Development of novel, rare earth doped lanthanum strontium cobalt ferrite ceramics, synthesized by ion-exchange promoted sol-gel processing

Meera Rhiannon Davidson

Submitted in accordance with the requirements for the degree of Doctor of Philosophy

University of Leeds

School of Chemical and Process Engineering

August 2025

Intellectual Property and Publication Statements

I confirm that the work submitted is my own and that appropriate credit has been given where reference has been made to the work of others. I was responsible for generating, intercepting and analysing the data, Figures, Tables and writing of this thesis. The contributions of the other authors for this thesis are detailed as below.

Dr Adrian Cunliffe – Collected the thermal analysis (TGA/DSC/DTG) data on the metal-alginate beads which forms as part of Chapter 4 and 6 during the COVID rules.

Dr Thomas Brown – Collected the XRD data using the Empyrean in the Braggs Centre, Leeds for both the crushed calcined nanopowders and crushed sintered pellets using Professor Brown's grant to obtain high resolution XRD diffraction patterns which forms as part of Chapters 4-7.

Mr Macauley Hough – Assisted me when performing the SEM in the Braggs Centre on both crushed nanopowders and sintered whole pellets using Professor Brown's grant to obtain high resolution images for Chapter 4-7.

Dr Tristan Lowe – As part of the Free Beamtime NXCT grant via the University of Manchester, the parameters were set and 3D data was collected using the Micro-CT on the crushed dried metal alginate and calcined nanopowder samples which forms as part of Chapter 4 and 6. Dr Jiaqi Xu – As part of the Henry Royce Institute grant via the University of Manchester, the sintered LPSCF33428 pellet was prepared using the Thermo Scientific Helios 5 Laser-Plasma Focused Ion Beam (FIB). Nano-CT was used to collect data upon the prepared sintered LPSCF33428. Dr Mozhdeh Mehrabi – Collected the porosity data using the Avizo software obtained from the CT on dried and calcined LPSCF33428, LNSCF33428 and NSCF6428 and the sintered LPSCF33428 pellet.

Mr **S**tuart Micklethwaite – Prepared and collected the data and the video using FIB-SEM sintered LSCF6428 and LPSCF33428 pellet as detailed in Chapter 8.

Dr Matthew Rodgers – As part of my collaboration with the School of Physics and Astronomy, SQUID-VSM was used to collect magnetic data on both the crushed calcined nanopowders and sintered pellets as detailed in Chapter 8.

Acknowledgements

I would like to thank my primary supervisor, Professor Andy Brown for his time, encouragement and support. The challenges of the PhD were made less difficult owing to his sensitive grasp of how my dyslexia affected me. He has, by patiently modifying and adapting his supervisory style to accommodate my dyslexia, trained me not just to be rigorous in my approach to my research but also to think and write critically, logically and precisely.

I would like to thank my co-supervisors; Professor Oscar Cespedes, School of Physics and Astronomy for his time and advice. He has always been available to answer any questions I might have. I have also really appreciated his hands on training on Raman in the Braggs Centre and for offering me the use of the SQUID-VSM. Professor Andrew Bell for his kindness. Despite a very heavy overseas lecture schedule, he managed to find time to advise me on my fabrication and train me in spectroscopy work. Dr Ali Hassanpour has always made time to advise me and check on my wellbeing. I would also like to thank him for introducing the XCT scheme to me and helping me with my initial grant proposal.

I would like to thank the technicians, Robert Simpson and Diane Cochrane for helping me with lab bookings and for training me on certain bits of equipment. I would also like to thank Ben Douglas for training me on the BET machine and offering me the use of the vacuum oven.

I would like to convey my thanks to all the people I mentioned in Intellectual Property and Publication Statements. I deeply appreciate the time and effort they put into helping me. I would also like to thank Dr Faye East for training me on the XRD machine and to access to the XRD software remotely for the first two years of my PhD.

I want to thank Dr Ali Hassanpour's research group for their weekly meeting which served as a great source of support and information. I would like to thank Professor Andrew Bell's research group for all their advice on lab procedures and machinery.

I would especially like to thank Dr Darren Dixon-Hardy, my Postgraduate Director of Studies for the first two years of my PhD, for his kindness, encouragement and support.

I would like to thank my mother, Vanitha, for always encouraging me to try new things and not let my disability stand in the way of anything I wanted to do. She has been a constant source of support and encouragement. I want to thank my father, Ian, for all his concern, advice on practical matters as well as for driving back and forth between Scotland and Leeds. My

sister, Sharada, has always been my inspiration. She has supported me, guided me and encouraged me always.

I would like to thank the EPSRC for my DTP studentship without which I would never have been able to complete my PHD. I am also very grateful to University of Manchester for my two grants to do XCT work. I would also like to think Professor Andrew Brown for helping me fund XRD and SEM work. Professor Oscar Cespedes also helped me fund my VSM work for which I am very grateful.

Abstract

Lanthanum strontium cobaltite ferrite, $La_{0.6}Sr_{0.4}Co_{0.2}Fe_{0.8}O_{3-\delta}$ or LSCF6428 is a mixed ionic and electronic conductivity (MIEC) cathode material suitable for use in solid oxide fuel cells (SOFCs) operating at intermediate temperatures (ITs) between 600 - 800 ºC. In this work, LSCF6428 and rare earth doped LSCF i.e. LPSCF33428, LNSCF33428 and NSCF6428 were synthesised using the sodium alginate mediated, sol gel method and the resulting structural, porous and performance properties of sintered ceramics investigated as cathode materials for IT-SOFCs. Dried, 3 wt% alginate + metal oxide sol-gel beads were calcined at 800 ºC for LSCF6428, LPSCF33428, LNSCF33428 and 775 ºC for NSCF6428. XRD analysis revealed nanopowders (of ~ 40 nm crystallite size) to be in the expected rhombohedral structure for LSCF and to have between 94-96% phase purity. SEM/EDX suggest Sr deficiency and Fe enrichment of the rhombohedral phase (apart from NSCF6428) due to the presence of second phase $SrCO_3$ and probably α-Fe_2O_3 (likely to be retained after calcination in air). SEM and XCT reveal that nanoparticle agglomeration results in significant microporosity. The size of the pores range from 30-50 nm, based on SEM and N_2 adsorption analysis, and are similar for both the undoped and rare earth doped LSCFs. The specific surface area for the calcined nanopowders meet target requirements of between 5-7 m^2/g for SOFCs.

The calcined nanopowders were sintered at 1000 ºC for 1 h to produce LSCF6428 and rare earth doped LSCF microstructures suitable for IT-SOFCs cathode materials i.e. of 70-90 % density. Microstructural analysis by nano-XCT and serial sectioning FIB-SEM reveal grain size and phase inhomogeneity not detected by XRD (the latter suggesting 70 nm crystallites in a single phase). A nanocrystalline, porous grain structure plus areas of dense, micrometre size grains and separate iron rich areas are all detected by FIB-SEM (the latter likely being the α-Fe_2O_3 predicted by thermal analysis of the calcined material and by magnetometry of the sintered ceramics). Overall, the sintered ceramics meet the target criteria of 25-40% porosity, with < 100 nm average crystallite size and < 100 nm average pore size by bulk measures.

Electrical symmetrical cell testing of LSCF doped with praseodymium in a half-cell format (LPSCF3342/YSZ) showed a decrease in total polarization resistance compared to an equivalent LSCF6428 half-cell, suggesting that oxygen adsorption, desorption and surface diffusion for oxygen reduction reactions at the interface of a cathode and electrolyte in a SOFC would all be improved. There is potential for further improvement if more homogeneous microstructures were to be produced. However, it is clear from this thesis that rare earth dopants such as Pr can enhance the performance of a LSCF based cathode in an IT-SOFCs.

Table of Contents

List of Tables

List of Figures

Abbreviations

(G)	Guluronic acid
(M)	Mannuronic acid
"a"	Unit Cell of the perovskite
1D	One Dimensional
2D	Two Dimensional
2θ	2 theta
3D	Three Dimensional
Å	Angstroms
AFM	Antiferromagnetic
ALG	Alginate
ASR	Area Specific Resistance
Ba	Barium
BET	Brunauer-Emmett-Teller
Bi_2O_3	Bismuth Oxide
BJH	Barrett-Joyner-Halenda
BSCF	Barium Strontium Cobaltite Ferrite ($Ba_{0.5}Sr_{0.5}Co_{0.8}Fe_{0.2}O_{3-\delta}$)
BSE	Backscattered Electrons
CO_2	Oxalate
C_2O_4	Ceria
cm^{-1}	Raman Shift
cm^3/g	Pore Volume
CO	Carbon monoxide
Co	Cobalt
CO_2	Carbon dioxide
CPE	Constant Phase Element
CT	Computed Tomography
Cu	Copper
CVD	Chemical Vapour Decomposition
DSC	Differential Scanning Calorimetry
DTG	Derivative thermogravimetry
e^-	Electron
EC	Ethyl Cellulose
EDX	Energy Dispersive X-ray Spectroscopy
E_{OCV}	Open Circuit Cell
eV	Activation Energy
FC	Field Cooled
Fe	Iron
FIBSEM	Focused Ion Beam-Scanning Electron Microscope
FM	Ferromagnetic
g/cm^3	Density
GDC	Gadolinium doped ceria
GOF	Goodness of Fit
h	Hour
H_2	Hydrogen gas
H_2O	Water

Hc^-	Negative Coercivity
H_c^+	Positive Coercivity
HS	High Spin
HT	High Temperature
ICDD	International Centre for Diffraction Data
IT	Intermediate Temperature
IUPAC	International Union of Pure and Applied Chemistry
K	Magnetic Anisotropy
kOe	Kilo oersted
kV	Kilovolt
La	Lanthanum
LaCrO3	Lanthanum Chromate
LaFeO3	Lanthanum Ferrite
LaMnO3	Lanthanum Manganite
LaNiO3	Lanthanum Nickelate
LAP	Leeds Alginate Process
LCO	$LaCoO_3$
LNSCF33428	Lanthanum Neodymium Strontium Cobaltite Ferrite ($La_{0.3}Nd_{0.3}Sr_{0.4}Co_{0.2}Fe_{0.8}O_{3-\delta}$)
LPSCF33428	Lanthanum Praseodymium Strontium Cobaltite Ferrite $La_{0.3}Pr_{0.3}Sr_{0.4}Co_{0.2}Fe_{0.8}O_{3-\delta}$)
LSC	Lanthanum Strontium Cobaltite
LSCF6428	Lanthanum Strontium Cobaltite Ferrite ($La_{0.6}Sr_{0.4}Co_{0.2}Fe_{0.8}O_{3-\delta}$)
LS	Low Spin
LSF	Lanthanum Strontium Ferrite
LSGM	Lanthanum Strontium Gallium Magnesium
LSM	Lanthanum Strontium Manganite
LZO	La_2Zr2O_7
MIEC	Mixed Ionic and Electronic Conductor
M_r	Magnetic Remnant
M_S	Maximum Magnetization Saturation
mW	Megawatts
N_2	Nitrogen Gas
Nd	Neodymium
NiO	Nickel Oxide
Ni-YSZ	Nickel-Yttria Stabilized Zirconia
nm	Nanometres
NO_3	Nitrate
NSCF6428	Neodymium Strontium Cobaltite Ferrite ($Nd_{0.6}Sr_{0.4}Co_{0.2}Fe_{0.8}O_{3-\delta}$)
°	Degree
O_2	Oxygen gas
O^{2-}	Oxygen Ion
°C	Temperature
Oe	Oersted
Oh	Orthorhombic
ORR	Oxygen Reduction Reaction
P	Adsorbate Equilibrium Pressure
PEM	Polymer Electrolyte Membrane

Pm3m	Cubic
Po	Saturation pressure
PPD	Power Peak Density
Pr	Praseodymium
Pt	Platinum
PVA	Polyvinyl Alcohol
PVD	Physical Vapour Decomposition
R	Gas constant
R1, R2, R3..	Resistance of ORR processes
R3c	Rhombohedral
Ro	Ohmic resistance
R_{exp} (%)	Expected Pattern
rpm	Rotations per minute
RT	Room Temperature
R_{wp} (%)	Weighted Pattern
s	Seconds
S cm^{-1}	Ionic/Electronic Conductivity
ScSZ	Scandia Stabilized Zirconia
SDC	Samarium doped ceria
SDCC	Samarium-Doped Ceria Carbonate
SE	Secondary Electrons
SEM	Scanning Electron Microscope
SOFC	Solid Oxide Fuel Cell
SQR	Squareness
SQUID	Superconducting Quantum Interference Device
Sr	Strontium
$SrCO_3$	Strontium Carbonate
SZO	$SrZrO_3$
Tc	Transition Temperature
TEC	Thermal Expansion Coefficient
TGA	Thermogravimetric Analysis
TPB	Triple Phase Boundary
um	Micrometres
V	Voltage
VSM	Vibrating Sample Magnetometer
Wt%	Weight Percentage
XCT	X Ray Computed Tomography
XMT	X Ray Mirco tomography
XRD	X Ray Diffraction
YSZ	Yttria Stabilized Zirconia
Z'	Real Axis
Z''	Imaginary Axis
ZFC	Zero Field Cooled
Z_W	Warburg element
Ω	Ohms
λ	Wavelength (nm)
ρ	Relative Density

Chapter 1 - Introduction

Fuel cell technology was first developed in the 19th century and could be a "green" and sustainable alternative to traditional technologies that use carbon-based fuels. Proton exchange membrane fuel cells (PEMFCs) and solid oxide fuel cells (SOFCs) are the two most studied fuel cell types due to their reliable operation, fuel flexibility and greater range of power density for uses in a variety of energy applications. SOFCs in particular, however, are considered as an emerging form of clean energy generation for the 21st century as they enable a direct conversion of fuel from chemical to electrical energy without the risk of electrolyte release. The direct conversion capability of SOFCs is due to a dense, solid ceramic oxide electrolyte component along with porous anode and cathode electrodes, which distinguishes it from the liquid-based electrolyte that is used in the PEMFCs. [1-3]

Traditionally, SOFCs have operated at higher temperatures, typically between 800ºC – 1000ºC, and incorporated cathode materials such as lanthanum strontium manganite (LSM) to enable sufficient oxygen reduction reaction (ORR) at the surface and within the bulk of the material. However, long term use at high temperatures has resulted in faster material degradation rates and high costs.[4] Therefore, it has led researchers to shift to investigating operation at lower temperatures between 600ºC – 800ºC, known as intermediate temperature (IT) SOFCs. The decrease in operating temperature for LSM though, has led to higher activation energy for the cathode component compared to the other two components, the anode and the electrolyte. [5-9]. As a result, it causes sluggish oxygen reduction reaction (ORR) kinetics leading to a sharp increase in polarisation losses as the LSM is only an electronic conductor, where the reactions occur at the triple phase boundary (TPB) regions, and this is detrimental to the overall fuel cell performance. Researchers have been focusing on the development of mixed ionic and electronic conductor (MIEC) cathode materials to enable ORRs to occur across the entire bulk surface of the cathode material at ITs.[10-11] Attention has been drawn to a popular MIEC cathode with a perovskite type oxide structure, lanthanum strontium cobalt ferrite (LSCF) with a chemical composition of $La_{0.6}Sr_{0.4}Co_{0.2}Fe_{0.8}O_3$ (LSCF6428). This cathode material enables excellent electrochemical catalytic activity along with electronic conductivity and ionic conductivity of around 10^2 S cm^{-1} and 10^{-2} S cm^{-1} respectively at an operating temperature of 800 ºC. It also has sufficient catalytic activity for ORRs at this IT. However, the LSCF ceramic material has been known for its Sr segregation at the surface of the electrode material, which can impact negatively on the performance efficiency of the SOFC at ITs. [12-14]

Therefore, the choice of synthesis method to produce LSCF6428 is critical to ensure control of particle phase, size, homogeneity and chemical composition during calcination and sintering as this can influence the final microstructure and the performance efficiency of the material as a cathode. There have been a wide range of methods that have been investigated for the synthesis of LSCF6428, such as solid state, co-precipitation and hydrothermal routes.[12-14] However, the drawbacks with all these methods are that despite obtaining a high yield of nanopowder, they lead to introduction of impurities and inhomogeneities of the phase and grain size of the microstructure. As a result, attention has been drawn to the sol-gel method of production which enables the use of lower processing temperatures and superior control in the uniformity of the calcined particle size and shape to produce high purity nanopowders.[14-17]

The aim of this work is to investigate the synthesis and characterisation the LSCF6428 and rare earth doped LSCF (using Ln = Pr and Nd) using the sodium alginate ion exchange sol gel-based synthesis method (called the Leeds Alginate Process). Then to determine whether the effect of doping LSCF with the rare earth elements through this process influences porous microstructures to yield superior electrochemical performance in comparison to LSCF6428.

1.1. Motivation

The Leeds Alginate Process (LAP) was developed by a research group at the University of Leeds over a decade ago. The LAP is an alginate mediated ion exchange sol gel-based synthesis method, aimed at yielding high purity single phase metal oxide nanopowder at a relatively low cost. The LAP has been successful in synthesising anode and electrolyte materials such as NiO and $Ho_2Zr_2O_7$.[18] The synthesised electrolyte material was then further investigated for performance. Synthesising of the cathode material, LSCF has been done using the LAP with three different compositions by Rahayu et.al. [15] However, the product was not further characterised for homogeneity of the chemical composition and its porous properties of the LSCF6428. As a result, there has been no sintering procedure been investigated for the LSCF6428 where it has been synthesised using the LAP method.[15]

Cheaper transition metal dopants have been widely established for LSCF6428 to enhance catalytic activity for ORRs.[14] Rare earth dopants have been heavily studied and are emerging as preferred in electrolyte materials because of their capability to provide superior ionic conductivity, establishing a bulk pathway for excellent electrochemical performance at lower operating temperatures.[19-20] Rare earth elements such as Ce and Dy have also recently been used as dopants for IT cathode materials such as LSCF6428 to enhance the ORR activities at

ITs.[21-22] Like transition metals, rare earth elements, especially the lighter rare earth elements across the range of Ce to Nd, are preferred because of greater abundance in nature and lower cost. [19-21]

Findings in this thesis show how the LAP method influences the phase purity, the homogeneity and the individual metal element distributions of both the undoped LSCF6428 and rare earth doped LSCFs. The rare earth dopants, Pr and Nd i.e. LPSCF33428, LNSCF33428 and NSCF6428 were investigated to reveal similar porous properties and varied grain structure but potentially improved electrochemical performance in comparison to the undoped LSCF6428.

1.2. Structure of Thesis

This thesis consists of a total of nine chapters which are outlined below:

Chapter 1 covers a brief introduction of the research topic, the motivation of the work and the structure of the thesis. Chapter 2 provides an in-depth literature review of the benefits and drawbacks of the SOFC and its associated components, the anode, electrolyte and cathode, and material selection for those components. The synthesis, sintering and fabrication methods for the cathode material of interest, LSCF6428 are reviewed. A main summary is then given of the general aims and objectives for this thesis.

Chapter 3 provides a description of the experimental methods and characterisation techniques undertaken for this thesis. It provides detail on the LAP synthesis method used for the production of LSCF6428 and rare earth doped LSCF using Pr and Nd. Details on the sintering, pellet pressing and polishing of the calcined nanopowders of LSCF6428, rare earth doped LSCF and YSZ are given. Microstructural and electrical properties are provided from density measurements and impedance spectroscopy. The different property measurements undertaken in this work are described in this chapter. The working principles and theoretical basis of the thermal analysis techniques (TGA/DSC/DTG), X-ray Diffraction and basic Rietveld, Raman Spectroscopy and Scanning electron microscopy are all explained. Details of porosity measurement by N2 adsoprtion and X-ray tomography (XCT) and magnetic property measurement by VSM are provided.

Chapter 4-8 consist of a detailed description of the findings that make up the Results and Discussion Section of the thesis.

Chapter 4 describes the synthesis and homogeneity of the LSCF6428 produced using the LAP. It includes details of the thermal analysis of LSCF6428 prior to calcination, and structural

properties of the LSCF6428 nanopowder across different calcined temperatures. It also describes the findings of the investigation of the microstructural properties of the LSCF6428 nanopowder calcined at the selected temperature and gives a comparison of the porous properties between the LSCF6428 metal complex and the LSCF6428 nanopowder.

Chapter 5 describes the findings of the investigation of the structural, microstructural (homogeneity of the chemical composition, grain size etc), and porous properties of the sintered LSCF6428 across different sintering temperatures.

Chapter 6 describes the synthesis and homogeneity of LPSCF33428, LNSCF33428 and NSCF6428 produced using the LAP. It includes details of the thermal analysis of LPSCF33428, LNSCF33428 and NSCF6428 prior to calcination, and structural properties of the LPSCF33428, LNSCF33428 and NSCF6428 nanopowders across different calcined temperatures. It also describes the findings of the investigation of the microstructural properties of the LPSCF33428, LNSCF33428 and NSCF6428 nanopowders and comparison of the porous properties between the LPSCF33428, LNSCF33428 and NSCF6428 metal complexes and of LPSCF33428, LNSCF33428 and NSCF6428 nanopowders.

Chapter 7 describes the structural properties and homogeneity of the chemical composition of the sintered LPSCF33428, LNSCF33428 and NSCF6428 across different sintering temperatures. It also describes the findings of the investigation of the microstructural and porous properties at the selected sintering temperature of the sintered LPSCF33428, LNSCF33428 and NSCF6428.

Chapter 8 describes findings using 3-D characterisation by FIB-SEM sectioning of sintered LSCF6428 and LPSCF33428 and nano-XCT of sintered LPSCF33428 to reveal a varied porosity and grain structure. It also describes the magnetic properties between the selected calcined and sintering temperatures of LSCF6428, LPSCF33428, LNSCF33428 and NSCF6428. The electrical properties are also described from testing using a symmetrical cell consisting of sintered cathodes; LSCF6428, LPSCF33428, LNSCF33428 and NSCF6428 printed upon a YSZ electrolyte pellet.

Chapter 9 provides a conclusion to this research work and also provides suggestions on future work directions

References are listed at the end of the thesis.

Chapter 2 – Literature Review

2.1 Brief History of the Development of Fuel Cells

The field of fuel cell research was pioneered as a greener and alternative renewable energy source by William R Grove in the late 1830s. [3][6][9][23] However, fuel cells were only fully commercialised in 1889 by researchers, Langer and Mond.[24] The fuel cell, in which fuel oxidation takes place, can be described as an electrochemical device, since it is not dependent on a heat engine but on direct conversion of chemical to electrical energy. That contrasts with other popular alternative renewable energy sources such as solar or wind which typically rely on Carnot efficiency. [25]

A typical fuel cell is traditionally made up of a dense electrolyte sandwiched between an anode and cathode (porous electrodes) as shown in Figure 2.1. That is where the anode and cathode are exposed to both reducing and oxidising environments respectively.[15] There are also interfaces, anode/electrolyte and electrolyte/cathode, which establish the development of the triple phase boundary (TPB) active sites for oxidation and reduction to occur. The whole design is always connected via an external circuit (DC) between the anode and cathode component where the electrons are the main transporting medium. A DC current can be generated through the loading of energy sources where hydrogen (H_2) is introduced at the anode side and air (O_2) at the cathode side. That in turn, enables the DC current to be developed from the chemical potential of the electrolyte, which is an ionic conductor, establishing a cyclic procedure through the fuel cell itself. [2][6][8] [26-28]

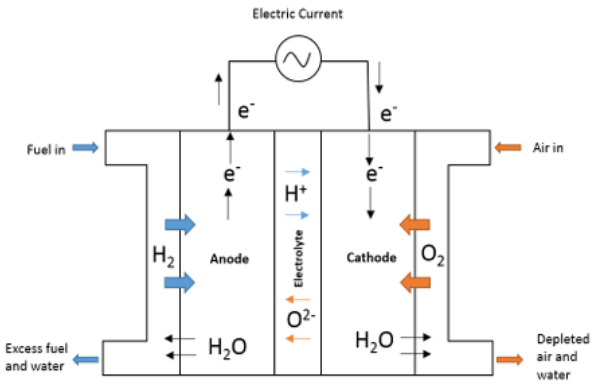

Figure 2.1: Schematic Design of a Solid Oxide Fuel Cell (SOFC) consisting of Anode (feed inward with chosen fuel), Electrolyte and Cathode (feed inward with air, typically oxygen) components [Taken from Afroze et.al.] [28]

Since their discovery, researchers have been experimenting with the continuous development and evolution of different types of fuel cells through material selection, synthesis and fabrication methods. Named differences between fuel cells is based on the type of electrolyte material that is used. [1][3][6][9] [23-24] [29-30] (see Table 2.1).

Table 2.1: Popular types of fuel cell using atmospheric O_2 as a cathode gas oxidant which have been researched. [3-5][23]

Type of Fuel Cells	**Electrolyte Phase**	**Anode Gas (Fuel)**	**Operating Temperature (°C)**	**Efficiency Range (%)**	**Power Density (kW)**	**Applications**
Alkaline	Liquid (Potassium Hydroxide)	Pure H_2	40 - 220	35 – 70	0.5 – 100	Mobile, space, military
Polymer Electrolyte Membrane	Liquid (Nafion)	Pure H_2	50 – 110	35 – 55	0.001 - 10^4	Portable, mobile and low power generation
Phosphoric Acid	Liquid (Phosphoric Acid)	H_2	175 – 210	37 – 45	100 - 10^7	Medium to large scale generation and CHP
Direct Methanol	Liquid (Methanol)	Liquid methanol	60 – 200	10 - 40	0.0001 -1	Mobile, portable
Molten Carbonate	Liquid (Lithium and Sodium Carbonate)	H_2, CH_4, methanol	550 – 650	50-70 (maximum if heat waste is used)	0.001 - 10^6	Large scale power generation
Solid Oxide	Solid (Ceramic or Perovskites)	H_2, CH_4, CO carbon hydrocarbons	400 – 1000	40-72	10-10^5	Vehicle auxiliary power units, medium to large scale power generation and CHP, off – grid power and micro-CHP

However, in recent years, Polymer Electrolyte Membranes (PEMs) and Solid Oxide Fuel Cells (SOFCs) have been the fuel cells researched the most, due to the significant power densities that these can achieve and the use of non-alkaline electrolyte materials which are not prone to liquid leakages in the SOFC case. The major issue though with PEMs is operation at temperatures above 150 °C can result in accelerated degradation and shorter lifetimes. [1]

Therefore, unlike the other classes of fuel cells referred to Table 2, the development of solid-state ceramic electrolytes means a SOFC can suppress gas leakage and corrosion. The solid state, along with the use of cheaper non-noble metals has led to higher device efficiency (typically over 70%) being recorded than was previously achieved with liquid-based electrolytes. That is because the ceramic electrolyte is able to operate effectively across a greater temperature range, typically between 800 - 1000 ^{o}C. This, therefore, allows for the use of fuel flexibility such as hydrocarbons which have been looked upon as alternatives that can be fed directly into SOFCs without the need for additional steps such as steam reforming for the production of a hydrogen stream. [1][3][8][23][31]

However, the constant use of higher operating temperatures (800-1000 ^{o}C) has been noted to be problematic in terms of the long-term sustainability of SOFCs, because issues such as phase transitions, sintering, interdiffusion, and poisoning all decrease durability. That has meant recent research has been aiming to reduce the operating temperature of SOFCs to a range typically between 400-750 ^{o}C i.e. intermediate temperature or IT-SOFCs. There are however major obstacles which can hinder progress when operating at lower temperatures: the increase of irreversible losses at the electrolyte/electrode interface; sluggish kinetics of the oxygen reduction reaction (ORR) at the cathode due to the large activation energy requirement; and increases in the thermal expansion coefficient (TEC) of the materials. [1][3][6-9][16][26][31-34]

Therefore, the single fuel cell which can be considered as a whole SOFC has been investigated to determine the main cause of irreversible losses at the electrolyte/electrode interface. The single fuel cell has an open voltage circuit (E_{OCV}) typically of above 1 V. To obtain the E_{OCV} for a single fuel cell, the E_{OCV} is calculated through the Nernst equation for SOFCs as shown in equation (2.1a) which considers the overall reaction for the whole SOFC when creating an E_{OCV}. However, it has been found that when the current load is connected to a single fuel cell, the E_{OCV} value has been estimated to decrease to around 0.5 – 0.7 V. That has led to the establishment of the actual cell voltage equation as shown in equation (2.1b), which considers all the different types of irreversible losses as mentioned earlier when the SOFC operates. [4][23][27][35]:

$$E_{OCV} = E_0 + ((RT_0)/nF)\, In \quad \frac{P(H_2)\sqrt{P(O_2)}}{(H2O)} \qquad (2.1a)$$

$$E = IR = E_{OCV} - \eta_{act} - \eta_{con} - \eta_{ohm} - \eta_{fcl} - \eta_{icl} \qquad (2.1b)$$

where E_o is the cell standard potential (electromotive force, emf V); R, the universal gas constant (8.314 J mol^{-1} K^{-1}); T_o, the cell reference temperature (K); n, the valence number of ions ($moles\ of\ electrons/mole$); F, Faraday's constant (C moles of electrons); and E = Actual cell voltage. Activation losses (η_{act}) occur where charges are built up at the electrolyte/electrodes interface from the activation energy barrier. Concentration (polarization) losses (η_{con}) happen with mass transfer loss in sustaining electrochemical reactions at the electrodes. Ohmic losses (η_{ohm}) typically occur at the electrolyte through a combination of ionic and electrical resistance contributions which are governed by the thickness and the ionic conductivity of the material itself. Losses associated with fuel crossover (η_{fcl}), the effect of fuel diffusion across the electrolyte, and also the internal current (η_{icl}), when the electrolyte suffers from leakage, have also has been mentioned as other irreversible losses, but only in a single recent review by Fallah et. al. [4] In the past though, η_{fcl} and η_{icl} were neglected and not included in the actual voltage equation (1b) in other review papers such as Jaiswal et.al., Nikonov et.al. and Zouhri et. al. [23] [36-37] That is also evident from Figure 2.2 which accounts for only the irreversible losses η_{act}, η_{con} and η_{ohm} , showing an inaccurate estimation of the actual cell voltage produced from the deduction of the E_{OCV}. [38]

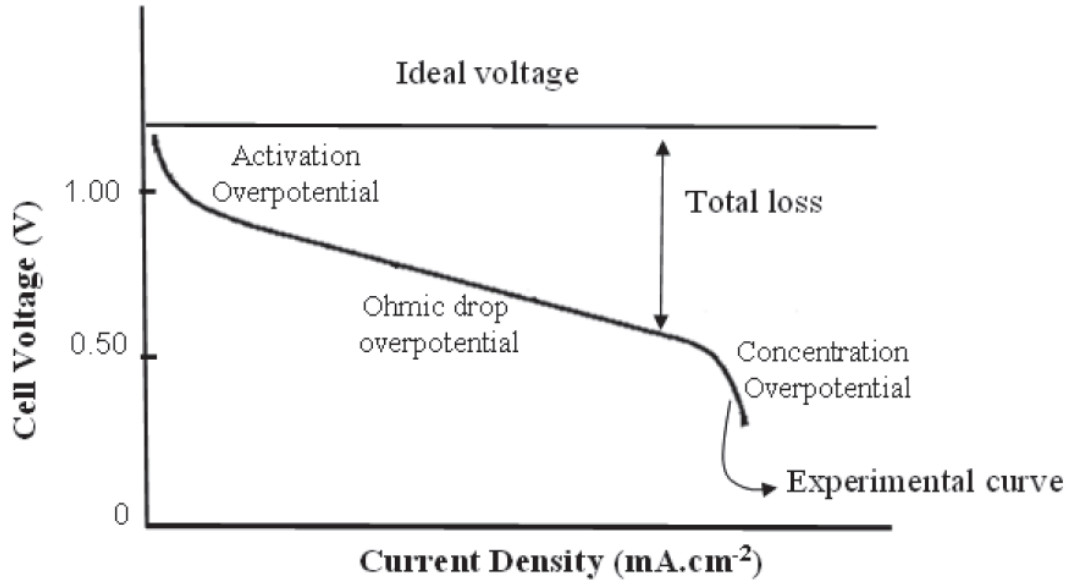

Figure 2.2: Schematic design of a voltage-current characteristics of SOFC in pure hydrogen as a fuel at 800 ºC neglecting η_{fcl} and η_{icl}.[Taken from Taroco et.al.] [38]

A typical single cell SOFCs has three main components: anode, electrolyte, and cathode where the irreversible voltage losses in equation (1b) occur. A SOFC is also made up of two minor components: interconnects and sealants, which do not have any contribution towards any losses

in reference to equation (1b). Although, the main function of interconnects and sealants is to enable the separation of gases to ensure proper maintenance of the whole SOFC. There are four typical configurations that have been manufactured: tubular, monolithic, planar, and integrated. However, from an industrial perspective, the SOFC single cell is commonly either in planar or tubular form as shown in Figures 2.3. The planar configuration (Figure 2.3a) is made up of a sandwiched rectangular form consisting of flat electrodes and an electrolyte, with the interconnects allowing for fuel and air to enter and flow to the anode and cathode respectively. While for tubular form (Figure 2.3b), the electrodes and the electrolyte are made into a long hollow tube where the fuel and air flow radially across the interior and exterior of the tube itself.[21]

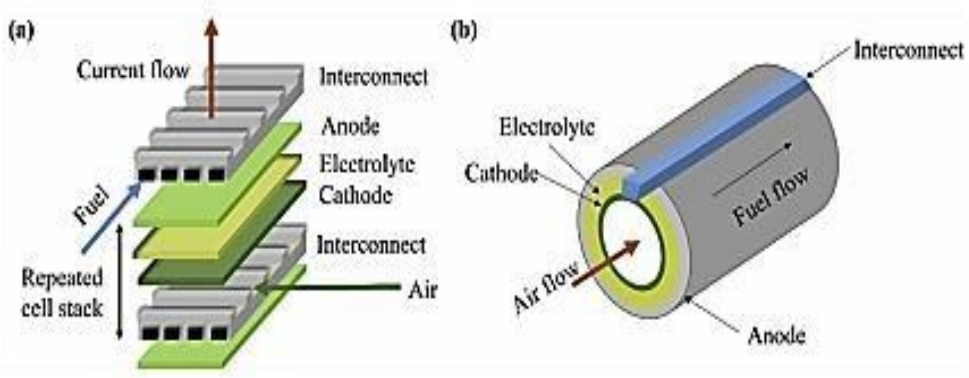

Figure 2.3: Schematic Designs showing a (a) planar SOFC (b) tubular SOFC [Taken from Ng et. al] [30]

Table 2.2 contrasts the various advantages and disadvantages between the tubular and the planar forms. The planar geometry has always been a popular choice of researchers due to its simpler design than the tubular form. Moreover, the planar form can offer a higher power density, is easier to fabricate and can be manufactured more cheaply than the tubular form. These are key factors when synthesising new materials for IT-SOFCs to obtain maximum electrochemical performance.[39]

Table 2.2: Comparison of different planar and tubular SOFC designs against working factors [30][39]

	Planar	**Tubular**
Electrical resistance	Lower	Higher
Power density	Higher	Lower
Manufacturing cost	Lower	Higher
Fabrication Ease	Easy	Difficult
High temperature sealing	Needed	Not really required
Start-up/cool down	Slower	Faster
Interconnect	Expensive	Difficult
Thermo-cycling stability	Fair	Good
Thermal stability	Lower	Higher

In addition, the planar cell configuration can be sub-categorised into either self-supporting or external supporting as described in Table 2.3. The self -supporting configuration is where one of the components consists of a thicker layer for the whole cell structure where its major function is to support the cell mechanically. While for the external supporting configuration, layers of equal thickness for the components are fabricated directly upon a support, consisting of either a porous or interconnect material. [39]

Therefore, in reference to Table 2.3, an electrolyte supported cell is unsuitable in research because of the significant thickness of the electrolyte which, from a review, is in the range of 80-250 μm, which for IT-SOFCs increases the irreversible losses and proportionally diminishes electrochemical performance. That has resulted in the electrode supported cells being typically selected for fabrication by researchers due to a thinner electrolyte layer of around 50 μm, so it can be operational at lower temperatures without affecting the electrochemical performance. The anode-supported cells tend to be researched more favourably than cathode supported cells due to the challenge of needing to use a fabrication method with a sintering temperature of above 1200 ºC to produce the cathode cell; which can intercalate the electrolyte material causing a poor electrochemical performance.[4] That makes it critical to select materials for each component to ensure that the SOFC fuel cell can operate as a whole at intermediate temperatures (ITs).

Table 2.3: Advantages and Disadvantages of Cell Configuration [4]

	Name of Cell Geometry	**Advantages**	**Disadvantages**
Self – Supporting	Anode	Lower operating temperatures via use of the thin electrolytes Highly conductive anode	Potential anode reoxidation Potential mass transportation limitation due to thick anode
Self – Supporting	Electrolyte	Strong backbone from the support of the dense electrolyte Uniform current density	High ionic resistance Higher operating temperatures to diminish ohmic losses due to thicker electrolyte
Self – Supporting	Cathode	Lower operating temperature via use of the thin electrolyte No cathode oxidation	Lower cathode conductivity Potential mass transportation limitation due to thick cathode
External Supporting	Interconnect	Thin components for lower operating temperatures Structure robustness especially from metallic interconnects	Interconnect oxidation when operating at higher temperatures Flowfield design limitation
External Supporting	Substrate	Thin components for lower operating temperatures Use of non-cell materials for support to improve properties	Discontinuous layers on porous structure Increase complexity

2.2 Anode Component and Material Selection

The anode, which can be termed as the "fuel electrode", is where the fuel is directly fed into the SOFC. The main reaction known as the hydrogen evolution reaction takes place at the anode/electrolyte interface.[34] The hydrogen gas is combined with the oxygen ions from the electrolyte resulting in a release of heat, electricity and water (as waste product) as shown in the corresponding equation reactions (2.2 – 2.3) [1]:

$$H_{2(gas)} \rightarrow 2H^+ + 2e^-(anode) \quad (2.2)$$

$$2H^+ + O^{2-}(electrolyte) \rightarrow H_2O(anode) \quad (2.3)$$

To ensure that reactions (2.2-2.3) can take place efficiently, it is essential that the key criteria for the anode are met: excellent electronic conductivity of greater than 100 S cm^{-1}, adequate ionic conductivity of about 10 S cm^{-1}, excellent chemical compatibility in a reducing environment with connecting components especially with the electrolyte and interconnect, good TEC matching with other components of the SOFC, excellent adhesion to the electrolyte component, large triple phase boundary (TPB) for catalytic and electrochemical activity, porosity of between 20-40% to provide fuel supply, capability to diminish poisonings such as coking, sulphur and chlorine species, ease of fabrication and low cost. [38]

Graphite and pure transition metals such as platinum (Pt), cobalt (Co), iron (Fe) and graphite were first considered for the anode component, however, there are several disadvantages: they are susceptible to corrosion; and they are expensive; which has resulted in them being ruled out for use as a single material-based anode. [29-30]

Therefore, nickel has been selected as the preferred candidate to act as a metallic nanoparticle material for HT-SOFCs because nickel possesses a high melting point of 1453 ºC and has one of the best electrochemical activities for the hydrogen oxidation reaction.[9] Nickel is also known to be cost effective given its approximate cost of €10.39/kg.[40] However, using nickel as an element alone has led to issues such as agglomeration, coarsening and self-sintering which can reduce the porosity.[9] That is purely down to the TEC value of nickel of 13.3 -16.9 $x10^{-6}$ K^{-1} in the range 20 – 1000 ºC compared to the electrolyte TEC ranging between 10.0 – 12.0 $x10^{-6}$ K^{-1} across the same temperatures. [31]

Therefore, nickel is used in a complex composite known as cermet, typically nickel-yttria stabilized zirconia (Ni-YSZ) that is made up of electronic and ionic conductors as shown in Figure 2.4. Thus, the anode has better electronic conductivity from the metallic material whilst the ceramic electrolyte material has better ionic conductivity (oxygen conducting or proton conducting). This is illustrated in Figure 2.4 which indicates the presence of the reaction sites at the TPB. The TPB is where the maximum electrochemical performance of the cell can be achieved through connection of ionic and electronic conductors and the gas phase (hydrogen) at one location.[30]

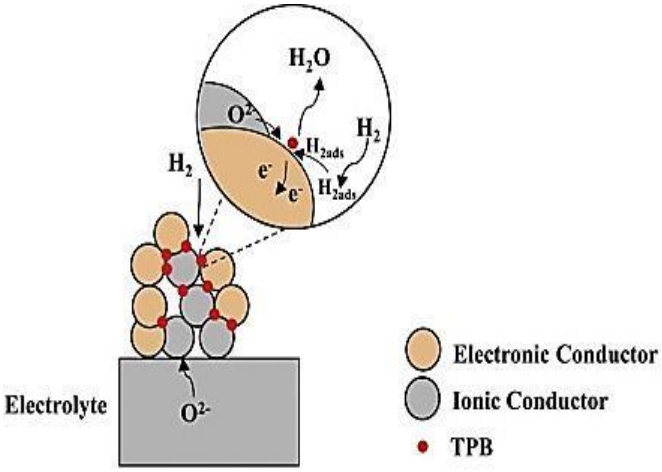

Figure 2.4: Schematic design of anode cermet (Taken from Ng et.al.) [30]

The cermet concept was first introduced by researcher Spacil, in which the nickel in the form of nickel oxide particles is dispersed onto an yttria stabilized zirconia skeleton (Ni-YSZ). [29-30] It had been agreed from several articles that 30 vol% nickel gives the ideal percolation threshold for ideal electronic conductivity. To ensure how Ni-YSZ can meet the requirement of providing sufficient power density, the 3-D structure has been analysed by X-ray Computed Tomography (XCT) over the last two decades. A study of a Ni-YSZ anode was carried out by Izzo et. al. using XCT volumetric data to reconstruct the actual 3D internal microstructure to provide a detailed examination of the pores and solid phases of the Ni-YSZ anode and used to calculate its structural parameters.[41] In another study, Hennan et.al. have extended this analysis through the use of nano-XCT to characterise the interconnectivity of the TPB regions of a Ni-YSZ anode at greater 3D resolution of ~ 100 nm; something which 2D microstructure characterisation cannot do easily.[42]

There have also been alternative options such as surface modification through the alloying of noble metals, sometimes termed as electrocatalysts, which have been of benefit in suppressing activation polarization. However, this is not a cost-effective approach given that platinum (Pt) and palladium (Pd) are expensive based on its approximate cost at €50000/kg and €22500/kg respectively.[30][40]

Therefore, copper (Cu^{2+}) has been highly used in recent years as another abundant and low-cost anode material with an approximate cost at €5.30/kg. Cu^{2+} has been classified as an electronic conductor and a protection element against side reactions from hydrocarbons. [31][40]-43] While, Cu-CeO_2 has stood out as a popular composite anode due to the high oxygen storage capacity provided by the ceria, enabling the incorporation of oxygen vacancies

and achieving an electronic conductivity of 5200 S cm^{-1}. By contrast the IT-SOFCs with nickel cermet anodes such as Ni-SDC and Ni-GDC achieve electronic conductivities of 570 S cm^{-1} and 1073 S cm^{-1} respectively. [43] The major disadvantages of copper over nickel is that it has a lower melting point temperature of 1083 ºC, meaning that it cannot be sintered at all at temperatures above 1200 ºC. Also, because of the copper abilities to suppress poisoning, it compromises its catalytic activity.[31]

Therefore, it is critical to ensure that the choice of anode, when sintered with the other components to form an anode supported cell, can achieve the appropriate electrochemical properties at lower operating temperatures.

2.3 Electrolyte Component and Material Selection

Electrolytes are a core component in any type of fuel cell, as first discovered by Nernst in 1899.[44] That is because it is responsible not only for the ion transportation between the electrodes, but also for determining the operating temperature of a cell, which in turn affects electrochemical performance. Therefore, the criteria that need to be met by a good electrolyte are as follows: [7][34]

1. The structure must be dense, gas tight and thin (<30 micro) with no porosity, to suppress interdiffusion of the electrode gases and current leakage.
2. Ionic conductivity must be greater than 10^{-2} S cm^{-1}, and there must be negligible electronic conduction to ensure an electronic transport number close to zero.
3. The TEC must be compatible with the electrodes from room temperature to operating temperature.
4. There must be no chemical interaction with the electrodes both during fabrication and under operating conditions, otherwise a blocking interface layers may form.
5. It must be structurally stable across a wide range of oxygen partial pressures from both anode and cathode environments.
6. The electrolyte must have excellent mechanical properties with a fracture resistance of greater than 400 MPa at room temperature.
7. The electrolyte must have a high peak power density (PPD) of 1 W cm^{-2} and an area specific resistance (ASR) of less than 0.3 Ω cm^2.
8. The cost of the material and its fabrication are also considered for its selection.

The oxygen (O^{2-}) ion conducting electrolytes type have been the most popular studied by researchers. The corresponding equation reaction (2.4) that needs to take place to ensure that the chemical potential of ions is established for the development of high ionic conductivity is: [45]

$$O_2\,(gas) + 2e^- \rightarrow O^{2-}\,(electrolyte) \quad (2.4)$$

The early versions of oxygen electrolytes were fluorite structured in the form AO_2 as shown in Figure 2.5 below.

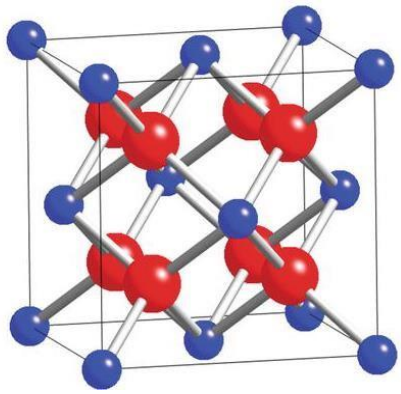

Figure 2.5: Schematic of the atomic packing of a Fluorite Structured Electrolyte with ceria cations (blue) and oxygen ions (red) [Taken from Omar] [46]

The tetravalent A^{4+} metal cations are located at the centre of the cubic faces of the fluorite structure, whilst the O^{2-} anions are tetrahedrally coordinated to the metal cations. That results in the creation of octahedral interstitial voids to enable a large, open structure, allowing for rapid diffusion of oxygen ions to occur whilst also enabling accommodation of dopants such as gadolinium or samarium which restricts the ceria from partial reduction to allow for sufficient ionic conductivity at ITs.[46]

O^{2-} conducting electrolytes which have evolved from HT-SOFCs to IT-SOFCS such as yttria stablished zirconia (YSZ), scandia stablished zirconia (ScSZ), samarium doped ceria (SDC), and gadolinium doped ceria (GDC) are classified as oxide ion fluorite deficient compounds. Bismuth oxide (Bi_2O_3) has also been popularly studied due to its superior ionic conductivity. The ionic radii mismatches for these electrolytes are shown in Table 2.4 which shows the differences between the host, cerium and the dopant cations, samarium and gadolinium for SDC and GDC. While the difference occurs between the host cation, zirconia and dopant cations, scandium and yttria for YSZ and ScSZ. The choice of host cation as mentioned earlier for Figure 2.5 provide a stabilised cubic fluorite structure while the dopants ensure electrical

neutral balance of the host cation, introduction of oxygen vacancies and lower migration activation energy to ensure sufficient ionic conductivity performance at ITs (typically below 800 ^{o}C).[45] These mismatches can also explain the stability at a given operating temperature and how it affects the activation energy requirements for ionic conduction.

Table 2.4: Ionic radii for cations [167]

Materials for Electrolyte	**Ionic radii(Å)**	**Coordination Number**
Zirconia (Zr^{4+})	0.84	8
Scandium (Sc^{3+})	0.87	8
Cerium (Ce^{4+})	0.97	8
Gadolinium (Gd^{3+})	1.053	8
Samarium (Sm^{3+})	1.079	8
Yttria (Y^{3+})	1.019	8
Magnesium (Mg^{2+})	0.89	8
Barium (Ba^{2+})	1.42	8
Lanthanum (La^{3+})	1.36	12
Strontium (Sr^{2+})	1.44	12

Table 2.5 summarises the advantages and disadvantages that each electrolyte material can give in relation to the ionic radii mismatch (Lanthanum, Strontium Gadolinium Magnesium Oxide in a perovskite structure is also included in the Table here).[19][36][46]

Table 2.5: Calculated ionic radii mismatch of the electrolytes and its Advantages and Disadvantages

Electrolyte Materials	**Ionic radii Mismatch(Å)**	**Advantages**	**Disadvantages**
YSZ [4][9][47]	1.019- 0.84 = 0.179	The doping of trivalent rare earth element such Y^{3+}: enables stabilisation of the cubic crystal structure of the ZrO_2 down to room temperature and also for the introduction of oxygen vacancies to enable superior ionic conductivity for HT-SOFCs ranging from 800 – 1000 ºC	Direct contact with other cathode materials like lanthanum strontium cobalt ferrite (LSCF) and lanthanum strontium cobaltite (LSC) leads to secondary phases being formed
ScSZ [4][7][9][23] [48-49]	0.87 – 0.84 = 0.03	The smaller mismatch compared with YSZ means ScSZ offers a much higher ionic conductivity of 0.3 S cm^{-1} at 800 ºC, typically higher than YSZ which is only 0.1 S cm^{-1}.	ScSZ has been neglected as an electrolyte material for IT-SOFCs because of its thermal aging at elevated temperatures and lack of abundance linked to high cost
GDC **SDC** [23][45-46] [50]	1.053 – 0.97 = 0.083 1.079 – 0.97 = 0.109	Trivalent rare earth cations enable the establishment of charge carriers to promote the polaron hopping mechanism, where charge transfer occurs between the dopant and the neighbouring extrinsic oxygen vacancies GDC has a smaller binding energy of only 0.17 eV compared to 0.64 eV and 0.38 eV for YSZ and ScSZ and can be operated at ITSOFCS between 500- 700 ºC	Pure ceria is exposed to low oxygen partial pressure or anode atmosphere, it results in structural distortion of the ceria structure due to the effect of the redox couple, Ce^{4+}/Ce^{3+}
Bi_2O_3 [6-7][23][48][51]	N/A	The disordered structure of the Bi_2O_3 and the high polarizability of Bi^{3+} has resulted in 10-100 times higher ionic conductivity than YSZ when at an operating temperature of 1000ºC	Reduced to metal; low melting point; poor thermodynamic stability under reducing conditions and at elevated temperatures above 804ºC; and high volatilization and toxicity from the Bi
LSGM [7][23][45][48]	A site -> 1.44 -1.36 = 0.08 B site ->1.053 – 0.89 = 0.163	Introduction of the dopants results in the creation of oxygen vacancies aimed for IT-SOFCs	influence the formation of secondary phases, especially with other perovskite cathode materials

It can be shown from Table 2.5 that rare earth dopants have traditionally been used to allow for superior ionic conductivity which is related to the ionic radii mismatch for the electrolyte materials. The explanation behind the difference in the operating temperature ranges of zirconia and ceria is due to their crystal structures under operating temperatures when in pure form. For pure zirconia, it undergoes phase transitions resulting in dramatic volume changes which affects its ionic conductivity, limiting the potential value of ZrO_2 as an electrolyte as shown in the phase transition equation (2.5). So rare earth elements have been selected to adjust the temperatures of the phase transitions.[47]

$$(> 1170\ ^{o}C) \qquad (> 2370\ ^{o}C) \quad (2680\ ^{o}C)$$

$$Monoclinic \leftrightarrow Tetragonal \leftrightarrow Cubic \leftrightarrow Liquid \tag{2.5}$$

While for pure ceria, it can maintain its cubic phase from room temperature to melting temperature (2400 ^{o}C). Unfortunately, pure ceria is also a poor oxygen ion conductor making it difficult for greater ionic conductivity to be generated at lower temperatures. That led to researchers investigating the effects of introducing trivalent rare earth cations such as gadolinium for the establishment of charge carriers to promote the polaron hopping mechanism, where charge transfer occurs between the dopant and the neighbouring extrinsic oxygen vacancies making it appealing for IT-SOFCs.[23][46] Bi_2O_3 has been neglected and not often studied as a potential electrolyte material due to its disadvantages, as shown in Table 2.6 compared to CGO and YSZ. [6][23] Whilst for the LSGM, it was one of the first perovskite materials to be developed. [7]

Table 2.6: Electrolytes and the TECs at different temperature ranges [34][36]

Oxygen conducting Electrolytes	**TEC ($x10^{-6}$ K^{-1}) at 800 ^{o}C**
YSZ	10
GDC	12.5
LSGM	10.4
ScSZ	10.3

Table 2.6 shows that TEC values for ceramic electrolytes are typically in the range 10 – 13 $x10^{-6}$ K^{-1} for an intermediate operating temperature of 800 ^{o}C (Bi_2O_3 is not included since it has not been highly researched experimentally). Therefore, the electrolyte TEC values are set as a

firm benchmark when selecting materials for the other components. TEC matching is important to ensure that chemical stability is achieved so that it matches with the other components of the SOFC. [36]

2.4. The Cathode Component and Material Selection

The cathode, which can also be termed as the "air electrode", is where the reduction of oxygen takes place, as shown in the following equation reaction (2.6).

$$O_2\,(gas) + 2e^{-}(cathode) \rightarrow O^{2-}\,(\text{electrolyte}) \qquad (2.6)$$

The rate of oxygen reduction is dependent on the operating temperature at which the fuel cell is running and upon the level of oxygen partial pressure. Therefore, high temperature and high oxygen partial pressure are fundamental to overcome the activation energy barrier where an equilibrium exists at the electrolyte/cathode in driving a variety of electrochemical and reaction kinetic mechanisms such as surface exchange and oxygen diffusion of the ORR.[1][50][52]

To ensure that reaction (2.6) can take place efficiently, it is essential that the following key criteria for the cathode are met [38][52]:

1. excellent electronic conductivity of > 100 S cm^{-1} and ionic conductivity of between 10^{-1}-10^{-4} S cm^{-1}
2. excellent chemical compatibility with connecting components especially with the electrolyte and interconnect
3. an oxidising environment
4. microstructure stability when fabricating and under the operating conditions of the fuel cell
5. good TEC matching with other components of the SOFC
6. sufficient catalytic activity for ORR
7. excellent adhesion to electrolyte component
8. large establishment of TPB for catalytic and electrochemical activity
9. porosity of between 20- 40% to provide air supply
10. ease of fabrication; and low cost.

A review by researchers, Yang et.al. has also set out the criteria for IT-SOFCs for achieving a power density of at least 1 W cm^{-2}, the electrolyte (ASRs) must have an ASR of below 0.15

Ω, while for the electrode the ASR must be below 0.30 Ω. [53] Therefore, there has been an ongoing evolution of cathode materials from conventional to novel to ensure that the resistance criteria are met along with excellent ORR activities.

Gustav Rose discovered the perovskite structure, $CaTiO_3$ back in 1839. However, the structure name "perovskite" was actually coined by a Russian mineralogical, L. A. Perovski[54]. The typical formula of the ideal perovskite oxide is ABO_3, as shown below in Figure 2.6.

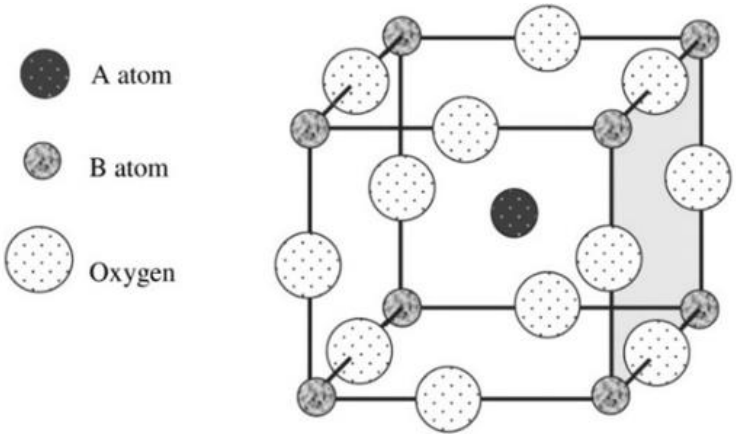

Figure 2.6: Schematic Diagram of ABO_3 ideal cubic perovskite structure [Taken from Jun et.al.] [55]

The A site cations, which are coordinated to 12 oxygen ions, consist of either rare earth or alkaline earth elements. While the B site cation which forms part of the BO_6 octahedra is coordinated to 6 oxygen ions consisting of transition metal elements as shown in Figure 2.6 [53] [55-56]. In turn, this structure has led to the synthesis and evolution of different perovskite structures aimed for efficient functioning of the cathode component of a SOFC. That is because materials with the perovskite structure often meet the required criteria, given above, for use as the cathode component of the SOFC.

2.4.1. Earlier Versions of Cathode Materials

Table 2.7: Properties of the earliest version of cathode materials based on, $LaMO_3$ where M is a transition metal [36][52]

Families [28]	Electronic Conductivity (S cm^{-1})	TEC (x10^{-6} K^{-1})	Tolerance factor (t)	Octahedral factor (μ)
$LaMnO_3$	115 (900 ºC)	11.2 (25 – 1000 ºC)	0.954 (HS) 0.985 (LS)	0.46 (HS) 0.41 (LS)
$LaCoO_3$	700 (750 ºC)	23.5 (100 – 700 ºC)	1.00	0.389
$LaCrO_3$	1 (1000 ºC)	9.5	0.996	0.4
$LaNiO_3$	-	-	0.996	0.4
$LaFeO_3$	-	-	0.954 (HS) 1.00(LS)	0.46 (HS) 0.393(LS)

Early attempts to create compounds with the perovskite structure used lanthanum located at the A site of the perovskite with different transition metals where M = Mn, Cr, Co, Ni or Fe located at the B site of the perovskite. The properties of these lanthanum-based perovskites are shown in Table 2.7. That is what led to rare earth perovskites ($LaMO_3$) being first introduced in 1926 by Goldschmidt as a cathode material through the use of lanthanum.[36][52] Goldschmidt was also the researcher who proposed the tolerance factor equation for perovskite oxides as shown in equation (2.7). The purpose behind the equation was to determine the structural stability and formability of the perovskite oxide when partial replacement of cations of the original perovskite composition had taken place. If the value of t = 1, the ideal cubic perovskite structure is likely obtained, however, if the value of t falls within the range between 0.9-1, the cubic perovskite structure is a reasonable possibility. In a study by Behara et.al., there are two possible reasons why the ideal perovskite structure is not obtained: either the mismatch of the relative size of the ionic radii of either the A/B site cations is too big; and/or the calcination temperature that is used to synthesise the perovskite structure is too low (mixed metal oxides).[57] For the ABO_3 perovskite structure, high symmetry cubic forms are achieved when a higher calcination temperature is used, typically > 1000 ºC. [57] When the calcination temperature is lower than 1000 ºC, the perovskite structure shifts away

from the ideal cubic structure in two ways: either by the B site off centring within the perovskite structure, resulting in high symmetry structure hexagonal/tetragonal phases; or the BO_6 octahedra tilt away from the centre leading to lower symmetry structures such as the rhombohedral or orthorhombic phases.[57-58] The high symmetry, tetragonal phase typically occurs when the structure consists of larger A site cation compared to the B site cation forming an order-disorder structure with ferroelectric properties. And for low symmetry phases, distortion upon octahedra tilting results in a phase transition to a rhombohedral or orthorhombic structure which is displacive for perovskites with smaller ionic mismatch.[57] Lanthanum was chosen since its ionic radius of 1.36 Å was closer to that of the ionic radius of the oxygen anion of 1.40 Å. As a result, this leads to a small ionic mismatch of only 0.04 Å between the La and a metal such as Sr which is critical to ensure effective electronic conduction and thermal stability.[19] However, the tolerance factor does not take account of the rotation or distortion of the BO_6 octahedra, so the octahedra factor equation is also proposed to account for this as shown in equation (2.8).

Lanthanum nickelate ($LaNiO_3$) data has rarely been reported as a pure cathode material (Table 2.7). That is because pure $LaNiO_3$ tends to decompose when operating temperatures are above 860 °C to $La_{n+1}Ni_nO_{3n+1}$ and NiO secondary phases.[59] Also, according to the calculated data of the tolerance (t) and octahedral factor (μ) in Table 2.7, and in reference to the equations (2.7) and (2.8) respectively, where r_A = radius of A site, r_B = radius of B site and r_O = radius of oxygen anion, even though the cubic phase is stable, the structure is prone to adopting a non-perovskite because of its octahedral factor being below the requirement of 0.41.

$$t = \frac{r_A + r0}{\sqrt{2}\, r_B + r0} \tag{2.7}$$

$$\mu = r_B / r_0 \tag{2.8}$$

While for lanthanum chromite ($LaCrO_3$), although it has one of the lowest TEC, it has suffered from poor electronic conductivity of only 1 S cm^{-1}.[44] Also, like the octahedral factor for $LaNiO_3$, it can adopt a non-perovskite structure so both will not be discussed any further this section.

While, the parent oxide lanthanum cobaltine ($LaCoO_3$) was reported to be the first perovskites oxide synthesised to be used as an electrocatalyst for oxygen reduction activity in 1970.[55] In turn, it has proven to be effective as a cathode material, possessing a high electronic

conductivity (typically over 1000 S cm^{-1}) compared to the other lanthanum based cathodes in Table 2.7 even at a lower operating temperature [7-9].

Table 2.8: Properties of LSF, LSM and LSC

Properties	**Lanthanum Strontium Ferrite (LSF)**	**Lanthanum Strontium Manganese (LSM)**	**Lanthanum Strontium Cobaltine (LSC)**
Electronic (800 ^oC)	>50 S cm^{-1} [3]	<200 S cm^{-1} [3]	1600 S cm^{-1} [3]
Electronic (700 ^oC)	90 S cm^{-1} [55]	180 S cm^{-1} [55]	1300 Scm^{-1} [55]
Ionic (800 ^oC)	0.005 S cm^{-1} [3]	<0.00000004 S cm^{-1} [3]	0.4 S cm^{-1} [3]
TEC(x10^{-6} K^{-1})	12.2 (30 -1000 ^oC) [55]	11.8 (30 – 1000 ^oC) [55]	19.1 (30 – 1000 ^oC) [55]

Moreover, a range of alkali metal dopants ("M") as shown in Table 2.8 have also been tried in the lanthanum-based perovskite, $LaMO_3$. From a study by Ji et.al. the substitution of the La^{3+} with a lower oxidation state cation such as either Sr, Ca or Ba leads to the generation of charge imbalance.[56] The charge imbalance could be either be compensated through alternation of the oxidation state of the transition metal located at the B site, or by generating oxygen vacancies in the perovskite lattice. Sr^{2+} was found to be the ideal choice from the alkali metal dopants because of a smaller ion size mismatch of only 0.08 Å between the La^{3+} and Sr^{2+} radii in comparison to the other alkali-based metals, with larger mismatches of 0.17 Å for Ba^{2+} and 0.1 Å for Ca^{2+}. [56]

LSM is currently considered to be the "state of the art" cathode material for maximising HT-SOFC benefits [36] because of its ideally small thermal mismatch and chemical stability with a TEC of 11.8 x10^{-6} K^{-1}.[3] The TEC of LSM is the lowest of any $LaMO_3$ cathode material in the temperature range 30-1000 ^oC. However, when operated below 800 ^oC, LSM does not have sufficient electronic conductivity given its value of only 180 S cm^{-1} at 700 ^oC, compared with the value for LSC of 1300 S cm^{-1}.[36] The lower electronic conductivity is thought to be caused by the diffusion of diatomic oxygen being severely limited at the TPB intersection points. That has resulted in the ORR being restricted, where LSM can provide only free surface energy for the ORR at the electrode/electrolyte TPB interface, and not within the cathode itself as a bulk pathway, limiting its electrochemical performance as shown in Figures 2.7(a) and (b). [60]

a.)

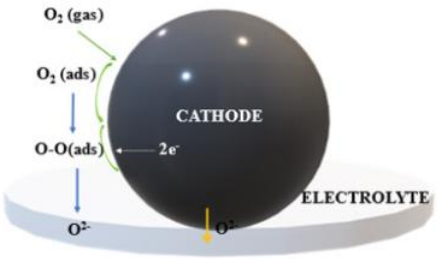

b.)

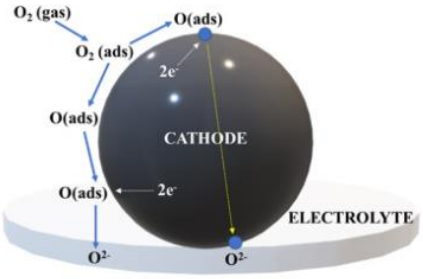

Figures 2.7: Schematic showing mixed ionic and electronic conductivity (MIEC) pathways in a SOFC cathode material (a) surface pathway of the cathode (b) bulk pathway of the cathode [Taken from Tahir et.al.][60]

While for Lanthanum Strontium Ferrite ($LaSrFeO_3$), although iron has a better thermal stability compared with cobalt in LSC, it suffers from both poor electronic and ionic conductivity. It can also be seen from Table 2.8 that the element cobalt fulfils a major role in providing high electronic conductivity through its redox properties to obtain a superior power efficiency. However, LSC has a relatively high TEC of 19.1 $x10^{-6}$ K^{-1} in reference to Table 2.8, which does not match the TEC values of the electrolyte materials in Table 2.6. Cobalt as an element is also relatively expensive. [3][55]

Therefore, the synthesis of an LSM-YSZ composite cathode was investigated as a method of adding a second phase, to increase the effectiveness of both the bulk and surface pathways, to reduce the losses from the ORR occurring at the interface, and to maximise the electrochemical performance of the SOFC. The disadvantage of this composite approach, when operating at elevated temperatures, is that the content of La^{3+} and Sr^{2+} interdiffusion occurs. That causes the formation of $La_2Zr_2O_7$ and $SrZrO_3$ from interaction with YSZ and due to the poor ionic conductivity of LSM it results in fewer oxygen vacancies within the remaining LSM. [61] That has led to researchers investigating superior mixed electronic and ionic based (MIEC) cathodes such as lanthanum strontium cobalt ferrite (LSCF) and barium strontium cobalt ferrite (BSCF) which provide superior properties for IT-SOFCs.[55]

2.4.2. Later Versions of Cathode Materials with the use of Rare Earth Element Doping

LSCF and BSCF belong to a family of perovskites which in recent years have been studied by many researchers as the major MIEC cathodes for IT-SOFCS. Both LSCF and BSCF cathodes have been investigated by numerous researchers to determine the optimal composition which

enable chemical stability, desirable performance such as ionic and electronic conductivity, and no phase transitions for IT-SOFCs. [62-63]

A study by Tai et.al. on the structure of $La_{0.8}Sr_{0.2}Co_{1-x}Fe_xO_3$ found that a higher content of Co of $x = 0.6$ possesses higher TEC when paired with lower TEC electrolytes which has led to chemical instability.[64] While the Sr content is more complicated due to the limitations that occur from either phase transitions or the solubility limit for the LSCF composition. A follow-up study by Tai el al. suggests that when the Sr content is less than 0.2 the rhombohedral phase stability is limited and there is a phase transition towards the orthorhombic symmetry. Therefore, when the Sr content is greater than 0.3, the rhombohedral phase is considered to be stable. However, the solubility limit of Sr in LSCF is 0.4.[65] From both studies, it has been found that varying content of cobalt and strontium in both the BSCF and LSCF heavily influences the chemical stability, phase transition and electrochemical properties.[64-65] Therefore, $La_{0.6}Sr_{0.4}Co_{0.2}Fe_{0.8}O_{3-\delta}$ perovskite oxide will be the focus for this work to ensure the chemical and phase stability of such a cathode material for IT-SOFCs.

Although the chosen optimal compositions of LSCF and BSCF have been frequently investigated for a range of properties, both compositions individually have disadvantages in relation to long term stability under performance conditions. Overall, it could affect the electrochemical performance, the ORR kinetics and surface diffusion if left unaddressed.

Table 2.9: Comparison of LSCF and BSCF perovskite oxide characteristics [53][55][62][66-69]

LSCF	**BSCF**
Operating at 800 ºC	Operating at 600 ºC
Temperature dependent	Non-Temperature dependent
Sr segregation influenced by the effect of sintering leading to long term instability when under operating conditions	Transition from cubic to hexagonal phase transition due to significance ionic difference between the Ba^{2+} and Sr^{2+}
Lead to the presence of secondary phases Co/Fe phases	Formation of carbonates from Ba and Sr rich phases when CO_2 presence in air

Therefore, when comparing the LSCF and BSCF as shown in Table 2.9, $Ba_{0.5}Sr_{0.5}Co_{0.8}Fe_{0.2}O_{3-\delta}$ has been shown to be a promising cathode for IT-SOFCs by Yang et.al. [53] BSCF was found to achieve a low ASR in the range 0.055−0.071 Ω and a PPD of 1010 W cm^{-2}, when paired with a SDC electrolyte and operated at 600ºC. [53][66] Unfortunately, in a study by Jun et. al., the MIEC BSCF cathode exhibits the largest TEC value of 24 x 10^{-6} K^{-1} in contrast to LSCF.[55] It is caused by the significant transition from the cubic to inactive hexagonal phase, due to the ionic mismatch of 0.16 Å between Ba^{2+} and Sr^{2+} ion radii at the A sites of BSCF (compared to 0.08 Å between La and Sr in LSCF). The ionic mismatch between the Ba^{2+} and Sr^{2+} has led to the BSCF being susceptible to CO_2 adsorption in air. At 1% concentration of CO_2 it can react with the Ba and Sr rich phases from the BSCF perovskite oxide composition to form carbonates when operating at temperatures below 900 ºC.[67] The formation of the carbonates has been known to negatively influence the ORR kinetics and surface diffusion when BSCF performance is measured. In turn, carbonate affects the electrochemical performance through the increase of ASRs and activation energies at IT-SOFCs.[55]

$La_{0.6}Sr_{0.4}Co_{0.2}Fe_{0.8}O_{3-\delta}$ has also been a popular mixed electronic and ionic conductor operating at 800 ºC. However, the major challenge for using LSCF has been long-term instability when operated for long hours because of the degradation mechanisms of interdiffusion and Sr^{2+} segregation on either the surface or the interface of the cathode as shown in Table 2.9. [62][68] The interdiffusion is caused when LSCF is paired with a yttria established zirconia electrolyte resulting in insulating phases such as $La_2Zr_2O_7$ (LZO) or $SrZrO_3$ (SZO) forming when sintered at 1100 ºC.[68] One of the potential causes of Sr segregation is due to the ionic radii mismatch and charge difference between Sr and La cations located at the A site of the LSCF [69]. Segregation influences the secondary phases, in particular the Co/Fe phase within the LSCF perovskite composition, which hinders the ORR leading to lower conductivity of the IT-SOFCs, adversely affecting performance. [68]

Therefore, to address the sluggish kinetics of the ORR, there has been a wide range of studies investigating the doping at either the A site or the B site of the perovskite oxides, BSCF and LSCF. Noble metals such as Pd and Pt (even though possessing excellent catalytic activity, as stated earlier in the anode section), are considered. As a result, there has been a shift in investigating dopants that are not only efficient for ORR but are also cheaper and in abundant supply. The transition elements such as Cu and Ni have been chosen in the past as main dopants due to their low cost and sufficient catalytic activity to permit electrochemical performance. However, there has been a recent trend in investigating rare earth elements other than cheaper

transition metal elements for doping the A/ B site of LSCF 6428.[21][70] This is due to the rare earth elements sufficient abundance especially for the lighter rare earth elements; La, Ce, Pr and Nd as shown in Figure 2.8. [70]

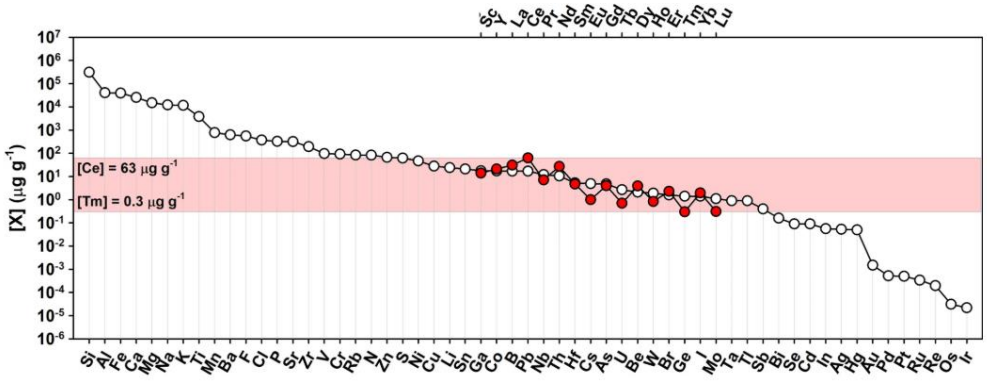

Figure 2.8: Concentrations in log scale of 73 elements in the upper continental crust lanthanides, Sc and Y are among those shown with the red circles. Red area shows a range of concentrations of a range of the rare earth elements defined by the least and most abundance [Taken from Dang et.al.] [70]

Rare earth elements have been in demand for use in magnets and catalytic applications with configurations of either $[Xe]4f^{n}\ 5d^{1}\ 6s^{2}$ or $[Xe]4f^{(n+1)}\ 5d^{0}\ 6s^{2}$. The 6s shell is responsible for the chemical bonding and therefore allowing for chemical similarity, greater polarizability for facilitating ionic conductivity, and stability of its oxidation state, $^{3+}$. [19][71-72] Moreover, electronegativity remains consistent at between 1.1-1.2 throughout the whole rare earth series. The electronegativity can provide the cathode protection against atmospheric gases such CO_2, CO and nitrogen oxide. [19]

However, their physical properties are different across the series due to the increasing number of unpaired electrons filling up the 4f energy shell. [19] The 4f energy shell of gadolinium provides only a weak shielding effect when surrounding the nucleus core, in comparison to its filled external shells, 5s and 5p as shown in Figure 2.9. [73] As a result of the weak shielding, an effect known as lanthanide contraction occurs, which leads to a continuous decrease in the rare earth cation ion radius as its atomic number increases. This in turn promotes the magnetic properties from which the energy is localised spatially from the electron's spin.[19] Lanthanum is classed to be diamagnetic, due to an electron absence in the 4f shell of its electronic configurations, compared to the other elements mid-series, which are paramagnetic due to the presence of unpaired electrons. [19][71][73]

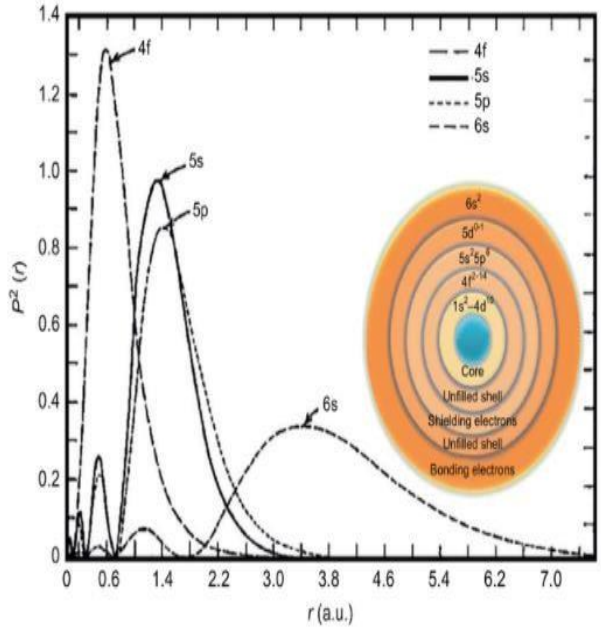

Figure 2.9: The distance from the nucleus against the electron probability of gadolinium [Taken from Rivera et.al.] [73]

A study by Liu et. al. on $Ba_{0.5}Sr_{0.5}Co_{0.7}Fe_{0.28}Ln_{0.02}O_{3-\delta}$ (BSCF) investigated the effect of rare earth doping using Ln = La^{3+}, Ce^{3+} and Praseodymium (Pr^{3+}).[74] Pr^{3+} was the rare earth doping that enabled superior ORR catalytic activity, structural stability and electrochemical properties at the B site of the BSCF perovskite at intermediate operating temperatures. Pr doping gave the best polarization resistance of 0.026 Ω cm^{-2} at 700 °C and power density of 1083 W cm^{-2}.[69] While in a study by Zhou et.al the Ce has been used for A site doping of $La_{0.6}Sr_{0.4}Co_{0.2}Fe_{0.8}O_3$.[21] Doping with Ce^{3+} is seen as also being a cheaper alternative than using noble metals such as Pt with a content limit of x = 0.6 providing suitable oxygen vacancies. [21]

The rare-earth element Ce is commonly aimed for IT-SOFC electrolytes because of its high abundance and its effective ionic conductivity for superior ORR catalytic activities when substituted for the lower valent cation, La^{3+}. However, there has been no extended studies as of yet on partial replacement of the La^{3+} with the other lighter rare earth elements from the series on the LSCF chemical composition $La_{0.6}Sr_{0.4}Co_{0.2}Fe_{0.8}O_3$ i.e. using Pr^{3+} or Nd^{3+} .[21] There has been a study by Mohammadi et.al. , using a heavier rare earth element, Dy for doping the $La_{0.6}Sr_{0.4}Co_{0.2}Fe_{0.8}O_3$ for partial replacement of the La^{3+} cation.[22] However, due to the significant ionic radii mismatch between Sr and Dy, using a concentration content of 0.3 mol and 0.6 mol led to the formation of the secondary phase, $SrCO_3$ despite being able to obtain a

smaller particle size to that of the LSCF at the same calcination temperature of 700 ºC. The Dy is also not in high abundance compared to the lighter rare earth elements as shown in Table 2.8. [22]

While for Nd, in a study by Heydari ey.al., by investigating $Ln_{0.6}Sr_{0.4}Co_{0.2}M_{0.8}O_{3-\delta}$ where Ln = La, Nd and Sm and M = Mn, Fe and Ni, the phase obtained for NSCF6428 was orthorhombic due to the tilting of the octahedra leading to a decrease in lattice parameters when synthesising using solid state methods.[75] However, there has been little work in the comparison of how the lighter rare earth doping using a sol-gel synthesis method, such as sodium alginate precursors, influences the LSCF structure and its associated ORR processes for IT-SOFCs performance. Although, Nd has been found to be a popular lighter rare earth element for doping for MIEC cathode as it is classified to have significant electronic conductivity in a study for Nd doped BSCF.[76] It has also been investigated in a study by Samreen et.al. where the CGO electrolyte is co doped with Nd and mixed with a LSCF cathode to form a composite cathode, NCGO-LSCF. 5% co doped Nd for GCO in LSCF was recognised as the potential composite cathode for IT-SOFCs which enabled the improvement of the oxygen diffusion and charge transfer rate of the ORR.[77] A study on LSCF by Ghogomu et al. altered the content of Co which had a significant influence on the magnetization due to the relationship between three different spin states of the cobalt that co-exist at different temperatures within the LSCF system.[78] The rare earth elements alter structural properties and typically influence the magnetic properties due to the effects of tilting of the octahedra in the original perovskite structure, especially Nd , as reported by Das et.al.[79]

Overall, rare earth materials stand out for improvements of not only ionic conductivity for oxide ion electrolyte materials but potentially for a wider range of properties such as structural stability under environmental conditions, magnetic properties and ORR activities which could benefit IT SOFCs operating at lower operating temperatures. Therefore, for this work, Pr and Nd will be used as dopants in place of La in $La_{0.6}Sr_{0.4}Co_{0.2}Fe_{0.8}O_3$ cathode materials.

2.5. Synthesis methods for LSCF perovskite cathodes

The selection of a synthesis method is the most essential step for the manufacturing of any individual components of a whole SOFC structure.

The synthesis methods for LSCF6428 that have been commonly used for SOFCs components are classified as: top-down approach such as solid state sintering of mixed oxide powders produced by ball milling; and bottom-up using nanoparticle synthesis methods such as co-precipitation, hydrothermal and sol gel, as shown in Table 2.10.[80]

The top-down approach is where the bulk material is broken systemically into the formation of finer nanoparticles. Out of the top-down approaches, the solid-state technique achieves the highest yield of product, is low cost and is a simpler method as shown in Table 2.10.[81-82] The solid-state method had been investigated thoroughly for synthesising LSCF in numerous studies. However, milling can introduce secondary phases into the final product, resulting in the need for higher calcination temperatures to meet the required phase purity standard of > 90%. Another disadvantage is the inhomogeneity of the particle sizes of the mixed or milled powders. [82-84]

As an alternative, the use of wet chemical methods has been tried to produce an almost pure phase with uniform distribution of particle size and shape of microstructure thus providing a high surface area synthesis of a cathode material. This can be carried out without grinding, which impacts the inhomogeneity of the final cathode material. [84]

The bottom-up approach is a self-assembly process in which chemical and physical forces are utilised at the nanoscale from starting materials that are dispersed at the atomic or molecular scale i.e. synthesis and formation of target nanomaterials from interconnected clusters of atoms. The bottom-up approach results in the assembly of the atoms/molecules into a complex nanostructure, as shown in the Figure 2.10. The bottom-up approach can enable production of compositionally homogenous nanoparticles of controlled size. [80][85]

A study by Mostafavi et.al, used co-precipitation for the synthesis of LSCF6428 due to its ability to produce ultrafine nanopowders.[84] However, co-precipitation is dependent on the pH of the precursor and rigorous washing to obtain high purity final products and this can make the methodology quite complex.[84] A study by Garcia et.al., identified undesired secondary phases such as La_2O_3 and $SrCO_3$ which have been induced into the perovskite lattice and require a higher temperature calcination for removal, running the risk of enhanced grain growth

in the process. Hydrothermal synthesis is another bottom-up technique that has been used for the production of high purity cathode materials.[86] Hydrothermal synthesis is described as a self-cleansing process, where during the synthesis of the material particle growth takes place that assists the removal of impurities in the pure crystalline form. However, there can be a need for further annealing to ensure purity of the material. Therefore, a combination method of citrate based-hydrothermal synthesis has been investigated as an alternative for synthesising functional cathode materials for IT-SOFCs.[86] Citrate is classified as a small molecule consisting of three carboxylic acids, which has typically been used for sol gel processing to enable binding of metal cations. [87]

There has been a transition by researchers towards using the sol gel process as a synthesis method to synthesize LSCF6428 nanopowders. This has involved the use of citrate as a precursor material in several studies for LSCF6428.[83][86] Use of citrate has led to difficulty in controlling the stability and homogeneity of the metal-citrate complexes and so additional agents such as bases are required to modify pH of the citrate containing dispersion to ensure efficient binding of the metal cations.[87]

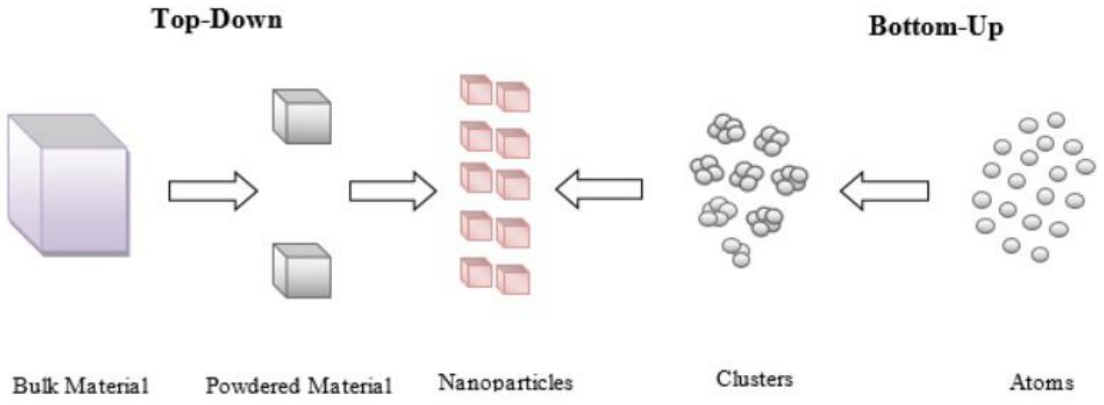

Figure 2.10: Schematic Diagram of the Top-Down and Bottom-Up approaches to synthesis of homogenous nanostructures [Taken from Pandey et.al.] [80]

Table 2.10: Comparison of different synthesis methods [80-86]

Popular Methods for LSCF6428	**Solid State**	**Sol - Gel**	**Hydrothermal**	**Co-precipitation**
Cost	Low/Medium	High	Medium	Medium
Purity %	< 99.5	>99.9	>99.5	>99.5
Composition control	Poor	Excellent	Excellent	Good, High
Morphology control	Poor	Moderate	Good, High	Moderate
Particle Size (nm)	>=1000	>=10	>=10	>=10
Calcination	Yes	Yes	No	Yes
Milling	Yes	Yes	No	Yes
Scalability	Yes, due to the simple method of obtain high yield product but there is risk of introducing impurities.	Yes, due to the use of low temperature processing. However, there is risk of batch consistency in relation to the uniformity of nanopowders.	Yes, due to use of single step to enable reproducible production of high quality nanopowders. However, there is a need of further annealing to ensure purity.	Yes, due to the use of mild conditions to control parameters such as pH. Although, its complex method makes it difficult to achieve a perfect batch consistency.

The sol gel method was originally carried out by Ebelman in 1846 and involved metal alkoxides for the synthesis of silica used for basic applications, especially biological.[88] Since

then, the sol gel method has been widely extended to synthesis of advanced materials such as metal oxides for the synthesis of nanoparticles with superior properties for the production of ceramics and glass. The sol gel procedure consists of simple steps which can be classified as a "one pot" approach. [54][85][87] The procedure for using a typical sol gel process is outlined in the flow diagram shown in Figure 2.11. The liquid, when mixed with the precursor materials, forms as a colloidal solution which promotes the suspension of solid particles in a liquid through a process known as hydrolysis. The interconnects that form between the solid particles and liquid results in a gel. This gelation is an ion exchange procedure between the colloidal nanoparticles that form in the solution, resulting in a three-dimensional network which can be described as an "egg box" model. [54][80][85][87][89] The water and organic matrix can be thermally detached from the gel network (calcined), causing disruption to the stuctures and producing homogenous metal oxide nanoparticles. Sol gel processing allows for the randomness of the solution state to be trapped at an atomic level promoting homogeneity and stability in the formation of metal oxide nanoparticles on gelation and calcination. [87]

There have been significant differences in synthesis methods that have been used in powder preparation for LSCF6428 perovskite oxides which has resulted in differences in relation to the crystal phases formed, typically cubic and rhombohedral. A key possibility to consider is the choice of calcination temperature. That led to a study that was carried out by Utomo et al. where three different synthesis methods were chosen, i.e. sol gel, solid-state and co-precipitation routes, to investigate how each method influences particle size, shape, purity, and morphology of the final LSCF composition. In relation to the sol gel process compared to the solid state and co precipitation processes, the formation of the LSCF perovskite oxide occurs at a lower temperature of below 650 ºC and with enhanced uniformity of a small, nanoparticle size (< 100 nm). That indicates that the choice of synthesis methods results in LSCF with different characteristics of grain size, porosity and phase purity being synthesised, despite having the same nominal elemental composition.[83] The use of different calcination temperatures can also influence different phase formation such as cubic or rhombohedral for the LSCF6428.

However, the degree of drying of the gel is the most critical step of the sol gel procedure, which is dependent on the degree of formation of a porous structure within the gel. The choice of drying method used can influence parameters such as pore volume, and the shape and size of the established metal oxide precursor nanoparticle prior to calcination. It can also influence the level of densification of the established ceramics. The drying of a sol gel, as represented by

equation (2.9) below, forces a linear shrinkage of the solid porous structure from the liquid where variables are the capillary pressure (Pc), surface tension (y/v), pore volume (Vp), surface area (Sp) and thickness of a surface adsorbed layer (-y/v). There are three different popular drying methods which have been investigated, each of which form a unique gel network structure as shown in Table 2.11. The thermal drying or xerogel network structure has been selected for the formation of SOFC components in previous work by Sunnela et. al. and Wang et.al. [90-91]

$$Pc = -\frac{-\gamma/v}{(2\left(\frac{Vp}{Sp}\right)-\theta)} \tag{2.9}$$

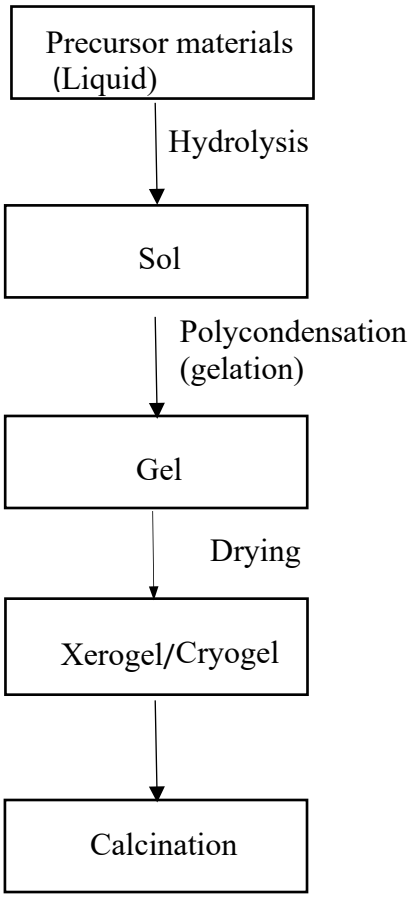

Figure 2.11: Schematic diagram of a Sol gel flow chart [90-91]

A comparison between the freeze-drying, ambient pressure drying and supercritical drying methods is shown in Table 2.11. The difference in drying methods for the sol gel will determine the formation of the structure within the gel network and in particular the levels and size of pores.

Table 2.11: Comparison of the Ambient Pressure, Freeze and Supercritical Drying [87] [90 - 91]

Ambient Pressure (Thermal) Drying	**Freeze Drying**	**Supercritical Drying**
Removal of liquid with replacement of air	Maintains the gel structure through freezing that is then dried through sublimation	Original gel network remains intact
Collapse/Shrinking of the gel network so could result in low pore volume, large surface area and easy densification of the final ceramic through heating.	Maintains the pore volume of the gel and decreases the surface area. Shrinkage is lower compared to Xerogel	Results in a higher pore volume and surface area
Xerogel	Cryogel	Aerogel

Overall, the standout advantages that sol gel processing has over the conventional methods is listed in Table 2.10 and these are: lower operating temperatures, high yield of product, cost effective and final product homogeneity of complex inorganic materials that can be controlled through trapping the randomness of the molecules in solution during synthesis, all leading to control of porosity, particle size and composition of the final material. However, the drawbacks are a major challenge to scale-up to an industrial scale: it can be expensive to run due to the use of expensive raw materials (use of 99.9999% purity) and the process of drying and sintering can be time consuming to ensure the target criteria for a material's desired properties are being met. [81][87][89] Therefore, it is critical here to ensure that the raw material (precursor) chosen for synthesising the LSCF6428 cathode materials enable homogeneity and stability to be achieved but are also cost effective.

2.5.1 Properties of sodium alginate for sol gel synthesis of the LSCF perovskite cathode

For the sol gel procedure there have been a range of materials that have been investigated for synthesising a metal oxide nanoparticle, such as citrate as mentioned earlier which had potential for enabling the gelation step.[87] In recent years though, there has been a shift in the choice of the materials for the sol gel procedure towards those which are environmentally friendly, low cost and require low processing temperatures. The use of polymer chemistry has been the current trend for sol gel processing due to the diverse and well-defined structures of polymers such as pectin, maltose, starch, and alginate, compared to small molecules. The polymers enable direct interaction with the metal ions to form metal oxides. In previous research maltose, starch and alginate were compared and alginate was preferred due to the ability to coordinate metal cation bonds with the alginate through the carboxylate groups when in solution (dues to alginate's good water solubility). Sodium alginate was originally used in the food and biomedical industries because its binding capability is temperature independent compared to the other materials that have been mentioned.[87] [92-93] In the last decade, the sodium alginate sol gel method has been used to synthesize anode and electrolyte materials and is seen as a promising alternative to the other conventional methods. [93-96] However, the method has only been recently utilised for one popular MIEC cathode material, LSCF, compared to the prior, successful use for synthesis of electrolyte materials.[15]

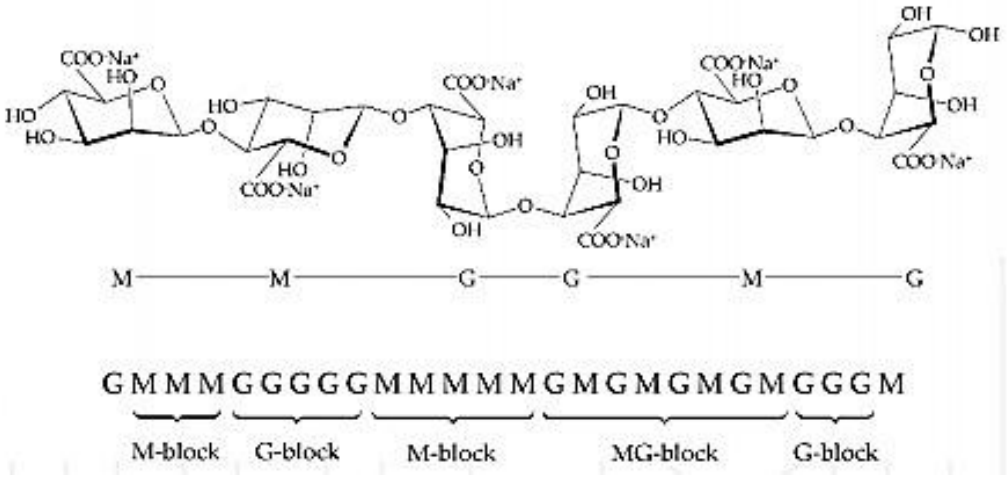

Figure 2.12: Schematic diagram of the molecular structure of sodium alginate in chain conformation. [Taken from Sardar et.al.] [93]

Figure 2.12 shows the sequence within the alginate molecule both molecularly and genetically, being made up of different ratios of α-L-guluronic acid (G) and 1, 4 linked β-D-mannuronic acid (M) residues linked together covalently into copolymer blocks.[93][97-99] It has been found that the presence of a divalent metallic cation, when crosslinked with the alginate, establishes a gelation mechanism known as an egg dimer where each metallic cation is bound to the 4 guluronate monomers. [98-99] The alginate molecule can also provide stronger interchain bonding because of its large molecular weight which is technically between 32-400 kDa. This class of polysaccharides are attractive for ion exchange because they are made up of natural biomass resources which are non-toxic, biocompatible and of sufficient strength compared to synthetic polymers (which are typically hydrogels, termed as cross-linked hydrophilic networks). [15] [92-96]

The sodium alginate is unique as a precursor for the sol gel process because it is extracted from the cell wall of a brown algae seaweed, so it is environmentally friendly. Its structure consists of long chains of linked mannuronic acid (M) and guluronic acid (G) units, arranged in a block-wise pattern [97] as already shown.

The steps in the extraction process can be summarised as follows:

Brown seaweed -> Algal material -> Alginic acid -> Sodium alginate -> Pure Sodium Alginate

The extraction can occur from a variety of seaweed sources such as *Laminaria hyperborea*, or *Ascophyllum nodosum*, each uniquely classified with different chemical compositions (i.e. different ratios of G, M and GM blocks). The G-G, M-M and G-M co-polymer are logically sequenced in relation to the anionic polysaccharide which can be arranged as either heterogeneous or homogenous form. The different sequencing has been reported to greatly impact the physiochemical properties such as viscosity, water absorption uptake and sol/gel formation of sodium alginate.[97][99] It has been found that the pH concentration, molar mass, and temperature can impact on the physiochemical properties of the sodium alginate gel. It also has been found that the ratio of M-M, G-G and MG co polymers can characterise the state of the gel in relation to the physiochemical properties as shown in Table 2.12 below. [99-100]

Table 2.12: The different types of blocks within a sodium alginate structure and its characteristics [99-100]

Blocks	Characteristics	Diagram of the Blocks [Taken from Hu et.al.] [99]
M	Higher M:G ratio can result in higher water absorption and better ionic exchange with the divalent metallic ions. Enables formation of soft and elastic gel.	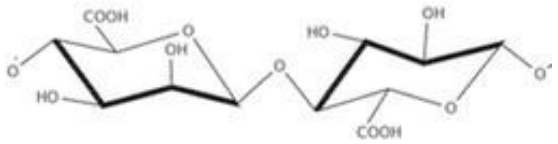
G	Higher G:M ratio can result in a stiffer, stronger and brittle gels due to the hindered rotation compared to the M block.	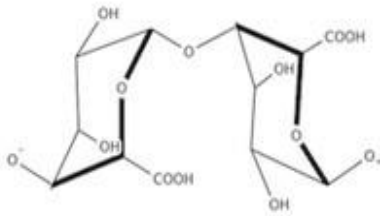
M/G	Higher M/G content allows for higher flexibly and shrinkage of the sodium alginate gels.	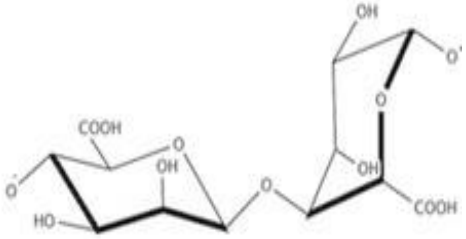

There are also key parameters that need to be addressed regarding the selection of the metal cation as part of the ion exchange process in alginate binding. [101] In turn, the metal cation can affect the effectiveness of the alginate adsorption to enable the gelation mechanism of the egg box formation to occur.[99] The production of well-defined spherical beads upon gelation is dependent on the content of the G blocks (alternating the level of metal binding) in the alginate, controlling the particle size of the beads themselves as well as the gelling mechanism.[98] The increased viscosity from an increased average molecular mass (M_v) of the sodium alginate can also affect the condition of the gel through its relationship with the intrinsic viscosity[η] as shown in equations (2.10 –2.12). Where η is the polymer solution's viscosity, η_o is the pure solvent's viscosity, η_{sp} is the specific viscosity, and K and α are parameters which are related to the viscometric constants.[102]

$$[\eta] = lim_{c->0} [\eta_{sp}/c] \quad (2.10)$$

$$\eta sp = (\eta - \eta 0)/ \eta 0 \quad (2.11)$$

$$[\eta] = K(M_v)^{\alpha} \quad (2.12)$$

It has also been found that the choice of metal cation other than sodium for the binding of the alginate has a massive influence regarding its elastic modulus and strength. From a study by Yang et. al., it has been agreed that trivalent cations such as iron and aluminium give a stronger and stiffer material compared to divalent metals such as strontium and calcium, Figure 2.13a.[103] Sodium alginate itself has poor strength and poor elastic modulus despite excellent stretchability as also shown in Figure 2.13b. The enhancement of mechanical properties with di and trivalent metal ion binding to alginate is considered to be due to them forming a 3-dimensional (3D) network with the alginate resulting in a compact network structure. [103] Although, the main concern is that even though these provide better properties the trivalent cations may be unsuitable for gelling because of their instability (e.g. reversible transition from ferric to ferrous iron) and or toxicity in biological processes (e.g. Fenton chemistry of Fe). [99]

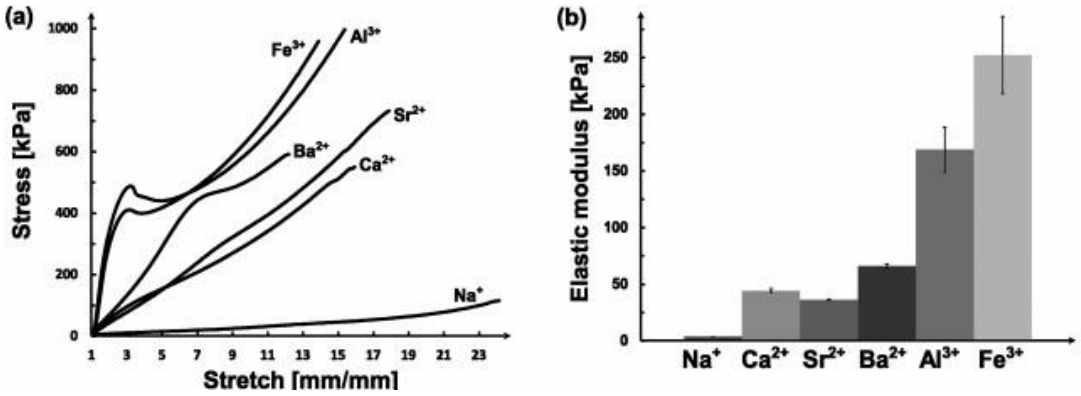

Figure 2.13: a) the stress-strain performance of metal ion alginate gels b) the elastic modulus of the metal ion alginate gels [Taken from Yang et.al.] [103]

2.5.1b Calcination of the metal-alginate gels to produce homogenous nanopowders of LSCF

Calcination is classified as the final stage of sol gel synthesis and is also known as heat treatment. As shown earlier in Figure 2.11(Section 2.5), calcination takes place straight after the drying of the metal complex.[91] It can also be shown clearly that the heat treatment of for example a silica gel (used in earlier sol gel synthesis) is divided into three parts: dehydration;

decomposition in the case of the work here, of the dehydrated anhydrous metal alginate; and densification of the final ceramic product as shown in Figure 2.14 below.[103]

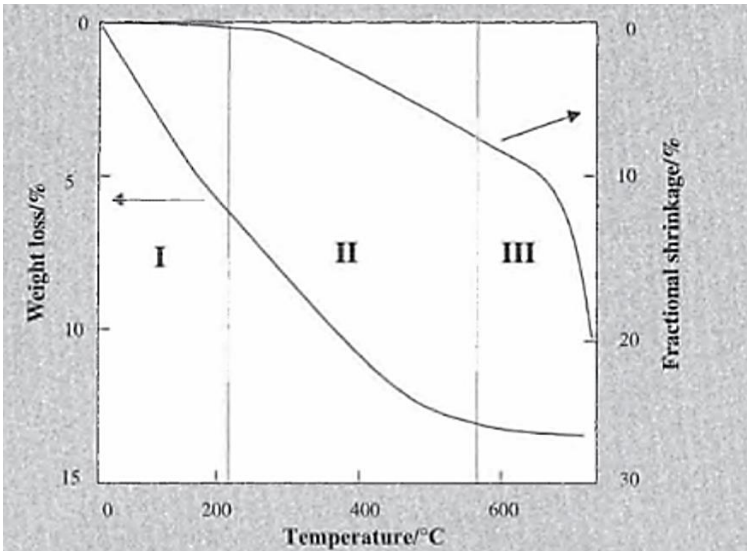

Figure 2.14: Stages of decomposition and densification of a silica gel in relation to Weight Loss % and Shrinkage % [Taken from Wright et.al.] [104]

Dehydration occurs when heating up to 200 ºC because pore surface water is desorbed from the metal alginate leading to mass loss and leaving behind a dehydrated anhydrous metal alginate. Then decomposition, which is the critical stage of calcination, occurs typically between 200 ºC – 700 ºC where a combination of additional mass loss and shrinkage of the metal alginate occurs. The increase of thermal energy is sufficient to breakdown the alginate and cause the loss of organic components, leaving behind a porous matrix and structural relaxation from the alginate (this process will be described in detail in Chapters 4 and 6). Heating in this temperature range ultimately results in the formation of the target metal oxide and can favour densification and a decrease in the surface area of the newly formed material itself. At temperatures greater than 700 ºC, there is no further mass loss, although there is still an increase in structural relaxation and full densification towards a ceramic.[104] The key heat treatment parameters for this process are the calcination temperature and heating/cooling rate, which can also influence the properties of the resulting ceramic such as porosity and density. [105-109]

The heating rate has been investigated for sodium alginate and alginic acid under different atmospheric conditions (O_2 and N_2) and heating rates of 5 ºC/min, 10 ºC/min and 20 ºC/min over a temperature range from RT to 1000 ºC. It was revealed from the study by Guo et. al. that the heating rate influences the resolution and timing analysis of the thermogravimetric (mass-loss or TG) curve for this process.[100] 10 ºC/min was shown to be optimum heating

rate for alginate to allow for a clear resolution TG curve to identify the main chemical mechanisms from the initial dehydration, through the decomposition events to the formation of a metal oxide. [100]

The choice of metal cation can alter the temperature requirements of the dehydration and decomposition reactions. Divalent and trivalent metal-alginates, with cations such as alkali (Ba and Sr), transition metals (Cr, Al, Fe, Co) and earlier series of the rare earth elements (La and Ce), have been widely investigated by researchers in examining the removal of heavy metal ions from freshwater. The strength of the chelating bonds such as ionic and covalent (within functional groups such as carboxylic acid and hydroxyl) was found to influence the varied production of the intermediate fragments such as hydroxides, carbonates and oxalates. [105-109] Production of these fragments will be detailed for LSCF6428-alginate gels in Chapter 4.

As discussed earlier in Section 5.1 of this Chapter, there have been different precursors used for the sol gel synthesis that undergo the thermal decomposition process for the production of the MIEC LSCF perovskite oxide nanopowders that can be subsequently sintered for use/testing as SOFC cathodes. The major drawbacks of the precursors are the cost effectiveness and the byproducts that are obtained after the decomposition and release of volatiles occurs. The use of the alginate sol gel process specifically has been investigated by the Leeds Alginate Group to synthesise LSCF-alginate beads and undertake calcination. [15] There has so far been detailed thermal analysis of rare earth lanthanides such as lanthanum and cerium.[108] However, praseodymium and neodymium have yet to be investigated in the synthesis with alginate including the thermal behaviour in relation to their decomposition characteristics upon calcination.

2.5.2 Sintering method of the synthesised LSCF cathode material

After calcination, the next steps towards the establishment of the optimum cathode ceramic LSCF material for IT-SOFCs is through the sintering procedure. The sintering procedure requires control of parameters such as grain size, relative density, porosity and densification. It is critical that the cathode microstructure is densified to a specific level of porosity to enable gas diffusion when in use as a SOFC and with a finer grain size to maintain plenty of reaction sites but high relative density in between, and with appropriate mechanical and TEC properties overall for superior electrochemical performance. [110-111]

Similar to the study by Tai et.al. much work has been undertaken investigating the optimal elemental compositions of the LSCF in relation to the content of Co and Sr in LSCF.[64] The

sintering behaviour of five different LSCF compositions is investigated in a study by Möbius et al. in order to determine the main sintering parameters ranging from dwell time, sintering temperature, shrinkage rates (that influence the densification), and porosity.[112] Varying the sintering temperature between 900 and 1100 ºC is shown to be the main parameter influencing the degree of densification and porosity.[112] However, the sintering time for LSCF6428 is also critical, as longer sintering times of either 3 or 6 hours results in either cracks or undesired secondary phases in the microstructure.[112] That is consistent with another study by Solovyev et. al., who stated that the sintering temperature of the cathode should take place between 900 – 1100 ºC. Operating at temperatures above 1100 ºC with a SOFC half-cell can introduce unwanted phases which can interfere with the electrochemical performance and increase the polarisation resistance for ORR. [113]

The sintering procedures for calcined LSCF6428-alginate complexes are set out in a study by Sardar et al. Sintering was conducted using both single and two step sintering as the microstructure must be densified with controlled porosity such that it performs well as an IT-SOFCs. From a study using the sodium alginate for sintering of the electrolytes, $Ho_2Zr_2O_7$ and $Ho_2Hf_2O_7$ properties such as grain structure and density have been examined by XRD.[93][114] However, for the perovskite cathode to perform efficiently within IT-SOFCs, there needs to be a balance between densification and porosity, which are the criteria to meet the MIEC properties as discussed in Section 2.5.1 e.g. nanoscale grains with 20-40% porosity.[38]

X-ray micro tomography (XMT) has been used to study freeze dried NiO (synthesised using the sodium alginate sol gel) aimed for anodes for IT-SOFCs by Wang et. al., and this characterisation has proven to be another efficient way to examine microstructure to determine particle size and morphology in relation to a material's porosity before and after freezing.[65] The technique is strictly limited to only 1 micrometre resolution resulting in critical nanoscale information being missed out. Due to the complex nature of an alginate derived LSCF cathode, further analysis needs to be undertaken to determine the homogeneity between the surface and bulk composition of the LSCF. That has led to researchers to investigate a variety of approaches of both 3-D characterisation and modelling techniques to study the porous electrodes of for LSCF compositions for SOFC cathodes from a volumetric perspective. Focused ion beam scanning electron microscopy (FIB-SEM) has been a popular direct experimental method for the examination of 3-D microstructure by serial milling and imaging, a technique that was first

used for anode based NiO-YSZ composites and later expanded to LSCF cathodes.[41] [115-117]

There has been no work done in optimising the sintering procedure using a single step method for synthesising perovskite LSCF6428 using the sodium alginate sol gel method. There has also been little work done in investigating how additional rare earth dopants to La and the chosen synthesis method influence the sintering behaviour of modified LSCF6428 compositions to affect the structural, porosity and microstructure properties of the cathode. The work presented here will address this area of uncertainty.

2.5.3 Fabrication of LSCF cathode half cells for electrical performance testing

The fabrication method used for the half-cell is also of great importance to ensure that binding between the electrode and electrolyte occurs without secondary phases impacting the interface. Physical and chemical vapour deposition (PVD and CVD) are very expensive fabrication techniques while ink printing is a suitable alternative as it is simpler and cheaper and can also be used for upscale production. The thickness of the electrolyte is critical to address sluggish kinetics in relation to the hindrance of ORR kinetics and surface diffusion, as discussed in Section 2.4.1. Synthesis of a planar cell is also the simplest choice for efficient testing (Fig 2.3). The choice of fabrication method for a half-cell can influence the polarisation resistance. [118-120] The slurry ink is typically made up of ceramic particles, binder, solvent and dispersant. 60:40 can be chosen as a typical solid: liquid ratio in a slurry ink for fabrication of the cathode material. When the solid content increases to up to 70 wt% it leads to an increase in cracking of the deposited microstructure. Screen painting is a low cost and simple method for fabricating planar SOFCs and has potential use for mass production. The ink quality is critical as it influences the final properties of the sintered half-cell.[119]

The use of the binder is key to improve the particle network strength within the cathode ink. Hydroxyl group-based binders are typical as they allow for the quality of the final product to be obtained so it is critical that a balance between the solid content and binder ratio is considered.[118][120-122] Ethyl cellulose (EC) is a linear polymer structure which consists of branches and allows for homogenous pore size formation which enables a fine and uniform microstructure on sintering. The solvent and binder affect the dispersibility and stability of the ink paste. [120-122]

A study by Jamale et. al, where EC was used as the binder and terpineol was used as the solvent for screen printing of LSCF onto a GCO pellet which were then sintered at 1000 ºC for 2 h. The effects of the screen printing resulted in porous but continuous bonding to the substrate pellet as shown by SEM/EDX imaging. That establishment of the interface between LSCF and GCO without undesired secondary phases allows for ORR processes at IT in the SOFC half cells.[123]

There has been little work on investigating the IT-SOFCs half cell performance of rare earth doping of LSCF. There have been past work on rare earth doped MIEC cathodes using Pr and Nd in BSCF and with a GCO electrolyte. In both cases, Pr and Nd exhibit significant enhancement in electronic conductivity, oxygen diffusion and catalytic activity compared to the undoped BSCF when tested at 600 ºC. This is thought to be due to the formation of oxygen vacancies from the substitution of Ba^{2+} with trivalent Pr and Nd ions. However, ionic conductivity was difficult to measure due to the rare earth elements enhancing the electronic conductivity of MIEC cathode bonded to the GCO electrolyte. [76][124] A study by Lei et. al., investigated the LSCF/YSZ/LSCF half-cell by using YSZ as an electron blocker to limit electronic current and enable measurement of ionic conduction to better understand oxygen ion diffusion for IT-SOFCs. From the impedance measurements between 600 – 800 ºC, the dense LSCF exhibited ionic conductivity with an activation energy of 1.26 eV but high sintering temperatures of 1600 ºC were used due to the choice of pressing method used for making the YSZ pellets.[125] There has been limited work on undoped LSCF/YSZ and rare earth doped LSCF/YSZ on how the rare earth elements influence the ORR processes of the electrolyte/cathode interface and this work will address this knowledge gap.

Research Aim and Objectives

The overall aim of my PhD research is for the synthesis and characterisation of a novel LSCF6428 material through doping with rare-earth dopants (Ln = Nd, Pr) at the A site of the LSCF6428 perovskite structure, produced using the sodium alginate sol gel methodology. That will determine whether this substitution of La for Pr and or Nd enables favourable properties such as enhanced phase or porous microstructures and whether this leads to superior electrochemical performance, aimed for IT-SOFCs that can operate below 800 ºC.

Objectives

1. Synthesize and analyse LSCF6428 using sodium alginate, ion-exchange, sol gel processing.

- Analyse the LSCF6428-alginate beads using TGA and calcination at chosen temperatures for formation of LSCF6428 nanopowders. Then characterise the LSCF6428 nanopowder using XRD, Raman Spectroscopy, SEM/EDX, XCT and BET to examine its structural and porous properties.

2. Single doping the rare earth elements, Pr and Nd at the A site of the LSCF6428 cathode using the same synthesis method as the LSCF6428, sodium alginate ion-exchange, sol gel processing.

- Analyse the LPSCF33428, LNSCF33428 and NSCF6428-alginate beads using TGA and calcination at chosen temperatures for formation of LPSCF33428, LNSCF33428 and NSCF6428 nanopowders. Then characterise the LPSCF33428, LNSCF33428 and NSCF6428 nanopowders using TGA, XRD, Raman Spectroscopy, SEM/EDX, XCT and BET for comparison of the structural and porous properties.

3. Uniaxial press and sinter LSCF6428

- Analyse the sintering temperature range of 900 ºC to 1100 ºC for LSCF6428 and characterise using XRD, Raman Spectroscopy, SEM/EDX, Density Measurements (Archimedes and Geometrical) and BET. Analyse for comparison of the structural, porous properties and densification across the sintering temperature range.

4. Uniaxial press and sinter rare earth doped LSCFs; LPSCF33428; LNSCF33428 and NSCF6428
    - Analyse the sintering temperature range of 900 ºC to 1100 ºC for rare earth doped LSCFs; LPSCF33428, LNSCF33428 and NSCF6428 and characterise using XRD, Raman Spectroscopy, SEM/EDX, Density Measurements (Archimedes and Geometrical) and BET. Then analyse for comparison of the structural, porous properties and densification against the prior sintered LSCF6428.

5. Analyse the 3-D, densified microstructure of the sintered materials

    - Analyse the densified microstructures of the sintered LSCF6428 ceramic and sintered LPSCF33428 ceramic using FIB-SEM and EDX to determine the homogeneity of the porosity, grain structure and chemical composition and compare the two. Then characterise a sintered LPSCF33428 pellet using nano-CT to determine homogeneity of the densification through the effect of Pr doping of LSCF across the whole pellet.

6. Analyse the magnetic properties of calcined nanopowders and sintered ceramics of LSCF6428, LPSCF33428, LNSCF33428 and NSCF6428 for comparison of the effect of rare earth doping and its structural parameters upon magnetization.

7. Analyse the ac impedance performance of half cells of LSCF6428/YSZ, LPSCF33428/YSZ, LNSCF33428/YSZ and NSCF6428/YSZ

    - Analyse the ac impedance performance of the half cells at temperature ranges between 400-500 ºC for LSCF6428/YSZ and LPSCF33428/YSZ, at temperature ranges of 400-550 ºC and 400-500 ºC for Nd doped LNSCF6428/YSZ and NSCF33428/YSZ, and at temperature ranges between 550 -750 ºC for LSCF6428/YSZ and LPSCF33428/YSZ using the appropriate equivalent circuit models. Then interpret the data for activation energies and area specific resistance of the ORR processes to enable comparison between the undoped and doped LSCF/YSZ half cells to relate doping to the performance efficiency of ORR for IT-SOFCs.

Chapter 3 – Experimental Methods and Characterisation Techniques

Introduction

The structural, porous and electrical properties of the ceramic perovskite oxide cathode material are greatly dependent on the processing and fabrication methods used throughout this study. The aim here is to synthesis a ceramic cathode material with a porosity of between 20-40%, as referred to in Chapter 2, Section 2.3. Explanations of the method of sintering and fabrication of the Sodium alginate sol gel are referred to in Chapter 2, Sections 2.5.2 and 2.5.3 respectively, as part of the making of the novel ceramic cathode material.

Various analytical, 3D, magnetic and performance characterisation methods were used to examine the structure, porosity and homogeneity of the materials, both the undoped LSCF6428 and rare earth doped LSCF i.e. LPSCF33428, LNSCF33428 and NSCF6428.

3.1. Sodium Alginate Ion Exchange Sol gel

The Leeds Alginate Process (LAP), which has been established over a decade within the research group, is well known for the synthesis of metal alginate beads for other fuel cell components such as the anode, i.e. NiO, and electrolyte, i.e. $Ho_2Hf_2O_7$. [93][96] Sardar et.al. had trialled the synthesis of the MIEC cathode, lanthanum strontium cobaltite ferrite (LSCF6428) for the first time in 2020 using only 4wt% alginate in the form of metal - alginate beads.[15] For this work, as discussed earlier in the literature review in relation to establishing a cost-effective synthesis method, the LSCF6428 material was synthesised using both the 3wt% and 4wt% alginates. The mass residue of the 3wt% and 4wt% alginates were compared to determine what wt% alginate would be used as a set point for the rare earth doped LSCF i.e. LPSCF33428, LNSCF33428 and NSCF6428.

The stoichiometric measurements were done from the relevant inorganic metal nitrates hexahydrate, which act as precursor salts for particular compositions as shown in Table 3.1 below, using a Sartorius electronic balance to a precision of +/- 0.001g.

Table 3.1: The Purity, suppliers and CAS codes of the nitrate reagents and alginic acid, sodium salt

Raw Powder	Purity	Supplier	CAS Code
$La(NO_3)_3.6H_2O$	99.99	Merck, Darmstadt, Germany	10277-43-7
$Sr(NO_3)_2$	≥99.0%	Merck, Darmstadt, Germany	10042-76-9
$Co(NO_3)_2.6H_2O$	≥99.9%	VMR Chemical, Belgium	10026-22-9
$Fe(NO_3)_3.9H_2O$	≥99.9%	Scientific Laboratory Supplies,Ltd	EEC Label: 233-899-5
$Pr(NO_3)_3.6H_2O$	99.9	BioServ, Callbre Scientific Company	13746-96-8
$Nd(NO_3)_3.6H_2O$	99.999%	BioServ, Callbre Scientific Company	14483-17-7
Alginic acid sodium salt	-	Sigma-aldrich	9005-83-3

Details of the quantities of each raw powder used to synthesise the $La_{0.6}Sr_{0.4}Co_{0.2}Fe_{0.8}O_{3-\delta}$ composition can be seen in the equations below.

Table 3.2: The moles and formula mass of the individual elements required for the synthesising the composition of LSCF6428

Elements	Moles	Formula Mass (g/mol)
Lanthanum (La)	0.6	138.91
Strontium (Sr)	0.4	87.62
Cobalt (Co)	0.2	58.93
Iron (Fe)	0.8	55.85
Oxygen (O)	3	16.00

The quantity of raw powder (m) was calculated by multiplying the atomic fraction (n) of each element from the chemical composition in LSCF6428 with the formula mass of each element (Mr) from Table 3.2 according to the formula (3.1) shown below:

$$\mathrm{n} = \frac{\mathrm{m}}{\mathrm{Mr}} \tag{3.1}$$

La: 0.6 mole x 138.91 g/mol = 83.34 g

Sr: 0.4 mole x 87.62g/mol = 35.05 g

Co: 0.2 mole x 87.62g/mol = 11.79 g

Fe: 0.8 mole x 87.62g/mol = 44.68 g

O: 3 mole x 87.62g/mol = 48.00g

Total: 222.85 g

Each element was then divided by the total and multiplied by the quantity in grams to be produced as shown in the formula (2.2) below. Therefore, for 20g of the LSCF6428 nanopowder, the quantity of the La content required would be:

$$\left(\frac{83.34\ g}{222.85\ g}\right) * 20\ g = 7.4796\ g \tag{3.2}$$

However, the metal nitrate hexahydrate consists of water molecules that are chemically bound to the metal nitrate compounds as shown in Table 3.3. The molecular weight of the La is divided by the total molecular weight of the metal nitrate hexahydrate to obtain the % of La content present in the metal nitrate hexahydrate as shown in formula (2.3) below .

Table 3.3: % Metal Content from the Nitrate reagents obtained from equation (3.3)

Elements	**Total Molecular Mass (g/mol)**	**Mass of the Individual Metal (g/mol)**	**% of Metal content**
$La(NO_3)_3.6H_2O$	433.01	138.91	32.079
$Sr(NO_3)_2$	211.63	87.62	41.403
$Co(NO_3)_2.6H_2O$	291.03	58.93	20.25
$La(NO_3)_3.9H_2O$	404.00	55.85	13.823

$$\%\mathrm{La} = \left(\frac{138.9005\ \mathrm{g}}{433.0114\ \mathrm{g}}\right) * 433.0114\ \% = 32.079\% \tag{3.3}$$

To ensure that the La content obtained from the La $(NO_3)_3.6H_2O$ is 100%, the 100% is divided by the % of the La content multiplied by the La content required for the synthesis of LSCF6428 as shown in formula (3.4) below.

$$\text{La content} = \left(\frac{100\%}{32.079\%}\right) * 7.4796\ g = 23.316\ g \text{ (rounded to 3 decimal places)} \quad (3.4)$$

The overview of the synthesis of LSCF6428 is described in the flow chart diagram below in Figure 3.1

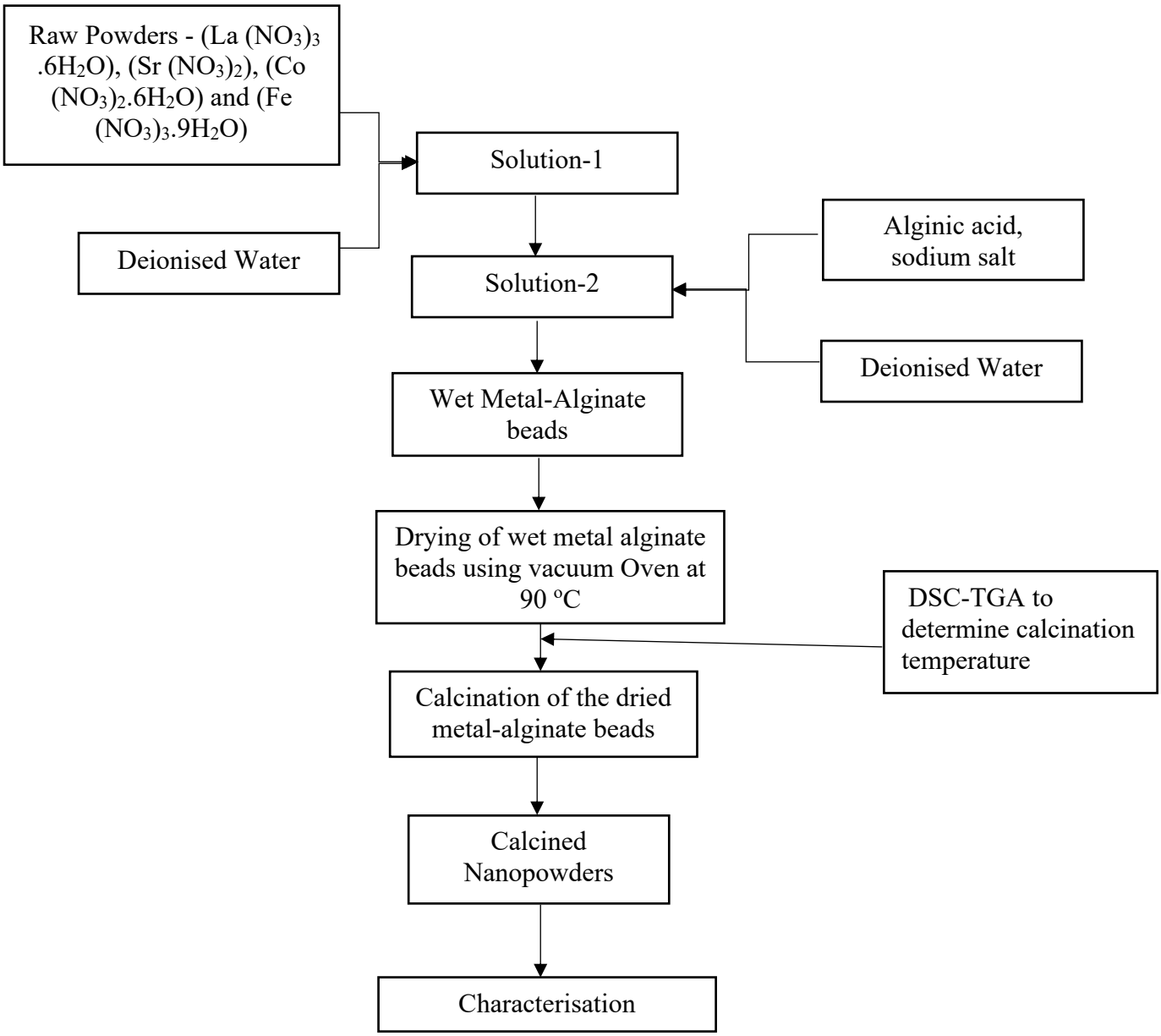

Figure 3.1: Overview of the sodium alginate sol gel synthesis process for LSCF6428

Figure 3.2: Sodium Alginate mixture (left, yellowish thick solution) and Aqueous Metallic Ion Solution (LSCF6428) (Right, dark red clear liquid) both mixed using a magnetic stirring rod.

The quantities selected for each of the inorganic metal salt materials were dissolved in 200 ml of deionised water in a beaker, carried out using a magnetic stirrer operating at around 500 rpm for around half an hour until fully dissolved. A complex aqueous metallic ion "solution 1" was formed as shown in Figure 3.2. The organic salt solution sodium alginate ("solution 2") was diluted to obtain 4 wt% and 3 wt% concentrations. This was carried out by dissolving the stoichiometric quantity of sodium alginate in 200 ml of deionised water in a beaker, stirring under a magnetic stirrer at around 500 rpm to incorporate, then reduced to 200rpm until fully dissolved after about four hours. The sodium alginate solution was then left overnight to ensure the solution was homogeneous (no air bubbles) prior to use. Afterwards, the sodium alginate solution is transferred into a 20cm^3 hypodermic syringe by dragging the syringe up slowly, ensuring that no air bubbles are formed. The preparation of the metal-alginate wet beads was carried out under a fume hood operating at ambient temperature and pressure. Then a 16G (1.194 nm diameter) stainless steel needle attached to a 20 cm^3 hypodermic syringe was used to drip the sodium alginate solution into the complex metallic ion solution beaker (likely containing the La^{3+}, Sr^{2+}, $Co^{3+/2+}$ and Fe^{3+} ions) to transform the sodium alginate solution immediately into wet metal-alginate beads. The height of the hypodermic syringe, held around 5 cm above the beaker, was critical to ensure that the sodium alginate solution was given sufficient falling time to form a spherical bead (4-5mm in diameter) before coming into direct contact with the complex metallic ion solution 1.

Figure 3.3: The ion exchange between the sodium alginate beads and the LSCF6428 nitrate solution at 200rpm.

The wet metal alginate beads will then be maintained in a gelling phase for 24 hours under a gentle magnetic stirrer operating at 200rpm as shown in Figure 3.3. That will ensure that enough time is given for a complete ion exchange of the Na+ with the La^{3+}, Sr^{2+}, $Co^{3+/2+}$ and Fe^{3+} likely to occur within the complex aqueous metallic ion solution.

Figure 3.4: The filtered metal-alginate beads of the LSCF6428

The wet metal-alginate beads will then be separated from the complex aqueous metallic ion solution through a stainless-steel sieve (5mm) as shown in Figure 3.4. The collected wet metal-alginate beads are extensively washed and rinsed with deionised water several times for the removal of any unreacted material. The wet metal-alginate beads are finally dried in a dried vacuum oven/hot plate at 90 ºC for 24 hours (or until a constant weight is reached) to produce fully dried metal alginate beads as shown in Figure 3.5 below.

Figure 3.5: The wet metal alginate beads of LSCF6428 before drying (left) and the dried metal alginate beads of LSCF6428 after drying in a vacuum oven at 90 ºC

Then the calcination temperature is determined using a characterisation technique combining differential scanning calorimetry, thermogravimetric analysis and differential thermogravimetric analysis (DSC/TGA/DTG) for both the 4 wt% and 3 wt% LSCF6428 composition. As discussed in Chapter 4.1, due to the 3wt% LSCF6428 retaining a greater mass residue of 44.1% compared to the 4wt% LSCF6428 of only 29.9%, 3 wt% alginate is selected for the synthesis of the rare earth doped LSCF compositions i.e. LPSCF33428 containing $Pr^{+3/+4}$ ions, LNSCF33428 and NSCF6428 containing Nd^{3+} ions, and the procedure used for the synthesis of the LSCF6428 is repeated.

Then all four compositions are stored in plastic tubes which are then stored in a vacuum desiccator to prevent any humidity or air affecting the materials.

3.1.1. Calcination

The dry metal alginate beads are placed in an alumina crucible with an alumina tile lid on top prior to calcination.

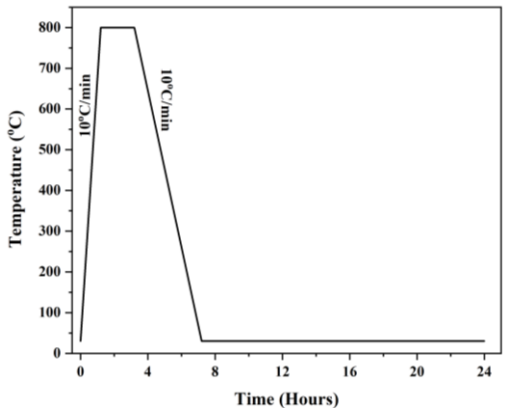

Figure 3.6: Calcination profile of the optimal calcined temperature of LSCF6428 at 800 °C

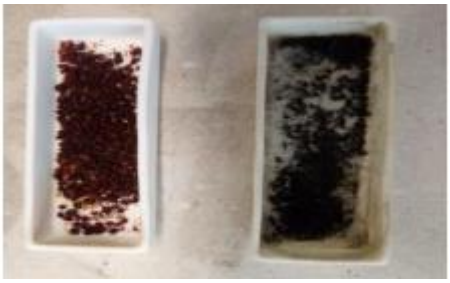

Figure 3.7: The dried dark red powder LSCF6428 (left) before calcination and the grey ash powder LSCF6428(right) after calcination at 800 °C for 2h

Then the dry metal alginate beads of the 3wt% LSCF6428, LPSCF33428, LNSCF33428 and NSCF6428 compositions are then calcined at three different temperatures, 750 ºC, 775 ºC and 800 ºC, for about 2 hours under an ambient atmosphere at 10 ºC/min as shown in the calcined profile from Figure 3.6. That will ensure the removal of alginate, and that the metallic beads are fully transformed into perovskite oxide nanopowders as shown in Figure 3.7.

Then all four compositions of the calcined nanopowders are stored securely in plastic tubes and stored in a vacuum desiccator prior to further analysis work.

From there, the four compositions of the calcined nanopowders will then be examined through characterisation techniques as discussed in Section 3.2 in relation to their phase purity, structural and porous properties and homogeneity of their compositions prior to pelleting and sintering.

3.1.2. Pelleting

Following the calcination, the calcined nanopowders chosen from the optimal calcined temperature were pressed with a 13 mm diameter steel die on a uniaxial press as shown in Figure 3.8 below. The amount of nanopowder used to make the pellets is in accordance with the formula (3.5) shown below which is dependent on the theoretical density obtained from the XRD Rietveld of the optimal calcined temperatures of both undoped LSCF6428 and rare earth doped LSCF. Then the pump handle is used to build up the pressure to 0.4 ton for 5 minutes to obtain the shape of the pellet then increased further to a pressure of 2 tons for 10 minutes. To release the pressure, the pressure release handle is turned anticlockwise. The pellet is then placed on top of a standard pellet made of the same composition in an alumina crucible to prevent contamination of the composition before undertaking the sintering procedure.

$$\rho = \frac{m}{\pi r^2 t} \tag{3.5}$$

Where r = radius of the steel die, t= thickness of the pellet, m= mass of nanopowder used to make the pellet, ρ = relative density of the pellet

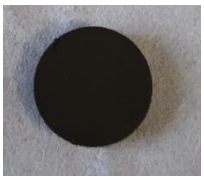

Figure 3.8: Appearance of the calcined LSCF6428 nanopowder at 800 ºC pressed to form pellet prior to sintering

Before the pellets are sintered, each pellet is measured for its diameter and thickness using the vernier callipers in mm (rounded to 2 decimal places)

3.1.3. Single Step Sintering

Sintering has been used for ceramic production where the thermal energy is used to obtain dense ceramics. The thermal treatment needs to take place at below melting point to ensure that the nanopowders are bonded to each other. A study by Möbius et.al. investigated sintering behaviour of the individual compositions of the LSCF to determine the suitability of the sintering temperatures. [112] The sintering procedure can be shown in Figure 3.9 where the heating rate increases at 3 ºC/min from RT to a sintering temperature at 1000 ºC, with a dwell time of 1h, then cooled down at 3 ºC/min from 1000 ºC to RT as shown in Figure 3.9 below. The other sintering temperatures that were used are detailed in Chapters 5 and 7.

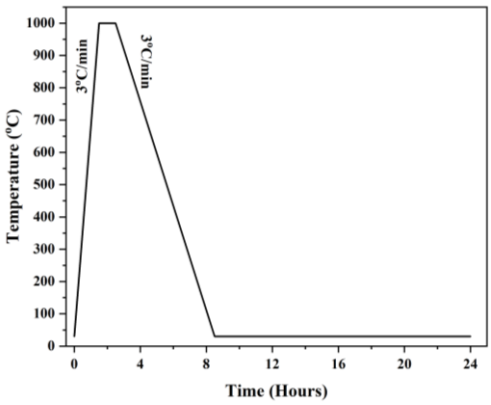

Figure 3.9: Sintering profile of the optimal sintering temperature for all four compositions; LSCF6428, LPSCF33428, LNSCF33428 and NSCF6428 pellets

After sintering, the sintered pellets are measured for its diameter and thickness using the vernier callipers in mm (rounded to 2 decimal places).

3.1.4. Fabrication of the YSZ powder

8.7mol% of YSZ (MEL Chemicals, Manchester) was mixed with 1wt% AC Optinax, which is use as a binder for the YSZ, in a 500ml beaker filled with water and then heated to a temperature of around 150 ºC until all the liquid has evaporated and the YSZ powder becomes dry.

3.1.5. Pressing of the YSZ pellet

A 13 mm diameter steel die on a uniaxial press was used to create pellets from the dried YSZ powder. Then the pump handle was used to build up the pressure to 0.4 tons for 2 minutes to obtain the shape of the pellet then is further increased to a pressure of 2 tons for 5 minutes. The typical relative density for the YSZ of 5.9 g/cm^3 as defined from the literature was used for this work. [126]

3.1.6. Sintering of the YSZ pellet

Six different sintering temperatures (1300, 1350, 1400, 1450, 1500, 1550 ºC) were used for this work, to determine the optimal sintering temperature of YSZ for reaching the relative density of above 99%.[1] As described in Chapter 8, Session 8.4, 1400 ºC was selected as shown in Figure 3.10 below.

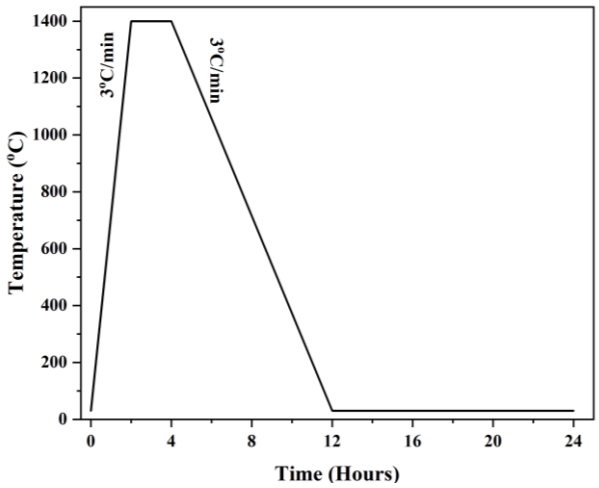

Figure 3.10: Sintering profile of the YSZ pellet

The heating rate occurs at 3 ºC/min from RT to sintering temperature at 1400 ºC with dwell time for 2h then it cooled down at 3 ºC/min from 1400 ºC to RT.

3.1.7. Cathode Slurry and Half Cell

The binder solution was made up by putting 100 mL of deionised water into a beaker containing a magnetic stirrer with 8g polyvinyl alcohol (PVA) (Sigma Aldrich) as the binder and 2g Dispex AA 4040 (BSAF) as the dispersant and then
stirred at room temperature for four hours until the solution was clear.

Figure 3.11: Schematic diagram of the half cell cathode (black slurry)/YSZ pellet (white)

A ratio of 60:40 wt% solid content of calcined cathode nanopowder (from the chosen optimal calcined temperature) to the solvent, PVA and Dispex solution was used to make the cathode slurry ink. A piece of tape with a hole in the middle was placed onto one side of the sintered YSZ pellet which was then placed onto a white tile prior to painting the cathode slurry. The slurry was painted over the hole onto sintered YSZ pellet using a paint brush with a width of 5mm until it was fully covered. The painted wet slurry was then left out for one hour at room temperature until it was fully dried before the tape was removed. The application was repeated on the other side as shown in Figure 3.11. The LSCF6428/YSZ half-cell was then placed into an alumina crucible on top of a standard sintered YSZ pellet to prevent contamination with the alumina.

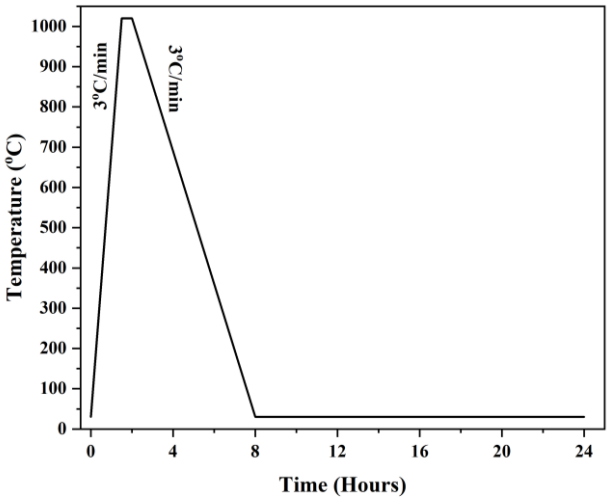

Figure 3.12: Sintering profile of the half-cell cathode/YSZ pellet

Sintering was done at a heating rate at 3 ºC/min from RT up to a final temperature of 1020 ºC held for half an hour then cooled down at 3 ºC/min to RT as shown in Figure 3.12.

3.2 Thermogravimetric Analysis, Differential Scanning Calorimetry and Derivative thermogravimetry (TGA/DSC/DTG)

Thermal analysis, first developed back in the 1960s, is done by generating or applying heat through the function of temperature and time. That results in material property changes of composition, structure and mass as shown in the equation below. That property is carefully monitored using temperature programming using the furnace temperature sensors and controllers. The term "programming" is key, ensuring that the sample property is carefully monitored and continuously measured throughout, to record any forms of chemical and physical changes that take place when undergoing cycles of heating or cooling across a range of temperatures over measured time as shown in equation (3.6). [127]

$$Temperature/Time \propto Sample\ Property \tag{3.6}$$

The thermal analysis measurements that were undertaken in this work are detailed below.

Thermogravimetric Analysis (TGA) measures the sample mass loss or gain against the change of temperature over time to identify decomposition, thermal stability, oxidative, volatile and adsorption or desorption behaviour of a sample. TGA can also determine the rate limiting steps of a reaction occurring in a sample. The use of TGA for complex reactions can limit precise analysis. Therefore, the derivative of a thermogravimetric analysis (DTG) curve against the temperature range used can simplify TGA analysis. That will enable better resolution of thermal events and more precise identification of the rate of the mass loss at reaction peaks that occur at a given temperature. [127-128]

Differential Scanning Calorimetry (DSC) measures the heat flux at a sample by measuring the difference of temperatures between the sample and an inert reference material undergoing heating or cooling at the same time and rate. The heat flow can be used to identify enthalpy changes, glass transitions and any forms of exothermic or endothermic peak reactions

occurring in a sample. DSC can be carried out during heating, cooling or when isothermally held at a constant temperature. [127-129]

The main components of the DSC/TGA/DTG equipment that need to be considered for thermal analysis are the material that holds the sample and the reference, the furnace, and temperature programmer and recording instrumentation. The following need to be considered when specifying and fabricating these critical components as shown in Figure 3.13 below: [127][129]

(1) Alumina, which has a high sintered density, is the preferred material for the sample and reference crucibles, to ensure that the crucibles do not react with the samples (typically the crucibles are 1-20 cm in height). Thermocouples are used to ensure that the heating is thoroughly uniform throughout. Correct sample preparation is also essential to ensure that the small mass of the sample to be analysed is homogenous.

(2) The furnace must not be contaminated. A suitable atmospheric or inert gas must be selected to minimise the effect of corrosive gases.

(3) Temperature programmer and recording. The choice of scanning and heating rate are important to ensure that sequential reactions are not overlapped.

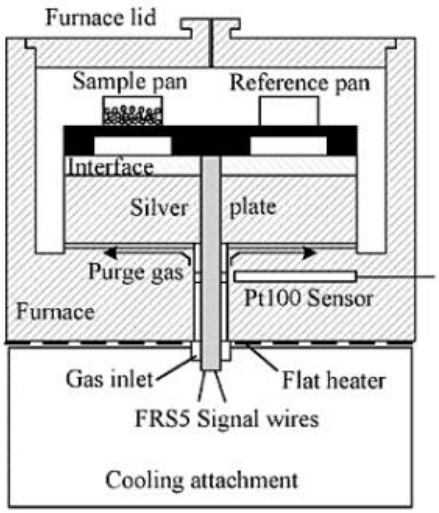

Figure 3.13: A typical DSC/TGA equipment set up [Taken from Wagner et.al.][127]

Prior to thermal analysis, 20 mg of the dried metal-alginate beads for LSCF6428, LPSCF33428, LNSCF33428 and NSCF6428 were crushed with a mortar and pestle into a powder to ensure that the material was homogenous. The thermal analysis of the dried metal - alginate beads was performed using a Mettler Toledo STAR-e, UK, model. Both the DSC and TGA data were collected simultaneously, with a gas flow rate set at 10 mL min^{-1} and a heating rate of 10 °C min^{-1}. The temperature programming is set at a temperature range from room temperature to 1000 ºC until the mass of the sample stabilises to a constant level, regardless of any further temperature increases. The DTG data were obtained by differentiating the TGA data.

Combined analysis of DSC/TGA/DTG and XRD results will determine the calcination temperatures to be used for obtaining calcined nanopowders of 90% phase purity or better prior to sintering whilst meeting industrial powder production standards.

3.3. X-ray Diffraction (XRD) Analysis

XRD is used to reveal the crystallography of both calcined nanopowders and sintered pellets throughout this work, including the effects of rare earth doping upon the phase purity, crystal structure, lattice parameters and crystallite size.[130]

The information on the experimental diffraction pattern is obtained when the material sample, in powdered form, is irradiated with coherent, single wavelength X-rays that diffract by constructive interference following reflection or scattering from the orderly arrangement of atomic structures of crystalline materials. The X-rays are generated by accelerating electrons towards a Cu metal target. Electrons striking the Cu metal target of sufficient high energy knock out an electron from the inner shell of the Cu metal target e.g., the K shell orbital. This leads to a transfer of an electron from one of the outer shells (L or M) to drop down to fill in the vacant site in the K shell orbital. The effect of the transfer between the two shell orbitals involved causes a release of energy in the form of *K*α or *K*β X rays when electrons fall from the L and M shell orbital respectively. However, the Kα radiation is more intense than the Kβ due to the vacant site of the K shell being occupied by the electron from the L shell rather than the M shell. The Kβ X-ray can be filtered out from the X ray diffractometer as shown in Figure 3.14 below. While the Kα radiation can split into Kα1 and Kα2 when electrons transition from the L shell (specifically the 2p3/2 and 2p1/2 orbitals) fill a vacancy in the K shell (n=1).

However, the Kα2 radiation and scattering can be stripped out by computer software after the diffraction peak pattern is obtained. [130-131]

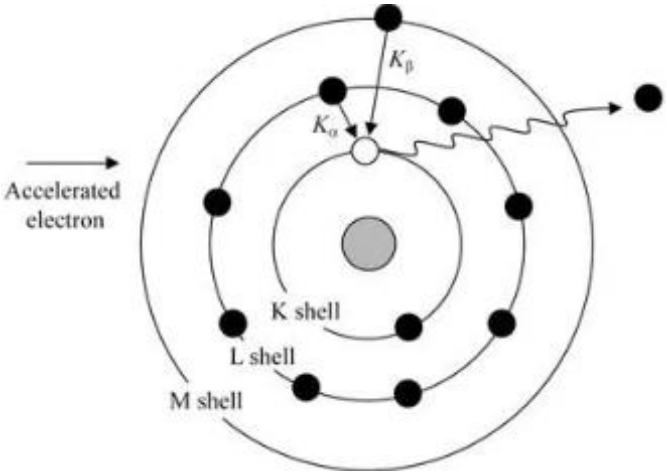

Figure 3.14: Schematic representations of the electronic transitions in an atom with the X ray emissions represented by the arrows [Taken from Lee et.al.][130]

As the X-ray diffraction is constructive interference of scattered waves from a crystalline material, the path difference of the sample may be calculated through Bragg's Law which is given by the equation (3.7) below: [131-135]

$$n\lambda = 2\,d\,sin\,\theta \qquad (3.7)$$

where n =integer, λ = wavelength of the monochromatic X-rays (1.54 Å for Cu $K\alpha_1$), d = atomic spacing, θ = diffraction angle. Figure 3.15 shows an X-ray diffractometer with three main components: X-ray source, sample and detector. The diffracted signal is collected by the detector at a range of different angles in a diffractometer circle. [130-135]

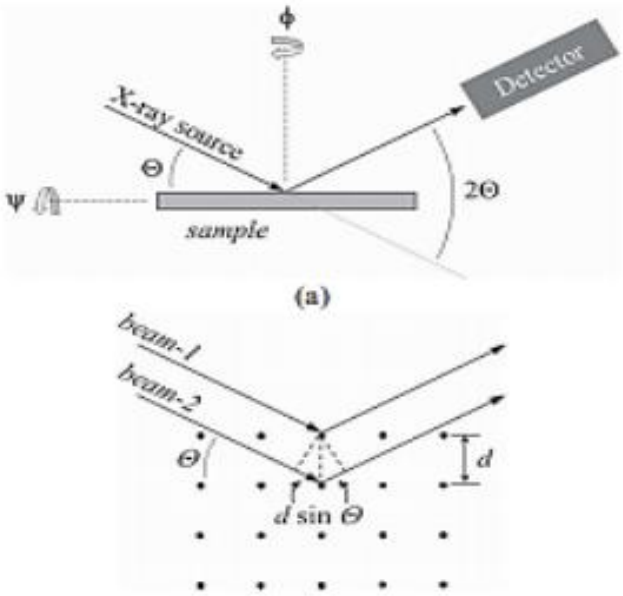

Figure 3.15: The principle of the X-ray diffractometer in relation to Bragg's Law. [Taken from Greenberg et.al.] [133]

However, Bragg's Law does not always provide a realistic measurement because it only applies to a perfect crystal structure. Crystallite size and strain can broaden peaks in a diffraction pattern. Crystallite size is given by the Scherrer equation (3.8) which originated in 1918 and accounts for the different width of the peaks in relationship to the crystallite size. [134-135]

$$Dv = \frac{k\lambda}{\beta cos\theta} \qquad (3.8)$$

where Dv = volume averaged crystallite size of the sample, k = shape factor, λ = X-ray wavelength, θ = diffraction angle and β = full width at half maximum of peak. The crystallite size of the sample is always inversely proportional to the width of the peak in a XRD pattern. [134-135]

The shape factor (reflection and crystal form), k is a value close to 1 but is dependent on the crystallite shape and hkl (Miller indices which describe the orientation of a crystal plane) reflection of the d spacing planes. It can vary between 0.62 – 2.08, however, the most common shape factor value which has been used is 0.89 and was used in this study. Peak broadening can also result from micro-strain, lattice distortion, instrumental broadening and texture. [135]

Figure 3.16: Crushing of the calcined LSCF6428 nanopowder using mortar and pestle (Left) and crushed LSCF6428 nanopowder placed in stainless steel sample holder prior to XRD measurement (Right)

To obtain a powder pattern indexable to a crystal structure, the sample must contain many crystals of random orientation resulting in a wide range of peaks being detected at different 2θ. [134-135] The sample is ground with a mortar and pestle until a powder size of typically below 45 micrometres is achieved. Then the powder is packed densely into a X by Y sample holder that is filled so the powder level is the same as the surrounding surface of the stainless steel sample holder as shown in Figure 3.16. Cu Kα radiation (1.5418 Å) was applied under a static ambient atmosphere. A step size of 0.02° was used for high resolution data. The recording of the XRD patterns was carried out through a 2θ range of 20-80 degrees. XRD data were collected using an Empyrean XRD diffractometer and indexed using the X'Pert HighScore Plus software.

XRD was performed on both crushed calcined nanopowders and sintered pellets to assess phase purity and structural parameters of the probed crystal structures obtained by the diffractometer. Short scans of 30 mins were obtained for the sintered pellets to check for the presence of any glassy phase. Longer scans of 12 h were performed to obtain high resolution data, enabling a more in depth analysis that included obtaining basic unit cell parameters and other structural parameters.

Data analysis of the experimental diffraction patterns of both the calcined nanopowders and sintered pellets were performed on the HighScore plus software using profile peak fitting and comparison to reference files from the ICDD. The matched profiles were then fitted manually to the experimental diffraction patterns. The basic form of unit cell parameters was carried out

to determine the unit cell parameters, volume and theoretical density of the calcined nanopowders and sintered pellets.

3.4. Raman Spectroscopy

Raman spectroscopy is a non-destructive optical scattering technique used for studying molecular vibrations from a sample, e.g. individual metal oxides within the LSCF composition. This occurs by direct interaction or vibration of molecules in the sample caused by the monochromatic incident radiation. A laser generating monochromatic radiation is applied to the sample. For Raman activation, the sample must be under some form of electric dipole polarizability (E) when it is undergoing forms of vibrational motion(α). The level of intensity of the Raman effect that is produced is proportional to the level of polarizability change (μ) as shown in equation (3.9). [136]

$$\mu = \alpha E \tag{3.9}$$

The laser source which is used is dependent on what is being investigated in the sample itself as shown in Figure 3.17. Minimal sample preparation time is required. [136]

When inelastic collision occurs between the molecules of the sample and the monochromatic incident radiation, scattered radiation is formed. The scattered radiation leads to a Raman shift in frequency due to the change in polarizability ($\partial\alpha$) from the induced molecular vibration with respect to a change in the vibrational amplitude (∂Q) being greater than 0 as shown in the equation (3.10) below. This shift can occur from individual metal oxide molecules within the perovskite oxide composition and is dependent on the electronegativity forming the electron cloud around the chemical bond. [136-138]

$$\frac{\partial \alpha}{\partial Q} \neq 0 \tag{3.10}$$

When the scattered radiation frequency is equal to the frequency of incident radiation, this is known as Rayleigh scattering, while when the scattered radiation frequency has a different frequency from the incident radiation, this is known as Raman scattering as shown in Figure 3.17. [136-138]

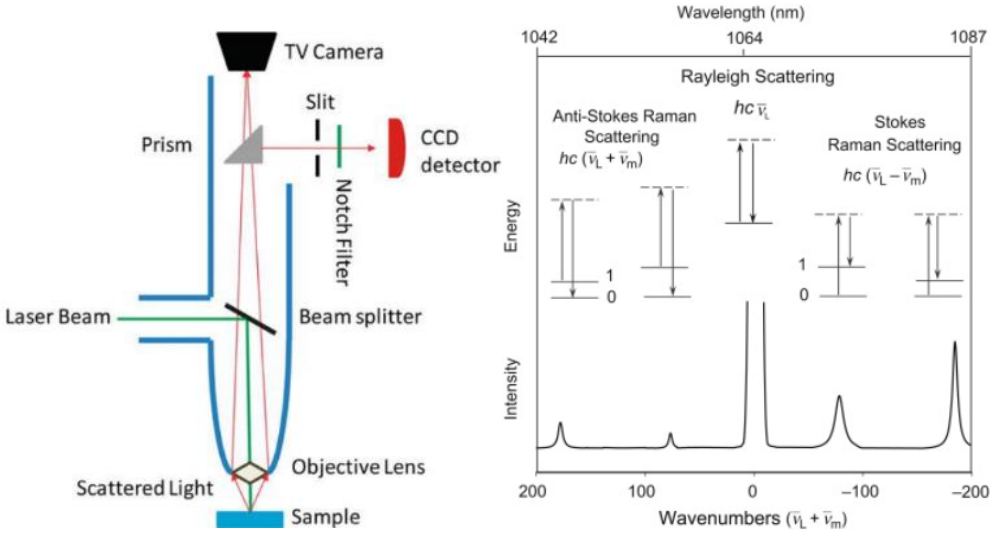

Figure 3.17: Schematic diagram of a Raman microscope (left)[Taken from Do Nascimento, G.M] [138] and (Right) [Taken from Larkin,P] [136] schematic illustration of the Rayleigh scattering and Raman scattering (Anti Stokes and Stokes) where vL represents the upward arrow is the laser excitation frequency (higher in energy compared to the molecular vibrations) while vM represents the downward arrow which is scattered radiation frequency that remains unchanged in Rayleigh scattering but results in higher or lower frequency in Raman scattering.

The Raman spectra were measured using a Horiba Jobin Yvon spectrometer over a range of 100 cm^{-1} – 1000 cm^{-1} at 532 nm incident wavelength with parameters set at 600 lines per mm grating set with a 250 nm hole and 50x objective lens.[6] For the calcined crushed nanopowders of LSCF6428, LPSCF33428 and NSCF6428, 25% power and an acquisition time of 50 s with an average accumulation of 20 was used to obtain Raman spectra. While for the sintered pellets of LSCF6428, LPSCF33428 and LNSCF33428, 10% power and an acquisition time of 100 s with an average accumulation of 40 was used to obtain Raman spectra. The Raman signals were calibrated with respect to the reference signals of a silicon wafer around 520 cm^{-1} prior to Raman analysis.

3.5. Scanning Electron Microscopy / Energy Dispersive X-ray Spectroscopy (SEM/EDX)

SEM equipped with EDX spectroscopy was used to study the homogeneity, agglomeration, average pore size, crystallite size and grain growth for the dried, calcined and sintered material, including how the rare earth dopants influence these parameters for the doped LSCF compositions.

XRD gave average crystallite sizes of below 100 nm for the calcined powders and SEM can provide a greater resolving power of down to 0.5 nm compared to light which is limited to 200 nm at best. The greater resolving power enables details of the topological, morphological features and crystallite size to be investigated in the calcined powders. The SEM can also provide a resolution for three-dimensional imaging of the sample at a higher magnification of around 50 times better than light microscopy. [139-141]

For SEM electrons are accelerated to wavelengths shorter than light. When the primary electron beam penetrates either the surface of a nanopowder or pellet, the electrons scatter from a range of different depths and generate signals which are collected by detectors to produce images as shown in Figure 3.18.[142] The signals that are generated are proportional to the depths at which they occur; secondary electrons (SE) are produced from the inelastic collision events that occur near the surface of the sample which consist of a lower energy of < 50 eV and a resolving power of less than 10 nm. The effect of the lower energy and resolving power of SE provides topological information of the microstructure. Backscattered electrons (BSE) are produced from multiple elastic collisions that are scattered back from a deeper level in the sample and consists of higher energy, primary electrons typically > 50 eV and a lower resolution than SE imaging. The effect of the higher energy of BSE leads to “Z” contrast (or atomic number) imaging due to more or a brighter contrast of scattering from higher atomic number elements. [139-141]

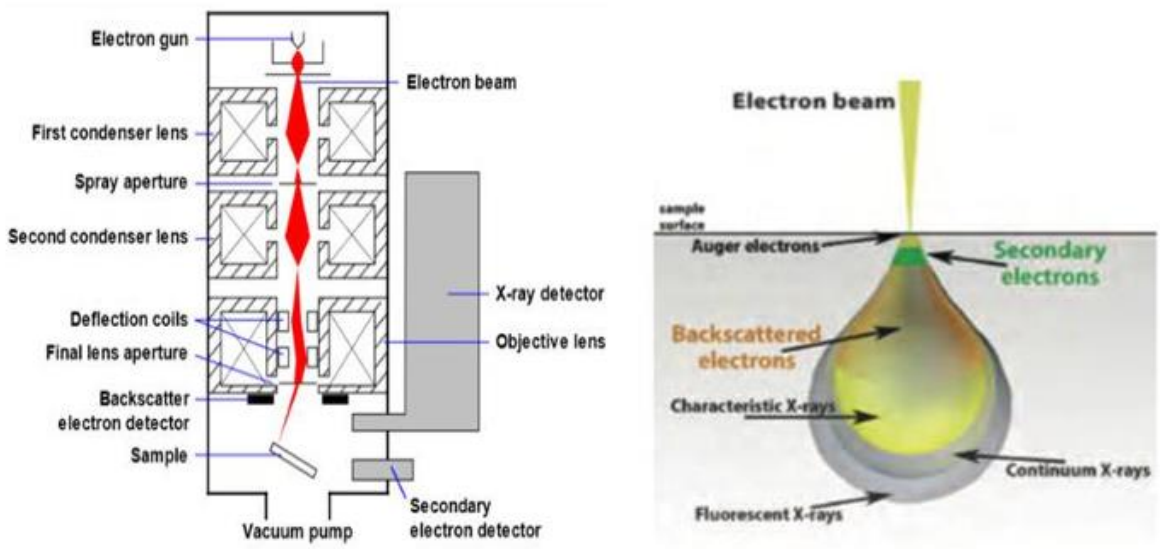

Figure 3.18: Schematic illustration of the SEM microscope (left) and the different penetration levels of the electron with interact with the sample (right) [Taken from Mohammed et.al.][142]

A detector or spectroscopy may be used, EDX works in conjunction with the SEM imaging and can provide a clear elemental mapping of the LSCF and rare earth doped LSCF compositions. This enables homogeneity of the individual metallic elements to be visualised and any significant differences identified, such as deficiency or excess of elemental content. [143]

Figure 3.19: A CitoVac machine used for pellet samples to remove excess air from the epoxy resin

Sintered pellets were mounted in silicon moulds and set in resin (Beuchler EpoThin 2 epoxy 2 resin was used and mixed with EpoThin 2 corresponding epoxy harder in accordion to the manufacturer instructions). The CitoVac is used to control the mass of resin into the silicon moulds and remove excess air to retain the porosity of the sintered pellets as shown in Figure 3.19. It was ground using progressively finer silicon carbide powder down to P240 (ground at 200 rpm by turning it at 180 degrees), P600 (turning it at 90 degrees to remove the original scratches from the P240) and P2500 (for 8 mins).

Prior to polishing to produce a flat surface for imaging and elemental analysis, resin mounted, sintered pellets were washed using deionised water then mild detergent then deionised water and lastly, isopropanol and dried by heater to remove any surface impurities. Polishing was undertaken using Texmet P microcloths and TMetaDi-2 diamond suspensions at 3 micrometres on the Buehler EcoMet 300 grinder/polisher, the ground sintered pellets were polished for 30 s to eliminate scratches, producing a flat surface prior to acid etching to reveal the surface grain structure.

The samples were placed onto adhesive carbon pads fixed to an aluminium SEM stub. Prior to analysis under the SEM, both samples were sputter coated with a 10 nm amorphous carbon layer for calcined nanopowders and a 20 nm layer for sintered pellets, mounted in the epoxy resin. The SEM Hitachi SU8230 high performance cold field emission instrument was used where the accelerating voltage was 2 kV with images being taken both in SE and BSE mode at 5x up to 60,000x magnification.

The pore size distribution for the chosen optimal calcined temperature of the 4 compositions was measured using the ImageJ software and an upper estimate was used for selected areas of the images.

TheTM3030Plus Desktop SEM in conjunction with EDX was used to examine the homogeneity of the chemical composition of both the calcined nanopowders and sintered pellets of the undoped LSCF6428 and rare earth doped LSCF i.e. LPSCF33428, LNSCF33428 and NSCF6428. The voltage used was 15 kV with images being taken both with SE and BSE ranging between 50x and 5000x magnification.

3.6. X-ray Computed Tomography, XCT

XCT is a non-destructive technique by which the penetrating X-rays are used to obtain a series of 2D radiographs of the dried beads and calcined nanopowders from different directions and are compiled into a 3D view. [144-145] For example Wang et. al. have investigated the synthesis of NiO anode nanopowders using this process however, the minimum voxel size that could be used was between 1-3 micrometres. [96]

In this study, dried metal alginate complexes and calcined perovskite metal oxide nanopowders, undoped LSCF6428 and rare earth doped LSCF i.e. LPSCF33428, LNSCF33428 and NSCF6428 were crushed using a mortar and pestle, and approximately 10 mg placed into 3 mm diameter polyamide tubing glued to an aluminium nail. The samples were then mounted and an initial low-resolution scan was conducted in a Versa 620 micro-CT at the University of Manchester, UK. The voltage was 80 kV with a power of 12.5 W, a 4x objective magnification lens was used, with the X ray source and detector distances of 10 mm and 20 mm respectively giving a voxel size of 1.1 μm^3. Due to the differences in agglomeration between the crushed dried and calcined nanopowders, the exposure times were set up differently, for the dried samples 2 s was used while for the calcined samples, 6 s was used to enable 2006 projections to be taken when the sample is rotated by 360^o.

For the sintered LPSCF33428 pellet a pre-preparation was required before undertaking Nano-CT analysis. A Thermo Scientific Helios 5 Laser-Plasma Focused Ion Beam (FIB) microscope was used to prepare the sintered LPSCF33428 pellet into a pillar for CT scanning. Laser sputtering was used to make a trench on the bulk sample and leave a block of 60 x 60 x 200 μm followed by using the focused ion beam to trim it several times down to a 35 x 35 x 100 μm pillar, then the pillar was lifted out and welded on to a pin top using platinum.

The LPSCF33428 pellet was then mounted in the nano scale Zeiss Xradia 810 Ultra, Nano-CT at the University of Manchester, UK. The voltage was 35 kV with a power of 2.5 W, a 20x magnification objective lens was used, with source and detector distances of 1 mm and 1 mm respectively giving a voxel size of 0.128 μm^3 with an exposure time of 1 s to enable 731 projections to be taken when the sample is rotated by 360^o.

The Avizo software was used for the visualise of projections to obtain relevant information in relation to the pore volume fraction and pore size distribution of the dried metal alginate complexes and calcined metal oxide perovskite oxide nanopowders by extracting the sub volume and greyscale thresholding of each of the selected 20 individual grains of both the undoped LSCF6428 and rare earth doped LSCF i.e. LPSCF33428, LNSCF33428 and NSCF6428. The procedure was repeated for the sintered LPSCF33428 pellet at 1000 ^{o}C at the selected 10 different areas with the pellet.

3.7. Brunauer-Emmett-Teller and Barrett-Joyner-Halenda, BET and BJH Analysis

N_2 physisorption analysis was used to determine porosity of the rare earth doped LSCF composition in comparison to the undoped LSCF6428. The experimental method known as gas physisorption was used, where the equilibrium Van der Waals forces between the gas molecules and solid particles at a given pressure occurs.[146]

The BET model (equation 3.12) is an extension of the Langmuir model (equation 3.11) (which considers only a monolayer of gas molecules interacting with the solid surface where q = number of adsorbed molecules, α = surface area occupied by one molecule, N = the Avogadro's number and M = molecule's molecular mass) which calculates the specific surface area (S) of the adsorbed molecules by considering multilayer adsorption, where W = quantity of adsorbed gas, Wm = quantity of absorbed gas by monolayer, P and Po = adsorbate equilibrium and saturation pressures respectively and C = BET constant.[146-147]

$$S = \frac{q*\alpha*N*10^{-20}}{M} \qquad (3.11)$$

$$\frac{1}{w[\frac{P}{P0-1}]} = \frac{C-1}{WmC}(\frac{P}{P0}) + \frac{1}{WmC} \qquad (3.12)$$

While the BJH model (equation 3.13) is used for calculating the pore size distribution following N_2 adsorption. The model works through the estimation of the capillary condensation in which the mesopores and micropores are filled with multilayers of gas molecules under saturation gas pressure to determine the radius (r) of internal pores that gas molecules are adsorbed on.

$$r = \frac{2\gamma V}{RT\ In\ (\frac{P0}{P})} \qquad (3.13)$$

Where γ = liquid – vapour tension , V = molar mass of the liquid , R = gas constant, T = temperature in Kelvin and P/Po = relative pressure of the liquid (where P and Po are the actual and saturated vapor pressures of adsorbate respectively).[147]

Before specific surface area and adsorption/desorption measurements were undertaken, the empty glass tubes were cleaned using mild detergent and deionised water before being placed in an ultrasonic bath to remove any impurities to limit contamination. After that, the glass tubes were rinsed with a combination of acetone and water and left to dry in an oven.

The empty glass tubes and their stoppers were weighed, before putting around 20 mg of the sample into the glass tube and weighing it again before degassing the samples. The degas was done in two stages; first at 80 ºC for 10-15 minutes and then increased to around 200 ºC for 3 hours, to remove any organic molecules and moisture, and then cooled for 10-15 minutes. The sample in the glass tubes with the stoppers were then weighed again to obtain the final mass of the sample after the degas procedure.

The BET specific surface area and adsorption/desorption measurements were taken using approximately 20 mg of the crushed calcinated nanopowders using the micromeritics TriStar surface area and porosity analysis under liquid nitrogen at 77 K and were left overnight to ensure completion.

3.8. Density Measurements

To be able to obtain bulk density measurements of sintered pellets, two different methods were conducted due to differences in how the displacement of the pellet in liquid is conducted. The Geometrical method uses a dry method using the equation below by measuring the area and volume of the pellet to obtain the relative density.[148] The Archimedes method used is based on the Archimedes principle in states that the buoyant force exerted on the object immersed in a fluid is equal to the mass of the fluid that the object displaces. This principle is the simplest method used for calculating the relative density of the sintered pellet. [149]

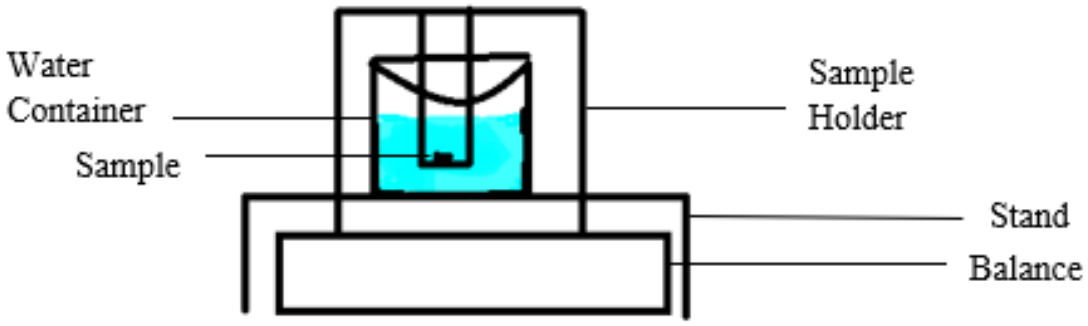

Figure 3.20: Archimedes method set up

The main relative density (ρ) equation (3.14) can be shown below which can be adapted, where m = mass of the pellet, V= volume of water

$$\rho = \frac{m}{V} \qquad (3.14)$$

The Geometrical relative density equation (3.15) for the sintered pellet is shown below, where m = mass of the dry pellet after being sintered r = radius of the pellet after being sintered, t = thickness of the pellet after being sintered.

$$\rho = \frac{m}{\pi r^2 t} = \text{g/cm}^3 \qquad (3.15)$$

The calculation for the Archimedes relative density equation (3.16) for the sintered pellet is shown below, where W_1 = weight of the sintered pellet in air, ρw = density of water used as fluid (water at RT is 0.997 g/cm^3), W_2 = wet weight of the sintered pellet (in water).

$$\rho = \frac{W1\rho w\,(g)}{W1\,(g) - W2(g)} = \text{g/cm}^3 \qquad (3.16)$$

The thickness shrinkage equation (3.17) gives a measure of the shrinkage behaviour of the pellet on sintering, assuming that it is isotropic as shown below.

$$Thickness\ Shrinkage = \frac{difference\ before\ and\ after\ sintering\ pellet}{before\ sintering\ pellet} \qquad (3.17)$$

3.9. Focused Ion Beam-Scanning Electron Microscope, FIB-SEM

The SEM objective lens is limited to observing the external shape and surface of the pellet. Hidden information of the inner structure of the pellet can be obtained by making a series of thin slices through the sample, imaging the surface after each slice and then reconstructing the imaged volume. For the FIB-SEM, an energetic ion beam erodes the pellet surface to expose an area or section of the varied grain structure and the pores of the pellet itself to allow 3D

reconstruction.[150-151] This approach is known as “slice and view” or serial sectioning where milling and imaging of the pellet occurs sequentially throughout the procedure as shown in Figure 3.21.

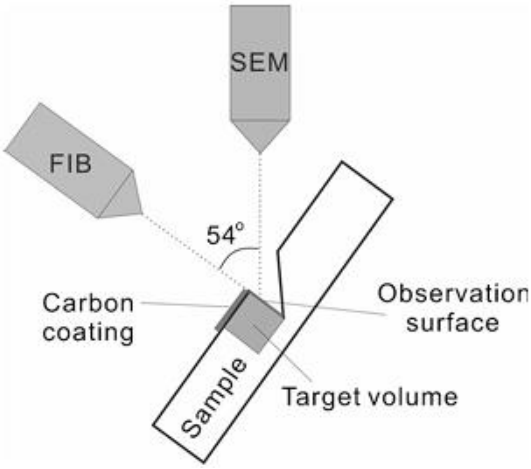

Figure 3.21: Schematic illustration of FIB-SEM set up where the FIB and SEM mills away and images respectively the sample. [Taken from Meffert et.al.][150]

Prior to FIB-SEM, the LSCF6428 and LPSCF33428 pellets are prepared by grinding manually using silicon carbide paper which gradually decreases roughness from Grade [P600], [P1200], [P2500] and grinding at 250 r.p.m. contra-rotation. Then, both the LSCF6428 and LPSCF33428 pellet are polished manually using the Textmet C- 6 mm for 5 min, Trident 3 mm for 4 min, Trident 1 mm for 2 min at 250 r.p.m. contra-rotation. Final polishing was done using the (automated) Automatic Chemonet Mastermet 0.06 um Colloidal Si, for 10 min with a 150 r.p.m. contra-rotation, head 30 r.p.m., contra-force 10 N. The polished sintered LSCF6428 and LPSCF33428 pellets which were resin mounted were etched with 50 mL deionised water + 3 mL HCl + 3 drops HF for 100 s.

The FIB-SEM was undertaken with milling at a depth of 20 nm in thickness and then imaging. The LPSCF33428 serial sectioning was conducted on the Tescan AmberX Plasma FIB-SEM. The LSCF6428 serial sectioning was conducted on the FEI Helios G4 CX DualBeam FIB-SEM.

3.10. Superconducting Quantum Interference Device with a Vibrating Sample Magnetometer, SQUID-VSM

A superconducting quantum interference device (SQUID) - vibrating sample magnetometer (VSM) known as the SQUID-VSM in the Condensed Matter Physics Group, Bragg Centre for Materials Research, Leeds was used to assess magnetic properties of the calcined and sintered LSCFs. This is because a) second phases were identified by other techniques such as XRD and because the spin states of Co and Fe may affect whether a phase is paramagnetic, ferromagnetic, ferrimagnetic or antiferromagnetic. SQUID-VSM is a superconducting magnet device which has better sensitivity than a room temperature VSM as outlined in the Table 3.4 below. [152-154]

Table 3.4: Comparison between the SQUID and VSM [152-154]

SQUID (suitable for temperature dependent magnetization curve)	**VSM (suitable for field dependent magnetization curve)**
Highly sensitive to ultralow magnetic signals up to 5 $x10^{-4}$ (T).	Costly and low sensitivity device due to bulky electromagnets
Signal to noise ratio improved with noise thresholds nearly 3 ft $Hz^{-1/2}$	Time resolution of the signal is low for signal to noise ratio
Quantitative magnetometry with 1 x 10^{-8} electromagnetic units making it useful for studying weak magnetic materials but it can only detect magnetic flux.	Useful for detecting magnetic properties such as magnetic moments from cobalt/iron nanoparticles across a board range of fields at room temperature

VSM is based on Faraday's Law and the fact that mechanical vibrations of a magnetic sample are picked up by conducting coils as a change in flux. The change in flux leads to the vibrator receiving a signal from across a wide range of magnetic fields to obtain what is known as a field dependent magnetization curve of a sample, and providing measurement of parameters such as saturation magnetization M_s, coercive field H_c and remanent magnetization M_r. While the SQUID involves a superconducting loop consisting of Josephson junctions attached to

superconducting pick-up coils. Along with a superconducting shield, it enables the motion of the sample to be slow, keeping the magnetic field constant and suppressing the influence of external magnetic fields.[153-157] SQUID can be classified into two types; low temperature (LT) and high temperature (HT) superconductors where the SQUID are immersed in liquid helium (4.2 K) or liquid nitrogen (77 K) respectively (this is dependent upon the transition temperature of the selected superconducting material used in the SQUID). For this work, a liquid helium SQUID is used for the SQUID-VSM as shown in Figure 3.22 below.[157]

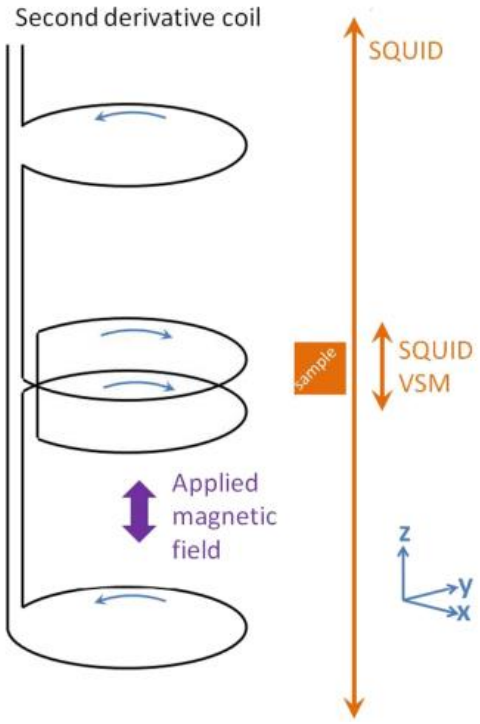

Figure 3.22: Schematic pickup coil in the SQUID and SQUID VSM systems used, arrows indicate the direction of the current. The orange box indicates the vertical centre of the sample (z-axis). The vertical arrows indicate the direction the sample travels during the measurement. [Taken from Dennis et. al.] [158]

Prior to the measurements, approximately 10 mg of the chosen crushed, calcined nanopowders and sintered pellets of LSCF6429, LPSCF33428, LNSCF3428 and NSCF6428 were measured using a Sartorius electronic balance to a precision of +/- 0.001 g. Then the samples were placed into a capsule and sealed with white tape prior to being put into the brass sample holder. The SQUID-VSM was checked to ensure the liquid helium level was at 17 L or above and the pressure below 15 Torr and to ensure no build-up of ice and water vapour, then analysis was carried out on the temperature and field dependent magnetization of each sample.

The field dependent magnetization curve (magnetic field against magnetization) is used to determine how the rare earth dopants of LSCF influence the magnetic behaviour compared to the undoped LSCF. The crushed, calcined nanopowders were measured at 2 K and 300 K while the crushed sintered pellets were measured only at 300 K. This was done by setting the parameters as follows for various temperature ranges: below 10 K (2-10 K) – temperature ramp range set to 1 K/min; 10 to 100 K – temperature ramp range set to10 K/min; 100 to 300 K – temperature ramp range set to 20 K/min with a field ramp rate of 500 Oe. To be able to obtain M_s, H_c and M_r, and compensate for the trapped flux in the superconducting coils, subtract 30 Oe to the applied magnetic fields on the first half of the measurement from 20000 Oe to -20000 Oe and then add 30 Oe to the second half (from -20 000 Oe to 20 0000 Oe) to obtain the true magnetic field values and divided by 1000 to obtain *k*Oe.

The temperature dependent magnetization curve (temperature against magnetization) is used to provide additional information in relation to the formation of the secondary phase, α -Fe_2O_3, and the spin states of cobalt ions in the rare earth doped LSCFs compared to the undoped LSCF. The measurements were over a temperature range between 2 K and 400 K, at 10 mT and 2 T plus a 100 Oe field is applied to enable demagnetisation to depopulate the spin bands and populate the spins to obtain what is known as the zero field cooling (ZFC) minus the field cooling (FC) or ZFC-FC curve.

3.11. Electrical Impedance Spectroscopy

SOFCs are assumed to operate in a quasi-steady state as described in a study by Wu et.al. through the use of modelling to predict the performance efficiency of the SOFC. [159]

Impedance spectroscopy is a non-destructive method for separating out the different contributors to a sample's total electrode polarisation (from a mixed ion and electron conductor such as LSCF). Properties such as the charge transfer, oxygen adsorption and dissociation of the oxygen reduction reaction (ORR) for the LSCF/YSZ and rare earth doped LSCF/YSZ can be understood and the losses described. For spectra to be obtained, the impedance of a material is measured as a function of the frequency of an applied alternating current (AC). For a fuel cell, the frequency has been studied over a wider range typically between 10kHz for high frequency to 10mHz for low frequencies to be able to obtain the typical processes that take place from the ORR of a cathode component.[160]

As described above, the half-cell fabrication using the cathode slurry ink painted over a YSZ pellet creates an electrode-electrolyte interface (cathode/YSZ) to undergo what is known as symmetrical cell testing. When the half-cell undergoes an electrochemical reaction, it leads to charge separation occurring, where the electrons accumulate at the electrode side while the ions accumulate at the electrolyte side, where the electrolyte is behaving like a capacitor (double layer interface) as shown in Figure 3.23 below. This is critical in understanding the individual ORR processes that are typically undertaken for a MIEC cathode.[161]

To obtain the impedance measurements, an Ametek Solarton Analyser was used, and data were analysed using the Modulab XM MTS software. The analyser was connected to a tube furnace and the sintered cathode slurry printed and sintered on both sides of the YSZ pellet, which was painted with sliver paint to ensure conductivity of the half-cell, which was mounted into a quartz rig and connected to Pt wires. It was heated at a between 450 ^{o}C to 800 ^{o}C in 50 ^{o}C intervals. The frequencies used were set between 1 MHz and 0.01 Hz with an absolute amplitude of 10 mV and average over 3 cycles.

The Modulab software fitted a model to the experimental data that can be used to calculate parameters such as activation energy and area specific resistance (ASR) (the equations for these fittings are described in Chapter 8). The models used are described in Chapter 8 and are dependent on both the operating temperatures used and the nature of the rare earth elements in the doped LSCFs, as these influence the contributors of the total polarisation of the ORR for the cathode component.

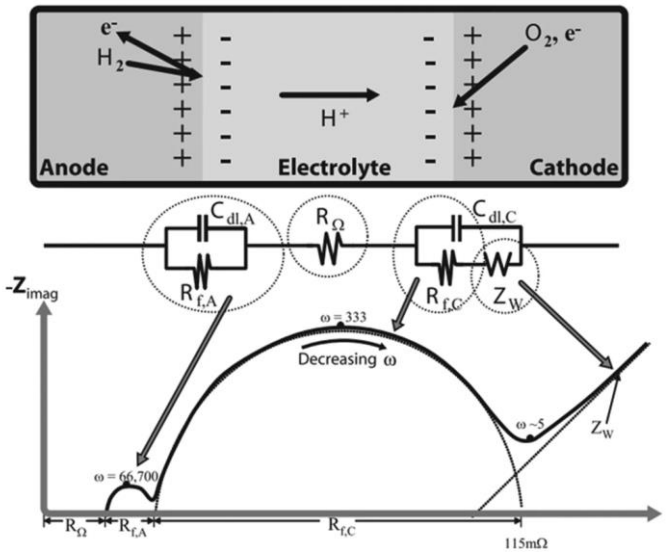

Figure 3.23: A typical schematic of an equivalent circuit model for a fuel cell where C_{dl} represents the capacitor and R_f represents kinetic resistance of the electrochemical cell of the charge double layer formation (electrode-electrolyte), R_0 represents the ohmic resistance from the electrolyte, Z_w is the Warburg circuit element for modelling the diffusive nature of the fuel cell. [Taken from Pandey et.al.] [161]

The equivalent circuit model constructed from the Modulab software in relation to the half-cell is used to outline the detailed kinetics of the ORR for the cathode electrode and consists typically of R_0 and $R_{||CPE}$ (which represent a system showing a depressed semicircular impedance arc passing through the origin). R_0 contributes to the ohmic losses that are omitted from the total electrode polarisation equation.[160-161] The Warburg element, in addition to R_0 and $R_{||CPE}$ is used only for the NSCF6428/YSZ and has been used for investigating Nd doped MIEC cathodes such as BSCF6428.[76] This is to address the diffusive nature of additional electrons from the Nd^{3+} which is a non-diamagnetic element compared to the La element in the undoped LSCF6428.

Results and Discussion Section

Chapter 4 – Synthesis and Characterisation of Calcined $La_{0.6}Sr_{0.4}Co_{0.2}Fe_{0.8}O_{3-\delta}$

4.1. Microstructure Characterisation of the metal-alginate complex of LSCF6428

For the novel sodium alginate sol gel method of $La_{0.6}Sr_{0.4}Co_{0.2}Fe_{0.8}O_{3-\delta}$ synthesis (discussed in Chapter 2), it is essential to investigate how the ion exchange mechanism between the chelating agent, sodium alginate and the metallic nitrates functions when under magnetic stirring. The general reaction mechanisms which are undertaken during the ion exchange between each metallic salt nitrate and the polysaccharide molecule, sodium alginate (Na-ALG) prior to thermal treatment can be shown in the following chemical equations below (4.1-4.4), in which the chemical formula of the sodium alginate is Na-ALG= $C_6NaH_7O_6$ and x = number of water molecules. [105-109][162-166]

$$La(NO_3)_3.\,6H_2O + 3(Na-ALG) \rightarrow (La^{3+}-ALG)_3.\,xH_2O + 3NaNO_3 \quad (4.1)$$

$$Sr(NO_3)_2 + 2(Na-ALG) \rightarrow (Sr^{2+}-ALG)_2 + 2NaNO_3 \quad (4.2)$$

$$Co(NO_3)_2.\,6H_2O + 2(Na-ALG) \rightarrow (Co^{2+}-ALG)_2.\,xH_2O + 2NaNO_3 \quad (4.3)$$

$$Fe(NO_3)_3.\,9H_2O + 3(Na-ALG) \rightarrow (Fe^{3+}-ALG)_3.\,xH_2O + 3NaNO_3 \quad (4.4)$$

As shown above, the equations describe how the effects of the ion exchange can lead to Na^+ situated in the alginate macromolecule being replaced by polyvalent metal ions to form cross linked metal alginates as referred to by Zaafarany, Hassan and Khairou. [105-107][109][164]. The coordination of the alginate with a metal cation (M), is due to the carboxylic acid from the alginate binding to the metal cation to form a three-dimensional egg box-like structure and the chemical formula then becomes $C_{12}H_{14}O_{11}M$. [35]. Zaafarany and Hassan have both studied a range of metal ions with different valences cross linked in the alginate structure that behave differently in relation to electrical properties of a final heat treated metal oxide.[108][163]

Therefore, investigation was carried out here on a crushed metal-alginate complex using a scanning electron microscope with energy dispersive spectroscopy (SEM-EDX) to determine

the effect of ion exchange on the shape and size of the metal-alginate bead complex formation prior to its thermal decomposition.

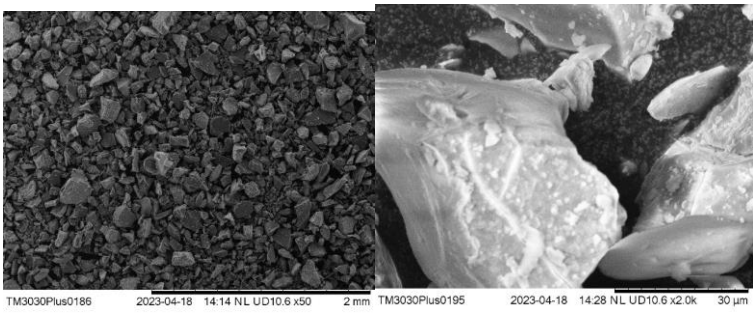

Figure 4.1: SEM images of the metal-alginate complex of LSCF6428 precursors. Left (Low magnification) and Right (High magnification) of crushed metal-alginate beads

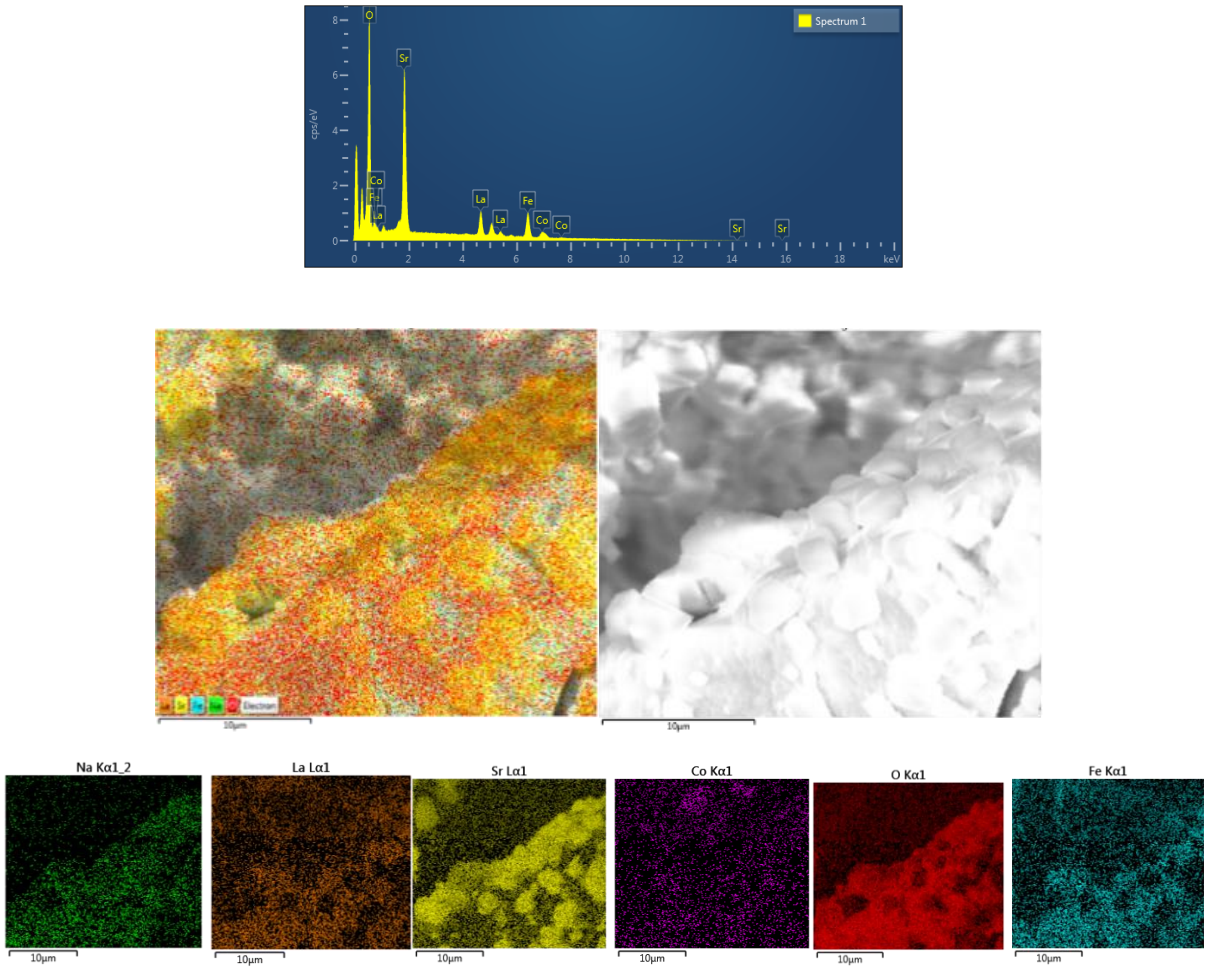

Figure 4.2: (Above) SEM image and EDX spectrum of metal-alginate complex of LSCF6428 precursor (Below) showing the presence of all the key metal elements for LSCF6428 with elemental maps showing some Sr segregation but otherwise a homogenous distribution of the elements.

From the SEM images in Figure 4.1, the effect of the ion exchange between the sodium alginate and the metal cations can be observed. An appearance of a smooth metal-alginate complex bead even when crushed to different size particles is seen throughout (Figure 4.1). From a higher magnification view, the size of the metal-alginate beads is estimated to be around 20 μm prior to thermal decomposition (Figure 4.1). Elemental analysis by EDX suggests that all the multivalent metal cations, La, Sr, Co and Fe have been successfully exchanged into the alginate structure (Figure 4.2), consistent with other reports by Zaafarany and Hassan. [105][107-108][109][166]. The elemental maps indicate that the La, Fe, Co and Na are homogenously distributed throughout a bead, whereas Sr and O are somewhat concentrated and clustered. The distribution could be due to the difference in bond strengths of each of the metal cations with the alginate gel, particularly those of the Sr and O ions. Sr^{2+} is known to have the highest ionic radius of 1.44 Angstroms and a stable valence of 2+ as shown in Table 4.1. This would affect the coordination chemistry and charge density when the Sr^{2+} binds with the alginate (mainly consisting of oxygen ions) unlike the other multivalent metal cations which have either a small valence and larger ionic radius. [166-167][168]

Table 4.1: Elements of the LSCF6428 with Valences and Ionic Radii [167]

Elements of LSCF6428	**Valence**	**Ionic Radius (Å)**
Lanthanum (La)	+3	1.36
Strontium (Sr)	+2	1.44
Cobalt (Co)	+2 +3	0.545 0.53
Iron (Fe)	+3	0.645
Oxygen (O)	-3	1.40

However, from two-dimensional characterisation alone it is difficult to tell the precise distribution between the alginate and the metal cations. Notably sodium alginate has been classified as more porous than calcium and cobalt alginate, but this porosity is not that evident by SEM alone suggesting it may be internal to the particles.[169]

4.2. Thermal Characterisation of the LSCF6428

Thermal analysis has been carried out to determine the calcination temperature requirement for homogenisation of the LSCF6428 precursor when undertaking the 3 wt% sodium alginate sol

gel method. DTG/TGA/DSC are used to observe the thermal decomposition of the metal alginate complex and the (assumed) formation of a perovskite oxide nanopowder as shown in Figure 4.3.

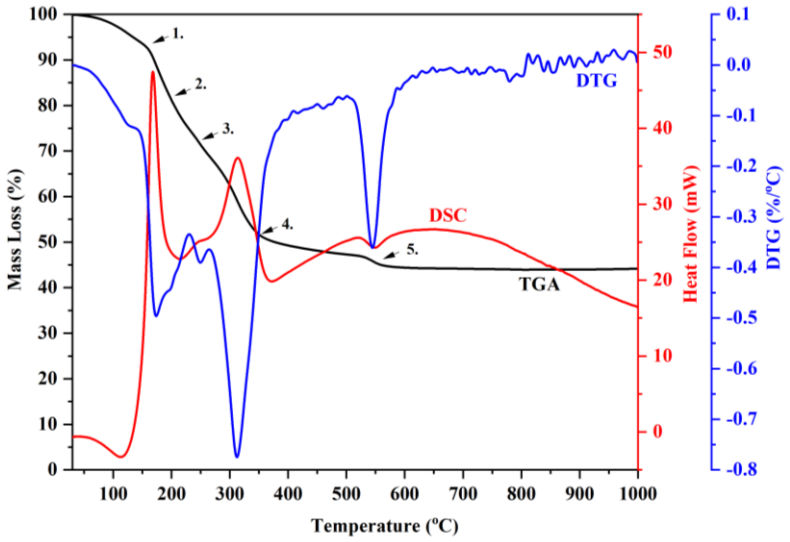

Figure: 4.3: DSC/TGA/DTG analysis of LSCF6428 in 3 wt% of alginate. Five decomposition steps are marked with numbered arrows in the plot.

Table 4.2: TGA of 3 wt% LSCF6428 alginate analysis

Stages	**TGA Temperature Range, °C**	**Weight Loss, %**
1	38.6 – 118.7	5.7
2	127.9 – 163.7	19.8
3	177.3 – 282.9	6.0
4	321.3 – 430.2	21.2
5	546.8 – 591.4	2.1
Final Mass		44.1

Table 4.3: DSC of 3 wt% LSCF6428 alginate analysis

Steps	**DSC Temperature Peak, °C**	**Types of Peaks**	**Integral (J/g)**
1	116.1	Endothermic	-
2	167.5	Exothermic	172
3	245.3	Exothermic	3.9
4	312.8	Exothermic	261
5	554.2	Endothermic	-20.1

Table 4.4: DTG of 3 wt% LSCF6428 alginate analysis

Stages	DTG Peak, ºC	Weight Loss, %
1	128.6	-0.12
2	173.4	-0.5
3	249.3	-0.39
4	312.5	-0.77
5	544.7	-0.36

From the thermal analysis, thermal decomposition of the metal alginate complex of LSCF6428 occurs in five stages of mass loss (%) at increasing temperatures until a constant mass residue is reached by ~ 600 ºC, as shown in Figure 4.3 and Tables 4.2-4.4. Thermal behaviour of the alginic acid has been previously investigated to determine when each specific processes occur i.e. dehydration, decomposition and residue formation and at what temperature in accordance with the TGA/DSC analysis until a final (assumed) single-phase perovskite oxide is produced above 600 ºC. [165]

The first stage of decomposition takes place at around 100 ºC, typically involving the loss of water as indicated from the small mass loss peak from the DTG profile. Around this temperature, the process of dehydration of the metal-alginate complex of LSCF6428 occurs through the removal of excess/adsorbed water molecules from the metal-alginate complex resulting in a mass loss that is typically less than 10% of the total original mass as referred to in Table 4.1.

The chemical equations (4.5-4.8) below describe the endothermic process of water removal from the metal-alginate complex as shown in the DSC peak located at 116.1 ºC. [15] [105-109][164][166]

$$(La^{3+} - ALG)_3.xH_2O \rightarrow 3La - ALG + xH_2O \quad (4.5)$$

$$(Sr^{2+} - ALG)_2.xH_2O \rightarrow 2Sr - ALG + xH_2O \quad (4.6)$$

$$(Co^{2+} - ALG)_2.xH_2O \rightarrow 2Co - ALG + xH_2O \quad (4.7)$$

$$(Fe^{3+} - ALG)_3.xH_2O \rightarrow 3Fe - ALG + xH_2O \quad (4.8)$$

The second and third stages of thermal decomposition of the metal-alginate complex occur after the dehydration process, i.e. at temperatures above 100 ºC as shown by all the DSC/TGA/DTG profiles where the largest mass loss occurs (%). This can be described as

oxidative decomposition. This is due to the initial breakdown of the metal-alginate complex with a sudden mass loss of around 20% as shown by the steepness of the TGA curve and the reactions by can be explained by the chemical equations below (4.9-4.12). [15] [105-109][164][166] [170-173] The sharp mass loss is caused by the rapid breakdown of the partially ionic bonds between the metallic cations and the functional groups in the alginate (carboxylic acid and hydroxyl acid). The exact temperatures as seen in the temperature range are related to the chelation strength in accordance with the valence of the metal cations consisting of a combination of 2^+ and 3^+.[166][168] The DSC exothermic peak in this region has a temperature of 167.4 ºC, the peak consistently has a heat flow value at around 50 mW, and the main process is the formation of intermediate compounds (carbonate (CO_3)/ oxalate (C_2O_4)) and the bulk formation of by-products of carbon dioxide and water. Sr is an alkali earth metal and is the only metal cation in the LSCF composition to have a stable 2^+ oxidation state as discussed by Zaafarany et.al.[31] That resulted in the formation of strontium carbonate compared to the rare earth, La and transition state elements, Co and Fe. [105][108][171][173]

$$2LaC_{18}H_{21}O_{17} + O_2 \rightarrow La_2(C_2O_4)_3.nH_2O + xCO_2 + yH_2O \quad (4.9)$$

$$SrC_{12}H_{14}O_{11} + O_2 \rightarrow SrCO_3 + xCO_2 + yH_2O \quad (4.10)$$

$$CoC_{12}H_{14}O_{11} + O_2 \rightarrow CoC_2O_4 + xCO_2 + yH_2O \quad (4.11)$$

$$FeC_{18}H_{21}O_{17} + O_2 \rightarrow FeC_2O_4.nH_2O + xCO_2 + yH_2O \quad (4.12)$$

$$La_2(C_2O_4)_3.nH_2O \rightarrow La_2(C_2O_4)_3 + nH_2O \quad (4.13)$$

$$FeC_2O_4.nH_2O \rightarrow FeC_2O_4 + nH_2O \quad (4.14)$$

Stage three of the decomposition is indicated clearly by the DTG curve with a mass loss % of below 10%. This process is where the metastable, hydrated La and Fe oxalate lose the additional water as shown in equations (4.13-4.14) above and this completes the formation of the anhydrous oxalates. [170][173] The presence of the intermediate anhydrous oxalates and carbonate is due to the full rupture of the metal-alginate complex. It typically alters the mass loss during that stage as it occurs below the temperature (300 ºC) that enables the compounds of carbonate and oxalate to decompose further and form stable metal oxides [15]

At stage 4 of the decomposition, there is a second significant mass loss of more than 15% at a temperature at 312.8 ºC, as indicated by another large exothermic DSC peak in the profile as

well as the large mass loss DTG peak (Figure 4.3). That is likely to lead to the major phase transformation to compounds of lanthanum dioxycarbonate and iron oxide. The carbon monoxide formed from the La and Fe as shown in the chemical equations (4.15-4.16) when under an air atmosphere is expected to be oxidised by oxygen to form carbon dioxide as shown in the chemical equation 4.17.[170][173] It is at this stage when the remaining G and M blocks from the polysaccharide alginate are fully oxidised from the anhydrous oxalates with the exception of cobalt. [166][168] This is due to the bridging oxygen between the blocks that are broken down and released (requiring higher activation energy than simply for the exchange of metal ions), resulting in the bulk formation of by-products of carbon dioxide. [166] The by-products are released by the initial process of the thermal breakdown of linkages of the weaker covalent bonds such as G-G, M-M and G-M. Malektaj et.al. report the breaking of the linkages occurring at temperatures above 250 ºC.[168] Ultimately, this decomposition is the alginate undergoing pyrolysis of its monosaccharide units and new stable metal-oxide bonding occurs as described in the final stage. [168] Simultaneously, the LSCF metal oxide compound (assumed to be a perovskite) begins to form where the TGA curve begins to level out and become constant. [15] [105-109][164][166]

$$La_2(C_2O_4)_3 + O_2 \rightarrow La_2O_2CO_3 + 3CO + CO_2 \quad (4.15)$$

$$FeC_2O_4 + O_2 \rightarrow 2FeO + 3CO + CO_2 \quad (4.16)$$

$$2x\ CO + xO_2 \leftrightarrow 2x\ CO_2 \quad (4.17)$$

At the final stage, the formation of metal oxides that enable the production of LSCF6428 occurs as shown from equations (4.18-4.21), at a temperature near 600 ºC. Here, there is only a small mass loss indicating the loss of excess oxygen from the LSCF6428. This is also indicated by a small endothermic peak in the DSC profile.[15] The metal oxides formed as shown in chemical equations (18-21) are what is expected from when thermal decomposition takes place in air conditions.[170-173] There is no further loss of mass above this temperature indicating the complete synthesis of a stable metal oxide/s with a mass residue of 41.1%.[15] The residue obtained is significantly higher for 3 wt% alginate-LSCF6428 compared to 4 wt% alginate-LSCF6428 as reported by the Leeds Alginate Group.[15] To determine how the mass of alginate has affected the mass residue of 41.1%, a comparison between the 4 wt% alginate-LSCF6428 is carried out as shown in Figure 4.4 and Tables 4.5-4.7.

$$La_2O_2CO_3 \rightarrow La_2O_3 + 3CO_2 \quad (4.18)$$

$$SrCO_3 \rightarrow SrO + CO_2 \quad (4.19)$$

$$3CoC_2O_4 + 2O_2 \rightarrow Co_3O_4 + 6CO_2 \quad (4.20)$$

$$2FeO + O_2 \rightarrow \alpha\text{-}Fe_2O_3 \quad (4.21)$$

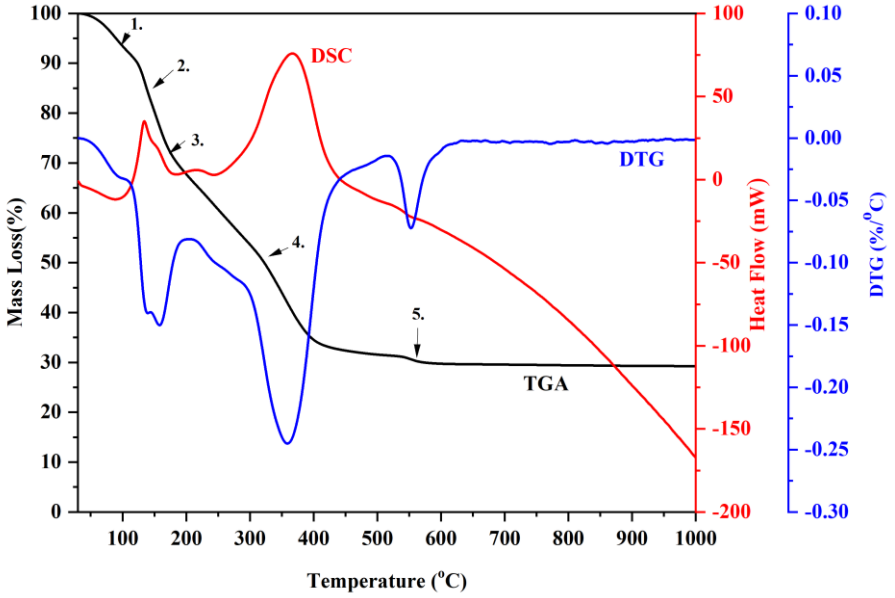

Figure 4.4: DSC/TGA/DTG analysis LSCF6428 calcination in 4 wt% alginate gels. Five decomposition steps are marked by numbered arrows in the plot.

Table 4.5:TGA of 4 wt% LSCF6428 alginate analysis

Stages	**TGA Temperature Range, °C**	**Weight Loss, %**
1	36.5 – 96.8	7.7
2	109.3 – 200	26.6
3	227.2 – 254.1	9.8
4	321.4 – 420	23.5
5	523.2 – 576.8	2.1
Final Mass		29.9

Table 4.6: DSC of 4 wt% LSCF6428 alginate analysis

Stages	**DSC Temperature Peak, °C**	**Types of Peaks**	**Integral (J/g)**
1	96.8	Endothermic	-205
2	134	Exothermic	335.8
3	217.5	Exothermic	-
4	367.8	Exothermic	2230
5	443.4	Endothermic	-

Table 4.7: DTG of 4 wt% LSCF6428 alginate analysis

Stages	DTG Peak ^{o}C	Weight Loss, %
1	91.5	-0.03
2	139.5 and 158.2	-0.14 and -0.15
3	255.2	-0.10
4	358.7	-0.25
5	552.7	-0.07

It is noticeable from stage 4, as shown in Figures 4.3 and 4.4, that the amount of alginate affects the heat flow significantly at ~ 300 ^{o}C, as for 4 wt% LSCF6428, the DSC peak is broader and higher in heat flow value, at about 75 mW as shown in Figure 4.4, compared to 3 wt% LSCF6428 where the DSC peak is narrower and sharper and has a value of 50 mW as shown in Figure 4.3. The total energy required for the complete decomposition towards stable metal oxides using 4 wt% alginate is 8.6 times greater than the 3 wt% alginate.

The explanation behind this is the difference in the activation energy required to break completely the strong ionic bonds between the M-O within the alginate structure [166][168]. A similar finding was investigating in the preparation of $La_{0.7}Sr_{0.3}Co_{0.5}Fe_{0.5}O_3$ through the combustion synthesis where different propellants (urea, glycine, citric acid and sucrose) were used to determine how each influence the mass of residue and temperature requirement for decomposition. From the findings, urea and sucrose enabled more control of the combustion reaction which lead to high purity and crystallinity of the perovskite LSCF phase.[174]

The greater quantities of alginic acid and sodium salt within the alginate solution could have led to greater quantities of carbon dioxide and water needing to be burned off for 4 wt% compared to the 3 wt%. Simultaneously, the intermediate compounds formed from the previous stage also decompose still resulting in the formation of the thermodynamically stable metal oxides. [105-109][164][166] The smaller % in final mass residue as recorded in Tables 4.5 and as shown in Figures 4.4 and 4.3 for 4 wt% (29.1 %) compared to 3 wt% alginate (44.1 %) respectively is due to greater quantities of volatiles being burned off in the former. A similar effect occurred where a study was conducted by varying the alginate concentration in a hydroxyapatite/alginate composite; it was found that with the composite compared with pure alginate, a greater residue mass loss was obtained.[175] The purpose of using 3 wt% sodium

alginate sol gel method compared to 4 wt% was to achieve a higher quantity of residue given the difficulties the sol gel method has with producing material at a large scale. However, despite varying the alginate concentration, no further loss of mass residue occurred above 750 ^{o}C. It is difficult to tell from thermal analysis alone how temperature affects the purity, crystal symmetry and metal ion incorporation into a single perovskite LSCF6428 metal oxide phase [15] and the following analysis will explore that.

4.3 Structural Characterisation of calcined LSCF6428 nanopowders

To confirm the phase purity and crystal symmetry of the LSCF6428, the nanopowders were calcined at different temperatures and then investigated by room temperature XRD. The results are shown in Figures 4.5 and 4.8. Basic whole pattern fitting (HighScore software) was used to examine the experimental diffraction patterns within the LSCF6428.[176]

The peak fitting will address the peak splitting of the rhombohedral crystal symmetry by whole pattern fitting of the experimental diffraction peaks with a reference pattern.[176-177] When comparing with the reference pattern of the cubic phase, there is an absence of peak splitting throughout the diffraction pattern peaks.[177] That, therefore, will provide a guide in determining the temperature at which a potential dual phase crystal composite of the LSCF6428 perovskite transitions towards a single-phase, rhombohedral crystal structure. [176]

This conflicts with previous work on 4 wt% LSCF6428 carried out by the Leeds Alginate group where all the diffraction peaks were labelled with cubic Miller indices using only the ICDD rhombohedral file without any demonstration of Bragg peak splitting at the cubic (220) peak at 68^{o} 2θ. There were also impurity phases of strontium carbonate present and similar trends have also occurred in other work on calcination of LSCF6428 [15]

For this work, four calcination temperatures, 700, 750, 775 and 800 ^{o}C were used and powder diffraction patterns were analysed by whole pattern fitting to obtain information on the crystal structure/s in relation to lattice parameters, crystallite size and the presence of any second phases. This information is summarised in Tables 4.8-4.9. Thus, the analysis may be used to identify the optimum calcination temperature. That is because the presence of any small impurities is unwanted, especially strontium carbonate $SrCO_3$ (due to its insulator properties) as this can have a severe effect on the electrochemical performance of LSCF6428, given its MIEC nature, and so hinder its use for IT-SOFCs.[178]

The exact choice of calcination temperature is therefore important as it influences the phase purity of the crystal structure of the final LSCF6428. A purity of more than 90% is typically required for lab scale powder production of the perovskite phase. Single phase purity of an IT-SOFCs cathode, $SrFe_{0.5}Ti_{0.5}O_3$ has been investigated in a similar manner. [179]

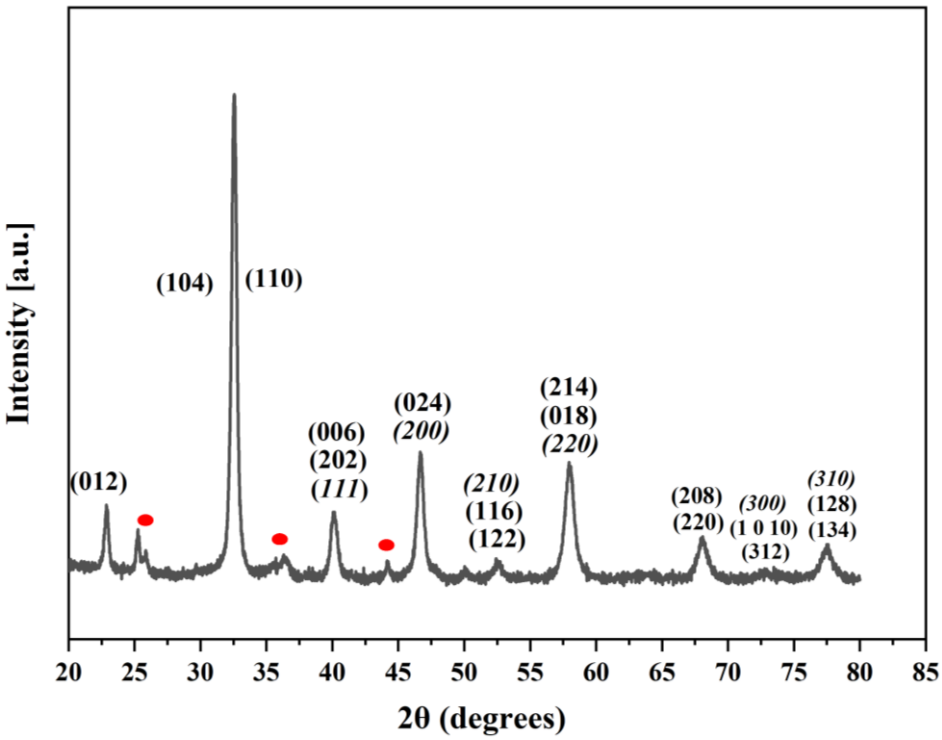

Figure 4.5: XRD patterns of 3 wt% crushed LSCF6428 nanopowders calcined for 2 h at temperature of 700 °C (grey line), indexed to ICDD, 04-017-2448 – R3c normal font and indexed to ICDD 04-023-4431- Pm3m italic font. Red circles indicate $SrCO_3$ peaks present (indexed to ICDD 01-078-4340)

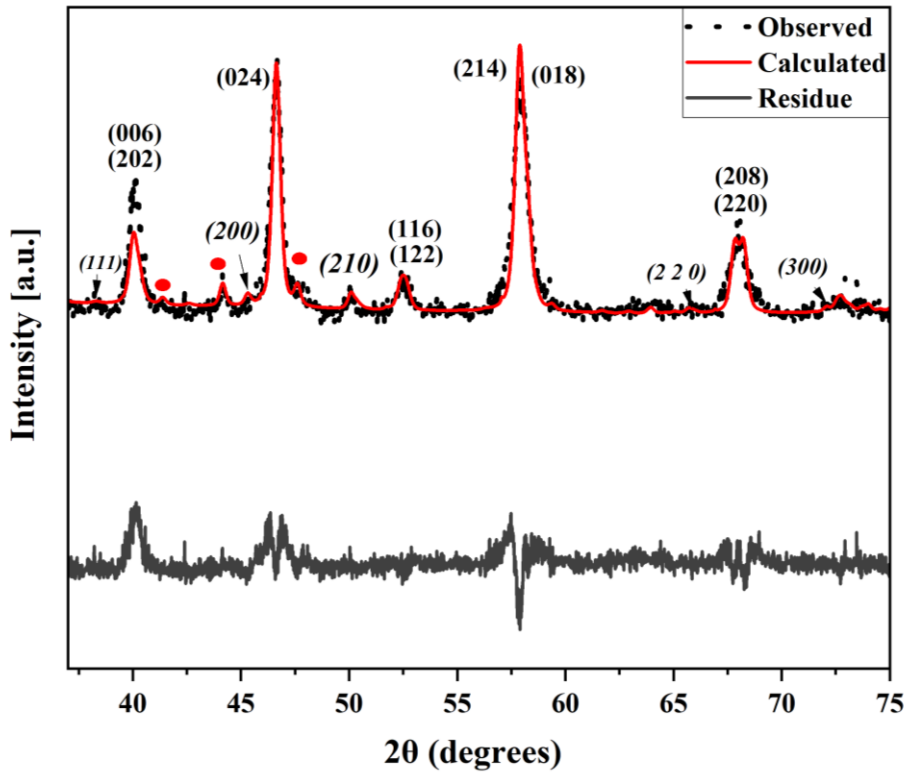

Figure 4.6: Whole pattern fitting of the cubic structure of the 700 ºC crushed calcined LSCF6428 nanopowder – peaks are indexed using ICDD 04-023-4431 and red circles indicate $SrCO_3$ peaks present (indexed to ICDD 01-078-4340)

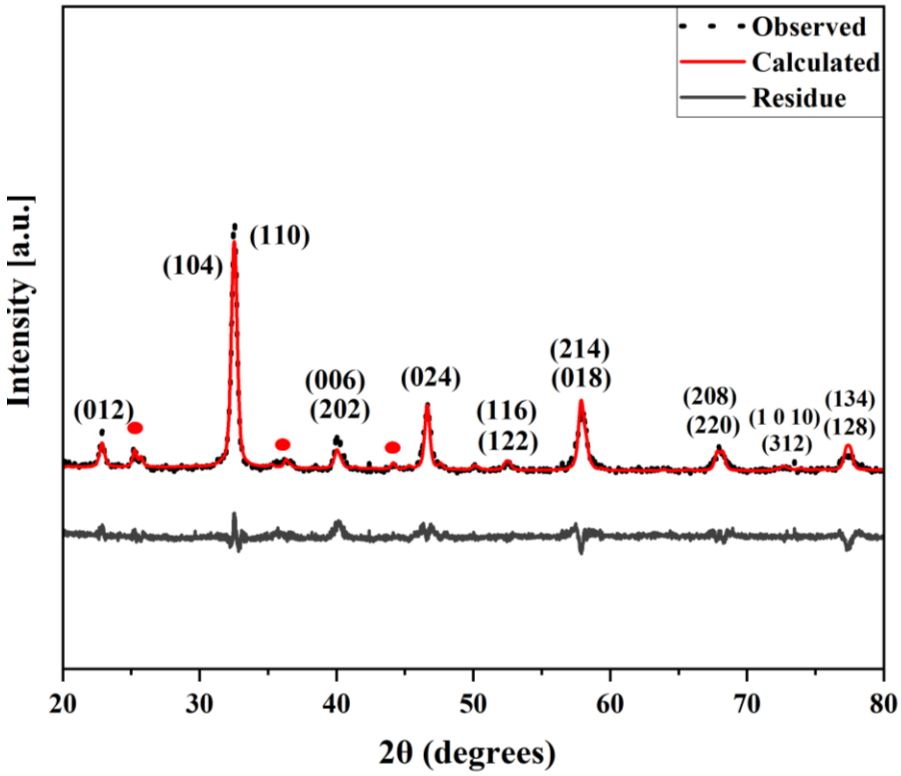

(a.)

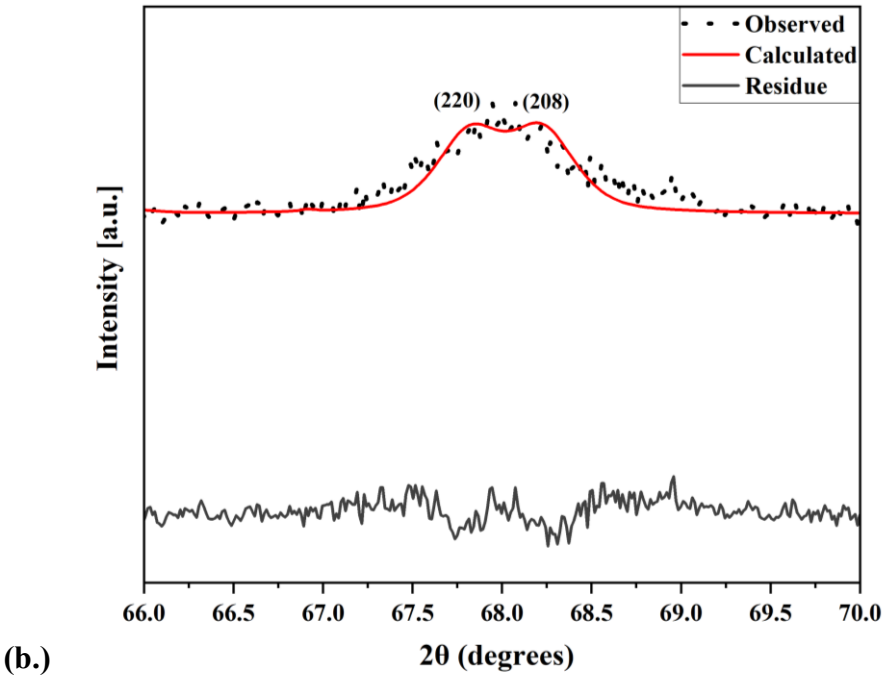

Figure 4.7: a) Whole pattern fitting of the rhombohedral structure of 700 ºC crushed calcined LSCF6428 nanopowder with experimental data (black line), reference file (red line), residue (grey line) – peaks are indexed using ICDD 04-017-2448 and red circles indicate $SrCO_3$ peaks present (indexed to ICDD 01-078-4340) **b**) Zoom in of the fitting of the rhombohedral structure of the 700 ºC crushed calcined LSCF6428 nanopowder, indicating potential peak splitting at the (220)/(208) peak 68º 2θ.

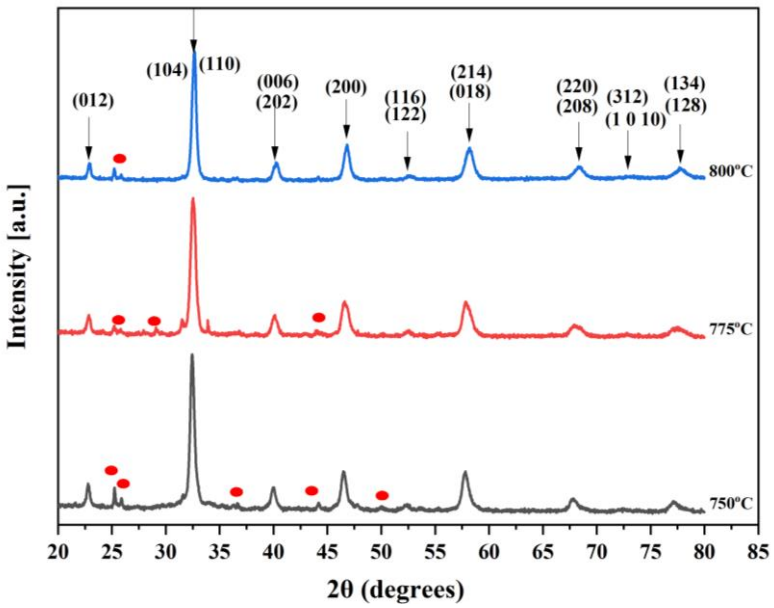

Figure 4.8: XRD patterns of 3 wt% crushed LSCF6428 nanopowders calcined for 2 h at temperatures of 750 ºC (grey line), 775 ºC (red line) and 800 ºC (blue line). (indexed to ICDD, 04-017-2448- R3c), Red circles indicate $SrCO_3$ peaks present (indexed to ICDD 01-078-4340)

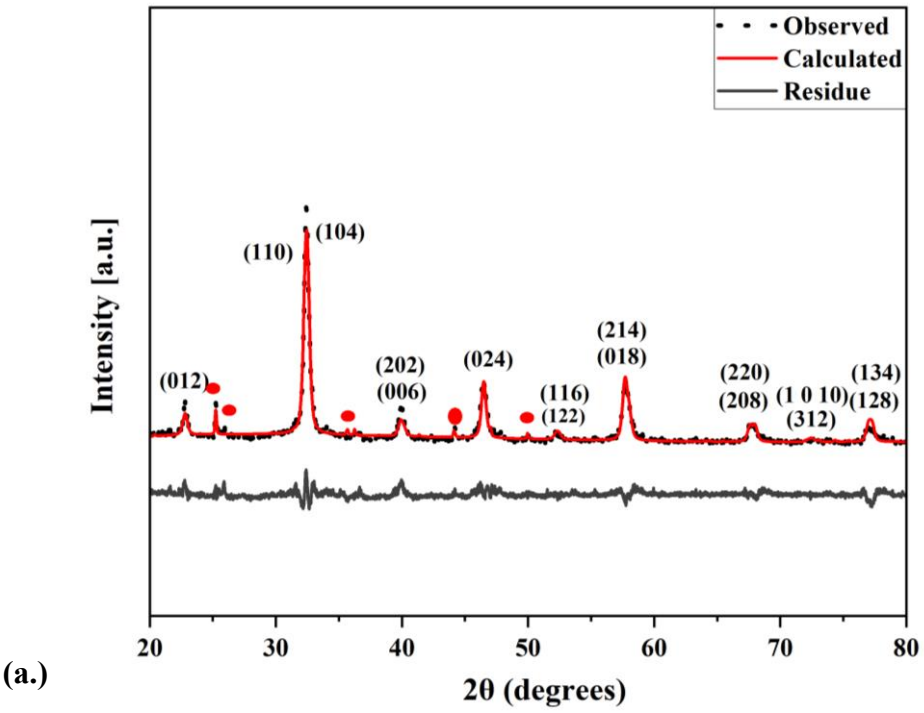

(a.)

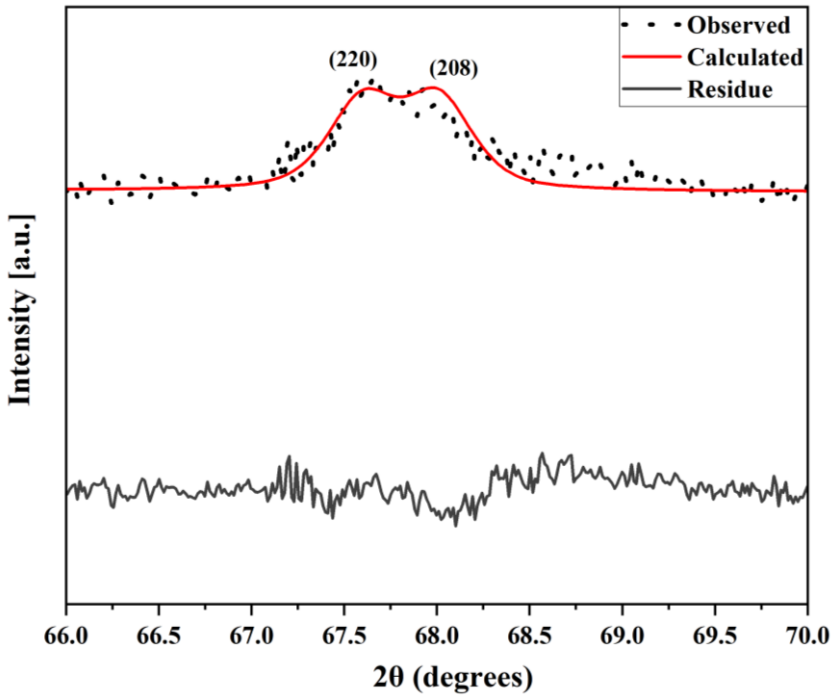

(b.)

Figure 4.9: a) Whole pattern fitting of the rhombohedral structure of 750 ºC calcined crushed LSCF6428 nanopowder with experimental data (black line), reference file (red line), residue(grey line) – peaks are indexed using ICDD 04-017-2448 and red circles indicate $SrCO_3$ peaks present (indexed to ICDD 01-078-4340) **b**) Zoom in of the whole pattern fit of the rhombohedral structure of 750 ºC crushed calcined LSCF6428 nanopowder indicating peak splitting located at (220)/(208) 68º 2θ.

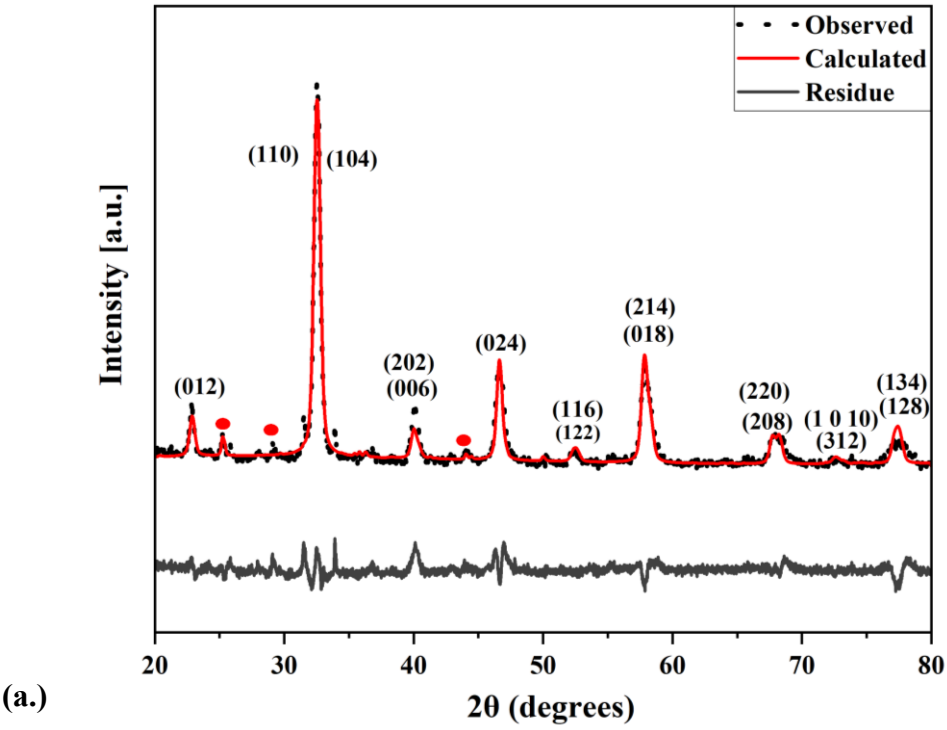

(a.)

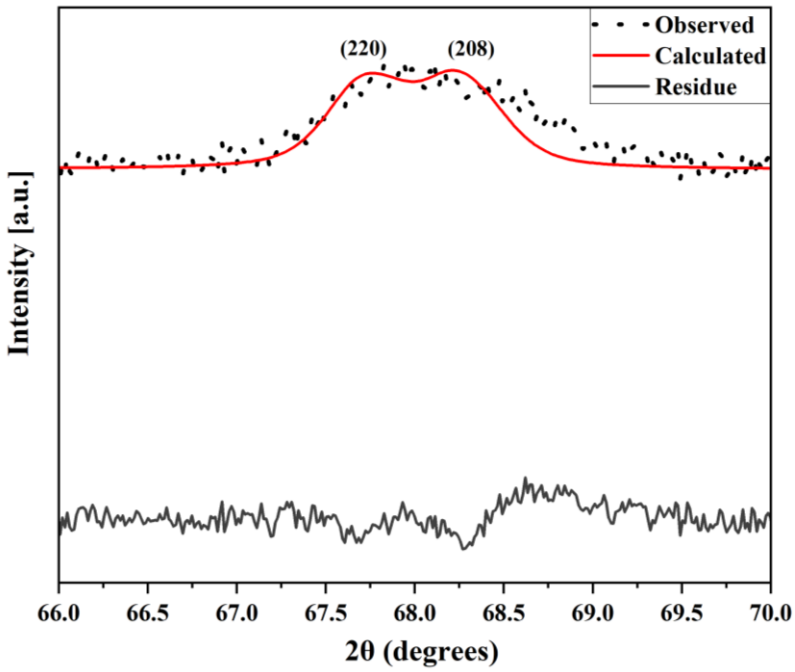

(b.)

Figure 4.10: a) Whole pattern fitting of the rhombohedral structure of 775 °C crushed calcined LSCF6428 nanopowder with experimental data (black line), reference file (red line), residue(grey line) – peaks are indexed using ICDD 04-017-2448 and red circles indicate $SrCO_3$ peaks present (indexed to ICDD 01-078-4340) **b)** Zoom in of the fitting of the rhombohedral structure of 775 °C crushed calcined LSCF6428 nanopowder indicating peak splitting located at (220)/(208) 68° 2θ.

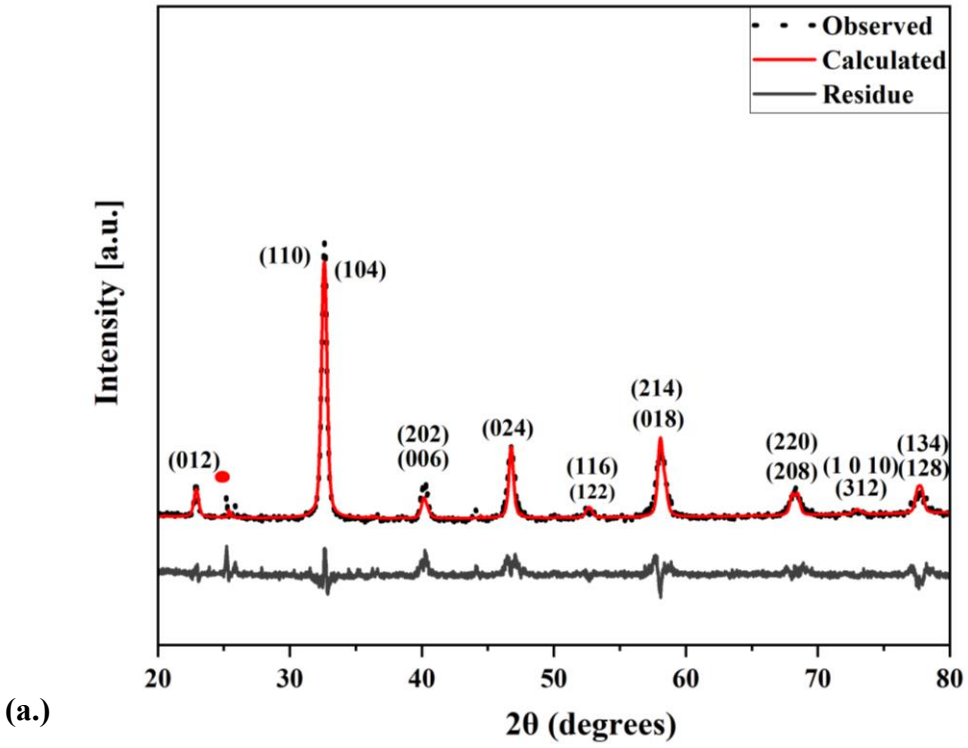

(a.)

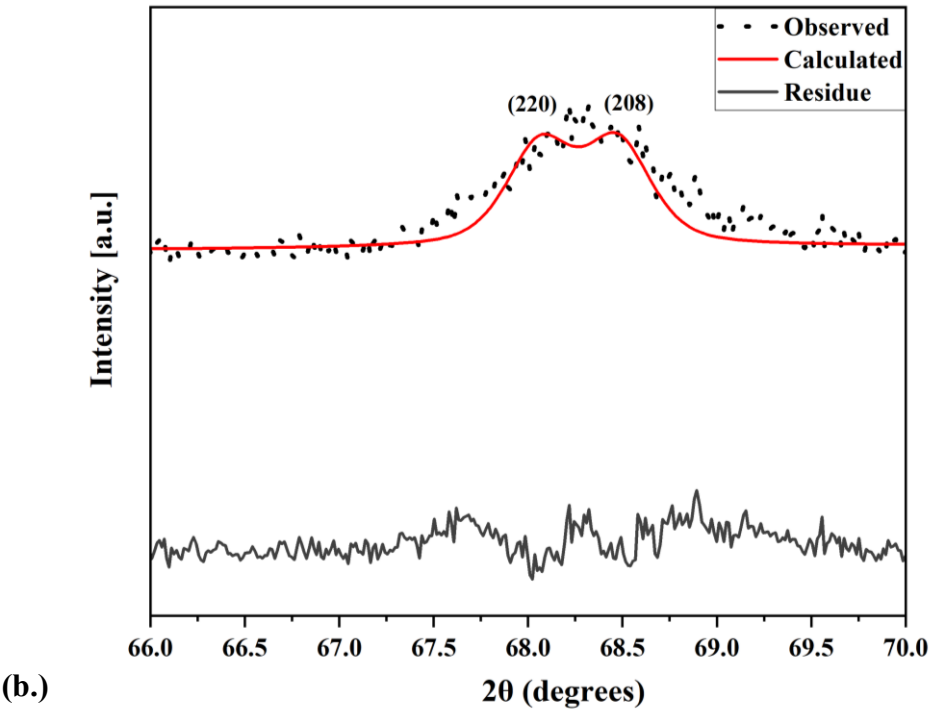

(b.)

Figure 4.11: a) Whole pattern fitting of the rhombohedral structure of 800 ºC crushed calcined LSCF6428 nanopowder with experimental data (black line), reference file (red line), residue(grey line) – peaks are indexed using ICDD 04-017-2448 and red circles indicate $SrCO_3$ peaks present (indexed to ICDD 01-078-4340) **b)** Zoom in of the pattern fitting of the rhombohedral structure of 800 ºC crushed calcined LSCF6428 nanopowder indicating peak splitting located at 68º 2θ.

At the calcined temperature, 700 ºC the XRD diffraction patterns were fitted to a mixture of the cubic and rhombohedral structures (ICDD) (Figures 4.5-4.7). By 750 ºC, the crystal symmetry transitions from the dual phase, cubic-rhombohedral structure to the single pure rhombohedral structure (Figure 4.8- 4.9). At temperatures higher than 750 ºC, only the rhombohedral phase is observed (Figures 4.8,4.10-4.11). Up to this point, there has been limited in-depth work revealing the presence of a dual phase cubic/rhombohedral $La_{0.6}Sr_{0.4}Co_{0.2}Fe_{0.8}O_3$ by XRD [15][83][86] [180-183] however as this mixture transitions to a single rhombohedral phase when calcining above 750 ºC this finding will not be explored any further here.

All the patterns for material calcined at 750 ºC and above (Figures 4.8-4.11), show reasonable fitting of the rhombohedral reference patterns to the experimental diffraction data. That is confirmed by the quantitative fitting values shown in Table 4.8 (the quality factor values for the fits are all below 10%). The fitting of the calcined LSCF6428 for this work using the alginate sol gel method reveals the R_{wp}, values to be slightly lower by nearly twice the value compared to prior work of the calcined LSCF6428 synthesised using the solid-state method. [180] The difference between the values is the choice in synthesis method that could potentially be affecting the homogeneity thus the phase purity of the final nanopowder.

It can be shown from Figure 4.8 and Table 4.8 that there is a clear trend with the (%) perovskite phase purity as the calcination temperatures increases. The highest perovskite oxide phase content of 96 % was achieved at 800 ºC and only one strontium carbonate peak was present. A similar trend occurred in past work such as investigating the relationship between the calcination temperature and presences of secondary phase in the LSCF6428 system. [15]

Table 4.8: Whole pattern fitting of structural parameters and average crystallite size and phase purity of rhombohedral (R3c) LSCF6428 at different calcination temperatures of 750, 775 and 800 ºC ((R_{wp}(%)) weighted pattern, (R_{exp} (%)) expected pattern and goodness of fit (GOF))

Temperature (^{o} C)	Mean Crystalline Size(nm)	R_{exp} (%)	R_{wp} (%)	GOF	Mirco-Strain (%)	Perovskite Phase Purity (%)
750	21.7	5.470	4.621	0.844	0.45	83.5
775	16.4	2.289	4.174	1.823	0.30	84.0
800	22.7	6.462	5.506	0.852	0.25	96.3

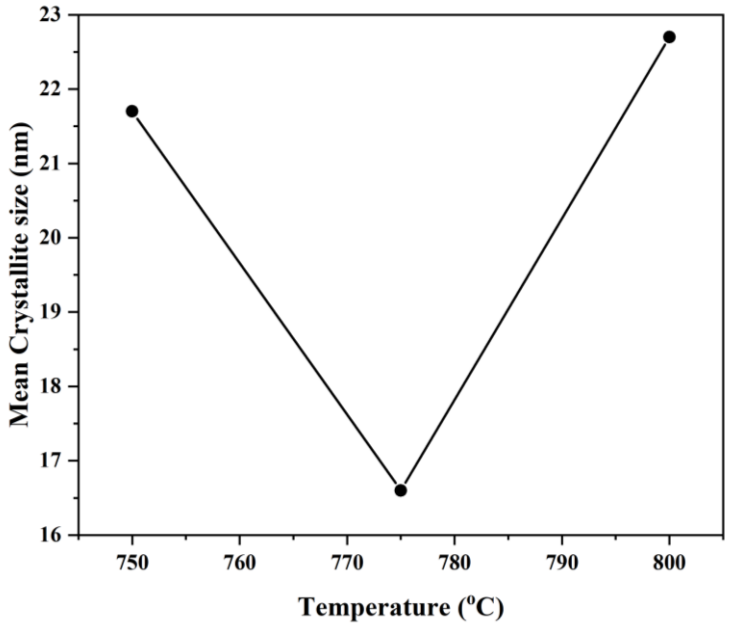

Figure 4.12: Temperature (ºC) vs Mean crystallite size (nm) of the LSCF6428 perovskite oxide where the black dots refer to as the experimental data.

The purity of the nanopowder is also known to affect the mean crystallite size. A study by Zhou et al., found a clear trend; when the %wt cellulose used increased, both the $SrCO_3$ impurity and crystallite size for LSCF6428 decreased.[184] For each calcined nanopowder for this work, the crystallite size was calculated using the Scherrer equation (as ref to in Chapter 3) obtained from all the diffraction main perovskite peaks. It can be seen from Figure 4.12 that there is no clear trend between the crystal size and calcination temperature. Overall, a nanoscale crystalline size is retained at 800 ºC and the highest phase purity (%) of the LSCF6428 also occurs at 800 ºC as seen from Table 4.8, indicating the near complete formation of the LSCF6428 crystal

structure. To get a better overview into the formation of the crystal structure across the temperature range tested, the lattice parameters of the LSCF6428s at different calcination temperatures are shown in Table 4.9 and these were obtained from the whole pattern fitting for the LSCF6428 nanopowders.

Table 4.9: Unit Cell dimensions (rounded to three decimal places), Theoretical Density and Volume (rounded to two decimal places) of rhombohedral (R3c) LSCF6428 at different calcination temperatures of 750, 775 and 800 ºC

Temperature (^{o} C)	**a (Å)**	**b (Å)**	**c (Å)**	**Volume (Å)**	**Theoretical Density (g/cm^3)**
750	5.543± 0.015	5.543	13.470	358.48± 3.4	10.82± 0.105
775	5.539± 0.016	5.539	13.430	356.93± 4.7	10.87± 0.105
800	5.515± 0.025	5.515	13.382	351.50± 4	11.03± 0.11

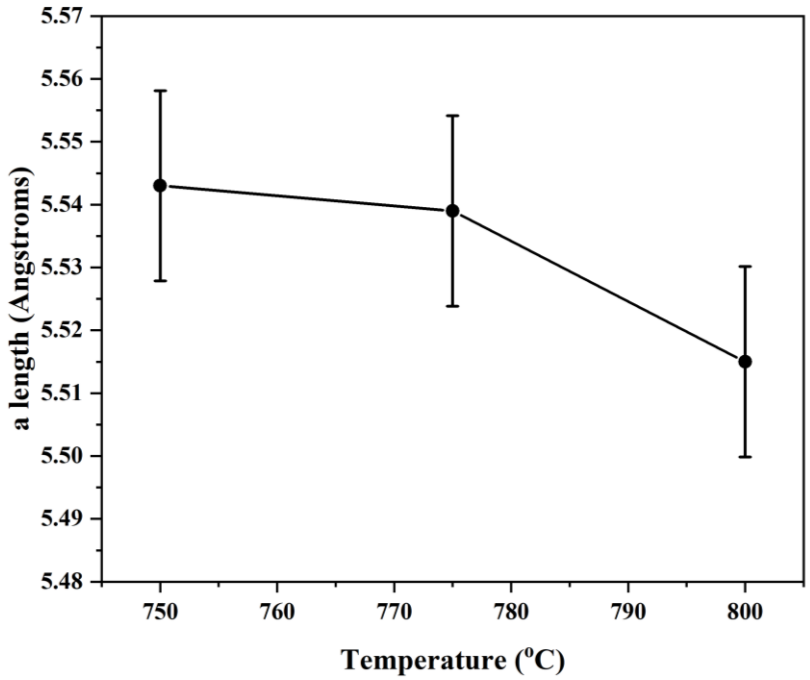

Figure 4.13: Temperature (ºC) vs Rhombohedral lattice parameter, "a" length (Angstroms) of the LSCF6428 perovskite oxide where the black dots refer to as the experimental data points along with the error bars.

Table 4.9 shows that the lattice parameters of LSCF6428 change as the calcination temperature is increased. Increasing the calcination temperature from 750 ºC onwards, predominantly

lowers the lattice parameter "a" length of the perovskite lattice structure as shown in Figure 4.13. The decrease in the lattice parameter can be referred to a study by Mineshige et.al. where a Sr deficiency trend of the chemical composition, LSCF6428 was being investigated; as the Sr deficiency increased, the "a" length lattice parameter increases.[185] Therefore, it suggests that as the calcination temperature increases, the strontium content of the chemical composition, LSCF6428 increases and this is also consistent with the decreasing amount of $SrCO_3$ second phase in the XRD patterns (since the number of $SrCO_3$ peaks drops in the XRD patterns as calcination temperature increases) as shown in Table 4.8 and Figure 4.13. The lattice parameter "a" length also influences the volume to density relationship of the LSCF6428 samples.

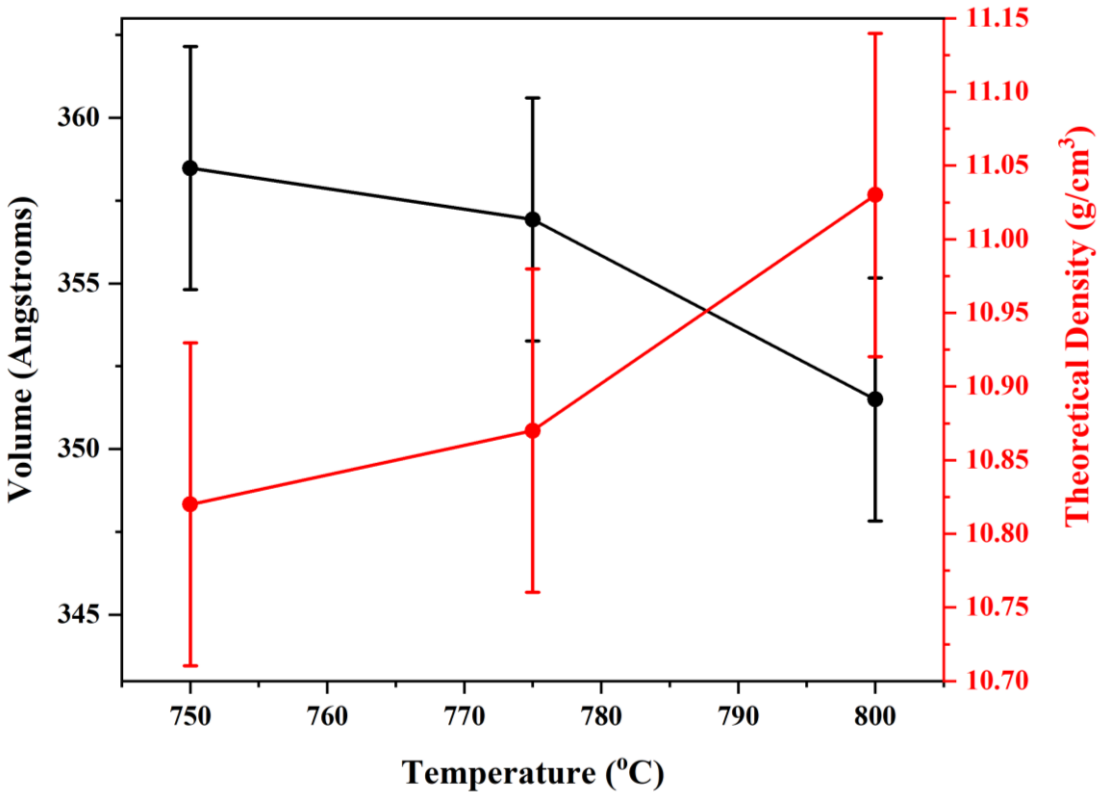

Figure 4.14: Temperature (°C) vs Rhombohedral Volume (Angstroms- black line with error bars at black dots refer to as experimental data points) and Theoretical Density (g/cm^3- red line with error bars at red dots refer to as experimental data points) of the LSCF6428 perovskite oxide

Table 4.9 shows there is an inverse relationship between the volume and the density when the crystal symmetry of the LSCF6428 is single phase at a calcination temperature of 750 °C and above. As referred to by Waller et.al. the trend in the decrease in "a" length lattice parameter decreases the lattice volume, as the calcination temperature increases, which results in the

change in density as shown in Figure 4.14.[186] That is similar to a study by Kostogloudis et. al. where the chemical composition of the A site deficient, LSCF6428 was being investigated by modifying its strontium content and examining its effects upon the crystal symmetry and its parameters. It was found that as the Sr deficiency decreases there was an increase in the unit cell volume of the crystal perovskite oxide structure because of the increase of the a length lattice parameter. [187] When the temperature was greater than 950 ºC, there was a complete decomposition of the $SrCO_3$ (similar to this study) decreasing the A site deficiency thus decreasing both the "a" lattice parameter and unit cell volume.[186]

The trends that are shown in Figures 4.13 and 4.14 are related to the single-phase purity of the perovskite lattice. Ismail et. al. [182] also show strontium deficiencies at the A sites of the LSCF6428 are affected by the calcination temperature. When the calcination temperature goes beyond a transition temperature of 700 ºC, the strontium is incorporated into the perovskite lattice, resulting in an absence of the strontium carbonate impurity phase from the diffraction pattern. There is also the sudden change in "c" length value after the transition temperature which is caused by the increased density of the LSCF6428 from the crystal structure changes to rhombohedral, along with the decrease in unit cell volume as referred to here in Table 4.9.

The structural tolerance factors and reference diffraction patterns of the cubic and rhombohedral reference phases of LSCF6428 are given in Table 4.10. The value of the tolerance factor calculated for the rhombohedral phase fitted to the calcined patterns above 750 ºC is 0.975 and is in close agreement to the calculated value of 0.979 in the literature. [188] Taken together these data suggest there is a transition calcination temperature of 750 ºC above which a stable perovskite oxide has been formed.

Table 4.10: Structural Tolerance Factors of the LSCF6428 corresponding with the space group (Pm-3m – cubic – 04-023-4431) and (R3c – Rhombohedral-04-017-2448)

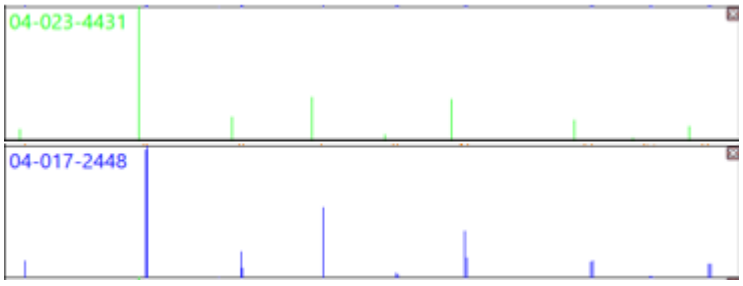

Space group	Tolerance Factor
Pm-3m	1
R3c	0.975

4.4 Raman Spectroscopy of the calcinated LSCF6428 nanopowder

X ray diffraction is not sensitive to the metal oxide vibration bonds and the distortion of the anion lattice of the perovskite oxide. The use of another method is therefore required, to get an insight into some fine structural details of the LSCF6428 perovskite oxide, such as the octahedral distortion and oxygen motion. [189] Raman spectroscopy is a suitable method, as was used by earlier studies on the $LaCoO_3$ rhombohedral structure.[190]

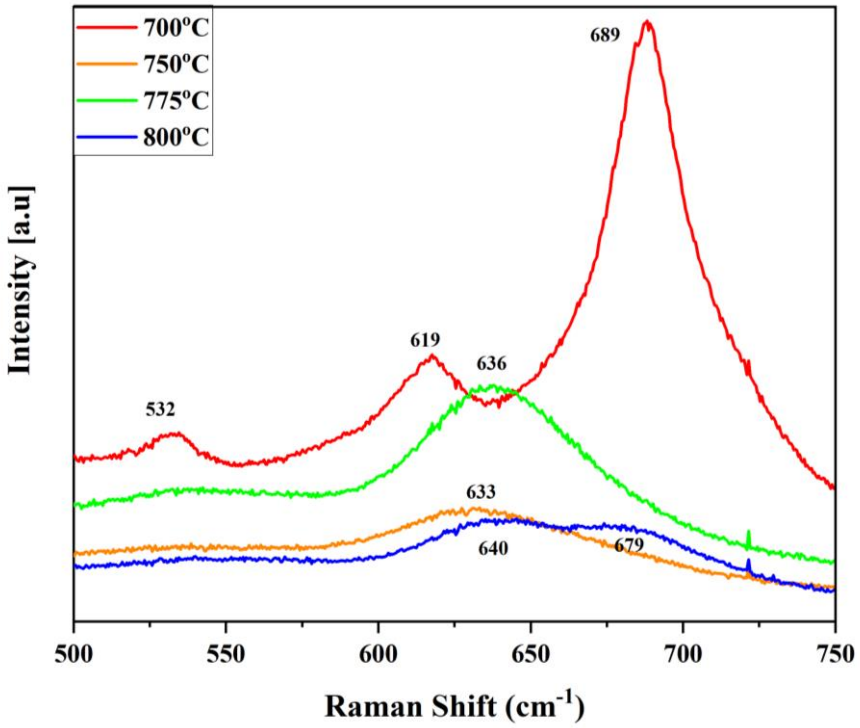

Figure 4.15: Raman Spectra of LSCF6428 nanopowders calcinated at 700 ºC, 750 ºC, 775 ºC and 800 ºC with excitation wavelength of 532 nm.

Past Raman studies have detected the LSCF perovskite phase, typically in the range of 500 – 700 cm^{-1}. The Raman spectra of the LSCF6428 of the four different calcination temperatures were examined in the range of 500 – 800 cm^{-1} and are shown in Figure 4.15. From the results there is clear relationship between the crystal symmetry and the number of peaks present. It can be seen that the dual phase (cubic and rhombohedral) of the LSCF6428 when calcinated at 700 ºC has three sharp peaks located at 532 cm^{-1}, 619 cm^{-1} and 689 cm^{-1} in Raman Spectroscopy (Figure 4.15). When the calcination temperature is increased beyond 700 ºC this results in the transition to a single phase, rhombohedral structure of LSCF6428, matching the trend of the decrease intensity of the diffraction patterns as the temperature increases from 750 ºC onwards.

The sharp peak at 532 cm^{-1} only appears when the LSCF6428 was calcinated at 700 ºC indicating the stretching of the oxygen tilting octahedra due to the A site chemical composition deficiency of strontium from the LSCF6428 perovskite.[190] The cubic phase in the dual phase material at 700 ºC is not Raman active by symmetry for an ideal cubic perovskite and it is thought that the main contribution to this first order scattering is caused by the effect of disorder. Since the Raman spectra are acquired at room temperature, researchers have found that many of the ideal cubic perovskites studied are distorted when measurements are undertaken which could have potentially led to the appearance of the 532 cm^{-1} peak. [191-192]

However, when the calcination temperature increases beyond 700 ºC, the 532 cm^{-1} peak disappears from the spectra due to the transition to a single-phase, potentially more ordered, rhombohedral structure and the decreasing trend for the lattice parameter "a" length of the perovskite lattice, indicating less Sr deficiency which is consistent with the decrease of $SrCO_3$ as shown in Figure 4.8. There is also a shift of the 619 cm^{-1} peak to higher wave numbers due to the local structural changes through the decrease in "a" length of the crystal symmetry lattice of the rhombohedral structure calculated from the XRD, which affects the volume and thus the density of the perovskite oxide structure as seen in Figures 4.13-4.14.[193]

Overall, 800 ºC will be selected as the calcination temperature for further work as it meets the criteria of creating a single-phase material and achieving 96 % purity of the rhombohedral crystal structure, in comparison to the other calcination temperatures where either or both the phase purity and single-phase crystal structure criteria are not met.

Given that the 800 ºC has met the purity requirement, to get a further insight behind the impurity, $SrCO_3$ and how it affects the chemical composition of the LSCF6428 SEM-EDX was used to determine the elemental distribution of the calcined LSCF6428 at 800 ºC.

4.5 Microstructure Characterisation of the 800 ºC calcinated LSCF6428 Nanopowder

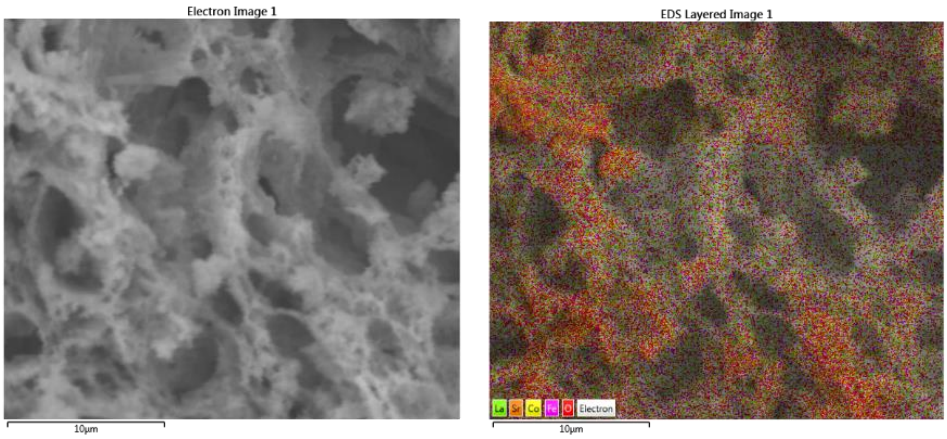

Figure 4.16: SEM image of calcined 800 ºC LSCF6428 nanopowder. Left (Before EDX scan) and Right with overlaid elemental X-ray maps from EDX

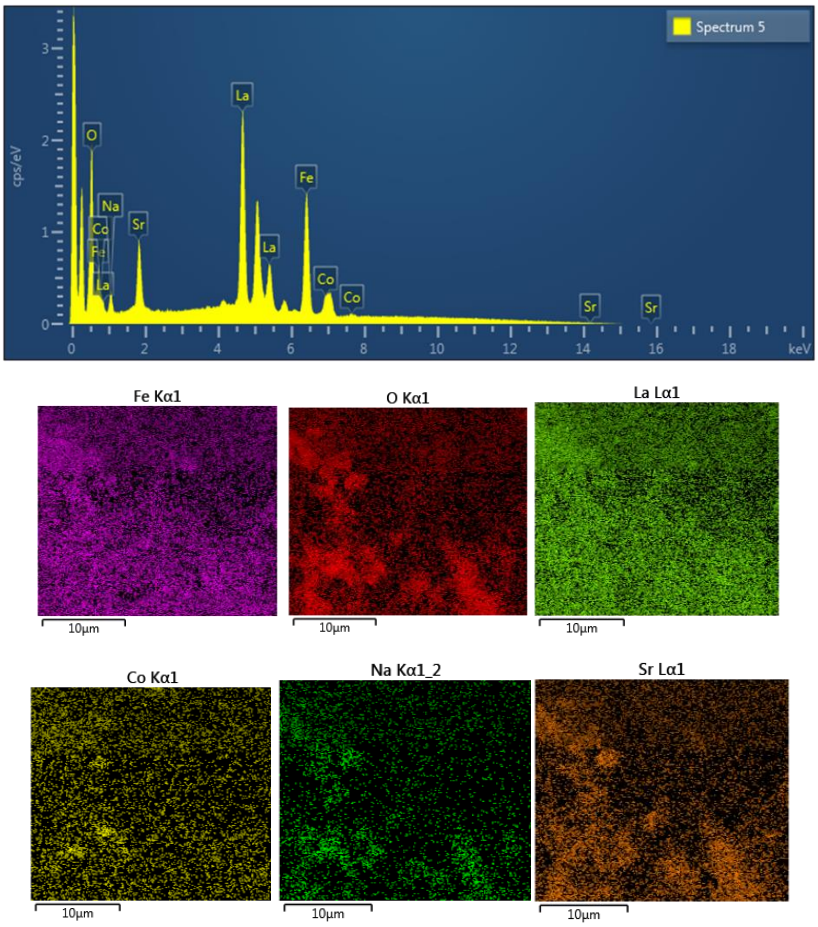

Figure 4.17: (Above) EDX spectrum of crushed calcined LSCF6428 nanopowder (Below) showing the presence of all the key metal elements for LSCF 6428 with elemental maps

showing some deficient Sr, excess Na but otherwise a homogenous distribution of the LSCF6428 elements

Table 4.11: 800 °C calcined LSCF6428 comparison of EDX measured composition (by assuming stoichiometry) and the expected composition.

Elements	Measured Composition	Expected Composition
Iron (Fe)	0.89	0.8
Strontium (Sr)	0.12	0.4
Lanthanum (La)	0.67	0.6
Sodium (Na)	0.15	-
Cobalt (Co)	0.16	0.2

SEM imaging (Figure 4.16) shows the formation of a porous material on calcination and that it has an agglomerated, fine particle (or crystal) surface. The structure of a porous nanopowder is caused by the complete thermal decomposition of the polysaccharide alginate structure. EDX spectroscopy and elemental mapping give an indication of the homogeneity of the metal cations in the nanopowder (Figure 4.17). All the elements for the perovskite metal oxide are present but with varied degrees of concentration in relation to the quantitative data from Table 4.11. The O and C have been omitted from the Table 4.11 because of the presence of the carbon support pad where the sample is placed. The measured composition shows the La and Fe elements are highly concentrated and homogeneously distributed throughout. The measured Co composition is close to the expected composition compared to the Sr which is significantly deficient in comparison to the other elements in the nominal LSCF6428 composition.

There has been limited study into the elemental distribution by SEM -EDX in relation to the LSCF6428 composition and homogenous distribution of the multivalent metal cations to examine any A site deficiency of strontium in LSCF6428 associated with this synthesis method of sol gel involving ion exchange. [182-183][194]. As for this work, there is a small presence of Na^+, and this suggests that not all the Na^+ present in the alginate has been fully exchanged with the multivalent metal cation which could have significantly impacted the Sr^{2+}. As seen in the Table 4.11, the chemical composition estimates are close to the expected composition although there is deficiency in strontium which is consistent with the presence of a small $SrCO_3$ second phase peak in the XRD diffraction pattern (Figure 4.8).

4.6 X-ray Computed Tomography (XCT) Characterisation between the metal alginate complex of LSCF6428 and 800 ºC calcinated LSCF6428 nanopowder

XCT was conducted to provide the 3D reconstruction on both the dried metal–alginate complexes and the chosen 800 ºC LSCF6428 calcinated nanopowder as shown in Figure 4.18 below. There have been no past studies in examining the homogeneity of the sodium alginate sol gel throughout the crushed samples of both dried and calcined material using XCT. However CT analysis of organics containing metal cations has been done for 'metallic' powders used for additive manufacturing (AM) to determine the level of porosity within the powders.[194-196] Using these approaches here will provide the key information as to whether the calcination of the LSCF6428 through the chosen synthesis method has led to the production of a successful uniform, porous and homogenous LSCF6428 nanopowder.

Dried LSCF6428 – Slice 75/2006

a.)

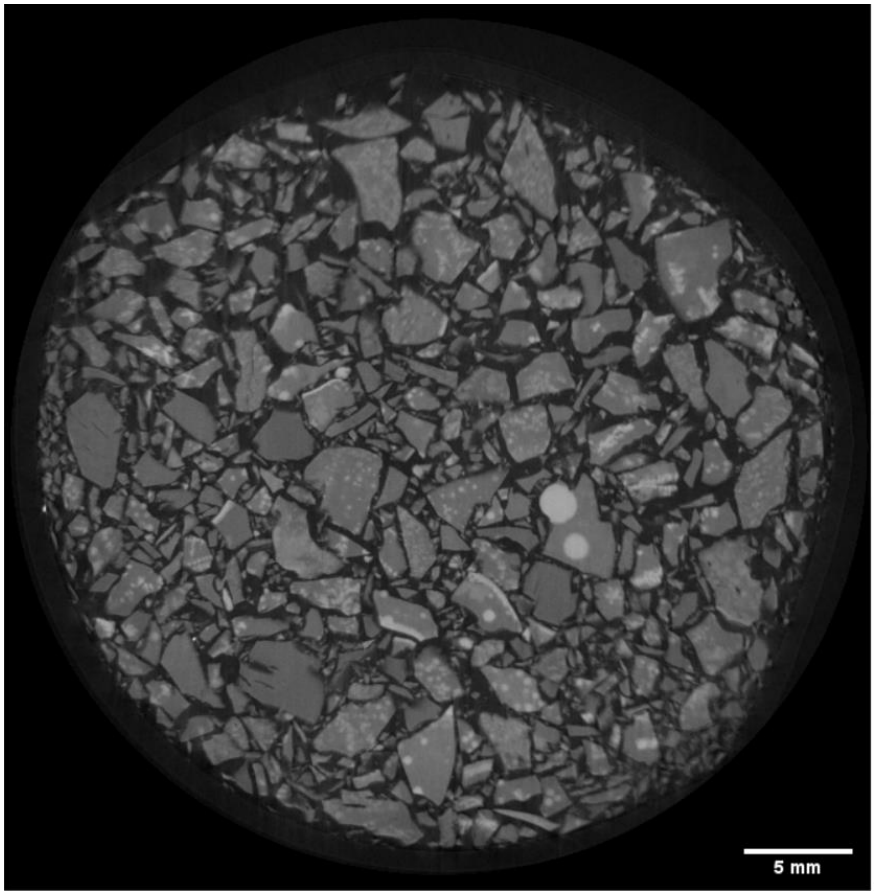

b.)

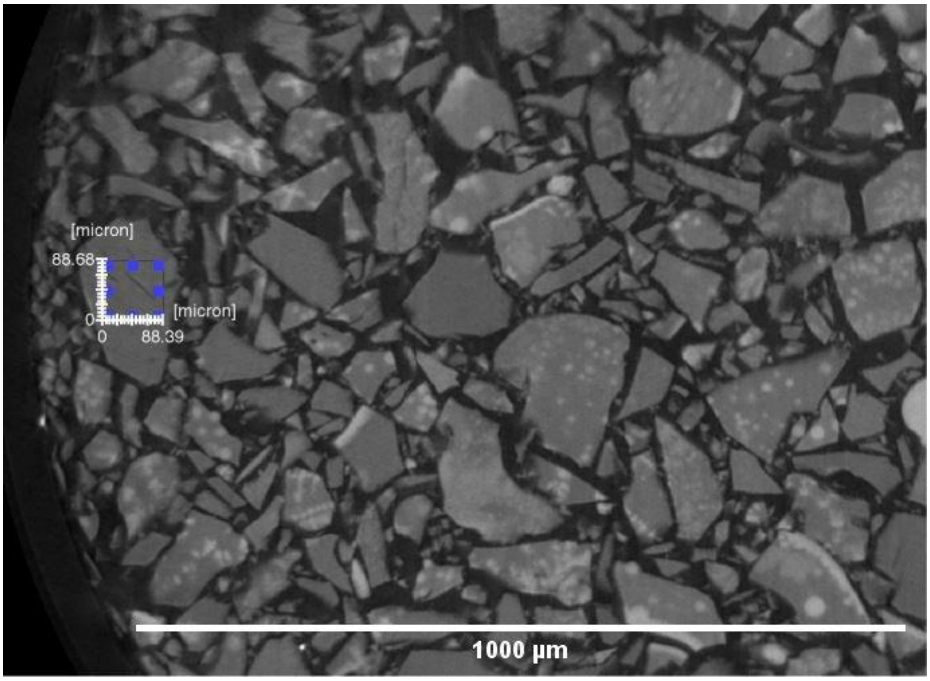

Calcined LSCF6428 – Slice 1465/2006

c.)

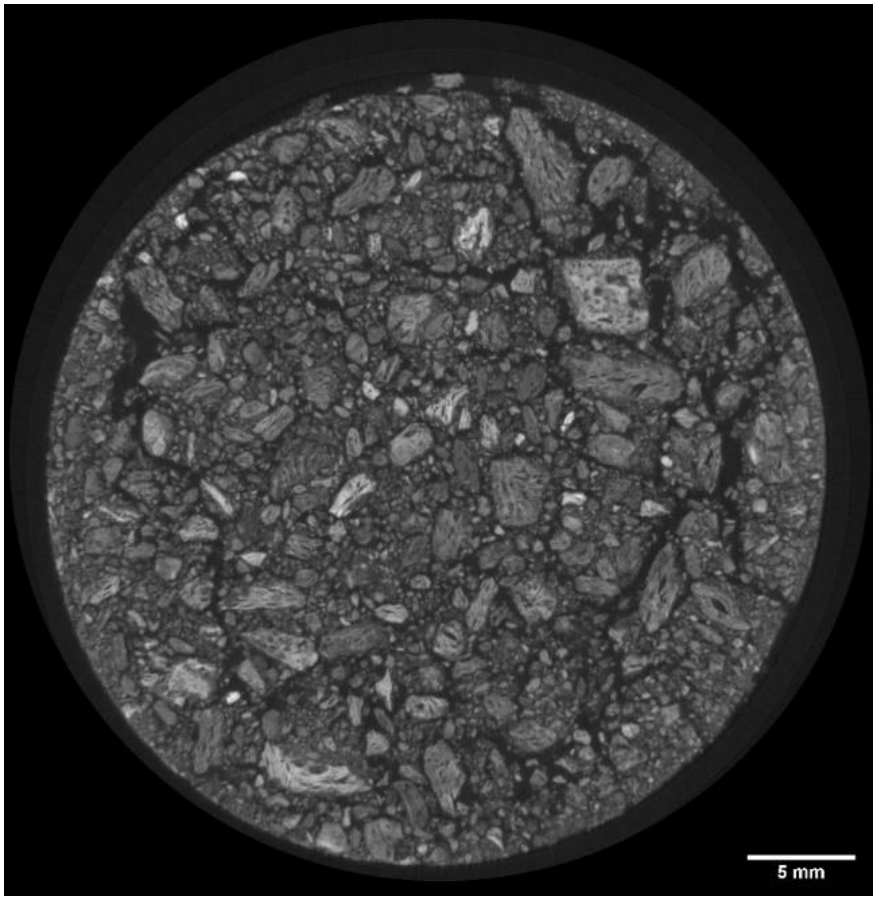

d.)

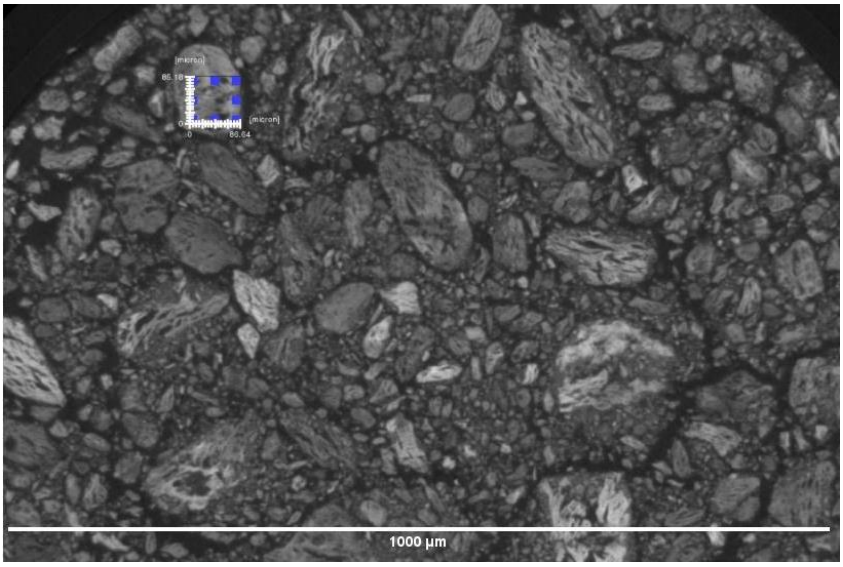

Figure 4.18: a.) Cross sectional morphological of metal-alginate complex of LSCF6428 from Micro-CT **b.)** Thresholded image of white box region (measured in micron) where the pore size distribution was taken from one of the selected 20 grains. **c.)** calcined perovskite oxide of LSCF6428 from Micro-CT **d.)** Thresholded image of white box region (measured in micron) where the pore size distribution was taken from one of the selected 20 particles.

(a.)

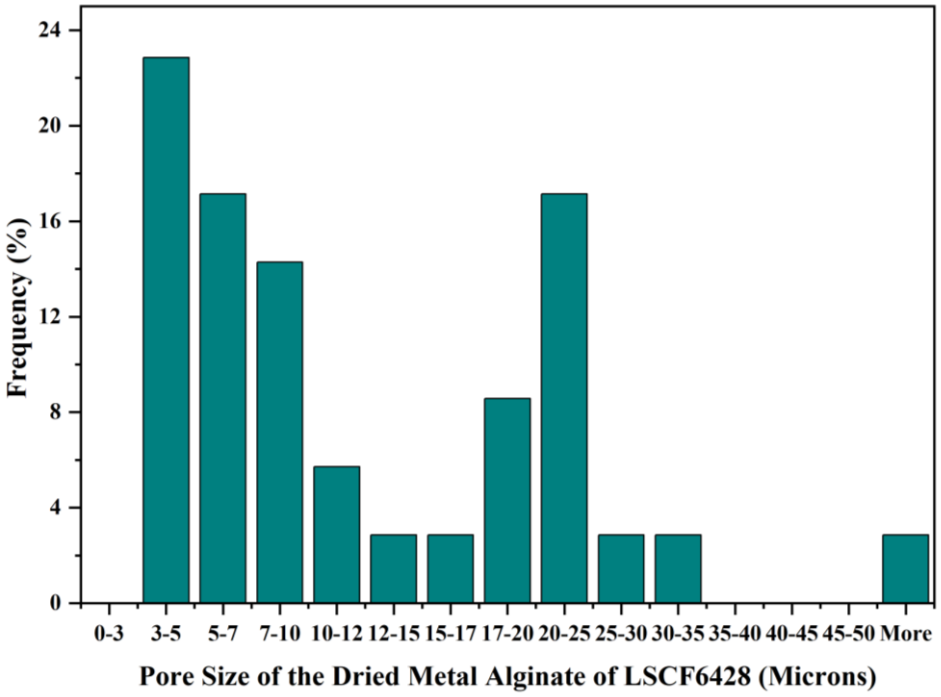

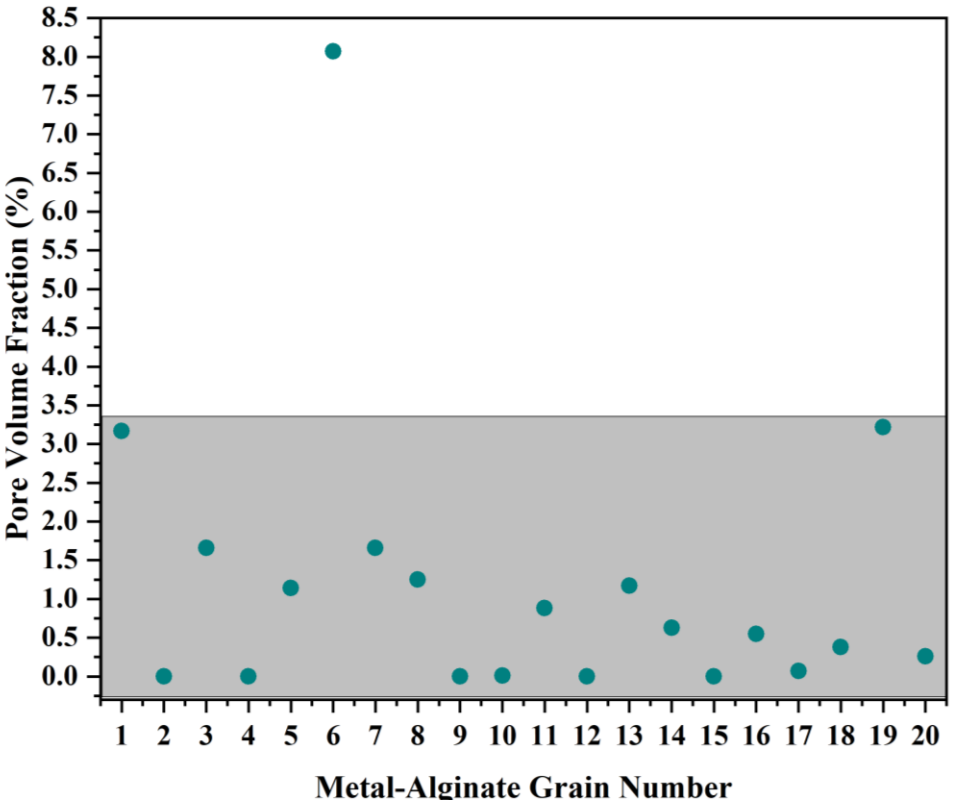
Pore Volume Fraction (%)
8.5
8.0
7.5
7.0
6.5
6.0
5.5
5.0
4.5
4.0
3.5
3.0
2.5
2.0
1.5
1.0
0.5
0.0
1 2 3 4 5 6 7 8 9 10 11 12 13 14 15 16 17 18 19 20
Metal-Alginate Grain Number

(b.)

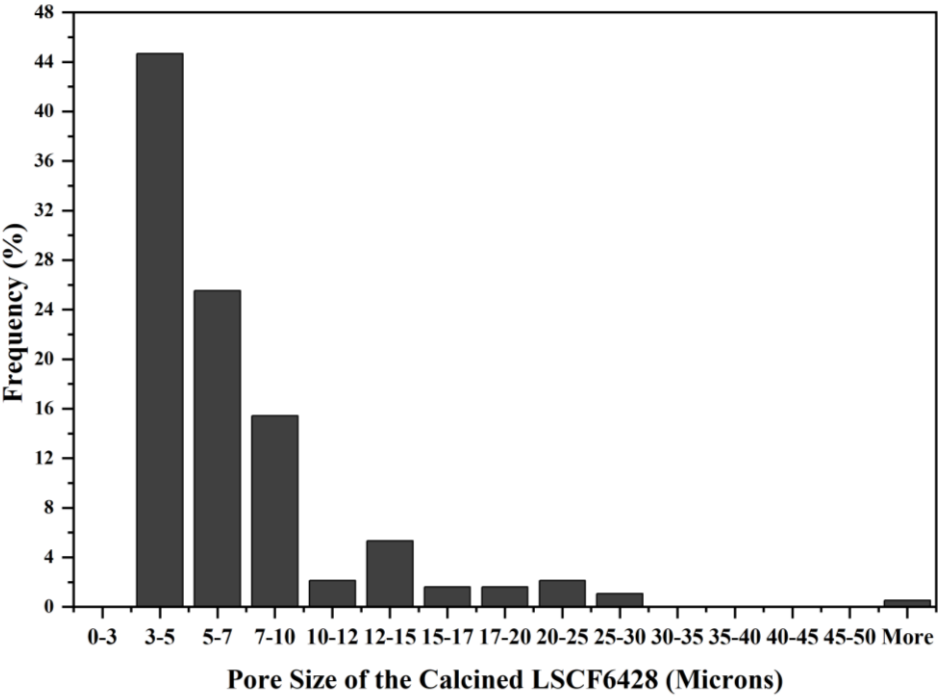
Frequency (%)
48
44
40
36
32
28
24
20
16
12
8
4
0
0-3 3-5 5-7 7-10 10-12 12-15 15-17 17-20 20-25 25-30 30-35 35-40 40-45 45-50 More
Pore Size of the Calcined LSCF6428 (Microns)

(c.)

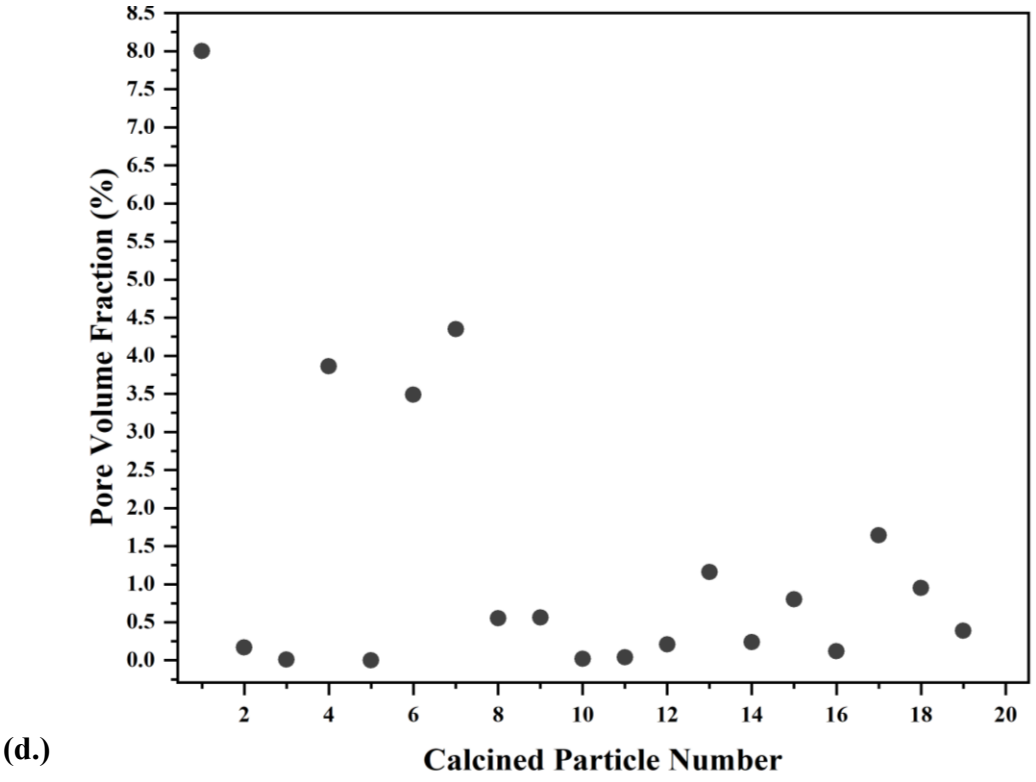

(d.)

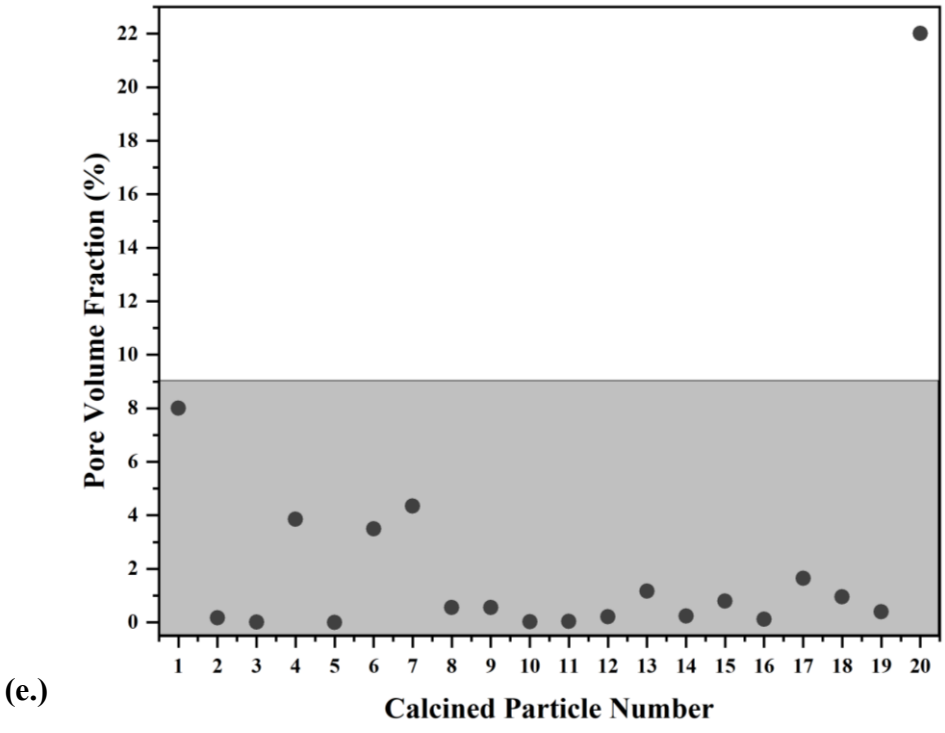

(e.)

Figure 4.19: (a) : Pore size distribution of the dried metal alginate complex of LSCF6428 (b) volume fraction of pores of the dried metal alginate complex of LSCF6428 (c) Pore size distribution of the calcinated 800 ºC LSCF6428 nanopowder (d) volume fraction of pores of calcinated 800 ºC LSCF6428 nanopowder (e.) zoom in grey box from (d.)

The 2D projection images as shown in Figure 4.18 reveal significant differences between the homogeneity of the grain sizes before and after calcination. The metal alginate complexes exhibit different grain sizes with facet features but (black) pores within these grains and some contrast inhomogeneity is visible (the black air background is pore space occurring within the acrylamide tube itself). The effect of encapsulation of the alginate is like that seen in work focusing on the effects of asphalt mastic for formation of metallic particles where pores were located within. [194]

Compared to the SEM images, the Micro-CT images can also distinguish the difference between the alginate and metal cations for the dried metal-alginate complex depending upon atomic mass. The white contrast indicates the presence of potentially excess metal cations, in relation to the measured composition shown in Table 4.11 while the grey indicates the presence of organic material coming from the mixture of metal cations in the grain (Figure 4.18a - 4.18b). This is consistent with a study investigating the calcium alginate capsules that are distributed throughout an asphalt mastic imaged using Micro-CT. [197] However, calcination degrades the alginate structure upon the effects of thermal decomposition, enabling the homogeneity of the perovskite oxide nanopowders to be established and distributed uniformly throughout (although some inhomogeneity and porosity is clearly visible; Figure 4.18c-d). That causes the effect of agglomeration in the individual grains with the appearance of an increased porous nature compared to the dried metal alginate.

To determine the pore size distribution, a threshold approach was used to analyse porosity across 20 grains.[145][194] It can be seen when comparing the images with pore size distribution, there is a broader pore size distribution in the dried metal alginate due to the encapsulating of the alginate harder outer shell and the lack of uniformity throughout the microstructure (Figure 4.19 a and b). While for the calcined nanopowder, there is a narrower pore size distribution with the % of the 3–5-micron range being doubled which suggests the formation of more homogenous pores occurring in the microstructure itself (Figure 4.19 c and d). It can also be seen from the cross section the grey values are more even in the calcined material, i.e there is fewer density differences in the calcined material.

4.7. Porous Characterisation of the 800 ºC calcined LSCF6428 nanopowder using SEM method

The previous characterisations of the calcined LSCF6428 nanopowder such as XRD and Raman Spectroscopy have analysed the structure at a nanoscale and XCT the pore size but SEM can combine the analysis of primary particle size and porosity. That combination will

enable the final cathode material to be operated effectively as an IT-SOFCs. The calcined nanopowder SEM surface images were analysed further using the ImageJ software to determine the pore size distribution and what the average of the pore size was.

(a.)

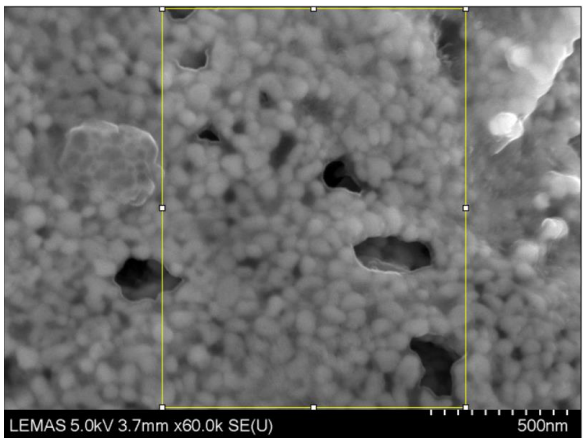

(b.)

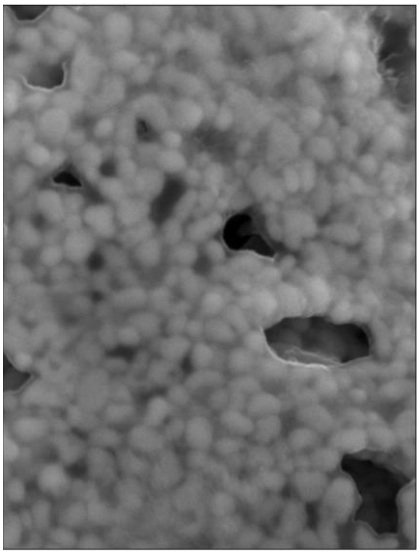

(c.)

(d.)

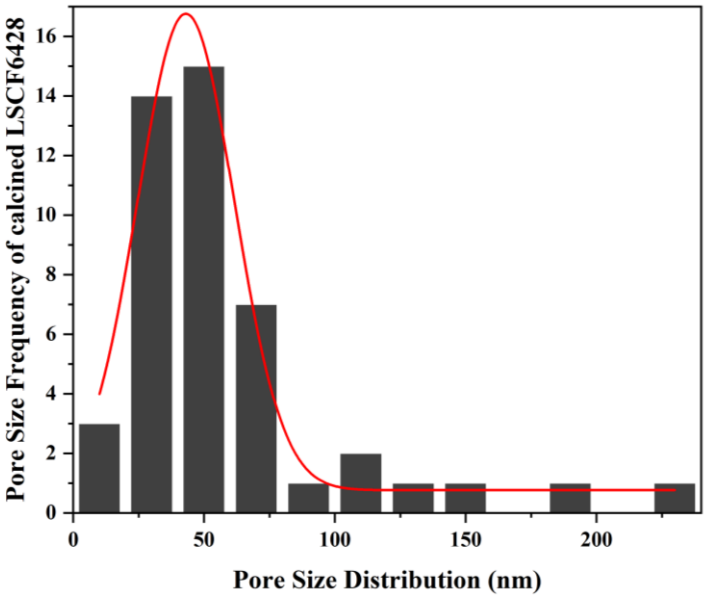

Figure 4.20:(a.) Secondary SEM image of LSCF6428 calcinated at 800ºC (b.) secondary electron image with yellow box used for pore size measurement (inset) (c.) Thresholded image of yellow box region where black is taken to be pore structure (d.) SEM pore size distribution of the 800 ºC calcined nanopowder of LSCF6428.

The SEM image was examined at high magnification as shown in Figure 4.20. The primary particle size of the nanopowders is small (a few 10s of nm and is consistent with the crystallite size of ~ 16 nm determined by XRD) and the primary particles are clearly agglomerated with pores around them. To obtain a realistic measurement of porosity, the SEM image was thresholded to distinguish between the particles (light grey features), the organic material (mid grey features) and pores (black features). Like with the narrower calcined pore size distribution of the LSCF6428 obtained from the XCT as shown in Figure 4.19, there also appears to be a similar trend occurring when measured at the nanoscale. Figure 4.20 shows that the pore size distribution of the calcined LSCF6428 is concentrated between 25 – 75 nm and analysis gives an average pore size of 43 nm confirming that nanoscale production had taken place. This average pore size is not far off from that of the study by Ismail et.al. where a 38 nm average pore size was achieved [182]

4.7. Porous Characterisation of the 800 ºC calcined LSCF6428 nanopowder using BET method

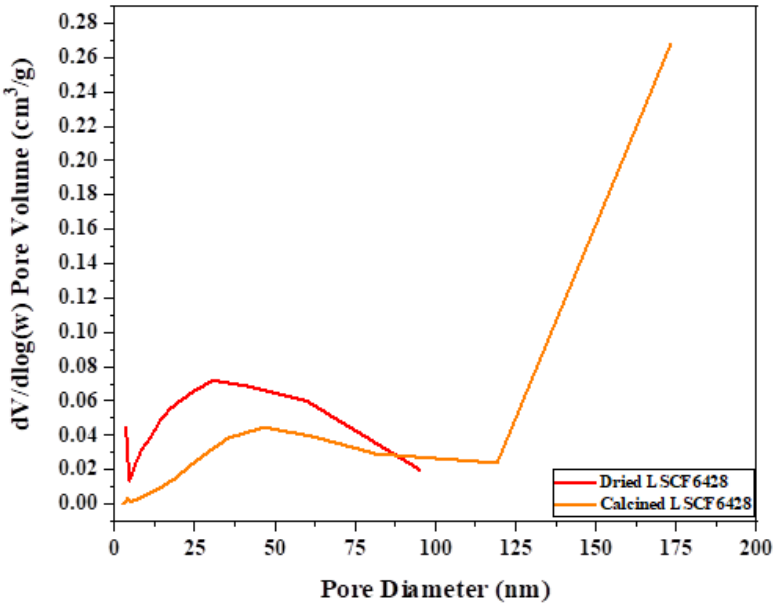

Figure 4.21: Pore size distribution of the dried metal – alginate complex of LSCF6428 and calcinated nanopowder of LSCF6428 using BET method.

Table 4.12: The single perovskite oxide of the dried metal alginate complex of LSCF6428 and calcined nanopowder (LSCF6428 calcined at 800 ºC)

Samples	Total Pore Volume (dried) (cm^3/g)	Total Pore Volume (calcined) (cm^3/g)	Average Pore Size (dried)(nm)	Average Pore Size (calcined)(nm)
LSCF6428	0.075	0.041	15.1	37.0

Since the SEM is limited to focusing on only one specific location, the pore size distribution was measured by nitrogen adsorption using the BJH method which can measure the whole surface area of the nanopowder. The method was used to analyse the size of the open pores of the calcined LSCF6428 and for comparison with the dried metal alginate complex. For the calcined LSCF6428, the curve shows a pore size distribution that ranges between 25 nm and 75 nm (Figure 4.21), which is similar to that which has been obtained by SEM from the ImageJ software (Figure 4.20). These pore sizes are consistent with other reports. [180][182][198] It can also be seen in relation to Table 4.12 that based on the qualitative explanation between the

LSCF6428 calcined perovskite oxide that the average pore size is 37 nm which is close to what has been obtained from ImageJ.

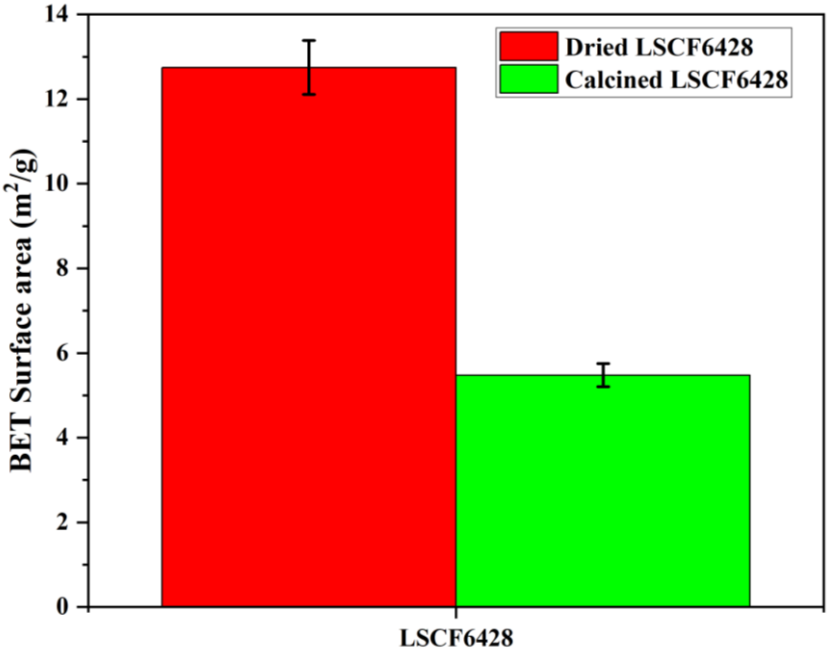

Figure 4.22: BET specific surface area investigated dried metal alginate complex of LSCF6428 (red bar) and 800 ºC calcined perovskite oxide nanopowder of LSCF6428 (green bar) with corresponding error bars.

Table 4.13: BET specific surface area of dried and calcined at 800ºC LSCF6428 nanopowder

LSCF6428	**BET specific surface area (m^2/g)**
Dried	12.75 ± 0.092
Calcined at 800ºC	5.48 ± 0.025

The changes in pore volume and pore size on going from dried to calcined nanopowder in Table 4.12 matches with the trend in the decrease in BET surface area as shown in Figure 4.22 and Table 4.13 but also with the key findings of the other characterisation techniques in this work. The significant reduction in the BET specific surface area value during the calcination process by half to 5.48 m^2/g is due to an increase in powder agglomeration (SEM and XCT images) despite the decomposition and shrinkage of the alginate structure. The value obtained for the calcinated LSCF6428 of both the specific surface is like that reported in a previous study where the value was 5.07 m^2/g and for an average pore size of 37.7 nm and the synthesis method chosen was solid state.[180][182][198] The solid-state method is known to yield

inhomogeneity of nanopowders and the results here are similar. The minor differences are due to the extent of the agglomeration which could affect the ORR activity and its conduction pathways of the final cathode material after sintering.

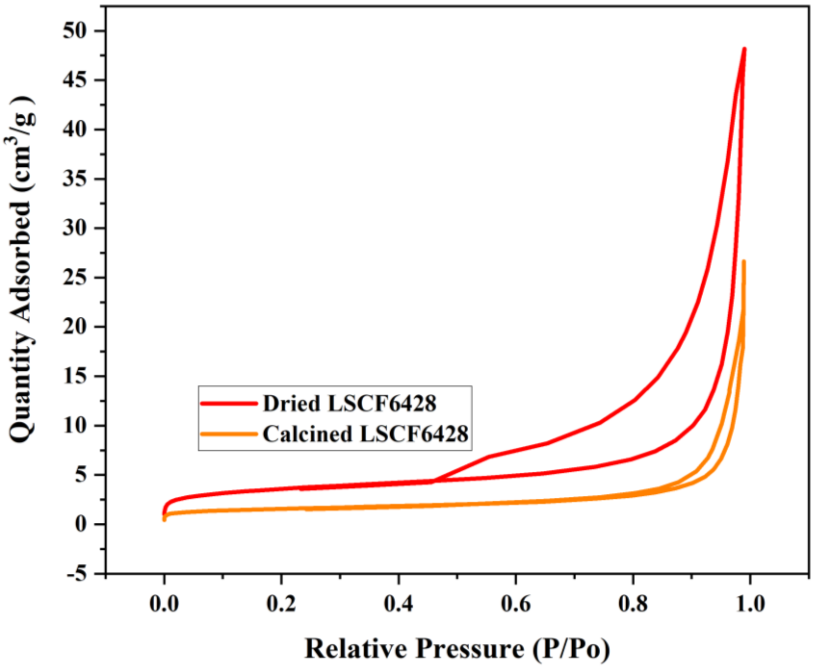

Figure 4.23: The BJH nitrogen adsorption and desorption isotherm of the dried metal – alginate complex of LSCF6428 and calcinated nanopowder (LSCF6428 calcinated at 800ºC)

To determine how the relationship between the pore size distribution and specific surface area behaves when adsorbed gases are applied. The nitrogen adsorption isotherm curve of the LSCF6428 was measured using the BJH method as shown in Figure 4.23. The results obtained were used to determine the adsorption mechanism of the LSCF6428 qualitatively. As can be seen from the isotherm, there is capillary condensation of the material taking place at relatively high pressure. It can be seen that the adsorption is not limited to the higher-pressure range between the 0.82 to 1.0 (p/p_0). Based on the IUPAC in accordance with the literature, the LSCF6428 nanopowder is of Type IV in relation to its mesoporous structure, its wider pore size distribution and shape of the hysteresis loop consists of a combination of, Type H1/ H3 of hysteresis loop.[199].

The value of the specific surface area recommended for IT-SOFCs cathodes has ranged typically between 5-7 m^2/g to ensure good practical application, so the current material meets the criteria for the sintering procedure. It is thought that the specific surface area when undergoing sintering will affect the rate of densification of the nanopowders through enhanced reactivity and shrinkage rate of the pellet.

Summary – Chapter 4

The choice of the 3 wt% over the 4 wt% metal alginate complex for the sol-gel synthesis of LSCF6428 revealed through thermal analysis an increase in final mass of 14.2% of calcined material in the 3 wt% complexes. Calcination of the sol-gel complexes was shown by XRD analysis to produce LSCF6428 nanopowder (of ~30-40 nm grain size) and calcination at 800 ^{o}C was chosen for further characterisation out of the four different calcination temperatures trialled (from 700 to 800 ^{o}C). At 800 ^{o}C, XRD shows LSCF6428 forms with a rhombohedral structure, a phase purity of 96% was achieved which meets the target criteria of over 90% purity and this was not accomplished for any of the calcination temperatures below 800 ^{o}C. Second phase $SrCO_3$ was detected by XRD even in the nanopowder calcined at 800 ^{o}C, and corresponding Sr deficiency of the main LSCF6428 phase was identified by SEM/EDX spectral and mapping analysis (giving an estimated Sr content of 0.12 (atomic ratio of Sr to all metal cations) vs the expected content of 0.2) whilst the other metal cations were measured to be in appropriate amounts for the nominal composition. That suggested a relatively homogeneous distribution of metal cations throughout the microstructure after calcination. Such a homogenous distribution was also consistent with results from XCT of the LSCF6428 nanopowder calcined at 800 ^{o}C which also revealed nanoparticle agglomeration that establishes pores within the microstructure. The size of the pores based on the pore size distribution across both SEM and BET was consistent between the techniques and indicated an average pore size of around 40 nm i.e. similar to the grain size. Moreover, the calcined LSCF6428 met the specific surface area target of 5.48 m^2/g.

The next stage is to sinter the calcined nanopowder to study the development towards a working SOFC intermediate temperature cathode material.

Chapter 5 – Structural and Porosity Characterisation of Sintered $La_{0.6}Sr_{0.4}Co_{0.2}Fe_{0.8}O_{3-\delta}$

5.1. Structural Characterisation of sintered LSCF6428 pellets

Precursor nanopowders selected for sintering were calcined at 800 ºC and shown to be single phase, rhombohedral LSCF6482 by XRD (Section 4.1). The powder underwent uniaxial pressing (at 2 tons) to form pellets and was sintered at three different temperatures for 1 hour. A temperature range of 900 ºC to 1100 ºC was chosen to assess sintering behaviour of the LSCF6428 following similar conditions used by Jamale et.al. [200]

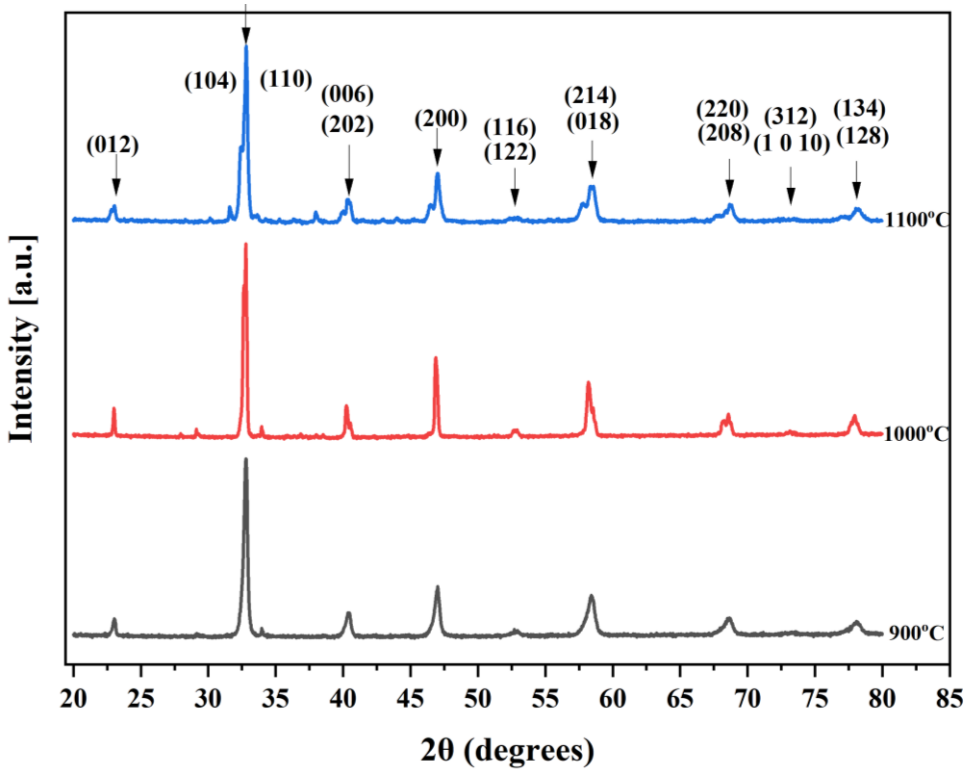

Figure 5.1 XRD patterns of 3 wt% LSCF6428 crushed pellets sintered for 1 h at temperatures of 900 ºC (grey line), 1000 ºC (red line) and 1100 ºC (blue line). (indexed to the rhombohedral phase in ICDD, 04-017-2448- R3c).

It can be seen from Figure 5.1 that the XRD diffraction peaks reveal critical information regarding rhombohedral peak splitting of the sintered LSCF6428 experimental diffraction patterns which were absent from the calcined LSCF6428 patterns. The number of diffraction pattern peaks with peak splitting increases with increasing sintering temperature across the 900 ºC to 1100 ºC range. To examine the effects of sintering, XRD diffraction patterns were indexed to the rhombohedral crystal symmetry using the ICDD based reference for the

perovskite crystal phase and peak fitting was used to fit the peak diffraction data as shown in Figures 5.2-5.4. Peak splitting of the 58°, 68°, 72° and 78° 2θ peaks is the focus of the analysis as these give a clear indication of the transition towards a lower symmetry rhombohedral structure, occurring at temperatures above 1000 °C as shown in Figures 5.2-5.4 and reported by others [185-186]. Diffraction peak splitting is present in other lanthanum-based oxides such as $LaCoO_3$ where studies have examined similar transition from higher to lower crystal symmetry [201-203]. Peak splitting is the characteristic feature identifying the rhombohedral space group, R3c. [204]

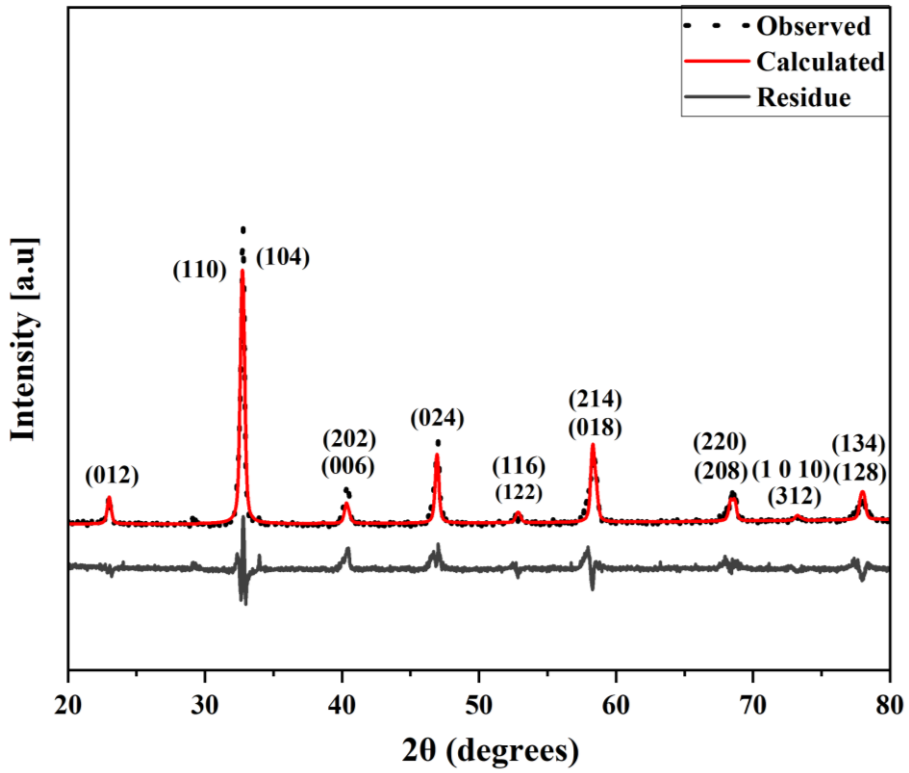

(a.)

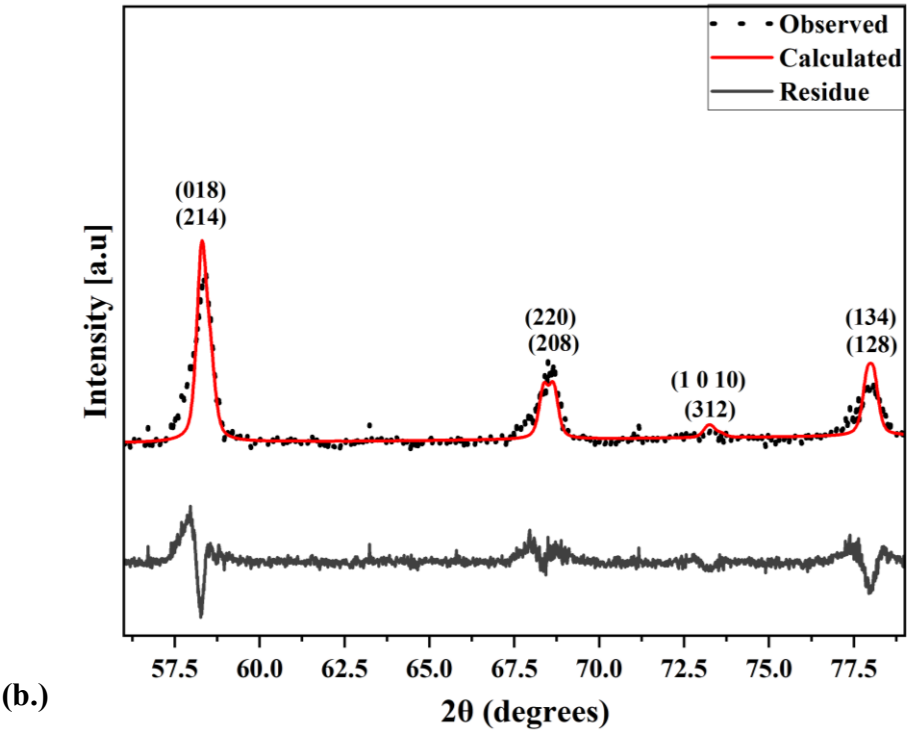

(b.)

Figure 5.2: **a)** Whole pattern fitting of the rhombohedral structure of a crushed LSCF6428 pellet sintered at 900 ºC with experimental data (black line), reference file fit (red line), residue (grey line) shown and peaks are indexed using ICDD 04-017-2448. b) Zoom in of the fitting of the rhombohedral structure of the 900 ºC crushed LSCF6428 nanopowder, indicating potential peak splitting at the (214)/(108), (220)/(208), (312)/(1 0 10) and (134)/(128) peaks 58º, 68º, 72º and 78º 2θ respectively.

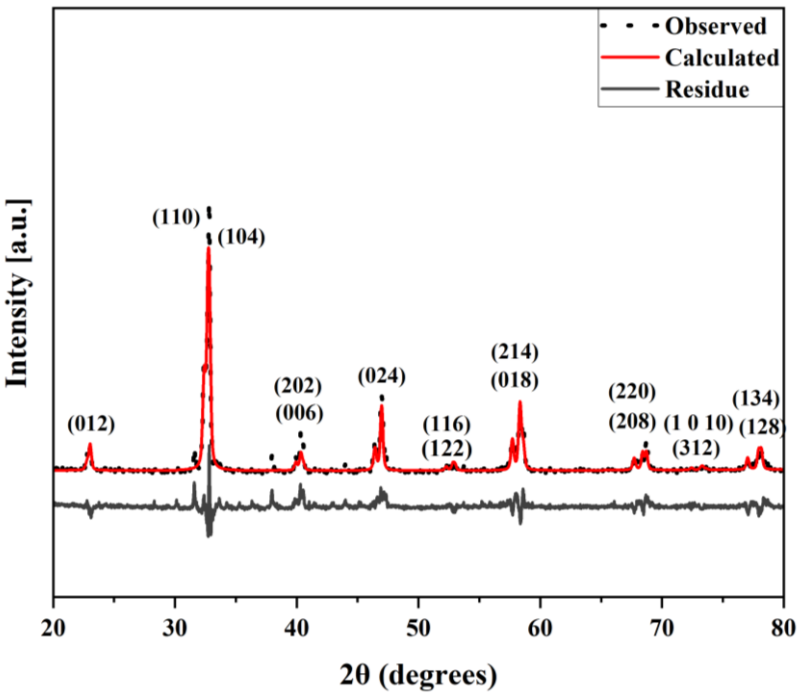

(a.)

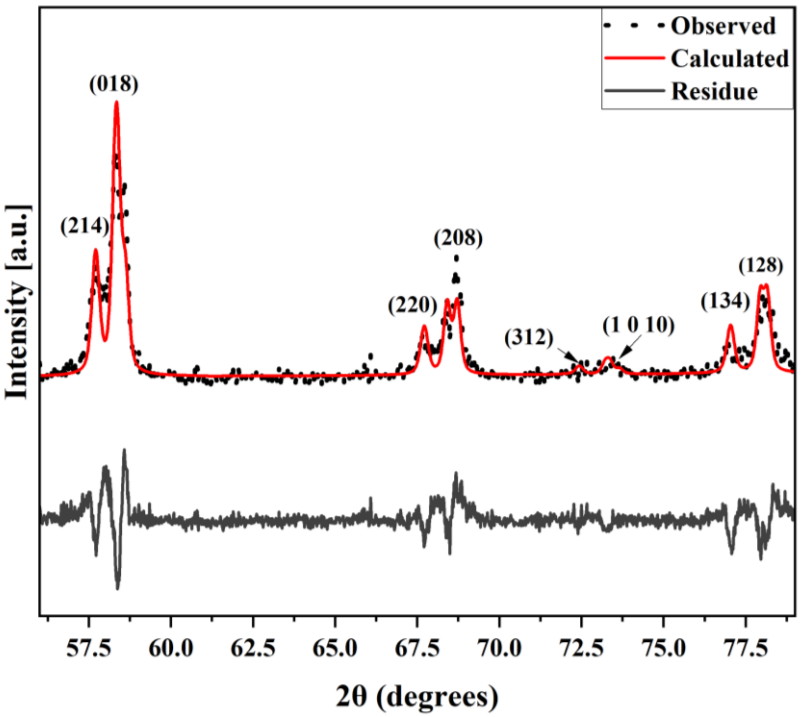

(b.)

Figure 5.3:**a)** Whole pattern fitting of the rhombohedral structure of a crushed LSCF6428 pellet sintered at 1000 ºC with experimental data (black line), reference file fit (red line), residue (grey line) shown and peaks are indexed using ICDD 04-017-2448. b) Zoom in of the fitting of the rhombohedral structure of the 1000 ºC crushed LSCF6428 nanopowder, indicating potential peak splitting at the (214)/(108), (220)/(208), (312)/(1 0 10) and (134)/(128) peaks 58º, 68º, 72º and 78º 2θ respectively.

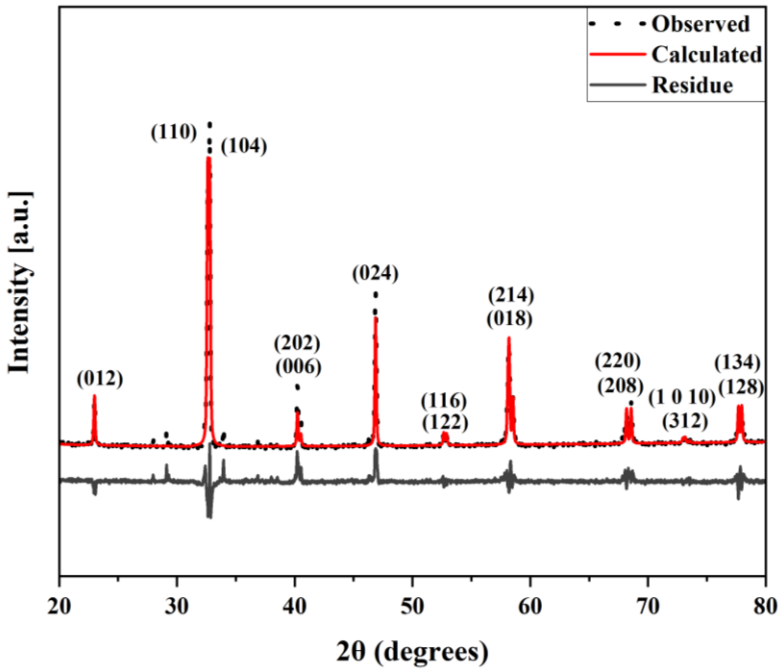

(a.)

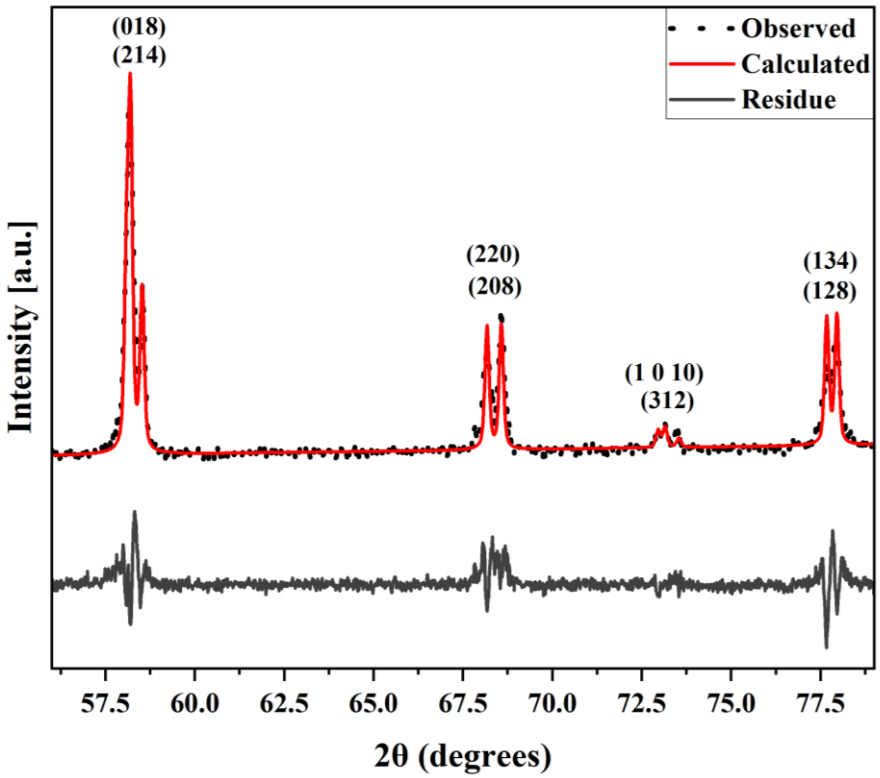

(b.)

Figure 5.4: **a)** Whole pattern fitting of the rhombohedral structure of a crushed LSCF6428 pellet sintered at 1100 ºC with experimental data (black line), reference file fit (red line), residue (grey line) shown and peaks are indexed using ICDD 04-017-2448. b) Zoom in of the fitting of the rhombohedral structure of the 1100 ºC crushed LSCF6428 nanopowder, indicating potential peak splitting at the (214)/(108), (220)/(208), (312)/(1 0 10) and (134)/(128) peaks 58º, 68º, 72º and 78º 2θ respectively.

Table 5.1: Whole pattern fitting of structural parameters, average crystallite size fit quality and micro strain of rhombohedral (R3c) LSCF6428 sintered at 900, 1000 and 1100 ºC ((r_{wp}(%)) weighted pattern, (R_{exp}(%)) expected pattern and goodness of fit (GOF))

Temperature (º C)	**Mean Crystalline Size (nm)**	**R_{exp} (%)**	**R_{wp} (%)**	**GOF**	**Mirco Strain (%)**
900	29.4	6.377	6.152	1.036	0.19
1000	38.4	7.028	6.439	1.091	0.15
1100	73.9	6.628	6.601	1.004	0.07

To examine the effects of sintering, whole pattern fitting of the XRD diffraction patterns was undertaken. From Figures 5.2-5.4, there seems to be a reasonable fitting of the reference

diffraction pattern to the experimental. The fits are measured using the quality factor values such as R_{wp} (%) where values < 10% indicate an acceptable fit while for GOF where values below 4% indicate a good fit and therefore are strong indicators of the formation of the rhombohedral phase. [179-180] Table 5.1 shows that these values are obtained for rhombohedral fits for all the sintering temperatures. Simultaneously, the FWHM of the diffraction peaks has also decreased significantly as the sintering temperature increases, indicating an increase in mean crystallite size of the LSCF6428 from 30 nm at 900 ºC to 75 nm at 1100 ºC and this is consistent with the decrease in micro strain (%) as shown in Table 5.1 and other reports [181].

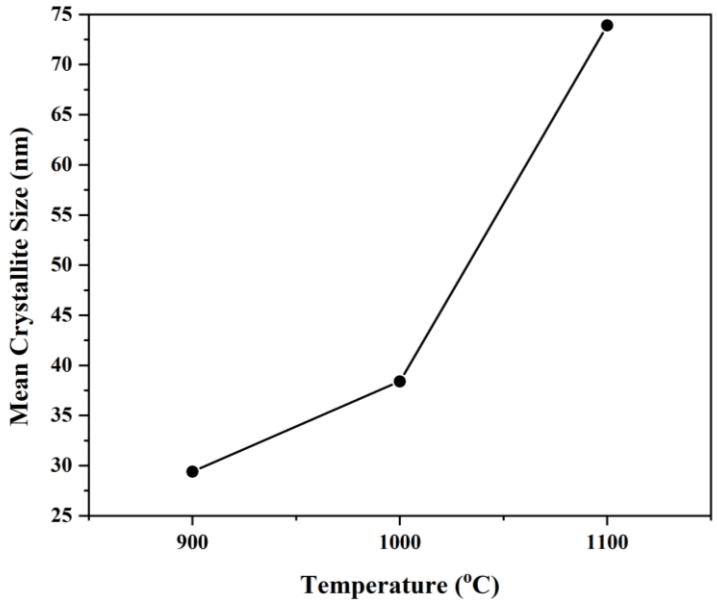

Figure 5.5: Temperature (ºC) vs Mean crystallite size (nm) of the crushed sintered LSCF6428 pellets where the black dots refer to the experimental data.

When the sintering temperature is increased from 900 ºC to 1000 ºC, there was an only small increase in crystallite size; however, when the sintering temperature was further increased from 1000 ºC to 1100 ºC, there was a much larger increase in crystallite size as shown in Figure 5.5. A similar effect occurs for other perovskite materials demonstrating the sensitivity of crystal growth of the microstructure on precise sintering temperature [179][205].

Table 5.2: Unit Cell dimensions (rounded to three decimal places), Theoretical Density and Volume (rounded to two decimal places) of rhombohedral (R3c) LSCF6428 at different sintering temperatures of 900, 1000 and 1100 ºC

Temperature (^{o} C)	**a (Å)**	**b (Å)**	**c (Å)**	**Volume (Å)**	**Theoretical Density (g/cm^3)**
900	5.487± 0.01	5.487	13.367	348.63± 1.47	11.12± 0.045
1000	5.485± 0.011	5.485	13.357	348.04± 1.46	11.14± 0.045
1100	5.503± 0.011	5.503	13.338	350.89± 1.51	11.05± 0.05

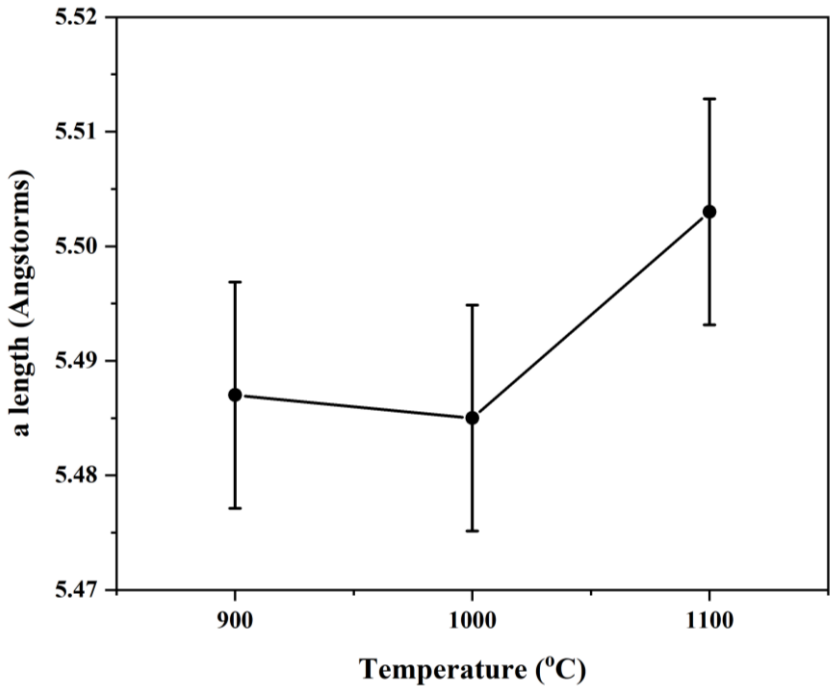

Figure 5.6: Temperature (ºC) vs Rhombohedral lattice parameter, "a" length (Angstroms) of the crushed sintered LSCF6428 pellets where the black dots are the experimental data points along with the error bars.

The effect of the sintering temperature on the perovskite lattice parameter, "a" length is shown in Figure 5.6. There is no clear trend between the sintering temperature and the "a" length lattice parameter. The slight decrease in "a" length between the 900 ºC and 1000 ºC led to a sudden change in relation to peak splitting from the XRD diffraction pattern as shown in Figure

5.1. However, there is then an increase in "a" length when the sintering temperature is increased from 1000 ºC to 1100 ºC, which is a similar the trend of a sudden increase in mean crystallite size of nearly double the value. The "a" length lattice parameter has been shown to decrease with increasing strontium incorporation into the LSCF6428 rhombohedral unit cell [185-187]. Given that there is no appearance of $SrCO_3$ impurity peaks in the XRD diffraction pattern, the change in "a" length lattice parameter of the perovskite oxide could be caused by the sintering temperature exceeding the melting temperature of the surface of the LSCF6428 [206]. However, in a study on sintering of different compositions of lanthanum strontium cobaltite ferrite for both different times and temperatures, both contraction and expansion of the "a" length lattice parameter have been reported [200]. The changes in "a" length lattice parameter also influence the volume and density parameters where there are changes when sintering at different temperatures from 900 ºC to 1100 ºC as shown in Table 5.2.

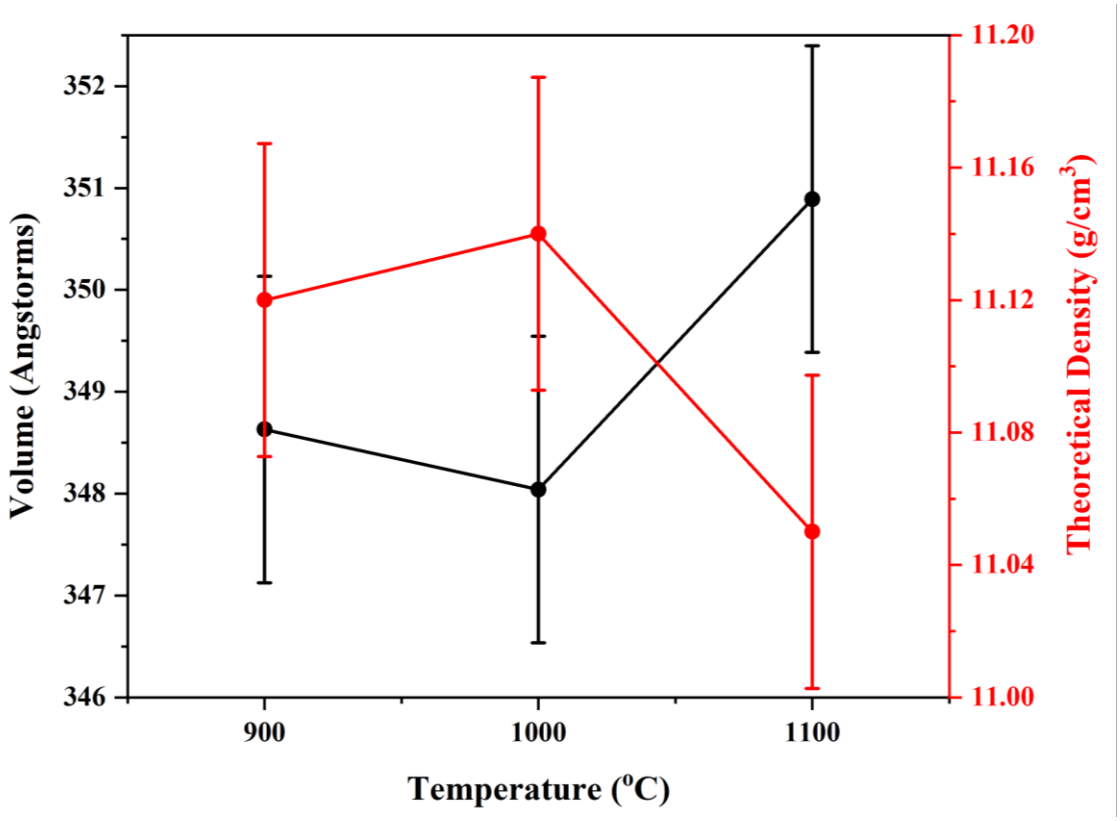

Figure 5.7: Temperature (ºC) vs Rhombohedral Volume (Angstroms- black line with error bars at black dots refer to as experimental data points) and Theoretical Density (g/cm^3- red line with error bars at red dots refer to as experimental data points) of the crushed sintered LSCF6428 perovskite oxide pellet.

When sintering between 900 ºC and 1000 ºC (see Figures 5.2-.5.3), the amount of diffraction peak splitting increases, suggesting that the complete transformation to space group R3c (from

simple cubic). However, the sudden decrease in the unit cell volume of the microstructure between 1000 ºC to 1100 ºC (Figure 5.7) could have been due to LSCF6428 exceeding its melting temperature between 1050 ºC and 1100 ºC and specifically the loss of Sr which will be further analysed using the SEM-EDX. Loss of Sr above 950 ºC has been reported in similar LSCF compositions [186].

5.2 Microstructure Characterisation of the sintered LSCF6428 Nanopowder

Each of the sintered pellets were crushed to a fine powder to ensure that a uniform layer distribution occurs over the carbon pad so that an in-depth analysis using SEM-EDX could take place. Surface SEM images are shown in Figures 5.8-5.10 and indicate the formation of a porous material.[113]. To get a detailed understanding into the effect of the sintering behaviour elemental distributions of the metal cations in the LSCF6428 sintered powder, elemental maps are shown in Figures 5.8-5.10. All the elements for the perovskite metal oxide are present but with a clear trend in the increase in concentration of the Sr element as the sintering temperature increases, as shown in Tables 5.3-5.5.

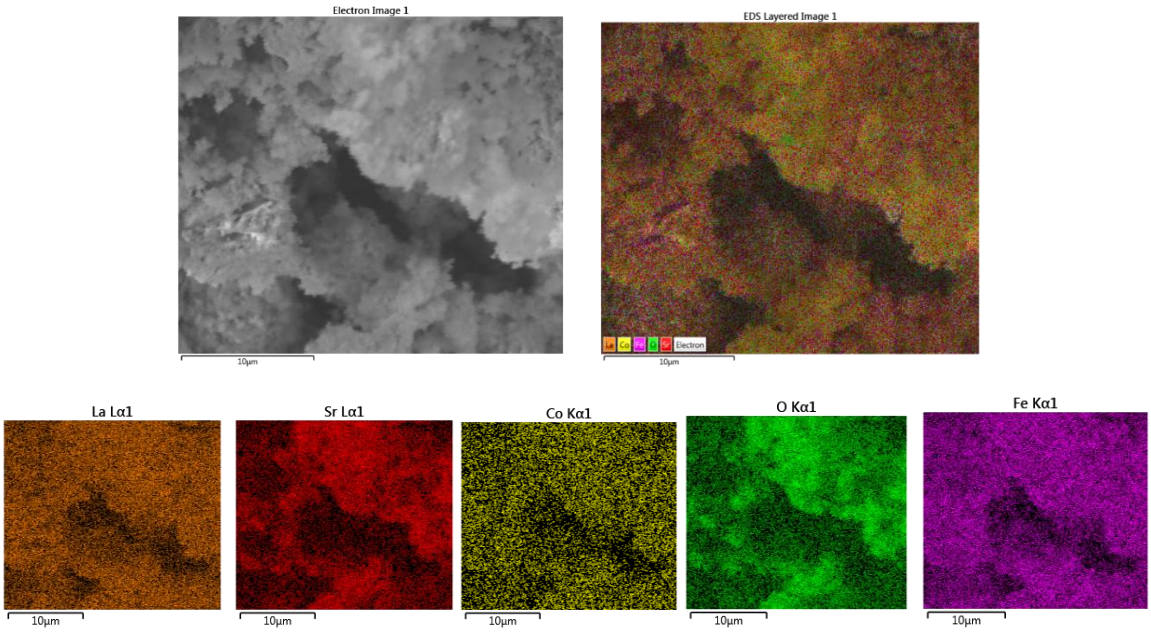

Figure 5.8: SEM image of LSCF6428 of crushed pellet sintered at 900 ºC. (Left) Secondary electron image, (Right) SE image overlaid with the elemental maps with individual elemental maps shown below, suggesting a homogenous distribution of the LSCF6428 elements.

Table 5.3: LSCF6428 sintered at 900 ºC with a comparison of EDX derived composition (assuming oxygen stoichiometry) with the expected composition indicated significant Sr deficiency.

Elements	Measured Composition	Expected Composition
Iron (Fe)	0.958	0.8
Strontium (Sr)	0.216	0.4
Lanthanum (La)	0.626	0.6
Cobalt (Co)	0.2	0.2

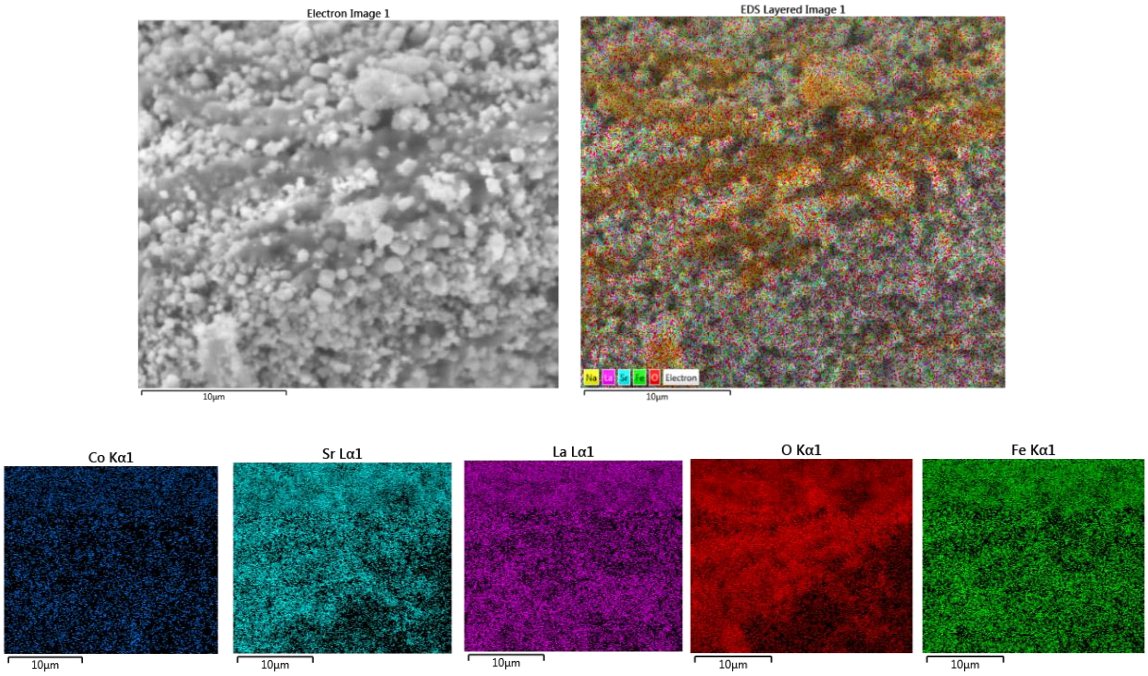

Figure 5.9: SEM image of LSCF6428 crushed pellet sintered at 1000 ºC. (Left) Secondary electron image, (Right) SE image overlaid with the elemental maps with individual elemental maps shown below, suggesting a homogenous distribution of the LSCF6428 elements.

Table 5.4: LSCF6428 sintered at 1000 ºC with a comparison of EDX derived composition (assuming oxygen stoichiometry) with the expected composition indicated significant Sr deficiency.

Elements	Measured Composition	Expected Composition
Iron (Fe)	0.911	0.8
Strontium (Sr)	0.295	0.4
Lanthanum (La)	0.576	0.6
Cobalt (Co)	0.182	0.2

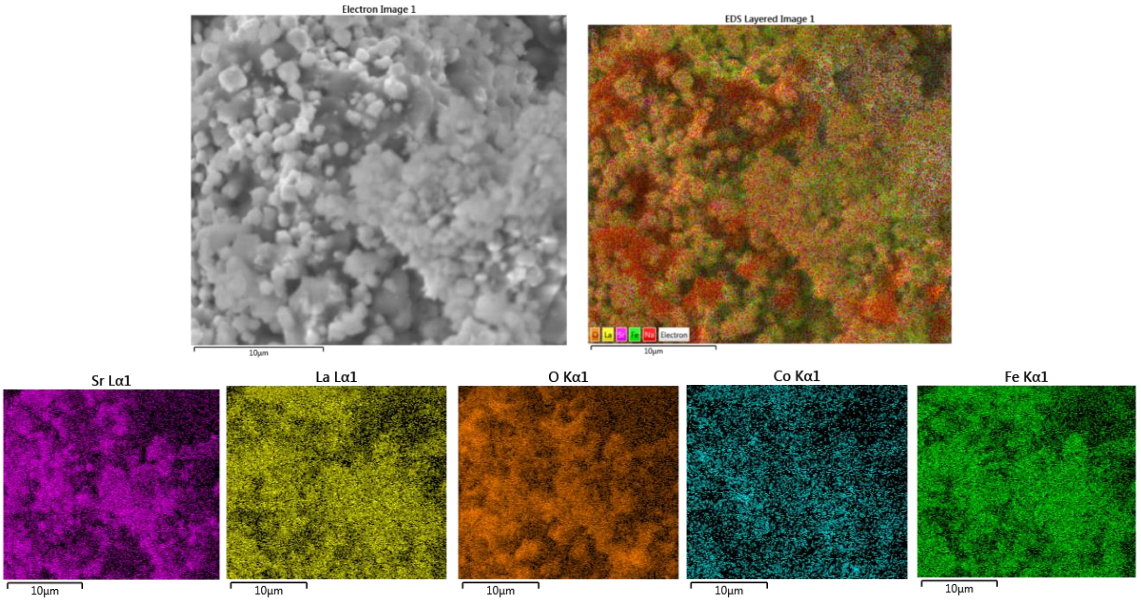

Figure 5.10: SEM image of LSCF6428 pellet sintered at 1100 ºC. (Left) Secondary electron image, (Right) SE image overlaid with the elemental maps with individual elemental maps shown below, suggesting a homogenous distribution of the LSCF6428 elements.

Table 5.5: LSCF6428 sintered at 1100 ºC with a comparison of EDX derived composition (assuming oxygen stoichiometry) with the expected composition indicated significant Sr deficiency.

Elements	Measured Composition	Expected Composition
Iron (Fe)	0.903	0.8
Strontium (Sr)	0.32	0.4
Lanthanum (La)	0.599	0.6
Cobalt (Co)	0.178	0.2

Overall, and despite the elemental maps looking homogenous, the analysis of EDX based elemental quantification by assuming oxygen stoichiometry suggests a slight enrichment in Fe, appropriate amounts of Co and La and a significant deficiency of Sr, as shown in Tables 5.3-5.5. This Sr deficiency reduces as the sintering temperature increases and this is consistent with the trend change in the decrease in 'c' lattice parameter and micro strain measured by XRD (Tables 5.1- 5.2). To determine how both the Sr element composition and the structural parameters affect the metal-oxygen vibrations and structural distortion of the LSCF6428 sintered at three different temperatures, the Raman spectroscopy was used.

5.3. Raman Spectroscopy of the sintered LSCF6428 nanopowder

The Raman spectra of the LSCF6428 for the three different sintering temperatures were examined in the Raman Shift range of 200 – 1000 cm^{-1} as can be seen from Figure 5.11. From the results there is a no linear trend in relationship between Raman intensity and sintering temperature.

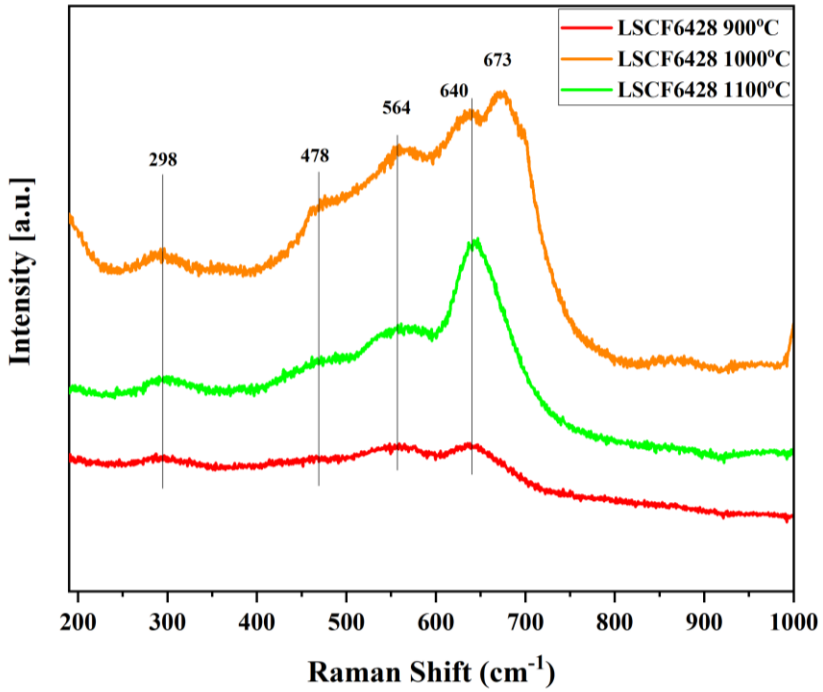

Figure 5.11: Raman Spectra of LSCF6428 crushed pellets after sintering at 900°C, 1000 °C, 1100 °C with excitation wavelength of 532 nm.

It can be seen from Figure 5.11 that the LSCF6428, when sintered at 1000 °C, has 5 main defined peaks that are identified at 298 cm^{-1}, 478 cm^{-1} ,564 cm^{-1}, 640 cm^{-1} and 673 cm^{-1}. This is due to the combination of increased peak splitting of the rhombohedral structure as shown in Figure 5.3, and a small mean crystallite size of 38 nm as referred to in Table 5.1.

However, for the powder sintered at 900 °C, there is a lower and weaker intensity in the Raman spectra, and peaks are less well defined and are broader. This is consistent with the decreased peak splitting of the rhombohedral structure in relation to the XRD peak fitting shown in Figures 5.2. While for the powder sintered at 1100 °C, the Raman intensity increases above the spectrum of the LSCF6428 sintered at 900 °C but the peaks are less well defined than for the LSCF sintered at 1000 °C.

The peak located at 298 cm^{-1} can be assigned to the oxygen octahedra tilting following work examining the Raman spectra peak positions of $LaFeO_3$ [207]. The peak located at 478 cm^{-1} may be due to octahedral rotation and is not so well defined at 900 ºC. While the peaks at 564 cm^{-1} and 640 cm^{-1} can be assigned to the Co/Fe – O bonds indicating the bending vibration and stretching vibration of the metal-oxide bonding respectively. Detection of the three peaks at, 478 cm^{-1}, 564 cm^{-1} and 640 cm^{-1} from this work is in line with a study carried out by using the micro-Raman at room temperature in investigating the metal-oxygen vibrations that characterised the rhombohedral structure of the $LaCoO_3$ perovskite oxide with positions located at 430 cm^{-1}, 557 cm^{-1} and 650 cm^{-1} [190].

However, for the 1000 ºC only, there is an additional peak detected at 673 cm^{-1} which is a similar match to a study which was carried out involving strontium substitution for lanthanum at the A site in the perovskite, $LaCoO_3$. The effect of the partially substituted strontium led to the transition of a broad peak from the LCO to a defined peak for the Sr doped LCO due to the distortion effect in the structure [208]. However, the 673 cm^{-1} peak disappears when the sintering temperature increases to 1100 ºC and transitions towards a single defined peak located around 650 cm^{-1} (perhaps due to the loss of Sr due to sintering at or above the melt temperature – as inferred by XRD and Figure 5.4 specifically). The effect of the splitting pattern at around 600 cm^{-1} (643 cm^{-1} and 673 cm^{-1} peaks) is similar to a stoichiometry study $SrFeO_{3-\delta}$ where there was a splitting pattern around these Raman wavenumbers [209]. In reference to the actual composition of the Sr element obtained from the EDX from Tables 5.3-5.5, the substitution of the Sr element decreases the deficiency at the A site of the LSCF6428, playing a key role in defining the peaks.

5.4. Density and SEM morphological of the sintered LSCF6428 nanopowder

To determine the density of the LSCF6428 cathode materials for all sintering temperatures ranging from 900 ºC to 1100 ºC, the Archimedes and Geometrical method was applied, as described in the methodology section, and the results are presented in Table 5.6 (rounded to 2 decimal points). [22][210]

There is a relationship between the sintering temperature and the parameters being analysed. As the sintering temperature increases, the density, both Archimedes and Geometrical increases because the porosity of the material decreases which is consistent with the increase in crystallite

size and the decrease in strontium deficiency. As the sintering temperature increases, the thickness shrinkage of the pellet decreases.

Table 5.6: Archimedes and Geometrical density (rounded to two decimal places), porosity (rounded to one decimal place) and pellet shrinkage ratio on sintering LSCF6428 at 900, 1000 and 1100 °C

Temperature (°C)	**900**	**1000**	**1100**
Archimedes Density (g/ cm^3)	7.26	8.29	9.85
Archimedes Porosity (%)	38.4	25.7	10.9
Geometrical density (g/ cm^3)	7.21	7.47	8.24
Geometrical Porosity (%)	34.7	32.3	25.3
Thickness Shrinkage	0.19	0.18	0.16

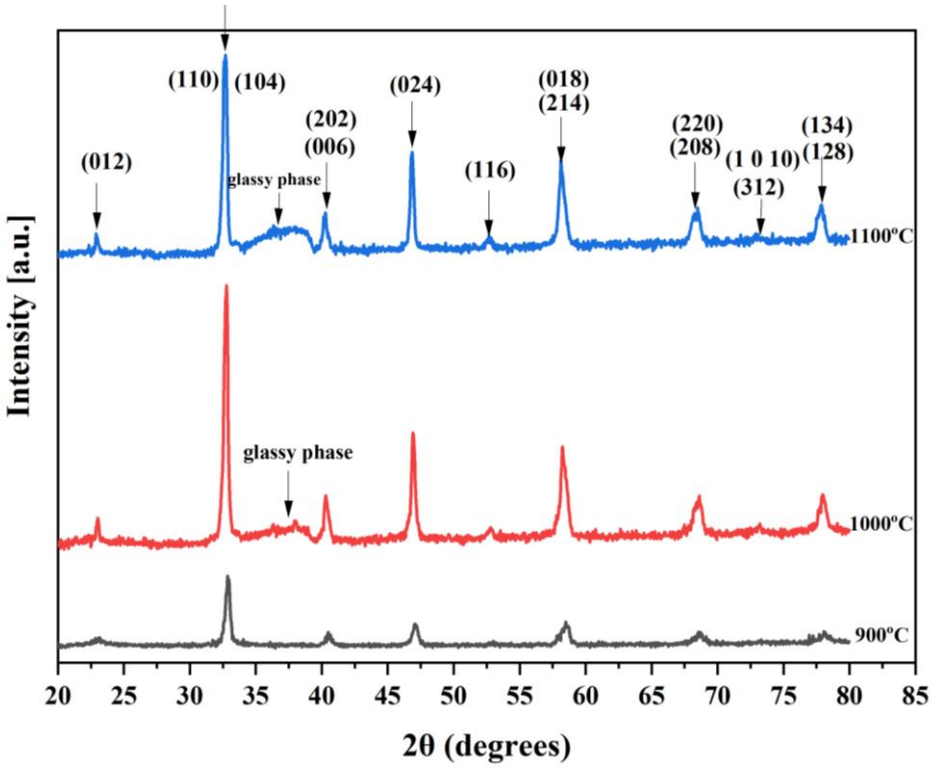

Figure 5.12: Bruker XRD patterns of 3 wt% LSCF6428 whole pellets sintered for 1 h at temperatures of 900 °C (grey line), 1000 °C (red line) and 1100 °C (blue line). (indexed to the rhombohedral phase in ICDD, 04-017-2448- R3c).

Based on the EDX result in relation to the Sr deficiency, whole pellets of LSCF6428, sintered at different temperatures, was examined further using XRD (as described in the methodology) to determine whether any additional phases were present other than the rhombohedral perovskite phase. From the XRD diffraction pattern, there is indication of a glassy amorphous phase forming between the 35 – 40 2θ range as shown in Figure 5.12. Trends can be recognised for the glassy amorphous phase and the Sr composition and crystallite size as the sintering temperature increases. Between the sintering temperatures of 900 ºC to 1000 ºC, the glassy amorphous phase appears whilst the Sr deficiency decreases suddenly from the measured Sr composition of 0.21 and 0.29 as referred to in Tables 5.3 and 5.4 respectively. However, for the sintering temperatures between 1000 ºC and 1100 ºC, the glassy amorphous phase increases which is consistent with the increase in the crystallite size of the perovskite phase from around 38 nm to 70 nm, along with a further decrease in strontium deficiency (to 0.32, Table 5.5). The effect of the strontium incorporation into the perovskite unit lattice has resulted in the formation of a second glassy amorphous phase within the LSCF6428 pellet. Therefore, the established microstructure of the LSCF6428 at three different sintering temperatures was examined further through SEM imaging to distinguish between the grain growth of the crystalline perovskite phase and the glassy, amorphous phase.

SEM images Figures 5.13-5.15 were obtained to observe densification, grain boundaries, grain growth and porosity for sintering temperatures of 900, 1000 and 1100 ºC. The SEM imaging threshold of the microstructure was determined through an upper estimate of the thresholding as shown in Figure 5.13-5.15c to distinguish between the formation of the grains and the porosity along with the selected areas in the yellow box as shown in Figures 5.13-5.15d.

At 900 ºC, from the secondary electron image, the microstructure does not densify effectively as interparticle necking is occurring showing only partially sintered grains (Figure 5.13). That has led to the retention of a small crystallite size. At 900 ºC, the pellet has undergone the first stage of the sintering mechanism known as initial neck formation. [111]. Secondary imaging (Figure 5.13 a) shows a lack of definition of grains and pores against a low contrast background matrix however very black pores that are about the same size as the white grains are visible in backscattered imaging (Figure 5.13b). There is a clear lack of grain growth in the BSE images consistent with the XRD measurements of a crystallite size of 30 nm (Table 5.1).

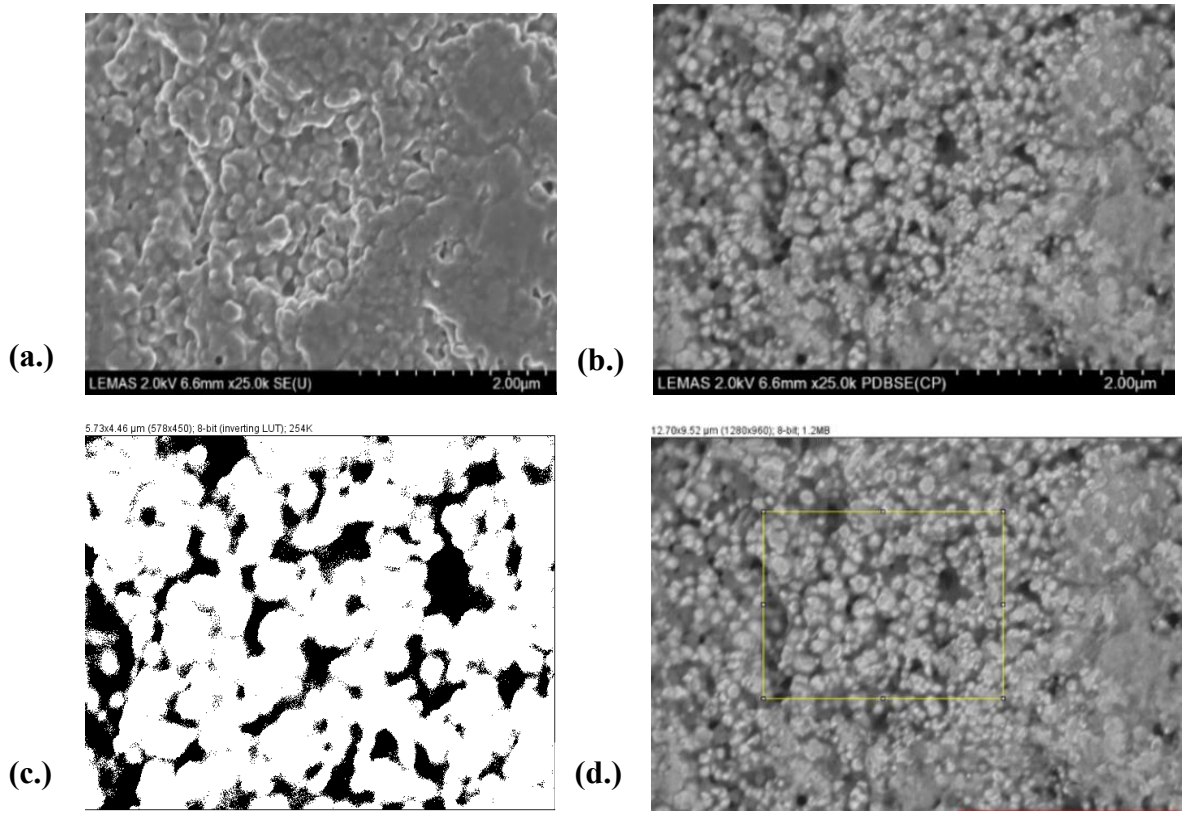

Figure 5.13: SEM images of the upper estimate of porosity sintered LSCF6428 pellet at 900 ^{o}C for 1 h a) secondary b) back scattered, c) backscattered with yellow box used for pore size measurement (inset) and d) thresholded image of yellow box region where black is taken to be the maximum pore structure.

When the sintering temperature is increased from 900 ^{o}C to 1000 ^{o}C, grain growth is clearly visible in both the secondary and backscattered images (Figure 5.14a. and b.). This is consistent with the transformation to the full rhombohedral structure measured by XRD (Figure 5.3) and other reports [211]. The increase in sintering temperature has also enabled the sintered grains to impinge on each other through neck growth to densify the ceramic however pores are still visible throughout the microstructure. The effect of the grain growth is consistent with the measured increase of the Archimedes density (Table 5.6) and the increase of mean crystallite size to 38.4 nm (Table 5.1). In comparison to the 900 ^{o}C sintered microstructure, it has caused the interconnected pore channels to become more closed off and reducing the area of porosity to 25% as shown in Table 5.6.

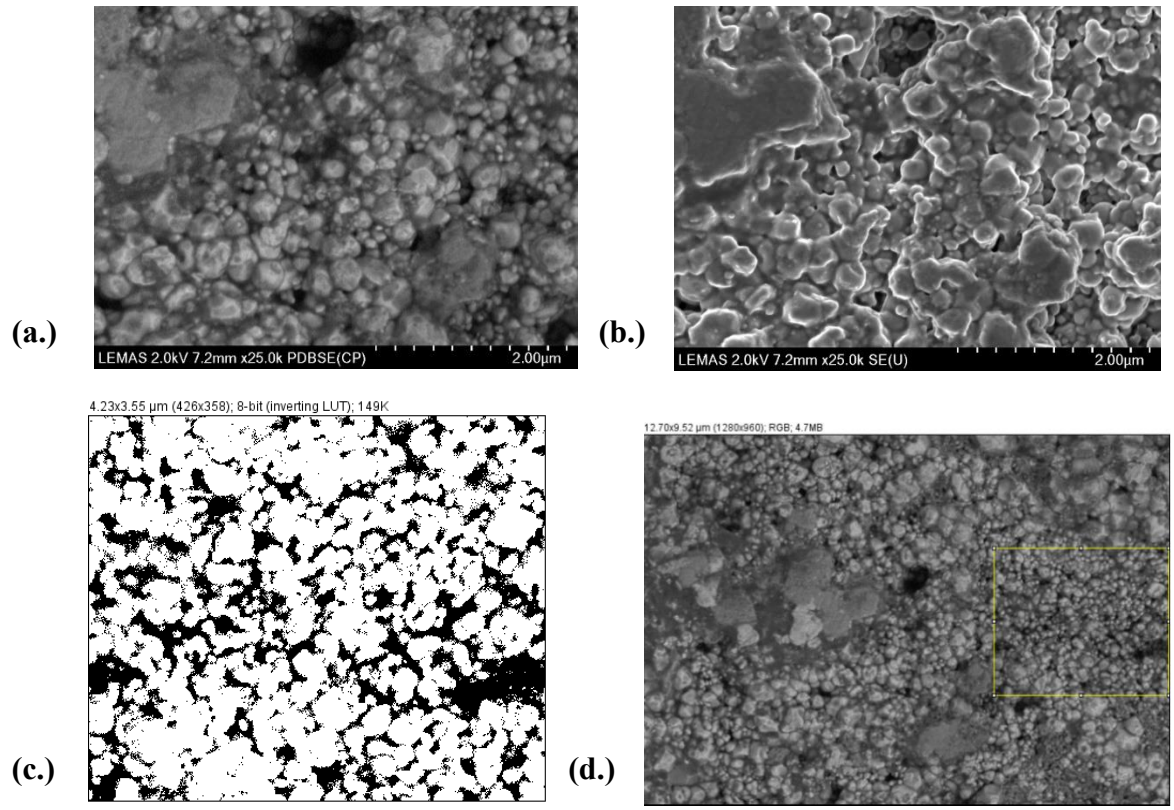

Figure 5.14: SEM images of the upper estimate of porosity of sintered LSCF6428 pellet at 1000 ºC for 1h a) secondary b) back scattered, c) backscattered with yellow box used for pore size measurement (inset) and d) thresholded image of yellow box region where black is taken to be the maximum pore structure.

At 1100 ºC, the sintering process reaches its final stage consistent with the sintering taking place at or above the melting temperature. Significant grain growth to micrometres and corresponding pore shrinkage are clearly visibly given the sudden decrease in area porosity of only 10% (Figure 5.15) Those factors have also caused significant densification (Table 5.6) yet the mean crystallite size is measured to only be 70 nm by XRD suggesting the grains in the SEM images are polycrystalline. Sintering temperature was found to have a greater influence on the porosity and densification of the microstructure compared to the effect of dwell time. To determine how the parameters of N_2 gas adsorption of the sintered LSCF6428 is affected by the sintering BET analysis was carried out.

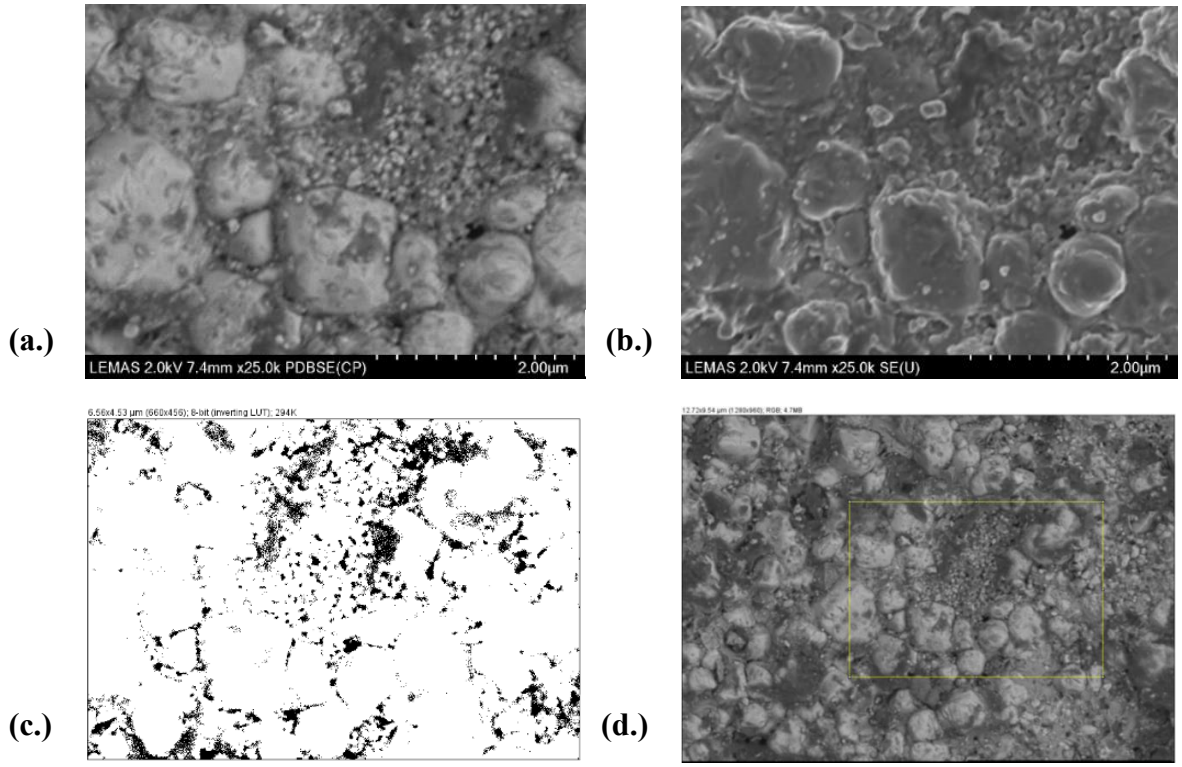

Figure 5.15: SEM images of the upper estimate of porosity of sintered LSCF6428 pellet at 1100 ºC for 1h a) secondary b) back scattered, c) backscattered with yellow box used for pore size measurement (inset) and d) thresholded image of yellow box region where black is taken to be the maximum pore structure.

5.5. Porous Characterisation of the sintered LSCF6428 nanopowder using BET method

Nitrogen adsorption isotherms of the sintered LSCF6428 samples were acquired and measured using the BJH method. Based on the IUPAC definitions, the LSCF6428 sintered at 900 ºC and 1000 ºC is of Type IV in relation to its mesoporous structure, its wider pore size distribution and shape of the hysteresis loop, which is a combination of, Type H1/ H3 of hysteresis loop (Figure 5.16). As can be seen from the isotherm, there is capillary condensation of the material taking place at relative high pressure. Whilst the adsorption is not limited at the higher pressure range between the 0.82 to 1.0 (p/p_0) which is a representation of the H3 hysteresis loop. However, for the 1100 ºC, the hysteresis loop has changed to Type H4 (despite it obtaining a similar specific surface area value to the 1000 ºC sintered LSCF6428), indicating the presence of silt shaped narrow pores which can be related to the SEM image as shown in Figure 5.15. [199]

Table 5.7: The total pore volumes and average pores sizes of LSCF6428 sintered at three different temperatures (derived from BJH analysis of N_2 adsorption/desorption isotherms).

Temperature (ºC)	Total Pore Volume (sintered) (cm^3/g)	Average Pore Size (sintered) (nm)
900	0.037	53.09
1000	0.024	68.76
1100	0.008	48.30

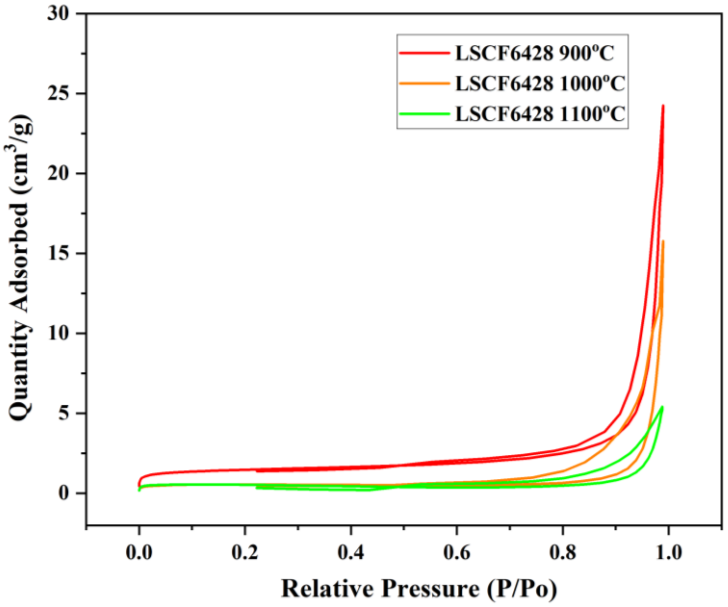

Figure 5.16: The BJH Nitrogen adsorption and desorption isotherm of crushed sintered pellet LSCF6428 at 900 ºC (red line),1000 ºC (orange line) and 1100 ºC (green line).

Pore size distribution is considered to be a significant parameter that affects sintering kinetics of a real powder compact.[108] The pore size distribution was measured using the BJH method for the analysis of N_2 adsorption and desorption isotherms. It can measure the whole surface area of a crushed sintered pellet to obtain quantitative information across the sintering range of 900 ºC to 1100 ºC. The method was used to analyse the size of the open pores of the sintered LSCF6428 samples. For the LSCF6428 sintered at 900 ºC, the curve shows a pore size distribution that ranges between 0 and 100 nm (Figure 5.17). It can be seen that the average pore volume remains ~ 50 nm across the three sintering temperatures (Table 5.7). However, there is a sudden decrease in the total pore volume on sintering above 1000 ºC (Table 5.7) consistent with the significant grain growth seen by SEM (Figure 5.15) and is potentially caused by the sintering temperature approaching the melting of the LSCF6428.

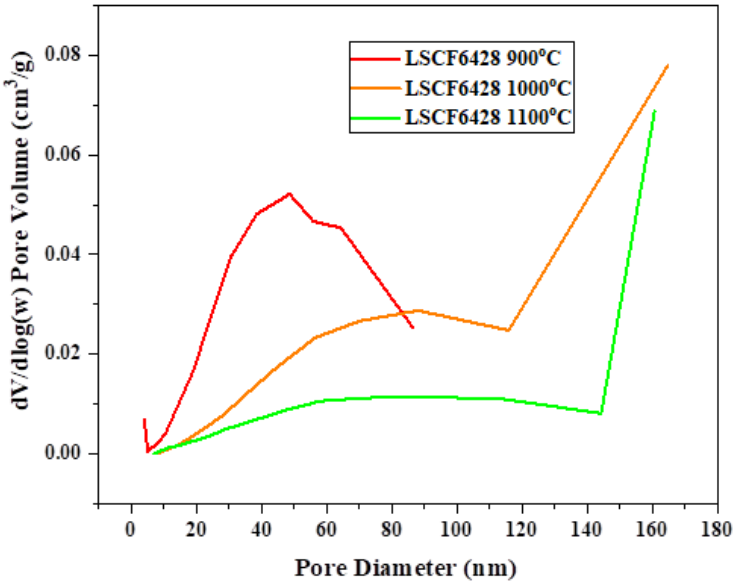

Figure 5.17: Pore size distribution of crushed sintered pellets of LSCF6428 sintered at 900 ºC (red line), 1000 ºC (orange line) and 1100 ºC (green line).

The pore size distribution appears to broaden with the increase in sintering temperature (Figure 5.17) even though the average remains relatively unaltered (Table 5.7). There is a decrease in BET surface area from 900 ºC to 1000 ºC then remaining constant at 1100 ºC (Figure 5.18 and Table 5.18). This is consistent with initial densification occurring between 900 ºC and 1000 ºC and densification with significant grain growth occurring above 1100 ºC. The values obtained for the LSCF6428 at 1000 ºC of the specific surface is similar to that reported in a previous study when LSCF6428 was directly sintered in air at 1000 ºC.[211]

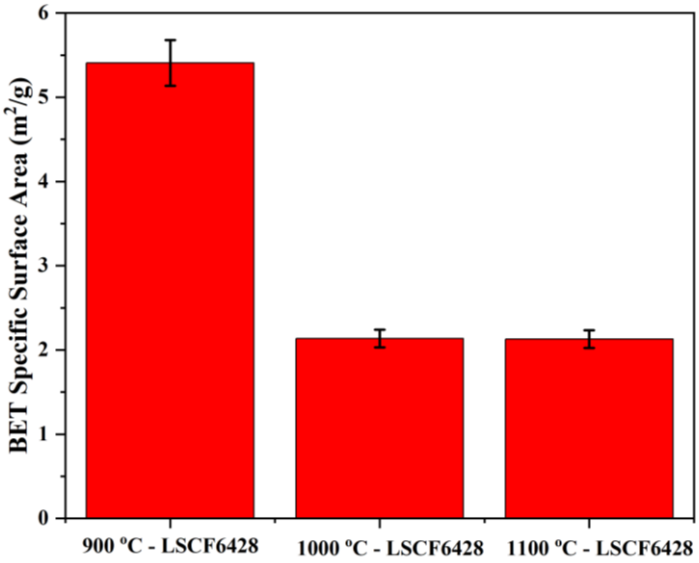

Figure 5.18: BET Specific Surface Area of the crushed sintering pellets of LSCF6428 at 900 ºC,1000 ºC and 1100 ºC with error bars.

Table 5.8: BET specific surface area values of the LSCF6428 crushed sintered pellets at three different sintered temperatures.

Temperature (°C)	**BET specific surface area (m^2/g)**
900	5.41 ± 0.033
1000	2.14 ± 0.029
1100	2.13 ± 0.027

Summary – Chapter 5

Sintering of the LSCF6428 rhombohedral single phase was achieved at 1000 °C while retaining a crystallite size of 40 nm i.e. without any apparent grain growth and with a porosity in the ceramic of 25% (which meets the porosity criteria of 20-40%) that was measured to be in the 50 nm size range by SEM. That was comparable to the crystallite size obtained by XRD (which confirmed a rhombohedral phase was produced). There is also evidence of a second/matrix phase between the grains in the SEM imaging which is consistent with the expected Sr deficiency in the LSCF6428 grains suggested by the XRD of the calcined material. SEM-EDX analysis however suggested Sr enrichment as estimates of Sr content relative to all metal cation ions was at 0.3 rather than the expected 0.2 from Chapter 4. Overall, the sintering at 1000 °C produces a LSCF6428 microstructure that would be suitable for IT-SOFCs cathode material despite evidence of the presence of some grain size and phase inhomogeneity within the 25% porosity ceramics.

Chapter 6- Synthesis and Characterisation of Calcined $La_{0.3}Pr_{0.3}Sr_{0.4}Co_{0.2}Fe_{0.8}O_{3-\delta}$ $La_{0.3}Nd_{0.3}Sr_{0.4}Co_{0.2}Fe_{0.8}O_{3-\delta}$ and $Nd_{0.6}Sr_{0.4}Co_{0.2}Fe_{0.8}O_{3-\delta}$

6.1 Microstructure Characterisation of the metal-alginate complexes of LPSCF33428, LNSCF33428 and NSCF6428

Late series lanthanide coordination with the alginate macromolecule have rarely been studied in detail compared to other divalent and trivalent metal cations (commonly transition metals) and the earlier elements of the lanthanide series such as lanthanum and cerium.[108-109][164][166] To determine how lanthanides other than lanthanum behave when undergoing sodium alginate sol gel, praseodymium and neodymium have been used as dopants for substitution with the host A site metal cation, lanthanum from the chemical composition LSCF6428. This chapter will determine how the behaviour of the dopants influences the structural properties and porosity of the calcined microstructure of Prx of Ndx doped L0.6-xSCF6428.

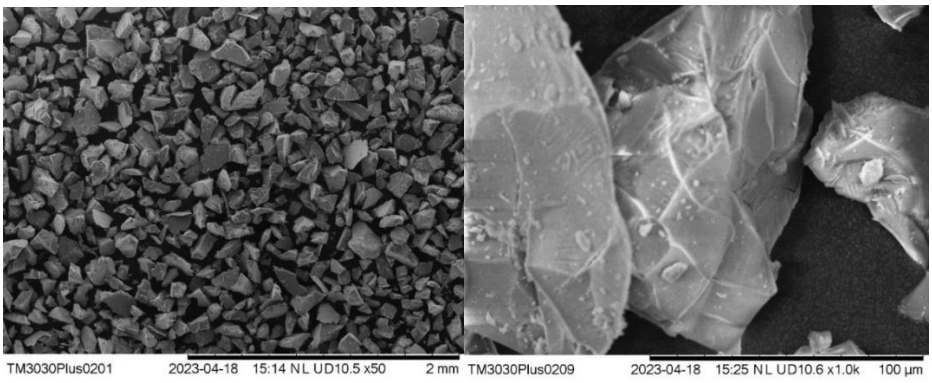

Figure 6.1: SEM images of the metal-alginate complex of LPSCF33428 precursors. Left (Low magnification) and Right (High magnification) of crushed metal-alginate beads

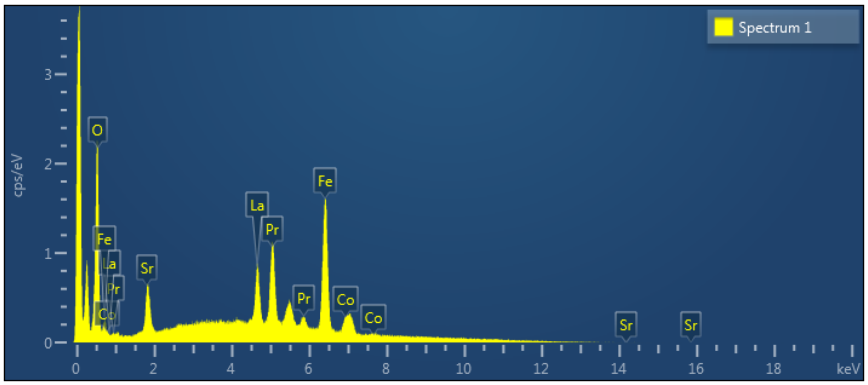

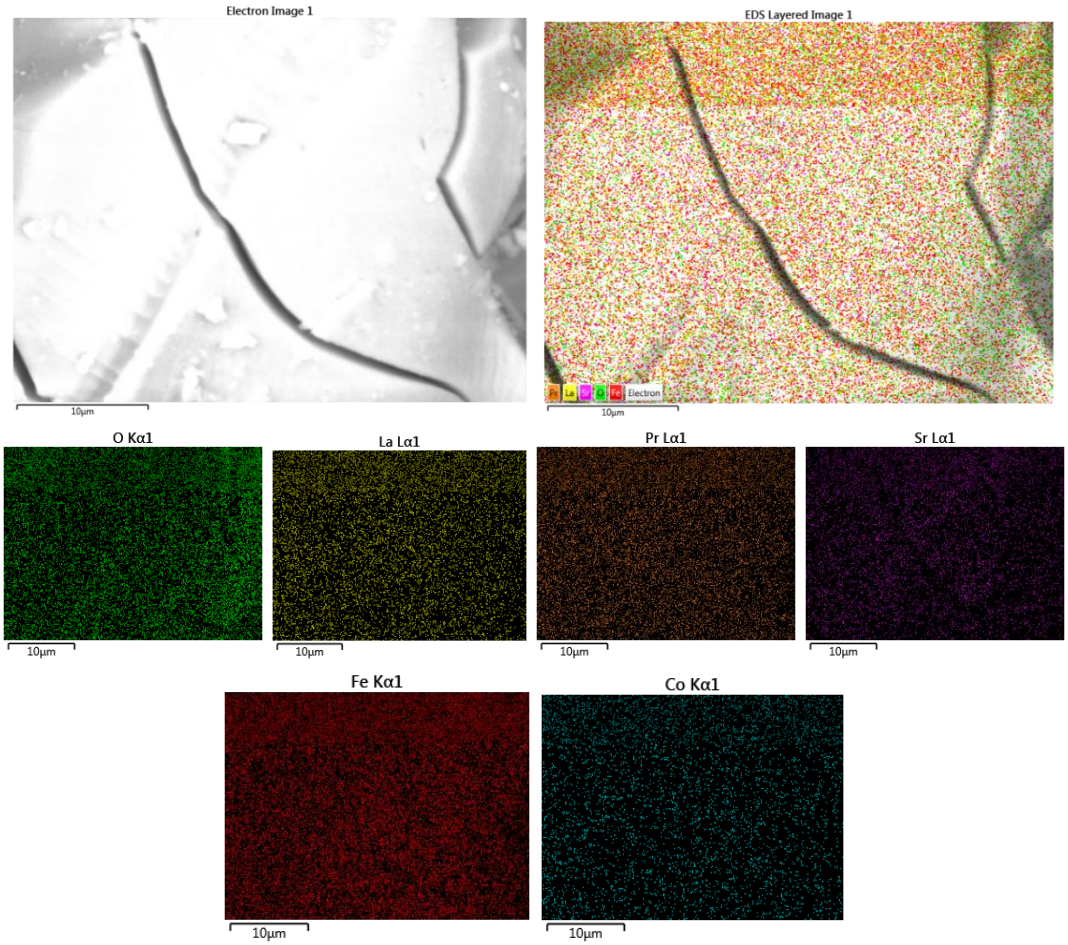

Figure 6.2: (Above) SEM image EDX spectrum of metal-alginate complex of LPSCF33428 precursor (Below) showing the presence of all the key metal elements for LPSCF33428 with elemental maps showing a homogenous distribution of the elements within a metal-alginate bead

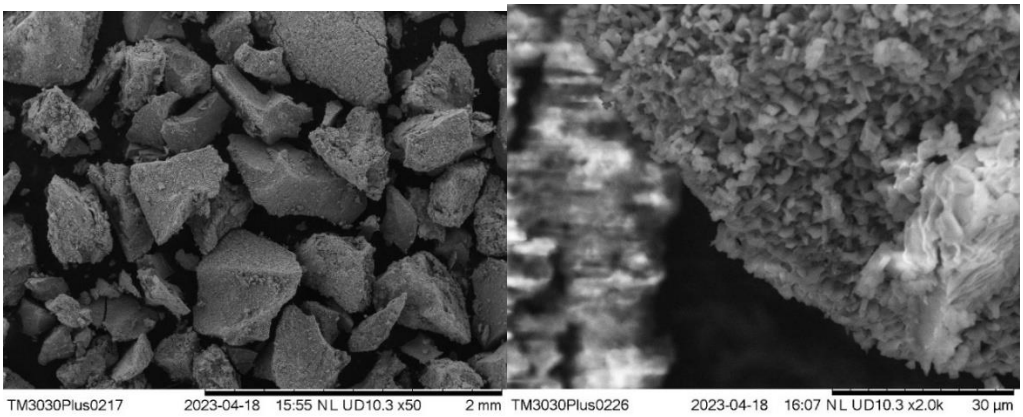

Figure 6.3: SEM images of the metal-alginate complex of LNSCF33428 precursors. Left (Low magnification) and Right (High magnification) of crushed metal-alginate beads

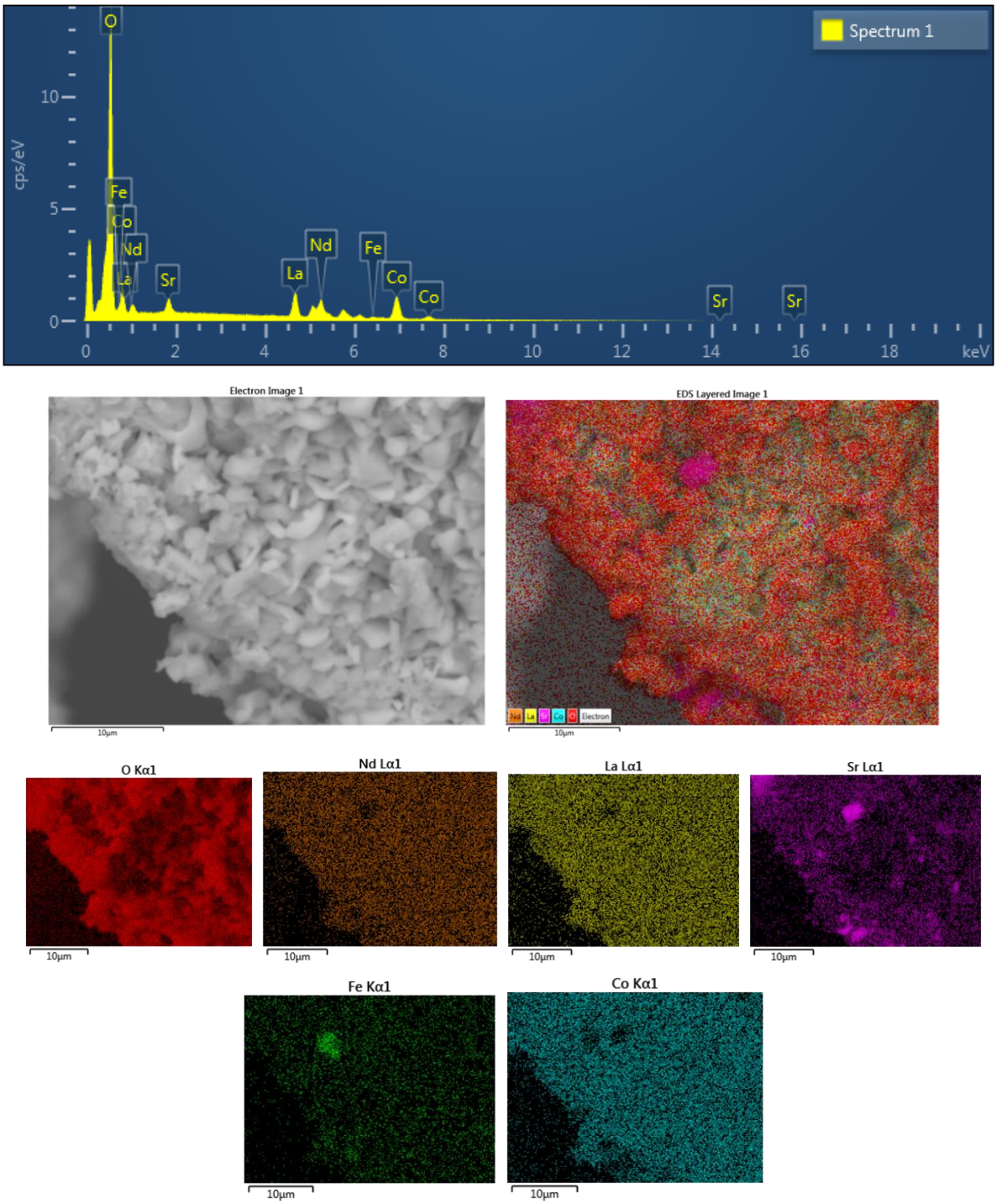

Figure 6.4: (Above) SEM image and EDX spectrum of metal-alginate complex of LNSCF33428 precursor (Below) showing the presence of all the key metal elements for LNSCF33428 with elemental maps showing some Sr and Fe segregation but otherwise a homogenous distribution of the elements within a metal-alginate bead

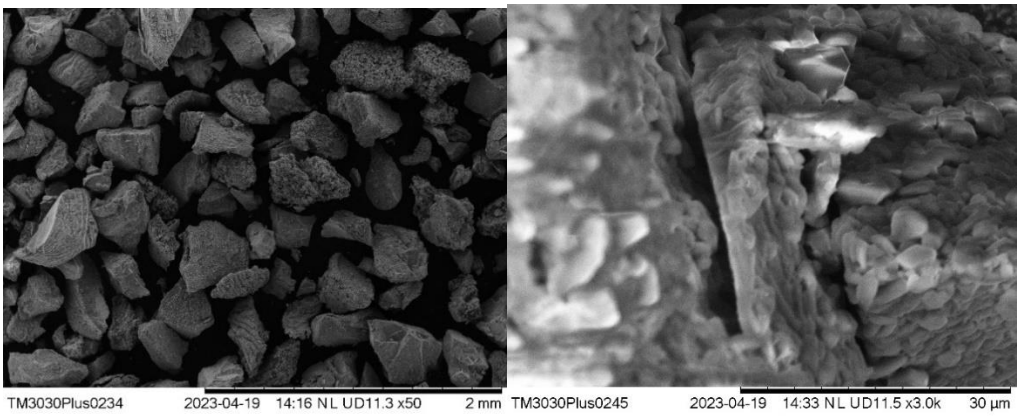

Figure 6.5: SEM images of the metal-alginate complex of NSCF6428 precursors. Left (Low magnification) and Right (High magnification) of crushed metal-alginate beads

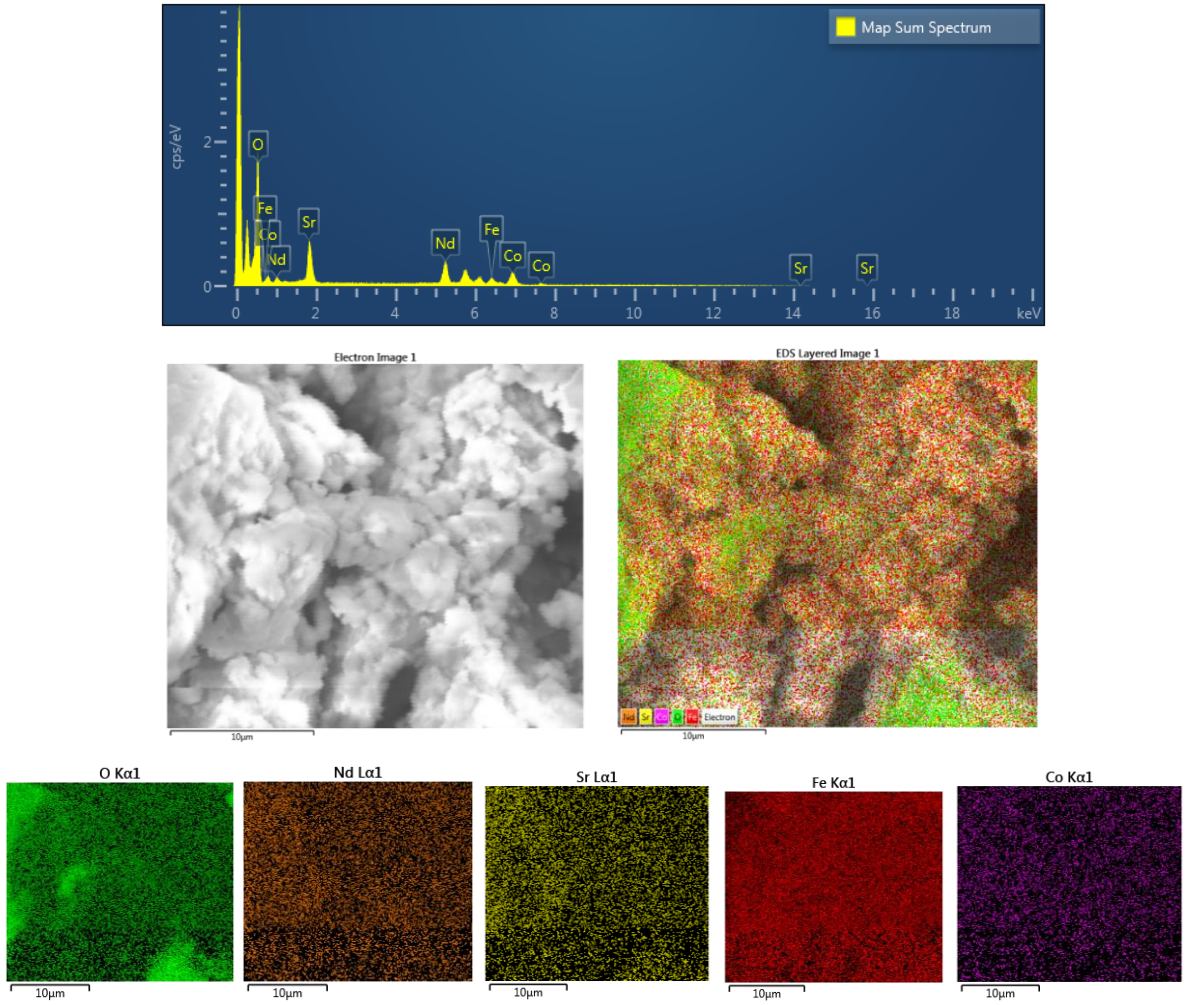

Figure 6.6: (Above) SEM image EDX spectrum of metal-alginate complex of NSCF6428 precursor (Below) showing the presence of all the key metal elements for NSCF 6428 with elemental maps showing some Sr segregation but otherwise a homogenous distribution of the elements of a metal alginate bead.

From the SEM images in Figures 6.1, 6.3 and 6.5 the effect of the ion exchange between the sodium alginate and the metal cations can be observed. It can be seen from the elemental analysis by EDX that all the multivalent metal cations, La, Sr, Pr or Nd, Co and Fe have been successfully exchanged into the alginate structure as shown in Figures 6.2, 6.4 and 6.6. The elemental maps indicate that all the multivalent metal cations for LPSCF33428 are homogenously distributed throughout a bead, whereas for Nd compositions (LNSCF33428 and NSCF6428), there is a more varied degree of metal cations distribution between the LNSCF33428 and NSCF6428. The Na element was omitted from the SEM/EDX analysis to determine the rare earth dopant behaviour effects upon the metal alginate complexes. That is done through the substitution of the host A site element, La from the starting or parent material by the dopant of either Pr or Nd. For the LNSCF33428, the elements, Sr and Fe are not homogeneously distributed while the O element is somewhat concentrated and clustered in comparison to the NSCF6428 as shown in Figure 6.4 and 6.6 respectively. The remaining multivalent cations, La, Nd and Co were homogeneously distributed between the LNSCF33428 and NSCF6428. Regardless, the size of the metal-alginate beads is estimated to be less than 100 μm prior to thermal decomposition for all the three rare earth doped LSCF compositions. It can also be observed that there is an appearance difference between the Pr and Nd doped LSCF. For the LPSCF33428 higher magnification imaging gives a smooth surface appearance to the crushed metal-alginate complex beads as shown in Figure 6.1. Whilst for the LNSCF33428 (Figure 6.3) and NSCF6428 (Figure 6.5) higher magnification imaging shows that the surface of the crushed metal alginate complex bead is not smooth in comparison to the LPSCF33428. Neodymium is hygroscopic, so it is possible water adsorption has roughened the surface and even causing the inhomogeneity of the O element distribution.[210][212] The study by Barbora et al., investigated how the influence of the lanthanide cations in the chemical composition, LSCF affect the thermal stability of the perovskite oxide.[210] That is due to numerous elemental properties, as shown in Table 6.1, which may affect thermal stability when the metal–alginate complexes undergo thermal decomposition towards a single phase perovskite oxide. Moreover, it is difficult to tell from the SEM images of the metal alginate complexes alone how thermal decomposition of the Pr and Nd doped LSCF will affect the precise distribution of the perovskite oxide composition when calcined in an oxygen atmosphere.

Table 6.1: Rare Earth Elemental properties associated with A-O bond where A = rare earth element [86]

Rare Earth Elemental Properties/ A-O bond	**La - O**	**Pr - O**	**Nd - O**
Ionic Radius for rare earth elements (Å)	1.36	1.30	1.27
Pauling electronegativity of rare earth	1.10	1.13	1.14
Electronegativitiy difference (between A cation and oxygen anion) of A - O	2.34	2.31	2.30
Ionic bond character (%)	74.56	73.65	73.35
Covalent bond character (%)	25.44	26.35	26.65
Electronic Configuration of Rare Earth Elements	$[Xe]4f^{1}5d^{1}6s^{2}$	$[Xe]4f^{3}6s^{2}$	$[Xe]4f^{4}6s^{2}$

The general reaction mechanisms which are undertaken during the ion exchange between each of the rare earth metallic salt nitrates and the polysaccharide molecule, sodium alginate (ALG) prior to thermal analysis can be shown in the chemical equations below (6.1-6.2), in which the chemical formula of the sodium alginate is Na-ALG = $C_6NaH_7O_6$ and x = the number of water molecules. [105-109][162-166] The other equations for the general ion exchange mechanisms that occur between the non-rare earth, polyvalent metal cations and the sodium alginate are described in Chapter 4 (Section 4.2).

$$\mathrm{Pr}(NO_3)_3.xH_2O + 3(Na - ALG) \rightarrow (\mathrm{Pr}^{3+} - ALG)_3.xH_2O + 3NaNO_3 \quad (6.1)$$

$$\mathrm{Nd}(NO_3)_3.xH_2O + 3(Na - ALG) \rightarrow (\mathrm{Nd}^{3+} - ALG)_3.xH_2O + 3NaNO_3 \quad (6.2)$$

The above equations describe how the effects of the ion exchange can lead to the Na^+ situated in the alginate macromolecule being replaced by rare earth ions to form cross linked metal alginates. The lanthanide ions can coordinate with the carboxyl groups from the alginate structure. Prior to the thermal analysis reported below each gel was dried however, the drying processes were different because the LSCF6428-alginate and LPSCF33428-alginate beads were dried in a vacuum oven, while the LNSCF33428-alginate and NSCF6428-alginate beads were dried on hot plates. The two drying processes suggested similar dehydration of the metal alginate gels as measured by changes in mass before and after drying, as shown in Table 6.2.

Table 6.2: Drying process, temperature and measured water loss of rare earth doped LSCF-alginate beads

Metal-Alginate Complexes	Drying Method	Measured Water loss %
LSCF6428	Vacuum Oven at 90 ^oC	90.1
LPSCF33428	Vacuum Oven at 90 ^oC	90.3
LNSCF33428	Hot plate drying at 90 ^oC	90.5
NSCF6428	Hot plate drying at 90 ^oC	91

6.2. Thermal Characterisation of the LPSCF33428, LNSCF33428 and NSCF6428

Thermal analysis has been carried out to determine the calcination temperature requirement for homogenisation of the LPSCF33428, LNSCF33428 and NSCF6428 beads prepared using the 3 wt% sodium alginate sol gel method. It will also determine how the effect of the dopants (rare earth) influence the thermal decomposition of the three metal alginate complexes and the final mass residue in comparison to the undoped LSCF6428 perovskite oxide (Chapter 4, Section 4.2). DTG/TGA/DSC are used to observe the thermal decomposition of the three different compositions of rare earth-based metal alginate complexes and the (assumed) formation of a perovskite oxide nanopowder as shown in Figures 6.7 – 6.9.

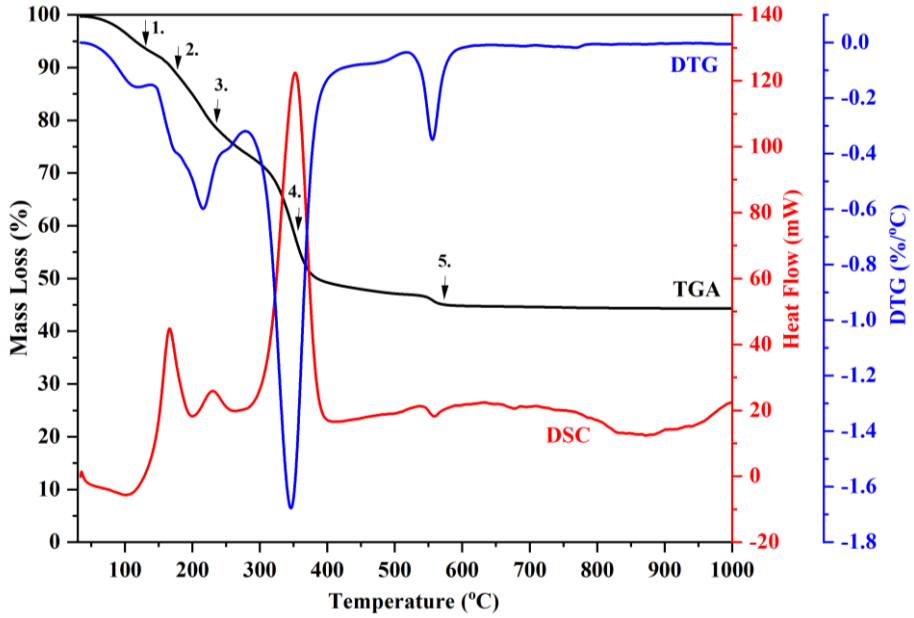

Figure: 6.7: DSC/TGA/DTG analysis of LPSCF33428 in 3 wt% of alginate. Five decomposition steps are marked with numbered arrows in the plot.

Table 6.3: TGA of 3 wt% LPSCF33428 alginate analysis

Stages	**TGA Temperature Range, °C**	**Weight Loss, %**
1	45.4 – 126.7	6.9
2	158 - 177.6	4.0
3	206.4-265.1	15.1
4	303 – 381.4	26.6
5	536.4 – 575.6	2.7
Final Mass		44.3

Table 6.4: DSC of 3 wt% LPSCF33428 alginate analysis

Steps	**DSC Peak, °C**	**Types of Peaks**	**Integral (J/g)**
1	109.7	Endothermic	-143.6
2	168.3	Exothermic	287.2
3	230.9	Exothermic	57.8
4	354.1	Exothermic	1436.4
5	559.8	Endothermic	-21.9

Table 6.5: DTG of 3 wt% LPSCF33428 alginate analysis

Stages	DTG Peak, °C	Weight Loss, %
1	110.7	-0.15
2	173.8	-0.39
3	215.3	-0.6
4	347.5	-1.67
5	557.1	-0.34

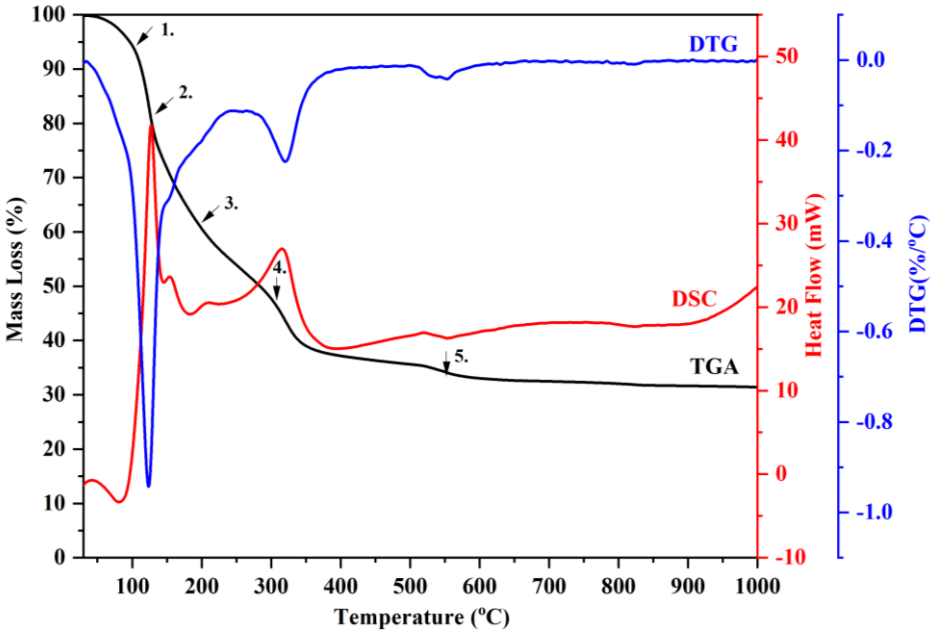

Figure: 6.8: DSC/TGA/DTG analysis of LNSCF33428 in 3 wt% of alginate. Five decomposition steps are marked with numbered arrows in the plot.

Table 6.6: TGA of 3 wt% LNSCF33428 alginate analysis

Stages	TGA Temperature Range, °C	Weight Loss, %
1	41.6 – 96.2	4.9
2	105.1 – 144.8	22.6
3	235.5 -284.0	11.0
4	301.4 – 345.6	16.7
5	504.3 – 570.7	4.0
Final Mass		31.4

Table 6.7: DSC of 3 wt% LNSCF33428 alginate analysis

Steps	DSC Peak, °C	Types of Peaks	Integral (J/g)
1	84.9	Endothermic	-
2	128	Exothermic	139.8
3	210.5	Exothermic	30.3
4	318.9	Exothermic	238.9
5	554.6	Endothermic	-13.9

Table 6.8: DTG of 3 wt% LNSCF33428 alginate analysis

Stages	DTG Peak, °C	Weight Loss, %
1	76.9	-0.13
2	123.9	-0.94
3	255.6	-0.11
4	321.7	-0.22
5	557.3	-0.03

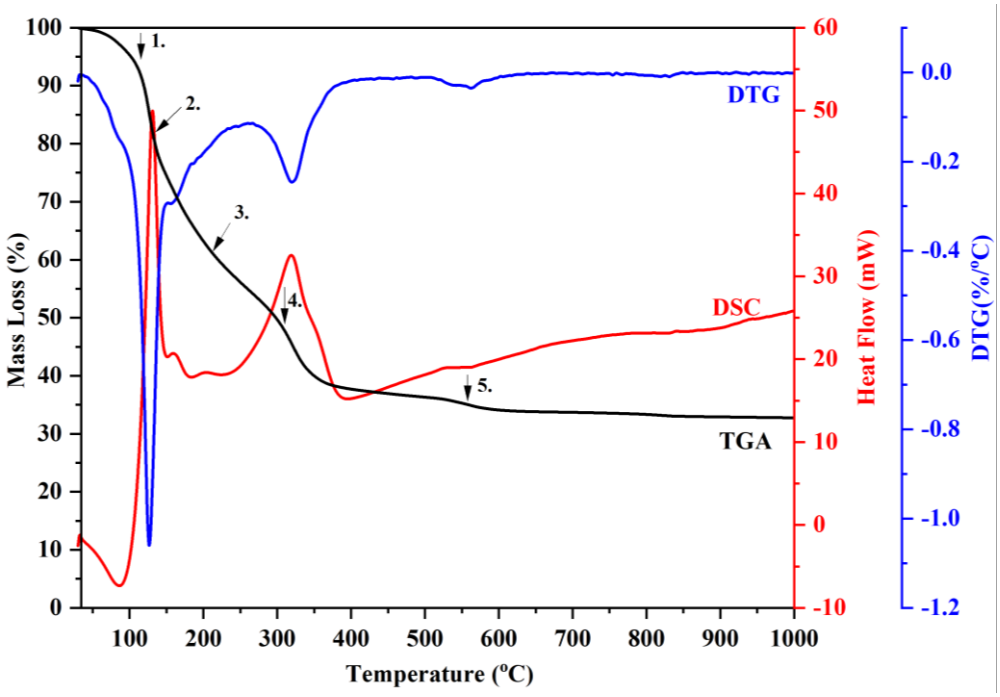

Figure: 6.9: DSC/TGA/DTG analysis of NSCF6428 in 3 wt% of alginate. Five decomposition steps are marked with numbered arrows in the plot.

Table 6.9: TGA of 3 wt% NSCF6428 alginate analysis

Stages	**TGA Temperature Range, ^{o}C**	**Weight Loss, %**
1	44.9 – 94.1	4.9
2	109.8 – 147.5	29.2
3	235.5 -284.0	11.0
4	300.9 – 345.6	17.3
5	440.2 – 582.4	4.9
Final Mass		32.7

Table 6.10: DSC of 3 wt% NSCF6428 alginate analysis

Steps	**DSC Peak, ^{o}C**	**Types of Peaks**	**Integral (J/g)**
1	88.8	Endothermic	-
2	131.6	Exothermic	148.8
3	206.2	Exothermic	7.5
4	319.5	Exothermic	545.9
5	560.1	Endothermic	-

Table 6.11: DTG of 3 wt% NSCF6428 alginate analysis

Stages	**DTG Peak, ^{o}C**	**Weight Loss, %**
1	84.6	-0.15
2	126.7	-1.06
3	167.9	-0.27
4	317.6	-0.24
5	554.1	-0.03

From the thermal analysis, the thermal decomposition of all the partially and fully substituted A site rare earth metal alginate complexes of LPSCF33428, LNSCF33428 and NSCF6428 occurs in five stages of mass loss (%) at increasing temperatures until a constant mass residue is reached by ~ 600 ^{o}C as shown in Figures 6.7-6.9 and Tables 6.3, 6.6 and 6.9. These stages have been reported before for these systems i.e. dehydration, decomposition and residue

formation, in accordance with this TGA/DSC/DTG analysis, before completion towards an (assumed) single-phase perovskite oxide. [165]

For the 3 rare earth doped LSCF compositions, the LNSCF33428 and the NSCF6428 complexes have a lower final residual mass of ~ 32 % compared to 44 % for the LPSCF33428 however the latter was the only complex dried in a vacuum oven as per LSCF which also had a final residual mass of ~ 44 %. In addition, the LNSCF33428 and the NSCF6428 complexes have a greater fraction of mass loss at stage 2 of the DTG peaks while LPSCF33428 as a greater fraction of mass loss at stage 4 of the DTG peaks as shown in Table 6.5, 6.8 and 6.11. The DSC peaks are also shifted to lower temperature for LNSCF33428 and NSCF6428 compared to the LPSCF33428 for stages 1, 2 and 4 as shown in Tables 6.4, 6.7 and 6.10. This suggests that as as the atomic number within the lanthanide series increases, the metal alginate reaction temperature decreases particularly for stages 1, 2 and 4 as shown in Figures 6.7-6.9 but the effect on the final melting temperature is not known as the samples were not heated above 1000 ^{o}C. In a study by Haeger et. al. however, it was observed that as the atomic number within the lanthanide series decreases, the melting temperature requirement may potentially increase. [213]

Regardless of the total amount of mass loss, for all the three different metal alginate complexes, the first stage of decomposition takes place at around 100 ^{o}C. At this temperature, a simple process of dehydration of the metal-alginate complexes occurs by the removal of excess and adsorbed surface water molecules from the metal-alginate complex, resulting in a mass loss that is typically less than 10 % of the total original mass, as referred to in Tables 6.3, 6.6 and 6.9. The dehydration for Pr is higher (measured as mass loss %) compared to Nd based complexes (6.9 vs 4.9% respectively) and this may be due to the different drying methods used here (Table 6.2). In a study of the thermal decomposition of Pr and Nd oxalate hydrate by Lv et.al and Li et.al both the Pr and Nd oxalate had similar mass loss % when using the same drying method (microwave field) prior to TGA/DSC/DTG analysis. [214-215]

The chemical equations (6.3-6.5) below describe the endothermic process of water removal from the metal-alginate complex as shown in Tables 6.4, 6.7 and 6.10, corresponding to the DSC endothermic peaks located at 109 ^{o}C and below 100 ^{o}C for the compositions of Pr and Nd respectively. Chemical equations for the other non-rare earth polyvalent metal cations can be referred to in Chapter 4, Section 4.2.

$$(Pr^{3+} - ALG)_3.xH_2O \rightarrow 3Pr - ALG + xH_2O \text{ (6.3)}$$

$$(Pr^{4+} - ALG)_4.xH_2O \rightarrow 4Pr - ALG + xH_2O \text{ (6.4)}$$

$$(Nd^{3+} - ALG)_3.xH_2O \rightarrow 3Nd - ALG + xH_2O \text{ (6.5)}$$

However, when dehydration occurs above 100 ºC, multiple processes are initiated, i.e. metal-alginate complex decomposition, alginate rupture and the formation of intermediate compounds that occur in stages 2 and 3 between the Pr and Nd doped LSCF all take place. There are differences in the steepness of the TGA curves for the Pr and Nd complexes. It is also clear for stage 2 that the DTG weight loss % for the Nd based compositions are around 3 times higher compared to the LPSCF33428 as shown in Figures 6.7-6.9, Tables 6.5, 6.8 and 6.11. Chemical equations (6.6-6.7) below show there is a sudden transition from metal-alginate to unstable metal oxalate intermediate compounds that are hydrated occurring here. Stage three of the decomposition is indicated clearly by the DTG curve with a mass loss % of below 10% for all three samples as shown in Tables 6.5, 6.8 and 6.11. Here as the temperature increases, the hydrated rare earth oxalates lose the additional water as shown in the chemical equations (6.8-6.9) below and this completes the formation of the anhydrous oxalates.

$$2PrC_{18}H_{21}O_{17} + O_2 \rightarrow Pr_2(C_2O_4)_3.nH_2O + xCO_2 + yH_2O \text{ (6.6)}$$

$$2NdC_{18}H_{21}O_{17} + O_2 \rightarrow Nd_2(C_2O_4)_3.nH_2O + xCO_2 + yH_2O \text{ (6.7)}$$

$$Pr_2(C_2O_4)_3.nH_2O \rightarrow Pr_2(C_2O_4)_3 + nH_2O \text{ (6.8)}$$

$$Nd_2(CO_3)_3.nH_2O \rightarrow Nd_2(C_2O_4)_3 + nH_2O \text{ (6.9)}$$

For easier comparison, the weight loss % from both the TGA and DTG between stages 2-3 for all the 3 compositions are combined in Tables 6.3, 6.5, 6.6, 6.8, 6.9 and 6.11. It is observed that the Nd based perovskite oxide compositions, when combined, are found to have a greater combined mass loss % than for the LSCF6428 and LPSCF33428.

This difference in mass loss of 14-21% is quite significant. The mass in weight loss % also influences the DSC temperature peak positions where the LPSCF33428 and LSCF6428 peaks are shifted to a 30 ºC higher temperature compared to the temperature peaks for LNSCF33428 and NSCF6428 at the same stage. This difference of mass loss % for the Nd based complexes of between 34%-40% total while for LPSCF33428 is only around 19% total for stages 2 and 3

combined. Oxalates are classified as unstable compounds so when exposed to air, tend to absorb water, although it can vary with each rare earth element depending on its hygroscopic nature. It is suggested that the Nd oxalate tends to absorb more moisture compared to the Pr oxalate. Indeed, the thermal decomposition of both Pr and Nd oxalate (synthesised using microwave fields) to metal oxides, with the removal of water of hydration and decomposition to form the intermediate oxalate, has been studied by TG-DSC analysis and shown to follow similar trends of mass loss % to this work. [214-217]

At stage 4 of the decomposition, there is a second significant mass loss of more than 15% for all three compositions. This loss is due to the decomposition of the remaining alginate and the unstable intermediate compound, i.e. breakdown of the rare earth oxalate. That is likely to lead to the major phase transformation to the metastable compounds of praseodymium carbon pentoxide and neodymium dioxycarbonate (monoclinic, Pr_2CO_5 and hexagonal, $Nd_2O_2CO_3$) as shown in the chemical equations (6.10-6.11) below. [214-217]. This process is explained in Chapter 4, Section 4.2. The carbon monoxide formed from the Nd as shown in the chemical equation (12) when under air atmosphere is expected to be oxidised by oxygen to form carbon dioxide. [156-157] In comparison to the earlier stages e.g. dehydration, the decomposition of LPSCF33428 has a greater mass loss of 26.6 % compared to the LNSCF33428 and the NSCF6428 of 16.7% and 17.3% respectively as shown in Table 6.6 and 6.9. In addition, the decomposition of LPSCF33428 has a large exothermic peak of 120 mW (3.5 and 4 times greater) than for the LNSCF33428 and NSCF6428 complexes, as shown in Table 6.3 and Figure 6.7 respectively. That is similar to the trend by Lv et. al. and Li et.al. for the decomposition of Pr and Nd oxalate, where the Pr loss is 23.22 % and Nd loss is 22.76 %.[215-216] However the difference of the mass loss % between the literature and this work is around 3-6% and is thought to be due to the nature of the atmosphere conditions used in each (argon vs air respectively). [156]

$$Pr_2(C_2O_4)_3 \rightarrow Pr_2CO_5 + 5/2\ CO_2 + O_2 \quad (6.10)$$

$$Nd_2(C_2O_4)_3 \rightarrow Nd_2O_2CO_3 + 2CO + CO_2 \quad (6.11)$$

$$2x\ CO + xO_2 \leftrightarrow 2x\ CO_2 \quad (6.12)$$

At the final step at a temperature near 600 °C, the formation of the three different metal oxide compositions occurs, as shown in the chemical equations (6.13-6.14) below, and there is only a small mass loss. This is the loss of carbon dioxide from the LNSCF33428 and the NSCF6428

complexes giving 4% mass loss in comparison to the LPSCF33428 complex of only 2.7%. This is also indicated by a small endothermic peak in the DSC profile.[15] That is also consistent with the Pr and Nd study by Liv et.al and Li et.al. where 3.69 % and 4.91 % mass loss occurred respectively. [154-155]

$$Pr_2CO_5 \rightarrow PrO_{1.83} + CO_2 \quad (6.13)$$

$$Nd_2O_2CO_3 \rightarrow Nd_2O_3 + CO_2 \quad (6.14)$$

There is no further mass loss above this temperature indicating the complete synthesis of a stable metal oxide with a mass residue of 44.4% for the LPSCF33428 and between 32 – 34% for the LNSCF33428 and NSCF6428. That trend is similar where the residue of $PrO_{1.83}$ was 50% for Nd_2O_3 and was 45% as the final residue obtained by Lv.et.al. and Li.et.al respectively. [215-216]

Overall, it shows that there is a difference in the thermal breakdown of the Pr and Nd alginate complexes despite the pre-drying method used and specifically that the intermediate compound, oxalates formed between stages 2 and 3 have different retention of moisture. [215-217]

6.3. Structural Characterisation of calcined LPSCF33428, LNSCF33428 and NSCF6428 nanopowders

To confirm the development of phase purity and type of crystal symmetry that occurs for LPSCF33428, LNSCF33428 and NSCF6428, the nanopowders were calcined at three different temperatures and then investigated using room temperature XRD. The results are shown in Figures 6.10, 6.13 and 6.17. Basic whole pattern fitting (HighScore software) was used to examine the experimental diffraction patterns.

There has been previous work on the MIEC perovskites, focussing on the composition of Ln = rare earth elements, where different light rare earth elements such as La, Pr and Nd were investigated for their impact on structural properties. [75][218-220] Although, in one study by Xu et. al. when the reference pattern was fitted to the experimental data, the diffraction peaks were not labelled but confirmed to be of a single-phase orthorhombic crystal structure.[219] However, in two studies by Heydair et.al., the diffraction peaks were labelled with Miller indices using only the ICDD file of orthorhombic crystal symmetry without any demonstration of Bragg peak splitting at 2θ.[75][220] Miller indices were also absent in other work in the investigation of the A site partially doping of LSCF6428 using lighter rare earth elements except for Ce and Dy. [21-22][218-219]

The peak fitting used here will address whether the peak splitting from the whole pattern fitting of the experimental diffraction peaks matches the reference pattern from either the rhombohedral or orthorhombic crystal symmetry.[176-177] When comparing with the reference pattern, whatever GOF value is the lowest will indicate the crystal symmetry of the rare earth doped LSCF6428.[177] That, therefore, will provide a guide in determining whether the substitution of the host A site element, Lanthanum with the lighter rare earth elements transitions towards a crystal structure of either rhombohedral or orthorhombic symmetry.

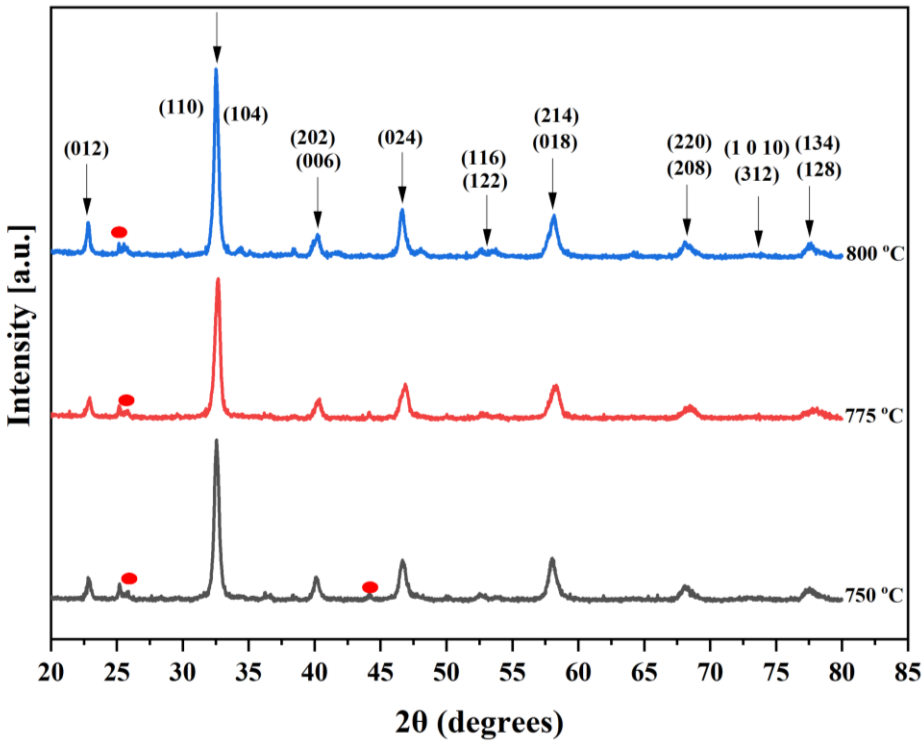

Figure 6.10: XRD patterns of 3 wt% crushed LPSCF33428 nanopowders calcined for 2 h at temperatures of 750 ºC (grey line), 775 ºC (red line) and 800 ºC (blue line). (indexed using profile fit), Red circles indicate $SrCO_3$ peaks present (indexed to ICDD 01-078-4340)

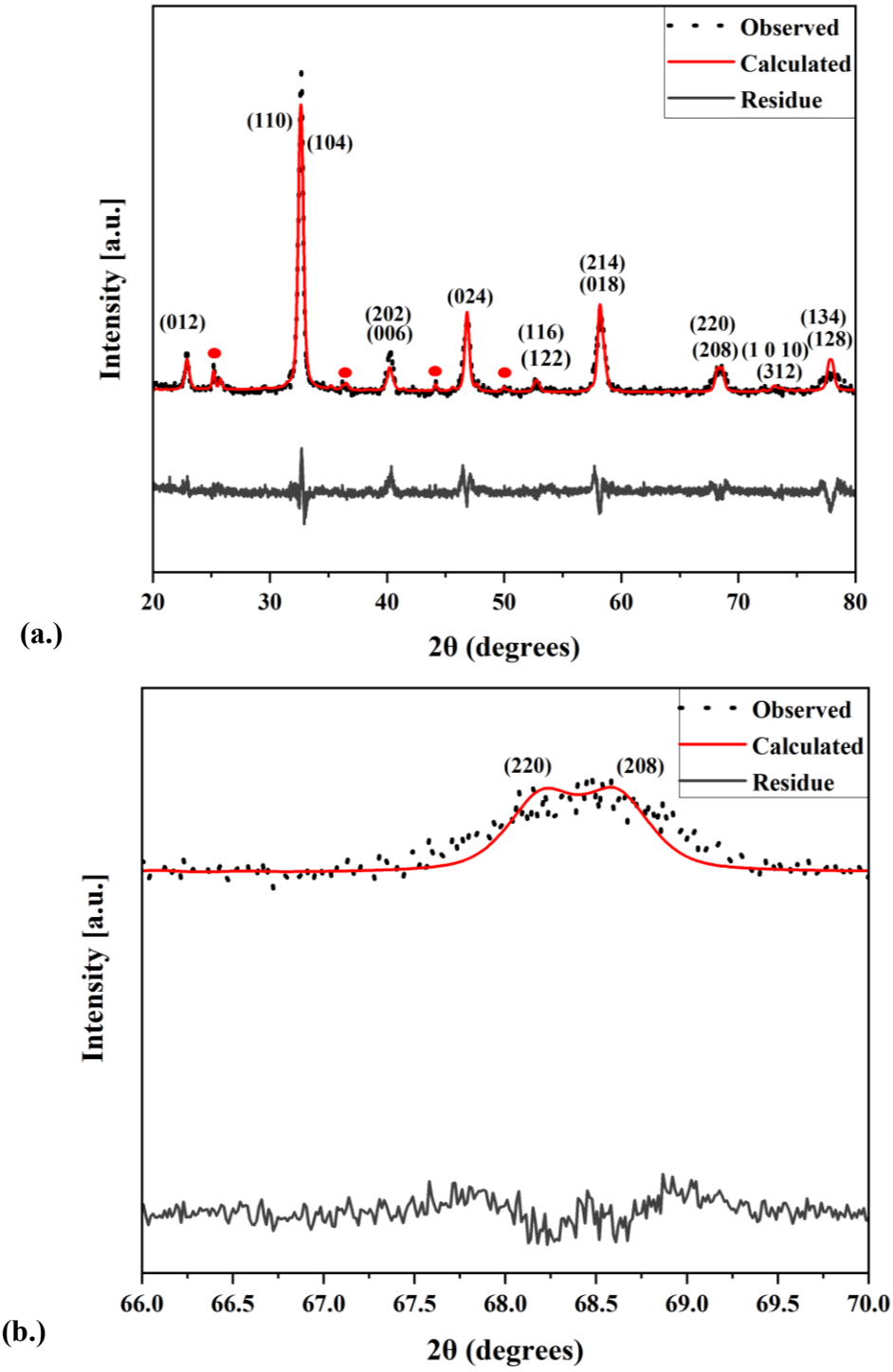

Figure 6.11: a) Whole pattern fitting of the rhombohedral (R3c) structure of 775 °C calcined crushed LPSCF33428 nanopowder with experimental data (black line), reference file (red line), residue (grey line) – peaks are indexed using ICDD 04-017-2448 and red circles indicate $SrCO_3$ peaks present (indexed to ICDD 01-078-4340) **b**) Zoom in of the fitting of the rhombohedral (R3c) structure of 775 °C calcined LPSCF33428 nanopowder indicating peak splitting located at (220)/(208) 68° 2θ.

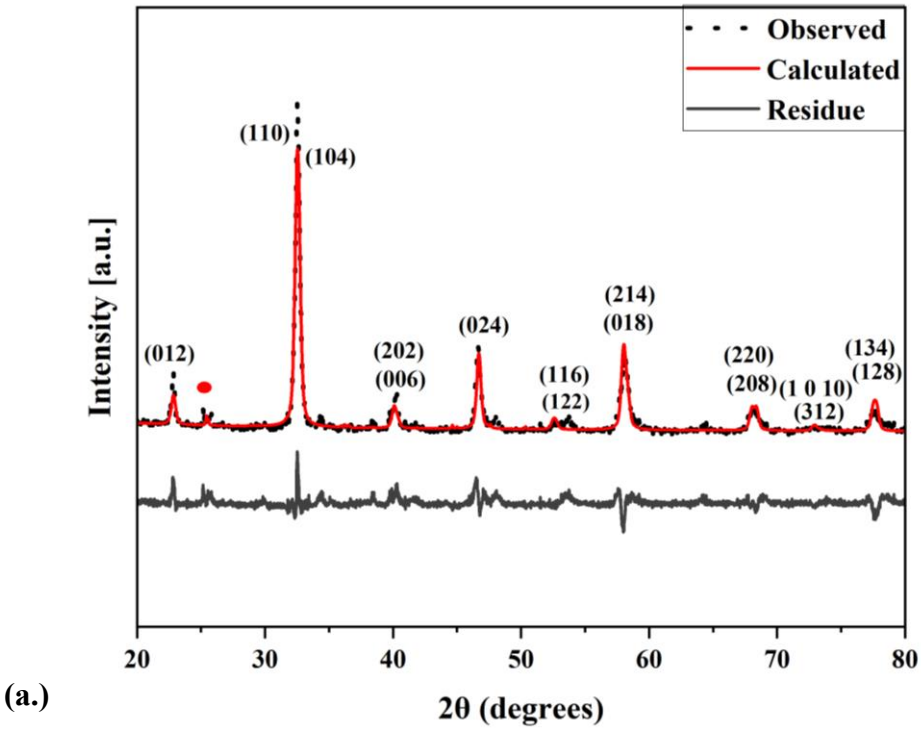

(a.)

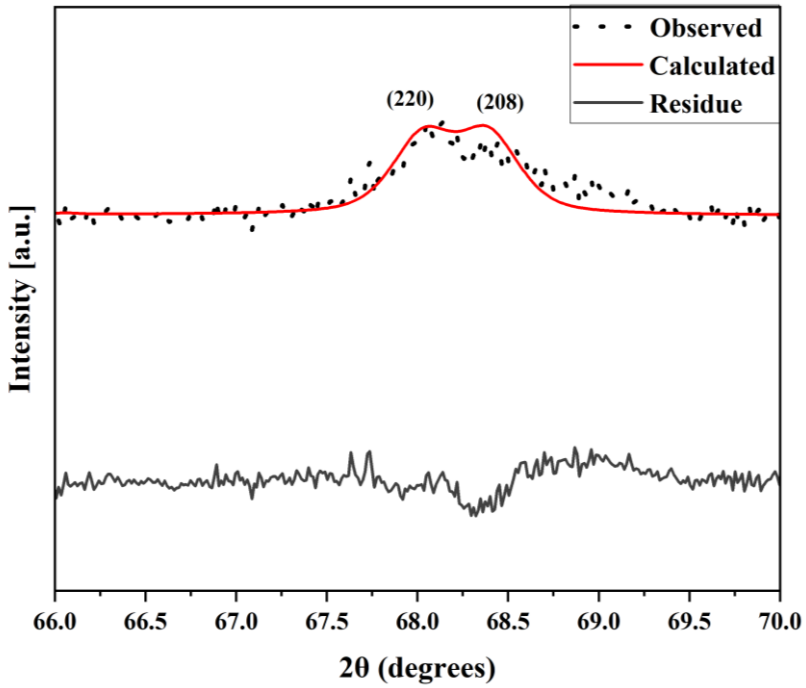

(b.)

Figure 6.12: a) Whole pattern fitting of the rhombohedral (R3c) structure of 800 ºC calcined crushed LPSCF33428 nanopowder with experimental data (black line), reference file (red line), residue(grey line) – peaks are indexed using ICDD 04-017-2448 and red circles indicate $SrCO_3$ peaks present (indexed to ICDD 01-078-4340) **b**) Zoom in of the fitting of the rhombohedral (R3c) structure of 800 ºC calcined LPSCF33428 nanopowder indicating peak splitting located at (220)/(208) 68º 2θ.

Table 6.12: Whole pattern fitting of structural parameters and perovskite phase purity of the rhombohedral (R3c) LPSCF33428 at different calcination temperatures of 775 and 800 ºC ((R_{wp}(%)) weighted pattern, (R_{exp}(%)) expected pattern and goodness of fit (GOF))

Temperature (º C) – R3c	**R_{exp}(%)**	**R_{wp}(%)**	**GOF**	**Perovskite Phase Purity (%)**
775	5.286	3.848	0.729	89
800	5.353	4.854	0.906	94

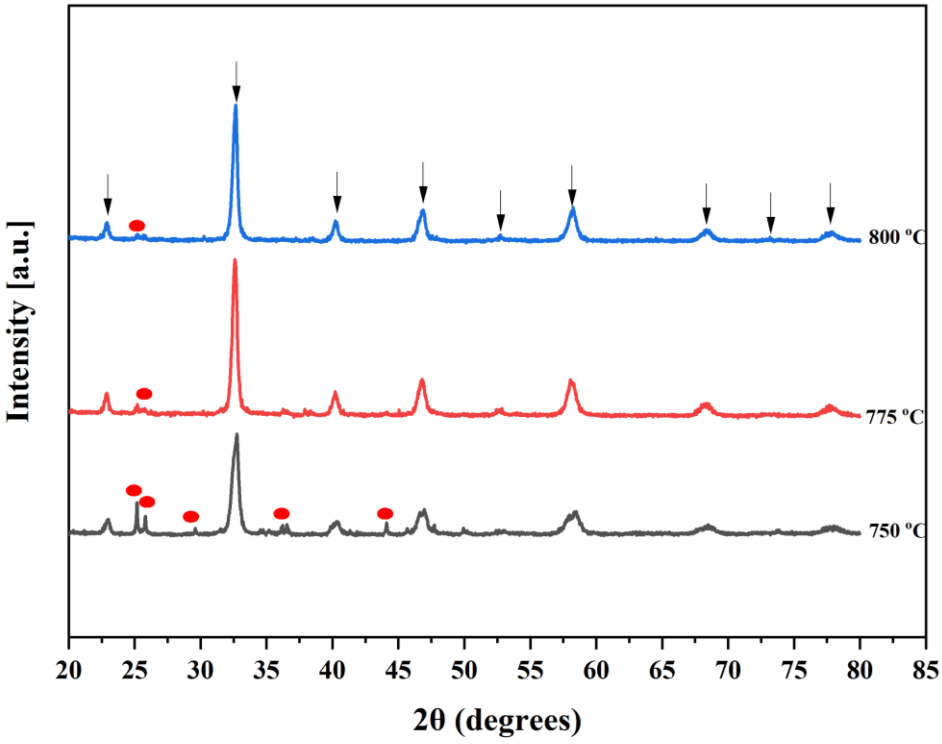

Figure 6.13: XRD patterns of 3 wt% crushed LNSCF33428 nanopowders calcined for 2 h at temperatures of 750 ºC (grey line), 775 ºC (red line) and 800 ºC (blue line)(indexed using profile fit). Red circles indicate $SrCO_3$ peaks present (indexed to ICDD 01-078-4340)

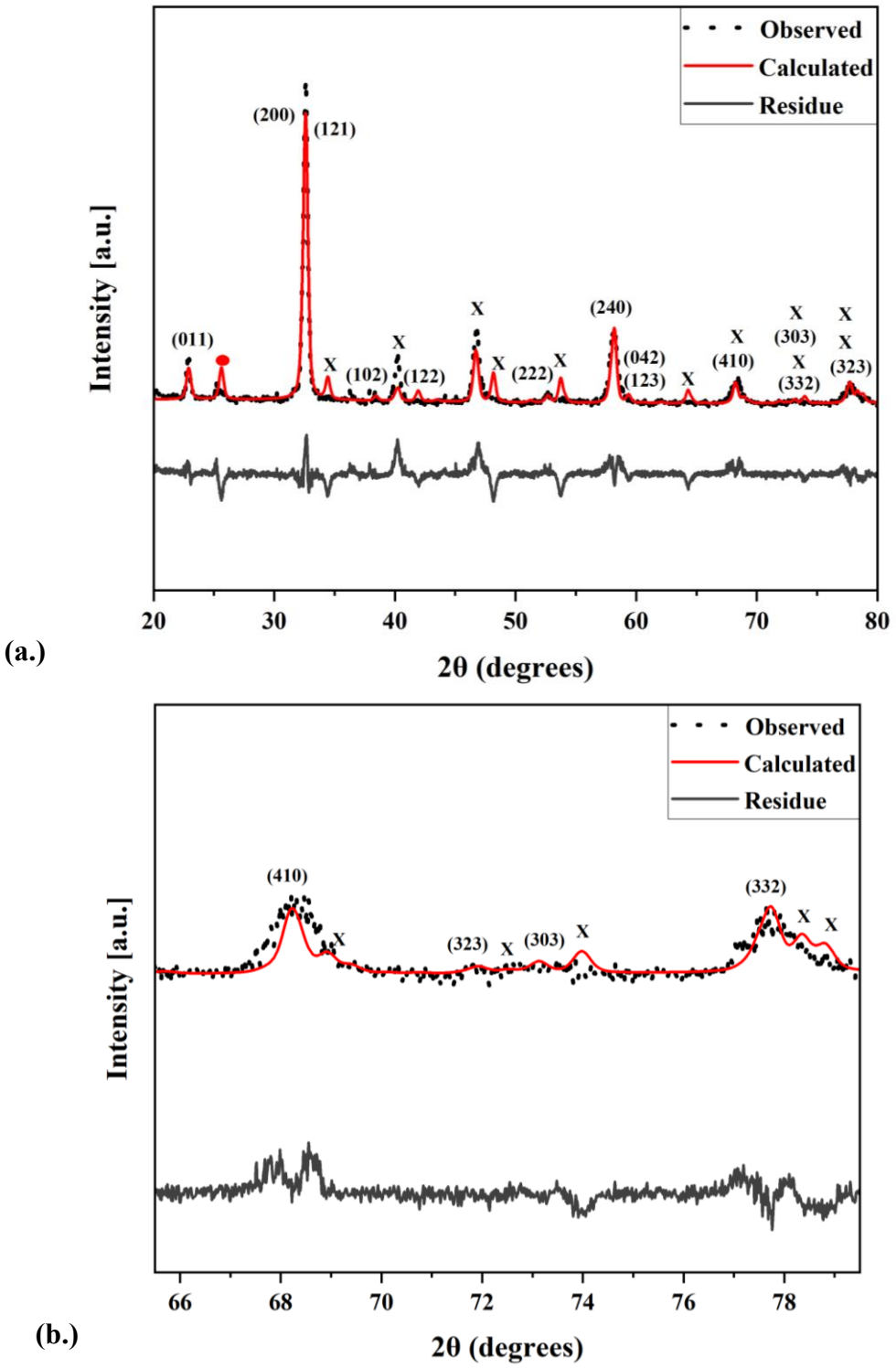

Figure 6.14: a) Whole pattern fitting of the orthorhombic (O_h) structure of 775 °C calcined crushed LNSCF33428 nanopowder with experimental data (black line), reference file (red line), residue (grey line) – peaks are indexed using ICDD 04-026-4876, red circles indicate $SrCO_3$ peaks present (indexed to ICDD 04-019-4340) and X represents mismatched/missing peaks **b**) Zoom in of the fitting of the orthorhombic (O_h) structure of 775 °C calcined LNSCF33428 nanopowder indicating peak splitting between 66°-79° 2θ.

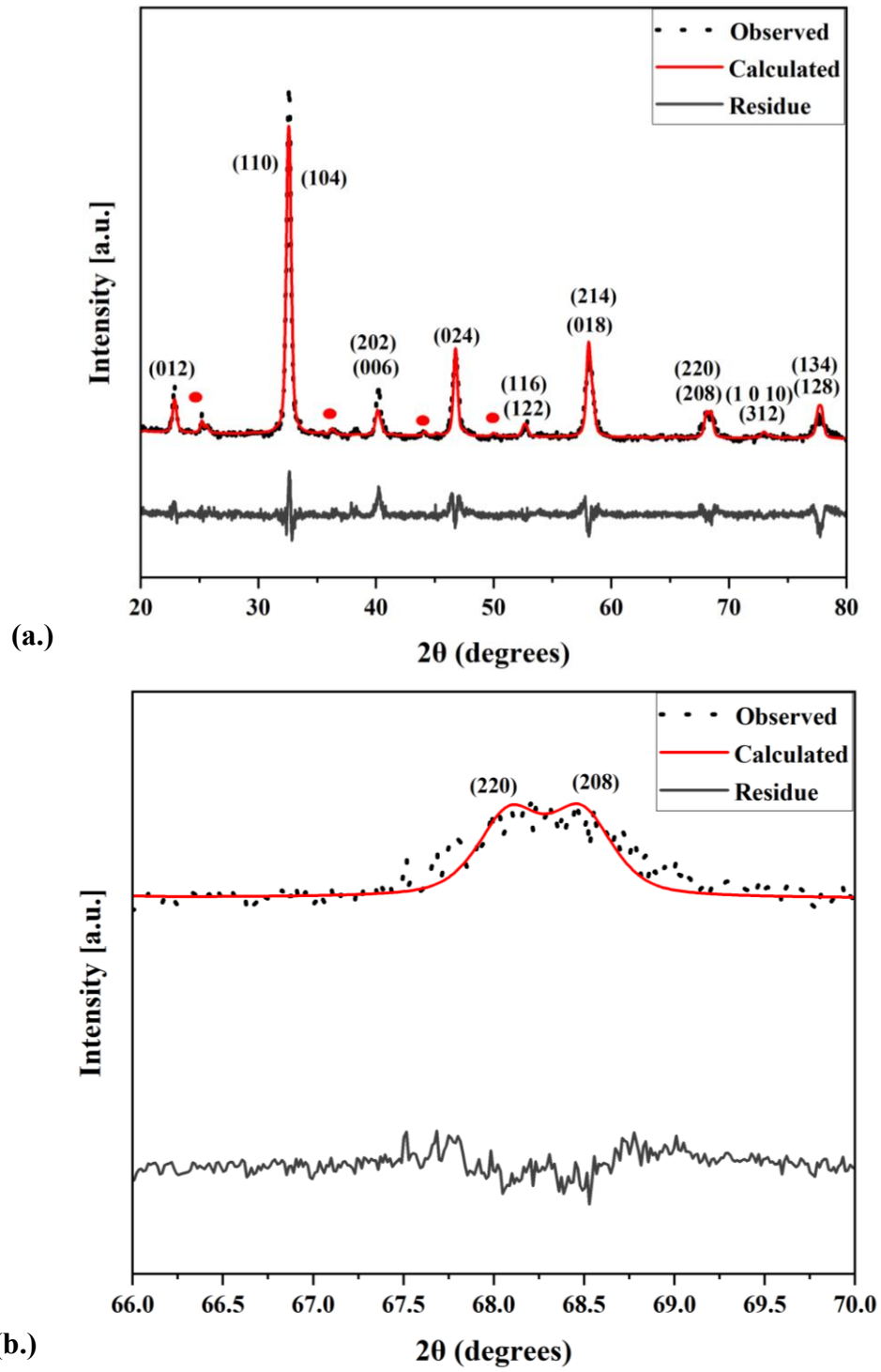

Figure 6.15: a) Whole pattern fitting of the rhombohedral (R3c) structure of 775 ºC calcined crushed LNSCF33428 nanopowder with experimental data (black line), reference file (red line), residue(grey line) – peaks are indexed using ICDD 04-017-2448 and red circles indicate $SrCO_3$ peaks present (indexed to ICDD 01-078-4340) **b**) Zoom in of the fitting of the rhombohedral (R3c) structure of 775 ºC calcined LNSCF6428 nanopowder indicating peak splitting located at (220)/(208) 68º 2θ.

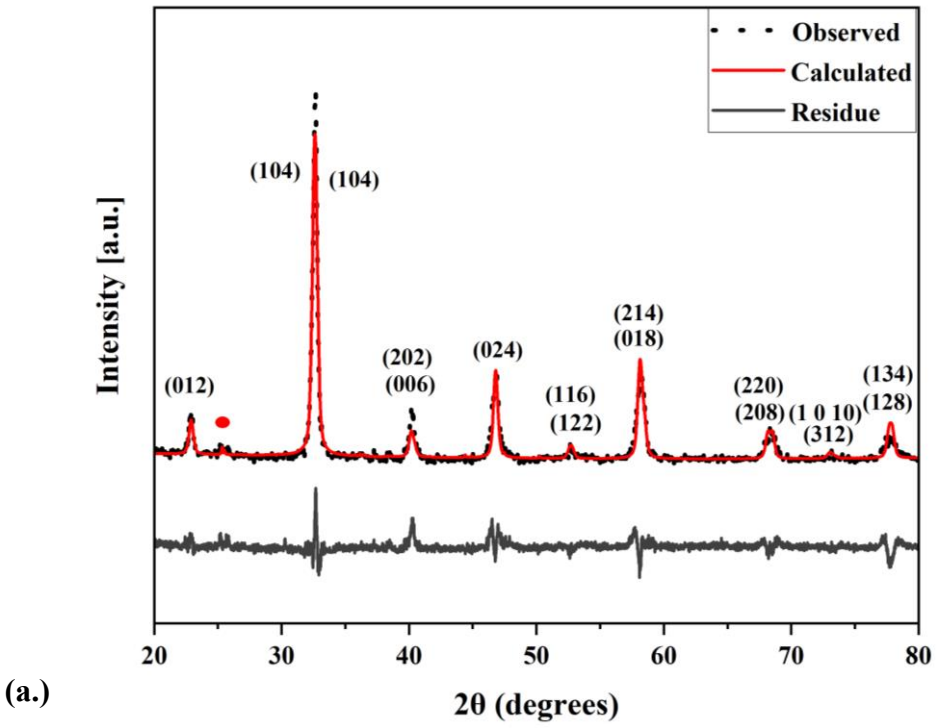

(a.)

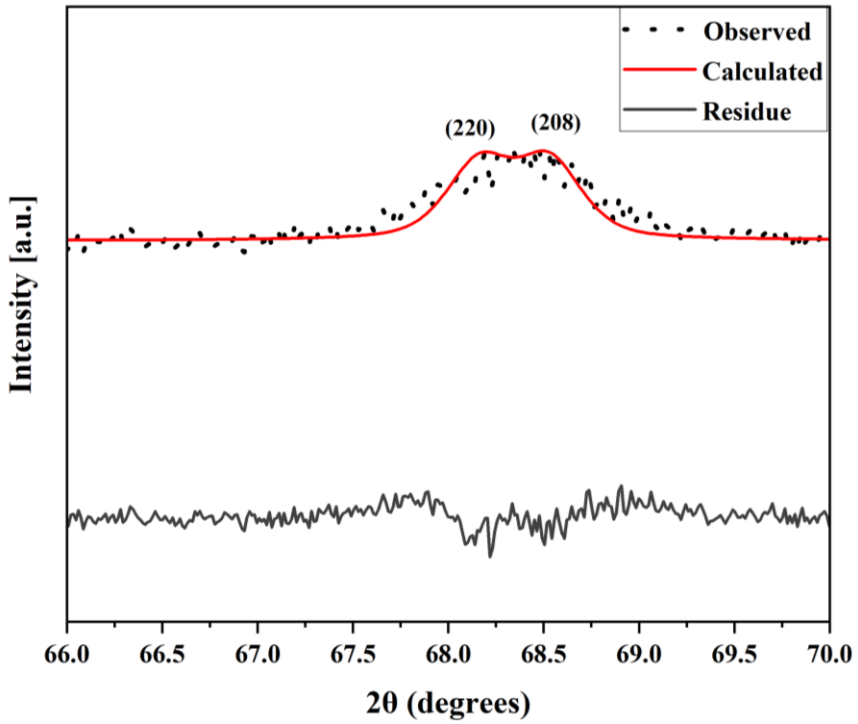

(b.)

Figure 6.16: a) Whole pattern fitting of the rhombohedral structure of 800 ºC calcined crushed LNSCF33428 nanopowder with experimental data (black line), reference file (red line), residue(grey line) – peaks are indexed using ICDD 04-017-2448 and red circles indicate $SrCO_3$ peaks present (indexed to ICDD 01-078-4340) **b**) Zoom in of the fitting of the rhombohedral structure of 800 ºC calcined LNSCF33428 nanopowder indicating peak splitting located at (220)/(208) 68º 2θ.

Table 6.13: Whole pattern fitting of structural parameters and perovskite phase purity of the rhombohedral (R3c) and orthorhombic (O_h) LNSCF33428 at different calcination temperatures of 775 and 800 ºC ((R_{wp}(%)) weighted pattern, (R_{exp}(%)) expected pattern and goodness of fit (GOF))

Temperature (^{o} C) – R3c	R_{exp}(%)	R_{wp}(%)	GOF	Perovskite Phase Purity (%)
775	5.423	4.36	0.832	92
800	5.475	4.314	0.788	96

Temperature (^{o} C) - O_h	R_{exp}(%)	R_{wp}(%)	GOF
775	5.245	7.012	1.336
800	5.475	6.486	1.885

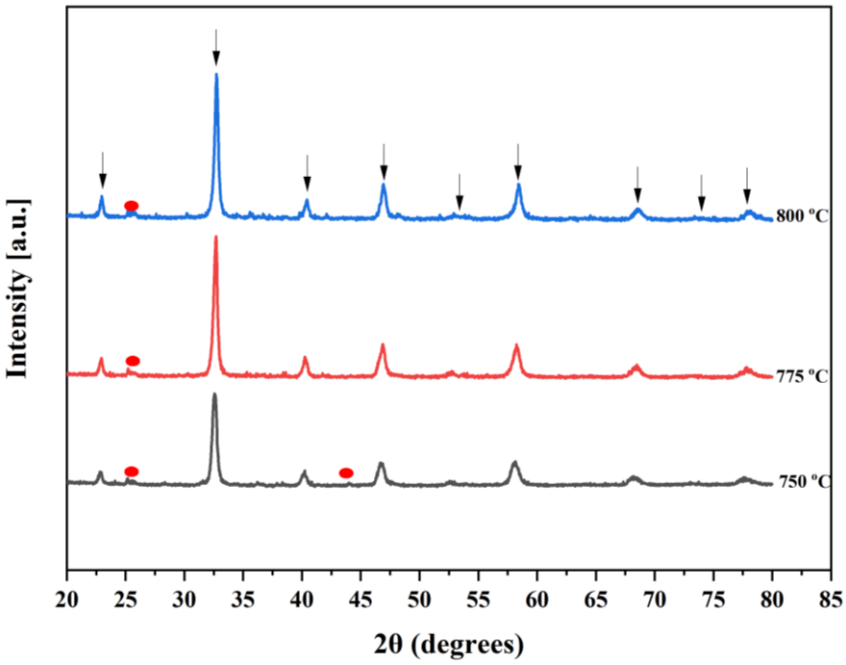

Figure 6.17: XRD patterns of 3 wt% crushed NSCF6428 nanopowders calcined for 2 h at temperatures of 750 ºC (grey line), 775 ºC (red line) and 800 ºC (blue line)(indexed using profile fit).Red circles indicate $SrCO_3$ peaks present (indexed to ICDD 01-078-4340)

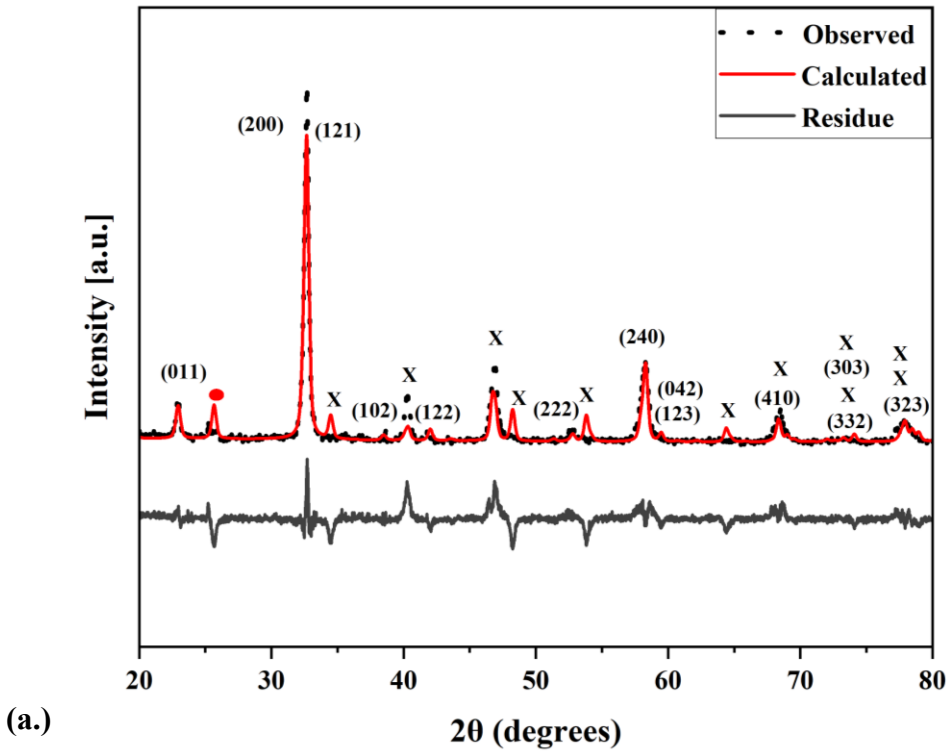

(a.)

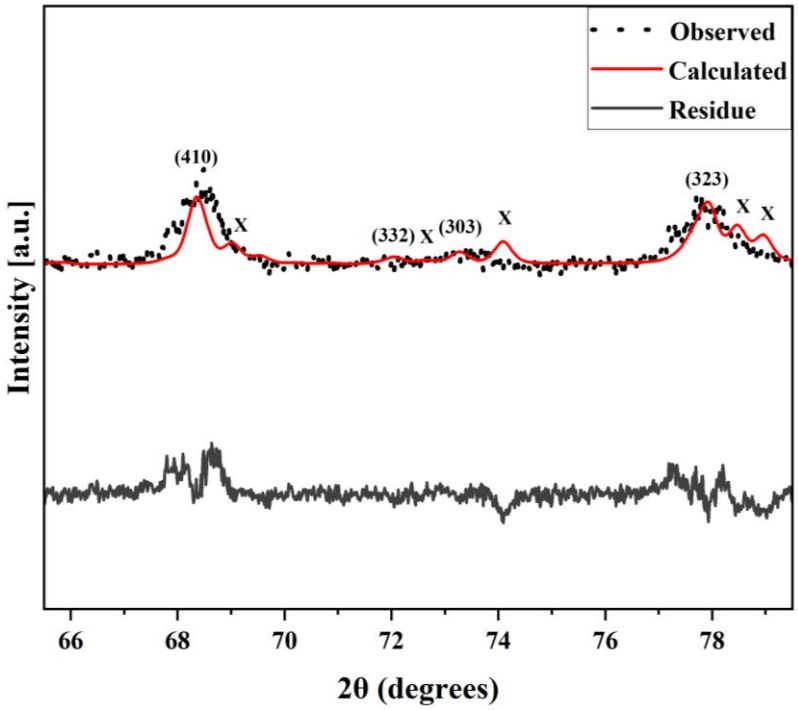

(b.)

Figure 6.18:a) Whole pattern fitting of the orthorhombic (O_h) structure of 775 ^oC calcined crushed NSCF6428 nanopowder with experimental data (black line), reference file (red line), residue(grey line) – peaks are indexed using ICDD 04-026-4876 , red circles indicate $SrCO_3$ peaks present (indexed to ICDD 01-078-4340) and X represents mismatched/missing peaks **b)** Zoom in of the fitting of the orthorhombic (O_h) structure of 775 ^oC calcined NSCF6428 nanopowder indicating peak splitting located between 66^o-79^o 2θ.

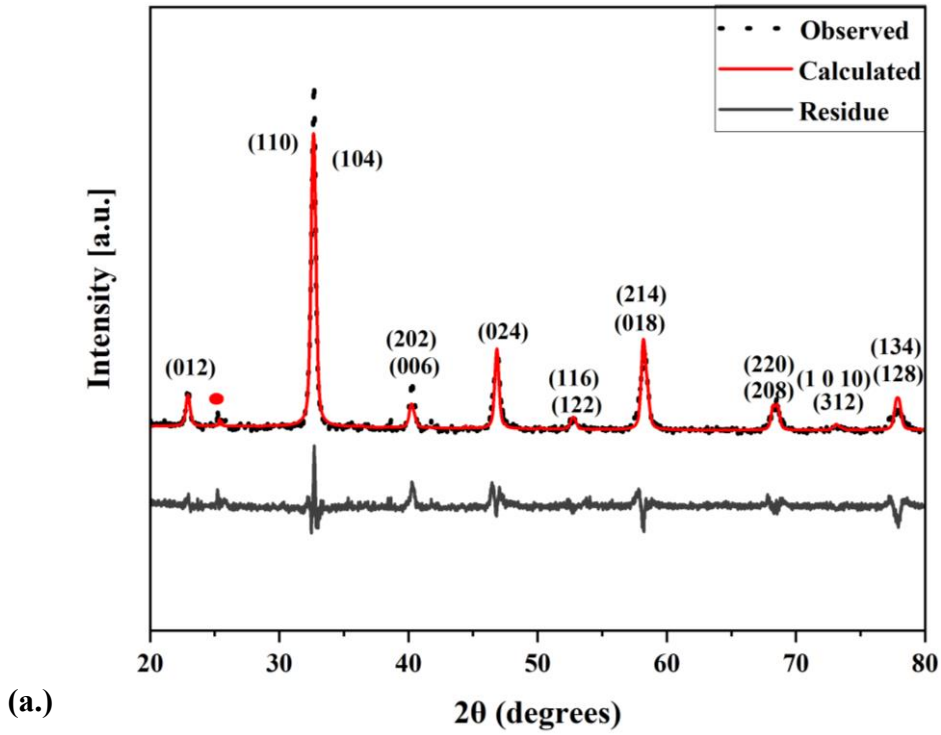

(a.)

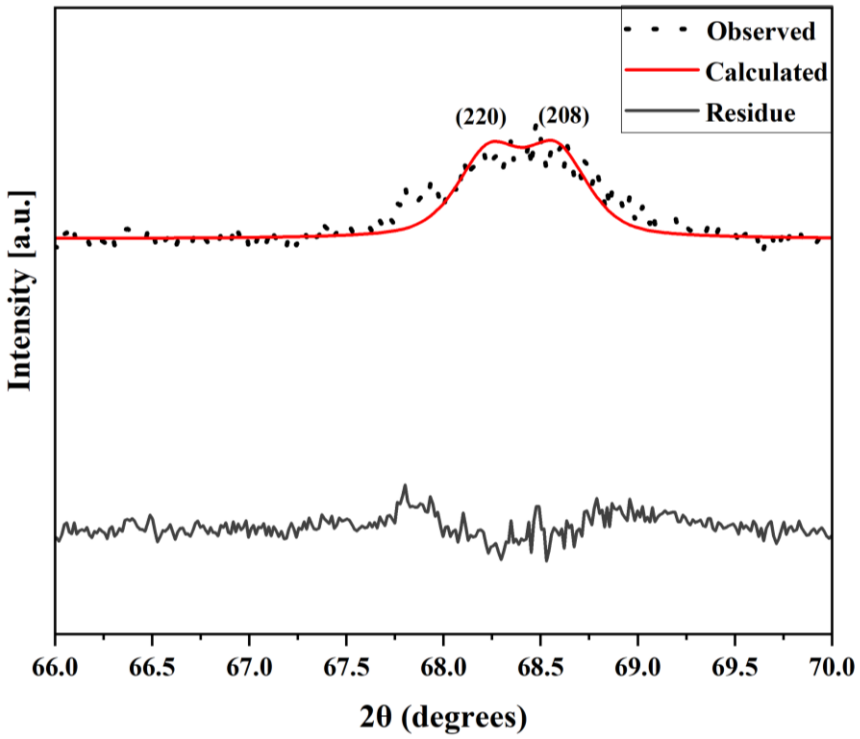

(b.)

Figure 6.19: a) Whole pattern fitting of the rhombohedral (R3c) structure of 775 ºC calcined crushed NSCF6428 nanopowder with experimental data (black line), reference file (red line), residue (grey line) – peaks are indexed using ICDD 04-017-2448 and red circles indicate $SrCO_3$ peaks present (indexed to ICDD 01-078-4340) **b**) Zoom in of the fitting of the rhombohedral (R3c) structure of 775 ºC calcined NSCF6428 nanopowder indicating peak splitting located at (220)/(208) 68º 2θ.

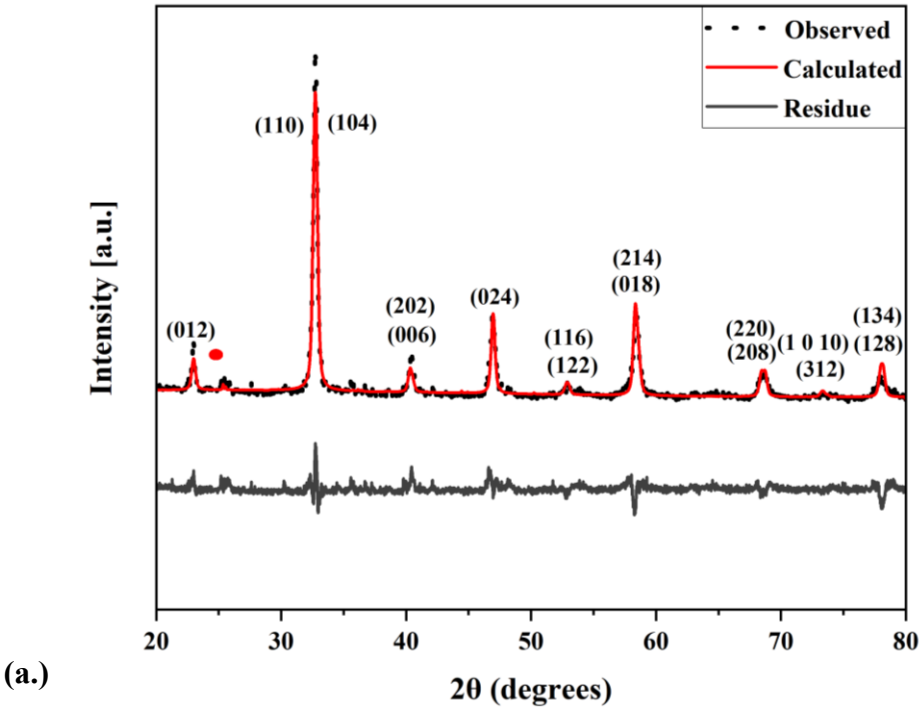

(a.)

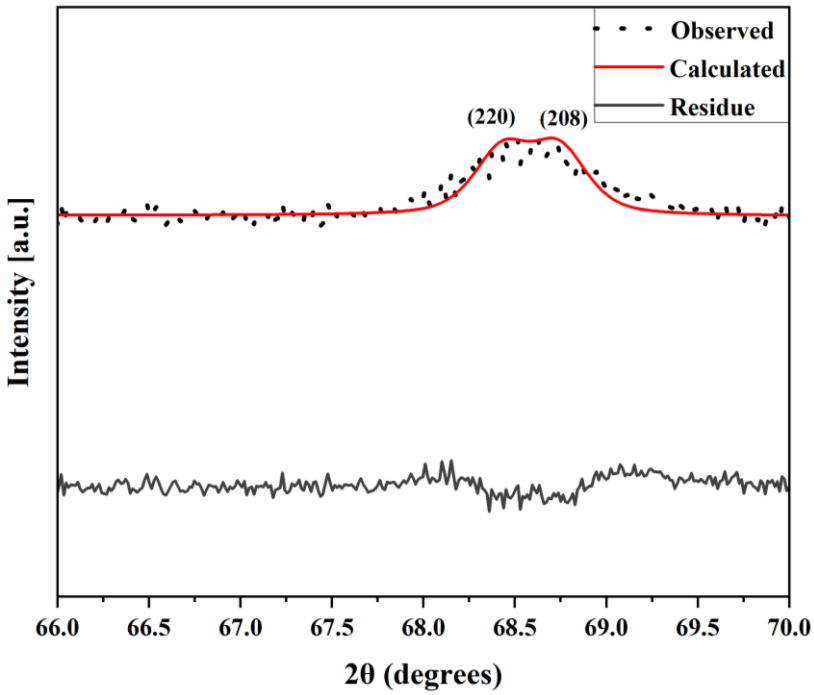

(b.)

Figure 6.20: a) Whole pattern fitting of the rhombohedral (R3c) structure of 800 ºC calcined crushed NSCF6428 nanopowder with experimental data (black line), reference file (red line), residue (grey line) – peaks are indexed using ICDD 04-017-2448 and red circles indicate $SrCO_3$ peaks present (indexed to ICDD 01-078-4340) **b**) Zoom in of the fitting of the rhombohedral (R3c) structure of 800 ºC calcined NSCF6428 nanopowder indicating peak splitting located at (220)/(208) 68º 2θ.

Table 6.14: Whole pattern fitting of structural parameters and perovskite phase purity of the rhombohedral (R3c) and orthorhombic (O_h) NSCF6428 at different calcination temperatures of 775 and 800 ºC ((R_{wp}(%)) weighted pattern, (R_{exp}(%)) expected pattern and goodness of fit (GOF))

Temperature (^{o}C) – R3c	**R_{exp} (%)**	**R_{wp} (%)**	**GOF**	**Perovskite Phase Purity (%)**
775	5.272	4.443	0.842	96.2
800	4.724	3.707	0.785	96.9

Temperature (^{o}C) - Ortho	**R_{exp}(%)**	**R_{wp}(%)**	**GOF**
775	5.272	6.609	1.254
800	4.724	5.008	1.06

The calcined temperature 750 ºC was omitted from the peak fitting analysis of the three different samples due to the phase purity being unlikely to meet the 90% phase purity criteria as shown in Figures 6.10, 6.13 and 6.17 and reported by Baharuddin et.al .[179] It can be seen from Table 6.1 that when calculating the tolerance factor for each rare earth doped composition, when the ionic radius of the lanthanides across the periodic table decreases, the tolerance factor of LPSCF33428, LNSCF33428 and NSCF6428 decreases below the value of LSCF6428.[218] The LSCF6428 diffraction pattern has been typically indexed to the rhombohedral crystal structure from this and past work. When there have been different lanthanide elements (other than lanthanum) involved for substitution in relation to the formula, there have been consistent reports of the effect of crystal structure transition from rhombohedral to orthorhombic when smaller ions are substituted in such that the lattice parameter, unit cell volume and Goldschmidt's tolerance factor are sufficiently decreased.[21-22][75][219-220] However, there has been limited in depth analysis of XRD peak pattern fitting on rare earth doped LSCF. For this current work, a mixture of the rhombohedral and orthorhombic crystal symmetry for

the Nd doped LSCF (LNSCF33428 and NSCF6428) (ICDD) were indexed separately to determine the most appropriate single phase fitting (Figures 6.14-6.16 and 6.18-6.20). Whilst the XRD diffraction patterns were fitted only to the rhombohedral crystal symmetry for LPSCF33428,the orthorhombic structure failed to match the diffraction patterns for any of the calcination temperatures for LNSCF33428 and NSCF6428 i.e. despite the substitution the unit cell volume has apparently not decreased sufficiently to transform the crystal symmetry so the 800 ºC XRD diffraction patterns of the orthorhombic structure are omitted.

All 3 different compositions calcined at 775 ºC and 800 ºC, show reasonable fitting of the rhombohedral reference patterns to the experimental diffraction data. Whilst for the orthorhombic reference patterns, there were either missing or mismatched peaks from the experimental data resulting in poor fitting, so these will be omitted from the rest of the section. That is confirmed by the quantitative fitting values shown in Tables 6.12, 6.13 and 6.14 (the quality factor values for the fits for rhombohedral are all below 1%).

It can show from Figures 6.10 and 6.13 that the highest single phase purity that also meets the 90% phase purity criteria is achieved at 800 ºC for the partially doped LSCF i.e. LPSCF33428 and LNSCF33428. However, for the fully substituted NSCF6428, it is achieved at 775 ºC (Figure 6.17). The chosen calcination temperature for each of the 3 samples will be examined further for their structural parameters and crystallite size to determine how the effects of the substitution of rare earth dopants with lanthanum influence the structural properties of the doped LSCF6428 in comparison to the undoped LSCF6428 as shown in Table 6.15.

Table 6.15: Unit Cell dimensions (rounded to three decimal places), Theoretical Density, Volume (rounded to two decimal places) and Mean Crystallite Size of Rhombohedral (R3c) LPSCF33428, LNSCF33428 calcined at 800 ºC and NSCF6428 calcined at 775 ºC.

Sintered Cathode Materials	**a (Å)**	**b (Å)**	**c (Å)**	**Volume (Å)**	**Theoretical Density (g/cm^3)**	**Mean Crystallite Size (nm)**
LPSCF33428	5.551 ± 0.034	5.551	13.396	351.81 ± 1.49	11.02 ± 0.04	23.6
LNSCF33428	5.550 ± 0.033	5.550	13.371	349.99 ± 1.5	11.08 ± 0.045	23.5
NSCF6428	5.494 ± 0.034	5.494	13.347	349.33± 1.47	11.1 ± 0.04	24.8

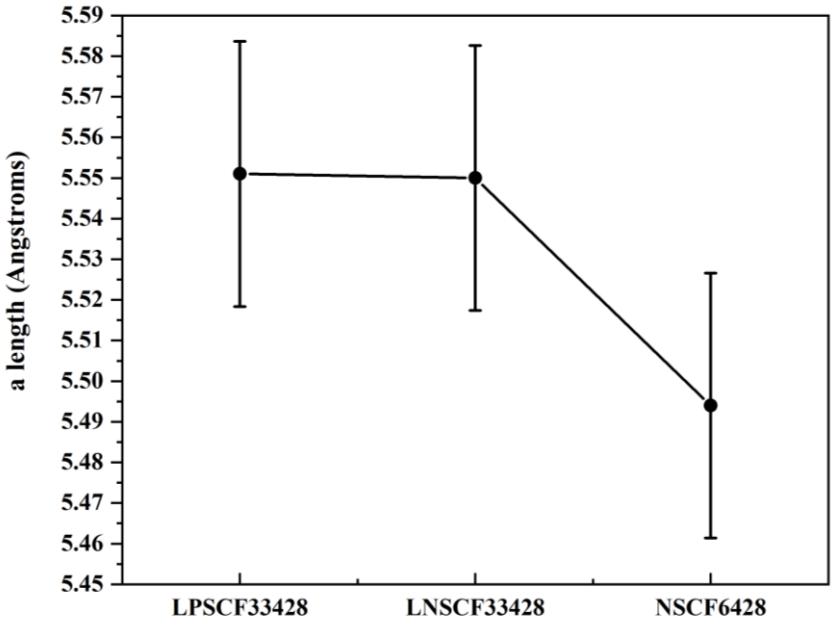

Figure 6.21: Temperature (°C) vs Rhombohedral lattice parameter, "a" length (Angstroms) of the calcined rare earth doped perovskite oxides where the black dots refer to as the experimental data along with the error bars.

LPSCF33428, LNSCF33428 and NSCF6428 phase purities were all confirmed to be around 96% and XRD peak diffraction patterns fitting were all indexed at the same symmetry, rhombohedral. The difference of "a" length of the crystal structure was examined in according to the rhombohedral structure. It can be seen from Figure 6.22 that the linear trend of a length lattice parameter decreases from LPSCF33428 -> LNSCF33428 -> NSCF6428. This is in agreement with previous work on the MIEC cathode, BSCF in relation for the substitution of rare earth dopants using Pr.[124] However, due to the phase purity not being 100 %, the effect of the $SrCO_3$ could have led to potential Sr^{2+} deficiency. In a study by Waller et.al., Sr^{2+} deficiency increase in the LSCF composition has led to an expansion of the "a" lattice parameter of the rhombohedral. Therefore, for this work, given the NSCF6428 has typically transformed into orthorhombic symmetry, the effect of Sr^{2+} deficiency could have inhibited the transformation and retain the rhombohedral symmetry as shown in for the undoped LSCF6428.[186]

Decreasing the average ionic radius predominantly lowers the lattice parameter "a" length of the perovskite lattice structure as shown in Figure 6.21. The decrease in the "a" length lattice parameter is referred to in a study by Xu et.al.[219] A composition was investigated with Ln = Pr, Nd and Sm, when La was replaced with small lanthanides ions, where the substitution led to the transition in crystal symmetry from rhombohedral to orthorhombic when calcined at 700

°C. However, there was no comparison provided between the ICDD data of either the rhombohedral or orthorhombic to index the presence of peak splitting.[219] In another study by Heydair, carried out nearly a decade later, the peaks were indexed for both the LSCF and NSCF, revealing the transition but there is limited information provided.[220] Therefore, this current work indicates that as the average ionic radius of the A site decreases, the a length lattice parameter of the rhombohedral crystal symmetry decreases linearly as shown in Figure 6.22, rather than transitioning to a different crystal symmetry as concluded from other work.[75][219-220] The lattice parameter "a" length also influences the volume to density relationship.

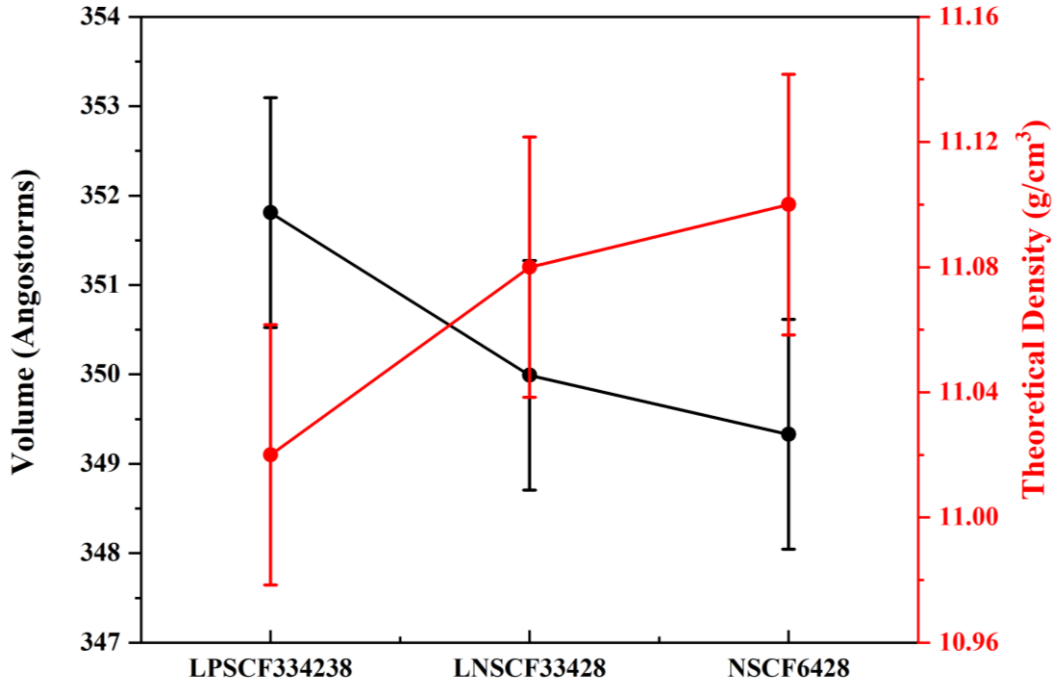

Figure 6.22: Temperature (°C) vs Rhombohedral Volume (Angstroms- black line with error bars at black dots refer to as experimental data points) and Theoretical Density (g/cm^3- red line with error bars at red dots refer to as experimental data points) of the calcined rare earth doped perovskite oxides

Figure 6.22 shows that there is an inverse relationship between the volume and the density for the phase purity of 96% and crystal symmetry of LPSCF33428, LNSCF33428 and NSCF6428. From earlier work on rare earth doped MIEC cathodes other than LSCF6428, researchers have always relied on basic XRD analysis rather than using peak fitting to obtain structural parameters to determine if there have been any shifts in XRD diffraction pattern peaks.[75][124][218-220] Without the peak fitting, it can be difficult to indicate the significance that rare earth doping has upon the crystal structure. In the last decade, there have

been two studies investigating rare earth doped LSCF materials such as Ce-LSCF which have looked at structural parameters to determine the effects of rare earth doping.[21] It can also be observed with the Dy-LSCF where the trend in the decrease in "a" length lattice parameter decreases the lattice volume, as the calcination temperature increases, which also results in the change in density.[22] This is consistent with this work on rare earth doping for the LSCF.

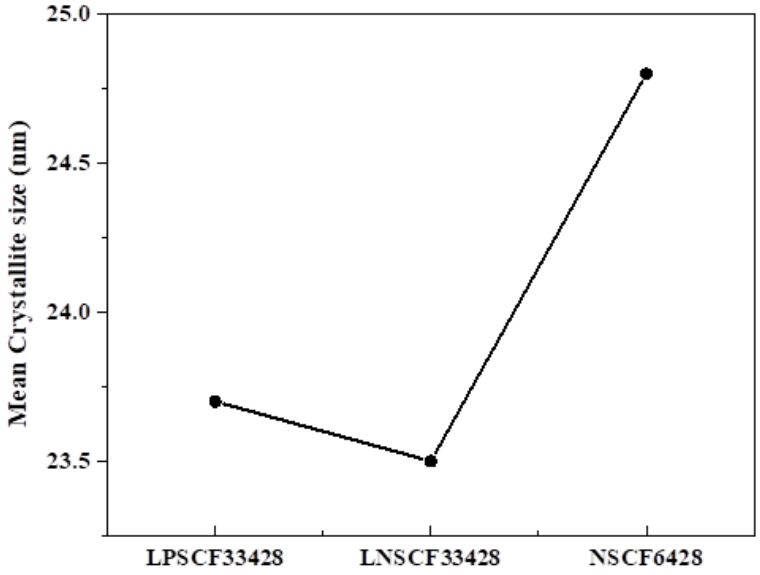

Figure 6.23: Temperature (°C) vs Mean crystallite size (nm) of the calcined rare earth doped perovskite oxide where the black dots refer to as the experimental data.

It has also been known that the effect of substituting dopants in the undoped LSCF6428 can influence the crystallite size as shown in Figure 6.23. That is due to the difference in ionic radius between the host and the dopant occupying the lattice space as shown in Table 6.1. From a study by Mohammadi et. al., rare earth Dy was substituted for lanthanum at the A site into the undoped LSCF6428 both partially (0.3 mol) and fully (0.6 mol) which influenced the crystallite size in a decrease from 28 nm for LDSCF33428 to 24 nm for LDSCF6428.[22] Here there is a trend from LNSCF33428 to NSCF6428 where there is an increase in crystallite size as shown in Figure 6.24, although the crystalline sizes for all 3 compositions are higher compared to the undoped LSCF6428 (21.5 nm as reported in Chapter 4, Section 4.3).

As the phase purity is not 100% for LPSCF33428, LNSCF33428 or NSCF6428, there is a possibility that the presence of second phase $SrCO_3$ could have led to Sr deficiency in the perovskite phase. XRD alone cannot determine how the crystalline size of the nanopowder affects the process of agglomeration and elemental homogenisation in relation to the developing microstructure of the perovskite oxide.

6.4. Microstructure Characterisation of the optimum temperature calcined LPSCF33428, LNSCF33428 and NSCF6428 Nanopowder

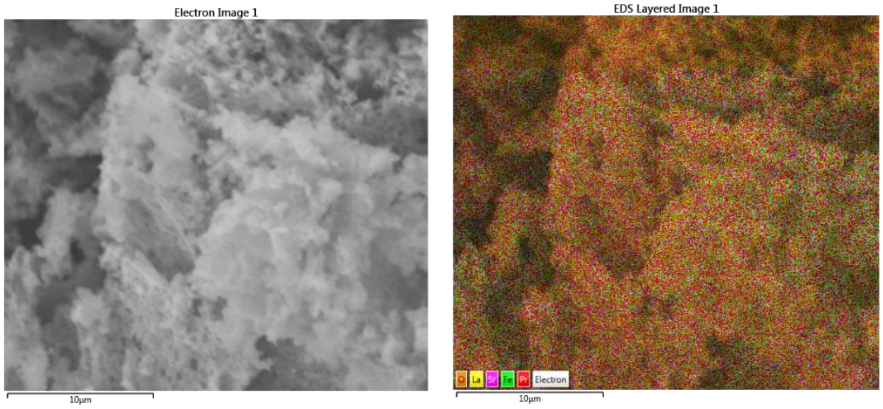

Figure 6.24: SEM image of calcined 800 ºC LPSCF33428 nanopowder. Left (Before EDX scan) and Right with overlaid elemental X-ray maps from EDX

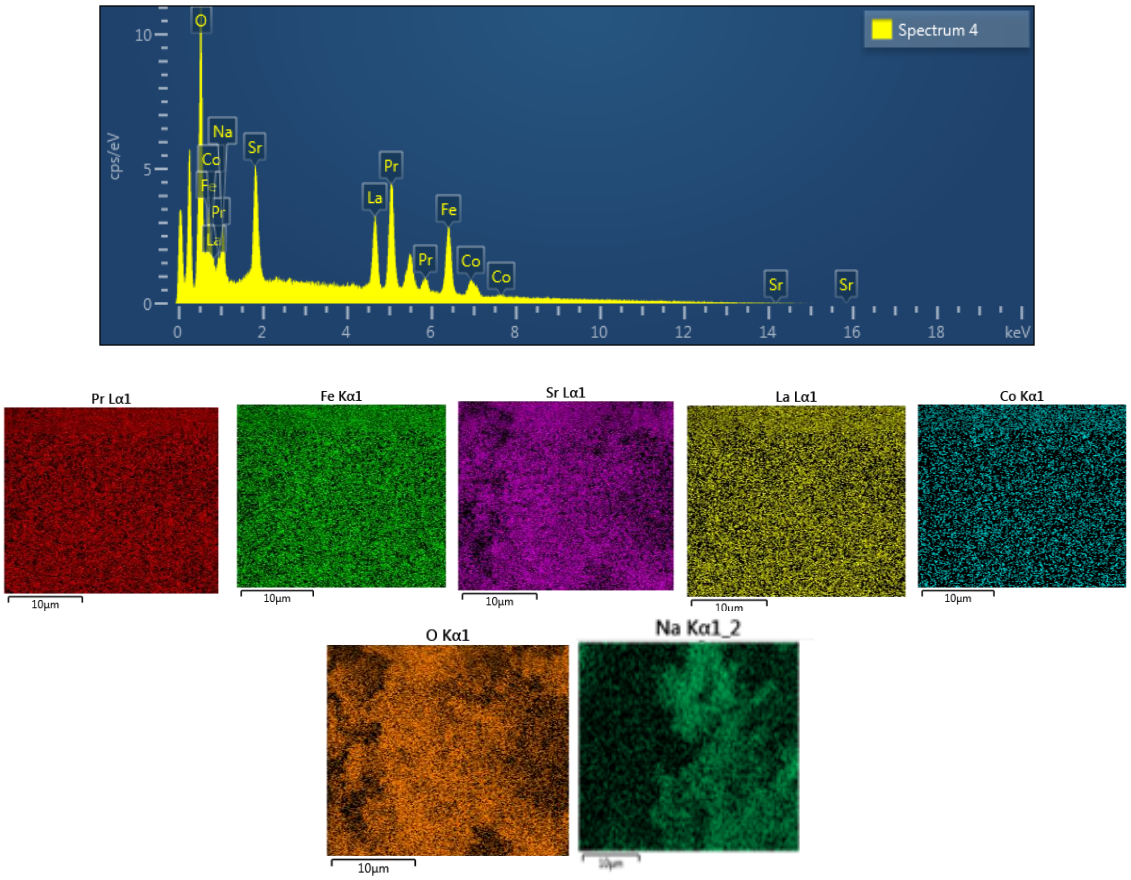

Figure 6.25: (Above) EDX spectrum of calcined LPSCF33428 (Below) showing the presence of all the key metal elements for LSCF 6428 with elemental maps showing some deficient Sr, excess Na but otherwise a homogenous distribution of the LSCF6428 elements in a calcined nanopowder.

Table 6.16: 800 ºC calcined LPSCF33428 comparison of EDX measured composition (by assuming stoichiometry) and the expected composition.

Elements	Measured Composition	Expected Composition
Iron (Fe)	0.83	0.8
Strontium (Sr)	0.20	0.4
Lanthanum (La)	0.37	0.3
Praseodymium (Pr)	0.34	0.3
Sodium (Na)	0.09	-
Cobalt (Co)	0.16	0.2

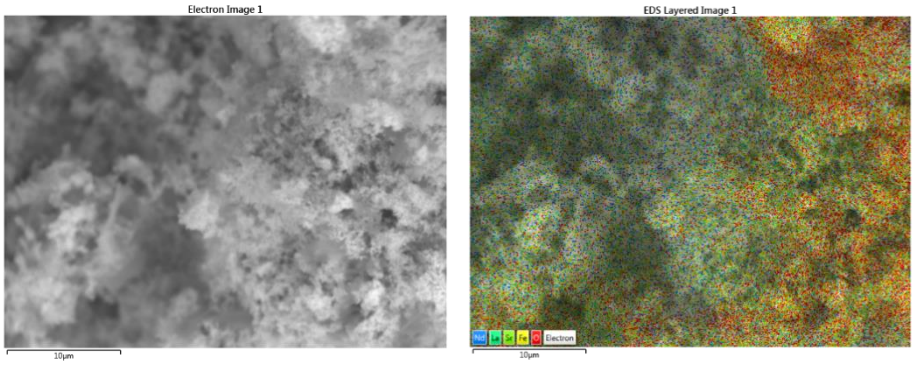

Figure 6.26: SEM image of calcined 800 ºC LNSCF33428 nanopowder. Left (Before EDX scan) and Right with overlaid elemental X-ray maps from EDX

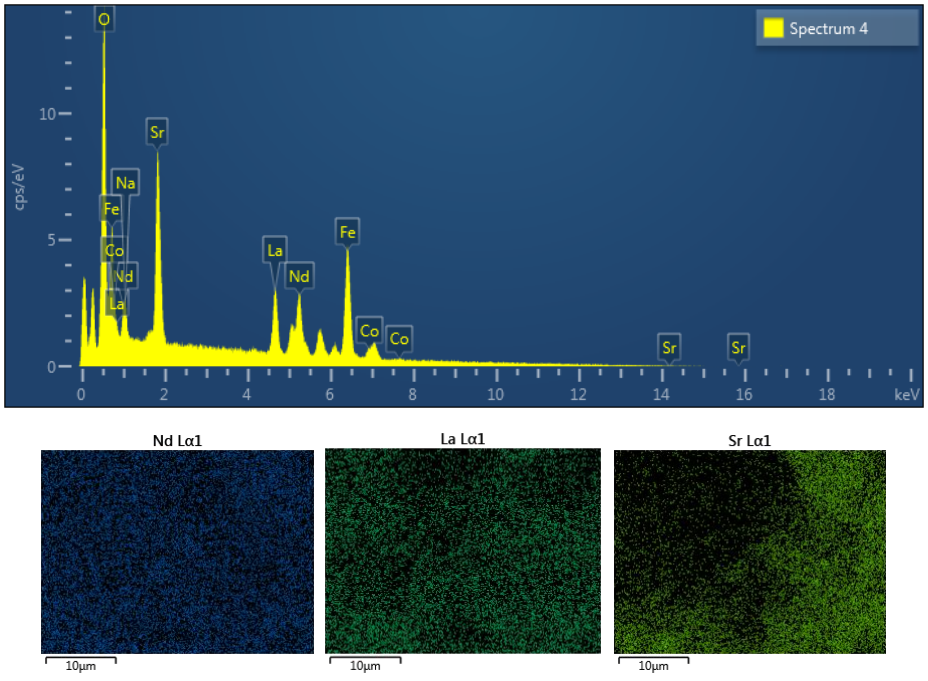

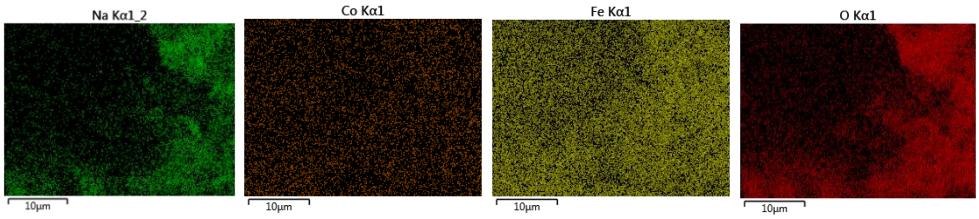

Figure 6.27: (Above) EDX spectrum of calcined LNSCF33428 (Below) showing the presence of all the key metal elements for LSCF 6428 with elemental maps showing some deficient Sr, excess Na but otherwise a homogenous distribution of the LSCF6428 elements from a calcined nanopowder

Table 6.17: 800 ^{o}C calcined LNSCF33428 comparison of EDX measured composition (by assuming stoichiometry) and the expected composition.

Elements	**Measured Composition**	**Expected Composition**
Iron (Fe)	0.92	0.8
Strontium (Sr)	0.17	0.4
Lanthanum (La)	0.25	0.3
Neodymium (Nd)	0.25	0.3
Sodium (Na)	0.26	-
Cobalt (Co)	0.13	0.2

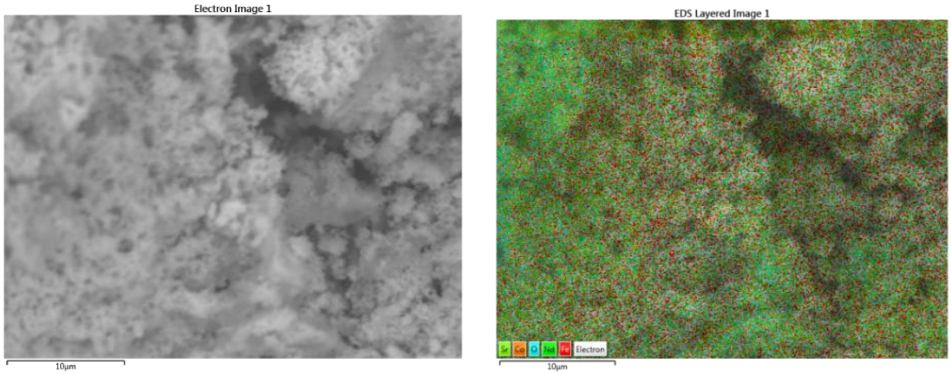

Figure 6.28: SEM image of calcined 775 ^{o}C NSCF6428 nanopowder. Left (Before EDX scan) and Right with overlaid elemental X-ray maps from EDX

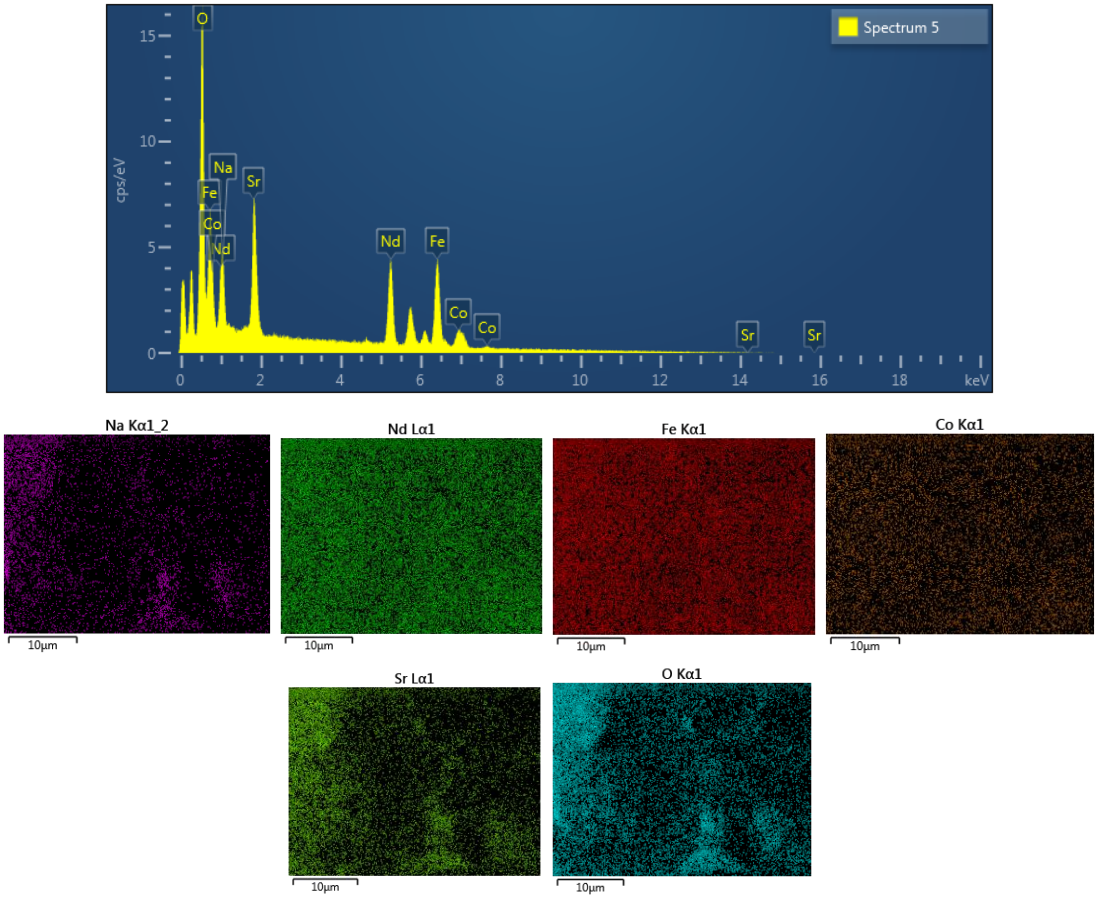

Figure 6.29: (Above) EDX spectrum of calcined NSCF6428 (Below) showing the presence of all the key metal elements for LSCF 6428 with elemental maps showing some deficient Sr, excess Na but otherwise a homogenous distribution of the LSCF6428 elements from a calcined nanopowder

Table 6.18: 775 °C calcined NSCF6428 comparison of EDX measured composition (by assuming stoichiometry) and the expected composition.

Elements	**Measured Composition**	**Expected Composition**
Iron (Fe)	0.69	0.8
Strontium (Sr)	0.20	0.4
Neodynium (Nd)	0.58	0.6
Sodium (Na)	0.38	-
Cobalt (Co)	0.15	0.2

SEM imaging (in Figures 6.24, 6.26 and 6.28) shows the formation of a porous material calcination of the LPSCF33428, LNSCF33428 and NSCF6428 and that the resulting material has an agglomerated, fine particulate (or crystal) structure. The structure of a porous nanopowder is created by the complete thermal decomposition of the polysaccharide alginate.

EDX spectroscopy and elemental mapping give an indication of the relative homogeneity of the metal cations in the nanopowder of the three different compositions (Figures 6.25, 6.27 and 6.29). LSCF-CuO synthesised using the sol gel method was investigated using SEM/EDX to show that the samples calcined at 600 – 900 ºC were pure along with the formation of porous microstructure. [221] Here all the elements for the perovskite metal oxide are present but with varied concentrations as seen in the quantitative data in Tables 6.15-6.17. O and C have been omitted from the Table 6.15-6/17 because of the presence of a carbon pad on which the sample is placed and absorption of C and O K X-rays affecting the measurements. The measured Co composition is close to the expected value for all 3 different compoistios and a similar pattern occurs for the LNSCF33428 with the elements La and Nd. That is compared to Sr which is significantly deficient at the A site for all the three different composites. Whilst the Fe element is significantly deficient for the NSCF6428 in comparison to the partially substituted perovskite oxide LNSCF33428 which has excess Fe as shown in Figure 6.29 and 6.27 respectively. The elements La and Pr within LPSCF33428 are also in excess as shown in Figure 6.26.

As the average ionic radius decreases at the A site, there is increased presence of the Na^+, and this suggests that not all the Na^+ present in the alginate has been fully exchanged with the multivalent metal cation, which could have significantly impacted the Sr^{2+}.[167] As seen in the Tables 6.15-6.17, the chemical composition estimates are close to the expected composition although there is deficiency in the strontium which is consistent with the presence of a small $SrCO_3$ second phase peak in the XRD diffraction pattern of the optimum calcination temperatures as shown in Figures 6.12, 6.16 and 6.19 given none of the three rare earth doped LSCF compositions achieved 100% perovskite phase purity.

6.5. Raman Spectroscopy of the calcined LPSCF33428 and NSCF6428 nanopowder

The choice behind acquiring Raman spectroscopy is similar to what is described in Chapter 4 Section 4.4 for the LSCF6428.

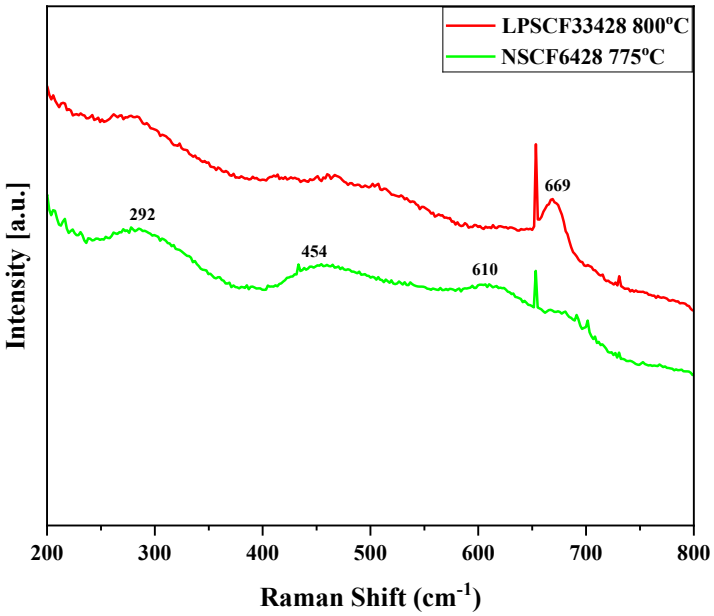

Figure 6.30: Raman spectra of LSCF6428 nanopowders calcined at 800 ºC for LPSCF33428 and 775 ºC for NSCF6428 and with excitation wavelength of 532 nm.

The Raman spectra of the rare earth doped LSCF6428 with the optimum calcination temperature were examined in the range of 200 – 800 cm^{-1} and are shown in Figure 6.30 to determine the difference of behaviour between the dopants, Pr and Nd. LNSCF33428 was omitted from the Raman due to complications with obtaining data at the selected Raman frequency. From the results there is clear relationship between the dopants and intensity of the peaks present. It can be seen for the LPSCF6428 when calcined at 800 ºC it has one sharp peak located at 669 cm^{-1} (Figure 6.31). While for the NSCF6428 when calcined at 775 ºC this results in the transition to three boarder peaks located at 292 cm^{-1}, 454 cm^{-1} and 610 cm^{-1}. There is also a decrease in the Raman intensity from the LPSCF to NSCF which is also consistent with the "a" length and lattice volume decrease from the XRD. It indicates that the substitution of lanthanum for neodymium could influences the distortion of the FeO6 octahedra due to the ionic radii mismatch of 0.17 A affecting the Fe-O coordination and stability of the crystal symmetry.

The sharp peak at 669 cm^{-1} only appears when the LPSCF6428 was calcinated at 800 ºC,and it has shifted to lower wavenumber compared to LSCF6428 indicating the effect of smaller symmetric stretching which is caused by the doping by a smaller rare earth ion.[62] The Raman position is similar to a study by Li et.al., when LSCFs were doped using other perovskites such as LSM to enhance the oxygen reduction activity and stability.[222] $PrMnO_3$ had the highest Raman intensity compared to the other perovskites. There is also possibility that the excess

iron which also tends to form redox couple especially with Sr deficiency could have led to this as well.[222]

However, for the NSCF6428, there were broader peaks which appeared at 292 cm^{-1} and 454 cm^{-1} which did not appear for LPSCF33428. These extra peaks indicate oxygen octahedra tilt and oxygen octahedra bending respectively. These may be an indication of the full rhombohedral-octahedral structure forming in the NSCF6428 while LPSCF33428 remains a rhombohedral structure. Certainly, increased calcination temperatures resulted in less Sr deficiency and a decrease in $SrCO_3$. LSCF6428 transitioned to a fully rhombohedral structure as shown in Chapter 4 Section 4.3 and reported by Anajafi et.al. [223]. There is also a shift of the 669 cm^{-1} peak to lower wave number due to the local structural changes through the decrease of the "a" length of the crystal symmetry lattice of the rhombohedral structure evident from the XRD. This also affects the volume and thus the density of the perovskite oxide structure as seen in Figures 6.23 and 6.22 respectively.

6.6. X – Computed Tomography Characterisation between the metal alginate complex of LPSCF33428, LNSCF33428 and NSCF6428 and the optimum calcined temperature of LPSCF33428, LNSCF33428 and NSCF6428 nanopowders

XCT was conducted to provide a 3D reconstruction for both the dried metal–alginate complexes and the optimum calcined rare earth doped nanopowders as shown in Figures 6.32-6.34 below. It has been found that neither the dried nor the calcinated samples of rare earth doped perovskite oxides have previously been examined using XCT for either homogeneity or porosity. However, ZK60 magnesium alloys with the addition of rare earth elements have been examined using micro-CT analysis to determine the effects that rare earth elements have upon the homogeneity and porosity within the microstructures. From the investigation, the use of 1.5 wt% of rare earth elements was found to improve the homogeneity of the alloy microstructure.[224] Images were thresholded to obtain the relative parameters such as volume fraction of pores, to provide key information for the comparison of the different rare earth dopants that influence the calcination of the doped LSCF6428 nanopowders microstructure in relation to its homogeneity and porosity.

Dried LPSCF33428 – Slice 1751/2006

a.)

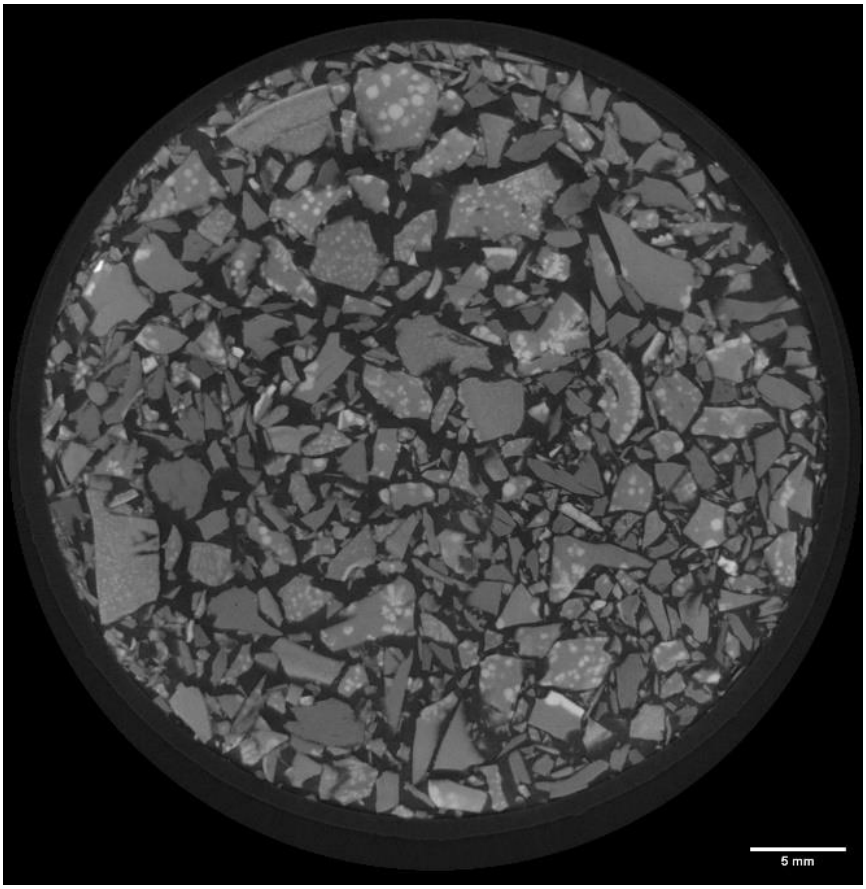

b.)

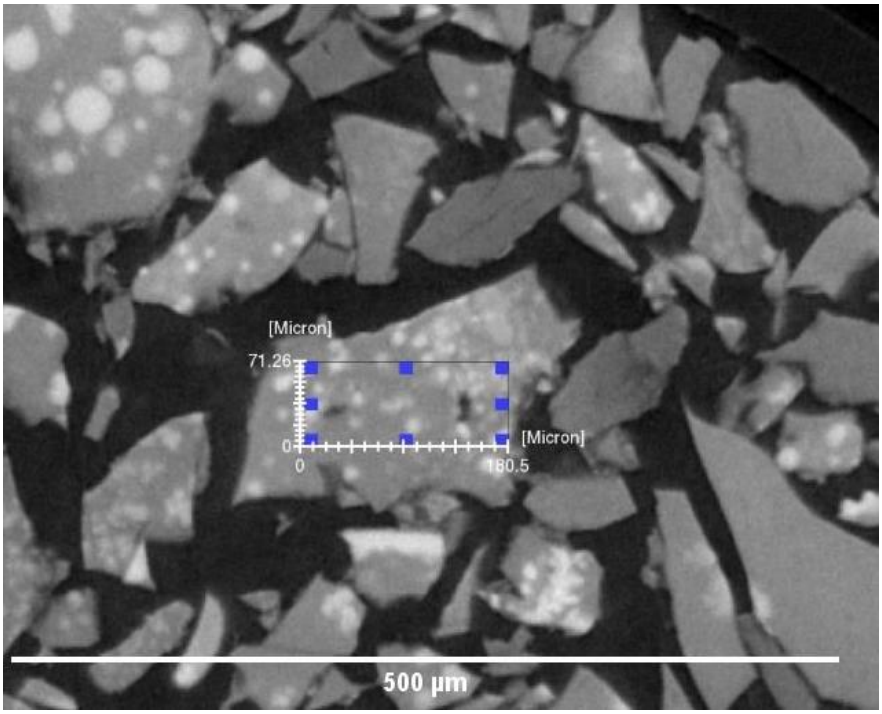

Calcined LPSCF33428 – Slice 565/2006

c.)

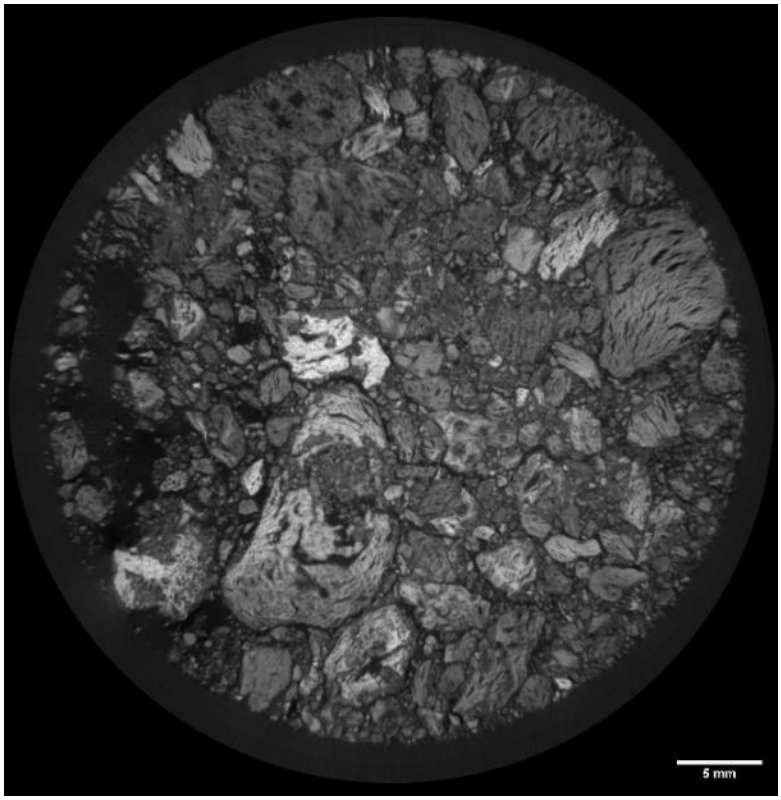

d.)

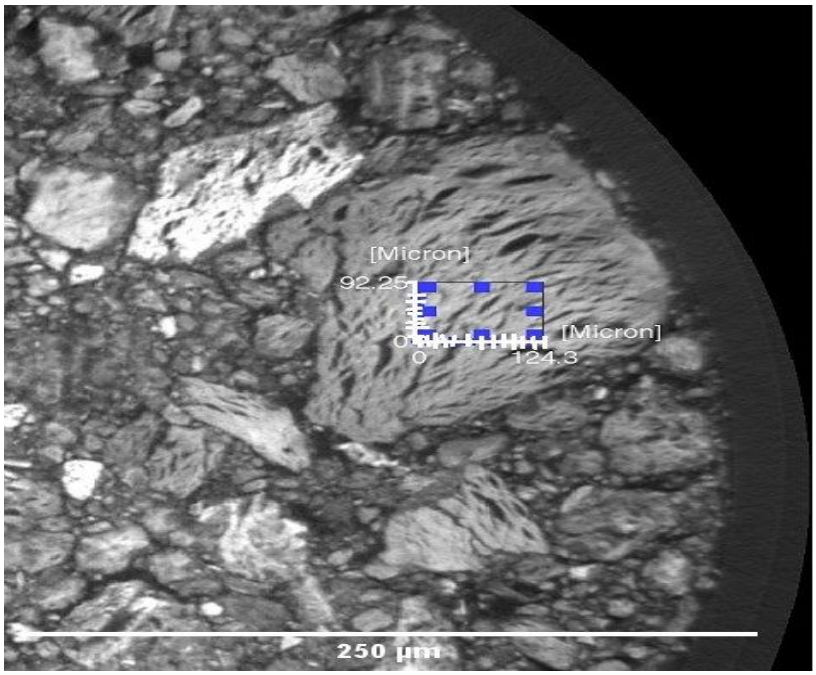

Figure 6.31: a.) Cross sectional morphological of metal-alginate complex of LPSCF33428 from Micro-CT **b.)** Thresholded image of white box region (measured in micron) where the pore size distribution was taken from one of the selected 20 grains. **c.)** calcined perovskite oxide of LPSCF33428 from Micro-CT **d.)** Thresholded image of white box region (measured in micron) where the pore size distribution was taken from one of the selected 20 particles.

Dried LNSCF33428 – 924/2006

a.)

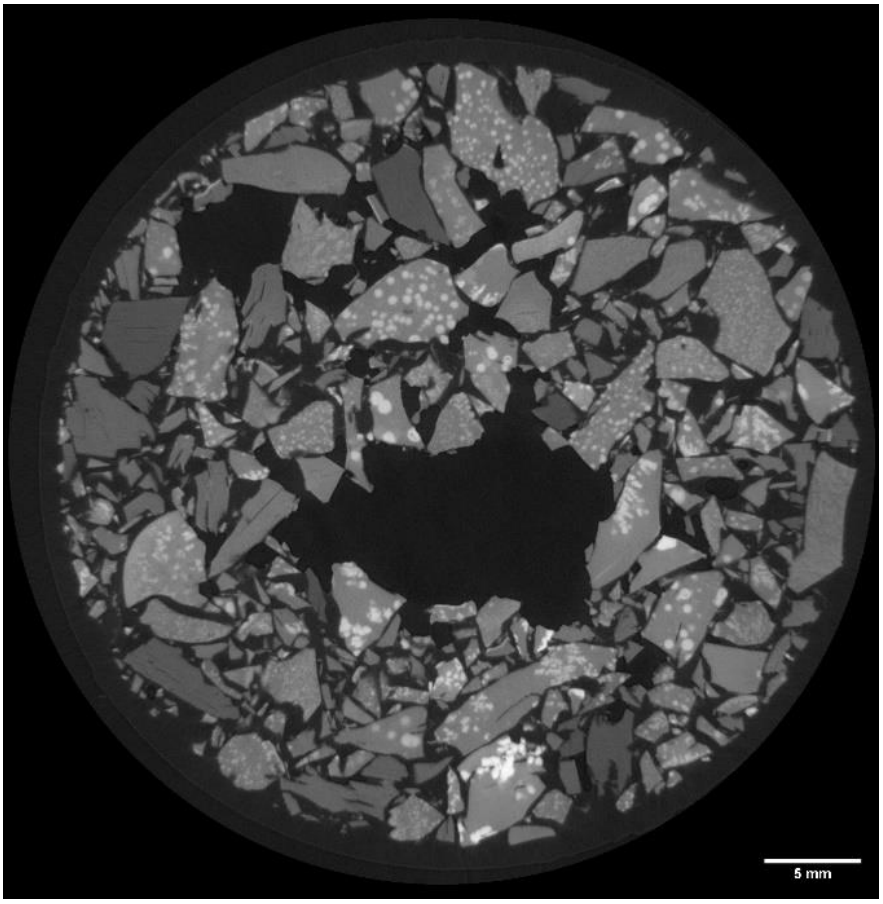

b.)

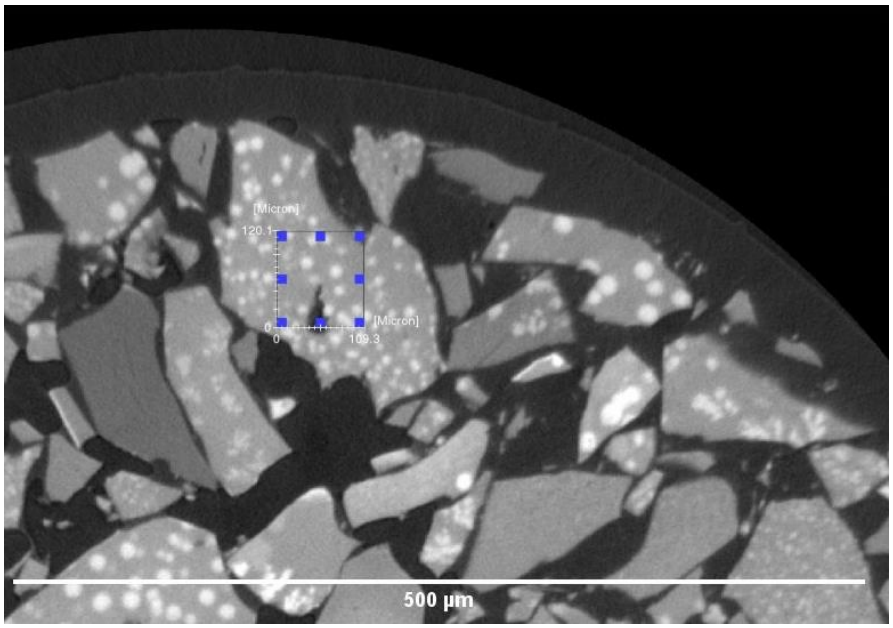

Calcined LNSCF33428 - Slice 1723/2006

c.)

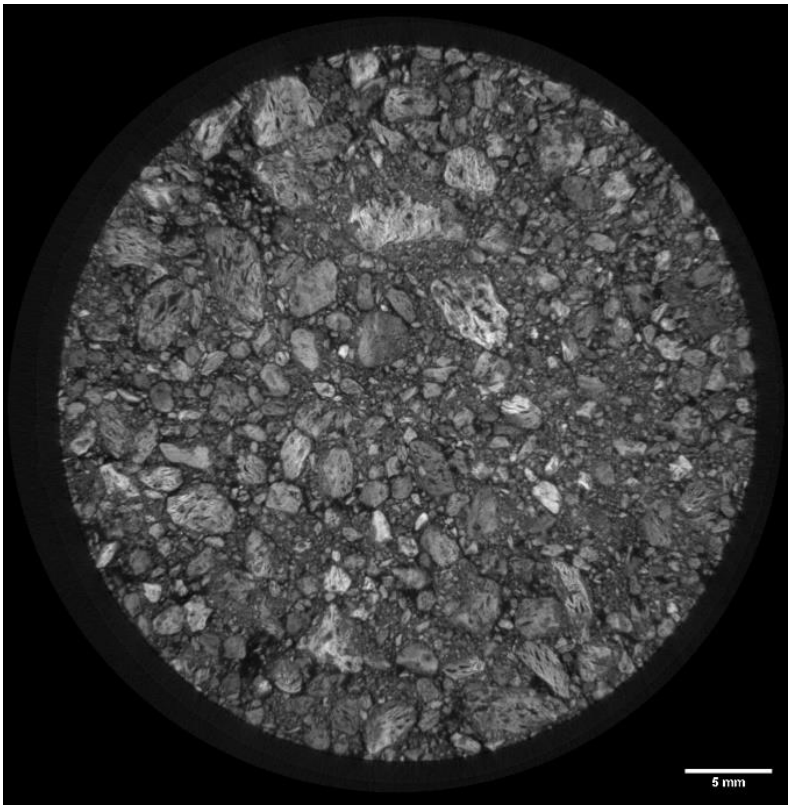

d.)

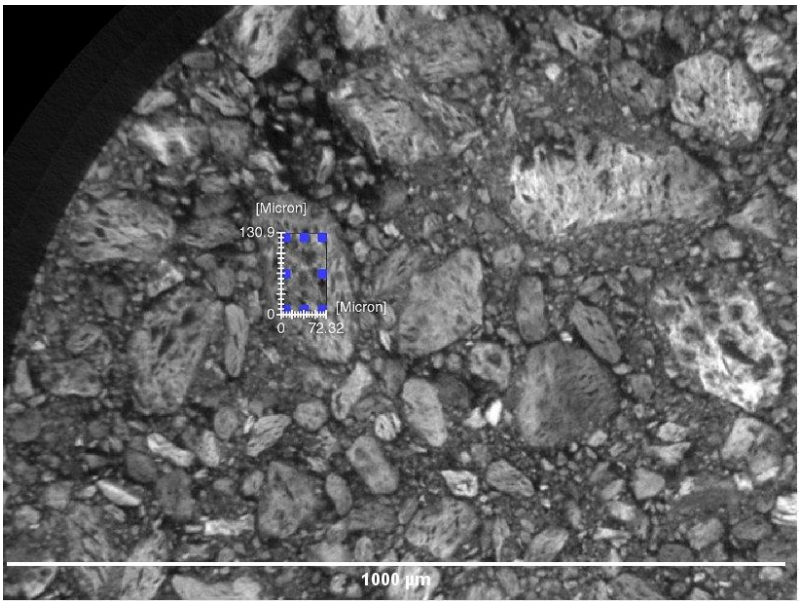

Figure 6.32: a.) Cross sectional morphological of metal-alginate complex of LNSCF33428 from Micro-CT **b.)** Thresholded image of white box region (measured in micron) where the pore size distribution was taken from one of the selected 20 grains. **c.)** calcined perovskite oxide of LNSCF33428 from Micro-CT **d.)** Thresholded image of white box region (measured in micron) where the pore size distribution was taken from one of the selected 20 particles.

Dried NSCF6428 – Slice 568/2006

a.)

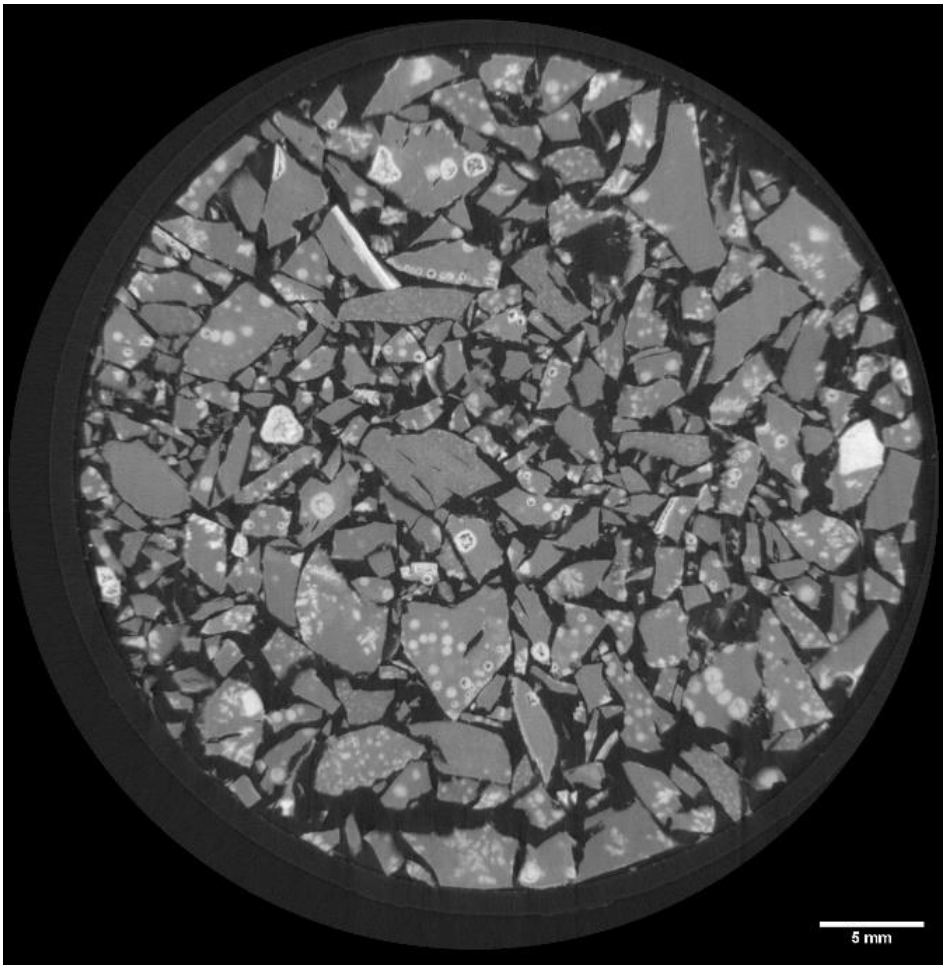

b.)

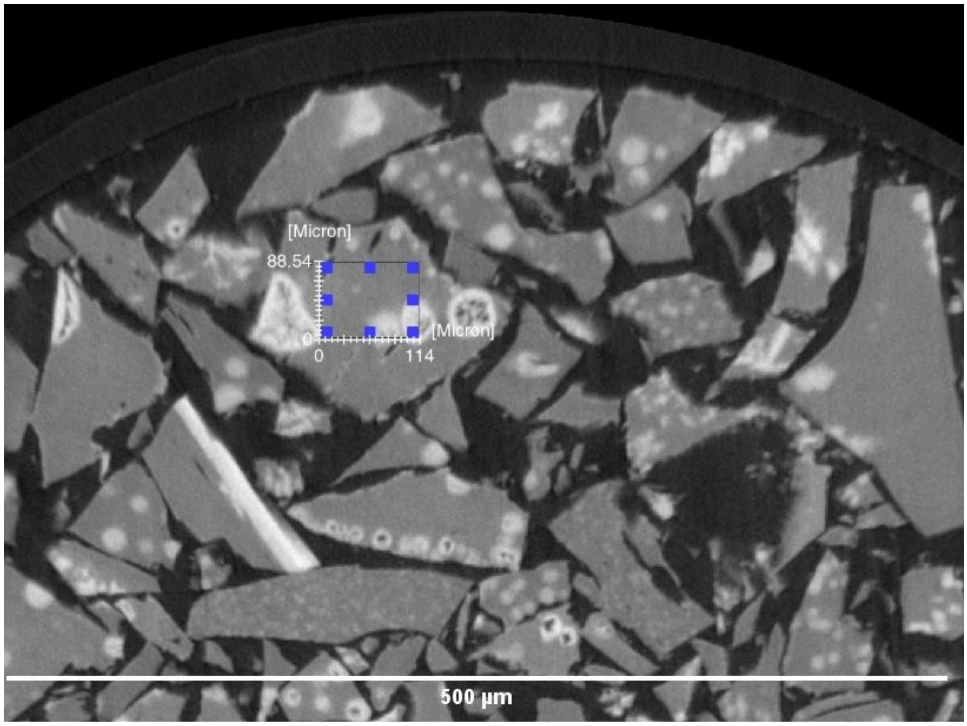

Calcined NSCF6428 – Slice 688/2006

c.)

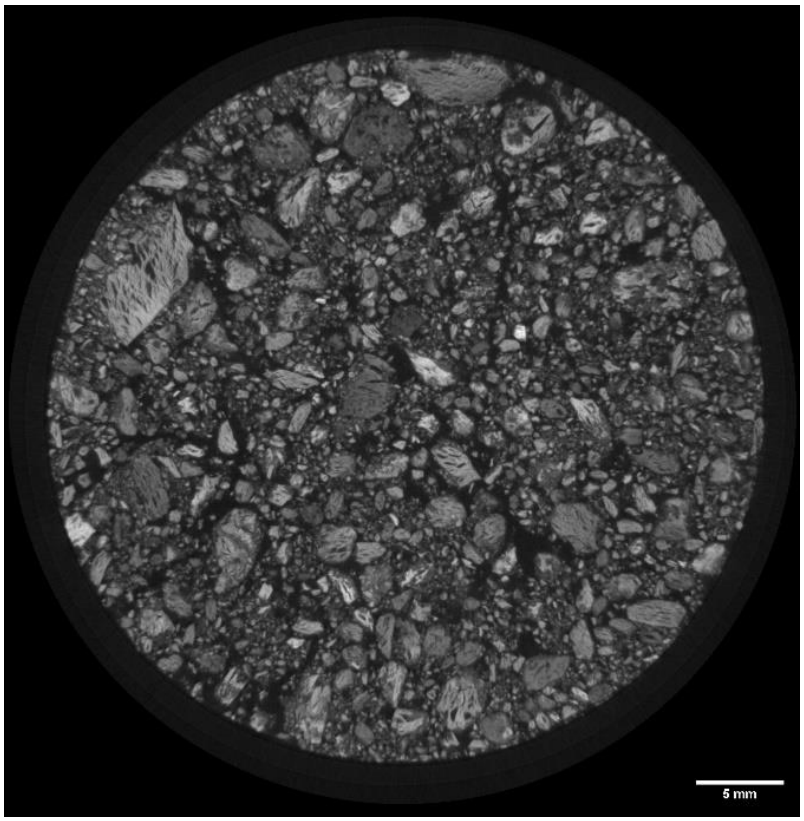

d.)

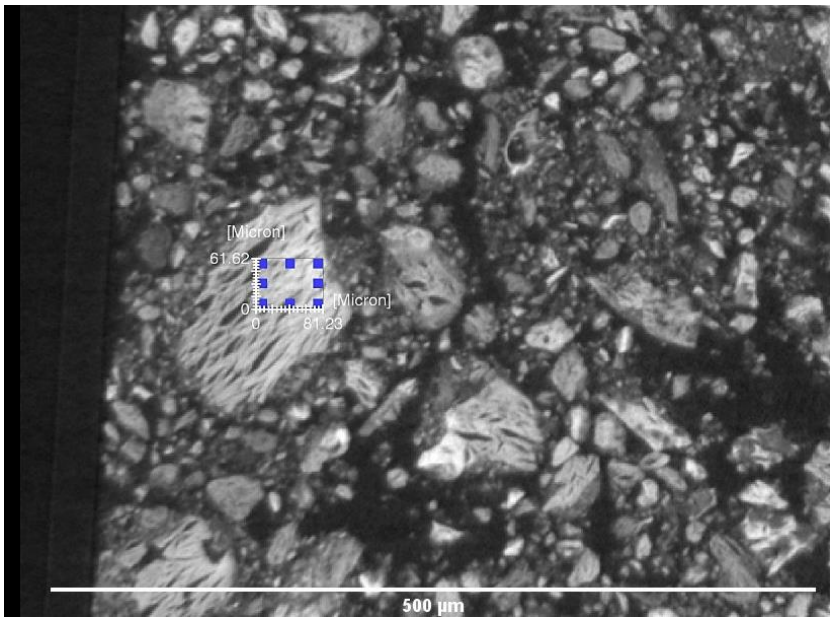

Figure 6.33: a.) Cross sectional morphological of metal-alginate complex of NSCF6428 from Micro-CT **b.)** Thresholded image of white box region (measured in micron) where the pore size distribution was taken from one of the selected 20 grains. **c.)** calcined perovskite oxide of NSCF6428 from Micro-CT **d.)** Thresholded image of white box region (measured in micron) where the pore size distribution was taken from one of the selected 20 particles.

a.)

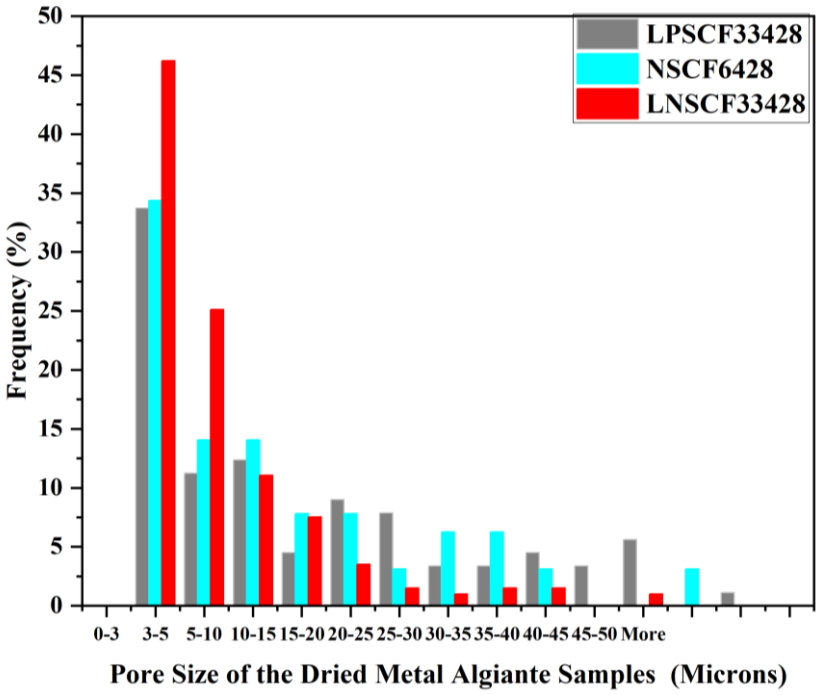
LPSCF33428
NSCF6428
LNSCF33428
Frequency (%)
0
5
10
15
20
25
30
35
40
45
50
0-3
3-5
5-10
10-15
15-20
20-25
25-30
30-35
35-40
40-45
45-50
More
Pore Size of the Dried Metal Algiante Samples (Microns)

b.)

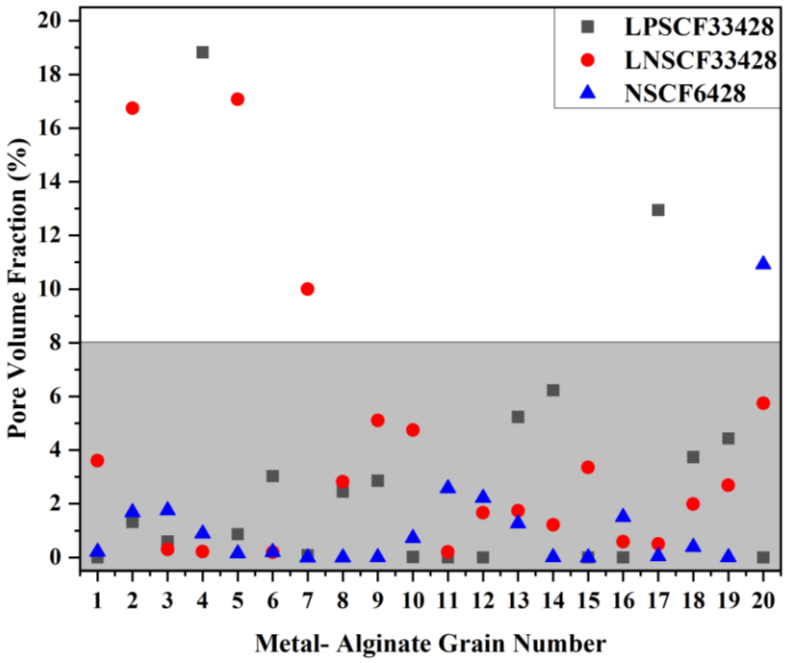
LPSCF33428
LNSCF33428
NSCF6428
Pore Volume Fraction (%)
0
2
4
6
8
10
12
14
16
18
20
1
2
3
4
5
6
7
8
9
10
11
12
13
14
15
16
17
18
19
20
Metal- Alginate Grain Number

c.)

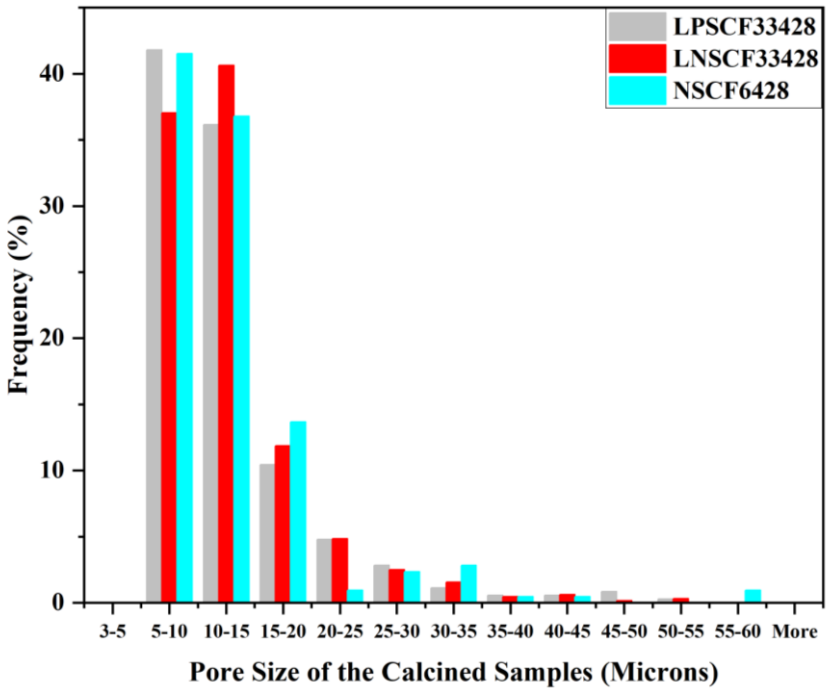

d.)

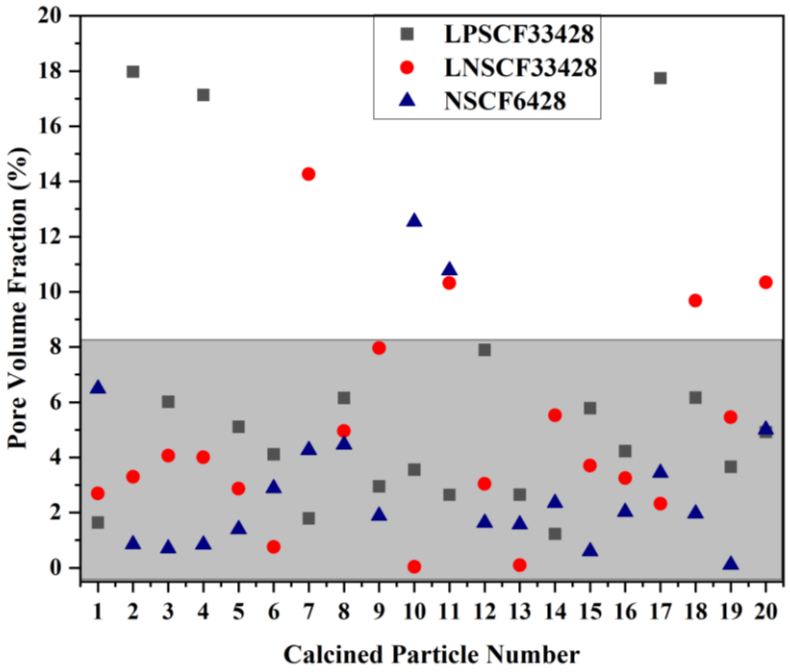

Figure 6.34: (a) Pore size distribution of the dried metal alginate complex of LPSCF33428, LNSCF33428 and NSCF6428 (b) volume fraction of pores of the dried metal alginate complex of LPSCF33428, LNSCF33428 and NSCF6428 (c) Pore size distribution of the optimum calcined temperature of LPSCF33428, LNSCF33428 and NSCF6428 nanopowder (d) volume fraction of pores (%) of the optimum calcined temperature of LPSCF33428, LNSCF33428 and NSCF6428 nanopowder

The 2D projection images as shown in Figures 6.31-6.33 reveal the significant differences between the homogeneity of the grain sizes before and after calcination for the three rare earth doped samples. As with the LSCF6428, rare earth doped metal alginate complexes exhibit different grain sizes with facet features, but with (black) pores within these grains and some contrasting inhomogeneity as shown from the white patches. However, the inhomogeneity is more pronounced with the LNSCF33428 and the NSCF6428, consistent with the EDX imaging in Figures 6.27 and 6.29 respectively.

The Micro-CT images can also distinguish the difference between the alginate and metal cations for the dried metal-alginate complex, depending upon atomic mass. The white indicates the presence of excess of the metal cation sodium in relation to the measured composition shown in Table 6.16-6.18, while the grey indicates the homogeneity of the organic material coming from the mixture of metal cations in the grain (Figure 6.31a-b, 6.32a-b, 6.33a-b). This is largely consistent with what was seen with the SEM imaging and Micro-CT imaging for the LSCF6428 in Chapter 4 Sections 4.5 and 4.6 respectively. For the calcination, as with the LSCF6428 in Chapter 4 Section 4.6, the effect of thermal decomposition degrades the alginate structure of the rare earth doped material. Although, the degree of homogeneity and agglomeration for the LPSCF33428, LNSCF33428 and NSCF6428 varies significantly as shown in Figures 6.31c-d, 6.33c-d 6.33d 6.34c-d respectively.

It can be seen, when comparing the Micro-CT images with pore size distribution, that there is a broader pore size distribution in the dried metal alginate due to similar reasons for the that occurred for the rare earth doped LSCF based on the sodium alginate sol gel methodology used for the LSCF6428 as stated in Chapter 4 Section 4.6 (Figure 6.34a and b). Although, when comparing the three rare earth doped samples, the LNSCF33428 pore size distribution of 3-10 microns has a frequency 10% higher from across the 20 grains examined compared to the LPSCF33428 and NSCF6428 as shown in Figure 6.34c. While for the calcined nanopowder, there is a narrower pore size distribution range with the % of the 5-10 micron range being doubled compared to the dried nanopowders, which suggests the formation of homogenous pores occurs in the microstructure itself (Figure 6.34 c and d).

6.7. Porous Characterisation of the optimum calcined temperature of LPSCF33428, LNSCF33428 and NSCF6428 nanopowder using SEM method

a.)

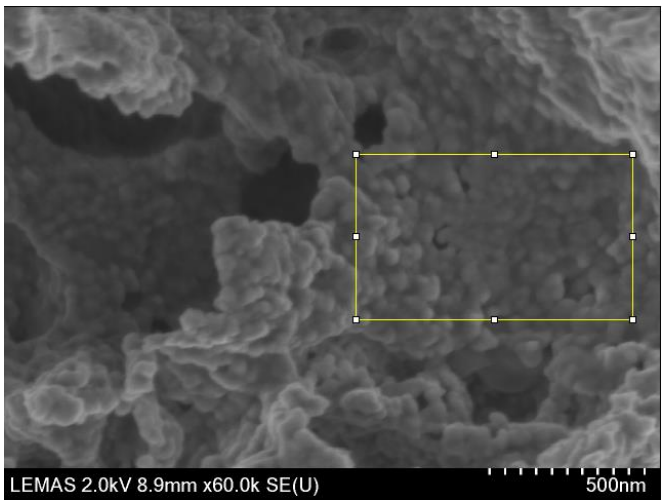

b.)

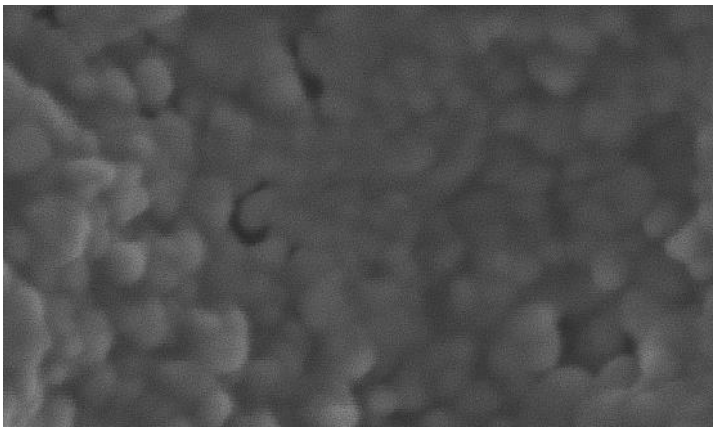

c.)

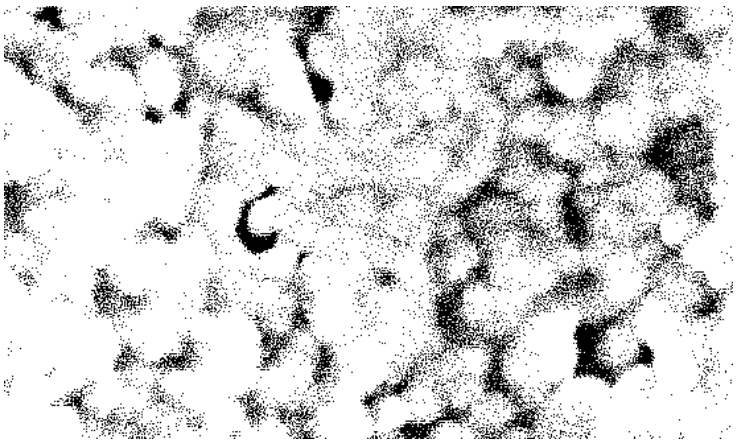

d.)

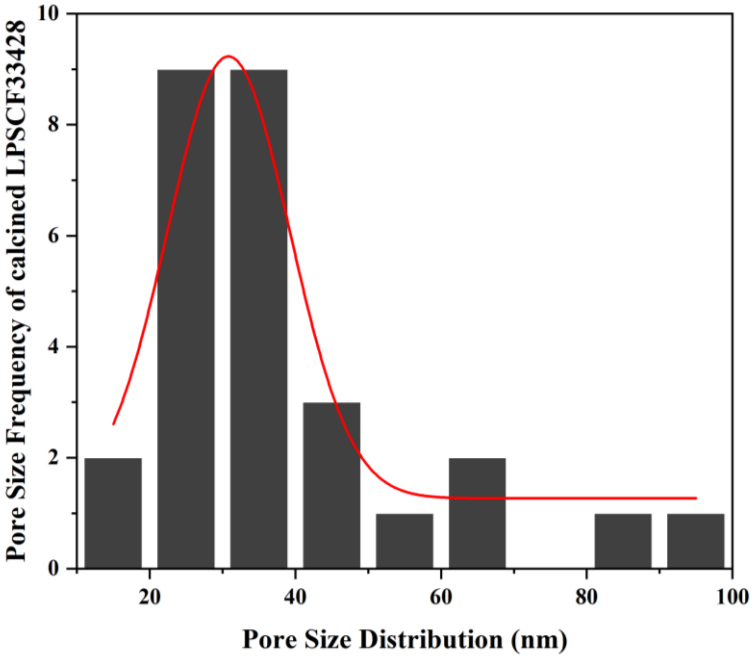

Figure 6.35:(a.) Secondary electron SEM image of LPSCF33428 calcined at 800ºC (b.) secondary electron image of an area used for pore size measurement (inset) (c.) Thresholded image of the selected area where black is taken to be the pore structure (d.) SEM pore size distribution of the 800 ºC calcined nanopowder of LPSCF33428

a.)

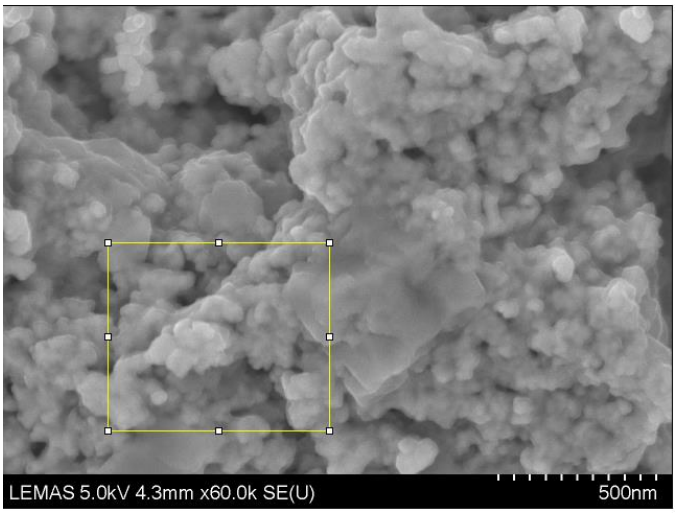

b.)

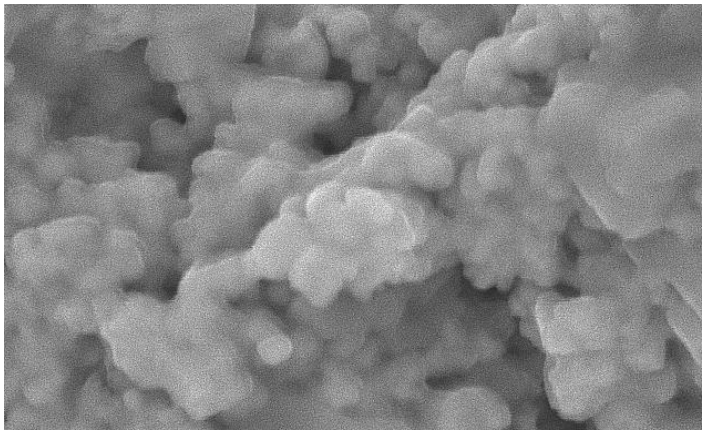

c.)

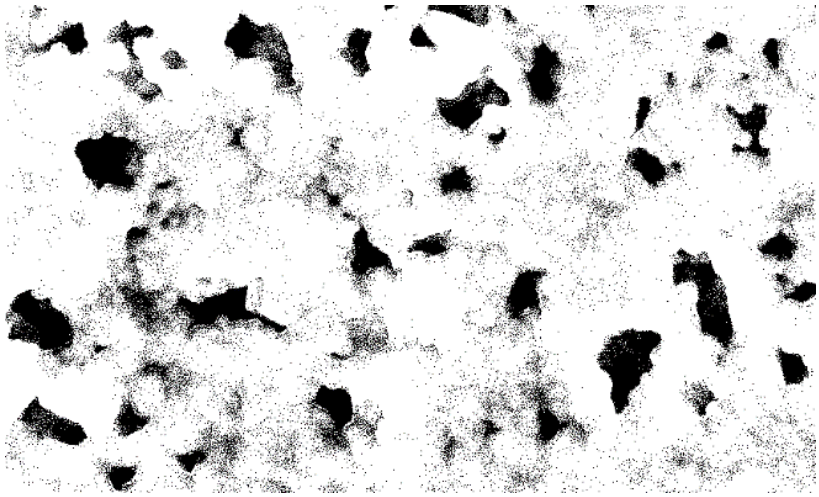

d.)

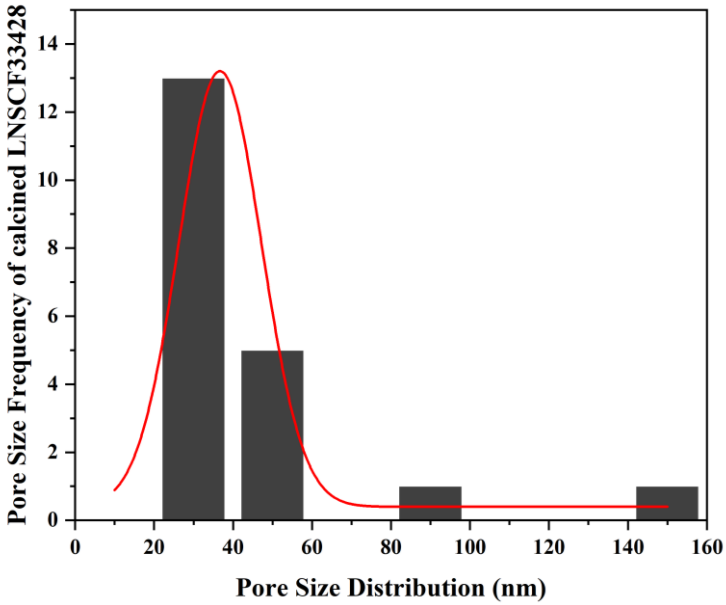

Figure 6.36:(a.) Secondary electron SEM image of LNSCF33428 calcined at 800ºC (b.) secondary image of the area used for pore size measurement (c.) Thresholded image of the selected area where black is taken to be the pore structure (d.) SEM pore size distribution of the 800 ºC calcined nanopowder of LNSCF33428.

a.)

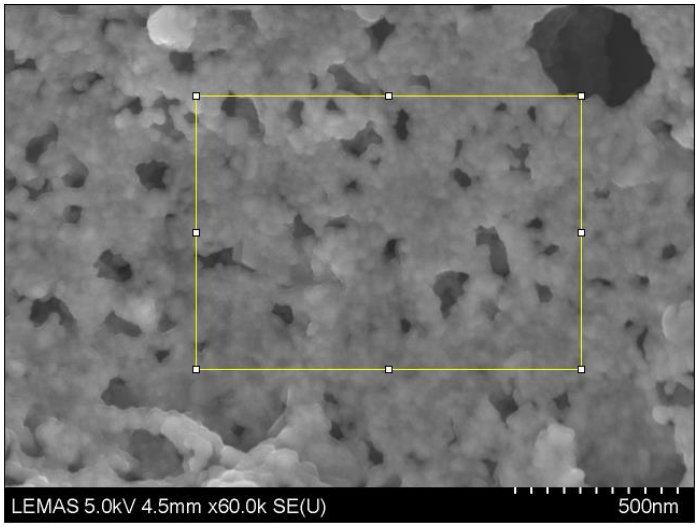

b.)

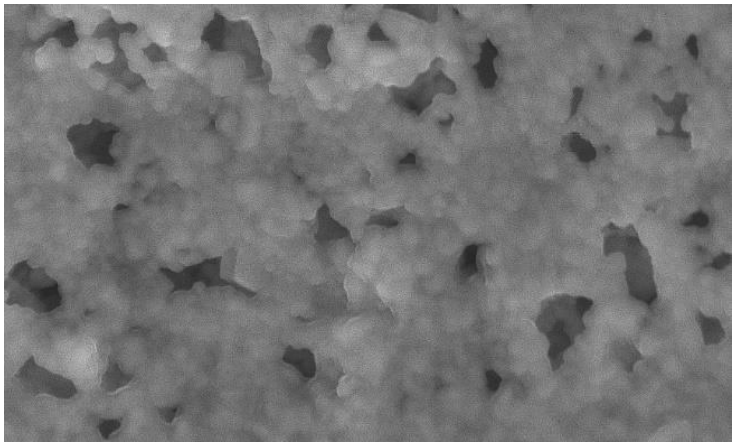

c.)

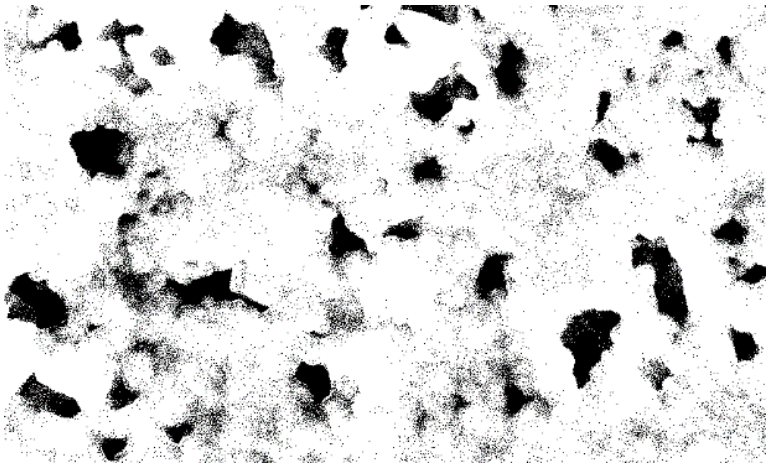

d.)

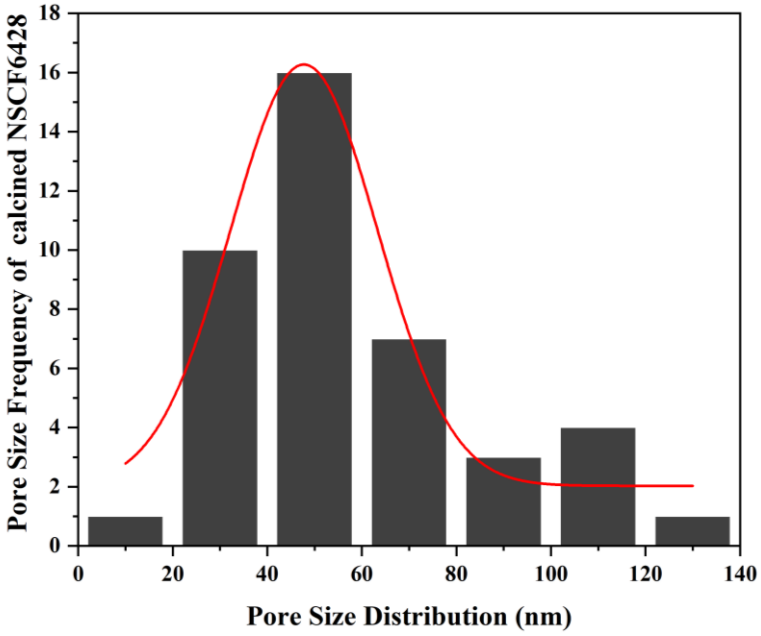

Figure 6.37:(a.) Secondary electron SEM image of NSCF6428 calcined at 775ºC (b.) secondary electron image of the area used for pore size measurement (c.) Thresholded image of selected area where black is taken to be the pore structure (d.) SEM pore size distribution of the 775 ºC calcined nanopowder of NSCF6428.

The calcined powders were examined using high magnification SEM imaging as shown in Figures 6.35-6.37a. The primary particle or grain size of the nanopowders is small and is consistent with the crystallite size of ~ 24 nm determined by XRD as shown in Figure 6.23. The primary particles/grains are clearly agglomerated with pores around them. To obtain a realistic measurement of porosity, an image contrast threshold was applied to an upper estimate to distinguish between the organic material (mid grey features) and pores (black features) as shown in Figures 6.35-6.37c. Figures 6.35-6.37d, show that the pore size distribution of the calcined three samples is concentrated within the range of 20 – 80 nm and analysis gives average pore sizes of 30, 38 and 47 nm for LPSCF33428, LNSCF33428 and NSCF6428. However, due to the lack of in-depth studies for SEM pore size distribution, and with the hygroscopic nature of the lanthanides, it is possible that there was a reaction from the effect in the retention of moisture from the atmosphere which led to the small increase in sizes across the series.[212]

6.8. Porous Characterisation of the optimum calcined temperature of LPSCF33428, LNSCF33428 and NSCF6428 nanopowder using BET method

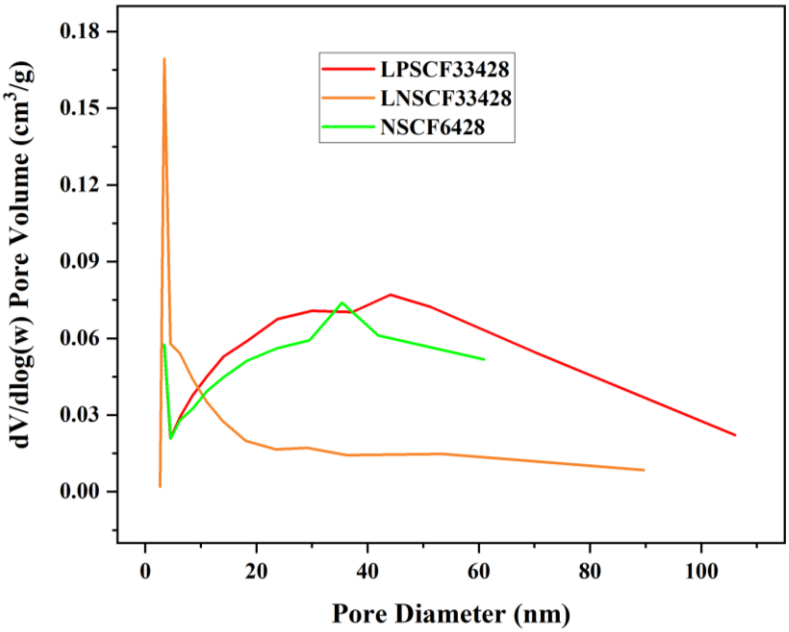

Figure 6.38: Pore size distribution of the dried metal – alginate complexes of LPSCF33428, LNSCF33428 and NSCF6428 using the BET method.

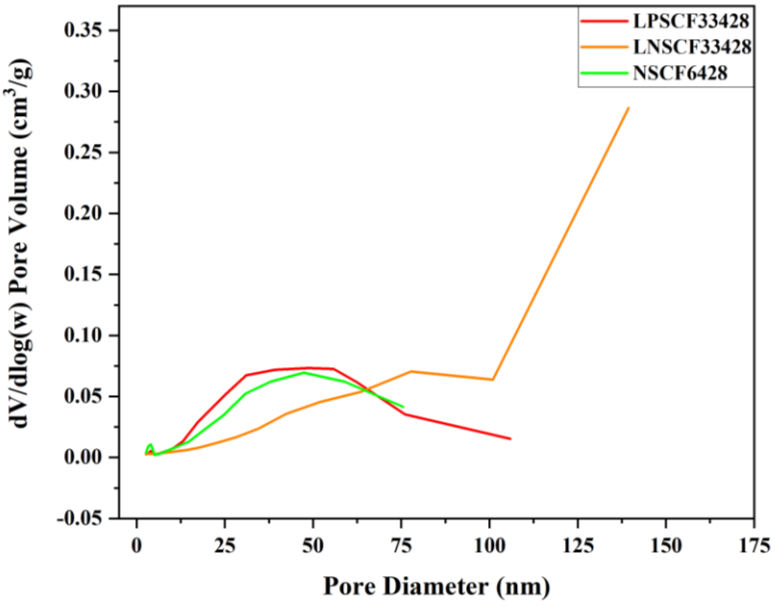

Figure 6.39: Pore size distribution of the optimum temperature calcined nanopowders of LPSCF33428, LNSCF33428 and NSCF6428 using the BET method.

Table 6.19: The single perovskite oxide of the dried metal alginate complex of LSCF6428 and optimum temperature calcined nanopowders of LPSCF33428, LNSCF33428 and NSCF6428.

Samples	Total Pore Volume (dried) (cm^3/g)	Total Pore Volume (calcined) (cm^3/g)	Average Pore Size (dried)(nm)	Average Pore Size (calcined)(nm)
LPSCF33428	0.083	0.048	32.11	30.28
LNSCF33428	0.061	0.048	12.68	38.92
NSCF6428	0.068	0.042	30.57	26.35

For the calcined LPSCF33428 and NSCF6428, the curve shows pore size distribution that ranges between 12.5 nm and 75 nm for the calcined material using the BET as shown in Figures 6.39 and 6.42 respectively. This finding is similar to that obtained by SEM from the ImageJ software analysis (Figure 6.35, 6.37). While for LNSCF33428 the pore sizes by SEM range between 25 nm to 100 nm (Figure 6.36). It can also be seen from Table 6.19, that the average pore size of each of the calcined materials is closer to the SEM values for the LPSCF33428 and LNSCF33428, but there is a difference of 21 nm between the SEM and BET values of NSCF6428. For the total pore volume across the three calcined samples, there is a slight decrease from the LNSCF33428 to NSCF6428. That could be due to the difference in methodology used between the SEM and BET, as the BET sample was degassed for removal of moisture prior to measuring while SEM was not.

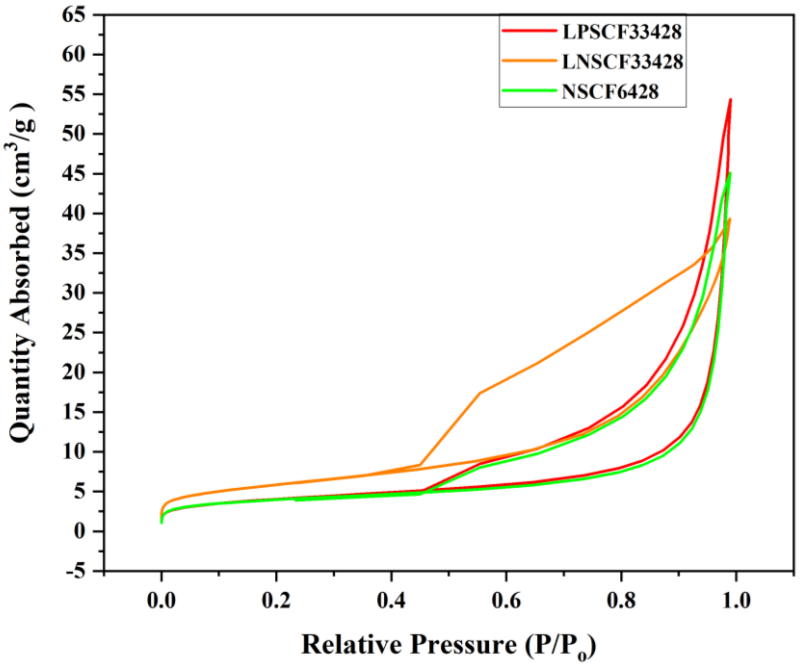

Figure 6.40: The BJH nitrogen adsorption and desorption isotherm of the dried metal–alginate complexes of LPSCF33428, LNSCF33428 and NSCF6428.

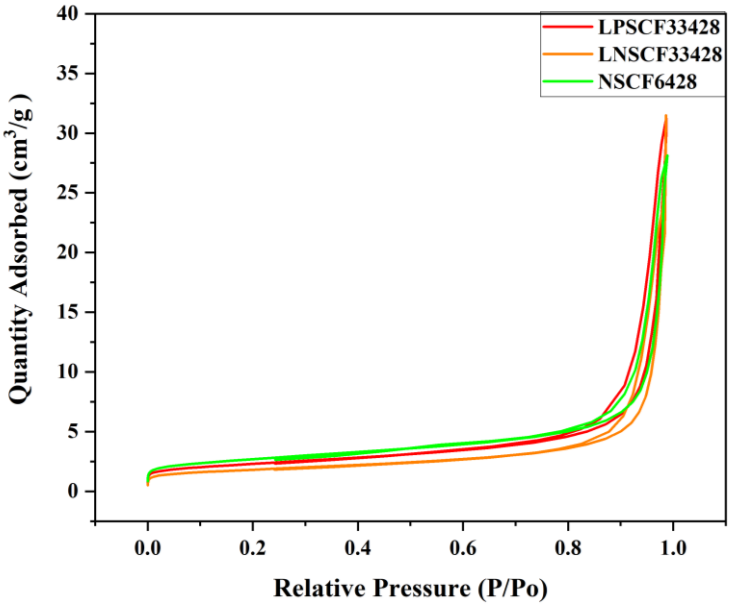

Figure 6.41: The BJH nitrogen adsorption and desorption isotherm of the optimum temperature calcined nanopowders of LPSCF33428, LNSCF33428 and NSCF6428.

To determine how the relationship between the pore size distribution and how the dopants behave when adsorbed gases are applied, nitrogen adsorption isotherm curves of the rare earth doped LSCFs were measured using the BJH method as shown in Figures 6.40-6.41. The results obtained were used to determine the adsorption mechanism of the rare earth doped LSCFs. As can be seen from the isotherms, for the dried samples there is a significance difference with the hysteresis loop of LNSCF33428 in comparison to the other two samples (Figure 6.40). The adsorption is not limited at the pressure range between the 0.45 to 1.0 (p/po). Nonetheless, based on the IUPAC definition, all the dried nanopowder isotherms are of Type V in relation to water absorption which typically occurs for mesoporous absorbents and in this case is consistent with the hygroscopic behaviours of the Pr and Nd dopants. The wider pore size distribution and the H3 shape of the hysteresis loop of the LNSCF33428 sample is consistent with the total pore volume trend in Table 6.19.[224] However, for the calcined rare earth doped samples, it can be seen that the adsorption is not limited at the higher-pressure range between 0.82 to 1.0 p/po as shown in Figure 6.42. Based on the IUPAC definition, the isotherms for these samples are of Type IV in relation to its mesoporous structure, its wider pore size distribution and shape of the hysteresis loop which all consist of a combination of Type H1 and H3 hysteresis loops.[199] i.e. once calcined and reacted the Pr and Nd are no longer as hygroscopic.

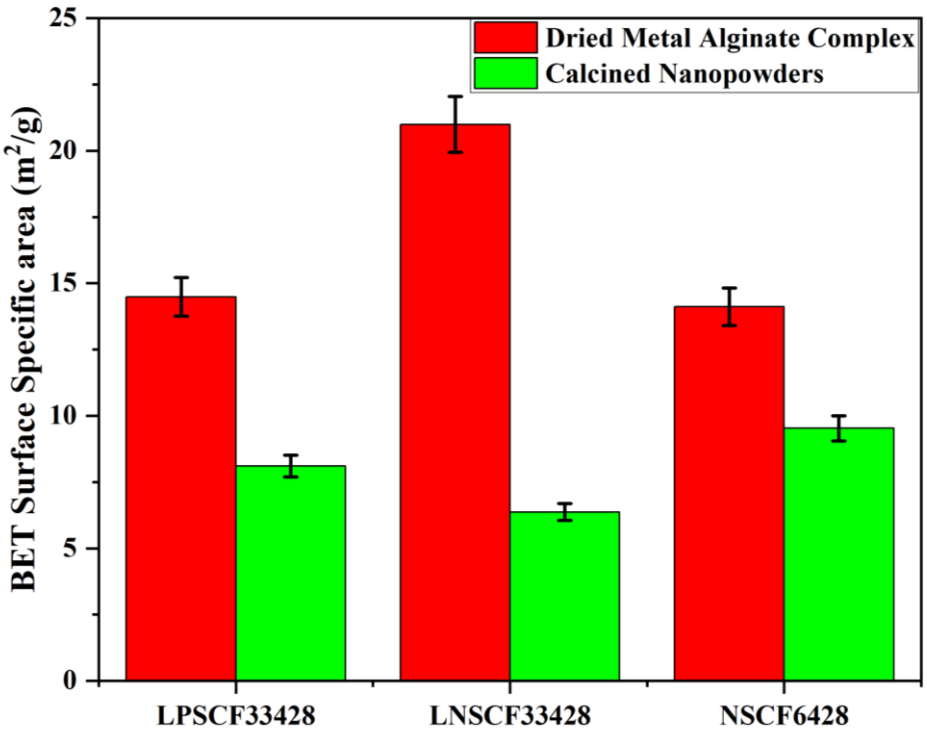

Figure 6.42: BET specific surface area investigated for the dried metal alginate complexes of LPSCF33428, LNSCF33428 and NSCF6428 (red bars) and for the optimum temperature calcined perovskite oxide nanopowders of LPSCF33428, LNSCF33428 and NSCF6428 (green bars) with error bars.

Table 6.20: BET surface area values of the dried and the optimum temperature calcined nanopowders of LPSCF33428, LNSCF33428 and NSCF6428.

Calcined rare earth doped LSCF nanopowders	**Dried BET specific surface area (m^2/g)**	**Calcined BET specific surface area (m^2/g)**
LPSCF33428	14.49 ± 0.451	8.11± 0.011
LNSCF33428	20.99 ± 0.511	6.53 ± 0.037
NSCF6428	14.11 ± 0.120	9.53± 0.067

The changes on going from dried to calcined nanopowder adsorption matches the trend in the decrease in BET surface area, which also matches other characterisation techniques such as XCT as shown in Figure 6.42 and Table 6.20. There is a significant reduction in the BET specific surface area value during the calcination process by more than ¾ to 6.53 m^2/g for LNSCF33428 and more than a ½ to 8.11 m^2/g and 9.53 m^2/g for LPSCF33428 and NSCF6428 respectively. This is due to an increase in powder agglomeration (SEM and XCT images) for LPSCF33428 and LNSCF33428 but for NSCF6428 there were separate grains rather than

agglomeration as shown in Figure 6.34b, which led to the highest surface area of the three calcined samples (of greater than 5 – 7 m^2/g). The value obtained for the calcinated NSCF6428 specific surface area is much higher compared to the transition metal doped LSCF where Cu and Ni were added to obtained surface areas of 4.17 m^2/g and 7.51 m^2/g respectively, where the synthesis method chosen on both occasions was sol gel.[221][226] The recommended minimum value of the specific surface area recommended for IT-SOFCs cathodes has ranged typically between 5-7 m^2/g to ensure good practical application so all three samples meet the criteria for the sintering procedure.

Summary – Chapter 6

The 3 wt% alginate sol-gels of the rare earth doped LSCFs; LPSCF33428, LNSCF33428 and NSCF6428 were successfully produced and calcined to yield single-phase, rhombohedral nanopowders comparable to the calcined LSCF6428 described in Chapter 4. The rare earth doped LSCF structures had similar 30-50 nm crystallite and grain sizes by XRD and SEM respectively while a small degree of compositional inhomogeneity was evident by SEM-EDX. The calcined rare earth doped LSCF pore sizes and specific surface areas were marginally lower and higher respectively compared to the LSCF6428 pore size of 40 nm and specific surface area of 5.48 m^2/g respectively.

Chapter 7 – Structural and Porosity of sintered $La_{0.3}Pr_{0.3}Sr_{0.4}Co_{0.2}Fe_{0.8}O_{3-\delta}$, $La_{0.3}Nd0_{.3}Sr_{0.4}Co_{0.2}Fe_{0.8}O_{3-\delta}$ and $Nd_{0.6}Sr_{0.4}Co_{0.2}Fe_{0.8}O_{3-\delta}$

7.1. Structural Characterisation of sintered $La_{0.3}Pr_{0.3}Sr_{0.4}Co_{0.2}Fe_{0.8}O_{3-\delta}$, $La_{0.3}Nd0_{.3}Sr_{0.4}Co_{0.2}Fe_{0.8}O_{3-\delta}$ and $Nd_{0.6}Sr_{0.4}Co_{0.2}Fe_{0.8}O_{3-\delta}$ pellets

The three rare earth doped lanthanum strontium cobalt ferrite (LSCF) nanopowders, LPSCF33428, LNSCF33428 and NSCF6428 selected for sintering were calcined at 800 ºC for LPSCF33428 and LNSCF33428 and at 775 ºC for the NSCF6428 based on the single phase, rhombohedral and perovskite phase purity by powder XRD patterns and analysis (Section 5.1). As stated in Section 5.1 (and Chapter 3, the methodology), the three nanopowders underwent uniaxial pressing (at 2 tons) to form pellets and were sintered at three different temperatures for 1 hour. The temperature range selected was between 900 ºC and 1100 ºC inclusive, as undertaken in Chapter 5 for the LSCF6428, to assess how the rare earth dopants, Pr and Nd influence the sintering behaviour in comparison to the undoped LSCF6428. [200] Given there has been limited information from a study by Kursan et al., where Nd-A-CO_3 (A= Sr, Ca), where A is the divalent alkaline earth elements was synthesised using ball milling and sintered at 1000 ºC and examined through SEM to determine how the A dopant influences the microstructural properties such as porosity. [227]

It can be seen from the profile fittings of the three sintered, rare earth doped samples from Figures 7.1, 7.5 and 7.10 that XRD diffraction reveals peak splitting of the sintered LPSCF33428, LNSCF33428 and NSCF6428 experimental powder XRD patterns which were absent from the calcined patterns in Section 6.3. To examine the effects of sintering in relation to its potential crystal structure formation of each crushed sintered sample, XRD diffraction patterns were indexed to rhombohedral and orthorhombic (LNSCF33428 and NSCF6428 only) crystal symmetry using the ICDD based reference for the perovskite crystal phase and peak fitting was used to fit the peak diffraction data as shown in Figures 7.2-7.4, 7.6-7.9 and 7.11-7.14. In earlier studies, sintered rare earth-based perovskite oxides such as $Pr_{1-x}Sr_xCoO_{3-\delta}$, $LnCoO_3$ (Ln = La, Pr, Tb) and Nd doped $LaCoO_3$ have been examined using reference files to confirm (the assumed) crystal symmetry of the diffraction pattern peaks.[228-230] As in Section 5.1 for the sintered LSCF6428 and Section 6.3 for the calcined rare earth doped LSCF, peak splitting of diffraction peaks at 68º and 78º 2θ is the focus of the analysis as these give a clear indication of the transition towards a lower symmetry structure, occurring at temperatures above 1000 ºC, as also reported by others [186-187]. Diffraction peak splitting is present in

other rare earth-based perovskites oxides where studies have examined similar transitions to either rhombohedral or commonly orthorhombic crystal symmetries.[75][228-233]

To examine the effects of sintering, whole pattern fitting of the XRD diffraction patterns was undertaken as described in the methodology by indexing the rhombohedral and orthorhombic reference patterns, except for LPSCF33428 where only the rhombohedral symmetry was indexed. From Figures 7.2-7.4,7.6-7.9 and 7.11 – 7.14 there seems to be a reasonable fitting of the reference diffraction pattern to the experimental however the rhombohedral structure always provides a better overall fit.

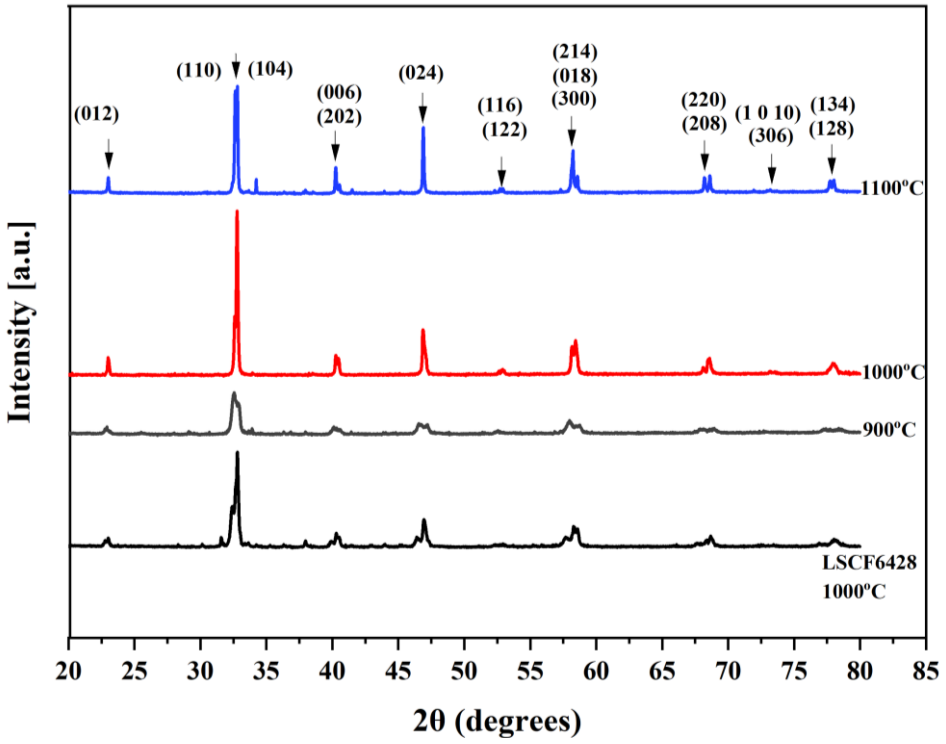

Figure 7.1: XRD patterns of 3 wt% LPSCF33428 crushed pellet sintered for 1 h at temperatures of 900 °C (grey line), 1000 °C (red line), 1100 °C (blue line) and LSCF6428 sintered at 1000 °C obtained from Section 5.1, Figure 5.1 (black line)

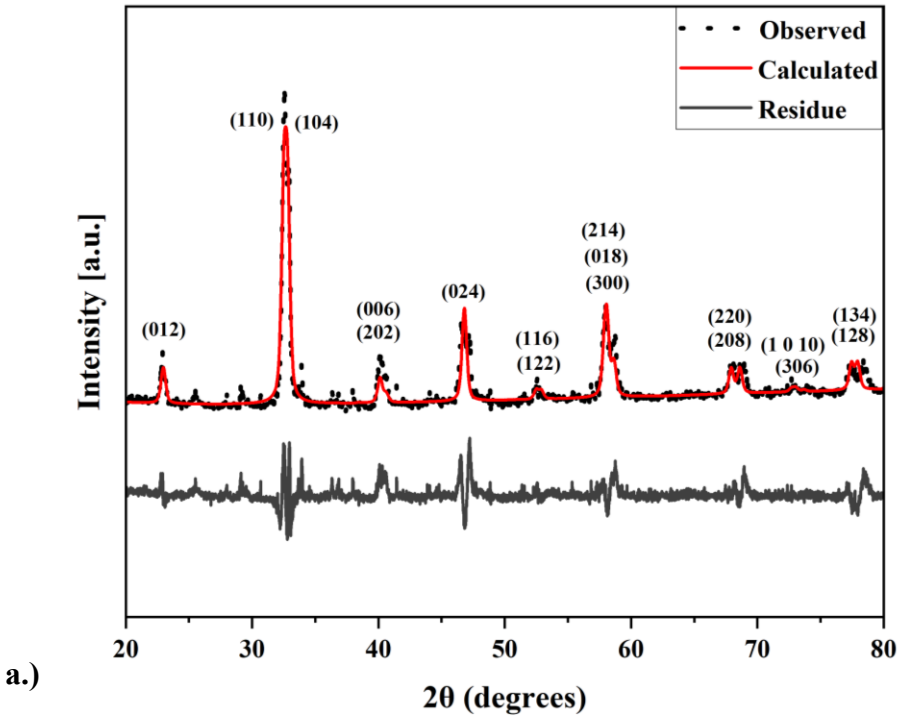

a.)

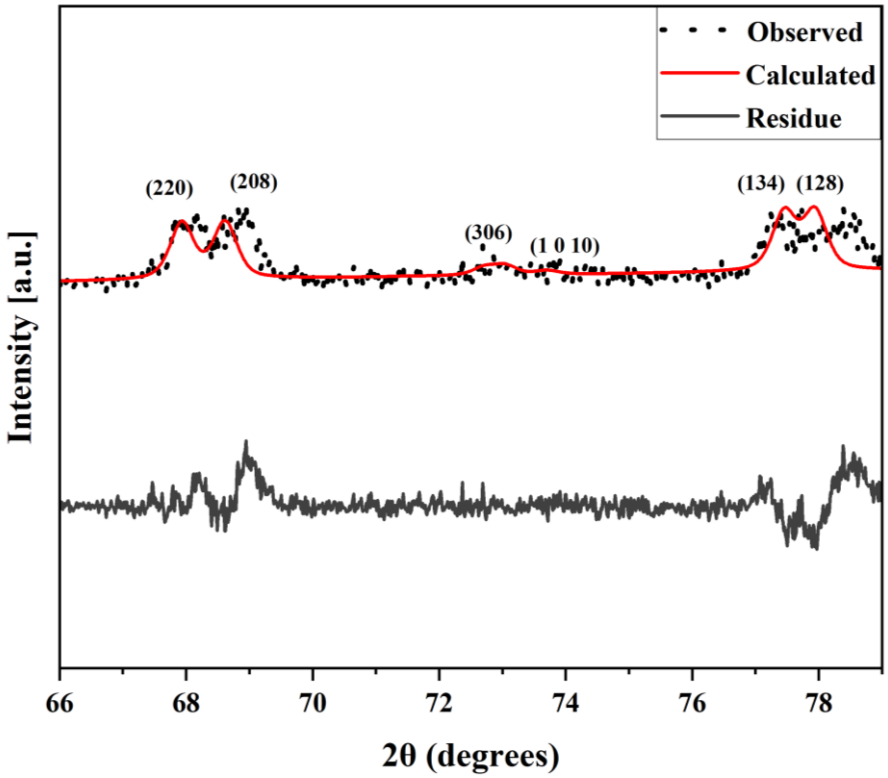

b.)

Figure 7.2: **a)** Whole pattern fitting of the rhombohedral (R3c) structure of a crushed LPSCF33428 pellets sintered at 900 ºC with experimental data (black line), reference file fit (red line), residue (grey line) shown and peaks are indexed using ICDD 04-017-2448. **b)** Zoom in of the fitting of the rhombohedral (R3c) structure of the 900 ºC crushed LPSCF33428 pellet, indicating potential peak splitting at the (220)/(208), (306)/(1 0 10) and (134)/(128) peaks 68º, 72º and 78º 2θ respectively.

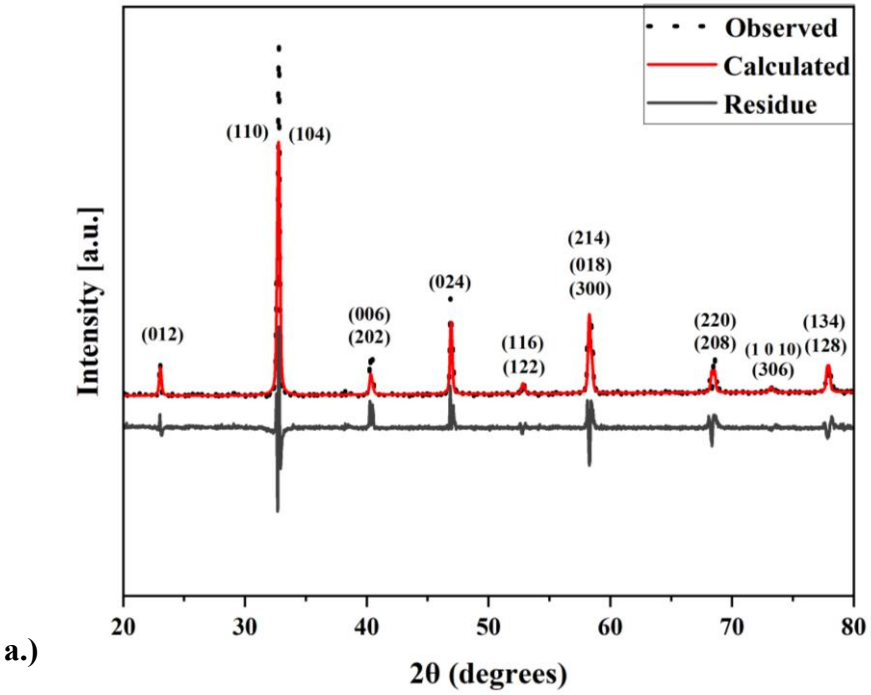

a.)

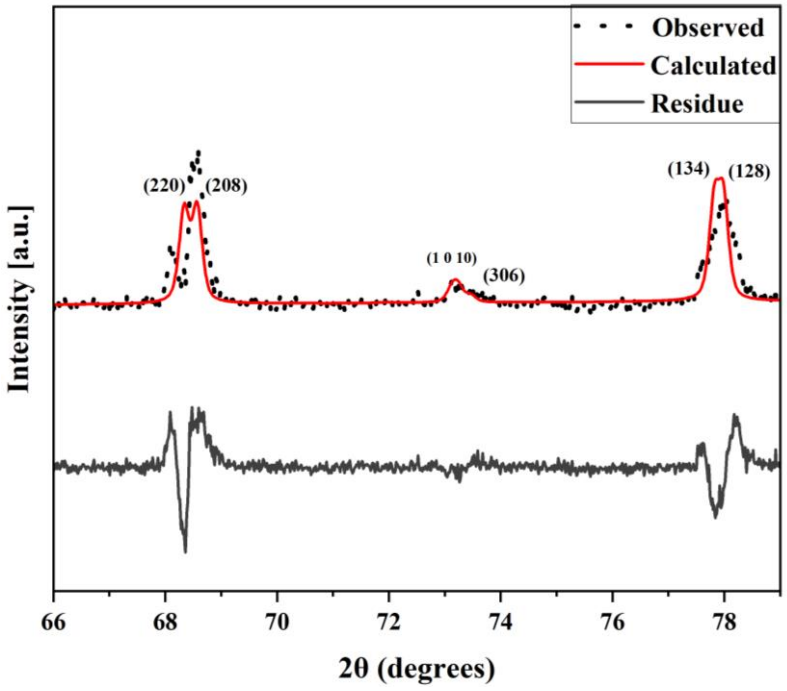

b.)

Figure 7.3: **a)** Whole pattern fitting of the rhombohedral (R3c) structure of a crushed LPSCF33428 pellet sintered at 1000 °C with experimental data (black line), reference file fit (red line), residue (grey line) shown and peaks are indexed using ICDD 04-017-2448. **b)** Zoom in of the fitting of the rhombohedral (R3c) structure of the 1000 °C crushed LPSCF33428 pellet, indicating potential peak splitting at the (220)/(208), (306)/(1 0 10) and (134)/(128) peaks 68°, 72° and 78° 2θ respectively.

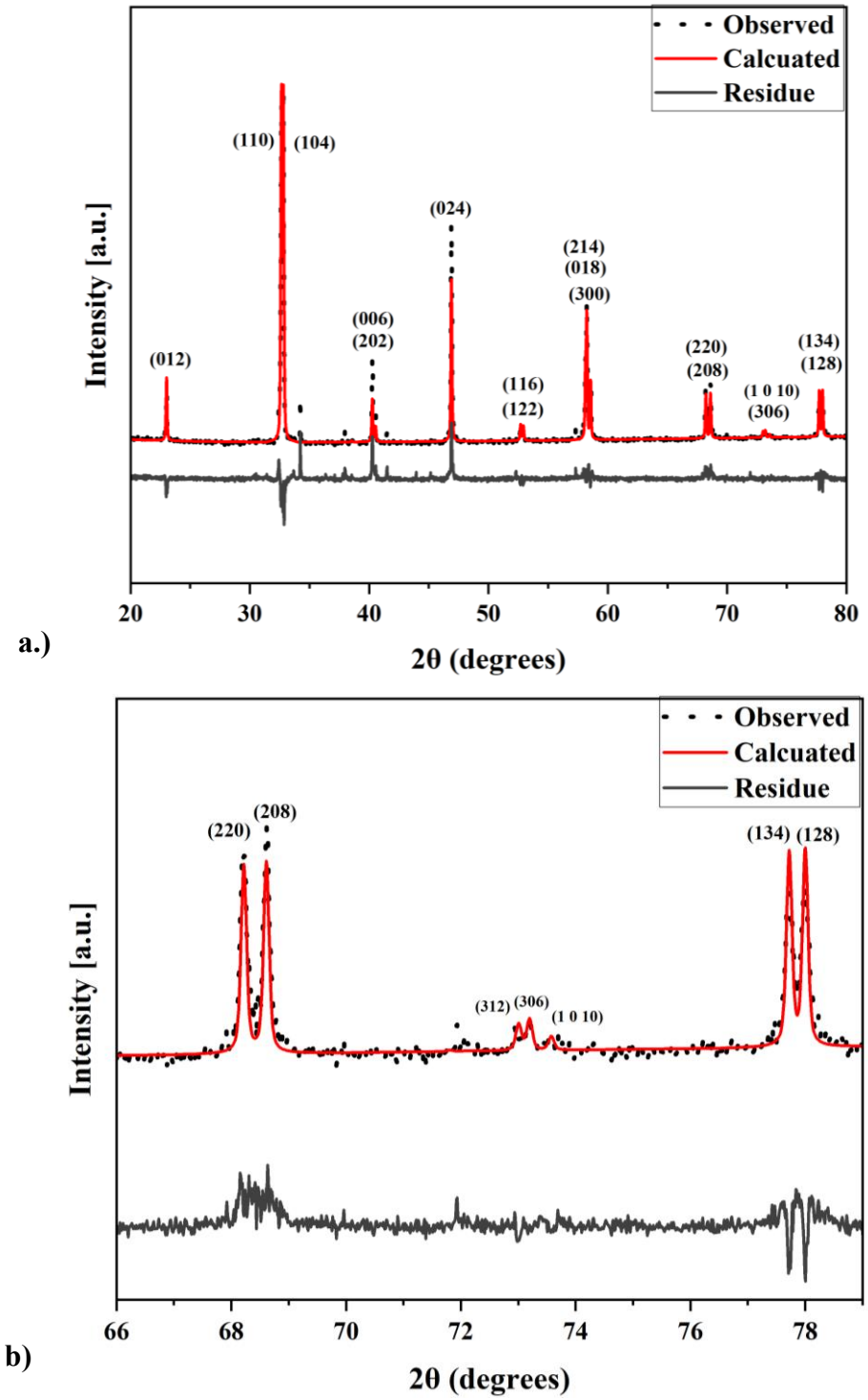

Figure 7.4: **a)** Whole pattern fitting of the rhombohedral (R3c) structure of a crushed LPSCF33428 pellet sintered at 1100 ºC with experimental data (black line), reference file fit (red line), residue (grey line) shown and peaks are indexed using ICDD 04-017-2448. **b)** Zoom in of the fitting of the rhombohedral (R3c) structure of the 1100 ºC crushed LPSCF33428 pellet, indicating potential peak splitting at the (220)/(208), (306)/(1 0 10) and (134)/(128) peaks 68º, 72º and 78º 2θ respectively.

Table 7.1: Whole pattern fitting of structural parameters, fit quality and micro strain of the rhombohedral (R3c) LPSCF33428 sintered at 900, 1000 and 1100 ºC (R_{wp}(%)) weighted pattern, (R_{exp}(%)) expected pattern and goodness of fit (GOF)

Temperature (ºC)	R_{exp} (%)	R_{wp} (%)	GOF	Micro Strain (%)
900	6.600	6.328	0.959	0.46
1000	6.744	6.696	0.993	0.18
1100	5.800	9.179	1.582	0.06

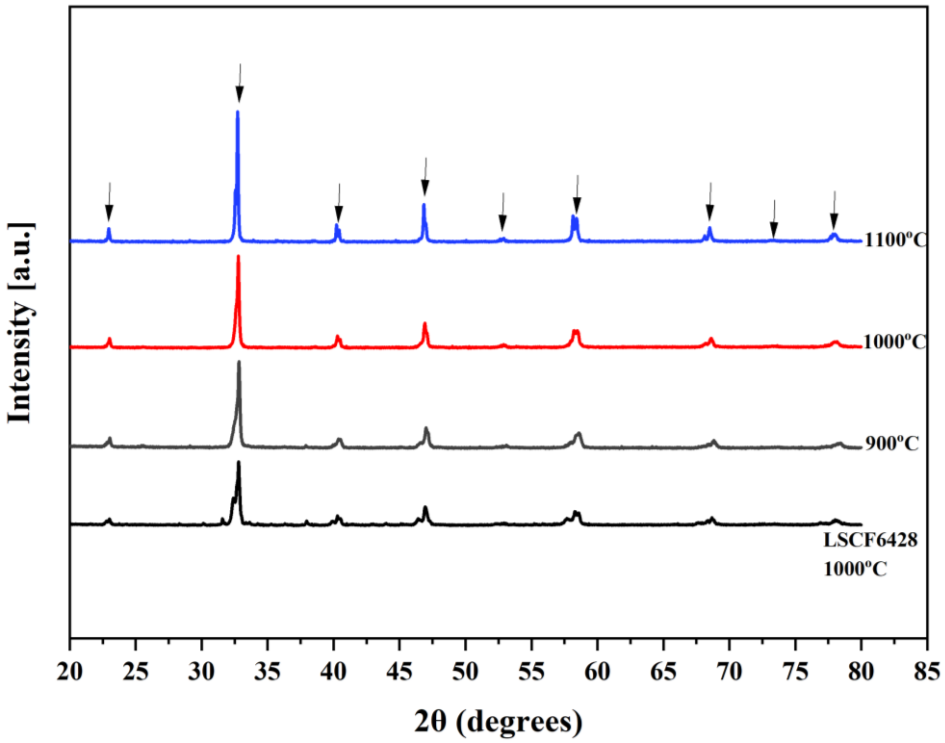

Figure 7.5: XRD patterns of 3 wt% LNSCF33428 crushed pellets sintered for 1 h at temperatures of 900 ºC (grey line), 1000 ºC (red line) and 1100 ºC (blue line) and LSCF6428 sintered at 1000 ºC obtained from Section 5.1, Figure 5.1 (black line)

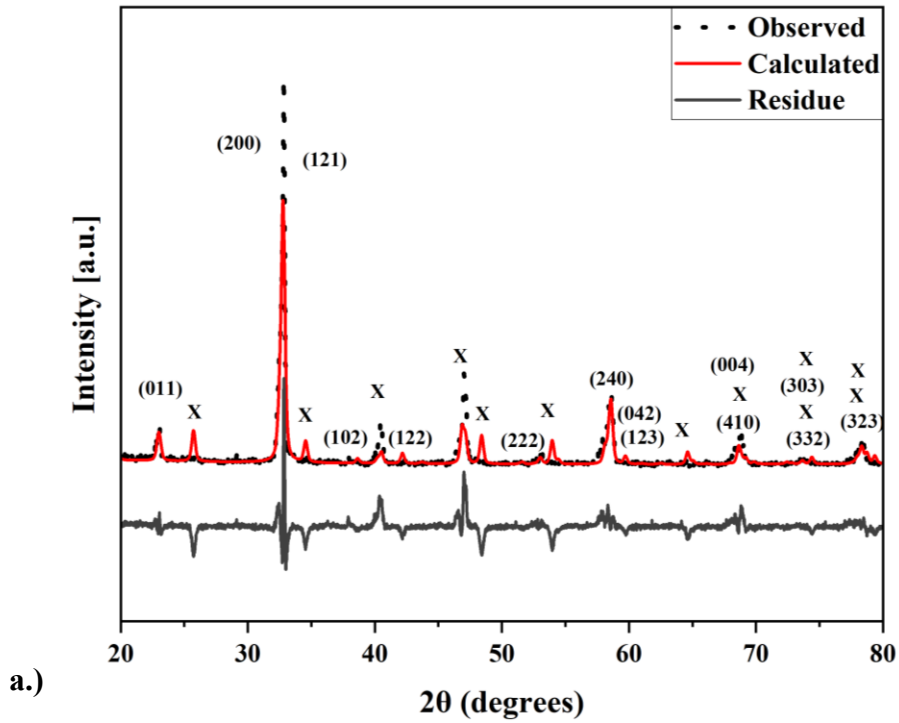

a.)

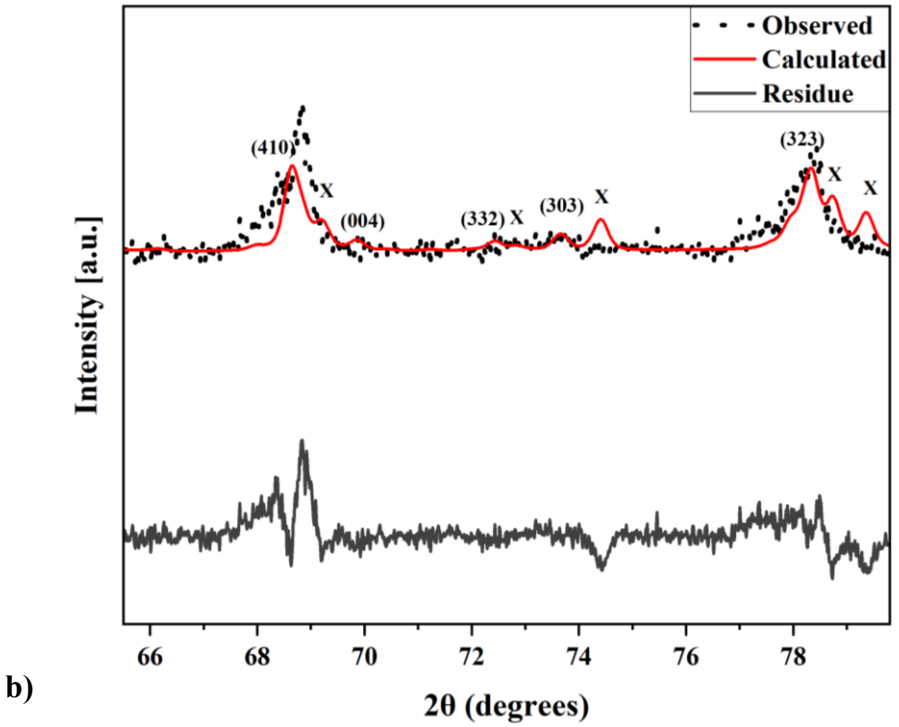

b)

Figure 7.6: **a)** Whole pattern fitting of the orthorhombic (O_h) structure of a crushed LNSCF33428 pellet sintered at 900 °C with experimental data (black line), reference file fit (red line), residue (grey line) shown and peaks are indexed using ICDD 04-026-4876 - O_h and X represents mismatched/missing peaks. **b)** Zoom in of the fitting of the orthorhombic (O_h) structure of 900 °C crushed LNSCF33428 pellet indicating peak splitting located between 66°-79° 2θ.

Table 7.2: Whole pattern fitting of structural parameters, fit quality and micro strain of the orthorhombic (O_h) LNSCF33428 sintered at 900, 1000 and 1100 ºC (R_{wp}(%)) weighted pattern, (R_{exp}(%)) expected pattern and goodness of fit (GOF)

Temperature (ºC) - Oh	**R_{exp} (%)**	**R_{wp} (%)**	**GOF**	**Micro Strain (%)**
900	5.033	8.532	1.693	0.32
1000	5.422	9.453	1.744	0.24
1100	5.307	11.418	2.151	0.15

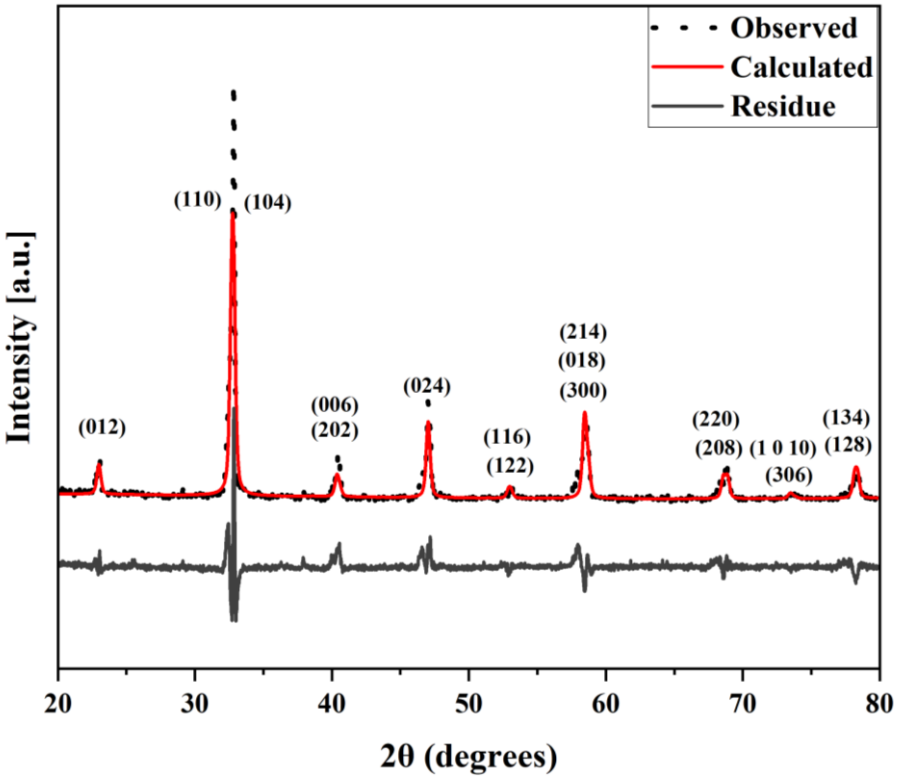

a.)

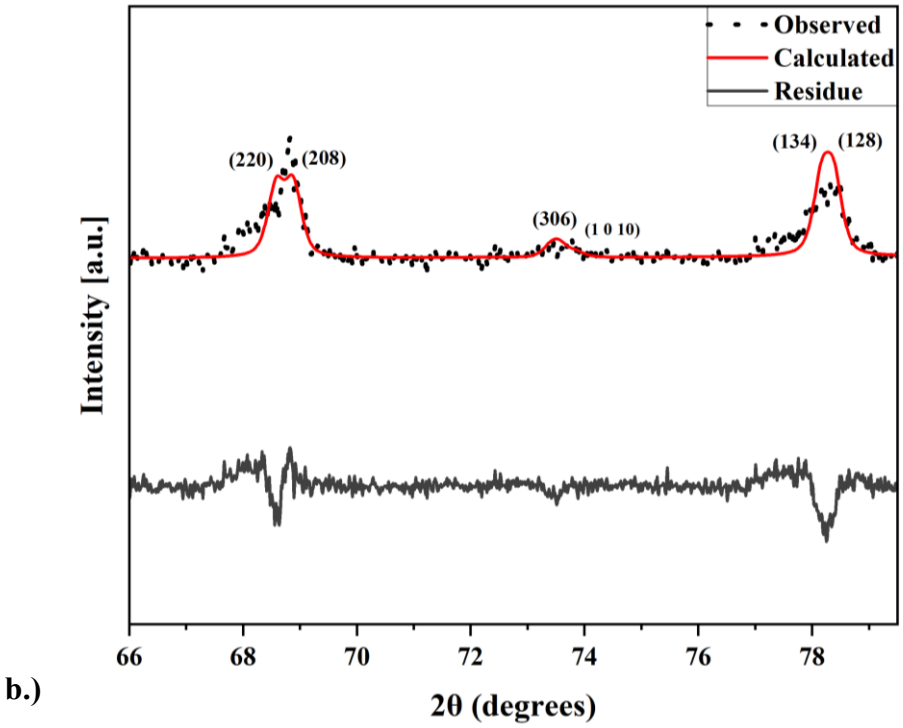

b.)

Figure 7.7: **a)** Whole pattern fitting of the rhombohedral (R3c) structure of a crushed LNSCF33428 pellet sintered at 900 ºC with experimental data (black line), reference file fit (red line), residue (grey line) shown and peaks are indexed using ICDD 04-017-2448. **b)** Zoom in of the fitting of the rhombohedral (R3c) structure of the 900 ºC crushed LNSCF33428 pellet, indicating potential peak splitting at the (220)/(208), (306)/(1 0 10) and (134)/(128) peaks 68º, 72º and 78º 2θ respectively.

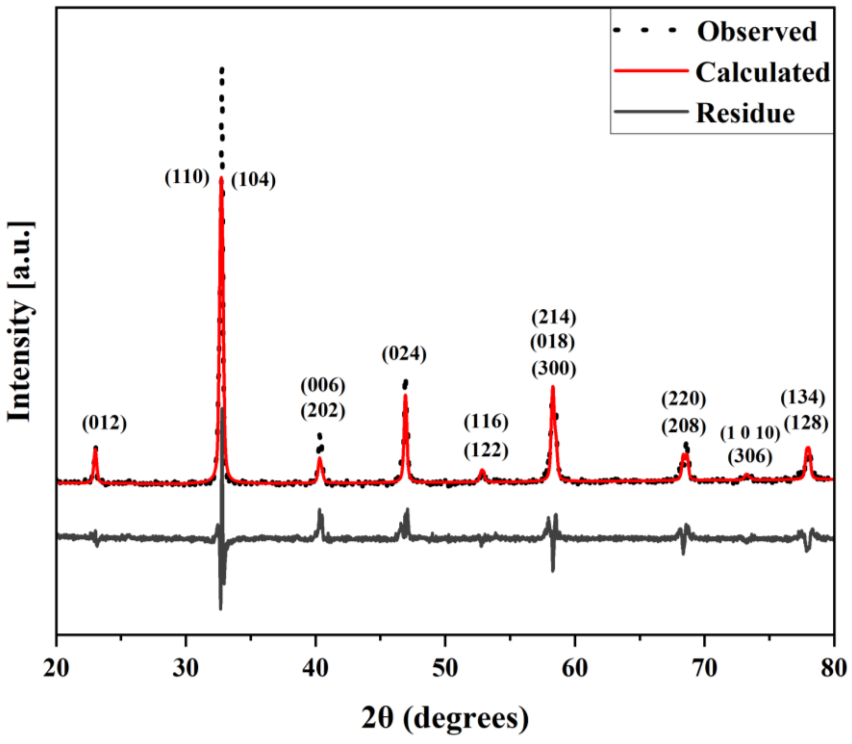

a.)

b.)

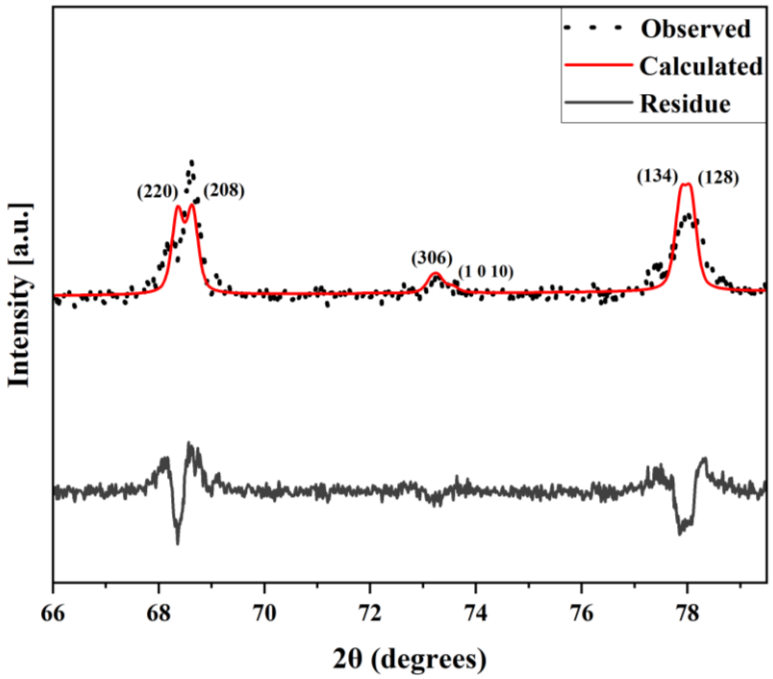

Figure 7.8: **a)** Whole pattern fitting of the rhombohedral (R3c) structure of a crushed LNSCF33428 pellet sintered at 1000 ºC with experimental data (black line), reference file fit (red line), residue (grey line) shown and peaks are indexed using ICDD 04-017-2448. **b)** Zoom in of the fitting of the rhombohedral (R3c) structure of the 1000 ºC crushed LNSCF33428 pellet, indicating potential peak splitting at the (220)/(208), (306)/(1 0 10) and (134)/(128) peaks 68º, 72º and 78º 2θ respectively.

a.)

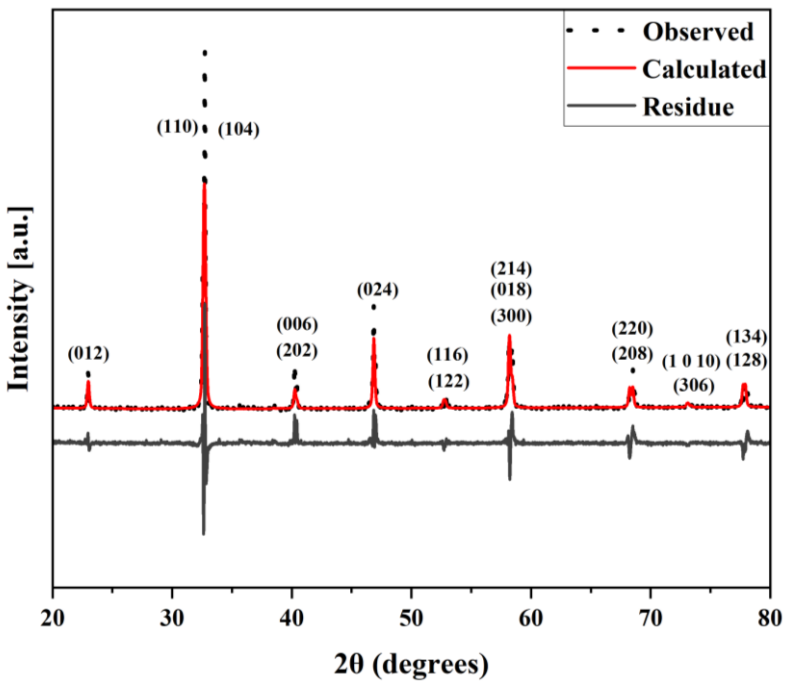

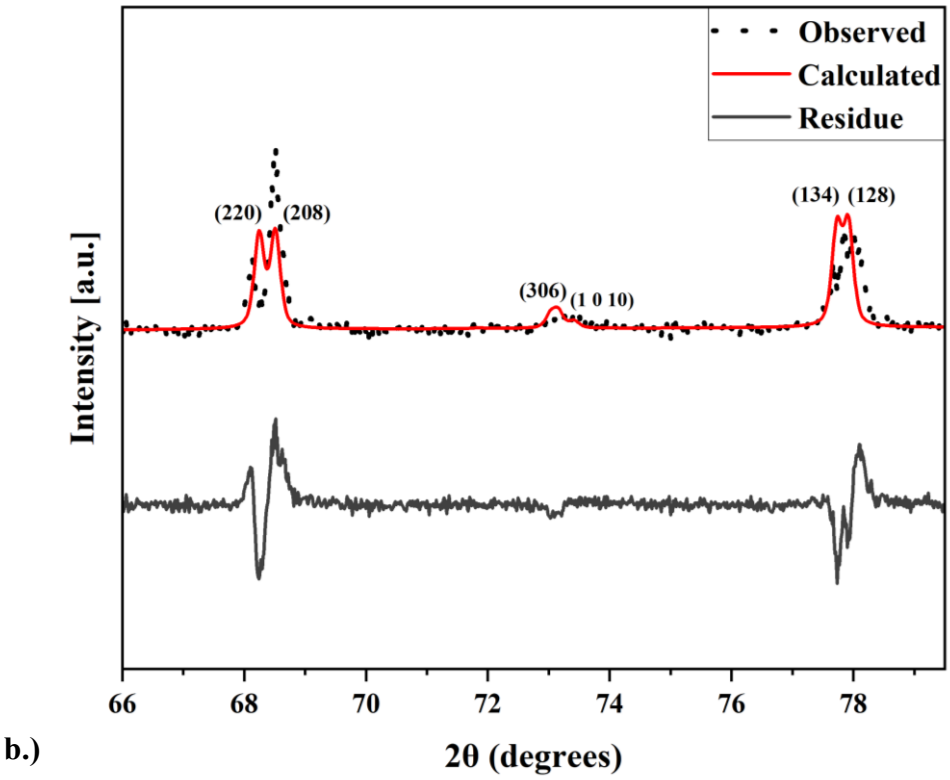

b.)

Figure 7.9: **a)** Whole pattern fitting of the rhombohedral structure of a crushed LNSCF33428 pellet sintered at 1100 ºC with experimental data (black line), reference file fit (red line), residue (grey line) shown and peaks are indexed using ICDD 04-017-2448. **b)** Zoom in of the fitting of the rhombohedral structure of the 1100 ºC crushed LNSCF33428 pellet, indicating potential peak splitting at the (220)/(208), (306)/(1 0 10) and (134)/(128) peaks 68º, 72º and 78º 2θ respectively.

Table 7.3: Whole pattern fitting of structural parameters, fit quality and micro strain of the rhombohedral (R3c) LNSCF33428 sintered at 900, 1000 and 1100 ºC (R_{wp}(%)) weighted pattern, (R_{exp} (%)) expected pattern and goodness of fit (GOF)

Temperature (ºC) – R3c	**R_{exp} (%)**	**R_{wp} (%)**	**GOF**	**Micro Strain (%)**
900	5.034	6.506	1.293	0.34
1000	5.422	6.198	1.142	0.24
1100	5.308	8.578	1.616	0.13

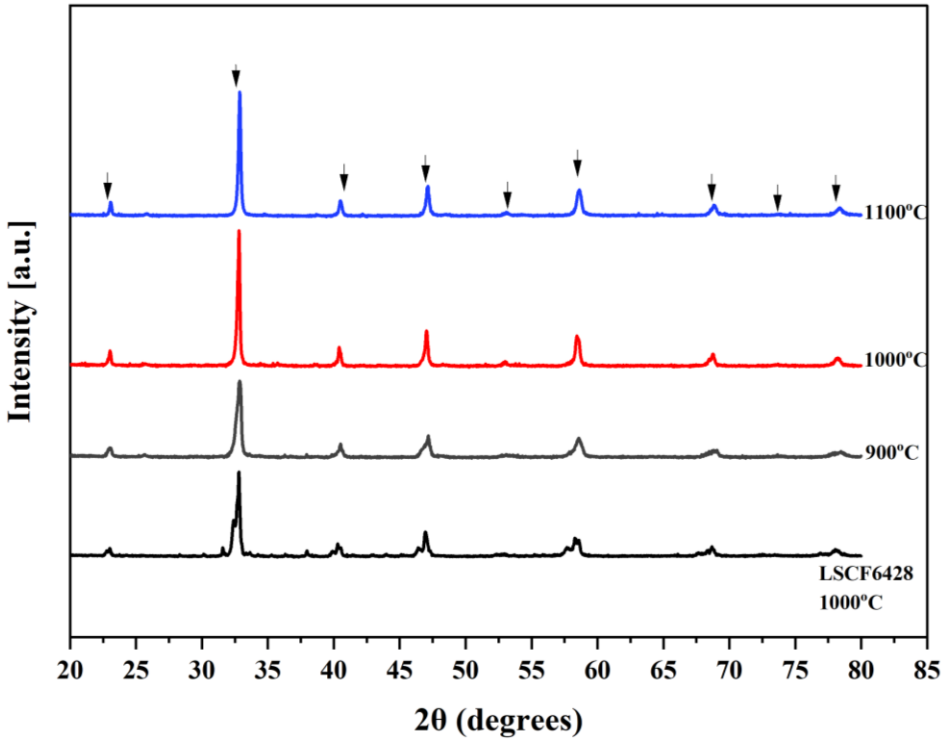

Figure 7.10: XRD patterns of 3 wt% NSCF6428 crushed pellets sintered for 1 h at temperatures of 900 °C (grey line), 1000 °C (red line), 1100 °C (blue line) and LSCF6428 sintered at 1000 °C obtained from Section 5.1, Figure 5.1 (black line)

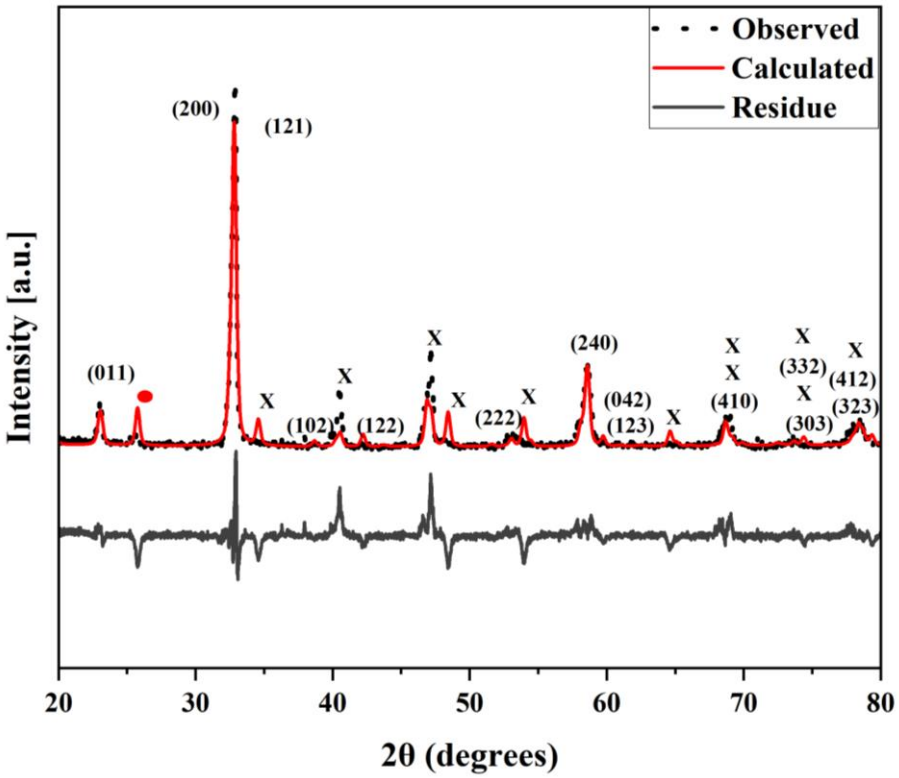

a.)

b.)

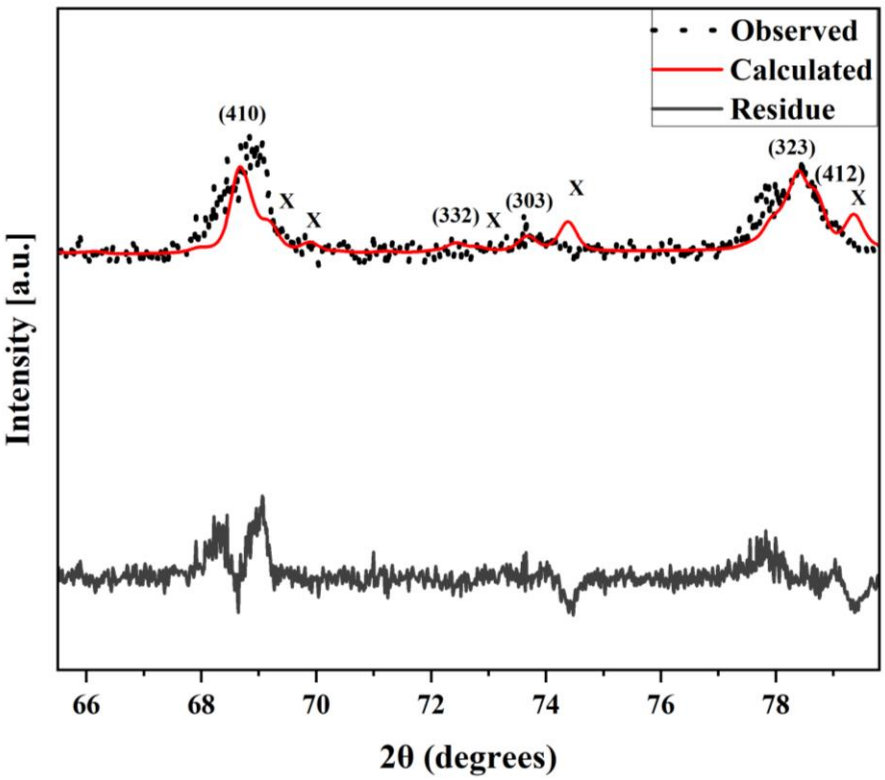

Figure 7.11: **a)** Whole pattern fitting of the orthorhombic (O_h) structure of a crushed NSCF6428 pellet sintered at 900 ºC with experimental data (black line), reference file fit (red line), residue (grey line) shown and peaks are indexed using ICDD 04-026-4876 and X represents mismatched/missing peaks. **b)** Zoom in of the fitting of the orthorhombic (O_h) structure of 900 ºC crushed NSCF6428 pellet indicating peak splitting located between 66º-79º 2θ.

Table 7.4: Whole pattern fitting of structural parameters, fit quality and micro strain of the orthorhombic (O_h) NSCF6428 sintered at 900, 1000 and 1100 ºC (R_{wp}(%)) weighted pattern, (R_{exp}(%)) expected pattern and goodness of fit (GOF)

Temperature (ºC) – O_h	**R_{exp} (%)**	**R_{wp} (%)**	**GOF**	**Micro Strain (%)**
900	5.109	6.551	1.305	0.36
1000	4.765	7.383	1.549	0.21
1100	5.298	7.692	1.452	0.21

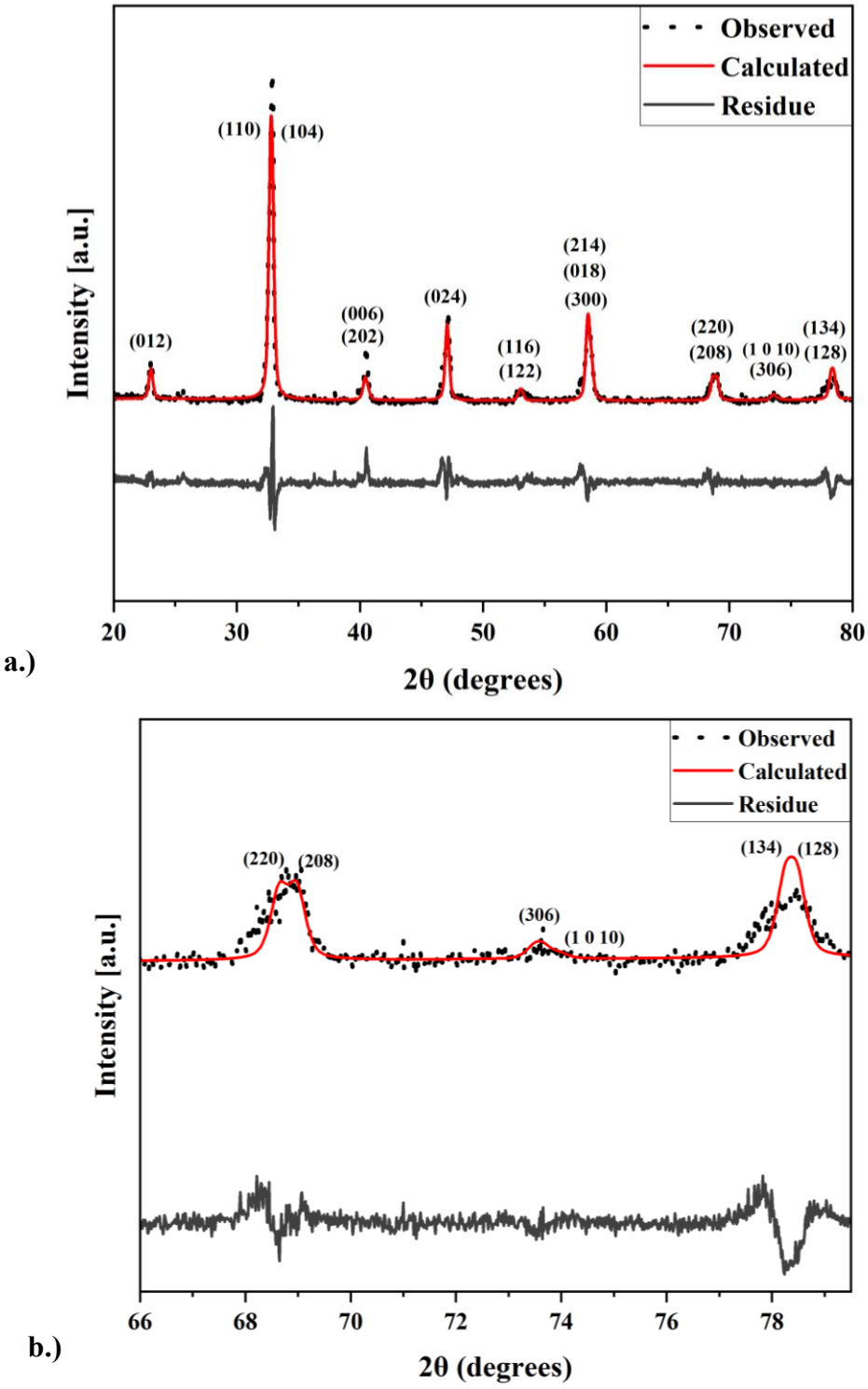

Figure 7.12: **a)** Whole pattern fitting of the rhombohedral (R3c) structure of a crushed NSCF6428 pellet sintered at 900 ºC with experimental data (black line), reference file fit (red line), residue (grey line) shown and peaks are indexed using ICDD 04-017-2448. **b)** Zoom in of the fitting of the rhombohedral (R3c) structure of the 900 ºC crushed NSCF6428 pellet, indicating potential peak splitting at the (220)/(208), (306)/(1 0 10) and (134)/(128) peaks 68º, 72º and 78º 2θ respectively.

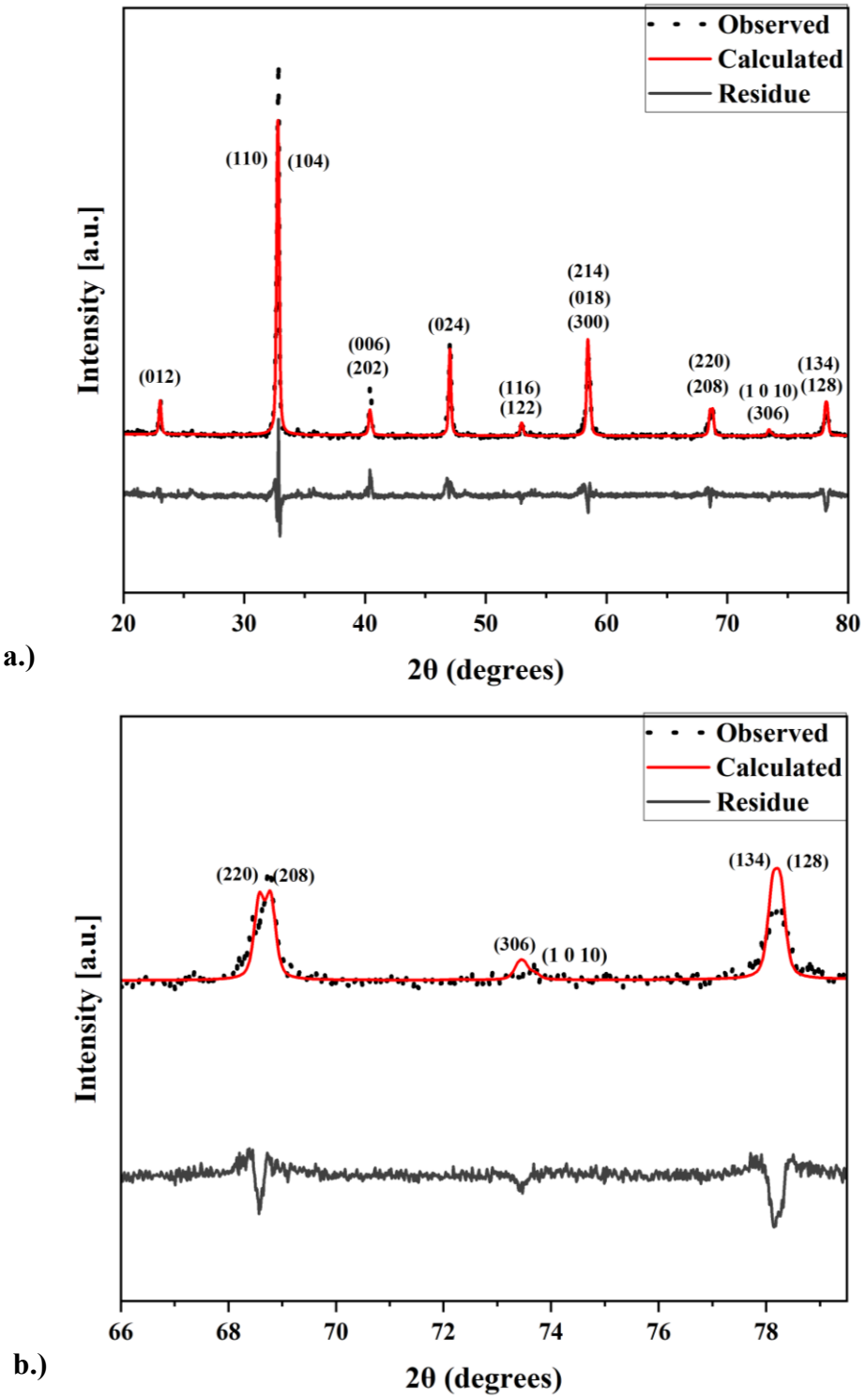

Figure 7.13: **a)** Whole pattern fitting of the rhombohedral (R3c) structure of a crushed NSCF6428 pellet sintered at 1000 ºC with experimental data (black line), reference file fit (red line), residue (grey line) shown and peaks are indexed using ICDD 04-017-2448. **b)** Zoom in of the fitting of the rhombohedral (R3c) structure of the 1000 ºC crushed NSCF6428 pellet, indicating potential peak splitting at the (220)/(208), (306)/(1 0 10) and (134)/(128) peaks 68º, 72º and 78º 2θ respectively.

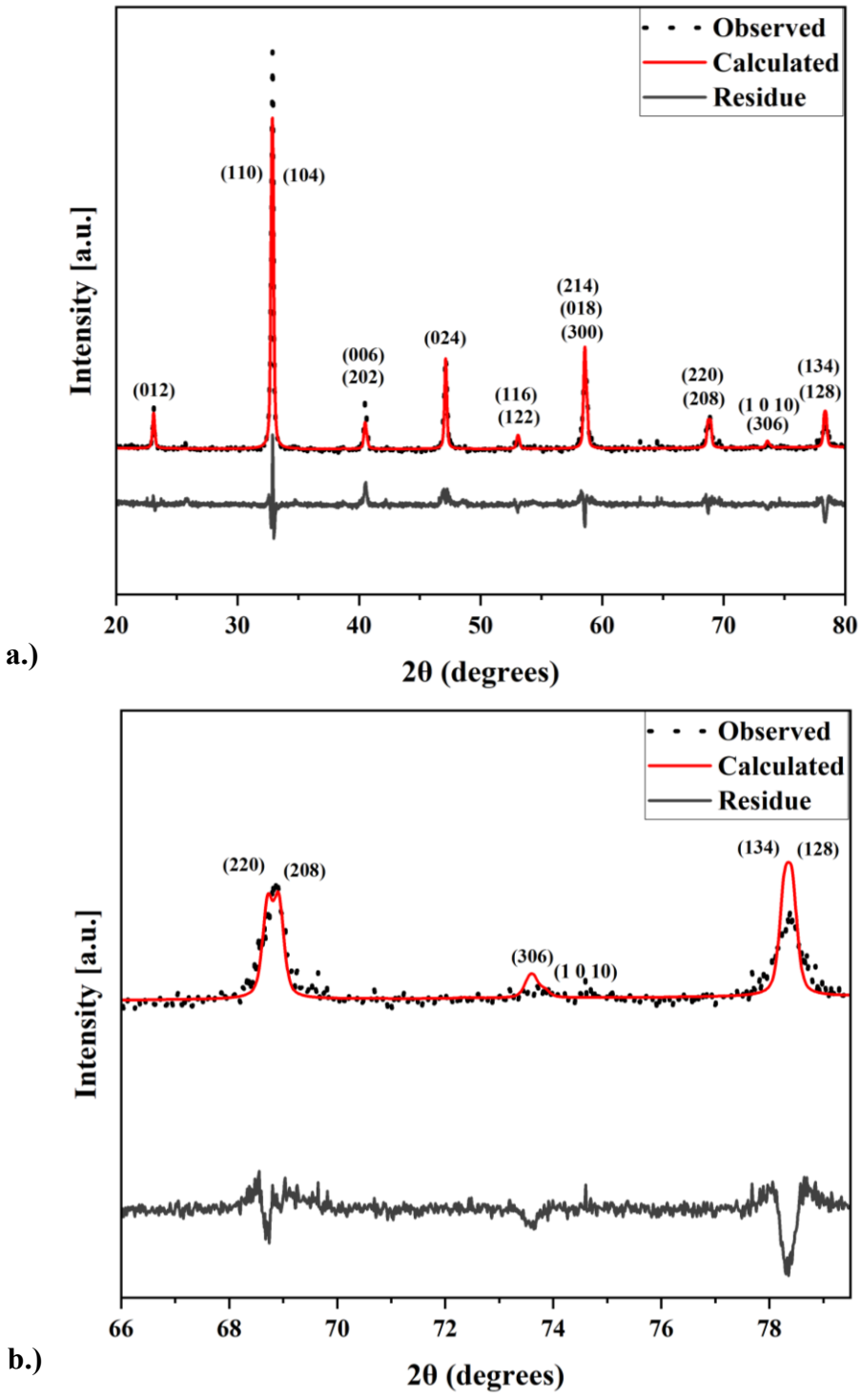

Figure 7.14: **a)** Whole pattern fitting of the rhombohedral (R3c) structure of a crushed NSCF6428 pellet sintered at 1100 ºC with experimental data (black line), reference file fit (red line), residue (grey line) shown and peaks are indexed using ICDD 04-017-2448. **b)** Zoom in of the fitting of the rhombohedral (R3c) structure of the 1100 ºC crushed NSCF6428 pellet, indicating potential peak splitting at the (220)/(208), (306)/(1 0 10) and (134)/(128) peaks 68º, 72º and 78º 2θ respectively.

Table 7.5: Whole pattern fitting of structural parameters, fit quality and micro strain of the rhombohedral (R3c) NSCF6428 sintered at 900, 1000 and 1100 ºC ((R_{wp}(%)) weighted pattern, (R_{exp} (%)) expected pattern and goodness of fit (GOF)

Temperature (ºC) – R3c	**R_{exp} (%)**	**R_{wp} (%)**	**GOF**	**Micro Strain (%)**
900	5.019	4.852	0.967	0.39
1000	4.766	4.363	0.916	0.19
1100	5.299	4.464	0.843	0.19

The above fits to the XRD patterns are measured using the quality factor values such as R_{wp} (%) where values < 10% indicate an acceptable fit, while for GOF values below 4% indicate a good fit in accordion to the literature as shown in Tables 7.1-7.5. [179-180] However, as with the calcined LNSCF33428 and NSCF6428 as described in Section 6.3, there are either missing or mismatched peaks for the Orthorhombic structure fit, as shown in Figures 7.6 and 7.11 with the 1100 ºC peak fitting figures being omitted from both the LNSCF33428 and NSCF6428. Moreover, for the NSCF6428 there is no formation of peaks at either 25 or 40 2-theta which in the study by Heydari et. al were visible and indicated the full transition towards an orthorhombic symmetry.[75] Furthermore, the GOF values for R3c are much lower than for the Orthorhombic structure, some are even below 1 such as LPSCF33428 and NSCF6428 suggesting a reasonable fitting to the experimental diffraction peaks of the R3c structure. Therefore, the rhombohedral symmetry was chosen to be examined further. Although, from the XRD peak fitting alone, it is difficult to pick the optimal sintering temperature for the rare earth doped cathodes compared to the sintered undoped LSCF6428. That is due to the possibility of Sr deficiency occurring in the distribution within the chemical composition especially given the hygroscopic nature of the Nd and carbonation behaviour of the strontium, as described in detail in the thermal analysis in Section 6.2.[212][234] Therefore, the use of SEM-EDX analysis was undertaken to examine the elemental distribution of the chemical composition of each rare earth doped sample to find an optimum sintering temperature for the elemental distribution of each rare earth doped LSCF crushed pellet.

7.2. Microstructure Characterisation of the sintered LPSCF33428, LNSCF33428 and NSCF6428 Nanopowders

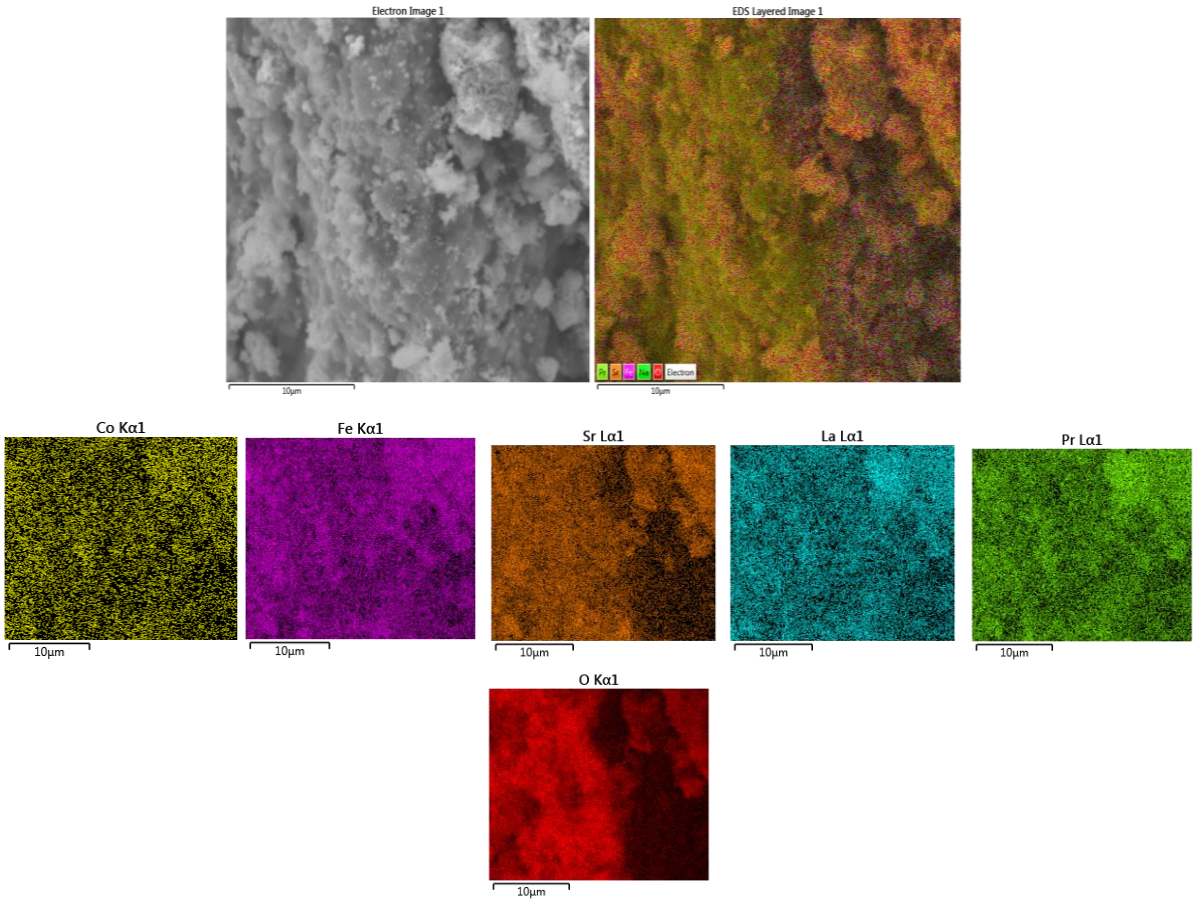

Figure 7.15: SEM image of an LPSCF33428 crushed pellet after sintering at 900 ºC . (Left) Secondary electron image, (Right) SE image overlaid with the elemental maps with individual elemental maps shown below, suggesting a relatively homogenous distribution of the LPSCF33428 elements.

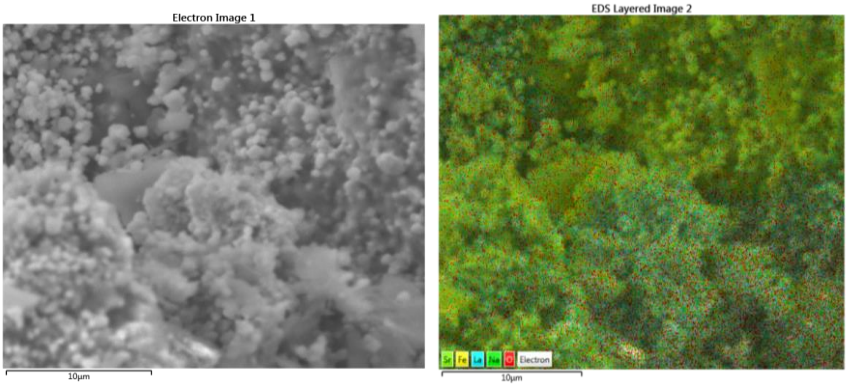

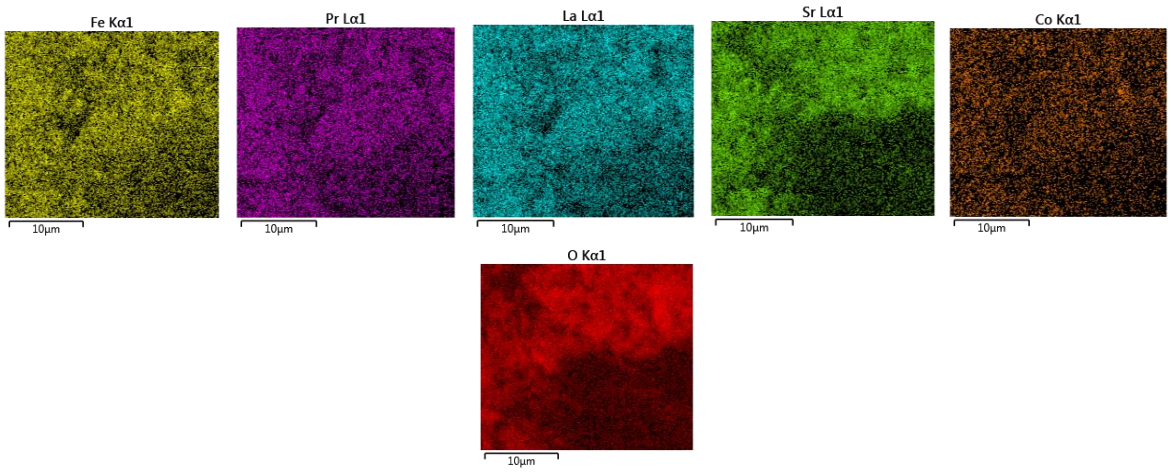

Figure 7.16: SEM image of LPSCF33428 of crushed pellet after sintering at 1000 ºC . (Left) Secondary electron image, (Right) SE image overlaid with the elemental maps with individual elemental maps shown below, suggesting a relatively homogenous distribution of the LPSCF33428 elements.

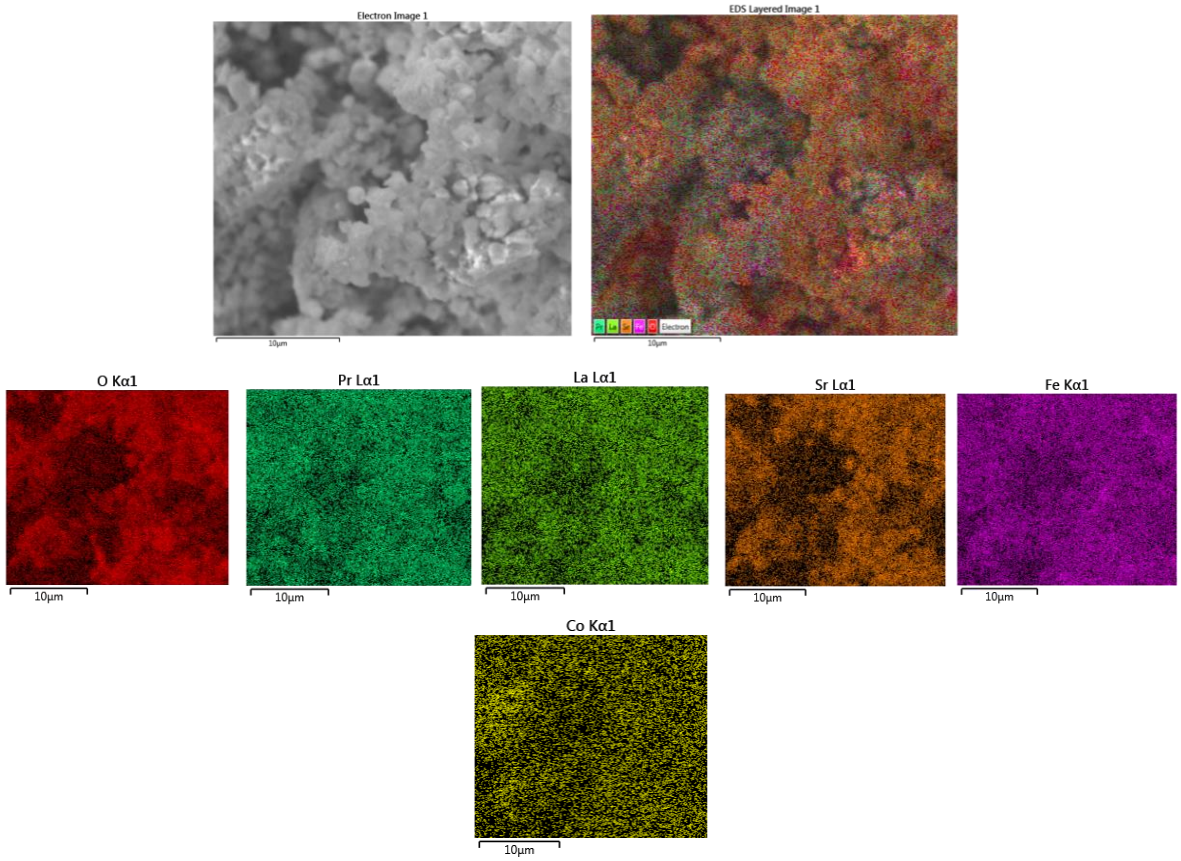

Figure 7.17: SEM image of LPSCF33428 of crushed pellet after sintering at 1100 ºC. (Left) Secondary electron image and (Right) SE image overlaid with the elemental maps with individual elemental maps shown below, suggesting a relatively homogenous distribution of the LPSCF33428 elements.

Table 7.6: LPSCF33428 sintered at 900 ºC,1000 ºC and 1100 ºC with a comparison of EDX derived composition (assuming oxygen stoichiometry) to the the expected composition indicated significant Sr deficiency and excess iron at each temperature.

Elements	Expected Composition	900 ºC	1000 ºC	1100 ºC
Iron (Fe)	0.8	0.88	0.88	0.93
Strontium (Sr)	0.4	0.35	0.34	0.29
Lanthanum (La)	0.3	0.28	0.3	0.29
Prasodynium (Pr)	0.3	0.31	0.3	0.33
Cobalt (Co)	0.2	0.17	0.17	0.15

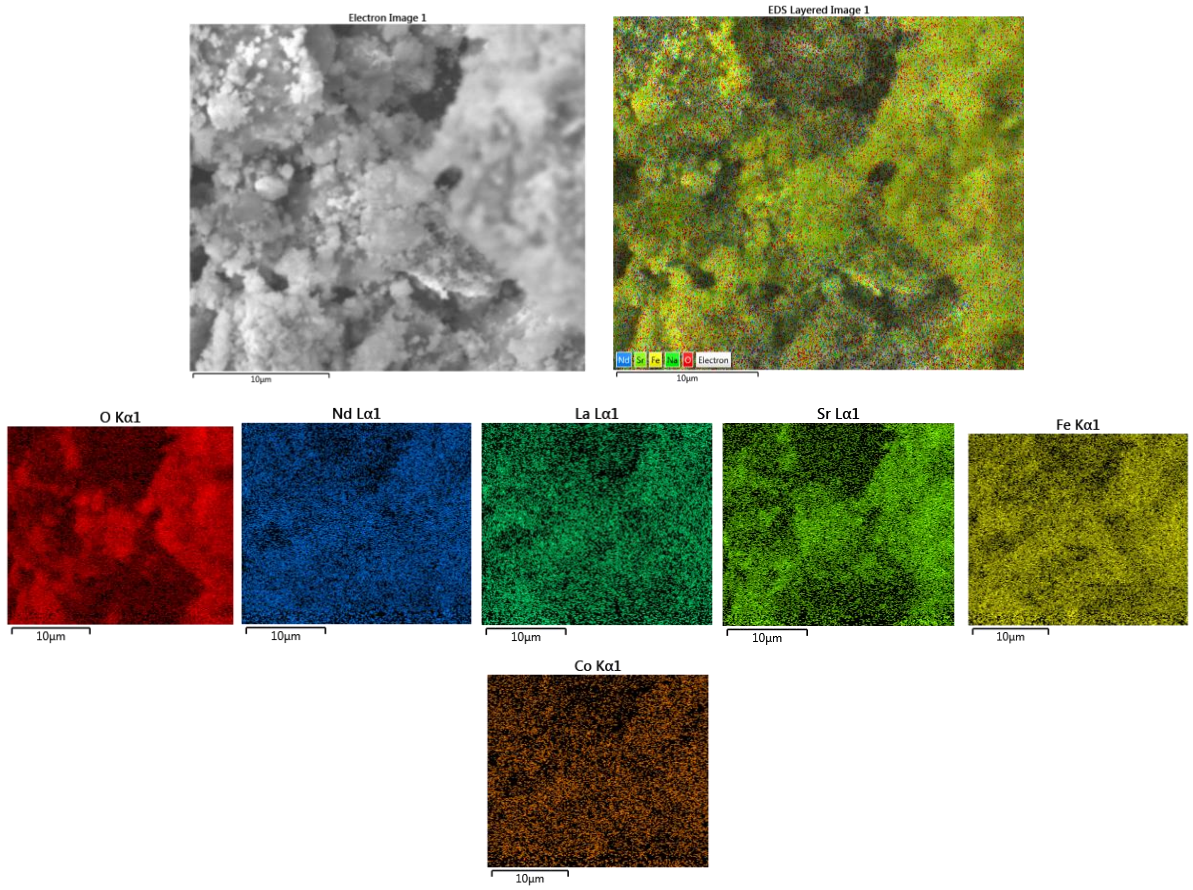

Figure 7.18: SEM image of LNSCF33428 of crushed pellet after sintering at 900 ºC . (Left) Secondary electron image, (Right) SE image overlaid with the elemental maps with individual elemental maps shown below, suggesting a relatively homogenous distribution of the LNSCF33428 elements.

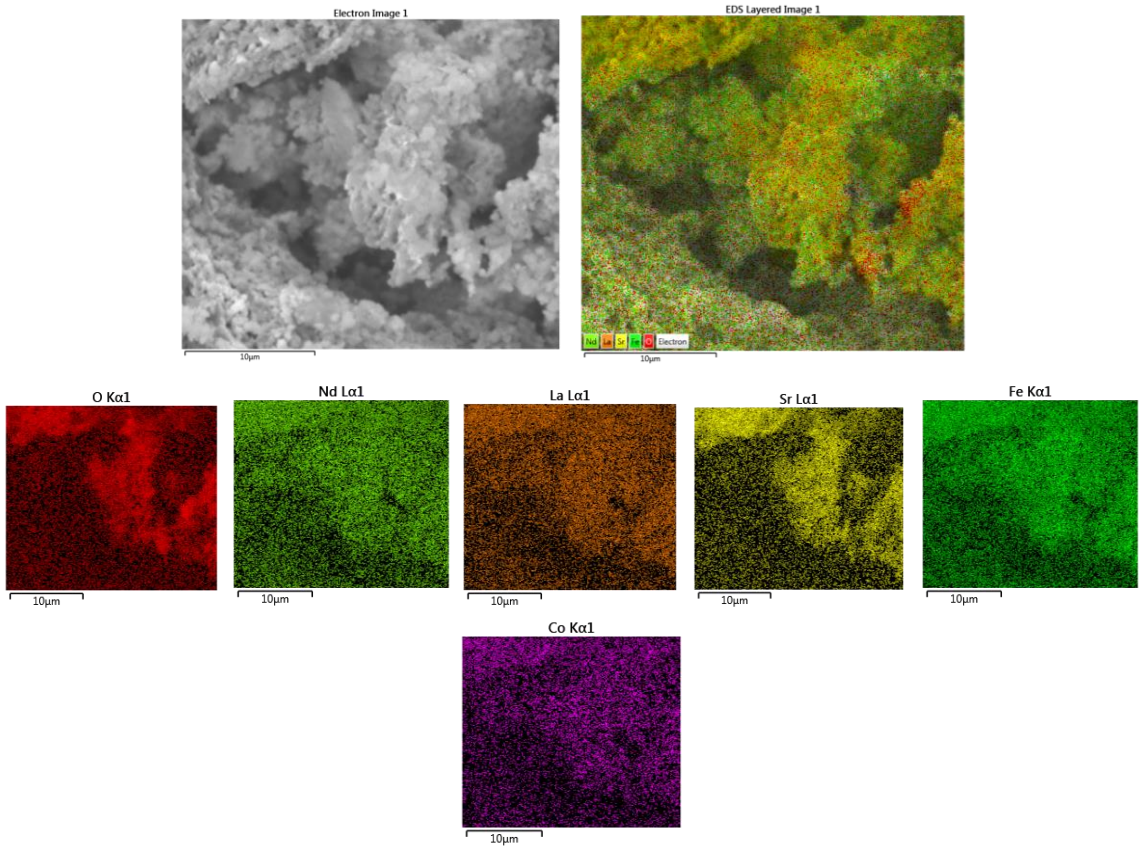

Figure 7.19: SEM image of LNSCF33428 of crushed pellet after sintering at 1000 ºC . (Left) Secondary electron image, (Right) SE image overlaid with the elemental maps with individual elemental maps shown below, suggesting a relatively homogenous distribution of the LNSCF33428 elements.

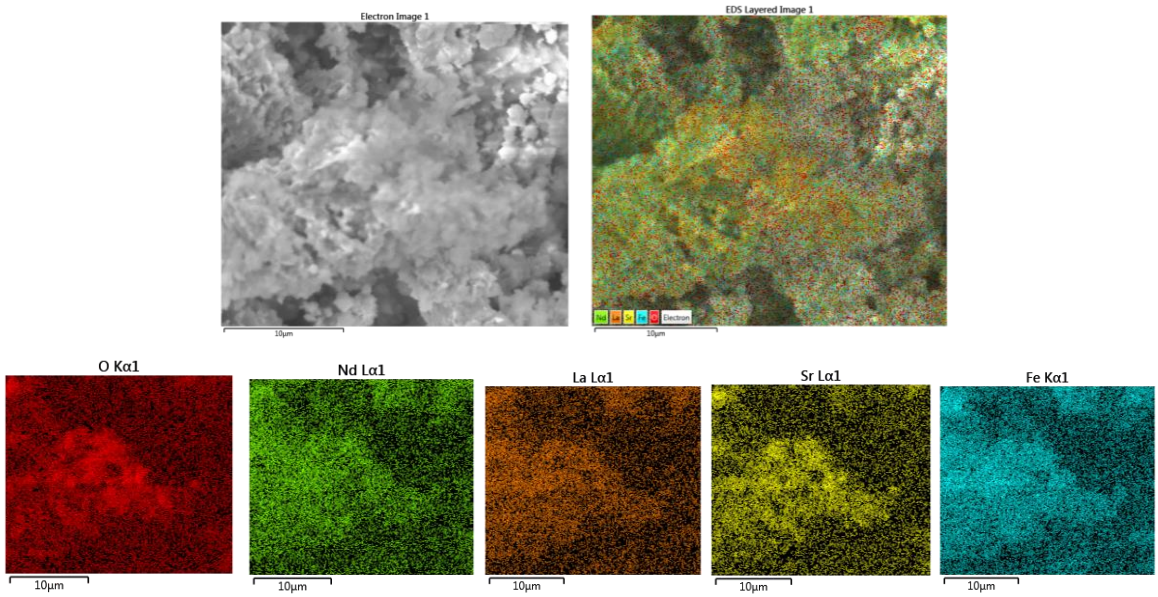

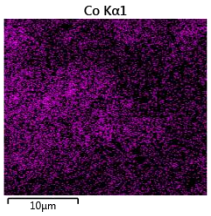

Figure 7.20: SEM image of LNSCF6428 of crushed pellet after sintering at 1100 ºC. (Left) Secondary electron image, (Right) SE image overlaid with the elemental maps with individual elemental maps shown below, suggesting a relatively homogenous distribution of the LNSCF33428 elements.

Table 7.7: LNSCF33428 sintered at 900 ºC,1000 ºC and 1100 ºC with a comparison of EDX derived composition (assuming oxygen stoichiometry) to the expected composition indicated significant Sr deficiency and excess iron at each temperature.

Elements	**Expected Composition**	**900 ºC**	**1000 ºC**	**1100 ºC**
Iron (Fe)	0.8	1.04	0.99	1.08
Strontium (Sr)	0.4	0.24	0.3	0.15
Lanthanum (La)	0.3	0.22	0.27	0.27
Neodymium (Nd)	0.3	0.35	0.30	0.35
Cobalt (Co)	0.2	0.15	0.15	0.16

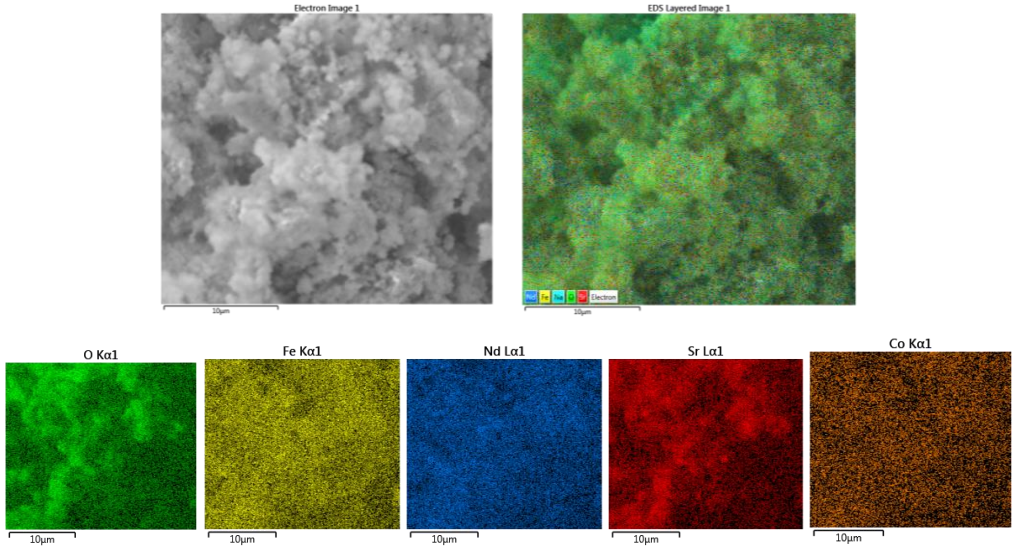

Figure 7.21: SEM image of NSCF6428 of crushed pellet after sintering at 900 ºC. (Left) Secondary electron image, (Right) SE image overlaid with the elemental maps with individual elemental maps shown below, suggesting a relatively homogenous distribution of the NSCF6428 elements.

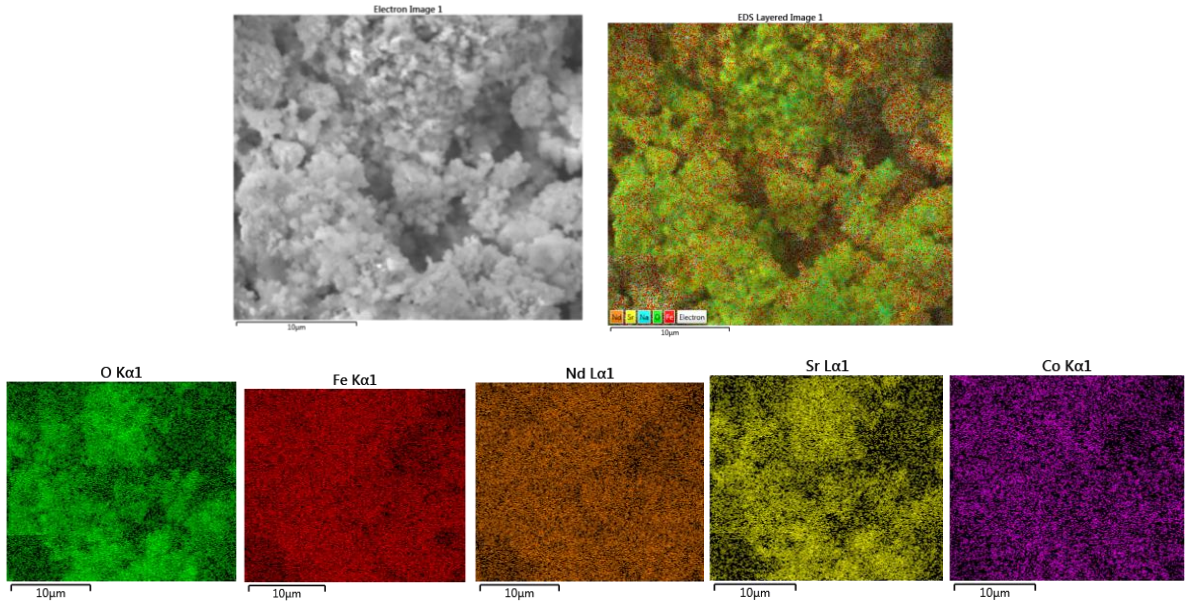

Figure 7.22: SEM image of NSCF6428 of crushed pellet after sintering at 1000 ºC. (Left) Secondary electron image, (Right) SE image overlaid with the elemental maps with individual elemental maps shown below, suggesting a relatively homogenous distribution of the NSCF6428 elements.

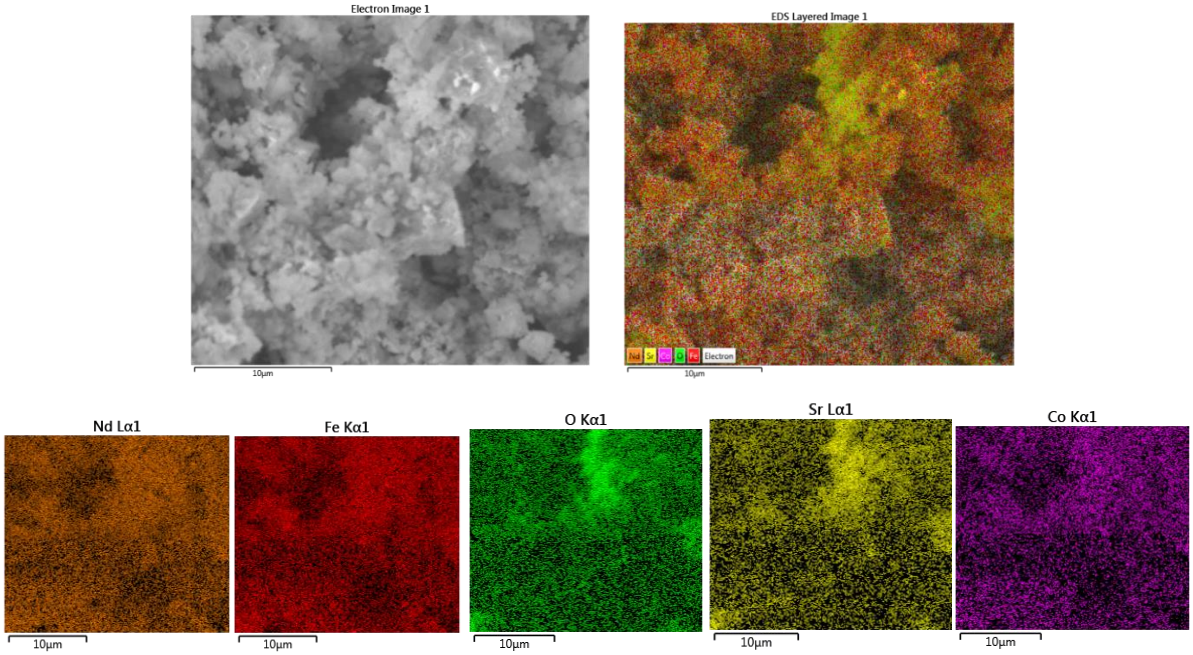

Figure 7.23: SEM image of NSCF6428 of crushed pellet after sintering at 1100 ºC. (Left) Secondary electron image, (Right) SE image overlaid with the elemental maps with individual elemental maps shown below, suggesting a relatively homogenous distribution of the NSCF6428 elements.

Table 7.8: NSCF6428 sintered at 900 ºC,1000 ºC and 1100 ºC with a comparison of EDX derived composition (assuming oxygen stoichiometry) with the expected composition indicated significant Sr deficiency and excess iron content at each temperature.

Elements	Expected Composition	900 ºC	1000 ºC	1100 ºC
Iron (Fe)	0.8	1.07	1.03	1.00
Strontium (Sr)	0.4	0.3	0.28	0.17
Neodymium (Nd)	0.6	0.45	0.55	0.66
Cobalt (Co)	0.2	0.19	0.16	0.18

Overall, and despite the elemental maps looking homogenous, the analysis of EDX based elemental quantification by assuming oxygen stoichiometry suggests a slight enrichment in Fe, appropriate amounts of Co, La, Pr, Nd and La and deficiency of Sr across the 3 rare earth doped samples as shown in Figures 7.15-7.23. For the LNSCF33428 and NSCF6428 containing the Nd element, there is a significant deficiency of Sr when the sintering temperature increases from 1000 to 1100 ºC, as shown in Tables 7.6-7.8. For NSCF6428 there is a significant trend as Nd content increases closer to the expected composition as the sintering temperature changes from 1000 to 1100 ºC, whereas the strontium content decreases away from the expected composition as shown in Table 7.8. In a study by Waller et.al., A-site deficient LSCF and $SrCO_3$ were heated above the decomposition temperature of $SrCO_3$ (of 950ºC) and the perovskite oxide structure changed from cubic to rhombohedral.[186] That is due to increased incorporation of Sr into the LSCF structure as seen by the sudden appearance of peak splitting of the XRD patterns. That contrasts with the significant Sr deficiency seen to be occurring here at a sintering temperature at 1100ºC for the Nd based cathodes (LNSCF33428 and NSCF6428) as shown in Figures 7.20 and 7.23. The LNSCF33428 and NSCF6428 Sr content here are 0.15 and 0.17 respectively (Table 7.9). Waller et. al., report that if the strontium content for LSCF is within the range between $0.15<Sr<0.2$, the cubic perovskite oxide structure was adopted however clear evidence of a rhombohedral structure is seen here by XRD (Figures 7.1 having peak splitting at 68º 2θ).[186]

Table 7.9: LPSCF334248, LNSCF33428, NSCF6428 sintered at 1000ºC with a comparison of EDX derived composition estimates establishing strontium deficiency and excess iron content along with the relevant rare earth content. LSCF6428 sintered at 1000 ºC data obtained from Section 5.2, Table 5.4

Sintered Cathode Materials at 1000 ºC	**Strontium (Sr)**	**Iron (Fe)**	**Lanthanum (La)**	**Praseodymium (Pr)**	**Neodymium (Nd)**
LPSCF 33428	0.34	0.88	0.3	0.3	NA
LNSCF 33428	0.3	0.99	0.27	NA	0.3
NSCF 6428	0.28	1.03	NA	NA	0.55
LSCF 6428 (Obtained from Section 5.2, Table 5.4)	0.3	0.91	0.58	NA	NA

As a result, the sintering temperature of 1000 ºC is chosen as the optimal sintering temperature for all three rare earth doped samples in relation to past studies despite the excess iron content from 0.88 for LPSCF33428 to 1.03 for NSCF6428 as referred to in Table 7.9. Further work will now be conducted into the structural parameters with comparison to the undoped LSCF6428 sintered at 1000 ºC and originally reported in Chapter 5.

7.3 Analysis of the Structural Properties of LPSCF33428, LNSCF33428 and NSCF6428 Pellets Sintered at 1000 ºC

Table 7.10: Unit Cell dimensions (rounded to three decimal places), Theoretical Density and Volume (rounded to two decimal places) of rhombohedral (R3c) LPSCF33428, LNSCF33428 and NSCF6428 sintered at 1000 ºC. LSCF6428 sintered at 1000 ºC data obtained from Section 5.2, Table 5.4

Sintered Cathode Materials	**a (Å)**	**b (Å)**	**c (Å)**	**Volume (Å)**	**Theoretical Density (g/cm^3)**
LPSCF33428	5.495 ± 0.009	5.495	13.399	350.32 ± 1.78	11.07 ± 0.055
LNSCF33428	5.489 ± 0.011	5.489	13.373	348.94 ± 1.86	11.11 ± 0.06
NSCF6428	5.471 ± 0.01	5.471	13.347	346.02 ± 1.98	11.21 ± 0.05
LSCF6428 (Obtained from Section 5.1, Table 5.2)	5.485 ± 0.011	5.485	13.367	348.63 ± 1.46	11.14 ± 0.045

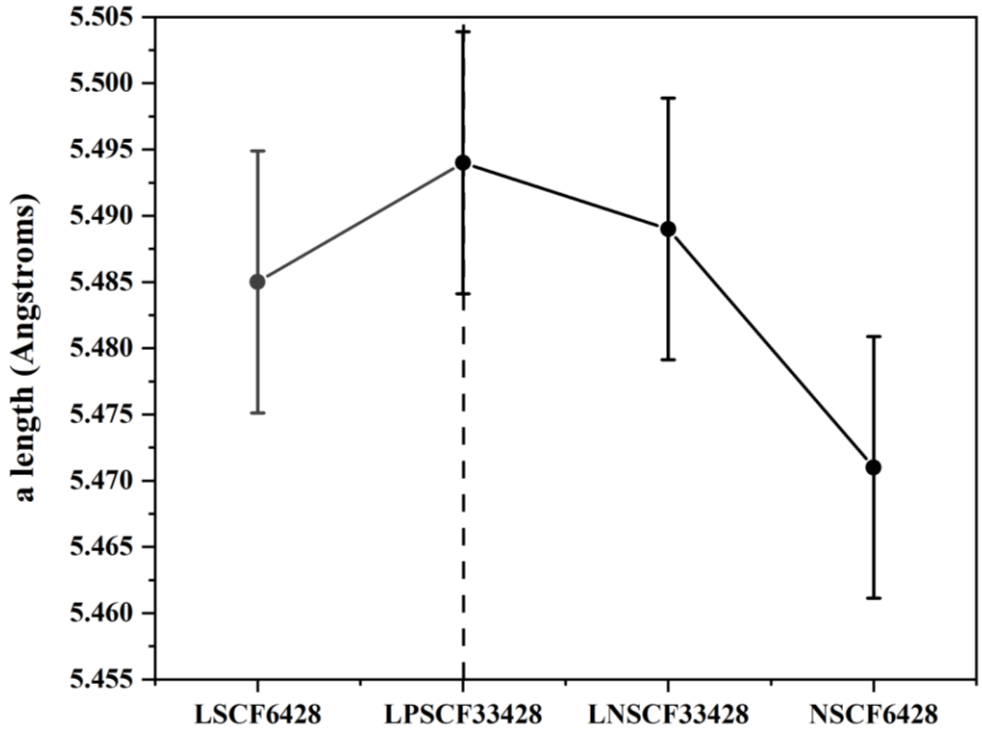

Figure 7.24: Temperature (°C) vs Rhombohedral lattice parameter, "a" length (Angstroms) of the crushed sintered LPSCF33428, LNSCF33428 and NSCF6428 pellets at 1000 °C where the black dots are the experimental data points along with error bars where the crushed LSCF6428 pellet was sintered at 1000 °C as reported in Section 5.1, Figure 5.6.

The effect of the strontium deficiency on each rare earth doped crushed pellet, sintered at 1000 °C on the perovskite lattice parameter, "a" length is shown in Figure 7.24 and Table 7.10. There is a decrease in "a" length lattice parameter in relation to a combination of strontium deficiency and potentially the excess Fe content from the EDX analysis as shown in Table 7.9 overall. Kostogloudis et.al. have reported the "a" length lattice parameter to increase with a decrease of strontium incorporation into the LSCF6428 rhombohedral unit cell. [57] Moreover, given that there is no appearance of $SrCO_3$ impurity peaks in the XRD diffraction pattern similar to the sintering of LSCF6428 in Section 5.1, the change in "a" length lattice parameter of the perovskite oxide could be caused by the dopant behaviour within the perovskite oxide, especially the Nd. The dopant behaviour described in Section 6.1, in relation to the hygroscopic nature and carbonation of the rare earth based perovskite oxides affecting the homogenous distribution of the elements when chemical mechanisms take place in humid environments. [75][212] The changes in "a" length lattice parameter trend also influences the volume and

density parameters where changes are seen in apparent relation to a combination of strontium deficiency, excess Fe content and increase in Nd content as shown in Table 7.10.

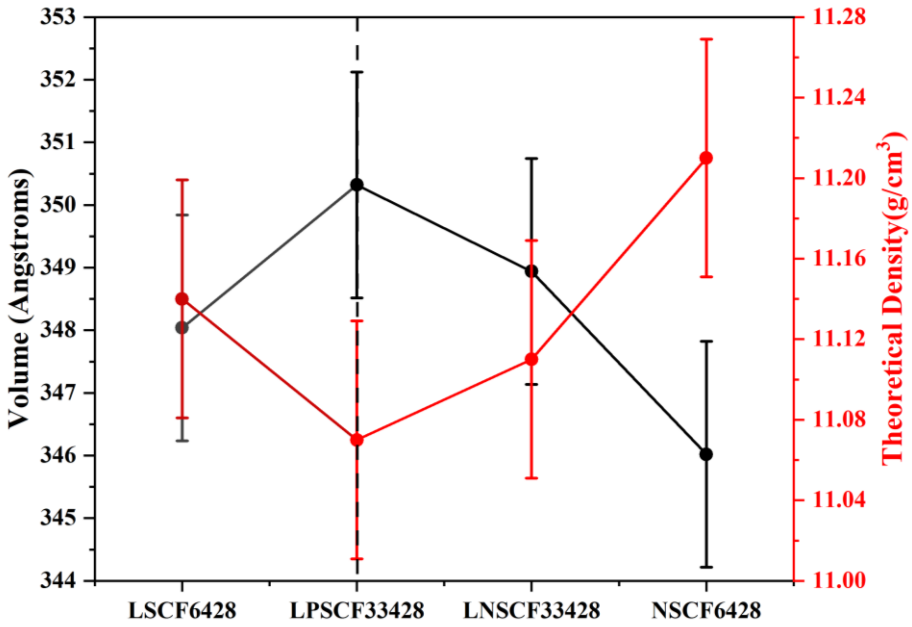

Figure 7.25: Temperature (°C) vs Rhombohedral Volume (Angstroms- black line with error bars at black dots refer to as experimental data points) and Theoretical Density (g/cm^3- red line with error bars at red dots refer to as experimental data points) of the crushed sintered LPSCF33428, LNSCF33428 and NSCF6428 pellets of perovskite oxide at 1000 °C while the grey dot (Volume) and dark red (Density) is the crushed sintered LSCF6428 pellet at 1000 °C experimental data points obtained from Section 5.1, Figure 5.7.

The "a" length lattice parameter influences the inverse relationship between the volume and density of the three rare earth doped materials sintered at 1000 °C as shown in Figure 7.25. The trend between the LPSCF33428 and LNSCF33428 given the small decrease in density is consistent with the "a" length lattice parameter trend which could be due to a combination of excess iron content and strontium deficiency as shown in Figure 7.26 and Table 7.9 respectively. However, the significant decrease in the unit cell volume and corresponding increase in the density of the microstructure between the LNSCF33428 and NSCF6428 trend (Figure 33) is due to the increase in Nd content of 0.55 as shown in Table 7.9. The increase in Nd content is consistent with the steep decrease in "a" length lattice parameter between the LNSCF33428 and NSCF6428.

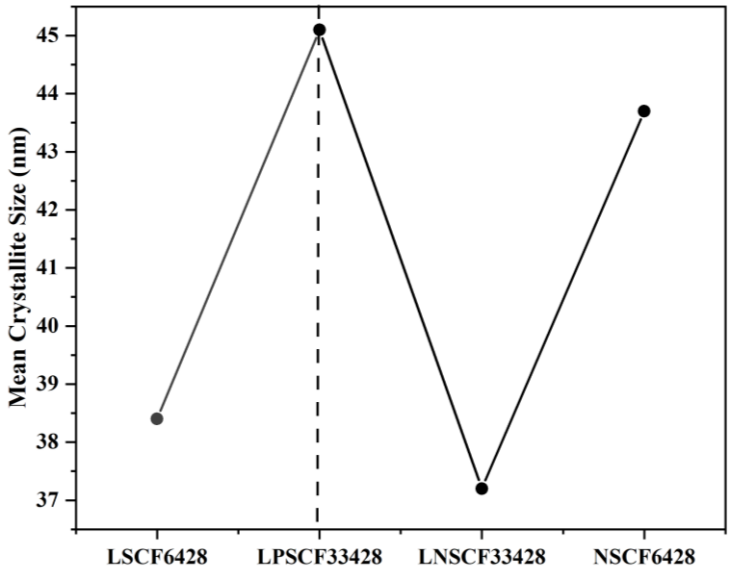

Figure 7.26: Temperature (ºC) vs Mean crystallite size (nm) of the crushed sintered LPSCF33428, LNSCF33428 and NSCF6428 pellets at 1000 ºC where the black dots refer to the experimental data while the grey dot is the crushed sintered LSCF6428 pellet at 1000 ºC experimental data point obtained from Section 5.1, Figure 5.5

Table 7.11: Mean Crystallite Size of sintered LPSCF33428, LNSCF33428 and NSCF6428 pellets at 1000 ºC and crushed LSCF6428 at 1000 ºC data obtained from Section 5.1, Table 5.1

Sintered Cathode Materials	**Mean Crystallite Size (nm)**
LPSCF33428	45.1
LNSCF33428	37.2
NSCF6428	43.7
LSCF6428	38.4

For the crystallite size, there is no trend from the LPSCF33428 to NSCF6428 when sintered at 1000 ºC regarding the substitution of host cation, lanthanum with the rare earth dopants, Pr and Nd as shown in Figure 7.26 and Table 7.11. The crystallite size of 37 nm for LNSCF33428 is similar to what has been obtained by Belina et.al. [233] The crystalline size of 44 nm for the NSCF6428, is similar to what has been obtained by Asad et.al.[230].

To determine how both the element composition of strontium, iron and neodymium and the structural parameters such as “a” length and density affect the metal-oxygen vibrations and structural distortion of the three different rare earth doped LSCF crushed pellets sintered at 1000 ºC, Raman spectroscopy was used.

7.4. Raman Spectroscopy of the LPSCF3428 and LNSCF33428 Nanopowders Sintered at 1000 ºC

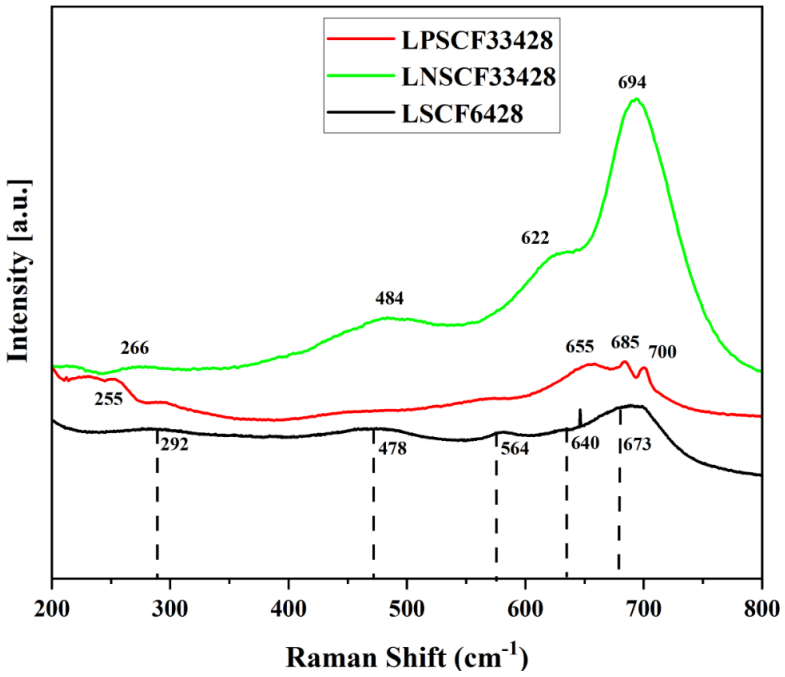

Figure 7.27: Raman Spectra of LPSCF33428 and LNSCF6428 crushed pellets after sintering at 1000 ºC with excitation wavelength of 532 nm while the sintered LSCF6428 crushed pellet at 1000 ºC was already reported in Section 5.3, Figure 5.11 with dashed lines for comparison.

NSCF6428 measurement was omitted from the Raman due to the strong fluorescence it outputted for the Raman, given its high Nd content as referred to in Table 7.9 (also see Methodology). It can be seen from Figure 7.27 that the LPSCF33428 has peak shifts located at 266 cm^{-1},484 cm^{-1},622 cm^{-1} and 694 cm^{-1} and LNSCF33428 peak shifts located 255 cm^{-1},655 cm^{-1},685 cm^{-1} and 700 cm^{-1} when sintered at 1000 ºC.

For the LPSCF33428 crushed nanopowder sintered at 1000 ºC, there is a lower and weaker intensity in the Raman spectra, and the peaks are less well defined. This is consistent with the excess iron content at 0.88 and Sr deficiency where the content is at 0.34 as shown in Table 7.9. While for the LNSCF33428 crushed nanopowder sintered at 1000 ºC, the Raman intensity increases above the spectrum of the LPSCF33428, the peaks are well defined, and broader where there is an increase in excess iron content at 0.99 and decrease of Sr content at 0.3 for this composition (Table 7.9). The appearance of the Raman spectra are similar to a study on Sr and Fe substituted $LaCoO_3$(LCO) by Alkan et.al.[208] The positions of the peaks of LPSCF33428 above 600 cm^{-1} are similar to the Sr10 and Sr20 substituted LCO, where its peaks are associated with a lower degree of Jahn Teller distortion of the cation octahedra given its

weaker appearance.[208] While for the LNSCF33428, the positions at 485 cm^{-1}, 622 cm^{-1} and 685 cm^{-1} are similar to the Fe20 substituted LCO positions at 472 cm^{-1}, 608 cm^{-1} and 678 cm^{-1} and are also boarder in appearance due to the orthorhombic distortions of rigid rotation of the octahedral cations [208].

The peaks located at 255 cm^{-1} and 266 cm^{-1} for LPSCF33428 and LNSCF33428 respectively are lower wavenumber compared to the undoped LSCF6428 due to the lower content of lanthanum and can be assigned to oxygen octahedra tilting following work by Nandy et.al. examining the Raman spectra peak positions of $LaFeO_3$. While the peaks located above 600 cm^{-1} can be assigned to the Co/Fe–O bonds indicating the bending vibration and stretching vibration of the metal-oxide bonds respectively. [207]. However, for the LNSCF33428 only, there is an additional peak detected at 484 cm^{-1} which is a similar match to a study by Alkan et.al, involving the iron substitution for lanthanum at the A site in the perovskite, $LaCoO_3$. The peak located at 484 cm^{-1} only for the LNSCF33428 may be due to octahedral rotation. The effect of the excess iron content led to the transition of a broader peak for the Fe20 doped LCO due to the distortion effect in the structure as referred to in a study by Alkan et. al in comparison to undoped LSCF6428. [208]

Overall, the differences in the positions and intensities of the peaks between the LPSCF33428 and LNSCF33428 are consistent with the partial substitution of the host cation lanthanum by the rare earth dopants.

7.5. Density and SEM Morphology of the LPSCF33428, LNSCF33428 and NSCF6428 Nanopowders Sintered at 1000 ºC

To determine the density of the three different rare earth doped cathode materials in comparison to the undoped LSCF6428 sintered at 1000 ºC, the Archimedes and Geometrical density methods were applied, as described in the methodology section. The results are presented in Table 7.12 (rounded to 2 decimal points). [22][210]

There is a relationship between the Pr and Nd dopants of LSCF and the parameters being analysed with lower densities for the Nd doped materials. Also, when comparing densities, there are significant differences between the values obtained from the Archimedes and Geometrical methods, which may correspond to the differences porosities. For the Archimedes density difference between the LPSCF33428 and LNSCF33428, there is a sudden decrease in both density and Archimedes porosity and as already reported there is a decrease in crystallite size from 45 nm to 37 nm for these compositions and a decrease in strontium content from 0.34

to 0.3 (Tables 7.11 and 7.9 respectively). The trend is also similar for the thickness shrinkage of the pellets where there is an increase from 0.17 to 0.21 as shown in Table 7.12. While for the geometrical method, there are no significant trends between the LPSCF33428 and LNSCF33428.

Given that the cathodes have all been sintered at the same temperature and for the same time of 1 hour, the significant differences in measurements between the LPSCF33428 to LNSCF33428 as referred to in Table 7.12 may be due to increased open porosity in the Nd doped materials. That could be due to the difference between the two density measurement techniques suggests that the significant open porosity in the samples which increases for the Nd doped material potentially because of the reduced elemental mixing as seen in the Nd doped LNFO3 in a study by Anajafi et.al.[233] In that study, the Nd concentrations was investigated on the study of Nd doped $LaFeO_3$, reports that for LNFO3, thickness shrinkage and therefore porosity could be caused by the restriction of the motions of particles at boundaries between the host cation La and dopant Nd.[233] To determine how the Nd influences the LNSCF33428 and NSCF6428 individually, the pellets were examined by the Bruker XRD to determine if there are any presence of additional or glassy phase among the crystalline phase of the sintered microstructure of the LPSCF33428, LNSCF33428 and NSCF6428. The presence of a glassy phase may suggest liquid phase sintering or melting and will affect density and therefore porosity

Table 7.12: Archimedes and Geometrical density (rounded to two decimal places), porosity (rounded to one decimal place) and pellet shrinkage ratio on sintering LPSCF33428, LNSCF33428, NSCF6428 whole pellets at 1000 ^{o}C and sintered LSCF6428 whole pellet at 1000 ^{o}C data obtained from Section 5.4, Table 5.6

Sintered Cathode Materials	**LPSCF33428**	**LNSCF33428**	**NSCF6428**	**LSCF6428 – 1000 ^{o}C**
Archimedes Density (cm^3/g)	7.61	6.76	6.62	8.29
Archimedes Porosity (%)	31.22	39.12	40.9	25.7
Geometrical Density (cm^3/g)	8.14	8.08	8.05	7.47
Geometrical Porosity (%)	26.5	27.3	28.2	32.3
Difference between Archemides and Geometrical Density (cm^3/g)	0.53	1.32	1.43	0.81

Difference between Archemides and Geometrical Porosity (%)	4.75	11.84	12.75	-6.5
Thickness Shrinkage	0.17	0.21	0.22	0.18

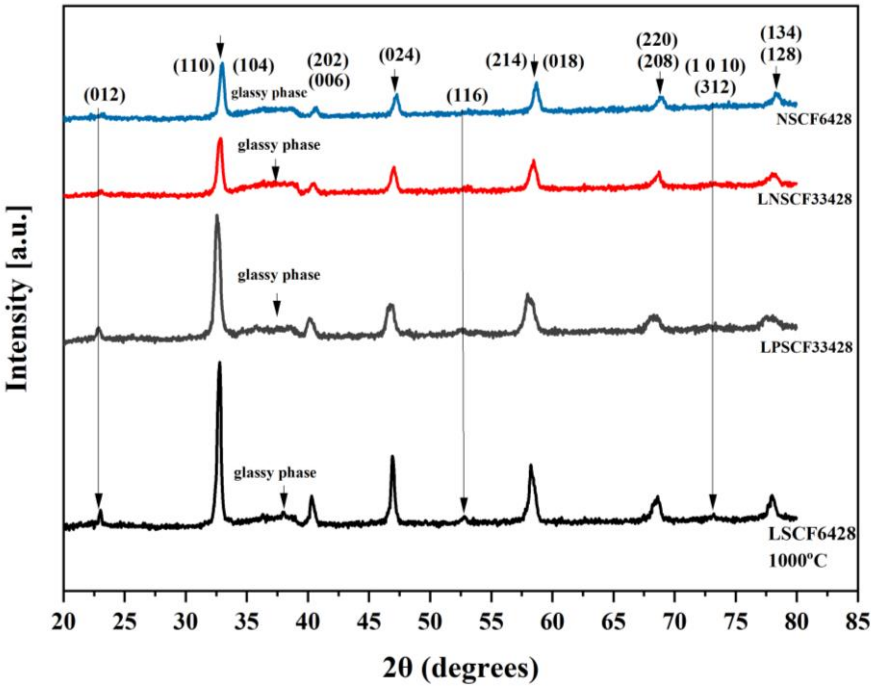

Figure 7.28: Bruker XRD patterns of 3 wt% whole pellets sintered for 1 h at 1000 ºC of LPSCF33428 (grey line), LNSCF33428 (red line), NSCF6428 (blue line) while the whole sintered LSCF6428 pellet at 1000 ºC (black line) was obtained from Section 5.4, Figure.5.12

Whole pellets of the 3 rare earth doped LSCF cathodes, sintered at the same temperature and time, were examined further using XRD (as described in the methodology) to determine whether any additional phases were present other than the rhombohedral perovskite phase. From the XRD diffraction patterns, there is an indication of a glassy amorphous phase forming between the 35º – 40º 2θ range as shown in Figure 7.28, potentially due to the excess Fe content and Sr deficiency as shown in Table 7.9. To establish the nature of this glassy phase SEM imaging of the pellet surfaces was undertaken.

SEM images (Figures 7.29-7.31) were obtained to observe densification, grain boundaries, grain growth, glassy phase presence and porosity of the three different rare earth doped LSCF cathode materials. For porosity measurement, the SEM imaging contrast threshold of the microstructure was determined through an upper estimate of the thresholding as shown in

Figures 7.29e-f and Figures 7.30-7.31g.-h., along with the selected areas in the yellow box as shown in Figures 7.29c.-d., 7.30-7.31e-f.

For the LNSCF33428, from the secondary electron image, it can be seen that the microstructure does not densify effectively, as interparticle necking is occurring in some certain areas of the microstructure showing only partially sintered grains (Figure 7.29 a-d). That has led to the retention of a small crystallite size in some areas of the microstructure and sudden inconsistent grain growth in other areas of the microstructure. The LNSCF33428 pellet has undergone the first stage of the sintering mechanism known as initial neck formation. [11] Secondary imaging (Figure 7.29a) shows a lack of definition of grains and pores against a low contrast background matrix, although there are very black pores visible in backscattered imaging (Figure 7.29b). There is a clear lack of grain growth in the BSE images consistent with the XRD measurements of a crystallite size of 37 nm in certain areas whilst grain growth is visible near a glassy phase as shown in Figure 7.29 b-d. This mixed microstructure is consistent with the Sr deficiency and excess iron content reported by EDX and the significant linear shrinkage of the sintered pellet of greater than 0.2 (Table 7.12). [233] The resulting open porosity can explain the significant differences between the two densities measurements in Table 7.12. This can be backed up with the study by Benila et.al. in refer to the LFO_3 in relation to the restricted diffusion at the boundaries between the La and Nd rich particles. [232]

(a.)

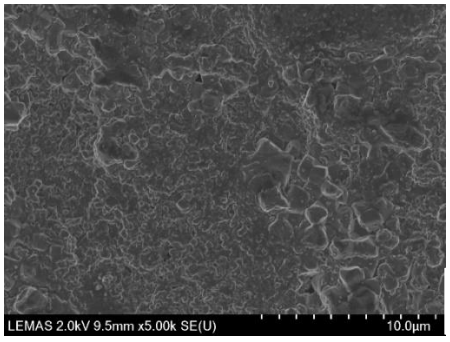

(b.)

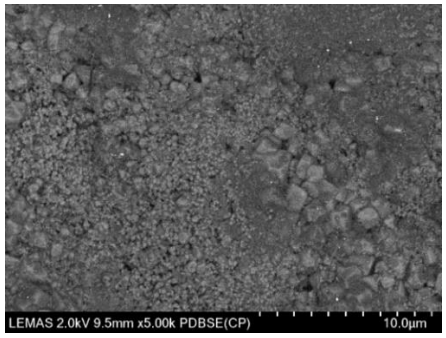

(c.)

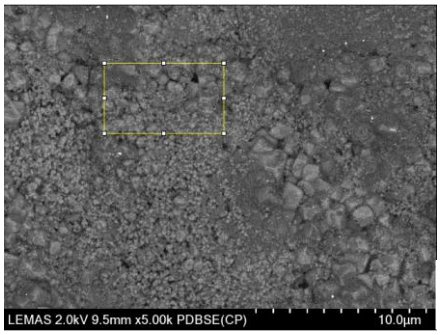

(d.)

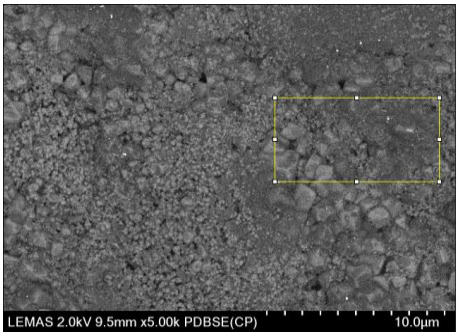

(e.) 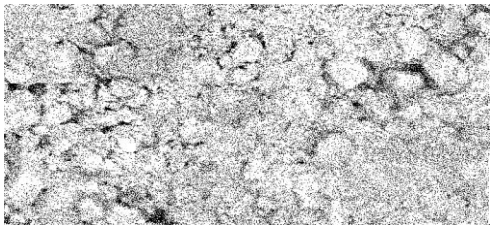 (f.) 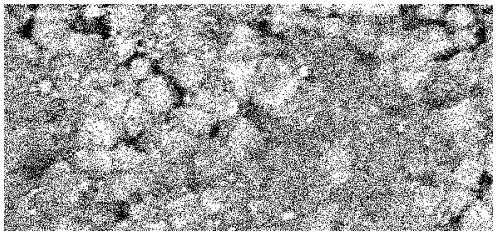

Figure 7.29: SEM images of sintered LNSCF33428 pellet at 1000 ºC for 1 h a) secondary b) back scattered, c) and d) backscattered with yellow box used for pore size measurement (inset) for geometrical and Archimedes respectively e) thresholded image of yellow box region where black is taken to be the maximum geometrical pore structure. f) thresholded image of yellow box region where black is taken to be the maximum Archimedes pore structure.

For LPSCF33428 and NSCF6428 pellets, only particle agglomeration with a (presumed) amorphous coating around the primary particles is visible by comparison of the secondary and backscattered images (Figure 7.30a.-d. and Figure 7.31a.-d.). This is consistent with the crystallite size measured by the XRD of approximately 40 nm (Figure 7.26) and is similar to the agglomeration of a study by Baker et. al., for Ag doped LSCF-SDCC [235]. The primary particles cluster in groups throughout the microstructure to form agglomerates which densifies the ceramic, however pores similar in size to the primary particles are still visible throughout the microstructure. The agglomeration is consistent with the presence of a glassy phase by XRD as shown in Figure 7.28 i.e. the agglomeration is the early stages of liquid phase sintering.

This agglomeration without grain growth is in contrast to the undoped LSCF6428 sintered at 1000 ºC (from Section 5.5) where there was significant grain growth to 70 nm and that also densification that resulted in a significant decrease of specific surface. To investigate further and measure specific surface areas of LPSCF33428 and NSCF6428, BET analysis was carried out on the crushed rare earth doped LSCF materials.

(a.) 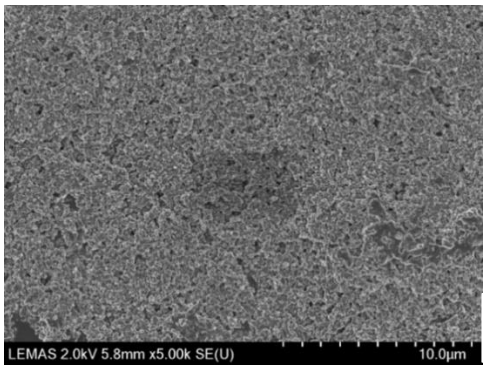

(b.) 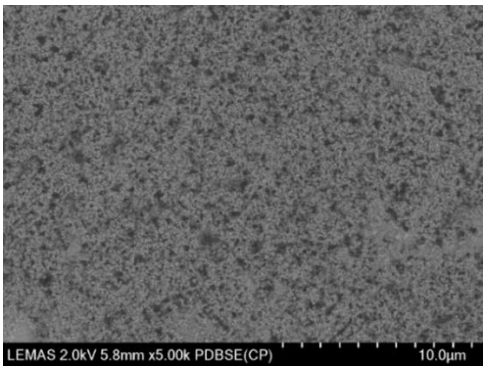

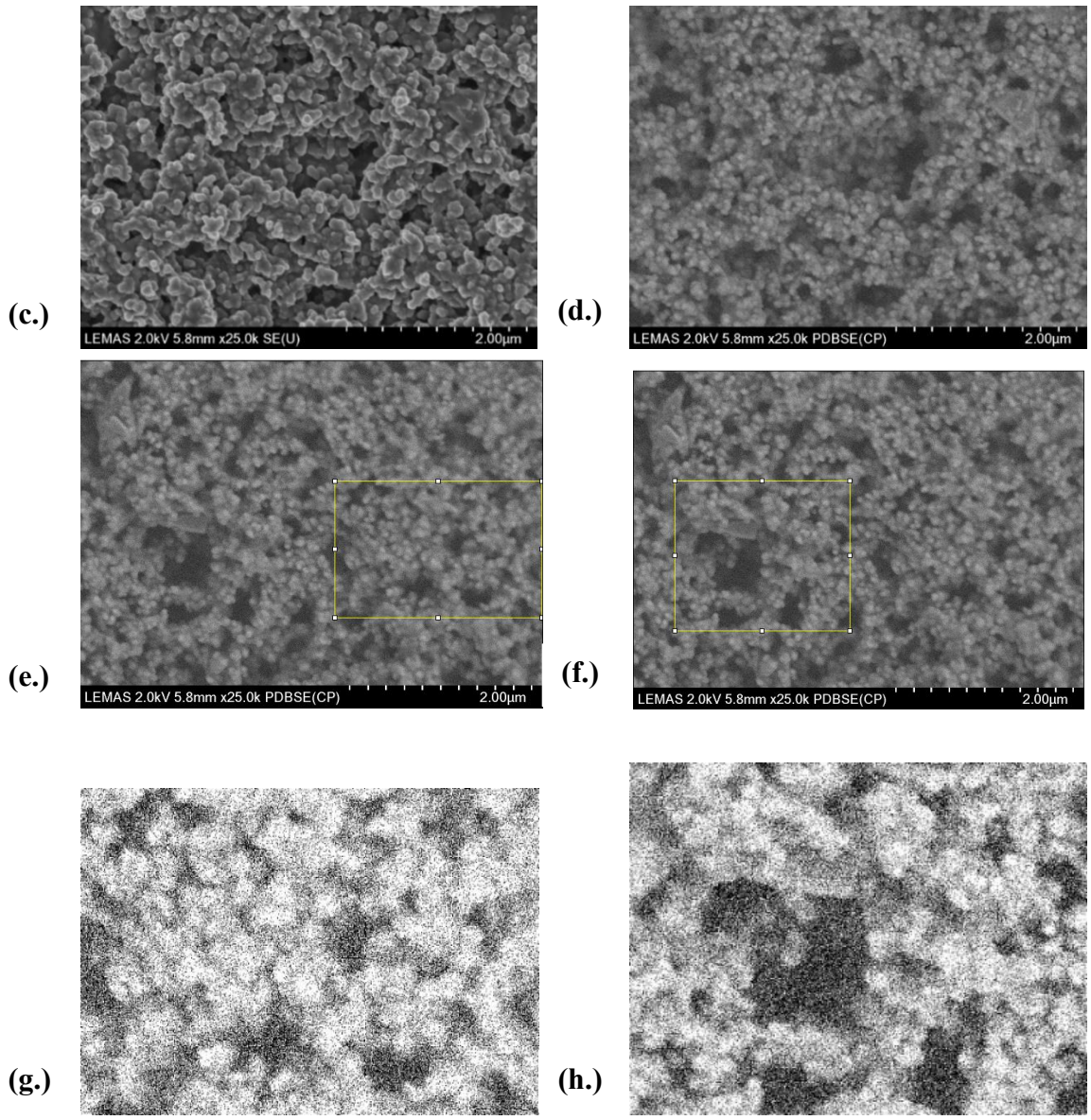

Figure 7.30: SEM images of sintered NSCF6428 pellet at 1000 ºC for 1 h a) and c) secondary b) and d) back scattered, e) and f) backscattered with yellow box used for pore size measurement (inset) for geometrical and Archimedes respectively g) thresholded image of yellow box region where black is taken to be the maximum geometrical pore structure h) thresholded image of yellow box region where black is taken to be the maximum Archimedes pore structure

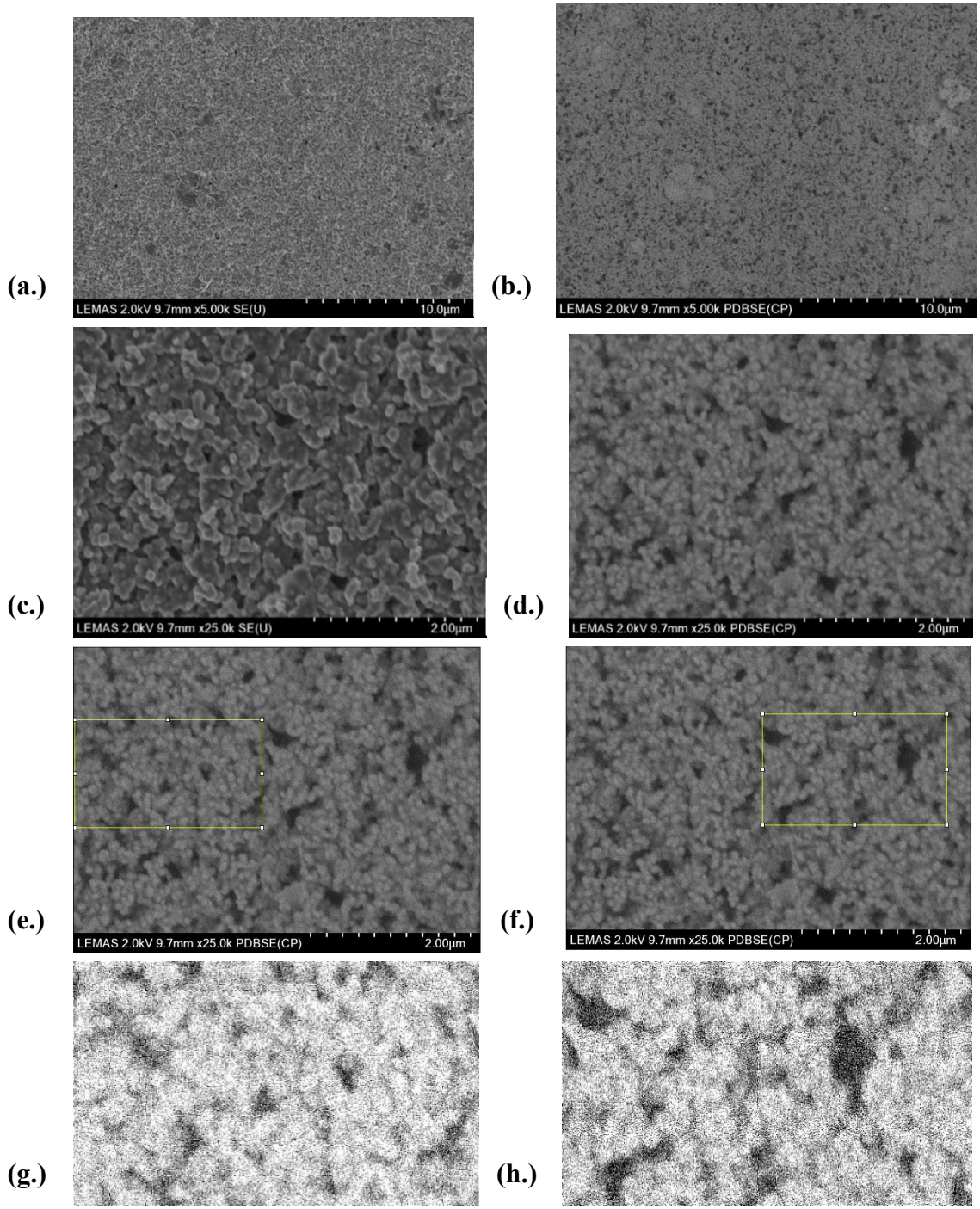

Figure 7.31: SEM images of sintered LPSCF33428 pellet at 1000 ºC for 1 h a) and c) secondary b) and d) back scattered, e) and f) backscattered with yellow box used for pore size measurement (inset) for geometrical and Archimedes respectively g) thresholded image of yellow box region where black is taken to be the maximum geometrical pore structure h) thresholded image of yellow box region where black is taken to be the maximum Archimedes pore structure

7.6. Porosity Characterisation of the LPSCF33428, LNSCF33428 and NSCF6428 Nanopowders Sintered at 1000 ºC using BET method

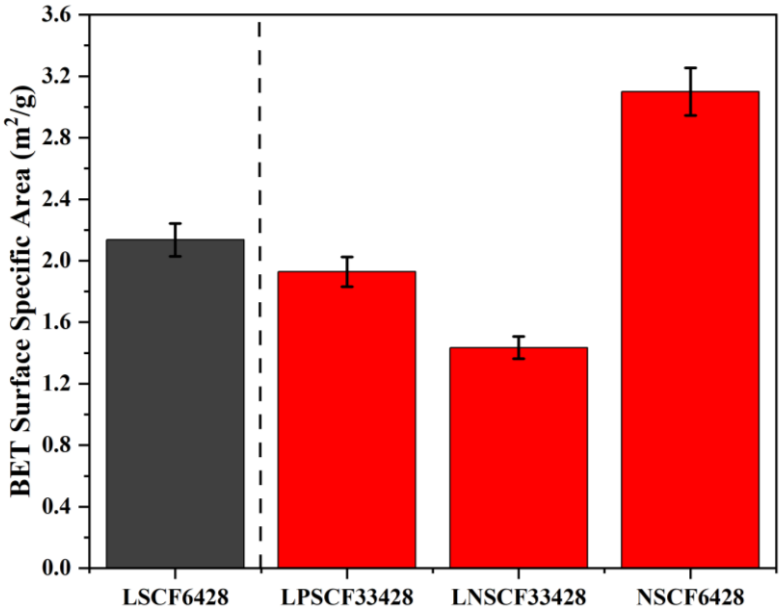

Figure 7.32: BET Specific Surface Area of the crushed sintering pellets of LPSCF33428, LNSCF33428 and NSCF6428 at 1000 ºC (red column) while also reported is the crushed LSCF6428 pellet sintered at 1000 ºC (black column) obtained from Section 5.5, Figure 5.18 with corresponding error bars.

Table 7.13: BET specific surface area values of the crushed LPSCF33428, LNSCF33428 and NSCF6428 pellets sintered at 1000 ºC and crushed LSCF6428 pellet sintered at 1000 ºC data obtained from Section 5.5, Table 5.8

Sintered Cathode Materials	BET specific surface area (m^2/g)
LPSCF33428	1.92 ± 0.068
LNSCF33428	1.43 ± 0.070
NSCF6428	3.10 ± 0.092
LSCF6428	2.14 ± 0.029

There is a significant decrease in BET surface area for LNSCF33428 of more than half compared with the NSCF6428 (Figure 7.32 and Table 7.13). This is consistent with the SEM images of mixed sintering in the LNSCF33428 only. The values obtained for the specific surface areas of LPSCF33428 and LNSCF6428 at 1000 ºC (as shown in Table 7.13) are lower than what has been reported in a previous study when LSCF6428 was directly sintered in air at 1000 ºC and when comparing LSCF6428 in this current work.[211] The explanation behind

the lower specific surface areas for the partially rare earth doped LSCFs is likely the presence of the glassy phase whose presence would increase relative to the pure LSCF because of the interdiffusion of dopants, either Pr or Nd as referred to by Benlia et.al. [232].

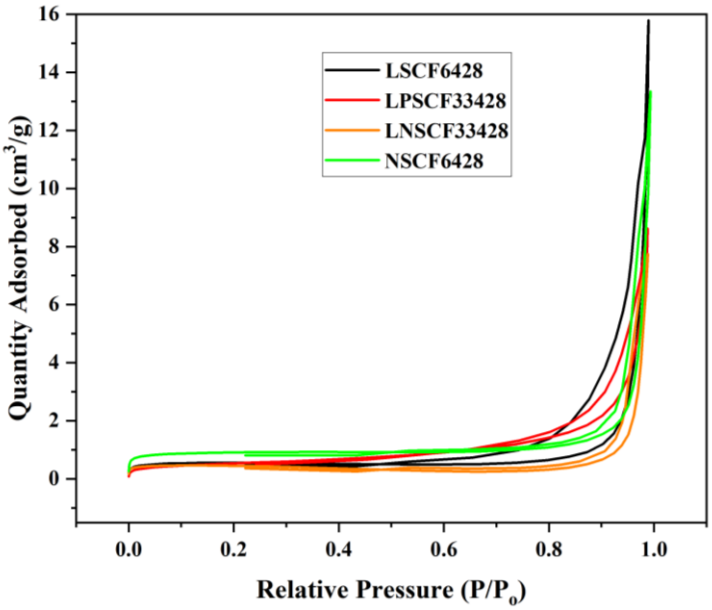

Figure 7.33: The BJH Nitrogen adsorption and desorption isotherm of crushed pellets sintered at 1000 ºC, LPSCF33428 (red line), LNSCF33428 (orange line), NSCF6428 (green line) and crushed LSCF6428 pellet sintered at 1000 ºC (black line) obtained from Section 5.5, Figure 5.16

Nitrogen adsorption isotherms of the sintered LSCF6428 samples were acquired and measured using the BJH method. Based on the IUPAC definitions, all 3 rare earth doped samples are Type IV in relation to their mesoporous structures and the shape of the hysteresis loops which are a combination of Type H1 and H3 hysteresis loops except for LNSCF33428 where it is only the H3 hysteresis loop representation (Figure 7.33). As can be seen from the isotherm, there is capillary condensation of the material taking place at relatively high pressure between the 0.75 to 1.0 (p/p_0), which is a representation of the H3 hysteresis loop for all three rare earth doped LSCF crushed sintered samples and is similar to the undoped sintered LSCF6428. [199]

Table 7.14: The total pore volumes and average pores sizes of LPSCF33428, LNSCF33428 and NSCF6428 sintered at 1000 ºC and LSCF6428 pellet sintered at 1000 ºC data obtained from Section 5.5, Table 5.7 (derived from BJH analysis of N_2 adsorption/desorption isotherms).

Sintered Cathode Materials	Total Pore Volume (sintered) (cm^3/g)	Average Pore Size (sintered)(nm)
LPSCF33428	0.013	26
LNSCF33428	0.012	59
NSCF6428	0.020	73
LSCF6428	0.024	69

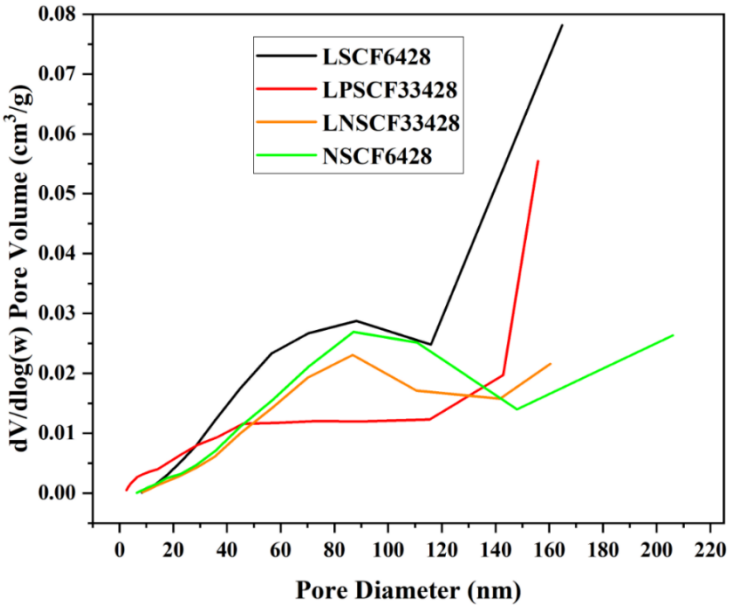

Figure 7.34: Pore size distribution of crushed pellets of LSCF6428 sintered at 900 ºC (red line), 1000 ºC (orange line), 1100 ºC (green line) and crushed LSCF6428 pellet sintered at 1000 ºC (black line) obtained from Section 5.5, Figure 5.17

For the LPSCF33428 and LNSCF33428, the curve shows a pore size distribution that ranges between 0 and 160 nm. While for NSCF6428, it ranges between 0 and 220 nm as shown in Figure 7.34. It can be seen that the total pore volume is lower for the three rare earth doped sintered LSCFs in comparison to the undoped sintered LSCF6428 as shown in Table 7.14 which is consistent with the difference in porosity and density measurements (Table 7.12) and may be due to an increase presence of glassy phase (Figure 7.28). However, the average pore size for the materials is not considered to be significantly different (based on the distribution of pore diameters in Figure 7.34).

Summary – Chapter 7

Sintering of LPSCF33428, LNSCF33428 and NSCF6428 rhombohedral phase ceramics has been achieved at 1000 ºC. With the Nd doped LSCF materials (LNSCF33428 and NSCF6428), there is a significant increase in porosity to a final value of 39-40%. For all rare earth doped ceramics i.e. LPSCF33428, LNSCF33428 and NSCF6428, the total pore volumes and final grain sizes are lower than for the undoped LSCF6428 sintered at the same temperature of 1000 ºC. The influence of the rare earth dopants upon the LSCF perovskite composition is thought to inhibit densification and grain growth compared to the undoped material. Overall though, the sintered rare earth doped LSCF materials produced are potentially suitable as cathodes for IT-SOFCs given that all the materials have a primary rhombohedral phase similar to the undoped sintered LSCF6428 and with an average crystallite size of < 100 nm, porosities in the range 20-40 % and pore sizes of <100 nm.

8. Three Dimensional Microstructure Characterisation, Magnetic Properties and Electrical Properties of $La_{0.6}Sr_{0.4}Co_{0.2}Fe_{0.8}O_{3-\delta}$, $La_{0.3}Pr_{0.3}Sr_{0.4}Co_{0.2}Fe_{0.8}O_{3-\delta}$, $La_{0.3}Nd_{0.3}Sr_{0.4}Co_{0.2}Fe_{0.8}O_{3-\delta}$ and $Nd_{0.6}Sr_{0.4}Co_{0.2}Fe_{0.8}O_{3-\delta}$

8.1. FIB-SEM Characterisation of the LSCF6428, LPSCF33428 ceramic pellets sintered at 1000 ºC

As described in the previous chapters, 5 and 7, the cathode pellets of the LSCF6428, LPSCF33428, LNSCF33428 and NSCF6428 that were sintered at 1000 ºC have been examined so far to obtain information on the phases, elemental compositions, microstructures and porosities of the crushed sintered pellets. For the sintered LSCF6428 (sintered at 1000 ºC for 1 hour), the mean crystallite size was 70 nm by XRD line broadening analysis, and the mean pore size was 68 nm as obtained by nitrogen porosimeter analysis.

Information obtained from the analysis so far came from only the crushed sintered pellets or the top surface. Up to here, it has been assumed that the microstructure is homogeneous e.g. grain phase, grain size distribution, elemental distribution and pore sizes do not vary across the pellets. This includes features that may well result from surface effects such as Sr segregation and resulting phase distributions. Sr segregation is a major concern for the LSCF6428 cathode

since operation is at elevated temperatures (> 600 ºC) and in oxidising environments both of which may influence the surface composition and structure of the perovskite oxide, potentially leading to formation of secondary phases and altering the performance of the cathode. This is confirmed by prior work it has reported that the temperature and time of the sintering can influence the microstructure by either the formation of secondary phases (as referred to in Chapter 4 and 5) or by modification of the main perovskite phase at exposed surfaces.[236-238] Ultimately, the long term the effect of elemental segregation can greatly affect the stability of the performance and the established mechanisms of the oxygen reduction reaction between the surface and bulk microstructure. [236-238] Therefore, detailed microstructure data across a sintered ceramic are an essential requirement to provide a direct link between structure and performance of the cathode material for SOFCs.[238]

FIB-SEM serial (cross-)sectioning has emerged as an effective route to 3D tomography characterisation of microstructures in LSCF6428 based materials to examine the effect of Sr segregation and to see if any secondary phase formation is present, both of which can significantly hinder the ORR performance.[238-240] Therefore, FIB-SEM sectioning with additional EDX will be used here for the LSCF6428 and LPSCF33428 materials sintered at 1000 ºC to determine the distribution of secondary phases, grain size plus porosity through the materials and link these to any Sr and Fe segregation. Nd based cathodes were not characterised by FIB-SEM due to time constraints.

FIB-SEM sectioning of the LSCF produced a serial dataset consisting of a total of 1000 cross section images that were taken and extracted as volumetric data. The data were used to determine how the sintering behaviour influences the distribution of grains, pores and phases of the LSCF6428 and LPSCF33428 pellets by selecting several areas of interest of the microstructure across the pellet. The use of EDX on a section helps determine if secondary phase formation has occurred by identifying Sr and Fe segregation in either the LSCF6428 or LPSCF33428 as shown in Figures 8.1 and 8.2.

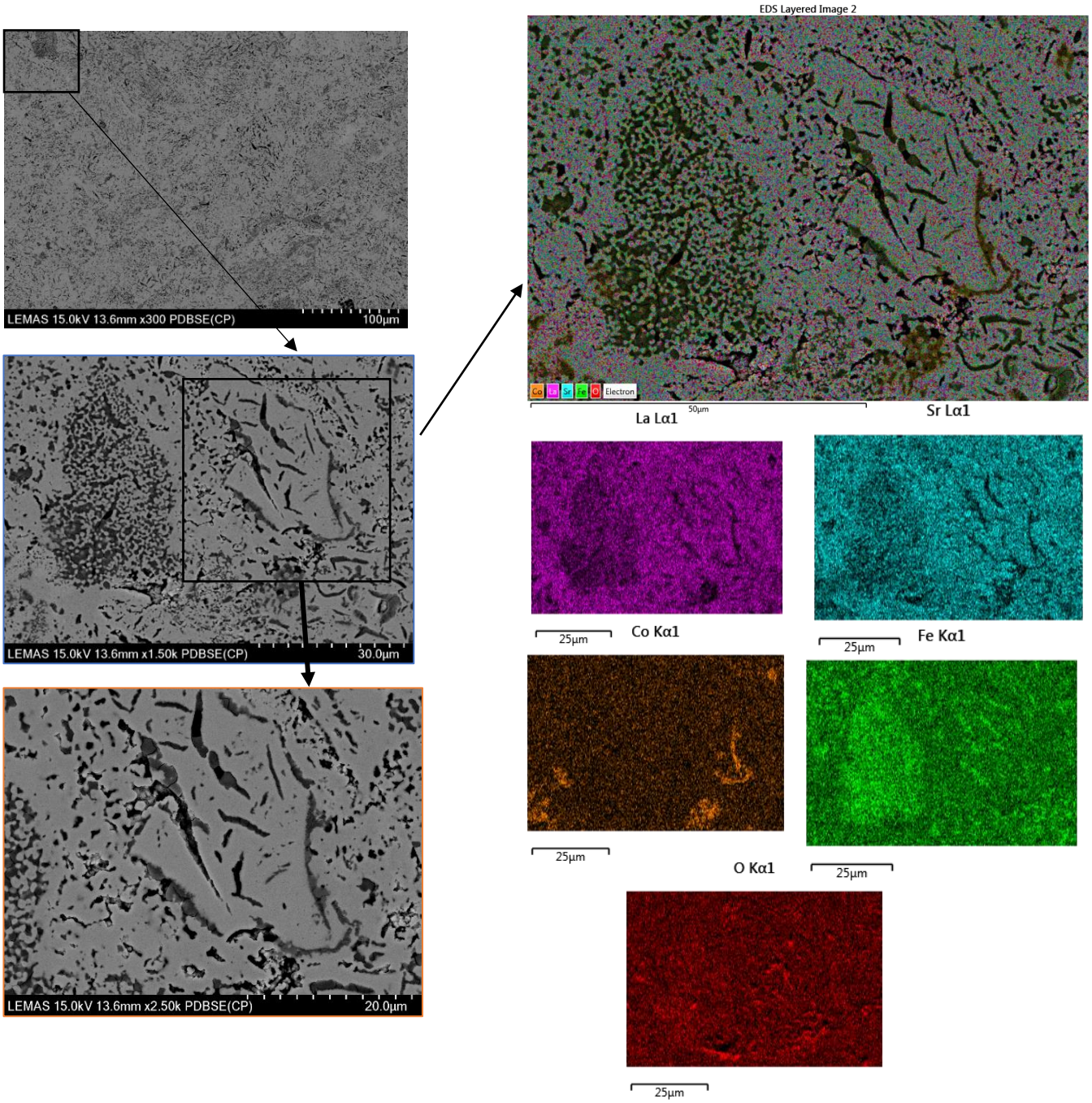

Figure 8.1: SEM, backscattered electron image of the polished and etched surface of a LSCF6428 pellet sintered at 1000 ºC for 1 h. EDX elemental maps of the sintered LSCF6428 showing the presence of all the key cations for LSCF 6428 with elemental maps showing some excess Fe occurring at the smaller size grains located around the Sr and La deficient regions but otherwise a homogenous distribution of the LSCF6428 elements (above).

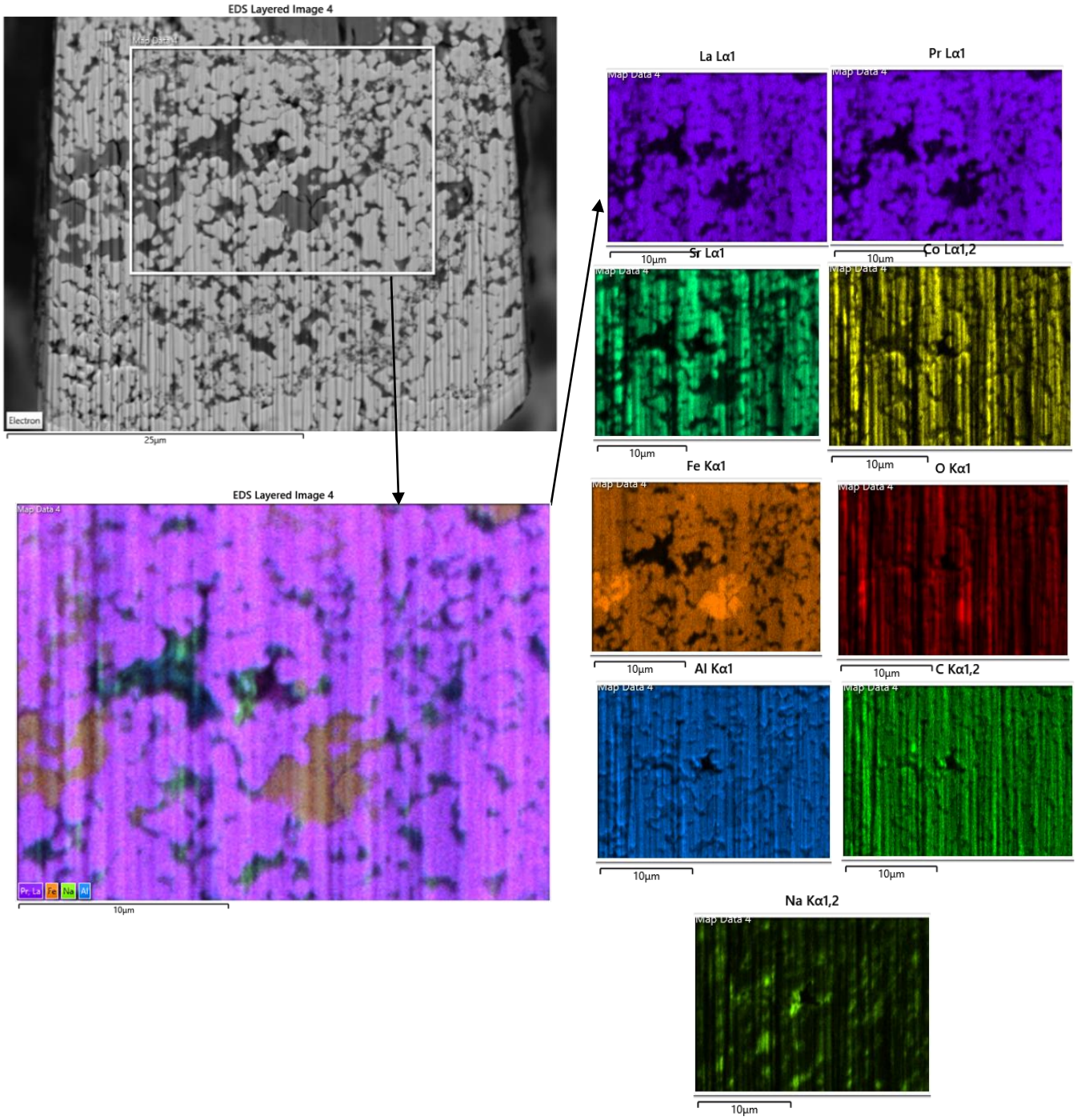

Figure 8.2: FIB-SEM, backscattered electron image of a plasma FIB sectioned LPSCF33428 pellet sintered at 1000 ºC for 1 h. EDX elemental maps showing some excess Fe occurring at the smaller size grains located around the Sr, La and Pr deficient regions but otherwise a homogenous distribution of the LPSCF33428 elements (above)

It can be seen from both the LSCF6428 and LPSCF33428 from Figure 8.1 and 8.2 respectively that cross-sectional images selected at lower magnification and examined further at high magnification reveal the presence of at least one secondary phases. The C and Al obtained from

the LPSCF33428 EDX is due to a carbon pad and an aluminium support rod (this sample was also used for XCT analysis, described in section 8.2). The EDX mapping clearly shows that the La, Pr, Sr and Co are homogeneously distributed throughout the large grained phase (white) of the microstructure across both the LSCF6428 and LPSCF33428 pellets. While iron is concentrated in specific areas of the microstructure for both the LSCF6428 and LPSCF33428, where either the finer crystalline grains or a matrix phase are formed respectively (dark grey contrast). He el. al. used STEM-EDX to detect Sr segregation between a LSCF6428 ceramic synthesised by sol gel processing and a yttria stabilized zirconia YSZ substrate. It was found there was a formation of a strontium rich layer (SRL) at the interface of the LSCF/YSZ and interface after polarisation for 12 hours and when examined at the interface (thickness 20 mm), there was presence of Fe and La in the thick SRL.[238] The information suggests that the presence of the Fe and La has been caused by the disintegration of the LSCF from the effect of Sr segregation. In this work excess iron content was detected at the surface of sintered LSCF by quantification of SEM-EDX spectra in the previous Chapter. Here the use of EDX elemental mapping via 3D FIB-SEM confirms the presence of excess iron content at the surface and within the bulk composition of the LSCF6428 and LPSCF33428 when sintered at 1000 ^{o}C. To determine if the second phase influences the porosity for the LSCF6428 within the bulk microstructure as discussed in previous work, the polished pellet was analysed further for pore connectivity within the sintered LPSCF33428 pellet. [239-240]

In the previous Chapters (4 and 6), porosity has been examined from both a micro and nano scale using XCT and BET respectively for crushed, calcined nanopowders. 12 representative cross sectional images from across the whole slice and view section of the LSCF6428 pellet sintered at 1000 ^{o}C were selected to illustrate how the porosity and microstructure are varied throughout the whole pellet, as shown in Figure 8.3.

1.Slice 10/1014

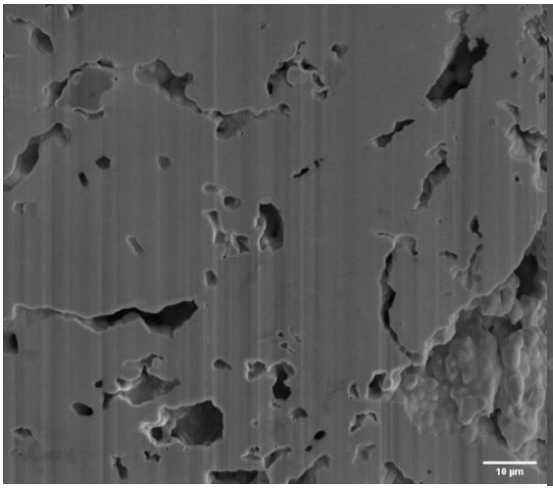

2. Slice 68/1014

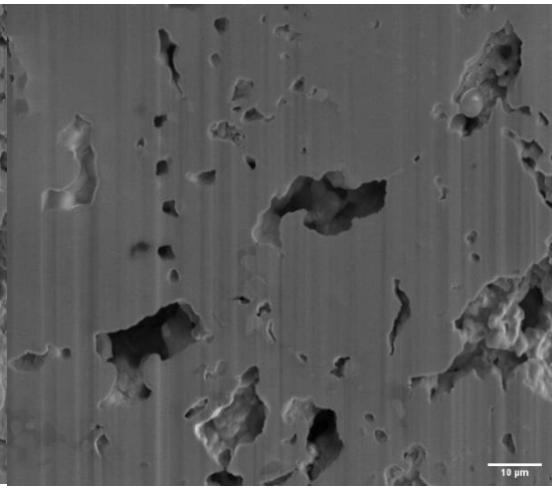

3. Slice 155/1014

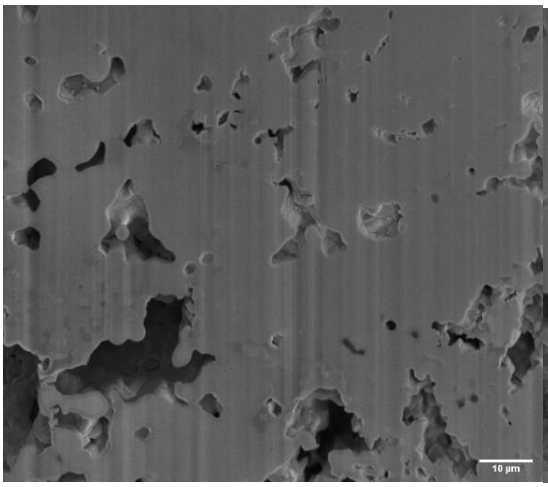

4. Slice 218/1014

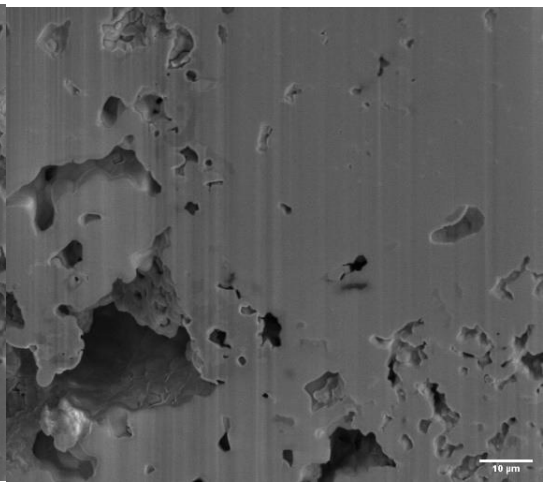

5.Slice 326/1014

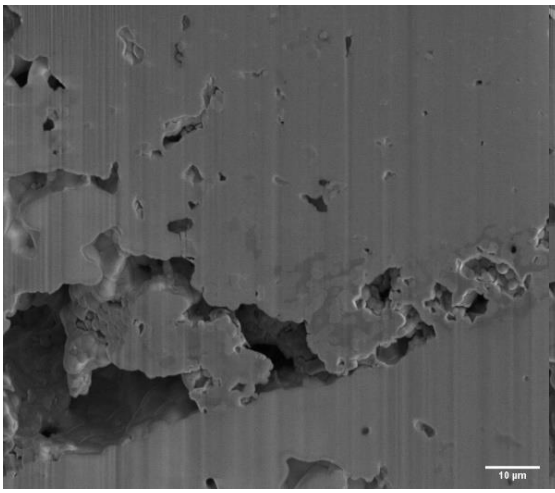

6. Slice 416/1014

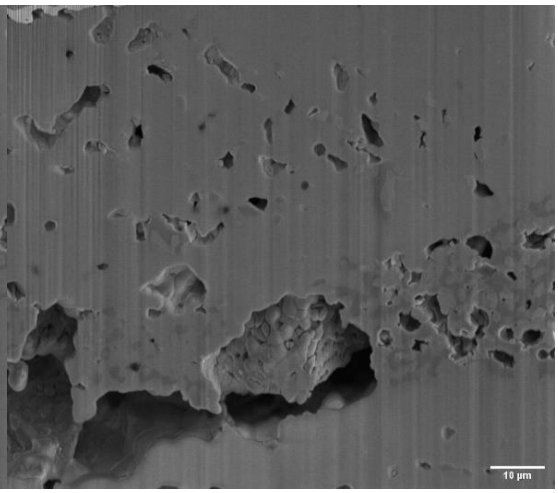

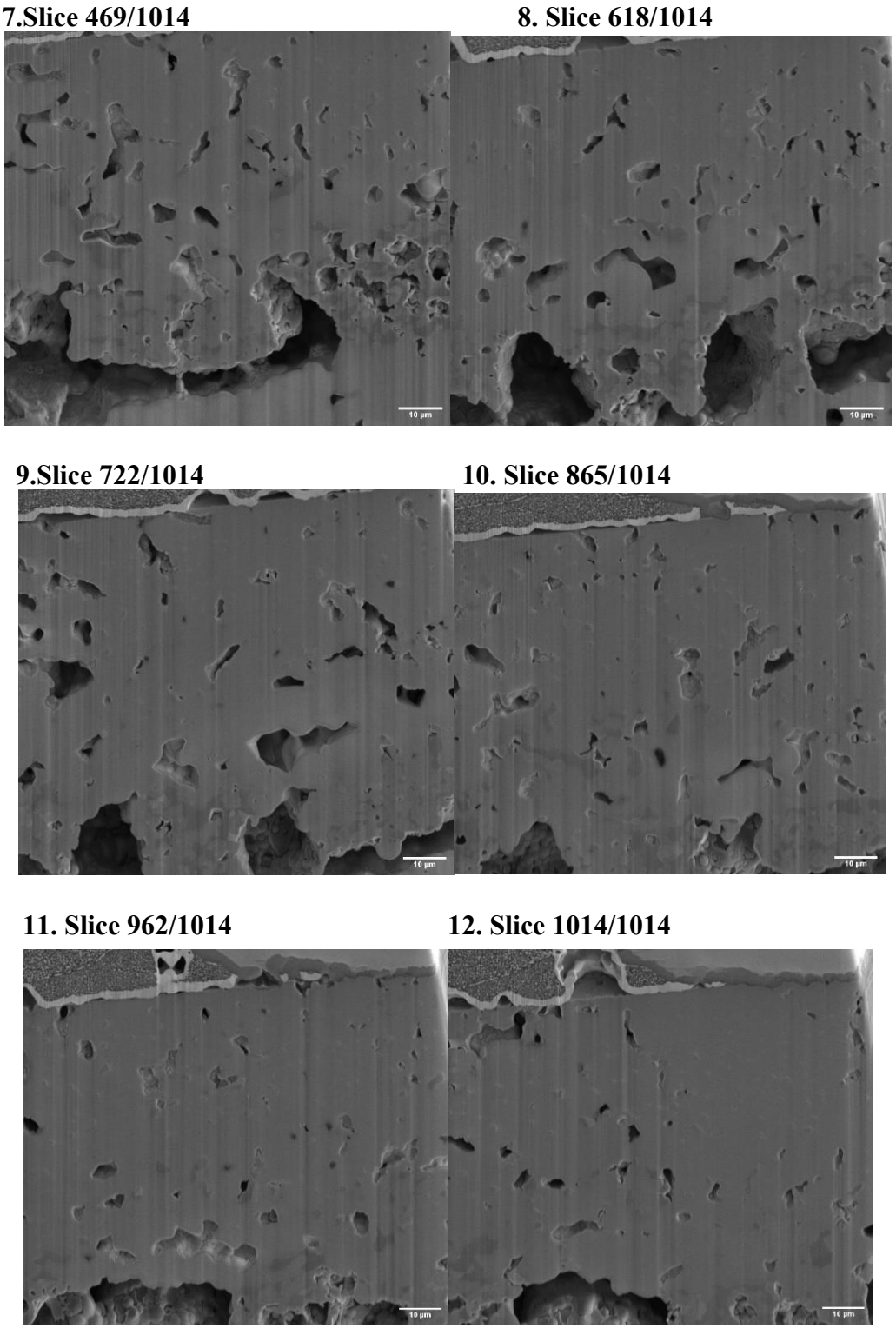

Figure 8.3: FIB-SEM slice and view SE images of freshly sliced sections of the LSCF6428 pellet sintered at 1000 ºC (sliced by Ga ion FIB) with the slice number given above each image (1014 slices of approximately 20 nm thickness each were cut in total). The porosity of 12 areas of interest from the surface, subsurface, in the middle and at the end of pellet are shown.

It can be seen from the slice and view images how the porosity varies greatly across the whole pellet of LSCF6428 (Figure 8.3). It confirms the varied densities of the microstructure, giving a complex, heterogenous network of porosity that meets the SOFC application criteria of 20-40% for LSCF6428 cathodes. Chen et. al., used FIB-SEM to determine how the porosity influences the mechanical properties of LSCF6428 porous ceramic films and bulk samples that were sintered between 900 ºC and 1200 ºC.[241] In relation to this work using FIB-SEM, Chen et al compared the difference of porosity levels between the film and bulk samples when sintered at the same temperature. It also showed how the difference of porosity levels between the film and bulk samples were consistent with the microstructure in relation to porosity and grain structure heterogenous network of porosity and grain structure was witness in the bulk sample which did not occur with the film. [241]

1.Slice 10/1014

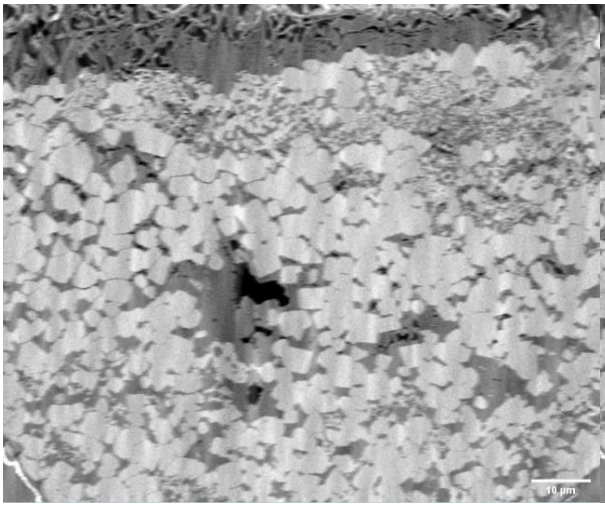

2. Slice 68/1014

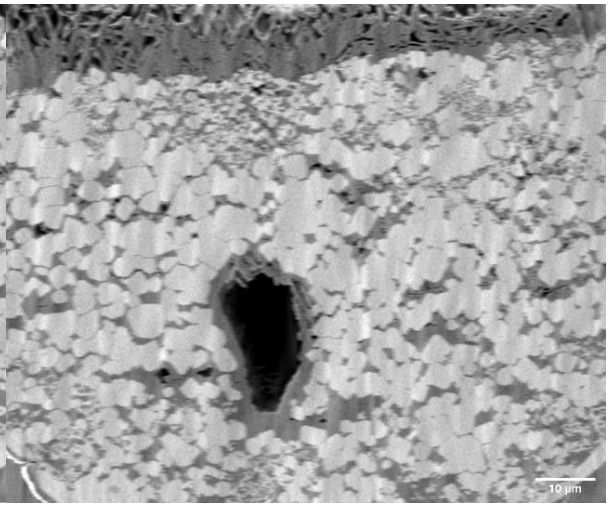

3. Slice 218/1014

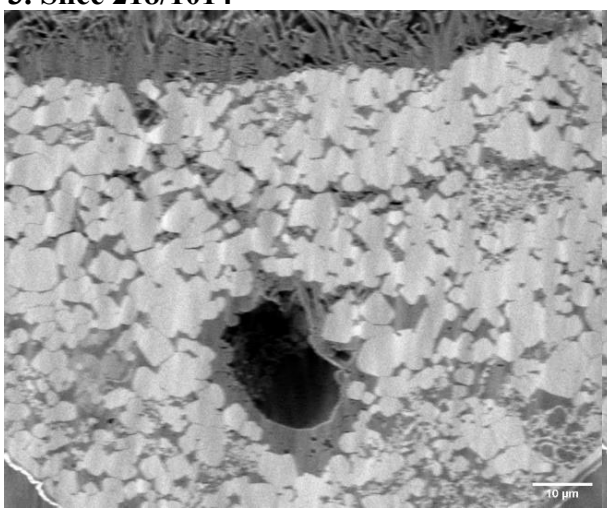

4. Slice 326/1014

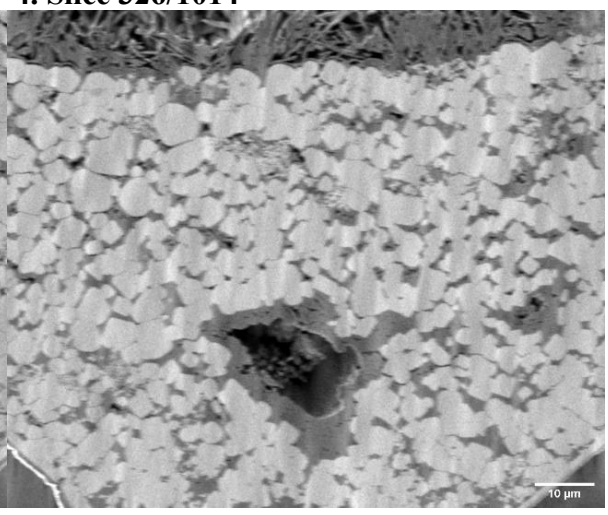

5.Slice 378/1014

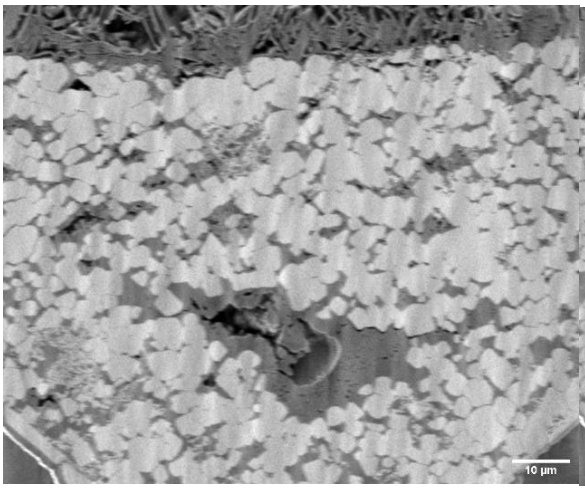

6. Slice 469/1014

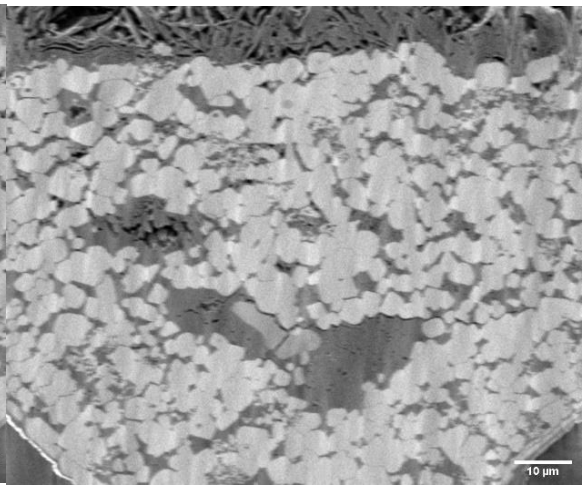

7.Slice 618/1014

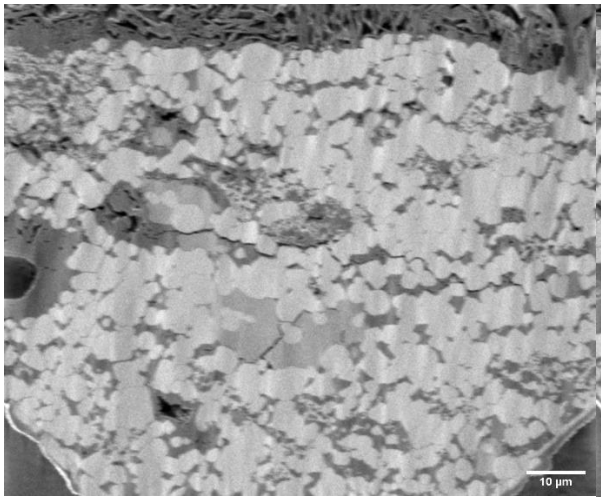

8. Slice 722/1014

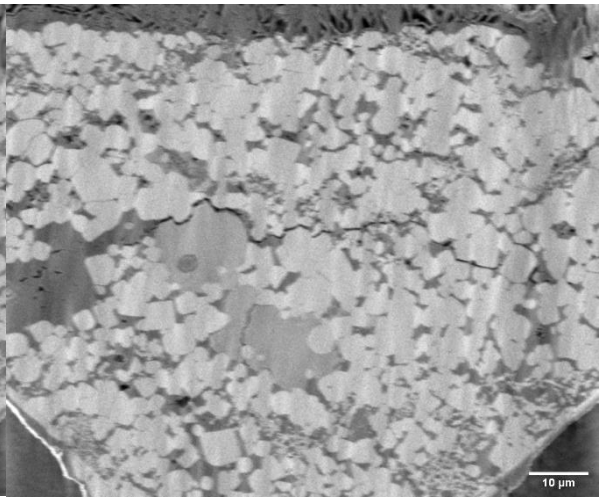

9. Slice 820/1014

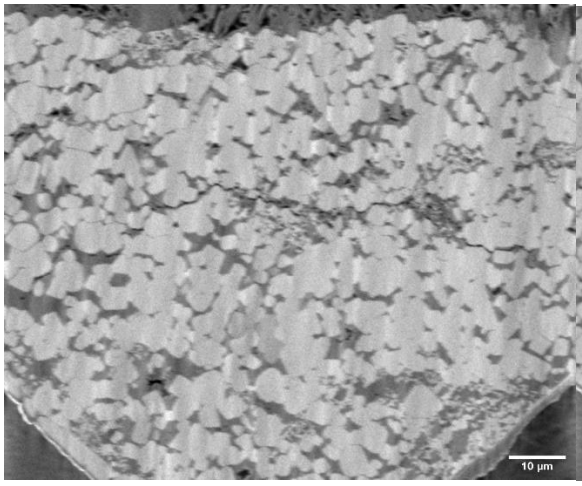

10. Slice 865/1014

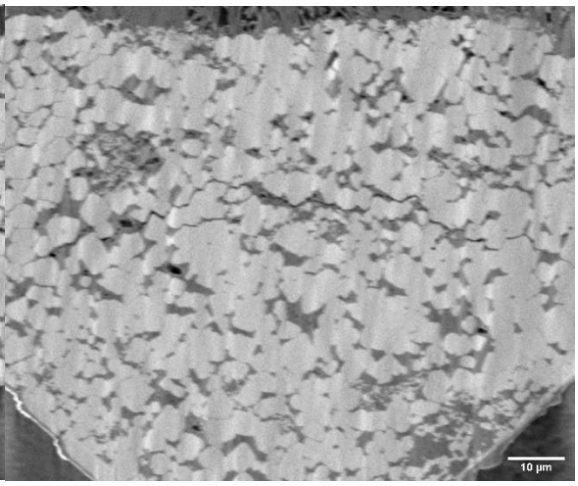

11.Slice 925/1014 **12.Slice 1014/1014**

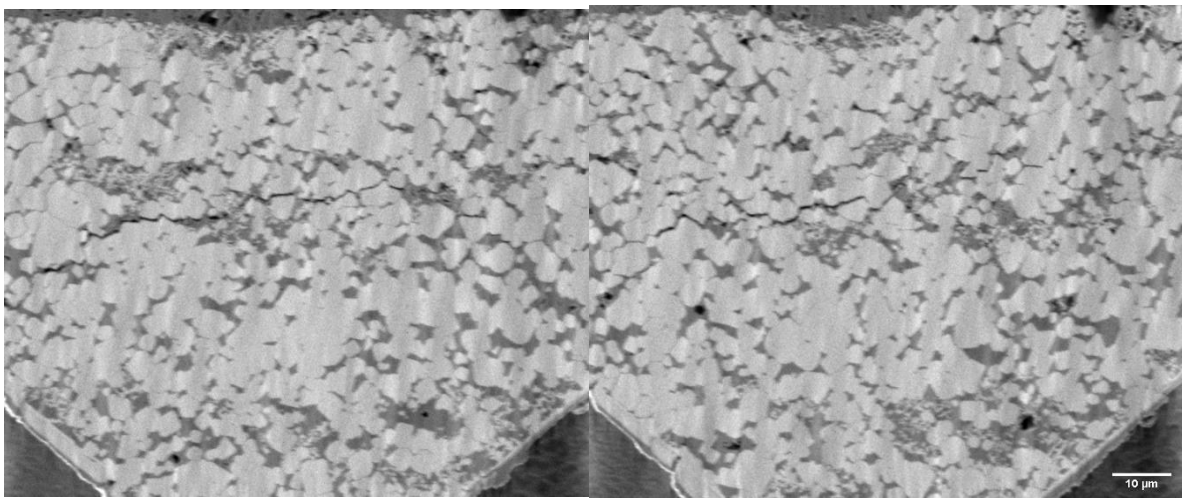

Figure 8.4: FIB-SEM slice and view BSE images of the LPSCF33428 pellet sintered at 1000 ºC sliced by plasma FIB. Pores and grain structure of 12 areas of interest from the surface, sub surface, middle and end of the pellet are shown, where pores are black, the matrix phase is white and a secondary phase is dark grey.

In a similar manner to the LSCF6428 the porosity, density and grain structure of the microstructure of LPSCF33428 have so far been analysed using XCT, surface SEM and bulk density measurements - Archimedes and Geometrical (Chapter 7). Here FIB slice and view reveals how grain sizes, porosity and phases vary across the sintered bulk composition of the LPSCF33428 sintered at 1000 ºC; selected cross-sectional images reveal microstructural inhomogeneity as shown in Figure 8.4. In line with what has been observed with the FIB-SEM EDX, identifying the secondary phase, rich in iron in LPSCF33428 (Figure 8.2). The presence of the secondary phase is seen throughout the LPSCF33428 sectioned microstructure. The formation of this and other secondary phases (of mixed grey levels in Figure 8.4) is potentially due to incomplete sintering and different grain sizes at 1000 ºC.

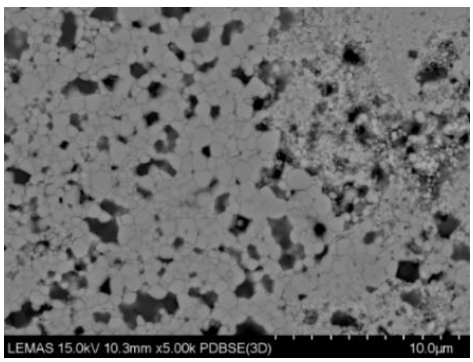

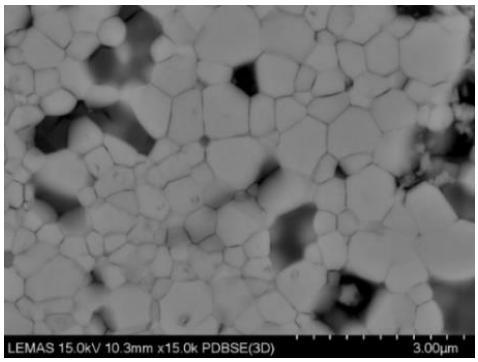

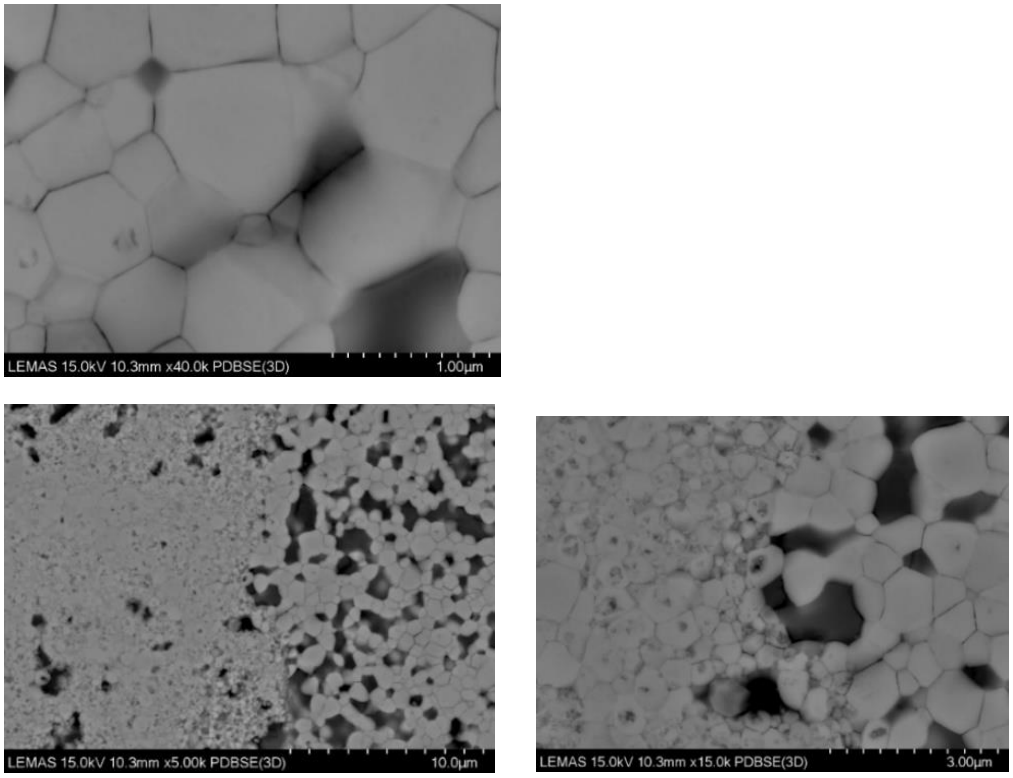

Figure 8.5: SEM based backscattered electron images of a mechanically polished and etched LSCF6428 pellet sintered at 1000 ºC revealing grain sizes and structure in the pellet. Areas of interest – smaller grain/crystallite sizes from a nano scale (of the iron-rich secondary phase in relation to Figure 8.1) and formation of larger matrix grains at a size in the micron scale.

Similar to the LSCF6428 (Figure 8.1), there is a mixture of fine and coarse grains amongst the sintered LSCF6428 bulk composition, as seen by the microstructure in Figure 8.5. Therefore, the FIB-SEM reveals a complex mixture of micron scale and nano scale grains and pores which were not detected by XRD average crystallite size analysis and BET porosity measurements respectively, as discussed in Chapter 7.

The disadvantage of conducting FIB-SEM for cathodes due to its porous nature is that the microstructural changes in use e.g. degradation throughout the whole pellet cannot be analysed due to the destructive method of removing the sample by the ion beam.[41] Therefore, to enable the examination of the microstructural changes of the sample directly in a non-destructive manner, there have been several papers that investigated the three-dimensional microstructure of anode components, Ni/YSZ of the SOFCs using nano-CT. Izzo et al. and Sheering et al. reconstructed the volume data of this nano-CT and visualised the bulk anode microstructure using 3D images to examine porosity, pore size distribution or pore volume fraction and make a direct comparison with other porous characterisation techniques such as Mercury porosimeter and FIB-SEM.[41][242] There has been XCT work reported for the cathode composite of

LSM-YSZ by Guan et al. who investigated the effect of sintering time and temperature and the evolution of the internal (bulk) microstructure of LSM reporting porosity and volume to surface area of the material. [243] Although, there was no direct comparison with other characterisation techniques that operate across the micro and nano scale i.e. the work may have been resolution limited. The LSM cathode is only an electronic conductor cathode material where as LSCF is a potential MIEC cathodes for IT-SOFCs so because pores and interfaces are more critical for ion conductivity it would be good to use nano-CT to investigate its microstructure and investigate how the rare earth dopant affect the LSCF6428 internal (bulk) microstructure and its microstructural parameters such as porosity in order to make a comparison with the other characterisations such as BET and FIB-SEM. The sintered LPSCF33428 pellet will be examined using the nano-CT to analyse in depth the pores of the pellet. Parameters such as pore volume fraction, pore size distribution and the aspect ratio (contributes to the pore volume) will be extracted.

8.2. Nano-CT Characterisation of the sintered LPSCF33428 pellet at 1000 ^{o}C

Nano CT was conducted to provide the 3D reconstruction of sintered LPSCF33428 without slicing and this was then destructively viewed by FIB-SEM (Figure 8.4). There have been no past studies investigating the inhomogeneity of densification and pores of sintered cathode pellets in relation to its bulk composition using nano-CT. However, there has been analysis of pores in shale gas samples by Garum et al., where comparison between FIB-SEM, nano -CT and nitrogen porosimeter (BJH method) were investigated to determine the populations of pores in relation to the volume and shape of the pores. [244] From the previous sections, where 20 individual grains were selected from calcined nanopowders and examined by micro-CT, pores greater than 1 mm were located in the grains and analysed for pore volume fraction (%) (Chapter 7). For the LPSCF33428 pellet however, using nano-CT results in the whole pellet being reconstructed as a 3D structure and 10 areas of interest with Cartesian coordinates (xy, xz and yz) of the pellet were analysed to determine the pore volume fraction (%) as shown in Figure 8.6 and from Table 8.1 [245]

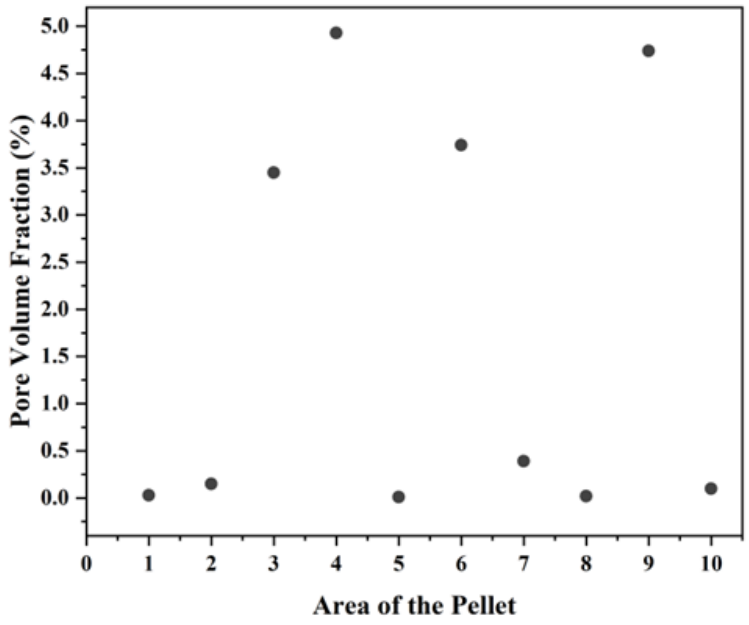

Figure 8.6: Pore Volume Fraction (%) of the LPSCF33428 pellet sintered at 1000 ºC across the 10 different areas of the pellet. Data were extracted from the images as shown in Figure 8.7.

Table 8.1: Data analysis of the selected area of the pellet and its corresponding pore volume fraction (%) Areas 1,2, 5, 7,8 and 10 are located from the centre whereas areas 3,4, 6 and 9 are from the edges in relation to the xz coordinates of the LPSCF33428 pellet sintered at 1000 ºC

Area of the pellet	**Location of the Pellet**	**Pore Volume Fraction (%)**
1	Centre	0.03
2	Centre	0.15
3	Edge	3.45
4	Edge	4.93
5	Centre	0.01
6	Edge	3.74
7	Centre	0.39
8	Centre	0.02
9	Edge	4.74
10	Centre	0.1

The essential microstructural parameter information of porosity obtained by nano-CT is shown in Figure 8.7 of the six different selected areas and should form a link with the BET and BJH work given in Chapter 7 to allow a better understanding of the porous nature of the internal

microstructure of the LPSCF33428 pellet. In addition, how the effect of sintering influences inhomogeneity within the bulk composition of the LPSCF33428 pellet as shown by FIB-SEM from Figures 8.2 and 8.4 can also be used.

0.01 % xy **0.01 % xz** **0.01 % yz**

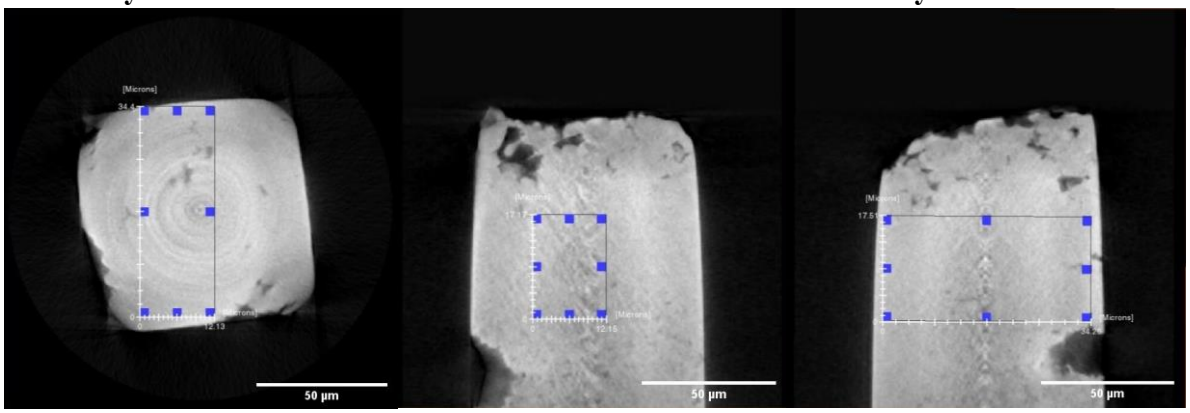

0.02 % xy **0.02 % xz** **0.02 % yz**

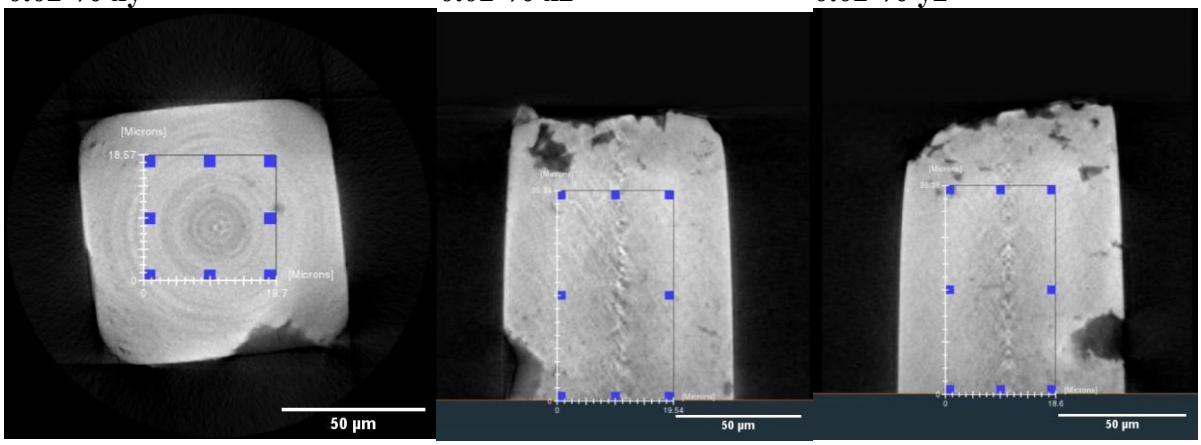

0.15 % xy **0.15 % xz** **0.15 % yz**

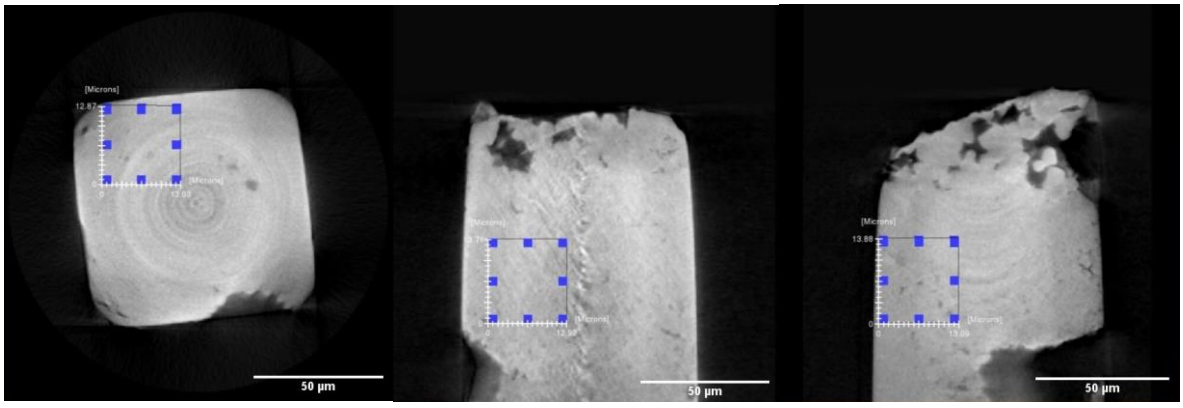

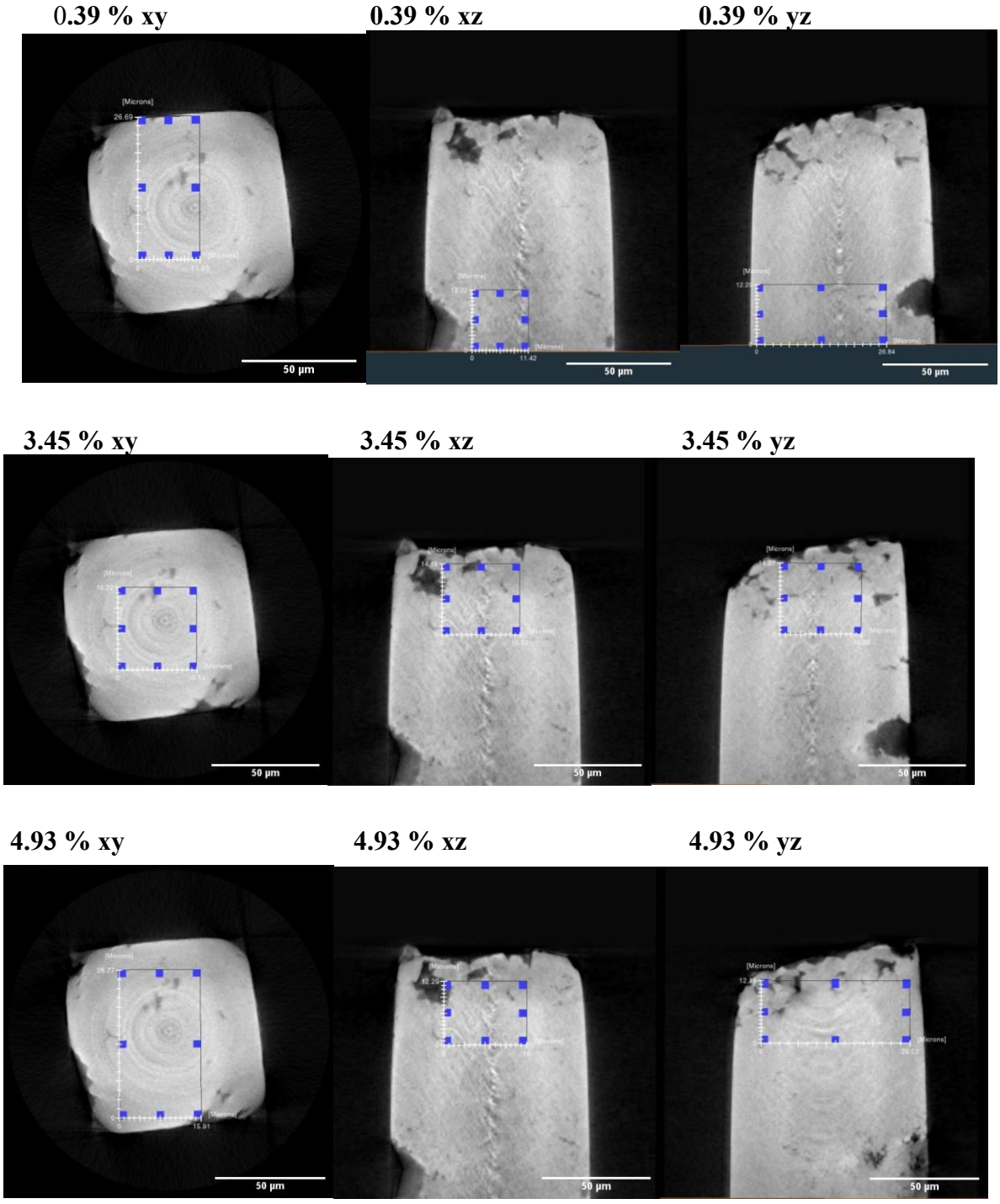

Figure 8.7: Nano-CT images of the areas of interest of the 6 different areas analysed at 3 cartesian coordinates (yz, xz and xy) of the sintered LPSCF33428 pellet sintered at 1000 ºC. Pores are seen as black and the bulk, matrix material white and the 6 analysis areas cover the edges and centre of the pellet. 0.01% from Area 5, 0.02% from Area 8, 0.15% from Area 2, 0.39% from Area 7, 3.45% from Area 3 and 4.93% from Area 4

The nano-CT for the LPSCF33428 pellet allows the whole pellet to be examined through taking 2D projection images without the effect of degradation, such that connectivity within the bulk microstructure, especially between small-scale pores is unaffected.

It can be shown clearly from Figure 8.6 in reference to the images of xz coordinate from Figure 8.7, where the different locations of the LPSCF33428 pellet are proportional to the pore volume fraction (%) located within the internal microstructure of the LPSCF33428 pellet. There is a clear trend that can be extracted from Figures 8.6 -8.7 and Table 8.1. The pore volume fraction (%) of above 3% occurs at the corners/edges or sub core sections of the sintered LSCF33428 pellet suggesting a decrease in densification here. While for the sections located at the core/centre of the pellet, there is a significant decrease in pore volume fraction as shown in Figure 8.7 consistent with increased densification. In comparison to the BJH where nitrogen adsorption was conducted to measure the internal surfaces of the pores, the use of the nano-CT enabled the examination of a 3D microstructure of the cathode to confirm that it less homogenous than suggested. Moreover, the relationship suggests that the timing and temperature of the sintering behaviour influences the inhomogeneity of densification throughout the whole internal (bulk) microstructure of the pellet. Therefore, the nano-CT information of the sintered pellet pore volume fraction (%) bridges the gap in relation to the varied densities and porosities previously examined by FIB-SEM (Figure 8.2 and 8.4), and the density measurements made in Chapter 7. The nano-CT measurements indicate that the frequency of the number of pores in relation to individual pore size may greatly vary from the surface to the bulk of a pellet.

The threshold approach was used to analyse the pore size distribution across the several different sections located within the bulk composition of LSCF33428 pellet as shown in Figure 8.8.[145][194]

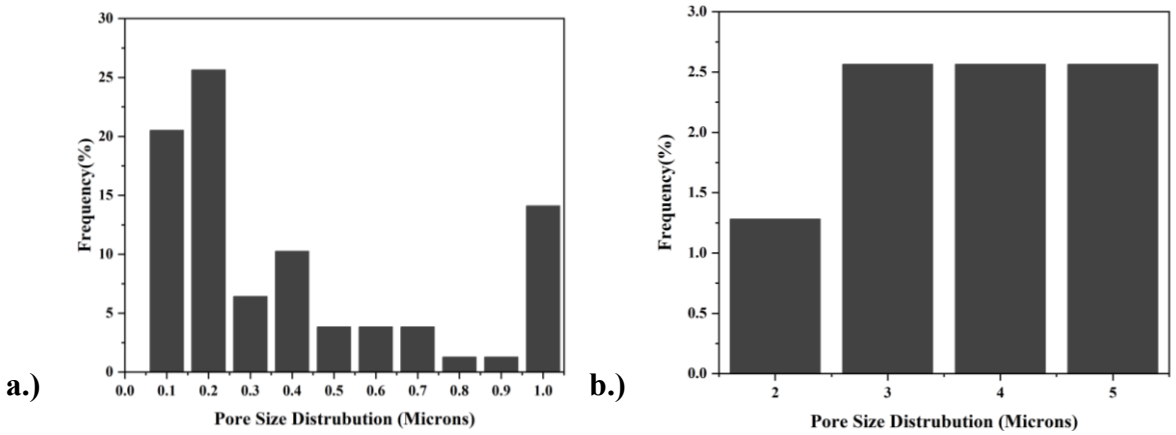

Figure 8.8: Pore Size Distribution of the LPSCF33428 pellet sintered at 1000 ºC against Frequency of pores of a) 0.1- 1 b) 2-5 microns

The pore size distribution of the sintered LPSCF33428 has a high frequency of pore sizes concentrated between 0.1 to 0.4 μm, suggesting a significant fraction of nanopores as well as a similar number (frequency of) large pores that are 1 μm (Figure 8.8a) although there was a significance decrease when greater than 1 um. While the BJH analysis in Chapter 7 provides a smaller range of pore sizes between 12.5 nm and 75 nm it is suggested the nano-CT detects these and larger pores. The BJH analysis however was carried out on crushed sintered LPSCF33428 pellet material, and the resulting H3 hysteresis loop suggested slit shaped pores.[199] Aspect ratio can be also measured on the nano-CT data to investigate this further.

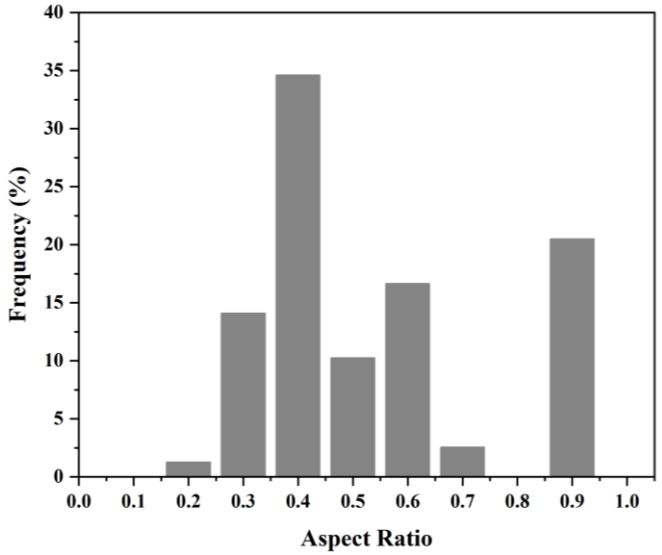

Figure 8.9: Aspect Ratio of the sintered LPSCF33428 pellet at 1000 ºC.

The aspect ratio has been a popular microstructure parameter used in past work to investigate the pore network of the shale used for gas diffusion. In reference to other work, researchers

have been obtaining convenient results through the representations of pores as ellipsoid with cauterising axes. [145][194] Obtaining the aspect ratio for the LPSCF33428 pellet from within the internal microstructure involves the calculation of the ratio of the largest to smallest length measurements across a pore. The aspect ratio can be defined from the calculation as one of either two forms, flat shaped penny oblate (aspect ratio less than 1) or needle shaped prolate (aspect ratio greater than 1). Since the BJH has its own limitations due to the shape of the individual pores which are not accounted for, the aspect ratios within the pellet will be obtained using the same threshold approach as the pore volume fraction from the 10 different areas within the internal microstructure. This, therefore, should provide a reasonable link to the previous sections where BJH using nitrogen absorption was used to analyse the average pore volume of the crushed sintered pellet. As shown in Figure 8.9, the aspect ratio varies greatly from 0.1 to 1 but the frequencies (%) that have been obtained are concentrated such that an aspect ratio of 0.4 has a frequency of 35% and an aspect ratio close to 1 has a frequency of 20% (Figure 8.9). The nano-CT indicates there is a greater presence of the oblate shape rather than the prolate shape pores, which is essential in determining the connectivity and the surface area of the pores within the internal microstructure of the pellet. FIB-SEM supports this finding (Figure 8.6)

Although, the limitations in the use of nano-CT are the resolution and that the voxel sizes set (65 nm) are bigger than for the BET measurements, the nano-CT that provides a bridge between the prior bulk pore and density analysis (Chapter 7) and the nano-to microscale analysis of FIB-SEM (Figure 8.1-8.5).

Overall, the sintered materials produced here are somewhat inhomogeneous in relation to varied porosity, particularly between the edge and centre of a sintered LPSCF33428 pellet (nano-CT data reveal this most clearly). At the edge of a pellet microscale pores dominate and Sr and Fe segregation are detected by SEM-EDX. FIB-SEM reveals that a secondary iron-rich phase is present throughout the whole LPSCF33428 sintered material and that fine grained nanomaterial is located near this phase while denser microscale grains of the main phase are seen further away, suggesting inhomogeneous sintering and corresponding porosity that follows this. However, towards the centre of a pellet nanoscale pores dominate by nano-CT, i.e. the core of a sintered pellet may be suitable for SOFC cathode material if the sintering were a bit more homogenous through acknowledging the mixed microstructure seen by FIB-SEM and the consistency of the bulk density measurements in Chapter 7.

8.3. Magnetic Properties of the crushed calcined nanopowders and sintered pellets of LSCF6428, LPSCF33428, LNSCF33428 and NSCF6428

Given the presence of the iron-rich second phase detected here by FIB-SEM, there has been prior analysis to determine how the concentration of iron in other perovskite chemical compositions such as $LaFe_xCo_{1-x}O_3$ and how it influences the structural parameters such as the tolerance factor and octahedra tilting. [246] The effects of the structural parameters of the perovskite oxide in relation to iron-based perovskite oxide cathodes such as $LaFeO_3$ and LSCF can influence the magnetic behaviour which could affect the electrical properties to the cathode performance for IT-SOFCs. [78][247] The iron has found to play a major role as G-type antiferromagnetic when located at the B cation site of the oxygen octahedra of a perovskite oxide in relation to the alignment of the magnetic interactions along the crystallographic direction. [135] There has also been work on rare earth doping for $LaFeO_3$ such as Sm^{3+} and Gd^{3+} which investigates how rare earth elements alter not just the structural properties but also the magnetic properties especially in recent work by Arman et.al. It was found to enhance the saturation magnetization, M_s due to the increase magnetic interactions not only from iron but from rare earth elements compared to $LaFeO_3$. [247-248] The cathode microstructure of LSCF and derivatives is also critical based on its size and shape as revealed here by SEM and micro-CT for nanopowders (Chapters 4 and 6) and FIB-SEM and nano-CT for sintered pellets (this Chapter). Although, there has been limited work with comparison between nanopowders and bulk perovskite oxide cathode materials, there has been work on other materials such as $MnFe_2O_4$ and $LaFeO_3$ nanostructures.[249-250] Therefore, measurements by VSM were investigated on both the crushed, calcined nanopowders from Chapters 4 and 6 and crushed sintered pellets from Chapters 5 and 7 for both undoped LSCF and rare earth doped LSCF to provide a direct link between how the effects of the iron, indicated in the FIB-SEM via EDX and rare earth doping influence the structural parameters measured from the previous chapters. The magnetization vs applied field for the crushed calcined nanopowders (chosen temperatures were 2K and 300K) and the crushed sintered pellets were analysed at 300K (RT only for the sintered pellets) as shown in Figures 8.10-8.11, 8.13. The ZFC-FC were also measured for the crushed calcined nanopowders as shown in Figure 8.12. The magnetic measurements are shown in Table 8.1-8.3. The magnetic anisotropy (K) is calculated as shown in equation 8.1.[251]

$$K = \frac{Hc * Ms}{0.96} \quad (8.1)$$

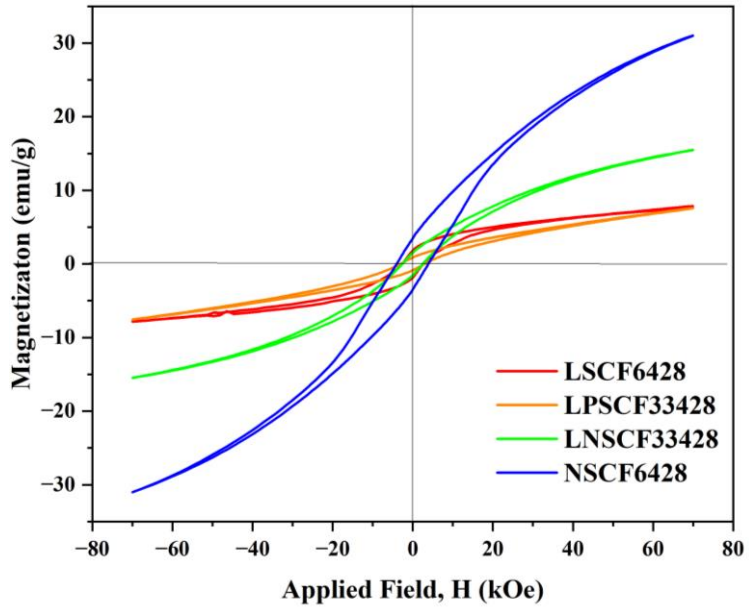

Figure 8.10: Low Temperature (2K) magnetic hysteresis loops (M-H) of crushed calcined nanpowders of LSCF6428, LPSCF33428, LNSCF33428 calcined at 800 ºC and NSCF6428 calcined at 775 ºC

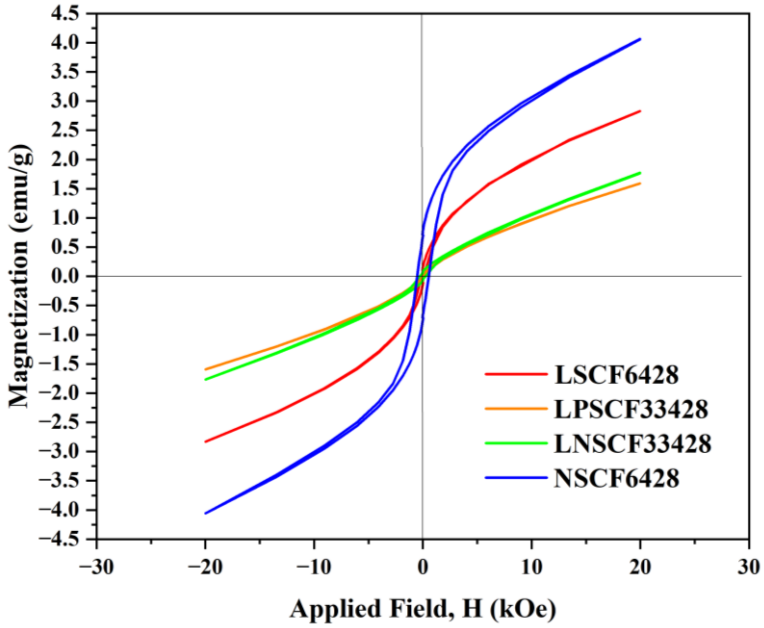

Figure 8.11: Room Temperature (300K) magnetic hysteresis loops (M-H) of crushed calcined nanpowders of LSCF6428, LPSCF33428, LNSCF33428 calcined at 800 ºC and NSCF6428 calcined at 775 ºC

Table 8.2: Magnetic parameters of low temperature (2K) of maximum magnetization saturation (M_s), positive direction coercivity (H_c+), negative direction coercivity (H_c-),

magnetization remanence (M_r) and magnetic anisotropy (K) of the crushed calcined cathode nanopowders

Calcined Cathodes – 2K	***M_s*** **(emu/g)**	***H_c+*** **(kOe)**	***H_c-*** **(kOe)**	***M_r*** **(emu/g)**	***K***
LSCF6428	7.65	2.66	-2.54	1.91	21.20
LPSCF33428	7.57	3.16	-2.97	0.89	24.91
LNSCF33428	15.48	2.60	-2.48	1.53	41.92
NSCF6428	31.04	3.98	-3.98	3.49	128.69

Table 8.3: Magnetic parameters of room temperature (300K) of maximum magnetization saturation (M_s), positive direction coercivity (H_c+), negative direction coercivity (H_c-), magnetization remanence (M_r) and magnetic anisotropy (K) of the crushed calcined cathode nanopowders

Calcined Cathodes - 300K	**M_s (emu/g)**	**H_c+ (kOe)**	**H_c - (kOe)**	**M_r (emu/g)**	***K***
LSCF6428	2.83	0.11	-0.10	0.13	0.29
LPSCF33428	1.20	0.03	-0.023	0.015	0.035
LNSCF33428	1.77	0.25	-0.20	0.086	0.46
NSCF6428	4.06	0.54	-0.53	0.77	2.28

Table 8.4: Magnetic parameters of room temperature (300K) of maximum magnetization saturation (M_s), positive direction coercivity (H_c^+), negative direction coercivity (H_c-), magnetization remnant (Mr) and magnetic anisotropy (K) of the crushed sintered cathode pellets at 1000 ^oC

Sintered Cathodes-300K	**M_s (emu/g)**	**Hc^+ (kOe)**	**Hc^- (kOe)**	**M_r (emu/g)**	**SQR = M_r/M_s**	**K**
LSCF6428	0.79	0.0044	-0.0026	0.0048	0.006	0.002
LPSCF33428	3.07	0.39	-0.40	0.78	0.25	1.25
LNSCF33428	1.62	0.026	-0.0019	0.19	0.12	0.043
NSCF6428	4.18	0.0095	-0.007	0.89	0.22	0.041

When the calcined nanopowders were analysed at room temperature (300 K), the shape of the M-H hysteresis loop is an S shape, as seen in Figure 8.10. It indicates antiferromagnet (AFM) behaviour due to presence of unsaturated magnetization at high fields with a weak ferromagnetic (WFM) component in accordion to the values of magnetization saturation (Ms) for both the undoped LSCF6428 and rare earth doped LSCF6428. The effect of the AFM, as referred to in other magnetic studies when iron is part of the perovskite oxide composition, is caused by the super exchange interaction of the Fe^{3+}-O_2-Fe^{3+}.While the WFM originates from a double exchange interaction between the iron ions. This is consistent with the other perovskite oxides cathodes doped with rare earth elements that have been studied such as $La_{1-x}Re_x FeO_3$ (Re = Nd, Sm and Gd), $Nd_{0.5}R_{0.5}FeO_3$ (R = La,Pr and Sm) and $La_{1-x}Pr_xFeO_3$.[251-252] The maximum magnetization for NSCF6428 is caused by an increase in effective magnetic moment by the Nd that is consistent with a study by Das et.al. which investigated the co-doping effect of Nd^{3+} and V^{5+} upon $LaFeO_3$.[253] However, in a study by Somvanshi et.al, when the content of Nd^{3+} exceeded 0.20 for the substitution of La^{3+} a sudden decrease in the Ms from 2 emu/g for 0.2 to 1.83 emu/g above was reported, due to unbalanced electron charges upon substitution of the La^{3+}. [252] That is consistent with the Ms of the LNSCF33428 where Ms is 1.77 emu/g, since the content of Nd^{3+} was 0.3, despite the Nd^{3+} having a significant effective magnetic moment as shown in Table 8.2. For LPSCF33428, the Ms was 1.20 emu/g for a content of content of 0.3 Pr^{3+}, the decrease in magnetization could have happened in the same manner as the LNSCF33428 as Pr^{3+} has a lower effective magnetic moment in this substitution.

For H_c, there is a shift in the hysteresis loop for the rare earth doped LSCF in comparison to the undoped LSCF from its origin from both the positive and negative direction as shown in Table 8.2. It is caused by an exchange bias effect which is exchange coupling due to the combination of AFM and FM interfaces – disorder and ordered spins which leads to spin glass like behaviour potentially due to the presence of the main phase and a second iron-rich phase, for both LSCF6428 and LPSCF33428, as seen by FIB-SEM EDX (Figure 8.1 and 8.2).[78][248][253-256]

While at the lower temperature region of 2 K in comparison to 300 K, the M-H hysteresis loops are wider but still with the presence of unsaturated magnetization at the high applied magnetic fields suggesting there is still AFM behaviour for both the undoped LSCF and rare earth doped LSCF. From the EDX in Chapter 7, when the Nd^{3+} content increases from 0.3 to 0.55, the 2 K

Ms is about 7.65 and 8.75 times greater for NSCF6428 and LNSCF33428 respectively compared to the Ms observed at a temperature of 300 K as shown in Figure 8.11. The effect of the sudden increase in Ms for Nd doped cathodes is due to a reducing thermal excitation for spin reorientations leading to an increase of the ferromagnetic component of the Nd doped cathode.[247-248][253] That is due to the non-magnetic La^{3+} where the lack of electrons in the 4f shell orbital compared to Nd^{3+} (where there are 3 electrons in the 4f shell), results in an increase of magnetic interactions, leading to enhanced magnetization for the Ms as shown in Table 8.3. The increase in the replacement of the La^{3+} by Nd^{3+} in the NSCF6428 is consistent with the change in structural tolerance factor and potential induction of tilting of the FeO_6 octahedra compared to the LSCF6428 and LPSCF33428. The NSCF6428 had the greatest Mr due to an increase in magnetic interactions coming from the Nd^{3+} ions along with the absence of nonmagnetic La^{3+}.[253] Therefore, to complete understand the effect the rare earth elements have on the magnetic behaviour, zero field cooling (ZFC) and field cooling (FC) curves are plotted for the crushed, doped-LSCF nanopowders in comparison to the crushed, undoped-LSCF nanopowders. across the entire temperature range from 2 K to above 300 K (Figure 8.12). This may also shed light on how the secondary iron-rich phase affects the magnetic properties of these materials.

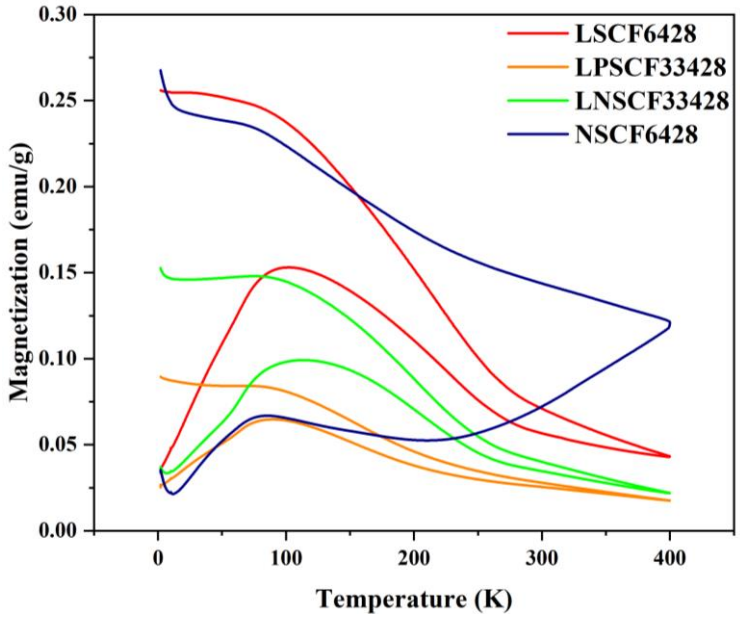

Figure 8.12: Temperature dependent ZFC and FC curves of the crushed, calcined nanopowders of LSCF6428, LPSCF33428, LNSCF33428 calcined at 800 ºC and NSCF6428 calcined at 775 ºC

Non overlapping ZFC and FC curves is known as a bifurcation and confirms the co-existence of a weakly ferromagnetic (WFM) and an antiferromagnetic (AFM) component that are irreversibly distinct from 400 K down towards 0 K as shown in Figure 8.12. The calcined NSCF6428 had the largest splitting below the transition temperature (Tc) in comparison to the undoped LSCF6428 and the partially doped LSCF6428. As the temperature increases from the 100 K to 400 K the LPSCF33428, LNSCF33428 and NSCF6428 nanopowder magnetization decreases steeply in both the FC and ZFC curves which suggest spin randomisation due to the increase of thermal excitation and AFM behaviour from the Fe^{3+}-O_2-Fe^{3+} especially at room temperatures.[253] When the temperature is below 100 K, all four nanopowders of the LSCF6428, LPSCF33428, LNSCF33428 and NSCF6428 decrease in the ZFC magnetization due to the presence of the small content of cobalt ions in the compositions. Ghogomu et.al., report that cobalt ions can exist in three different spin states which are temperature dependent compared to the two spin states of iron ions. Therefore, below 100 K there could be a transition from intermediate to low spin state. The effect of the transition from intermediate to low spin state is that cobalt ions become non-magnetic which would lead to a decrease in magnetization. [78] However, for the Nd doped cathodes, LNSCF33428 and NSCF6428, when the temperature decreases to below 2 K, there is a sharp increase in magnetization in both the ZFC and FC curves due to the increase dipolar interactions of the Nd^{3+}-Nd^{3+} which dominates the lower temperature region.[253]

Moreover, the effect of the Nd onsets ferromagnetic ordering of the LNSCF33428 and NSCF6428 nanopowders with the sudden decrease in temperature as seen in the widening of the hysteresis loops as shown in Figure 8.10. That is consistent with a study by Das et.al. where the co doping of the Nd^{3+} along with the V^{5+} into $LaFeO_3$ led to an increase in ferromagnetic order which enhances the magnetic properties when both the M-H hysteresis loop and ZFC-FC were examined. [253] Therefore, the ZFC-FC temperature dependent of the four nanopowders is consistent with the magnetic hysteresis M-H hysteresis loops when observed at 2 K and 300 K. Furthermore, a study by da Silva et.al. shows for the $La_{0.6}Sr_{0.4}FeO_3$ at 700 K (transition temperature), the exchange bias in the hysteresis loops indicated spin glass like behaviour which took place due to the impurity known as strontium hexaferrites of the $La_{0.6}Sr_{0.4}FeO_3$ perovskite material even when different fields (1 Oe and 100 Oe) were used. However, for this work, the measurements could only go to a maximum of 400 K so there is only an assumption that that there is spin glass like behaviour in the LSCF6428, LPSCF33428,

LNSCF33428 and NSCF6428 nanopowders however it would be consistent with the FIB-SEM via EDX identification of a secondary iron-rich phase which had likely to be formed. [255]

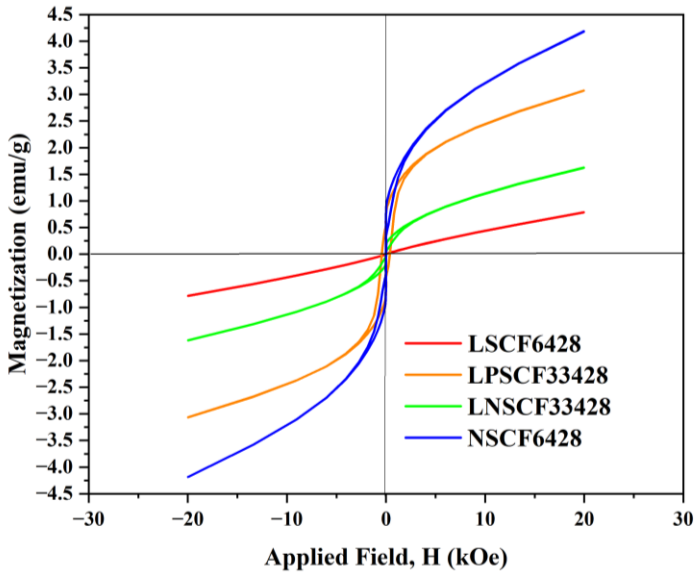

Figure 8.13: Room Temperature (300 K) magnetic hysteresis loops (M-H) of sintered crushed pellets of LSCF6428, LPSCF33428, LNSCF33428 and NSCF6428 sintered at 1000 ^{o}C for 1h

For the sintered cathode samples examined at 300 K for M-H, all the samples have been sintered 1000 ^{o}C and there is a dramatic change in the shape of the M-H hysteresis loops especially for the sintered LSCF6428 pellet as shown in Figure 8.13. This is due to the changes in the physical properties (microstructure) of the undoped LSCF and rare earth doped LSCF from the nanopowder precursors i.e. from agglomerated powder to sintered grains of size ranging from nano to micro scale (as indicated by the FIB-SEM via EDX in Figures 8.1-8.5). There has been limited work on comparison between nanopowder and sintered materials for MIEC perovskite oxide cathodes. However, there is a study by Aslibeiki et.al. where there was a comparison made between three different classifications of nanoparticle, bulk and films of $MnFe_2O_4$ for investigating how the difference in shape and size of the magnetic domains influence the magnetization. For the undoped LSCF here, Hc is very low.[249] That is consistent with a study by Kershi et. al., where the Ms was the lowest in undoped LSCF compared to doping with rare earth elements as the La^{3+} is paramagnetic and there are no electrons in the 4f shell to contributes to the magnetization. [257] From an independent analysis using the FIB-SEM via EDX on the sintered LSCF6428 pellet, there was the presence of a secondary iron-rich phase, of smaller crystallite size than the bulk composition. In the Silva et.al., from the ZFC-FC, the impurity strontium hexaferrites was identified which affect the

magnetization behaviour of the $La_{0.6}Sr_{0.4}FeO_3$. Therefore, the decrease in super exchange interactions from the iron ions due to the presence of secondary phase could have led to a sudden decline in magnetization from the 7.65 emu/g to 0.79 emu/g from calcined to sintered LSCF6428 as shown in Tables 8.2 and 8.4 respectively. While for the rare earth doped LSCF, there is still presence of weak ferromagnetic behaviour due to the unpaired electrons from the 4f shell orbital of the rare earth elements resulting in higher Ms compared to the LSCF6428. The NSCF6428 had the highest Ms as there is no paramagnetic La^{3+} in the chemical composition. Although, the LPSCF33428 had a higher magnetization compared to the LNSCF33428, it has a crystallite size of 45.1 nm from the XRD in Section 7.1 which influences a magnetic anisotropy of 1.25. The decrease in net magnetization of the LNSCF33428 is accompanied by a crystallite size of 37.1 nm which might lower the coercivity and magnetic anisotropy a small amount compared to the LPSCF33428 as shown in Table 8.4.[250]

Overall, it is suggested that rare earths influence the weak ferromagnetic behaviour of doped LSCF as seen from the hysteresis in Figure 8.13. For the partially rare earth doped LSCF, there is a combination of the crystallite size and the magnetic anisotropy which influences both the Ms and Hc as shown from Table 8.4. Moreover, given the low magnetic anisotropy of both the undoped LSCF and rare earth doped LSCF sintered cathode materials it indicates they are easy to demagnetise and suggested they could enable improvements in the efficiency of IT-SOFCs fuel cell performance.

8.4. Electrical Properties of the symmetrical cell of LSCF6428/YSZ, LPSCF33428/YSZ, LNSCF33428/YSZ and NSCF6428/YSZ using impedance spectroscopy

Impedance spectroscopy is an essential item of characterisation equipment, used here to determine how the microstructure of the undoped LSCF6428 and the rare earth doped LSCF sintered cathode materials influence the kinetics of the ORR mechanisms specifically aimed for IT-SOFCs.[258] Symmetrical cell testing is chosen as the performance measurement to identify the potential electrode materials for IT-SOFCs. The GDC electrolyte has been a popular choice for symmetrical cell testing with cathode materials by researchers due to its higher ionic conductivity, necessary for operating IT-SOFCs, compared to the more traditional YSZ which operated at high temperatures of 1000 ^{o}C. As described in previous sections, given that LSCF6428 is classified as a MIEC cathode, when LSCF6428 has been paired with the

GDC electrolyte it has led to superior MIEC, compared to LSCF + YSZ, when conducting impedance measurements.[259-260]

Although, from the section 8.3, due to the presence of electrons in the 4f shell in rare earth elements, the effect of doping rare earths in place of the non-magnetic La^{3+} has led to enhanced magnetic properties, especially for NSCF6428 regarding Ms, as referred to in Tables 8.2-8.4. This might also affect the value of electron conductivity occurring at the cathode/electrolyte interface which could influence the IT-SOFCs performance. The choice of sintering method for the undoped LSCF6428 and rare earth doped LSCF, can influence the surface and bulk composition of the microstructure in relation to the glassy, secondary iron-rich phase, and this might also significantly affect the performance of the sintered cathode/electrolyte half-cell. YSZ electrolyte has also been used for other purposes, for symmetrical cell testing other than that aimed for HT-SOFCs. YSZ is an electron blocker for unwanted electron conduction which can affect the measurements of individual electron processes of the ORR and it meets the criteria for ionic conductivity of 0.001 S cm^{-1} from Chapter 2, Section 2.3. Whereas GDC tends to have significant electronic conductivity when operating at temperatures for IT-SOFCs, because of the mixed valence from the ceria causing instability. [125][259] Therefore for this work, the undoped LSCF and rare earth doped LSCF cathode slurries were printed onto a YSZ electrolyte.

The YSZ pellet using 8.7 mol% Yttria was sintered at six different sintering temperatures prior to the painting and sintering of the cathode materials. It can be shown in Table 8.5 that the maximum density sintered YSZ reached was 98% at 1400 ^{o}C and at temperatures above this remained constant as shown in Table 8.5.

Table 8.5: The relative density (rounded to two decimal places) of the YSZ electrolyte pellet sintered at temperatures between 1300 – 1550 ^{o}C

Sintering Temperature (^{o}C)	**YSZ relative density (%)**
1300	90.23
1350	90.77
1400	98.3
1450	98.38
1500	98.64
1550	99.83

To ensure that the slurry of the cathode material is fully in contact with the YSZ electrolyte, to establish a good interface, the cathode materials were sintered at 1020 ºC, 20 ºC higher than the chosen optimal sintering temperature in preceding Sections and Chapters.

To obtain the measurements, Nyquist plots of the undoped LSCF and rare earth doped LSCF were conducted using the equivalent circuit models to resemble the kinetics and diffusion of the symmetrical cell, that are taking place within the cathode material. The equivalent circuit models will enable the measuring of frequencies over a temperature range of between 400-750 ºC that are targeted for IT- SOFCs. Therefore, it will outline the mechanisms of the ORR for each sintered cathode material performance. LSM/YSZ is a half-cell which has been investigated for use in HT-SOFCs in a study by Nielsen et.al, however, the model used is not suitable for this work due to LSM being classified as an electronic conductor compared to LSCF6428 which is a MIEC cathode. [261]

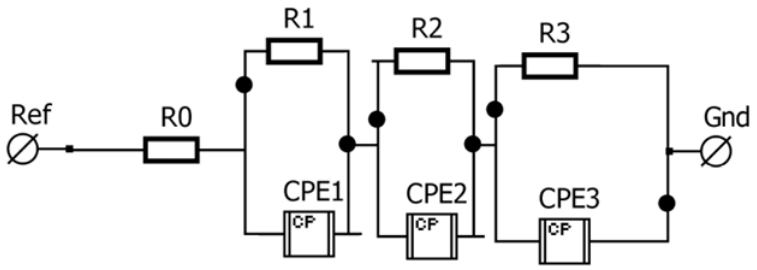

Figure 8.14: The Equivalent Circuit Model used for LSCF6428/YSZ and LPSCF33428/YSZ performed at 400 – 500 ºC

The first set of results is examined between a temperature range of 400 to 500 ºC for LSCF6428/YSZ and LPSCF33428/YSZ half-cells where the equivalent circuit model that is performed is referring to a study by Fan et.al.[262] which investigated the performance of low temperature ceramic fuel cells such as carbonate, which are operated at temperatures below 600 ºC as shown in Figure 8.14. The same equivalent model has been also performed with another MIEC alternative cathode in another study by Escudero et. al., for which the resistances were examined at operating temperatures greater than 600 ºC. [263] The equivalent circuit model consists of the ohmic resistance, R_0 of the YSZ electrolyte while the remaining components are associated with the cathode material which are made up of three R || CPE in series which describes the three ORR processes that contribute to the impedance of the cathode/electrolyte interface. R_0 is the ohmic resistance of the electrolyte, where the electrolyte/cathode interface, current collector and electrode are located. R_1 is associated with

the movement of the oxygen intermediates within the electrodes at high frequency, consisting of a semi-circle arc. R_2 is associated with the mid-frequency region, with charge transfers such as ions and electrons, consisting of a semi-circle. R_3 is associated with the tail occurring at the low frequency region such as non- charge-transfer, oxygen adsorption, desorption, dissociation and diffusion. The sum of (R_1 + R_2 + R_3) contributes to the total (electrode) polarisation resistance of the basic electrode processes that contribute to the incorporation of the resistances into the electrolyte interface which drives the electrochemical oxygen reduction reaction. CPE is a constant phase element, which represents the non-ideal and time dependent capacitor elements, which is discussed further in the methodology section.

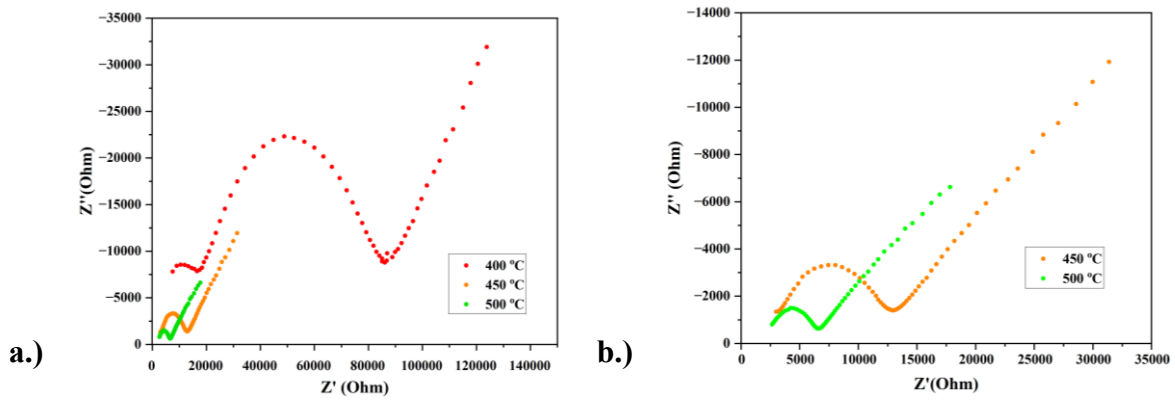

Figure 8.15: The Nyquist plots of the LSCF6428/YSZ symmetrical cell sintered at 1020 °C for 30 minutes performed at temperatures between 400 – 500 °C (b) zoom in Nyquist plots of temperatures between 400 – 500 °C

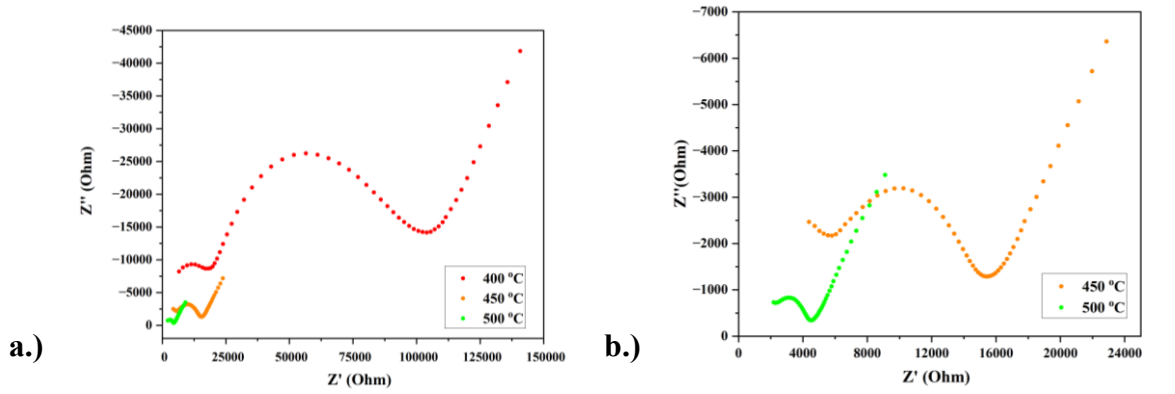

Figure 8.16: The Nyquist plots of the LPSCF33428/YSZ symmetrical cell sintered at 1020 °C for 30 minutes performed at temperatures between 400 – 500 °C (b) zoom in Nyquist plots of temperatures between 400 – 500 °C

From the Nyquist plots, when both the LSCF6428/YSZ and LPSCF33428/YSZ were performed at 400 °C in air, there were two complete semi-circle arcs (high and mid frequency)

and a tail extension (low frequency). Although, for both the LSCF6428/YSZ and LPSCF33428/YSZ half cells when performed at temperatures between 450 ºC and 500 ºC, there is one incomplete arc at high frequency, one complete arc and tail extension as shown in Figures 8.15 and 8.16. The Nyquist plots at 500 ºC in air for both the LSCF6428/YSZ and LPSCF33428/YSZ are similar with the Nyquist plots of the ceramic cell when performed at 500 ºC in air by a study by Fan et.al.[262] When the temperature increases, the high frequency arc slowly disappears while the mid frequency arc decreases in diameter and the tail decreases in size as shown in Figures 8.15 and 8.16. However, the R_1 resistance values are consistently lower for the LSCF6428/YSZ half-cell while the R_3 resistance values are consistently lower for the LPSCF33428/YSZ.

To determine how the rare earth elements affect the R_3 in comparison to the undoped LSCF6428/YSZ half-cell, the activation energies between 400 ºC to 500 ºC of R_1, R_2 and R_3 are calculated individually using the formula. A comparison between the individual activation energies across the temperature range can be used to determine the rate limiting mechanisms of the ORR. Then the experimental data of the individual resistances is plotted against a line fitting in accordion to the Arrhenius equations 8.2 and 8.3:

$$\mathrm{R} = \exp \mathrm{R'} + (-Ea/R\mathrm{T}) \tag{8.2}$$

$$ln\,\boldsymbol{R} = ln\,\mathrm{R'} + (-Ea/R)\ 1/T \tag{8.3}$$

The graph of ln(R) against 1/T, where $\boldsymbol{R}$ is the resistance, R' is the pre-exponential resistance and T is the temperature (in Kelvin). The slope of this line is equal to -Ea/R, where R is the ideal gas constant of 8.314 J mol^{-1} K^{-1} , Ea is the activation energy (kJ/mol). The activation energies for Ea_1 are consistent for both the LSCF6428/YSZ and LPSCF33428/YSZ so there is no effect on the oxygen intermediates with the influence of the rare earth element, Pr^{3+}. However, for the E_{a2}, the LSCF6428/YSZ of 0.56 eV is lower in comparison to the LPSCF33428 of 0.64 eV as shown in Figures 8.17 and 8.18 respectively. While for the LPSCF33428/YSZ, the E_{a3} is 0.83 eV in comparison to the LSCF6428/YSZ of 0.92 eV as shown in Figures 8.18 and 8.17 respectively. That suggests that the paramagnetic La^{3+} enables the increase efficiency in oxygen intermediates and charge transfer for the LSCF6428/YSZ half-cell, while the LPSCF33428/YSZ enhances the surface diffusion, oxygen adsorption and diffusion of the ORR processes overall due to the weak ferromagnetic contribution of Pr^{3+}.

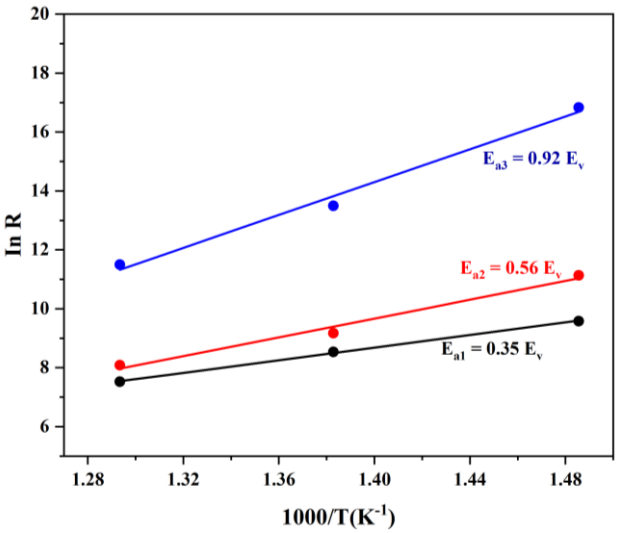

Figure 8.17: Temperature dependence Arrhenius plots of LSCF6428/YSZ symmetrical cell of best line fitting of the resistances performed at temperatures between 400 – 500 ºC to obtain individual activation energies of ORR, E_{a1} = high frequency, E_{a2} = mid frequency and E_{a3} = low frequency

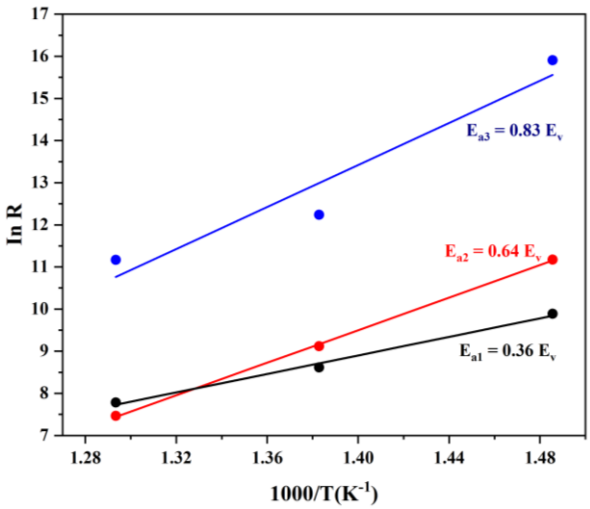

Figure 8.18: Temperature dependence Arrhenius plots of LPSCF33428/YSZ symmetrical cell of best line fitting of the resistances performed at temperatures between 400 – 500 ºC to obtain individual activation energies of ORR, E_{a1} = high frequency, E_{a2} = mid frequency and E_{a3} = low frequency

For the Nd doped cathodes, the LNSCF33428/YSZ and NSCF6428/YSZ half-cell Nyquist plots each had their own individual equivalent circuit model performed. For the LNSCF33428/YSZ half-cell, the same equivalent model for the LSCF6428/YSZ and LPSCF33428/YSZ was used as shown in Figure 8.14 and was only a good fit to the Nyquist

plots at the temperature of 400 ºC (which was omitted from this Chapter as a result due to the inability for comparison). Moreover, the Nyquist plots for the LNSCF33428/YSZ half-cell cannot be fitted to temperatures above 400 ºC in air with the equivalent circuit model as shown in Figure 8.14.

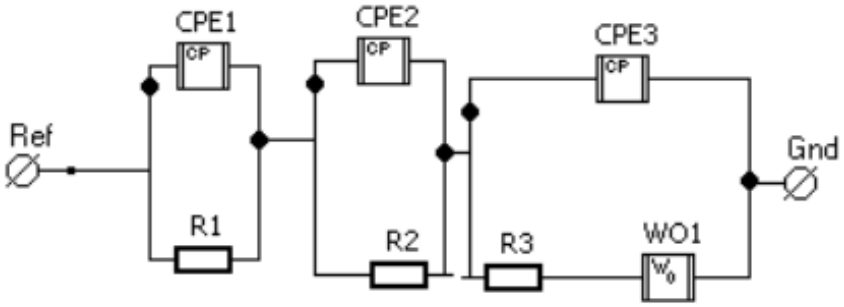

Figure 8.19: The Equivalent Circuit Model used for NSCF6428/YSZ performed at 400 – 500 ºC

Therefore, the NSCF6428/YSZ half-cell, which was investigated at temperatures ranging between 400 ºC to 500 ºC, the equivalent circuit model was adapted from Figure 8.14 to feature the Warburg open circuit element located at series 3 of the CPE and R_3 as shown in Figure 8.19 The Warburg element is due to surface diffusion limitations of the oxygen species from the increased presence of unpaired electrons coming from the 4f shell orbital of Nd as referred to in Table 6.1 from Section 6.1. The Warburg open circuit element was also used in the equivalent circuit to address the 45-degree off-set angle in the Nyquist plot. The equivalent circuit containing the Warburg element is also consistent with a study investigating the LSM-YSZ composite despite LSM only being an electronic conductor cathode.[261] The Warburg open circuit elements have also been incorporated into other equivalent circuit models for other Nd doped cathodes such as Nd doped BSCF and Nd-doped $LiNi_{0.5}Co_{0.2}Mn_{0.3}O_2$.[76][124][263-264]

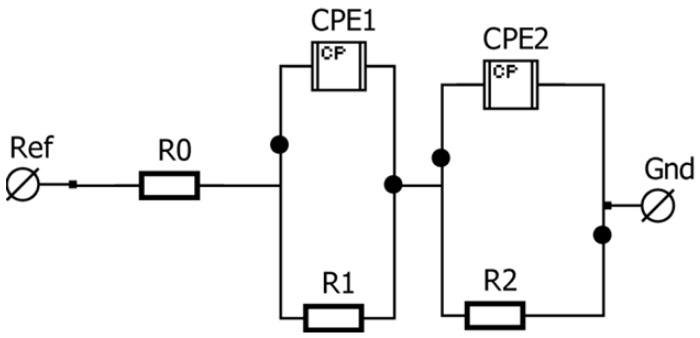

Figure 8.20: The Equivalent Circuit Model used for LNSCF33428/YSZ performed at 450 – 550 ºC and LSCF6428/YSZ and LPSCF33428/YSZ performed at 550 - 750 ºC

While, the LNSCF33428/YSZ half-cell measured between temperatures of 450 ºC and 550 ºC and the resulting Nyquist plots were fitted using the equivalent circuit model from a study by Jamale et.al. investigating the LSCF/GDC half-cell performance between the temperature range of 400 – 550ºC as shown in Figure 8.20. [261] There were incomplete semicircle outlines from both the high and low frequency ranges from Figures 8.21 and 8.22. The equivalent model for Nd doped material from Figure 8.20 performed as well as the equivalent circuit model used for temperatures between 400 - 500 ºC for the non-Nd doped cathode half cells as outlined in Figure 8.14. R_0 is ohmic resistance, where the electrolyte/cathode interface, current collector and electrode are located which consist of the resistance of the YSZ electrolyte itself. R_1 is associated with the high frequency region with the charge transfer such as ion and electron consisting of a semi - circle R_2 is associated with the other incomplete semi-circle occurring at low frequency region is the such a non-charge transfer, oxygen adsorption, desorption, dissociation and diffusion. As a result, the sum of ($R_1 + R_2$) contributes to the total (electrode) polarisation as described earlier in this section.[260]

From the Nyquist plot, for the NSCF6428/YSZ the high frequency incomplete arc disappears gradually and the low frequency tail decreases in length as the temperature increases while the mid frequency arc has decreased in height in comparison to LSCF6428/YSZ and LPSCF33428/YSZ as shown in Figure 8.21. While for the LNSCF33428/YSZ, the high frequency diameter decreases in size while the low frequency length decreases in line as shown in Figure 8.22. It suggests that there is a difference in behaviour between the partially doped and fully doped cathode consisting of Nd. As like the other half cells, the individual resistances obtained were plotted in accordion to the Arrhenius equation. It can be shown that with Ea_1, the charge transfer, the activation energies are consistent with what has been obtained from LSCF6428/YSZ and LPSCF33428/YSZ for the LNSCF33428/YSZ of 0.61 eV as shown in Figure 8.23. While for Ea_2, the oxygen adsorption and dissociation and surface diffusion there is a sudden decrease in activation energy for both the LNSCF33428/YSZ and NSCF6428/YSZ of 0.27 eV and 0.45 eV respectively. The trend is related to the combination of La^{3+} and Nd^{3+} which affected the charge imbalance of the chemical composition leading to mixed valences of the iron which affects the oxygen diffusion ability and the total polarisation resistance.[76] Although further work on Nd doped cathodes/YSZ half cells could not be performed at temperatures above 600 ºC due to the difficulties of stability of cell performance in air over the measurement period.

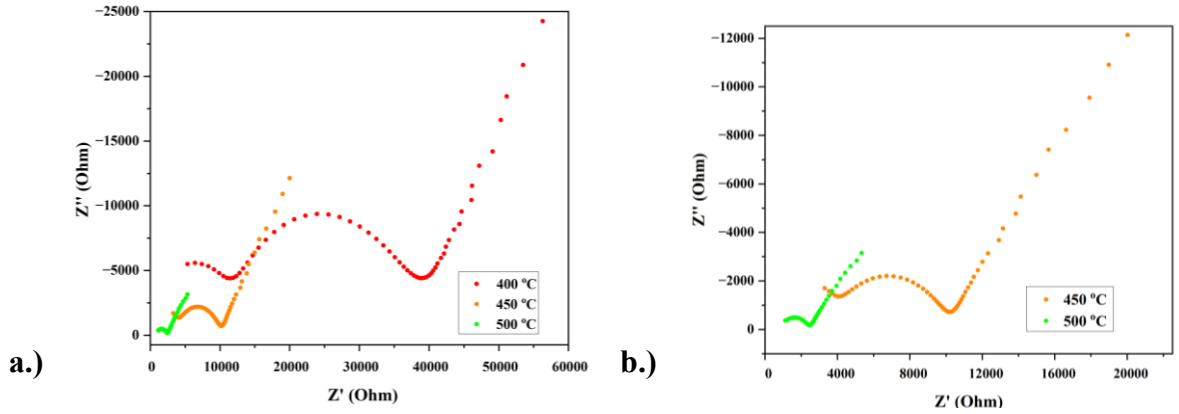

Figure 8.21: The Nyquist plots of the NSCF6428/YSZ symmetrical cell sintered at 1020 °C for 30 minutes performed at temperatures between 400 – 500 °C (b) zoom in Nyquist plots of temperatures between 400 – 500 °C

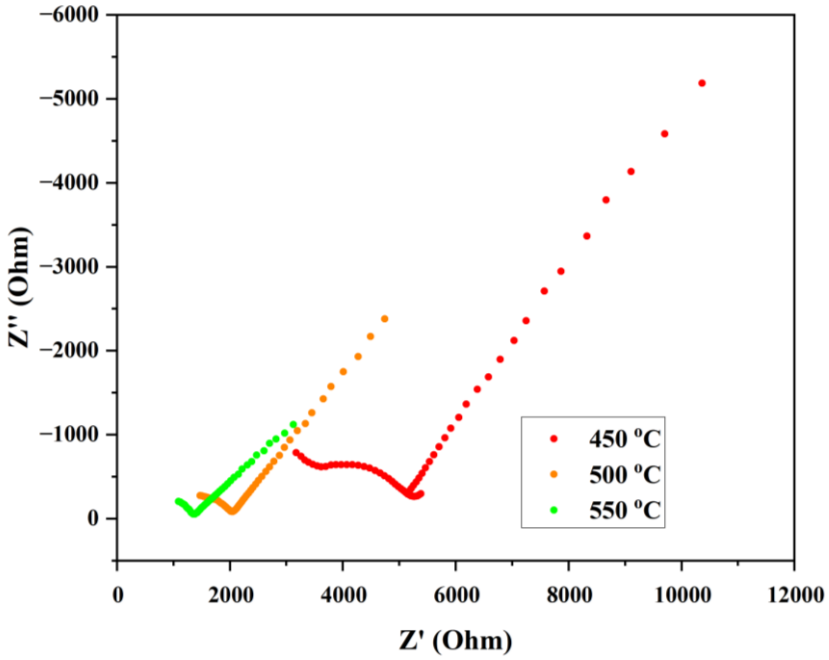

Figure 8.22: The Nyquist plots of the LNSCF33428/YSZ symmetrical cell sintered at 1020 °C for 30 minutes performed at temperatures between 450 – 550 °C (b) zoom in Nyquist plots of temperatures between 400 – 550 °C

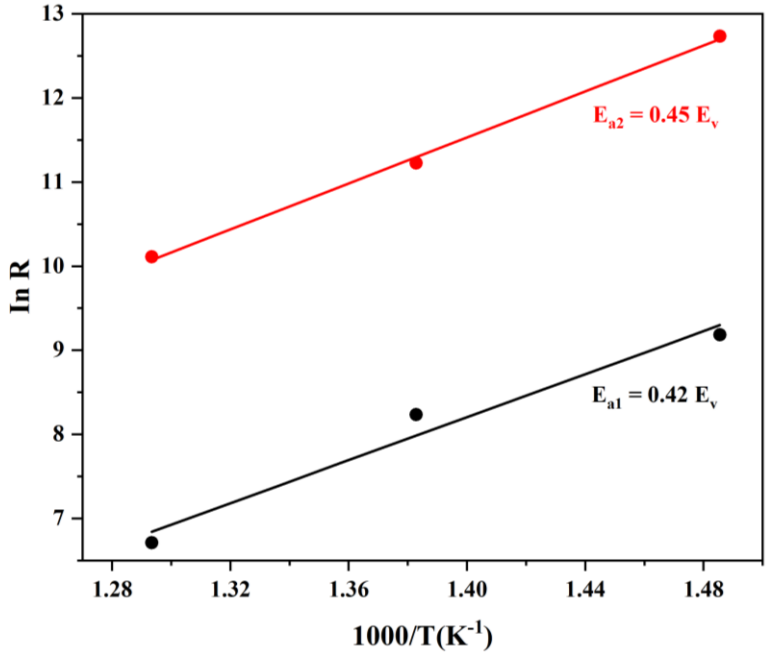

Figure 8.23: Temperature dependence Arrhenius plots of NSCF6428/YSZ symmetrical cell of best line fitting of the resistances performed at temperatures between 400 – 500 ºC to obtain individual activation energies of ORR, E_{a1} = high frequency, E_{a2} = low frequency

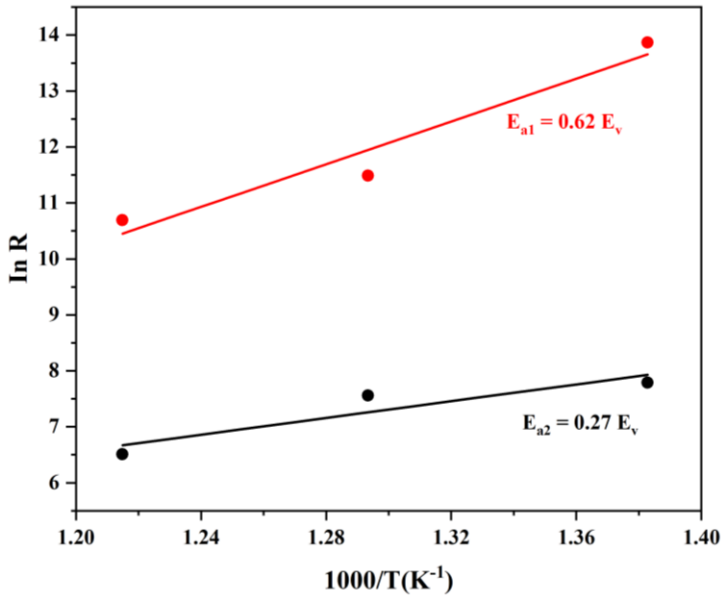

Figure 8.24: Temperature dependence Arrhenius plots of LNSCF33428/YSZ symmetrical cell of best line fitting of the resistances performed at temperatures between 450 – 550 ºC to obtain individual activation energies of ORR, Ea_1 = high frequency, Ea_2 = low frequency

The same equivalent circuit model used for the LNSCF33428/YSZ was used to obtain the Nyquist plots for the LSCF6428/YSZ and LPSCF33428/YSZ performed at temperatures between 550 - 750 ºC as shown in Figure 8.25. It is to determine how the higher temperatures

influence the cathode/electrolyte interface affect the activation energies of the individual mechanisms of the ORR.

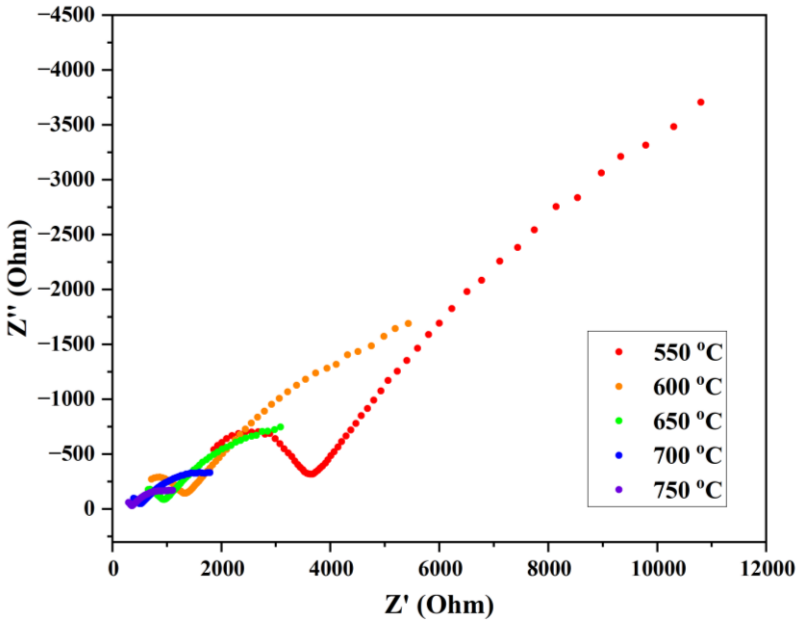

Figure 8.25: The Nyquist plots of the LSCF6428/YSZ symmetrical cell sintered at 1020 °C for 30 minutes performed at temperatures between 550 – 750 °C

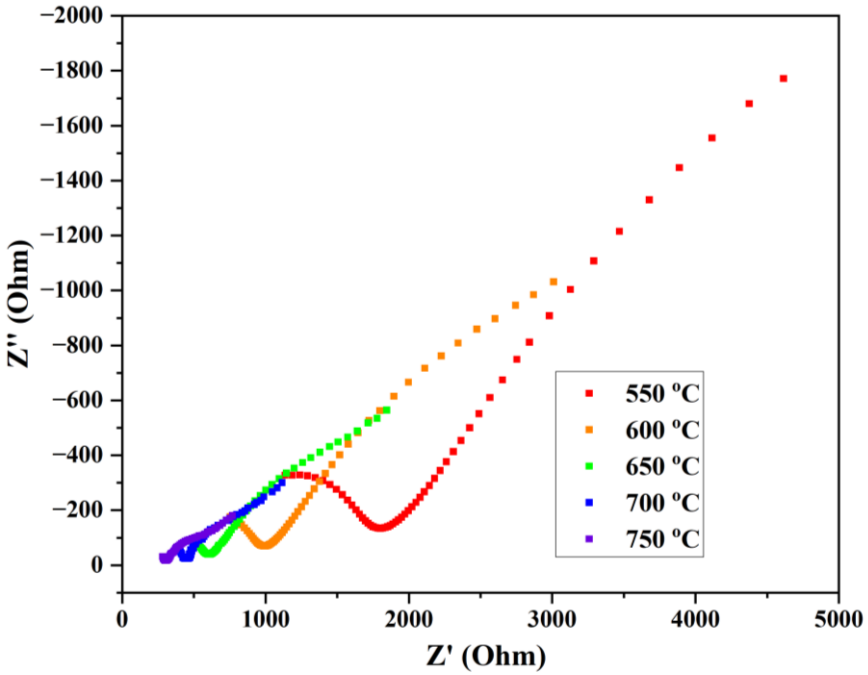

Figure 8.26: The Nyquist plots of the LPSCF33428/YSZ symmetrical cell sintered at 1020 °C for 30 minutes performed at temperatures between 550 – 750 °C

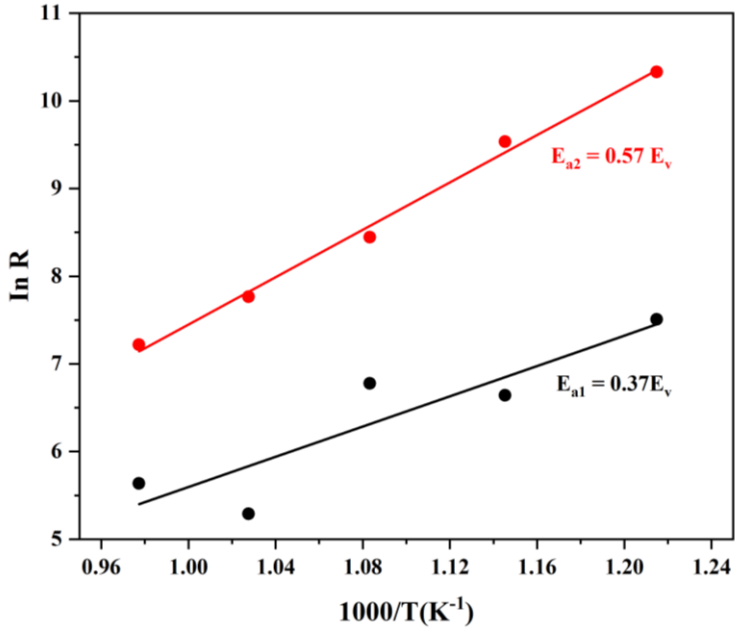

Figure 8.27: Temperature dependence Arrhenius plots of LSCF33428/YSZ symmetrical cell of best line fitting of the resistances performed at temperatures between 550 – 750 ºC to obtain individual activation energies of ORR, E_{a1} = high frequency, E_{a2} = low frequency

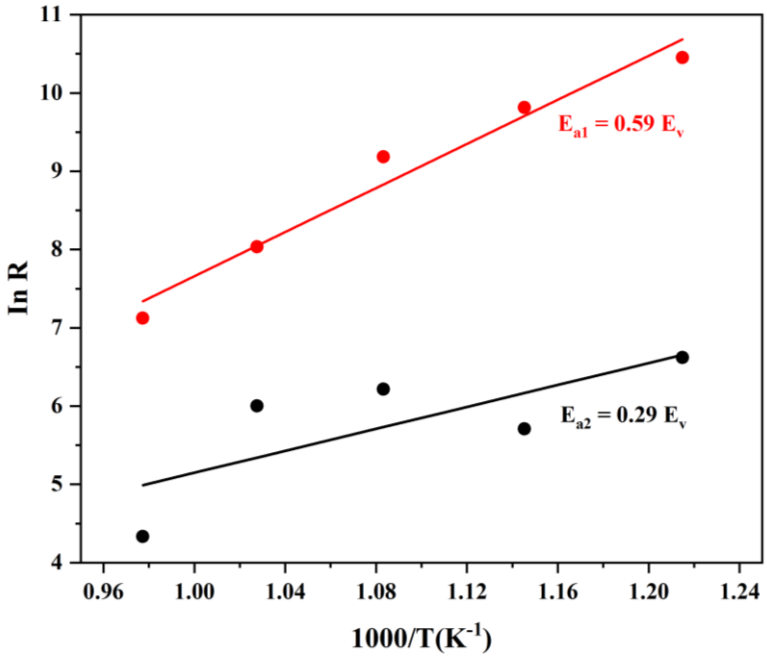

Figure 8.28: Temperature dependence Arrhenius plots of LSCF33428/YSZ symmetrical cell of best line fitting of the resistances performed at temperatures between 550 – 750 ºC to obtain individual activation energies of ORR, E_{a1} = high frequency, E_{a2} = low frequency

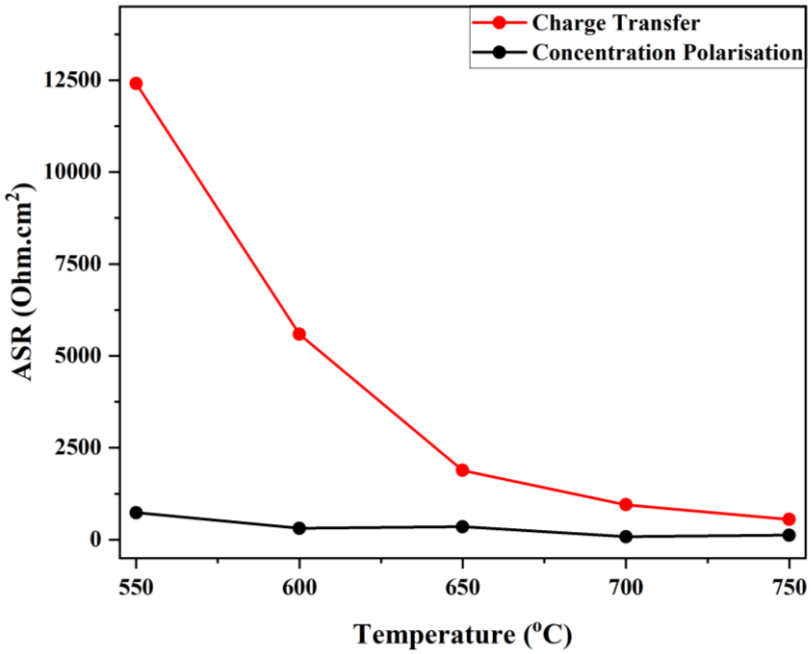

Figure 8.29: ASR of charge transfer and concentration polarisation reactions of the LSCF6428/YSZ symmetrical cell performed between 550 - 750 ºC

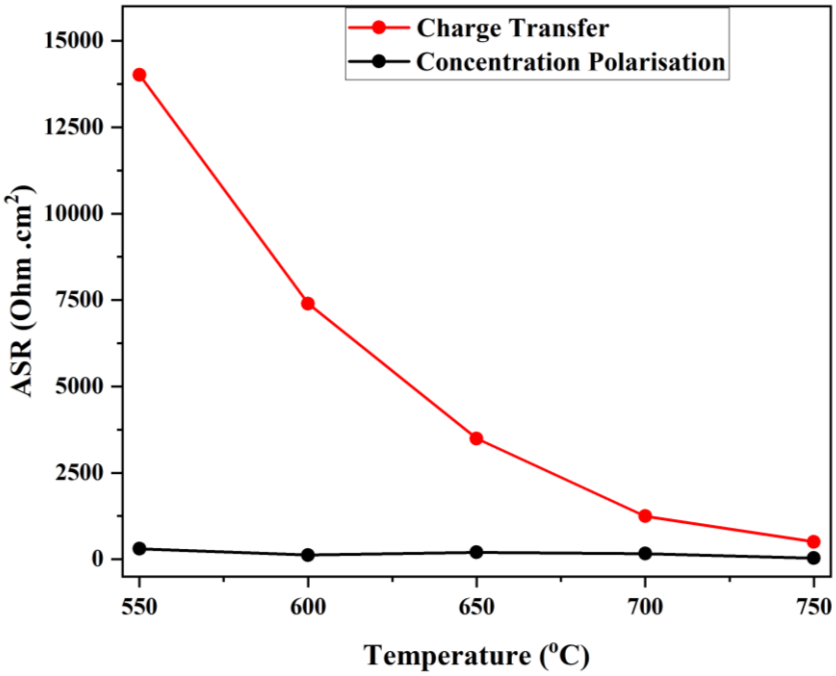

Figure 8.30: ASR of charge transfer and concentration polarisation reactions of the LPSCF33428/YSZ symmetrical cell performed between 550 - 750 ºC

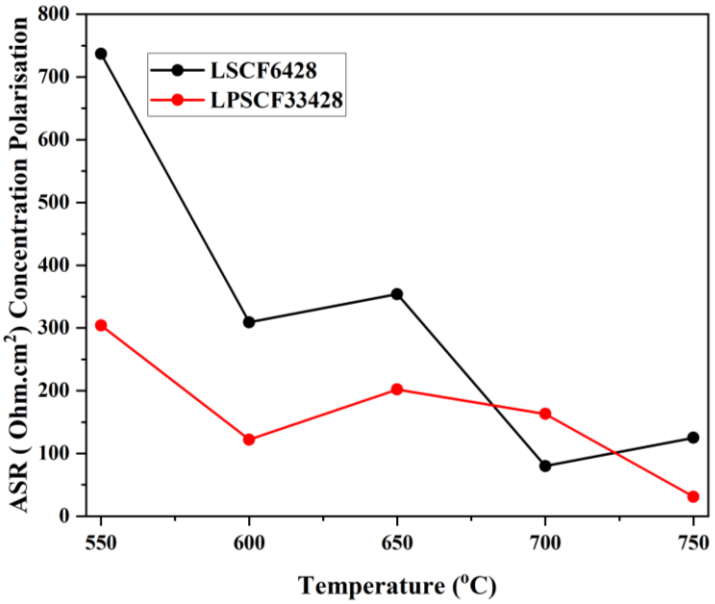

Figure 8.31: ASR concentration polarisation reactions of the LSCF6428/YSZ and LPSCF33428/YSZ symmetrical cell zoom in performed between 550 - 750 ºC

From the Nyquist plots, there is an incomplete arc at high frequency and a tail at low frequency, however, the temperature increases, the incomplete arc decreases in diameter at high frequency while the tail decreases in length and becomes an incomplete arc at low frequency when it reaches 700 ºC. That is consistent with the LSCF/GDC Nyquist plot when performed at lower temperatures between 400 ºC to 550 ºC using the same equivalent circuit model as shown in Figures 8.25 and 8.26.[260] Since the MIEC cathode is dependent upon the ionic conductivity and catalytic activity on the ORR for IT-SOFCs, the individual resistances obtained from the Nyquist plot were calculated using Arrhenius equation to determine its individual activation energies for each ORR process as with the lower temperature regions of below 600 ºC. [259] For the charge transfer, the activation energies between 550 – 750 ºC for both the LSCF6428/YSZ and LPSCF33428/YSZ of 0.57 eV and 0.59 eV as shown in Figures 8.27 and 8.28 respectively were consistent with the activation energies performed between 400 ºC -500 ºC from Figures 8.23 and 8.24. However, there was a sudden decrease in the activation energies for the oxygen adsorption, desorption and surface diffusion, Ea_2 for both LSCF6428/YSZ and LPSCF33428 when performed at 550 - 750ºC of 0.37 eV and 0.29 eV respectively in comparison to when performed between 400 – 500 ºC. Therefore, it was also critical to determine whether the influence of the rare earth element, praseodymium in air had an influence on the overall cell performance on the basis of the total polarisation resistance. Moreover, the ASR equation was used to calculate the charge transfer and the concentration

polarisation to determine the trend between 550 ºC - 750 ºC for the LSCF6428/YSZ and LPSCF33428/YSZ.[145] It can be seen clearly that the concentration polarisation reaction is significantly lower compared to the charge transfer reaction of the ORR process for both LSCF6428/YSZ and LPSCF33428/YSZ as shown in Figures 8.29 and 8.30. However, the LPSCF33428/YSZ has a concentration polarisation reaction of 30.96 Ohms which is about 4 times lower compared to the LSCF6428/YSZ of 125 Ohms as shown in Figure 8.31. It shows that the use of the mixed valence praseodymium, LPSCF33428 cathode enhances the oxygen adsorption, dissociation, surface diffusion of the overall cell performance of the ORR at ITs compared to the LSCF6428 cathode despite the use of the HT-SOFCs YSZ electrolyte which could decreases the total polarisation resistance. Therefore, the influence of the rare earth element doping upon MIEC cathodes for IT-SOFCs which enhances the oxygen adsorption, desorption and surface diffusion has also been consistent in other MIEC cathodes using the GDC electrolyte where Pr and Nd doped BSCF has also enhanced the oxygen adsorption, dissociation and surface diffusions at IT-SOFCS through lowering the total polarisation.[76][124] It has also occurred with cheap transition metal, Ni doped LSCF where the concentration polarization reaction ASR was lower compared to the charge transfer reaction. [226]

Summary – Chapter 8

This final chapter of the results has examined the homogeneity of the sintered LSCF6428 and rare earth doped LSCF pellets and tested the electrical performance of both. 3-D characterisation of the bulk structure of the LSCF and LPSCF by FIB-SEM and Nano-CT, has confirmed that the microstructures are inhomogeneous with densified micrometre grain size regions intermixed with regions of nanoscale grains resulting in varied porosity as well as an inhomogeneous grain structure. FIB-SEM with EDX also reveals an additional secondary 'matrix' phase that is rich in iron. The presence of this secondary phase may have led to a potential spin glass magnetic behaviour in these materials. The effects of Nd doping of LSCF (LNSCF33428 and NSCF6428) also enhances the ferromagnetic properties of the material compared to undoped LSCF6428. Overall, both the undoped LSCF6428 and rare earth doped LSCF sintered materials had low magnetic anisotropy of below 2 suggesting easy demagnetization that could help with efficiency for IT-SOFCs performance. The undoped LSCF6428/YSZ and LPSCF333428/YSZ half cells, produced by screen printing LSCF onto YSZ pellets and sintering at 1020 ºC, were electrically tested using impedance measurements

at temperatures between 550 ºC – 750 ºC (however Nd based cathodes could not be measured beyond 550 ºC). This was done to determine if the rare earth element doping influences the overall half-cell performance and / or the total polarisation resistance of the MIEC cathode materials despite the established inhomogeneity in microstructures. The LPSCF33428/YSZ polarisation resistance was significantly lowered at 30.96 Ohms compared to the undoped LSCF6428/YSZ half-cell at 125 Ohms with impedance loops. These results suggest that doping LSCF with the rare earth element, praseodymium enhances the cathode material by decreasing the total polarization resistance of the LPSCF33428/YSZ half-cell, suggesting that oxygen adsorption, desorption and surface diffusion at the interface would all be improved too. There is still potential for further improvement if more homogeneous microstructures were to be produced. This latter point will be addressed in the future work section in Chapter 9.

Chapter 9 – Conclusion and Future Work

9.1. Conclusion

Solid Oxide Fuel Cells (SOFCs), consisting of a dense solid ceramic oxide electrolyte with porous anode and cathode components, have emerged as a way of generating electrical energy directly from the chemical energy of a fuel. The cathode component, unlike the anode and electrolyte components, can severely hinder overall cell performance when operating at intermediate temperatures (ITs) due to high activation energies, along with sluggish kinetics from the electrochemical oxygen reduction reaction (ORR).

LSCF6428 has been chosen as popular mixed ion and electron conductor (MIEC) cathode to research for use in IT-SOFCs. Although, there have been some drawbacks with this choice, such as Sr segregation have been identified. Moreover, the choice of synthesis method and sintering procedure is critical as it establishes the homogeneity of the phases, grain structures and porosity of the final ceramic product which then influence the overall electrical performance at ITs.

Sol gel followed by calcination and sintering as a synthesis method has been a recent trend in research in comparison to other popular synthesis methods (such as solid state), this “bottom up” approach being used in an effort to address lack of homogeneity in cathode ceramics. Past work has already been carried out by the ion exchange, Leeds Alginate Process (LAP) group in investigating LSCF6428 synthesis using 4 wt% sodium alginate sol gel processing. However, there has been limited work done in obtaining critical information to demonstrate that the required cathode criteria are met, such as, e.g., measurement of the porosity to show that it is within the acceptable range for a SOFC cathode.

3 wt% alginate production of LSCF6428 is chosen over 4 wt% LSCF6428 as investigation revealed an increase in final mass above 600 ^{o}C for 3 wt% alginate compared to 4 wt%. While the difference in drying methods (vacuum and hot plate) influences the mass loss of the Nd based cathodes at stage 1 (dehydration) all samples revealed an initial loss of moisture at or below 100 ^{o}C. Above 100 ^{o}C (stage 2) oxidative decomposition of the alginate occurs, such that unstable intermediate compound, oxalates are formed from all the rare earth elements and transition metal elements (except for Sr) due to the coordination of the +3 oxidation state of these. While for Sr, carbonate is formed due to its +2 oxidation state. Moreover, due to the

difference in hygroscopic properties of the rare earth dopants Pr and Nd, there is greater loss of moisture in the Nd based materials compared to the LPSCF33428 and LSCF6428 materials.

Between 300ºC and 600 ºC decomposition of the oxalates occurs such that metal oxides form (stage 3 and 4) and start to mix to produce LSCF based phases. At this stage there is greater mass loss and energy release from the LPSCF33428 compared to the Nd based materials. That has led to a significant difference of around 12% between the final mass residue of the non-Nd based materials and the Nd based materials (the Nd based materials have a final mass residue of around 32% of the original mass, compared to 44% for non Nd based materials). There is no further mass loss above 750 ºC.

A temperature of 800 ºC was chosen as optimal for calcination for transformation to a near single phase ferrite of LSCF6428, LPSCF33428 and LNSCF33428, while for the NSCF6428 produced from the 3 wt% sodium alginate a temperature of 775 ºC was chosen. 94- 96% phase purity was obtained for the LSCF6428 and the three different rare earth doped LSCF composition nanopowders, all of which met the 90% phase purity criteria requirement for powder production of SOFC cathodes, with the crystal symmetry confirmed as single phase rhombohedral by powder XRD. The crystal symmetry was confirmed by Raman spectroscopy (except for LNSCF33428 due to complications with the spectrometer incident frequency) with an indication of structural distortions of octahedra evident in the acquired spectra at above 600 cm^{-1}.

100% phase purity was not achieved for any calcined LSCF powders in part due to the presence of impurity $SrCO_3$ that might also have inhibited the crystal symmetry transition to a single rhombohedral phase, especially for the rare earth doped LSCF. The effect of Sr^{2+} deficiency, as indicated by the SEM/EDX spectra and mapping, suggests for example that the NSCF6428 nanopowder crystal symmetry is retained as rhombohedral rather than being transformed to orthorhombic as reported in past literature. There was also a degree of inhomogeneity evidenced by the SEM/EDX and XCT for the LNSCF33428 nanopowder. All calcined powders, apart from the NSCF6428 nanopowder, showed iron enrichment by the SEM/EDX suggesting the α-Fe2O3 predicted to from at stage 4 of the thermal analysis is retained when the nanopowders were calcined in air. Although, the other metal cations such as La, Pr, Nd and Co were measured to be in appropriate amounts for the nominal composition of ferrite to be formed. That suggested a relatively homogeneous distribution of metal cations throughout the microstructure after calcination. Such a homogenous distribution was also consistent with

results from XCT for the LSCF6428 and rare earth doped nanopowders calcined at 800 ºC (not including NSCF6428 calcined at 775 ºC) which also revealed nanoparticle agglomeration that establishes pores within the microstructure.

The average crystallite and grain size of the ferrite phase in the undoped LSCF and 3 rare earth doped LSCF nanopowders after calcination was between 30-50 nm as detected by XRD and SEM. The size of the pores, based on the pore size distribution across both SEM and BET, were consistent for both the undoped LSCF6428 and rare earth doped LSCF and were also estimated to be centred around 30-50 nm. The specific surface area for the chosen calcined nanopowders met the specific surface area target requirements of between 5-7 m^2/g. Although, the specific surface area and average pore size for the rare earth doped LSCF was marginally higher and lower respectively in comparison to the undoped LSCF6428 of 5.48 m^2/g and 37.0 nm respectively.

Sintering of the LSCF6428 and rare earth doped LSCF calcined nanopowders was undertaken to understand the impact of densification on porosity and grain structure of the final ceramic product of LSCF6428. Sintering at 1000 ºC yielded by XRD rhombohedral single phase LSCF6428 and rare earth doped LSCF ceramics with average crystallite sizes of 40-45 nm being retained, i.e. without any apparent grain growth. Porosity of ~ 25% for the non-Nd ceramics and around 39-40% for the Nd based ceramics was estimated by geometric density measurement and confirmed by gas adsorption. The measured porosities of the sintered ceramics meet the porosity criteria for SOFC cathodes of 20-40%.

There is also evidence of mixed grain sizes and some second/matrix phase between the grains in the SEM imaging of the sintered ceramics which is consistent with the expected Sr deficiency and iron enrichment in the LSCF, and rare earth doped LSCF phase, suggested by the XRD of the calcined material. SEM-EDX analysis however indicated Sr enrichment, as estimates of Sr content relative to all metal cation ions was at 0.28 - 0.34, rather than the expected 0.2 suggesting other elements are lost to a second phase, particularly so for the sintered LPSCF33428. An Fe enriched matrix phase was detected suggesting incomplete transformation of the intermediate iron oxide phase yet the Fe content of the assumed LSCF grains relative to all metal cations was at 0.88-1.03 rather than the expected 0.69-0.92 suggesting other cation loss to a second phase too.

For all rare earth doped ceramics though i.e. LPSCF33428, LNSCF33428 and NSCF6428, the total pore volumes are lower than for the undoped LSCF6428 of 0.024 cm^3/g sintered at the

same temperature of 1000 ºC. Yet the influence of the rare earth dopants upon the LSCF6428 perovskite composition such as LPSCF33428 and LNSCF33428 is thought to inhibit densification because a lower specific surface area of 1.92 m^2/g and 1.43 m^2/g respectively is measured compared to the sintered undoped LSCF6428 of 2.14 m^2/g. Overall, sintering at 1000 ºC produces a LSCF6428 and rare earth doped microstructure that would be suitable for an IT-SOFCs cathode material. Despite evidence of the presence of some grain size and phase inhomogeneity, the sintered ceramics are within the target criteria of 25-40% porosity ceramics, < 100 nm average crystallite size and < 100 nm average pore size.

Ahead of electrical testing, the homogeneity of the sintered LSCF and rare earth doped LSCF sintered pellets was assessed in detail by 3-D characterisations of the bulk structure of both the LSCF and LPSCF by FIB-SEM and LPSCF33428 using Nano-CT. The volume analysis confirmed that the microstructures are inhomogeneous with densified micrometre grain size regions intermixed with regions of nanoscale grains, resulting in varied porosity as well as.

FIB-SEM with EDX also reveals an additional secondary 'matrix' phase that is rich in iron, potentially from the likely untransformed α-Fe_2O_3 as described in the thermal analysis. The presence of this secondary phase rich in iron oxide may have led to a potential spin glass magnetic behaviour in these materials as indicated by comparison of zero field and field cooling (ZFC-FC) curves. The effects of Nd doping of LSCF (LNSCF33428 and NSCF6428) also enhances the ferromagnetic properties of the material compared to undoped LSCF6428. Overall, both the undoped LSCF and rare earth doped LSCF sintered materials had low magnetic anisotropy of below 2, suggesting easy demagnetization that could help with efficiency for IT-SOFCs performance.

Undoped LSCF/YSZ and LPSCF/YSZ half cells were produced by screen printing LSCF onto YSZ pellets and sintering at 1020 ºC and were electrically tested using impedance measurements at temperatures between 550 ºC – 750 ºC (however Nd based cathodes could not be measured above 550 ºC). This was done to determine if the rare earth element doping influences the overall half-cell performance and / or the total polarisation resistance of the MIEC cathode materials, despite the established inhomogeneity in microstructures. Impedence loops show that the LPSCF33428/YSZ polarisation resistance was significantly lowered, at 30.96 Ohms, compared to the undoped LSCF6428/YSZ half-cell at 125 Ohms. These results suggest that doping LSCF with the rare earth element, praseodymium enhances the LSCF cathode material by decreasing the total polarization resistance of a half-cell, suggesting that

oxygen adsorption, desorption and surface diffusion at the interface would all be improved. There is still potential for further improvement if more homogeneous microstructures were to be produced.

In final conclusion the objectives of this thesis have been met. The ion exchange Leeds Alginate Process is successful in obtaining metal ferrite from an appropriate combination of La, Pr, Nd, Co, Sr and Fe that is near single phase and is suitable for use as an IT-SOFC cathode. The process is environmentally friendly and cost effective. Although, from undertaking analysis of the calcination and sintering products, there is inhomogeneity of the microstructure which has led to varied porosity and grain structure which could detrimentally influence the electrical performance of both the LSCF6428 and rare earth doped LSCF i.e. LPSCF33428, LNSCF33428 and NSCF6428 as SOFC cathodes. However, it is clear that rare earth dopants i.e. Pr can enhance the LSCF cathode performance in comparison to the undoped LSCF6428 counterpart.

To continue progress towards the overall aim of the thesis of improving IT-SOFC cathode performance of LSCF6428 material by doping with other rare earth elements a number of proposed suggestions are present in the future work section.

9.2. Future Work

Inhomogeneity of the microstructure of calcined and sintered metal-alginate sol-gel processing is required to be addressed to better understand the performance of the rare earth doped LSCF compared to its undoped LSCF6428 counterpart.

Therefore, the proposed future work in relation to this project include:

A) Investigate the most effective drying method of the ion exchanged sodium alginate sol gel beads i.e. vacuum heating versus plate drying, identifying the optimum shrinkage and dehydration due to the different hygroscopic nature of the rare earth dopants e.g. Pr and Nd.

B) Use variable temperature XRD to confirm the phases and phase transformation when heating from ion exchanged alginate beads to final calcined ferrite phase.

C) To improve homogeneity after sintering, increase the amount of calcined nanopowder production to > 100 g to enable the use of ball milling prior to pressing and sintering of a pellet. Moreover, considering other methods of pressing the pellet other than uniaxial compression (such as iso-pressing) to see if a more uniform densification of the final sintered cathode pellet can be achieved.

D) Vary the sintering procedure beyond just changing the maximum temperature e.g. heating/cooling rate, sintering time. Again this could enable more uniform densification, porosity and reduce second phase production, e.g. α-Fe_2O_3, across a whole pellet i.e. at both the centre and edge.

E) Use 3-D characterisation as a standard check of sintered material for example FIB-SEM and nano-CT for examining all pellets including the Nd doped LSCF would enable through comparison to identify and then address inhomogeneity (grain structure, pores and secondary phases) between re-processed undoped LSCF6428 and rare earth doped LSCF i.e. LPSCF33428, LNSCF33428 and NSCF6428.

F) Improve the fabrication of the half-cells for electrical testing i.e. because the LNSCF33428/YSZ and NSCF6428/YSZ could not be performed at temperatures above 550 ^{o}C, the fabrication of the half-cell needs to be addressed. This could be done by i) iso-pressing YSZ electrolyte pellet rather than uniaxial pressing prior to sintering and cathode ink printing or 2) finding an alternative method of uniformly cathode coating the YSZ electrolyte pellet e.g. improved ink printing, painting or spray coating (PVD) to ensure better electrical performances of the half cells

Chapter 10 - References

[1] Sazali, N., Wan Salleh, W.N., Jamaludin, A.S. and Mhd Razali, M.N., 2020, New Perspectives on Fuel Cell Technology: A Brief Review. *Membranes*, ***10***(5), pp.1-18 DOI:10.3390/membranes10050099

[2] Jo, S., Sharma, B., Park, D.H. and Myung, J.H., 2020,Materials and nano-structural processes for use in solid oxide fuel cells: a review. *Journal of the Korean Ceramic Society*, **57**, pp.135-151. DOI:10.1007/s43207-020-00022-3

[3] Irshad, M., Siraj, K., Raza, R., Ali, A., Tiwari, P., Zhu, B., Rafique, A., Ali, A., Kaleem Ullah, M. and Usman, A., 2016, A brief description of high temperature solid oxide fuel cell's operation, materials, design, fabrication technologies and performance. *Applied Sciences*, ***6***(3), pp.1-23 DOI: 10.3390/app6030075

[4] Fallah Vostakola, M. and Horri, B.A., 2021, Progress in Material Development for Low-Temperature Solid Oxide Fuel Cells: A Review. *Energies*, ***14***(5), pp.1-53 DOI: 10.3390/en14051280

[5] Bagotsky, V.S., Skundin, A.M. and Volfkovich, Y.M., 2015, Electrochemical power sources: batteries, fuel cells, and supercapacitors. *Wiley*, Ch.21 DOI: 10.1002/9781118942857

[6] Fan, L., Zhu, B., Su, P.C. and He, C.,2018, Nanomaterials and technologies for low temperature solid oxide fuel cells: recent advances, challenges and opportunities. *Nano Energy*, ***45***, pp.148-176. DOI: 10.1016/j.nanoen.2017.12.044

[7] Sreedhar, I., Agarwal, B., Goyal, P. and Singh, S.A., 2019, Recent advances in material and performance aspects of solid oxide fuel cells. *Journal of Electroanalytical Chemistry*, 848, pp.1-36 DOI: 10.1016/j.jelechem.2019.113315

[8] Hussain, S. and Yangping, L., 2020, Review of solid oxide fuel cell materials: cathode, anode, and electrolyte. *Energy Transitions*,**4**, pp.1-14DOI: 10.1007/s41825-020-00029-8

[9] Abdalla, A.M., Hossain, S., Azad, A.T., Petra, P.M.I., Begum, F., Eriksson, S.G. and Azad, A.K., 2018, Nanomaterials for solid oxide fuel cells: a review. *Renewable and Sustainable Energy Reviews*, **82**, pp.353-368.DOI: 10.1016/j.rser.2017.09.046

[10] Tahir, N.N.M., Baharuddin, N.A., Samat, A.A., Osman, N. and Somalu, M.R.,2021, "A review on cathode materials for conventional and proton-conducting solid oxide fuel cells." *Journal of Alloys and Compounds* ,**894**, pp.162458.
DOI: 10.1016/j.jallcom.2021.162458

[11] Rembelski, D., Viricelle, J.P., Combemale, L. and Rieu, M., 2012, Characterization and comparison of different cathode materials for SC-SOFC: LSM, BSCF, SSC, and LSCF. *Fuel Cells*, ***12***(2), pp.256-264.DOI: 10.1002/fuce.201100064

[12] Filonova, E. and Pikalova, E., 2023. Overview of approaches to increase the electrochemical activity of conventional perovskite air electrodes. *Materials*, ***16***(14), p.4967. DOI: 10.3390/ma16144967

[13] Jiang, S.P., 2019, Development of lanthanum strontium cobalt ferrite perovskite electrodes of solid oxide fuel cells-A review. *International Journal of Hydrogen Energy*, ***44***(14), pp.7448-7493.DOI: 10.1016/j.ijhydene.2019.01.212

[14] Guo, S., Wu, H., Puleo, F. and Liotta, L.F., 2015, B-Site Metal (Pd, Pt, Ag, Cu, Zn, Ni) Promoted $La_{1-x}Sr_xCo_{1-y}Fe_yO_{3-\delta}$ Perovskite Oxides as Cathodes for IT-SOFCs. *Catalysts*, ***5***(1), pp.366-391.DOI: 10.3390/catal5010366

[15] Rahayu, S., Fatah, A.A. and Kale, G.M., 2021, Facile Synthesis of lanthanum strontium cobalt ferrite (LSCF) nanopowders employing an ion-exchange promoted sol-gel process. *Energies*, ***14***(7), pp.1800-1810DOI: 10.3390/en14071800

[16]Bokov, D., Turki Jalil, A., Chupradit, S., Suksatan, W., Javed Ansari, M., Shewael, I.H., Valiev, G.H. and Kianfar, E., 2021. Nanomaterial by sol-gel method: synthesis and application. *Advances in Materials Science and Engineering*, pp.1-21. DOI: 10.1155/2021/5102014

[17] Arole, V.M. and Munde, S.V., 2014. Fabrication of nanomaterials by top-down and bottom-up approaches-an overview. *J. Mater. Sci*, *1*, pp.89-93.DOI: 10.1007/978-981-10-7751-7_8

[18] Sardar, S.; Kale, G.; Ghadiri, M.; Cespedas, O. ,2019, Structural Study of Holmium Zirconate Nanoparticles obtained through Carbon Neutral Sol-gel Process. *Thermochim. Acta* **676**, pp.120–129. DOI: 10.1016/j.tca.2019.04.003

[19] Wang, Q., Fan, H., Xiao, Y. and Zhang, Y., 2021, Applications and recent advances of rare earth in solid oxide fuel cells. *Journal of Rare Earths*, pp.1-14 DOI: 10.1016/j.jre.2021.09.003

[20] Li, X., Kuang, X. and Sun, J., 2020. Rare earth elements based oxide ion conductors. *Inorganic Chemistry Frontiers*, **8**(5), pp.1374-1398.DOI: 10.1039/D0QI00848F

[21] Zhou, F., Liu, Y., Zhao, X., Tang, W., Yang, S., Zhong, S. and Wei, M., 2018. Effects of cerium doping on the performance of LSCF cathodes for intermediate temperature solid oxide fuel cells. *International Journal of Hydrogen Energy*, **43**(41), pp.18946-18954. DOI: 10.1016/j.ijhydene.2018.08.041

[22] Mohammadi, N., Khakpour, Z., Maghsoudipour, A. and Faeghinia, A., 2021, A Study on Synthesis and Characterization of Dy-Doped $La_{0.6}Sr_{0.4}Co_{0.2}Fe_{0.8}O_{3-\delta}$ via the Coprecipitation Method. *Journal of Chemistry*., pp.1-10 DOI: 10.1155/2021/5577465

[23] Jaiswal, N., Tanwar, K., Suman, R., Kumar, D., Upadhyay, S. and Parkash, O., 2019, A brief review on ceria based solid electrolytes for solid oxide fuel cells. *Journal of Alloys and Compounds*, **781**, pp.984-1005. DOI: 10.1016/j.jallcom.2018.12.015

[24] Rafique, M., Nawaz, H., Shahid Rafique, M., Bilal Tahir, M., Nabi, G. and Khalid, N.R., 2018, Material and method selection for efficient solid oxide fuel cell anode: recent advancements and reviews. *International Journal of Energy Research*, ***43***(7), pp.2423-2446. DOI: 10.1002/er.4210

[25] Da Silva, F.S. and de Souza, T.M., 2017, Novel materials for solid oxide fuel cell technologies: A literature review. *International journal of hydrogen energy,* **42**(41), pp.26020-26036. DOI: 10.1016/j.ijhydene.2017.08.105

[26] Baharuddin, N.A., Muchtar, A. and Somalu, M.R., 2017, Short review on cobalt-free cathodes for solid oxide fuel cells. *International journal of hydrogen energy*, ***42***(14), pp.91499155. DOI: 10.1016/j.ijhydene.2016.04.097

[27] Chakraborty, U.K., 2018, Reversible and irreversible potentials and an inaccuracy in popular models in the fuel cell literature. *Energies*, ***11***(7), pp. 1-18 DOI: 10.3390/en11071851

[28] Afroze, S., Reza, M.S., Cheok, Q., Taweeku, J. and Azad, A.K., 2020. Solid oxide fuel cell (SOFC); A new approach of energy generation during the pandemic COVID-19. *International journal of integrated engineering*, **12**(5), pp.245-256.DOI: 10.30880/ijie.2020.12.05.031

[29] Kan, W.H., Samson, A.J. and Thangadurai, V., 2016, Trends in electrode development for next generation solid oxide fuel cells. *Journal of Materials Chemistry* A, **4**(46), pp.1791317932. DOI: 10.1039/C6TA06757C

[30] Ng, K.H., Rahman, H.A. and Somalu, M.R., 2018, Enhancement of composite anode materials for low-temperature solid oxide fuels. *International Journal of Hydrogen Energy*, **44**(58), pp.30692-30704. DOI: 10.1016/j.ijhydene.2018.01.073

[31] Liu, Y., Shao, Z. and Mori, T., 2020, Development of nickel based cermet anode materials in solid oxide fuel cells–Now and future. *Materials Reports: Energy*, **1**(1), pp. 1 – 26 DOI: 10.1016/j.matre.2020.11.002

[32] Rivard, E., Trudeau, M. and Zaghib, K., 2019, Hydrogen storage for mobility: a review. *Materials*, ***12***(12), pp. 1 -22 DOI: 10.3390/ma12121973

[33] Mahmud, L.S., Muchtar, A. and Somalu, M.R., 2017, Challenges in fabricating planar solid oxide fuel cells: A review. *Renewable and Sustainable Energy Reviews*, ***72***, pp.105-116. DOI:10.1016/j.rser.2017.01.019

[34] Zakaria, Z., Awang Mat, Z., Abu Hassan, S.H. and Boon Kar, Y., 2020, A review of solid oxide fuel cell component fabrication methods toward lowering temperature. *International Journal of Energy Research*, **44**(2), pp.594-611.DOI: 10.1016/j.rser.2017.01.019

[35] Ermis, K., 2019, Investigation on cobalt-free anodes and cathodes for solid oxide fuel cell. *Journal of Engineering Research and Applied Science*, ***8***(2), pp.1160-1167. DOI: 10.1016/j.ijhydene.2016.04.097

[36] Nikonov, A.V., Kuterbekov, K.A., Bekmyrza, K.Z. and Pavzderin, N.B., 2018, A brief review of conductivity and thermal expansion of perovskite-related oxides for SOFC cathode. *Eurasian Journal of Physics and Functional Materials*, **2**(3), pp.274-292. DOI: 10.29317/ejpfm.2018020309

[37] Zouhri, K. and Lee, S.Y., 2016, Exergy study on the effect of material parameters and operating conditions on the anode diffusion polarization of the SOFC. *International Journal of Energy and Environmental Engineering,* **7**(2), pp.211-224.DOI: 10.1007/s40095-015-0201-1

[38] Taroco, H.A., Santos, J., Domingues, R.Z. and Matencio, T., 2011. Ceramic materials for solid oxide fuel cells. *Advances in ceramics-Synthesis and Characterization, processing and specific applications*,2011 pp.423-446.DOI: 10.5772/18297

[39] Hossain, S., Abdalla, A.M., Jamain, S.N.B., Zaini, J.H. and Azad, A.K., 2017, A review on proton conducting electrolytes for clean energy and intermediate temperature-solid oxide fuel cells. *Renewable and Sustainable Energy Reviews,* **79**, pp.750-764.DOI: 10.1016/j.rser.2017.05.147

[40] Gandeepan, P., Müller, T., Zell, D., Cera, G., Warratz, S. and Ackermann, L., 2018, 3d transition metals for C–H activation, *Chemical Reviews*, **119**(4), pp.2192-2452. DOI: 10.1021/acs.chemrev.8b00507

[41] Izzo, J.R., Joshi, A., Grew, K., Chiu, W., Tkachuk, A., Wang, S. and Yun, W., 2008. Nondestructive reconstruction and analysis of solid oxide fuel cell anodes using X-ray computed tomography at sub-50 nm resolution. *ECS Transactions*, **13**(6), p.1. DOI: 10.1149/1.3271150

[42] Heenan, T.M., Bailey, J.J., Lu, X., Robinson, J.B., Iacoviello, F., Finegan, D.P., Brett, D.J.L. and Shearing, P.R., 2016. Three-phase segmentation of solid oxide fuel cell anode materials using lab based X-ray nano-computed tomography. *Fuel Cells*, **17**(1), pp.75-82.
DOI: 10.1002/fuce.201600176

[43] Shaikh, S.P., Muchtar, A. and Somalu, M.R., 2015, A review on the selection of anode materials for solid-oxide fuel cells. *Renewable and Sustainable Energy Reviews*, **51**, pp.1-8. DOI: 10.1016/j.rser.2015.05.069

[44] Akinyele, D., Olabode, E. and Amole, A. 2020, Review of Fuel Cell Technologies and Applications for Sustainable Microgrid Systems. *Inventions*, **5**(3), pp.1 - 35 DOI: 10.3390/inventions5030042

[45] Wang, F., Lyu, Y., Chu, D., Jin, Z., Zhang, G. and Wang, D., 2019, The electrolyte materials for SOFCs of low-intermediate temperature. *Materials Science and Technology*, **35**(13), pp.1551-1562.DOI: https://doi.org/10.1080/02670836.2019.1639008

[46] Omar, S., 2019, Doped ceria for solid oxide fuel cells. *IntechOpen* Ch.4., pp.44 -58 DOI: 10.5772/intechopen.79170

[47] Liu, T., Zhang, X., Wang, X., Yu, J. and Li, L., 2016, A review of zirconia-based solid electrolytes. *Ionics*, **22**(12), pp.2249-2262. DOI: 10.1007/s11581-016-1880-1

[48] Shi, H., Su, C., Ran, R., Cao, J. and Shao, Z., 2020 Electrolyte materials for intermediate temperature solid oxide fuel cells. *Progress in Natural Science: Materials International*, **30**(6), pp.764-774 DOI: 10.1016/j.pnsc.2020.09.003

[49] Kumar, A., Jaiswal, A., Sanbui, M. and Omar, S., 2016, Scandia stabilized zirconia-ceria solid electrolyte (xSc1CeSZ, 5< x< 11) for IT-SOFCs: Structure and conductivity studies. *Scripta Materialia*, **121**, pp.10-13. DOI:10.1016/j.scriptamat.2016.04.023

[50] Mahato, N., Banerjee, A., Gupta, A., Omar, S. and Balani, K., 2015, Progress in material selection for solid oxide fuel cell technology: A review. *Progress in Materials Science*, **72**, pp.141-337. DOI: 10.1016/j.pmatsci.2015.01.001

[51] Pesaran, A., Jaiswal, A. and Wachsman, E.D., 2019, Bilayer Electrolytes for Low Temperature and Intermediate Temperature Solid Oxide Fuel Cells–A Review, *Energy Storage and Conversion Materials*, Ch.1, pp.1-41 DOI: 10.1039/9781788012959-00001

[52] Kaur, P. and Singh, K., 2020, Review of perovskite-structure related cathode materials for solid oxide fuel cells. *Ceramics International*, **46**(5), pp.5521-5535. DOI: 10.1016/j.ceramint.2019.11.066

[53] Yang, G., Su, C., Shi, H., Zhu, Y., Song, Y., Zhou, W. and Shao, Z., 2020, Toward reducing the operation temperature of solid oxide fuel cells: our past 15 years of efforts in

cathode development. *Energy & Fuels*, **34**(12), pp.15169–15194 DOI: 10.1021/acs.energyfuels.0c01887

[54] Esposito, S., 2019. "Traditional" sol-gel chemistry as a powerful tool for the preparation of supported metal and metal oxide catalysts. *Materials*, **12**(4), p.668. DOI: 10.3390/ma12040668

[55] Jun, A., Kim, J., Shin, J. and Kim, G., 2016, Perovskite as a cathode material: a review of its role in solid-oxide fuel cell technology. *ChemElectroChem,* **3**(4), pp.511-530.

DOI: https://doi.org/10.1002/celc.201500382

[56] Ji, Q., Bi, L., Zhang, J., Cao, H. and Zhao, X.S., 2020, The role of oxygen vacancies of ABO3 perovskite oxides in the oxygen reduction reaction. *Energy & Environmental Science*, **13**(5), pp.1408-1428. DOI: 10.1039/D0EE00092B

[57] Behara, S. and Thomas, T., 2020. Stability and amphotericity analysis in rhombohedral ABO3 perovskites. *Materialia*, **13**, p.100819. DOI: 10.1016/j.mtla.2020.100819

[58] Khirade, P.P. and Raut, A.V., Perovskite structured materials: synthesis, structure, physical properties and applications. In Recent advances in multifunctional perovskite materials.London, *IntechOpen*. 2022. DOI: 10.5772/intechopen.106252

[59] Rehman, S.U., Shaur, A., Song, R.H., Lim, T.H., Hong, J.E., Park, S.J. and Lee, S.B.,. 2019, Nano-fabrication of a high-performance $LaNiO_3$ cathode for solid oxide fuel cells using an electrochemical route. *Journal of Power Sources*, **429**, pp.97-104. DOI: 10.1016/j.jpowsour.2019.05.007

[60] Tahir, N.N.M., Baharuddin, N.A., Samat, A.A., Osman, N. and Somalu, M.R., 2021. A review on cathode materials for conventional and proton-conducting solid oxide fuel cells. Journal of Alloys and Compounds, **894**, p.162458. DOI: 10.1016/j.jallcom.2021.162458

[61] Yang, Z., Guo, M., Wang, N., Ma, C., Wang, J. and Han, M., 2017, A short review of cathode poisoning and corrosion in solid oxide fuel cell. *International Journal of Hydrogen Energy*, **42**(39), pp.24948-24959. DOI: 10.1016/j.ijhydene.2017.08.057

[62] Giuliano, A., Carpanese, M.P., Panizza, M., Cerisola, G., Clematis, D. and Barbucci, A., 2017. Characterisation of $La_{0.6}Sr_{0.4}Co_{0.2}Fe_{0.8}O_{3-\delta}$–$Ba_{0.5}Sr_{0.5}Co_{0.8}Fe_{0.2}O_{3-\delta}$ composite as cathode for solid oxide fuel cells. *Electrochimica Acta,* **240**, pp.258-266.

DOI: 10.1016/j.rser.2021.111985

[63] Jiang, S.P., 2019. Development of lanthanum strontium cobalt ferrite perovskite electrodes of solid oxide fuel cells–A review. *International Journal of Hydrogen Energy*, **44**(14), pp.7448-7493. DOI: 10.1016/j.ijhydene.2019.01.212

[64] Tai, L.W., Nasrallah, M.M., Anderson, H.U., Sparlin, D.M. and Sehlin, S.R., 1995. Structure and electrical properties of $La_{1-x}Sr_xCo_{1-y}Fe_yO_3$. Part 1. The system $La_{0.8}Sr_{0.2}Co_{1-y}Fe_yO_3$. *Solid State Ionics*, **76**(3-4), pp.259-271. DOI: 10.1016/0167-2738(94)00244-M

[65] Tai, L.W., Nasrallah, M.M., Anderson, H.U., Sparlin, D.M. and Sehlin, S., 1995. Structure and electrical properties of $La_{1-x}Sr_xCo_{1-y}Fe_yO_3$. Part 2. The system $La_{1-x}Sr_xCo_{0.2}Fe_{0.8}O_3$. *Solid State Ionics*, **76**(3-4), pp.273-283. DOI: 10.1016/0167-2738(94)00245-N

[66] Shen, F. and Lu, K., Comparison of different perovskite cathodes in solid oxide fuel cells. *Fuel Cells*, 18(4),2018, pp.457-465. DOI: 10.1002/fuce.201800044

[67] Giuliano, A., Carpanese, M.P., Clematis, D., Boaro, M., Pappacena, A., Deganello, F., Liotta, L.F. and Barbucci, A., 2017. Infiltration, overpotential and ageing effects on cathodes for solid oxide fuel cells: $La_{0.6}Sr_{0.4}Co_{0.2}Fe_{0.8}O_{3-\delta}$ versus $Ba_{0.5}Sr_{0.5}Co_{0.8}Fe_{0.2}O_{3-\delta}$. *Journal of the electrochemical Society*, **164**(10), p.F3114. DOI 10.1149/2.0161710jes

[68] Yang, J., Chen, L., Cai, D., Zhang, H., Wang, J. and Guan, W., 2021. Study on the strontium segregation behavior of lanthanum strontium cobalt ferrite electrode under compression. *International Journal of Hydrogen Energy*, **46**(15), pp.9730-9740. DOI: 10.1016/j.ijhydene.2020.12.228

[69] Jiang, S.P., 2019, Development of lanthanum strontium cobalt ferrite perovskite electrodes of solid oxide fuel cells-A review. *International Journal of Hydrogen Energy,* **44**(14), pp.7448-7493. DOI: 10.1016/j.ijhydene.2019.01.212

[70] Dang, D.H., Thompson, K.A., Ma, L., Nguyen, H.Q., Luu, S.T., Duong, M.T.N. and Kernaghan, A., 2021. Toward the circular economy of Rare Earth Elements: a review of abundance, extraction, applications, and environmental impacts. *Archives of environmental contamination and toxicology*, **81**(4), pp.521-530. DOI: 10.1007/s00244-021-00867-7

[71] Lucas, J., Lucas, P., Le Mercier, T., Rollat, A. and Davenport, W.G., 2014, Rare earths: science, technology, production and use , *Elsevier Inc* , pp15-29.

[72] Zhou, J. and Fiete, G.A., 2020, Rare earths in a nutshell. *Physics Today*, **73**(1), pp.66 -67 DOI: 10.1063/PT.3.4397

[73] Rivera, V.A.G., Ferri, F.A. and Marega Jr, E., 2012, Localized surface plasmon resonances: noble metal nanoparticle interaction with rare-earth ions. *Plasmonics-Principles and Applications*, Ch.1pp.283-312. DOI: 10.5772/50753

[74] Liu, D., Dou, Y., Xia, T., Li, Q., Sun, L., Huo, L. and Zhao, H., 2021. B-site La, Ce, and Pr-doped Ba0. 5Sr0. 5Co0. 7Fe0. 3O3-δ perovskite cathodes for intermediate-temperature solid oxide fuel cells: effectively promoted oxygen reduction activity and operating stability. *Journal of Power Sources*, **494**, p.229778. DOI: 10.1016/j.jpowsour.2021.229778

[75] Heydari, F., Maghsoudipour, A., Alizadeh, M., Khakpour, Z. and Javaheri, M., 2015. Comparison of Thermal Expansion Coefficient in $Ln_{0.6}Sr_{0.4}Co_{0.2}M_{0.8}O_{3-\delta}$ (Ln= La, Nd, Sm and M= Fe, Ni, Mn) as Cathode Materials for Solid Oxide Fuel Cell. *Advanced Ceramics Progress*, **1**(1), pp.27-31. DOI:10.1007/s12034-015-0942-8

[76]Li, S., Lü, Z., Huang, X. and Su, W., 2008. Thermal, electrical, and electrochemical properties of Nd-doped $Ba_{0.5}Sr_{0.5}Co_{0.8}Fe_{0.2}O_{3-\delta}$ as a cathode material for SOFC. *Solid State Ionics*, **178**(35-36), pp.1853-1858. DOI: 10.1016/j.ssi.2007.11.016

[77] Samreen, A., Galvez-Sanchez, M., Steinberger-Wilckens, R., Arifin, N.A., Saher, S., Ali, S. and Qamar, A., 2020. Electrochemical performance of novel NGCO-LSCF composite cathode for intermediate temperature solid oxide fuel cells. *International Journal of Hydrogen Energy*, **45**(41), pp.21714-21721. DOI: 10.1016/j.ijhydene.2020.04.122

[78] Ghogomu, J.N., Nforna, E.A. and Lambi, J.N., 2015. Synthesis and Characterization of Lanthanum Strontium Cobalt Ferrite Nanoparticles Prepared by Thermal Decomposition of the Mixed Metal Acetylacetonates. *Inter. J. Engin. Research & Technology (IJERT),* **4**, p.907. DOI: 10.9734/ACSJ/2016/28010

[79] Das, S., Das, S., Bajorek, A. and Chakrabarti, P.K., 2024. Enhanced magnetic behavior of $LaFeO_3$ by co-doping with Nd^{3+} and V^{5+} substitution ($La_{0.8}Nd_{0.2}Fe_{0.95}V_{0.05}O_3$). *Journal of Magnetism and Magnetic Materials,* **606**, p.172333 DOI: 10.1016/j.jmmm.2024.172333

[80] Pandey, G., Rawtani, D. and Agrawal, Y.K., Aspects of nanoelectronics in materials development. I*n Nanoelectronics and Materials Development*.London, IntechOpen.2016
DOI: 10.5772/64414

[81] Shandilya, M., Rai, R. and Singh, J., 2016, Review: hydrothermal technology for smart materials. *Adv Appl Ceram***, 115**, pp.354–376. DOI: 10.1080/17436753.2016.1157131

[82] Abdul, M.A.S.A.K., Muchtar, A., Raharjo, J. and Khaerudini, D.S., 2022. A Review on the Process-Structure-Performance of Lanthanum Strontium Cobalt Ferrite Oxide for Solid Oxide Fuel Cells Cathodes. *International Journal of Integrated Engineering*, **14**(2), pp.121-137. DOI: 10.30880/ijie.2022.14.02.017

[83] Utomo, W.P., Ilham, A.M., Khoiroh, N., Nurherdiana, S.D., Pasicakti, G.P., Setyawati, M.Z. and Fansuri, H., 2019. Comparison of $La_{0.6}Sr_{0.4}Co_{0.2}Fe_{0.8}O_{3-\delta}$ perovskite synthesis methods and their effect on the particle size. *Rasayan Journal of Chemistry*, **12**(2), pp.697-706. DOI: 10.31788/RJC.2019.1225139

[84] Mostafavi, E., Babaei, A. and Ataie, A., 2015. Synthesis of nano-structured $La_{0.6}Sr_{0.4}Co_{0.2}Fe_{0.8}O_3$ perovskite by co-precipitation method. *Journal of Ultrafine Grained and Nanostructured Materials*, **48**(1), pp.45-52. DOI:10.7508/jufgnsm.2015.01.007

[85] Baig, N., Kammakakam, I. and Falath, W., 2021. Nanomaterials: a review of synthesis methods, properties, recent progress, and challenges. *Materials Advances*, **2**(6), pp.1821-1871. DOI:10.1039/D0MA00807A

[86] Garcia, L.M., Macedo, D.A., Souza, G.L., Motta, F.V., Paskocimas, C.A. and Nascimento, R.M., 2013. Citrate–hydrothermal synthesis, structure and electrochemical performance of $La_{0.6}Sr_{0.4}Co_{0.2}Fe_{0.8}O_{3-\delta}$ cathodes for IT-SOFCs. *Ceramics International*, **39**(7), pp.8385-8392. DOI: 10.1016/j.ceramint.2013.04.019

[87] Danks, A.E., Hall, S.R. and Schnepp, Z.J.M.H., 2016, The evolution of 'sol–gel'chemistry as a technique for materials synthesis. *Materials Horizons*, **3**(2), pp.91-112. DOI: 10.1039/C5MH00260E

[88] Thiagarajan, S., Sanmugam, A. and Vikraman, D., 2017. Facile methodology of sol-gel synthesis for metal oxide nanostructures. *Recent applications in sol-gel synthesis*, pp.1-17. DOI: 10.5772/intechopen.68708

[89] Modan, E.M. and Plasiasu, A.G. 2020, Advantages and disadvantages of chemical methods in the elaboration of nanomaterials. *The Annals of "Dunarea de Jos" University of Galati. Fascicle IX, Metallurgy and Materials Science*, **43**(1), pp.53-60. DOI: 10.35219/mms.2020.1.08

[90] Dervin, S. and Pillai, S.C., 2017, An introduction to sol-gel processing for aerogels. In Sol-Gel Materials for Energy, Environment and Electronic Applications. *Springer, Cham*., , pp. 1-22. DOI: 10.1007/978-3-319-50144-4_1

[91] Parashar, M., Shukla, V.K. and Singh, R., 2020. Metal oxides nanoparticles via sol–gel method: a review on synthesis, characterization and applications. *Journal of Materials Science: Materials in Electronics*, **31**(5), pp.3729-3749. DOI: 10.1007/s10854-020-02994-8

[92] Shaari, N. and Kamarudin, S.K., 2015, Chitosan and alginate types of bio-membrane in fuel cell application: An overview. *Journal of Power Sources*, **289**, pp.71-80. DOI: 10.1016/j.jpowsour.2015.04.027

[93] Sardar, S., Kale, G., Cespedes, O. and Ghadiri, M., 2020,Environmentally Sustainable Facile Synthesis of Nanocrystalline Holmium Hafnate ($Ho_2Hf_2O_7$): Promising New Oxide-ion Conducting Solid Electrolyte. *SN Applied Sciences*, **2**, pp.1-12. DOI: 10.1007/s42452-020-2336-9

[94] Rahayu, S., Forrester, J.S., Kale, G.M. and Ghadiri, M, 2018, Promising solid electrolyte material for an IT-SOFC: Crystal structure of the cerium gadolinium holmium oxide $Ce_{0.8}Gd_{0.1}Ho_{0.1}O_{1.9}$ between 295 and 1023 K, *Acta Crystallographica C,* **74**, pp. 236-239. DOI: 10.1107/S2053229617017946

[95] Wang, Z., Kale, G. M. and Ghadiri, M, 2012, Synthesis and characterisation of $Ce_xGd_{1-x}O_{2-\delta}$ nanopowders employing an alginate mediated ion-exchange process, *Chemical Eng. J.*, **198 – 199**, pp. 149 – 153 DOI: 10.1016/j.cej.2012.05.063

[96] Wang, Z., Kale, G. M., Yuan, Q. and Ghadiri, M, 2012. X-ray micro-tomography of freeze dried nickel alginate beads and transformation into NiO nanopowders, *RSC Advances*, **2**, pp. 9993 -9997. DOI: 10.1039/C2RA21171H

[97] Szekalska, M., Puciłowska, A., Szymańska, E., Ciosek, P. and Winnicka, K., 2016. Alginate: current use and future perspectives in pharmaceutical and biomedical applications. *International Journal of Polymer Science,* 8, pp.1-17 DOI:10.1155/2016/7697031

[98] Chuang, J.J., Huang, Y.Y., Lo, S.H., Hsu, T.F., Huang, W.Y., Huang, S.L. and Lin, Y.S., 2017. Effects of pH on the shape of alginate particles and its release behavior. *International Journal of Polymer Science*, **2017** (1), pp.1-9 DOI: 10.1155/2017/3902704

[99] Hu, C., Lu, W., Mata, A., Nishinari, K. and Fang, Y., 2021, Ions-induced gelation of alginate: Mechanisms and applications. *International Journal of Biological Macromolecules*,**177**, pp.578-888 DOI: 10.1016/j.ijbiomac.2021.02.086

[100] Guo, X., Wang, Y., Qin, Y., Shen, P. and Peng, Q., 2020, Structures, properties and application of alginic acid: A review. *International Journal of Biological Macromolecules*, **162**, pp.618-628. DOI: 10.1016/j.ijbiomac.2020.06.180

[101] Gao, X., Guo, C., Hao, J., Zhao, Z., Long, H. and Li, M., 2020, Adsorption of heavy metal ions by sodium alginate based adsorbent-a review and new perspectives. *International Journal of Biological Macromolecules*,**164**, pp4423 - 4434
DOI: 10.1016/j.ijbiomac.2020.09.046

[102] da Costa, M.P.M., Delpech, M.C., de Mello Ferreira, I.L., de Macedo Cruz, M.T., Castanharo, J.A. and Cruz, M.D., 2017, Evaluation of single-point equations to determine intrinsic viscosity of sodium alginate and chitosan with high deacetylation degree. *Polymer Testing*, **63**, pp.427-433. DOI: 10.1016/j.polymertesting.2017.09.003

[103] Yang, C.H., Wang, M.X., Haider, H., Yang, J.H., Sun, J.Y., Chen, Y.M., Zhou, J. and Suo, Z., 2013, Strengthening alginate/polyacrylamide hydrogels using various multivalent cations. *ACS applied materials & interfaces*, **5**(21), pp.10418-10422. DOI: 10.1021/am403966x

[104] Wright, J.D. and Sommerdijk, N.A., Sol-gel materials: chemistry and applications. London, *CRC press*, 2018

[105] Zaafarany, I., Khairou, K., Tirkistani, F., Iqbal, S., Khairy, M. and Hassan, R., 2012, Kinetics and Mechanism of Non-Isothermal Decomposition of Ca (II)-, Sr (II)-and Ba (II)-Cross-Linked Divalent Metal-Alginate Complexes. *International Journal of Chemistry*, **4**(6), pp.7-14 DOI: 10.5539/ijc.v4n6p7

[106] Said, A.A. and Hassan, R.M., 1993, Thermal decomposition of some divalent metal alginate gel compounds. *Polymer degradation and stability*, **39**(3), pp.393-397. DOI: 10.1016/0141-3910(93)90015-B

[107] Zaafarany, I.A., 2010, Non-isothermal decomposition of Al, Cr and Fe cross-linked trivalent metal-alginate complexes. *J. King Abdul. Uni*, **22**, pp.193-202. DOI: 10.4197/Sci.22-1.13

[108] Zaafarany, I., Khairou, K. and Hassan, R., 2010, Physicochemical studies on some cross-linked trivalent metal-alginate complexes especially the electrical conductivity and chemical equilibrium related to the coordination geometry. *High Performance Polymers*, **22**(1),pp.69-81. DOI: 10.1016/j.arabjc.2009.07.011

[109] Tirkistani[1], F.A. and Hassan, R.M., Kinetics and Mechanism of Non-Isothermal Decomposition of Some Cross-Linked Metal-Alginate Complexes Especially Trivalent Metal-Alginate Complexes. *Oriental Journal Of Chemistry*, **28**(2), pp.913-920

[110] Lóh, N.J., Simão, L., Faller, C.A., De Noni Jr, A. and Montedo, O.R.K., 2016, A review of twostep sintering for ceramics. *Ceramics International*, **42**(11), pp.12556-12572.

DOI: 10.1016/j.ceramint.2016.05.065

[111] Sutharsini, U., Thanihaichelvan, M. and Singh, R., 2018, Two-step sintering of ceramics. *Sintering of Functional Materials*, pp.3-22. DOI: 10.5772/68083

[112] Möbius, A., Henriques, D. and Markus, T., 2009. Sintering behaviour of $La_{1-x}Sr_xCo_{0.2}Fe_{0.8}O_{3-\delta}$ ($0.3 \leq x \leq 0.8$) mixed conducting materials. *Journal of the European Ceramic Society*, **29**(13), pp.2831-2839. DOI: 10.1016/j.jeurceramsoc.2009.04.003

[113] Solovyev, A.A., Ionov, I.V., Shipilova, A.V. and Maloney, P.D., 2018. Effect of sintering temperature on the performance of composite $La_{0.6}Sr_{0.4}Co_{0.2}Fe_{0.8}O_3$–$Ce_{0.9}Gd_{0.1}O_2$ cathode for solid oxide fuel cells. *Journal of Electroceramics*, **40**, pp.150-155.

DOI:10.1007/s10832-018-0114-5

[114] Sardar, S., Kale, G. and Ghadiri, M., 2021, Microstructure and impedance spectroscopy of high density holmium hafnate ($Ho_2Hf_2O_7$) from nanoparticulate compacts. *Materials Science and Engineering: B*, **265**, pp.1 -10 DOI: 10.1016/j.mseb.2020.114989

[115] Joos, J., Carraro, T., Weber, A. and Ivers-Tiffée, E. 2011, Reconstruction of porous electrodes by FIB/SEM for detailed microstructure modelling. *Journal of Power Sources*, **196**(17), pp.7302-7307. DOI: 10.1016/j.jpowsour.2010.10.006

[116] Joos, J., Ender, M., Carraro, T., Weber, A. and Ivers-Tiffée, E., 2012, Representative volume element size for accurate solid oxide fuel cell cathode reconstructions from focused ion beam tomography data. *Electrochimica Acta*, **82**, pp.268-276. DOI: 10.1016/j.electacta.2012.04.133

[117] Endler-Schuck, C., Joos, J., Niedrig, C., Weber, A. and Ivers-Tiffée, E., The chemical oxygen surface exchange and bulk diffusion coefficient determined by impedance spectroscopy of porous $La_{0.58}Sr_{0.4}Co_{0.2}Fe_{0.8}O_{3-\delta}$(LSCF) cathodes. *Solid State Ionics*,268, pp.67-79 DOI: 10.1016/j.ssi.2014.11.018

[118] Baharuddin, N.A., Abdul Rahman, N.F., Abd. Rahman, H., Somalu, M.R., Azmi, M.A. and Raharjo, J., 2020. Fabrication of high-quality electrode films for solid oxide fuel cell by screen printing: A review on important processing parameters. *International Journal of Energy Research*, **44**(11), pp.8296-8313. DOI: 10.1002/er.5518

[119] Muhammed Ali, S.A., Anwar, M., Baharuddin, N.A., Somalu, M.R. and Muchtar, A., 2018. Enhanced electrochemical performance of LSCF cathode through selection of optimum fabrication parameters. *Journal of Solid State Electrochemistry*, **22**, pp.263-273. DOI: 10.1007/s10008-017-3754-5

[120] Somalu, M.R., Muchtar, A., Daud, W.R.W. and Brandon, N.P., 2017. Screen-printing inks for the fabrication of solid oxide fuel cell films: A review. *Renewable and Sustainable Energy Reviews*, **75**, pp.426-439. DOI: 10.1016/j.rser.2016.11.008

[121] Piao, J., Sun, K., Zhang, N. and Xu, S., 2008. A study of process parameters of LSM and LSM–YSZ composite cathode films prepared by screen-printing. *Journal of Power Sources*, **175**(1), pp.288-295. DOI: 10.1016/j.jpowsour.2007.09.078

[122] Marani, D., Gadea, C., Hjelm, J., Hjalmarsson, P., Wandel, M. and Kiebach, R., 2015. Influence of hydroxyl content of binders on rheological properties of cerium–gadolinium oxide (CGO) screen printing inks. *Journal of the European Ceramic Society*, **35**(5), pp.1495-1504. DOI: 10.1016/j.jeurceramsoc.2014.11.025

[123] Jamale, A.P., Bhosale, C.H. and Jadhav, L.D., 2014. Electrochemical behavior of LSCF/GDC interface in symmetric cell: An application in solid oxide fuel cells. *Journal of Alloys and Compounds*, **623**, pp.136-139. DOI: 10.1016/j.jallcom.2014.10.122

[124] Chengjun, Z.H.U., Cuishan, Y.I. and Luomeng, C.H.A.O., 2011. Preparation and performance of Pr-doped $Ba_{0.5}Sr_{0.5}Co_{0.8}Fe_{0.2}O_{3-\delta}$cathode for IT-SOFCs. *Journal of Rare Earths*, **29**(11), pp.1070-1074. DOI:10.1016/S1002-0721(10)60600-X

[125] Lei, C., Simpson, M.F. and Virkar, A.V., 2022. Investigation of ion and electron conduction in the mixed ionic-electronic conductor-La-Sr-Co-Fe-oxide (LSCF) using alternating current (ac) and direct current (dc) techniques. *Journal of The Electrochemical Society*, **169**(1), pp.014506. DOI: 10.1149/1945-7111/ac43d8

[126] Panthi, D., Hedayat, N. and Du, Y., 2018. Densification behavior of yttria-stabilized zirconia powders for solid oxide fuel cell electrolytes. *Journal of Advanced Ceramics,* **7**(4), pp.325-335. DOI: 10.1007/s40145-018-0282-4

[127] Wagner, M., Thermal analysis in practice: fundamental aspects, Munich, Germany, Carl Hanser Verlag, 2018 DOI: 10.1007/978-1-56990-644-6

[128] Seifi, H., Gholami, T., Seifi, S., Ghoreishi, S.M. and Salavati-Niasari, M., 2020, A review on current trends in thermal analysis and hyphenated techniques in the investigation of physical, mechanical and chemical properties of nanomaterials. *Journal of Analytical and Applied Pyrolysis*, **149**, pp.1-14 DOI: 10.1016/j.jaap.2020.104840

[129] Gaisford, S., Kett, V. and Haines, P., Principles of thermal analysis and calorimetry. Eds 2, Cambridge, *Royal society of chemistry*.,2016

[130] Lee, M., X-ray diffraction for materials research: from fundamentals to applications. New York, *CRC Press*. 2017. DOI: https://doi.org/10.1201/b19936

[131] Bunaciu, A.A., UdriŞTioiu, E.G. and Aboul-Enein, H.Y., 2015. X-ray diffraction: instrumentation and applications. *Critical reviews in analytical chemistry*, **45**(4), pp.289-299. DOI: 10.1080/10408347.2014.949616

[132] Ali, A., Chiang, Y.W. and Santos, R.M., 2022. X-ray diffraction techniques for mineral characterization: A review for engineers of the fundamentals, applications, and research directions. *Minerals,* **12**(2), p.205. DOI: 10.3390/min12020205

[133] Greenberg, J., X-Ray Diffraction Imaging: Technology and Applications. Boca Raton, FL, USA, *CRC Press*. 2018 DOI: https://doi.org/10.1201/9780429196492

[134] Bunaciu, A.A., UdriŞTioiu, E.G. and Aboul-Enein, H.Y,. 2015, X-ray diffraction: instrumentation and applications. *Critical reviews in analytical chemistry*, **45**(4), pp.289-299. DOI:10.1080/10408347.2014.949616

[135] He, K., Chen, N., Wang, C., Wei, L. and Chen, J., 2018, Method for determining crystal grain size by x-ray diffraction. *Crystal Research and Technology*, **53**(2), pp.1-6 DOI: 10.1002/crat.201700157

[136] Larkin, P., 2017. Infrared and Raman spectroscopy: principles and spectral interpretation. *Elsevier*, p7-25 DOI: 10.1016/C2010-0-68479-3

[137] Bumbrah, G.S. and Sharma, R.M., 2016. Raman spectroscopy–Basic principle, instrumentation and selected applications for the characterization of drugs of abuse. *Egyptian Journal of Forensic Sciences*, **6**(3), pp.209-215.
DOI: 10.1016/j.ejfs.2015.06.001

[138] Do Nascimento, G.M., 2018. Introductory chapter: the multiple applications of Raman spectroscopy. [Online] InTech. DOI: 10.5772/intechopen.75795

[139] Kannan, M., Scanning electron microscopy: Principle, components and applications. *A textbook on fundamentals and applications of nanotechnology*, New Delhi, Daya Publishing House® A Division of Astral International Pvt,2018

[140] Khursheed, A., Scanning electron microscope optics and spectrometers. Singapore, World scientific, 2011 DOI: https://doi.org/10.1142/7094

[141] Davies, T.E., Li, H., Bessette, S., Gauvin, R., Patience, G.S. and Dummer, N.F., 2022. Experimental methods in chemical engineering: Scanning electron microscopy and X-ray ultra-microscopy—SEM and XuM. *The Canadian Journal of Chemical Engineering*, **100**(11), pp.3145-3159. DOI: 10.1002/cjce.24405

[142] Mohammed, A. and Abdullah, A., 2018, November. Scanning electron microscopy (SEM): A review. *In Proceedings of the 2018 international conference on hydraulics and pneumatics—HERVEX, Băile Govora, Romania* (Vol. 2018, pp. 7-9).

[143] Scimeca, M., Bischetti, S., Lamsira, H.K., Bonfiglio, R. and Bonanno, E., 2018, Energy Dispersive X-ray (EDX) microanalysis: A powerful tool in biomedical research and diagnosis. *European journal of histochemistry: EJH*, **62**(1), pp.1-11 DOI: 10.4081/ejh.2018.2841

[144] Withers, P.J., Bouman, C., Carmignato, S., Cnudde, V., Grimaldi, D., Hagen, C.K., Maire, E., Manley, M., Du Plessis, A. and Stock, S.R., 2021. X-ray computed tomography. *Nature Reviews Methods Primers*, **1**(1), p.18. DOI: https://doi.org/10.1038/s43586-021-00020-7

[145] Iacoviello, F., Lu, X., Mitchell, T.M., Brett, D.J. and Shearing, P.R., 2019. The imaging resolution and Knudsen effect on the mass transport of shale gas assisted by multi-length scale X-ray computed tomography. *Scientific Reports*, **9**(1), p.19465. DOI: 10.1038/s41598-019-55999-7

[146] Bardestani, R., Patience, G.S. and Kaliaguine, S., 2019. Experimental methods in chemical engineering: specific surface area and pore size distribution measurements—BET, BJH, and DFT. *The Canadian Journal of Chemical Engineering*, **97**(11), pp.2781-2791.

DOI: 10.1002/cjce.23632

[147] Mohammed, A., Ahmed, A.U., Ibraheem, H., Kadhom, M. and Yousif, E., 2022, July. Physisorption theory of surface area and porosity determination: A short review. In AIP Conference Proceedings (Vol. 2450, No. 1, p. 020007). *AIP Publishing LLC*. DOI: 10.1063/5.0093583

[148] Van Quyen, T. and Nagy, S., 2016, Development of Single Pelletizer Unit for Modelling Flat Die Pelletizer. *In International multidisciplinary Scientific Conference University of Miskolc* (Vol. 113, No. 1). DOI: 10.26649/musci.2016.006

[149] Mohazzab, P., 2017. Archimedes' principle revisited. *Journal of Applied Mathematics and Physics,* **5**(04), p.836. DOI: 10.4236/jamp.2017.54073

[150] Meffert, M., Wankmüller, F., Störmer, H., Weber, A., Lupetin, P., Ivers-Tiffée, E. and Gerthsen, D., 2020. Optimization of material contrast for efficient FIB-SEM tomography of solid oxide fuel cells. *Fuel Cells*, **20**(5), pp.580-591. DOI: 10.1002/fuce.202000080

[151] Mura, F., Cognigni, F., Ferroni, M., Morandi, V. and Rossi, M., 2023. Advances in focused ion beam tomography for three-dimensional characterization in materials science. *Materials*, **16**(17), p.5808 DOI: 10.3390/ma16175808

[152] Barmpatza, A.C., Baklezos, A.T., Vardiambasis, I.O. and Nikolopoulos, C.D., 2024. A Review of Characterization Techniques for Ferromagnetic Nanoparticles and the Magnetic Sensing Perspective. *Applied Sciences*, **14**(12), p.5134. DOI: 10.3390/app14125134

[153] Ripka, P., Magnetic sensors and magnetometers. 2nd Ed. Norwood, MA, USA, Artech house, 2021

[154] Sultan, K., Practical Guide to Materials Characterization: Techniques and Applications. John Wiley & Sons, 2022

[155] Buchner, M., Höfler, K., Henne, B., Ney, V. and Ney, A., 2018. Tutorial: Basic principles, limits of detection, and pitfalls of highly sensitive SQUID magnetometry for nanomagnetism and spintronics. *Journal of Applied Physics*, 124(16). DOI: 10.1063/1.5045299

[156] Khaneja, N., 2019. Squid magnetometers, josephson junctions, confinement and bcs theory of superconductivity. In Magnetometers-Fundamentals and Applications of Magnetism. *IntechOpen.* [Online] DOI: 10.5772/intechopen.83714

[157] Stolz, R., Schiffler, M., Becken, M., Thiede, A., Schneider, M., Chubak, G., Marsden, P., Bergshjorth, A.B., Schaefer, M. and Terblanche, O., 2022. SQUIDs for magnetic and electromagnetic methods in mineral exploration. *Mineral Economics*, **35**(3), pp.467-494.

DOI: 10.1007/s13563-022-00333-3

[158] Dennis, C.L. and Boekelheide, Z.A., 2016. Artifacts in magnetic measurements of fluid samples, *AIP Advances*, **6**(8), pp.1-15DOI:10.1063/1.4960457

[159] Wu, Z., Zhu, P., Huang, Y., Yao, J., Yang, F., Zhang, Z. and Ni, M., 2025. A comprehensive review of modeling of solid oxide fuel cells: from large systems to fine electrodes. *Chemical reviews*, **125**(4), pp.2184-2268. DOI: 10.1021/acs.chemrev.4c00614

[160] Kashyap, D., Dwivedi, P.K., Pandey, J.K., Kim, Y.H., Kim, G.M., Sharma, A. and Goel, S., 2014. Application of electrochemical impedance spectroscopy in bio-fuel cell characterization: A review. *International journal of hydrogen energy,* **39**(35), pp.20159-20170. DOI: 10.1016/j.ijhydene.2014.10.003

[161] Pandey, L., Kumar, D., Parkash, O. and Pandey, S., Analytical impedance spectroscopy: basics and applications. Boca Raton, *CRC Press,* 2023 DOI: 10.1201/9781003091387

[162] dos Santos Araújo, P., Belini, G.B., Mambrini, G.P., Yamaji, F.M. and Waldman, W.R., 2019, Thermal degradation of calcium and sodium alginate: A greener synthesis towards calcium oxide micro/nanoparticles. *International journal of biological macromolecules*,**140**, pp.749-760. DOI: 10.1016/j.ijbiomac.2019.08.103

[163] Said, A.A., Abd El-Wahab, M.M.M. and Hassan, R.M., 1994. Thermal and electrical studies on some metal alginate compounds. *Thermochimica acta*, **233**(1), pp.13-24. DOI: 10.1016/S0040-6031(99)80002-1

[164] Khairou, K.S., 2002. Kinetics and mechanism of the non-isothermal decomposition: I. Some divalent cross-linked metal-alginate ionotropic gels. *Journal of thermal analysis and calorimetry*, **69**, pp.583-588 DOI: 10.1023/A:1019920108863

[165] Soares, J.D.P., Santos, J.E., Chierice, G.O. and Cavalheiro, E.T.G., 2004. Thermal behavior of alginic acid and its sodium salt. *Eclética Química,* **29**, pp.57-64. DOI: 10.1590/S0100-46702004000200009

[166] Hassan, R.M. and Takagi, H.D., 2019. Degradation kinetics of some coordination biopolymers of transition metal complexes of alginates: influence of geometrical structure and strength of chelation on the thermal stability. *Material Science*, **1**(1), pp.1-6. DOI: 10.35702/msci.10003

[167] Shannon, R.D., 1976. Revised effective ionic radii and systematic studies of interatomic distances in halides and chalcogenides. *Foundations of Crystallography*, **32**(5), pp.751-767. DOI: 10.1107/s0567739476001551

[168] Malektaj, H., Drozdov, A.D. and deClaville Christiansen, J., 2023. Mechanical properties of alginate hydrogels cross-linked with multivalent cations. *Polymers*, **15**(14), p.3012.

DOI: 10.3390/polym15143012

[169] Pathak, T.S., Kim, J.S., Lee, S.J., Baek, D.J. and Paeng, K.J., 2008. Preparation of alginic acid and metal alginate from algae and their comparative study. *Journal of Polymers and the Environment*, **16**, pp.198-204. DOI: 10.1007/s10924-008-0097-4

[170] Balboul, B.A., El-Roudi, A.M., Samir, E. and Othman, A.G., 2002. Non-isothermal studies of the decomposition course of lanthanum oxalate decahydrate. *Thermochimica acta*, **387**(2), pp.109-114. DOI: 10.1016/S0040-6031(01)00834-6

[171] Ingier-Stocka, E. and Grabowska, A., 1998. Thermal analysis of cobalt (II) salts with some carboxylic acids. *Journal of thermal analysis and calorimetry*, **54**, pp.115-123.
DOI: 10.1023/A:1010116902412

[172] Chenakin, S.P. and Kruse, N., 2021. Surface compositional changes upon heating cobalt oxalate dihydrate in vacuum. *Vacuum,* **187**, p.110090.DOI: 10.1016/j.vacuum.2021.110090

[173] Ogasawara, H. and Koga, N., 2014. Kinetic modeling for thermal dehydration of ferrous oxalate dihydrate polymorphs: A combined model for induction period–surface reaction–phase boundary reaction. *The Journal of Physical Chemistry A*, **118**(13), pp.2401-2412.
DOI: 10.1021/jp500619q

[174] da Conceição, L., Silva, A.M., Ribeiro, N.F. and Souza, M.M., 2011. Combustion synthesis of $La_{0.7}Sr_{0.3}Co_{0.5}Fe_{0.5}O_3$ (LSCF) porous materials for application as cathode in IT-SOFC. *Materials Research Bulletin*, **46**(2), pp.308-314.
DOI: 10.1016/j.materresbull.2010.10.009

[175] Wulandari, W., Islami, D.M., Wellia, D.V., Emriadi, E., Sisca, V. and Jamarun, N., 2023. The effect of alginate concentration on crystallinity, morphology, and thermal stability properties of hydroxyapatite/alginate composite. *Polymers*, **15**(3), p.614. DOI: 10.3390/polym15030614

[176] Zou, Y., Ziegner, M., Malzbender, J. and Krüger, M., 2017. Investigation of rhombohedral-cubic phase transition of $La_{0.58}Sr_{0.4}Co_{0.2}Fe_{0.8}O_{3-\delta}$ using high temperature XRD. *Ceramics international*, **44**(3), pp.2822-2826.DOI: 10.1016/j.ceramint.2017.11.026

[177] Kim, D., Park, J.W., Chae, M.S., Jeong, I., Park, J.H., Kim, K.J., Lee, J.J., Jung, C., Lee, C.W., Hong, S.T. and Lee, K.T., 2021. An efficient and robust lanthanum strontium cobalt ferrite catalyst as a bifunctional oxygen electrode for reversible solid oxide cells. *Journal of Materials Chemistry A*, **9**(9), pp.5507-5521.DOI: 10.1039/D0TA11233J

[178] Samat, A.A., Pisor, M.S.A.A., Tajudin, M.A.F.M.A., Nawi, M.A.H.M., Darus, M., Osman, N. and Baharuddin, N.A., 2020, October. Phase formation and microstructure analyses

of $La_{0.6}Sr_{0.4}CoO_{3-\delta}$-$BaCe_{0.54}Zr_{0.36}Y_{0.1}O_{2.95}$ composite material prepared by solid state mixing method. In IOP Conference Series: Materials Science and Engineering (Vol. 957, No. 1, p. 012055). IOP Publishing. DOI: 10.1088/1757-899X/957/1/012055

[179] Baharuddin, N.A., Muchtar, A., Somalu, M.R., Anwar, M., Shaikh Abdul Kader Abdul Hameed, M.A. and Mah, J., 2018. Effects of sintering temperature on the structural and electrochemical properties of $SrFe_{0.5}Ti_{0.5}O_{3-\delta}$ perovskite cathode. *International Journal of Applied Ceramic Technology*, **15**(2), pp.338-348. DOI: 10.1111/ijac.12825

[180] Nurherdiana, S.D., Sholichah, N., Saputro, E.A., Jalil, M.J. and Fansuri, H., 2023. Crystallography Analysis on LSCF and LSM-based Perovskite Oxides. *Technium Romanian Journal of Applied Sciences and Technology,* 16, pp.405-410 DOI:10.47577/technium. v16i.10019

[181] Ghouse, M., Al-Yousef, Y., Al-Musa, A. and Al-Otaibi, M.F., 2010. Preparation of $La_{0.6}Sr_{0.4}Co_{0.2}Fe_{0.8}O_3$ nanoceramic cathode powders for solid oxide fuel cell (SOFC) application. *international journal of hydrogen energy*, **35**(17), pp.9411-9419. DOI: 10.1016/j.ijhydene.2010.04.144

[182] Ismail, I., Osman, N. and Md Jani, A.M., 2016. Tailoring the microstructure of $La_{0.6}Sr_{0.4}Co_{0.2}Fe_{0.8}O_{3-\alpha}$ cathode material: the role of dispersing agent. *Journal of Sol-Gel Science and Technology,* **80**, pp.259-266. DOI:10.1007/s10971-016-4102-4

[183] Simonenko, T.L., Simonenko, N.P., Simonenko, E.P., Sevastyanov, V.G. and Kuznetsov, N.T., 2021. Obtaining of $La_{0.6}Sr_{0.4}Co_{0.2}Fe_{0.8}O_{3-\delta}$ Nanopowder Using the Glycol–Citrate Method. *Russian Journal of Inorganic Chemistry*, **66**(4), pp.477-481. DOI: 10.1134/S0036023621040203

[184] Zhou, W., Shao, Z., Ran, R., Gu, H., Jin, W. and Xu, N., 2008. LSCF nanopowder from Cellulose–Glycine-Nitrate process and its application in Intermediate-Temperature Solid-Oxide fuel cells. *Journal of the American Ceramic Society*, **91**(4), pp.1155-1162. DOI: 10.1111/j.1551-2916.2007.02242.

[185] Mineshige, A., Izutsu, J., Nakamura, M., Nigaki, K., Abe, J., Kobune, M., Fujii, S. and Yazawa, T., 2005. Introduction of A-site deficiency into $La_{0.6}Sr_{0.4}Co_{0.2}Fe_{0.8}O_{3-\delta}$ and its effect on structure and conductivity. *Solid State Ionics*, **176**(11-12), pp.1145-1149. DOI: 10.1016/j.ssi.2004.11.021

[186] Waller, D., Lane, J.A., Kilner, J.A. and Steele, B.C.H., 1996. The structure of and reaction of A-site deficient $La_{0.6}Sr_{0.4-x}Co_{0.2}Fe_{0.8}O_{3-\delta}$ perovskites. *Materials Letters*, **27**(4-5), pp.225-228. DOI: 10.1016/0167-577x(95)00289-8

[187] Kostogloudis, G.C. and Ftikos, C., 1999. Properties of A-site-deficient $La_{0.6}Sr_{0.4}Co_{0.2}Fe_{0.8}O_{3-\delta}$-based perovskite oxides. *Solid State Ionics*, **126**(1-2), pp.143-151. DOI: 10.1016/s0167-2738(99)00230-1

[188] Sowjanya, C., Mandal, R., Abhinay, S., Mohanta, A., Das, S. and Pratihar, S.K., 2020. Effect of B-site substitution on the crystal structure, electrical conductivity and oxygen transport properties of $La_{0.5}Sr_{0.5}M_{0.2}Fe_{0.8}O_{3-\delta}$ (M= Co, Al, and Zn) perovskite. *Journal of Solid State Chemistry*, **285**, p.121237. DOI: 10.1016/j.jssc.2020.121237

[189] Siebert, E., Boréave, A., Gaillard, F. and Pagnier, T., 2013. Electrochemical and Raman study of $La_{0.7}Sr_{0.3}Co_{0.8}Fe_{0.2}O_{3-\delta}$ reduction. *Solid State Ionics*, **247**, pp.30-40.
DOI: 10.1016/j.ssi.2013.05.006

[190] Orlovskaya, N., Steinmetz, D., Yarmolenko, S., Pai, D., Sankar, J. and Goodenough, J., 2005. Detection of temperature-and stress-induced modifications of $LaCoO_3$ by micro-Raman spectroscopy. *Physical Review B—Condensed Matter and Materials Physics*, **72**(1), p.014122. DOI: 10.1103/PhysRevB.72.014122

[191] Gim, D.H., Sur, Y., Lee, Y.H., Lee, J.H., Moon, S., Oh, Y.S. and Kim, K.H., 2022. Pressure-Dependent Structure of $BaZrO_3$ Crystals as Determined by Raman Spectroscopy. *Materials*, **15**(12), p.4286. DOI: 10.3390/ma15124286

[192] Toulouse, C., Amoroso, D., Xin, C., Veber, P., Hatnean, M.C., Balakrishnan, G., Maglione, M., Ghosez, P., Kreisel, J. and Guennou, M., 2019. Lattice dynamics and Raman spectrum of $BaZrO_3$ single crystals. *Physical Review B*, **100**(13), p.134102. DOI: 10.1103/PhysRevB.100.134102

[193] Upasen, S., Batocchi, P., Mauvy, F., Slodczyk, A. and Colomban, P., 2015. Chemical and structural stability of $La_{0.6}Sr_{0.4}Co_{0.2}Fe_{0.8}O_{3-\delta}$ ceramic vs. medium/high water vapor pressure. *Ceramics International*, **41**(10), pp.14137-14147. DOI: 10.1016/j.ceramint.2015.07.035

[194] Wang, S. and Xu, B., 2021. Calibrated X-ray computed tomography for testing micro-scale pore defect in metallic powder particles for additive manufacturing. *Measurement: Sensors,* **18**, p.100110. DOI: 10.1016/j.measen.2021.100110

[195] Behnsen, J.G., Black, K., Houghton, J.E. and Worden, R.H., 2023. A review of particle size analysis with X-ray CT. *Materials*, **16**(3), p.1259. DOI: 10.3390/ma16031259

[196] Heim, K., Bernier, F., Pelletier, R. and Lefebvre, L.P., 2016. High resolution pore size analysis in metallic powders by X-ray tomography. *Case Studies in Nondestructive Testing and Evaluation,* **6**, pp.45-52. DOI: 10.1016/j.csndt.2016.09.002

[197] Xu, S., Liu, X., Tabaković, A. and Schlangen, E., 2019. Investigation of the potential use of calcium alginate capsules for self-healing in porous asphalt concrete. *Materials*, **12**(1), p.168. DOI: 10.3390/ma12010168

[198] Zhen, D., Zhao, B., Shin, H.C., Bu, Y., Ding, Y., He, G. and Liu, M., 2017. Electrospun porous perovskite $La_{0.6}Sr_{0.4}Co_{1-x}Fe_xO_{3-\delta}$ nanofibers for efficient oxygen evolution reaction. *Advanced Materials Interfaces*, **4**(13), p.1700146. DOI: 10.1002/admi.201700146

[199] ALOthman, Z.A., 2012. A review: fundamental aspects of silicate mesoporous materials. *Materials*, **5**(12), pp.2874-2902. DOI: 10.3390/ma5122874

[200] Jamale, A.P., Jadhav, S.T., Dubal, S.U., Bhosale, C.H. and Jadhav, L.D., 2015. Studies on the percolation limit of Ce0. 9Gd0. 1O1. 95 in $La_{0.6}Sr_{0.4}Co_{0.2}Fe_{0.8}O_{3-\delta}$–$Ce_{0.9}Gd_{0.1}O_{1.95}$ nanocomposites for solid oxide fuel cells application. *Journal of Physics and Chemistry of Solids*, **85**, pp.96-101.DOI: 10.1016/j.jpcs.2015.05.012

[201] Celorrio, V., Dann, E., Calvillo, L., Morgan, D.J., Hall, S.R. and Fermin, D.J., 2016. Oxygen reduction at carbon-supported lanthanides: The role of the B-site. *ChemElectroChem*, **3**(2), pp.283-291.DOI: 10.1002/celc.201500440

[202] Dragan, M., Enache, S., Varlam, M. and Petrov, K., 2019. Perovskite-type lanthanum cobaltite $LaCoO_3$: Aspects of processing route toward practical applications. In Cobalt Compounds and Applications. *IntechOpen.*[Online] Available at: http://dx.doi.org/10.5772/intechopen.86260.

[203] Takalkar, G., Bhosale, R.R., AlMomani, F., Rashid, S., Qiblawey, H., Saad, M.A.S., Khraisheh, M., Kumar, G., Gupta, R.B. and Shende, R.V., 2021. Thermochemical splitting of CO2 using solution combustion synthesized lanthanum–strontium–manganese perovskites. *Fuel*, **285**, p.119154. DOI: 10.1016/j.fuel.2020.119154

[204] Gálvez, M.E., Jacot, R., Scheffe, J., Cooper, T., Patzke, G. and Steinfeld, A., 2015. Physico-chemical changes in Ca, Sr and Al-doped La–Mn–O perovskites upon thermochemical splitting of CO_2 via redox cycling. *Physical Chemistry Chemical Physics*, **17**(9), pp.6629-6634. DOI: 10.1039/c4cp05898d

[205] Yu, X. and Li, X., 2017, June. The effect of sintering temperature on the performance of IT-SOFC $SrFe_{0.9}Sb_{0.1}O_3$-perovskite oxide. In 2017 6th International Conference on Energy and Environmental Protection (ICEEP 2017) (pp. 1162-1168). *Atlantis Press*.

[206] Abdul, M.A.S.A.K., Muchtar, A., Raharjo, J. and Khaerudini, D.S., 2022. A Review on the Process-Structure-Performance of Lanthanum Strontium Cobalt Ferrite Oxide for Solid Oxide Fuel Cells Cathodes. International Journal of Integrated Engineering, **14**(2), pp.121-137. DOI: 10.30880/ijie.2022.14.02.017

[207] Nandy, S., Theingi, M., Ghosh, S., Chae, K.H. and Sudakar, C., 2024. Influence of local structure and metal-oxygen hybridization on the electrical and magnetic properties of alkaline earth metal (Mg^{2+}, Ca^{2+}, Sr^{2+}) substituted $LaFeO_3$ ceramics. *Journal of Applied Physics*, **136**(10). DOI: 10.1063/5.0222233

[208] Alkan, B., Braun, M., Landrot, G., Rüdiger, O., Andronescu, C., DeBeer, S., Schulz, C. and Wiggers, H., 2022. Spray-flame-synthesized Sr-and Fe-substituted $LaCoO_3$ perovskite nanoparticles with enhanced OER activities. *Journal of Materials Science*, **57**(40), pp.18923-18936.DOI: 10.1007/s10853-022-07738-z

[209] Barkalov, O.I., Zaitsev, S.V. and Sedykh, V.D., 2022. Strontium ferrite $SrFeO_{3-\delta}$ ($2.50 \leq 3-\delta \leq 2.87$) studied by Raman and Mössbauer spectroscopy. *Solid State Communications*, **354**, p.114912. DOI: 10.1016/j.ssc.2022.114912

[210] Barbora, L., Singh, R., Shroti, N. and Verma, A., 2010. Synthesis and characterization of neodymium oxide modified nafion membrane for direct alcohol fuel cells. *Materials Chemistry and Physics*, **122**(1), pp.211-216 DOI: 10.1016/j.matchemphys.2010.02.036

[211] Muhoza, S.P., Taylor, T.H., Song, X. and Gross, M.D., 2021. The impact of sintering atmosphere and temperature on the phase evolution of high surface area LSCF prepared by in situ carbon templating. *Journal of The Electrochemical Society*, **168**(3), p.034519. DOI: 10.1149/1945-7111/abf062

[212] Gangwar, B.P., Maiti, S.C. and Sharma, S., 2017. Modifying the hygroscopic property of La_2O_3 by Pr, Sm and Nd doping. *Journal of Solid State Chemistry*, **256**, pp.109-115.
DOI10.1016/j.jssc.2017.08.036

[213] Haeger, T., Heiderhoff, R. and Riedl, T., 2020. Thermal properties of metal-halide perovskites. *Journal of Materials Chemistry* C, **8**(41), pp.14289-14311. DOI: 10.1039/D0TC03754K

[214] Zhang, W., Noble, A., Ji, B. and Li, Q., 2022. Effects of contaminant metal ions on precipitation recovery of rare earth elements using oxalic acid. *Journal of Rare Earths*, **40**(3), pp.482-490. DOI: 10.1016/j.jre.2020.11.008

[215] Lv, P., Zhang, L., Koppala, S., Chen, K., He, Y., Li, S. and Yin, S., 2020. Decomposition study of praseodymium oxalate as a precursor for praseodymium oxide in the microwave field. *ACS omega*, **5**(34), pp.21338-21344. DOI: 10.1021/acsomega.0c00505

[216] Li, Y., Lv, P., Li, S., Li, T., Yin, S., Zhang, L., Xu, Z. and Zhang, G., 2022. Facile Preparation and Characterization of Nd_2O_3 Powder by Calcination of Neodymium Oxalate in Microwave Field. *JOM*, pp.1-6. DOI: 10.1007/s11837-021-04986-3

[217] De Almeida, L., Grandjean, S., Vigier, N. and Patisson, F., 2012. Insights into the thermal decomposition of lanthanide (III) and actinide (III) oxalates–from neodymium and cerium to plutonium. *European Journal of Inorganic Chemistry*, *2012*(31), pp.4986-4999
DOI: 10.1002/ejic.201200469

[218] Lee, K.T. and Manthiram, A., 2006. Comparison of $Ln_{0.6}Sr_{0.4}CoO_{3-\delta}$ (Ln= La, Pr, Nd, Sm, and Gd) as cathode materials for intermediate temperature solid oxide fuel cells. *Journal of the Electrochemical Society*, **153**(4), p.A794. DOI: 10.1149/1.2172572

[219] Xu, Q., Huang, D.P., Chen, W., Zhang, F. and Wang, B.T., 2007. Structure, electrical conducting and thermal expansion properties of $Ln_{0.6}Sr_{0.4}Co_{0.2}Fe_{0.8}O_3$ (Ln= La, Pr, Nd, Sm) perovskite-type complex oxides. *Journal of alloys and compounds*, **429**(1-2), pp.34-39. DOI: 10.1007/s11595-007-3386-1

[220] Heydari, F., Maghsoudipour, A., Alizadeh, M., Khakpour, Z. and Javaheri, M., 2015. Synthesis and evaluation of effective parameters in thermal expansion coefficient of $Ln_{0.6}Sr_{0.4}Co_{0.2}M_{0.8}O_{3-\delta}$ (Ln= La, Nd and M= Mn, Fe) perovskite oxide. *Bulletin of Materials Science*, **38**, pp.1009-1014. DOI: 10.1007/s12034-015-0942-8

[221] Fatah, A.F., Mohamad, A.A., Muchtar, A. and Hamid, N.A., 2021. Physical characterization of LSCF-CuO via enhanced modified sol–gel method for intermediate temperature Solid oxide Fuel Cells (IT-SOFCs). *Materials Today: Proceedings*, **46**, pp.2052-2057. DOI: 10.1016/j.matpr.2021.03.141

[222] Li, X., Blinn, K., Chen, D. and Liu, M., 2018. In situ and surface-enhanced Raman spectroscopy study of electrode materials in solid oxide fuel cells. *Electrochemical Energy Reviews*, **1**(3), pp.433-459. DOI: 10.1007/s41918-018-0017-9

[223] Anajafi, Z., Naseri, M. and Neri, G., 2020. Gas sensing and electrochemical properties of rare earthferrite, $LnFeO_3$ (Ln= Nd, Sm). *Ceramics International*, **46**(17), pp.26682-26688. DOI: 10.1016/j.ceramint.2020.07.139

[224] Kastner, J., Zaunschirm, S., Rendl, S. and da Silva, E.P., 2021. Influence of rheocasting and rare earth metals on the 3D-microstructure of ZK60 Mg-alloy measured by multiscale X-ray computed tomography. *Materials Characterization*, **174**, p.110996. DOI: 10.1016/j.matchar.2021.110996

[225] Thommes, M., Kaneko, K., Neimark, A.V., Olivier, J.P., Rodriguez-Reinoso, F., Rouquerol, J. and Sing, K.S., 2015. Physisorption of gases, with special reference to the evaluation of surface area and pore size distribution (IUPAC Technical Report). *Pure and applied chemistry*, **87**(9-10), pp.1051-1069. DOI: 10.1515/pac-2014-1117

[226] Mohd Abd Fatah, A.F., Rosli, A.Z., Mohamad, A.A., Muchtar, A., SA, M.A. and Hamid, N.A., 2022. Electrochemical Evaluation of Nickel Oxide Addition toward Lanthanum Strontium Cobalt Ferrite Cathode for Intermediate Temperature Solid Oxide Fuel Cell (IT-SOFCS). *Energies*, **15**(14), p.5188. DOI: 10.3390/en15145188

[227] Kursun, C., Gogebakan, M., Uludag, E., Bozgeyik, M.S. and Uludag, F.S., 2018. Structural, electrical and magnetic properties of Nd–A–CoO_3 (A= Sr, Ca) perovskite powders by mechanical alloying. *Scientific Reports*, **8**(1), p.13083. DOI: 10.1038/s41598-018-31458-7

[228] Xie, R., Nie, Z., Hu, X., Yu, Y., Aruta, C. and Yang, N., 2021. Pr-doped $LaCoO_3$ toward stable and efficient oxygen evolution reaction. *ACS Applied Energy Materials*, **4**(9), pp.9057-9065. DOI: 10.1021/acsaem.1c01348

[229] Shu, K., Wang, C.H., Chen, G.T., Ji, Z.L., Yan, W.X. and Luo, F., 2024. Crystal structure and electrical properties of $LnCoO_3$ (Ln= La, Pr, Tb) perovskite. *Journal of Materials Science: Materials in Electronics*, **35**(33), p.2107. DOI: 10.1007/s10854-024-13874-w

[230] Asad, H., Ali, H., Ali, G., Ansar, M.T., Ramay, S.M., Alghamdi, E.A. and Atiq, S., 2023. Nanoscale engineering of structurally stable Nd-substituted $LaCoO_3$ as an electrode material for supercapacitors. *ECS Journal of Solid State Science and Technology*, **12**(4), p.043013.7 DOI: 10.1149/2162-8777/acce08

[231] Kostogloudis, G.C. and Ftikos, C., 2007. Oxygen nonstoichiometry in $Pr_{1-x}Sr_xCo_{0.2}B_{0.8}O_{3-\delta}$ (B= Mn, Fe, x= 0.2, 0.4) perovskite oxides. *Journal of the European Ceramic Society*, **27**(1), pp.273-277. DOI: 10.1016/j.jeurceramsoc.2006.02.044

[232] Benila, S.A. and Ferby, V.A., 2024. Envisioning the structural, morphological, optical, dielectric and electrical properties of Nd^{3+} ions doped $LaFeO_3$ nanoparticles–Study on effect of Nd^{3+} doping concentration. *Materials Science and Engineering: B*, **309**, p.117630. DOI: 10.1016/j.mseb.2024.117630

[233] Dasgupta, N., Krishnamoorthy, R. and Jacob, K.T., 2002. Crystal structure, thermal expansion and electrical conductivity of $Nd_{0.7}Sr_{0.3}Fe_{1-x}Co_xO_3$ ($0 \leq x \leq 0.8$). *Materials Science and Engineering: B*, **90**(3), pp.278-286. DOI: 10.1016/S0921-5107(02)00058-2

[234] Hong, J., Heo, S.J. and Singh, P., 2021. Water mediated growth of oriented single crystalline $SrCO_3$ nanorod arrays on strontium compounds. *Scientific reports,* **11**(1), p.3368.74 DOI: 10.1038/s41598-021-82651-0

[235] Bakar, M.S.A., Rahman, H.A., Mohammad, S.F., Ahmad, S. and Muchtar, A., 2017, October. Morphological and physical behaviour of LSCF-SDCC-Ag composite cathode with the incorporation of Ag as an additive element. In *Journal of Physics:* Conference Series (Vol. 914, No. 1, p. 012011). *IOP Publishing*. DOI: 10.1088/1742-6596/914/1/012011

[236] Li, Y., Zhang, W., Zheng, Y., Chen, J., Yu, B., Chen, Y. and Liu, M., 2017. Controlling cation segregation in perovskite-based electrodes for high electro-catalytic activity and durability. *Chemical Society Reviews*, **46**(20), pp.6345-6378. DOI: 10.1039/C7CS00120G

[237] Koo, B., Kim, K., Kim, J.K., Kwon, H., Han, J.W. and Jung, W., 2018. Sr segregation in perovskite oxides: why it happens and how it exists. *Joule*, **2**(8), pp.1476-1499. DOI: 10.1016/j.joule.2018.07.016

[238] Wang, H. and Barnett, S.A., 2017. Sr surface segregation on $La_{0.6}Sr_{0.4}Co_{0.2}Fe_{0.8}O_{3-\delta}$ porous solid oxide fuel cell cathodes. *ECS Transactions*, **78**(1), p.905. DOI: 10.1149/MA2017-03/1/143

[239] He, S., Saunders, M., Chen, K., Gao, H., Suvorova, A., Rickard, W.D., Quadir, Z., Cui, C.Q. and Jiang, S.P., 2018. A FIB-STEM study of strontium segregation and interface formation of directly assembled $La_{0.6}Sr_{0.4}Co_{0.2}Fe_{0.8}O_{3-\delta}$ cathode on Y_2O_3-ZrO_2 electrolyte of solid oxide fuel cells. *Journal of The Electrochemical Society*, **165**(7), p.F417.

DOI: 10.1149/2.0151807jes

[240] Soldati, A.L., Baqué, L., Troiani, H., Cotaro, C., Schreiber, A., Caneiro, A. and Serquis, A., 2011. High resolution FIB-TEM and FIB-SEM characterization of electrode/electrolyte interfaces in solid oxide fuel cells materials. *international journal of hydrogen energy*, **36**(15), pp.9180-9188. DOI: 10.1016/j.ijhydene.2011.04.121

[241] Chen, Z., Wang, X., Bhakhri, V., Giuliani, F. and Atkinson, A., 2013. Nanoindentation of porous bulk and thin films of $La_{0.6}Sr_{0.4}Co_{0.2}Fe_{0.8}O_{3-\delta}$. *Acta materialia*, **61**(15), pp.5720-5734. DOI: 10.1016/j.actamat.2013.06.016

[242] Shearing, P.R., Gelb, J. and Brandon, N.P., 2010. X-ray nano computerised tomography of SOFC electrodes using a focused ion beam sample-preparation technique. *Journal of the European Ceramic Society*, **30**(8), pp.1809-1814. DOI: 10.1016/j.jeurceramsoc.2010.02.004

[243] Guan, Y., Gong, Y., Liu, G., Song, X., Zhang, X., Xiong, Y., Wang, H. and Tian, Y., 2013. Analysis of impact of sintering time on microstructure of LSM-YSZ composite cathodes by X-ray nanotomography. *Materials Express*, **3**(2), pp.166-170. DOI: 10.1166/mex.2013.1116

[244] Garum, M., Glover, P.W., Lorinczi, P., Drummond-Brydson, R. and Hassanpour, A., 2020. Micro-and nano-scale pore structure in gas shale using Xμ-CT and FIB-SEM techniques. *Energy & Fuels*, **34**(10), pp.12340-12353. DOI: 10.1021/acs.energyfuels.0c02025

[245] Garum, M., Glover, P.W., Lorinczi, P., Micklethwaite, S. and Hassanpour, A., 2021. Integration of multiscale imaging of nanoscale pore microstructures in gas shales. *Energy & Fuels*, **35**(13), pp.10721-10732. DOI: 10.1021/acs.energyfuels.1c00554

[246] Abdel-Latif, I.A., Hegab, A.F., Azab, A.A. and Roumaih, K.M., 2023. Study on crystal structure, electrical and magnetic properties of $LaFe_xCo_{1-x}O_3$ prepared by sol-gel method. *Journal of Solid State Chemistry*, **325**, p.124144. DOI: 10.1016/j.jssc.2023.124144

[247] Arman, M.M., 2023. The effect of the rare earth A-site cation on the structure, morphology, physical properties, and application of perovskite $AFeO_3$. *Materials Chemistry and Physics*, **304**, p.127852. DOI: 10.1016/j.matchemphys.2023.127852

[248] Arman, M.M., 2025. The influence of rare earth doping on the structure, magnetic properties, and application of $LaFeO_3$ nanoparticles. *The European Physical Journal Plus*, **140**(3), pp.1-10. DOI: 10.1140/epjp/s13360-025-06092-8

[249] Aslibeiki, B., Kameli, P. and Ehsani, M.H., 2016. $MnFe_2O_4$ bulk, nanoparticles and film: A comparative study of structural and magnetic properties. *Ceramics International*, **42**(11), pp.12789-12795. DOI: 10.1016/j.ceramint.2016.05.041

[250] Thirumalairajan, S., Girija, K., Mastelaro, V.R. and Ponpandian, N., 2015. Investigation on magnetic and electric properties of morphologically different perovskite $LaFeO_3$ nanostructures. *Journal of Materials Science: Materials in Electronics*, **26**, pp.8652-8662.
DOI: 10.1007/s10854-015-3540-z

[251] Chanda, S., Saha, S., Dutta, A., Irfan, B., Chatterjee, R. and Sinha, T.P., 2015. Magnetic and dielectric properties of orthoferrites $La_{1-x}Pr_xFeO_3$ (x= 0, 0.1, 0.2, 0.3, 0.4 and 0.5). *Journal of Alloys and Compounds*, **649**, pp.1260-1266.
DOI: 10.1016/j.jallcom.2015.07.215

[252] Somvanshi, A., Husain, S., Manzoor, S., Zarrin, N. and Khan, W., 2019. Structure of nanocrystalline $Nd_{0.5}R_{0.5}FeO_3$ (R= La, Pr, and Sm) intercorrelated with optical, magnetic and thermal properties. *Journal of Alloys and Compounds*, **806**, pp.1250-1259.
DOI: 10.1016/j.jallcom.2019.07.333

[253] Das, S., Das, S., Bajorek, A. and Chakrabarti, P.K., 2024. Enhanced magnetic behavior of LaFeO3 by co-doping with Nd^{3+} and V^{5+} substitution ($La_{0.8}Nd_{0.2}Fe_{0.95}V_{0.05}O_3$). *Journal of Magnetism and Magnetic Materials*, **606**, p.172333. DOI: 10.1016/j.jmmm.2024.172333

[254] Li, J., Kou, X., Qin, Y. and He, H., 2002. Microstructure and magnetic properties of $La_{1-x}Sr_xFeO_3$ nanoparticles. *physica status solidi* (a), **191**(1), pp.255-259. DOI: 10.1002/1521-396X(200205)191:1<255: AID-PSSA255>3.0.CO;2-N

[255] da Silva, R.B., Soares, J.M., da Costa, J.A., de Araújo, J.H., Rodrigues, A.R. and Machado, F.L.A., 2018. Local iron ion distribution and magnetic properties of the perovskites $La_{1-x}Sr_xFeO_3$-γ. *Journal of Magnetism and Magnetic Materials,* **466**, pp.306-310. DOI: 10.1016/j.jmmm.2018.07.040

[256] Paul Blessington Selvadurai, A., Pazhanivelu, V., Jagadeeshwaran, C., Murugaraj, R., Mohammed Gazzali, P.M. and Chandrasekaran, G., 2017. An analysis on structural and magnetic properties of $La_{1-x}RE_xFeO_3$ (x= 0.0 and 0.5, RE= Nd, Sm and Gd) nanoparticles. *Applied Physics A*, **123**, pp.1-11. DOI: 10.1007/s00339-016-0651-1

[257] Kershi, R.M., Ali, F.M. and Sayed, M.A., 2018. Influence of rare earth ion substitutions on the structural, optical, transport, dielectric, and magnetic properties of superparamagnetic iron oxide nanoparticles. *Journal of Advanced Ceramics*, 7, pp.218-228. DOI: 10.1007/s40145-018-0273-5

[258] Murray, E.P., Sever, M.J. and Barnett, S.A., 2002. Electrochemical performance of (La, Sr)(Co, Fe)O_3–(Ce, Gd)O_3 composite cathodes. *Solid state ionics*, **148**(1-2), pp.27-34. DOI: 10.1016/S0167-2738(02)00102-9

[259] Chen, J., Liang, F., Liu, L., Jiang, S., Chi, B., Pu, J. and Li, J., 2008. Nano-structured (La, Sr)(Co, Fe)O_3^+ YSZ composite cathodes for intermediate temperature solid oxide fuel cells. *Journal of Power Sources*, **183**(2), pp.586-589. DOI: 10.1016/j.jpowsour.2008.05.082

[260] Jamale, A.P., Bhosale, C.H. and Jadhav, L.D., 2015. Electrochemical behavior of LSCF/GDC interface in symmetric cell: An application in solid oxide fuel cells. *Journal of Alloys and Compounds*, **623**, pp.136-139. DOI: 10.1016/j.electacta.2015.10.092

[261] Nielsen, J. and Hjelm, J., 2014. Impedance of SOFC electrodes: A review and a comprehensive case study on the impedance of LSM: YSZ cathodes. *Electrochimica Acta,* **115**, pp.31-45. DOI: 10.1016/j.electacta.2013.10.053

[262] Fan, L., Zhang, H., Chen, M., Wang, C., Wang, H., Singh, M. and Zhu, B., 2013. Electrochemical study of lithiated transition metal oxide composite as symmetrical electrode for low temperature ceramic fuel cells. *International journal of hydrogen energy*, **38**(26), pp.11398-11405.DOI: 10.1016/j.ijhydene.2013.06.050

[263] Escudero, M.J., Aguadero, A., Alonso, J.A. and Daza, L., 2007. A kinetic study of oxygen reduction reaction on La_2NiO_4 cathodes by means of impedance spectroscopy. *Journal of Electroanalytical Chemistry*, **611**(1-2), pp.107-116. DOI: 10.1016/j.jelechem.2007.08.006

[264] Jia, X., Yan, M., Zhou, Z., Chen, X., Yao, C., Li, D., Chen, D. and Chen, Y., 2017. Nd-doped $LiNi_{0.5}Co_{0.2}Mn_{0.3}O_2$ as a cathode material for better rate capability in high voltage cycling of Li-ion batteries. *Electrochimica Acta*, **254**, pp.50-58. DOI: 10.1016/j.electacta.2017.09.11